



National Library
of Canada

Acquisitions and
Bibliographic Services Branch

395 Wellington Street
Ottawa, Ontario
K1A 0N4

Bibliothèque nationale
du Canada

Direction des acquisitions et
des services bibliographiques

395, rue Wellington
Ottawa (Ontario)
K1A 0N4

Your file / Votre référence :

Our file / Notre référence :

NOTICE

The quality of this microform is heavily dependent upon the quality of the original thesis submitted for microfilming. Every effort has been made to ensure the highest quality of reproduction possible.

If pages are missing, contact the university which granted the degree.

Some pages may have indistinct print especially if the original pages were typed with a poor typewriter ribbon or if the university sent us an inferior photocopy.

Reproduction in full or in part of this microform is governed by the Canadian Copyright Act, R.S.C. 1970, c. C-30, and subsequent amendments.

AVIS

La qualité de cette microforme dépend grandement de la qualité de la thèse soumise au microfilmage. Nous avons tout fait pour assurer une qualité supérieure de reproduction.

S'il manque des pages, veuillez communiquer avec l'université qui a conféré le grade.

La qualité d'impression de certaines pages peut laisser à désirer, surtout si les pages originales ont été dactylographiées à l'aide d'un ruban usé ou si l'université nous a fait parvenir une photocopie de qualité inférieure.

La reproduction, même partielle, de cette microforme est soumise à la Loi canadienne sur le droit d'auteur, SRC 1970, c. C-30, et ses amendements subséquents.

UNIVERSITY OF ALBERTA

Multiscale Physical Modelling of an Upflow Solids-Contacting Clarifier

by

Brian Patrick Yaremko



A thesis submitted to the Faculty of Graduate Studies and Research in partial fulfillment of
the requirements for the degree of

Master of Science

in

Environmental Engineering

DEPARTMENT OF CIVIL ENGINEERING

EDMONTON, ALBERTA

SPRING, 1995



National Library
of Canada

Acquisitions and
Bibliographic Services Branch

395 Wellington Street
Ottawa, Ontario
K1A 0N4

Bibliothèque nationale
du Canada

Direction des acquisitions et
des services bibliographiques

395, rue Wellington
Ottawa (Ontario)
K1A 0N4

Your file Votre référence

Our file Notre référence

The author has granted an irrevocable non-exclusive licence allowing the National Library of Canada to reproduce, loan, distribute or sell copies of his/her thesis by any means and in any form or format, making this thesis available to interested persons.

L'auteur a accordé une licence irrévocable et non exclusive permettant à la Bibliothèque nationale du Canada de reproduire, prêter, distribuer ou vendre des copies de sa thèse de quelque manière et sous quelque forme que ce soit pour mettre des exemplaires de cette thèse à la disposition des personnes intéressées.

The author retains ownership of the copyright in his/her thesis. Neither the thesis nor substantial extracts from it may be printed or otherwise reproduced without his/her permission.

L'auteur conserve la propriété du droit d'auteur qui protège sa thèse. Ni la thèse ni des extraits substantiels de celle-ci ne doivent être imprimés ou autrement reproduits sans son autorisation.

ISBN 0-612-10810-4

Canada

UNIVERSITY OF ALBERTA

RELEASE FORM

Name of Author: Brian Patrick Yaremko

Title of Thesis: Multiscale Physical Modelling of an Upflow Solids-Contacting Clarifier

Degree: Master of Science in Environmental Engineering

Year Degree Granted: 1995

Permission is hereby granted to the University of Alberta to reproduce single copies of this thesis and to lend or to sell such copies for private, scholarly or scientific research purposes only.

The author reserves all other publication and other rights in association with the copyright in the thesis. Except as hereinbefore provided, neither the thesis nor any substantial portion thereof may be printed or otherwise reproduced in any material form whatsoever without the author's prior written permission.

A handwritten signature in black ink, reading "Brian Yaremko", is written over a horizontal line.

11240 - 35 Avenue NW
Edmonton, Alberta, Canada
T6J 3N2

January 4, A.D. 1995

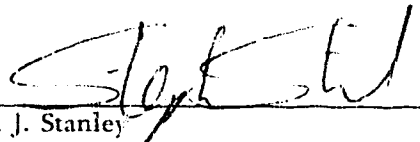
multas per gentes et multa per aequora vectus,
advenio has miseras, frater, ad inferias,
ut te postremo donarem munere mortis,
et mutam nequiquam adloquerer cinerem,
quandoquidem fortuna mihi tete abstulit ipsum,
heu miser indigne frater adempte mihi,
nunc tamen interea haec, prisco quae more parentum
tradita sunt tristi munere ad inferias,
accipe fraterno multum manantia fletu,
atque in perpetuum, frater, ave atque vale.

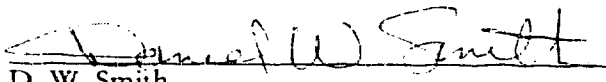
Gaius Valerius Catullus (84 B.C. - 54 B.C.)
Catulli Veronensis Liber, CI, 7

UNIVERSITY OF ALBERTA

FACULTY OF GRADUATE STUDIES AND RESEARCH

The undersigned certify that they have read and recommend to the Faculty of Graduate Studies and Research for acceptance a thesis entitled **Multiscale Physical Modelling of an Upflow Solids-Contacting Clarifier** submitted by Brian Patrick Yaremko in partial fulfillment of the requirements for the degree of Master of Science in Environmental Engineering.


S. J. Stanley


D. W. Smith


J. D. Dale

December 20, A.D. 1994

Abstract

Water treatment at the City of Edmonton's E.L. Smith Water Treatment Plant is currently performed in three generally identical circular upflow solids contact clarifiers. These clarifiers were analyzed by physical modelling at three different scales in hopes that the general hydraulic structure of the flow could be defined for a variety of structural configurations and that some consistent means of scale-up could be identified.

Average and turbulent velocities in the impeller-stream were measured either by laser-doppler velocimetry or with propeller meter, wherefrom dimensionless velocity profiles, pumping numbers, and turbulent dissipation rates were defined for a range of impeller speeds and for a number of structural configurations. Power consumption was measured by a rotary parallel shaft torque transducer, and dimensionless power numbers were defined for various structural configurations.

The following statements are offered as a general summary of the results of this study:

1. **The average and turbulent velocities in any direction which exist at a given point within the impeller-generated flow may be scaled as definite and approximately constant multiples of the impeller's tip-speed regardless of geometric scale and impeller angular velocity..**
2. **The estimated turbulent dissipation rate at a particular location within the impeller-generated jet-flow may be estimated by the expression**

$$\frac{u'^3}{\ell}$$

where the turbulent length-scale, ℓ , may be approximated as $\frac{1}{2}$ of the impeller's blade-height.

3. **For any particular model configuration, the dimensionless dissipation rate at a geometrically consistent location within the impeller-generated jet-flow, estimated as**

$$\frac{u'^3 / \ell}{v_{tip}^3 / b}$$

was shown to be a constant, regardless of both the impeller's angular velocity and the geometric scale of the model.

4. **The effects of a variety of geometrical modifications to the impeller-agitated mixing vessel were analyzed quantitatively according to the resultant effects upon both bulk flow-through and local turbulence.**

5. **Although the geometrical modifications to the impeller-agitated mixing vessel were found to affect the magnitude of the bulk flow-through, the local turbulence structure was found to be approximately unchanged.**
6. **The presence of a tangentially entering flow exerts considerable influence upon the local velocity field within the draught tube and is suspected to influence the local turbulent dissipation rate throughout a portion of the draught tube.**

This project was funded in part by the City of Edmonton, Public Works, Water Branch - I thank you.

The author also expresses his gratitude to the Natural Sciences & Engineering Research Council of Canada for its generous support over the last two years.

Special thanks are extended to Northwest Hydraulic Consultants Ltd. for providing technical assistance and free use of their facilities and equipment during the completion of this project.

Finally, thanks to all friends and family who supported me, financially or otherwise, during the completion of this project, Ago vobis omnibus gratias!

Table of Contents

1.0	Introduction	1
1.1	Coagulation and Flocculation in Water Treatment	1
1.2	Background	2
1.2.1	General Operation	2
1.2.2	Previous Studies	2
1.2.3	Impetus for the Current Study	3
1.3	Objectives of the Current Study	3
2.0	Review of Literature	6
2.1	Introduction	6
2.2	Dimensionless Parameters and Bulk Quantities	6
2.3	Power & Energy Consumption	9
2.3.1	General	9
2.3.2	Historical Review	9
2.4	Turbulence	13
2.4.1	Introduction	13
2.4.2	General Principles of Turbulent Flow	14
2.4.3	Historical Review	18
2.4.4	Length-Scale	25
2.5	Physical and Numerical Analyses	30
2.5.1	Introduction	30
2.5.2	Historical Review	30
3.0	Experimentation	37
3.1	Introduction	37
3.2	Apparatus	37
3.2.1	Dimensions, Scaling & Structure	37
3.3	Measurement	38
3.3.1	General	38
3.3.2	Location	39
3.3.3	Model Configurations & Operational Parameters	40
4.0	Results: Measured Quantities (no tangential inflow)	51

4.2	Velocities - General Properties of the Flow Field	51
4.2.1	Free Impeller - 1:55 & 1:41-Scale Models	51
4.2.2	Confined Impeller - 1:55 & 1:41-Scale Models	52
4.2.3	Northwest Hydraulic Consultants Model - no tangential inflow	54
4.2.4	Reverse-Flow	54
4.3	Torque and Power Consumption	55
4.3.1	General	55
5.0	Results: Derived Quantities (no tangential inflow)	81
5.1	Pumping Capacities	81
5.1.1	General	81
5.1.2	Results	82
5.2	Power Numbers	85
5.3	Turbulent Dissipation Rates	86
5.3.1	General	86
5.3.2	Dissipation Rate	86
5.3.3	Estimation & Confirmation of the Turbulent Length Scale	86
5.3.4	Results	88
6.0	Similarity (no tangential inflow)	94
6.1	General	94
6.2	Velocities	94
6.3	Pumping Discharges	98
6.4	Power Numbers	100
6.5	Dimensionless Rate of Turbulent Dissipation	103
6.5.1	Theoretical	103
6.5.2	the Non-Dimensionalization of ϵ	105
6.6	Conclusions	107
7.0	Effects of Configurational Changes (no tangential inflow)	165
7.1	Introduction	165
7.2	Effects upon Flow-Through	165
7.2.1	Draught Tube and Skirt	165
7.2.2	Draught Tube Baffles	167

7.2.3	Size of Orifice	168
7.2.4	Depth in Tank	169
7.3	Effects upon Turbulence, Turbulent Dissipation & Energy Consumption	170
7.3.1	Draught Tube and Skirt	170
7.3.2	Draught Tube Baffles	173
7.3.3	Size of Orifice	174
7.3.4	Depth in Tank	176
7.4	Conclusions	177
8.0	Inferences with Respect to Scale-Up (no tangential inflow)	189
8.1	Scaling and Similarity	189
8.1.1	General	189
8.1.2	Hydraulic Parameters	190
8.1.3	Power & Vessel-Averaged Energy Consumption	190
8.1.4	Turbulence	192
8.1.5	Other Processes	193
8.2	Application of Experimental Results to Scale-up Mechanisms	195
8.2.1	Introduction	195
8.2.2	The Full-Scale	196
8.2.3	Turbulent Dissipation Rate	197
8.2.3.1	Maintenance of the Local Turbulent Dissipation Rate	197
8.2.3.2	Flocculation	198
8.2.3.3	Dynamic Force	200
8.2.3.4	Floc Size	201
8.2.3.5	Rates of Physical and Chemical Processes	202
8.2.3.6	Summary	204
8.2.4	Scaling Based upon G and Power per Unit-Volume	204
8.2.4.1	Derivation	204
8.2.4.2	Duplication of the Full-Scale G and P/ ρ V	206
8.2.5	Maintenance of Constant Velocities	207
8.2.6	Maintenance of Constant Torque per Unit Volume	211
8.3	Concluding Remarks	211

9.0	Implications of Tangential Inflow	212
9.1	Introduction	212
9.2	General Operation	212
9.3	the Velocity Field - General Analysis	214
9.4	Flow Distribution Within the Draught Tube	215
9.4.1	General	215
9.4.2	Surface Efflux - the Velocities across the Top of the Draught Tube	215
9.4.3	Skirt Influx - Consideration of Velocities through the Skirt Opening	216
9.4.4	Velocity Profiles - Near-Side and Far-Side Measurements in Light of Flow Distribution	217
9.4.5	Conclusion	218
9.5	Pumping Capacities: Flow Numbers and the Recirculation Ratio	218
9.5.1	General	218
9.5.2	Flow Numbers	218
9.5.3	Recirculation Ratios	220
9.5.4	Use of Recirculation Ratios for Scale-up	223
9.6	Effects of Tangential Inflow on Turbulence and Turbulent Dissipation	224
9.7	General Consideration of Angular Velocity at the Full-Scale	226
10.0	Concluding Remarks - Modelling and Scale-Up	256
	List of References	259

List of Tables

Table 3-1	general properties of the scale-models	37
Table 3-2	summary of dimensionless radial locations used in the various trials	40
Table 3-3	summary of experimental conditions - all configurations & all scales	41
Table 3-4	intended effects of configurational change	42
Table 5-1	flow numbers - trials A01 and B01 free impeller	82
Table 5-2	flow numbers - trials A02 and B02 confined impeller: draught tube only	82
Table 5-3	flow numbers - trials A03, B03 & NHC trial 1 confined impeller: draught tube and skirt only	83
Table 5-4	flow numbers - trial A04 confined impeller: draught tube and constricted skirt opening	83
Table 5-5	flow numbers - trial A05 confined impeller: draught tube, skirt & baffles	84
Table 5-6	flow numbers - trial B06 confined impeller: draught tube, skirt & enlarged orifice	84
Table 5-7	flow numbers - trial B06 confined impeller: draught tube & skirt, with variable orifice opening and variable depth	84
Table 5-8	constant high-R, power numbers - all trials & configurations	85
Table 6-1	dimensionless characteristics of velocity near impeller's blade Ecodyne impeller, all scales, all observed ω 's - no tangential inflow	96
Table 6-2	dimensionless characteristics of velocity near impeller's blade various impellers, various scales - historical comparison	97
Table 6-3	historical review of flow numbers	99
Table 6-4	measured high-R, constant power numbers all trials & configurations	101
Table 6-5	historical review of power numbers	102
Table 6-6	maximum observed dimensionless dissipation rates near impeller	106
Table 6-7	historical review of maximum dimensionless dissipation rates near impeller	107
Table 7-1	flow numbers - effect of the skirt and draught tube on flow-through	166

Table 7-2	flow numbers - effect of draught tube baffles on flow-through	168
Table 7-3	flow numbers - effect of enlarged orifice on flow-through	169
Table 7-4	maximum observed dimensionless dissipation rates near impeller	170
Table 7-5	maximum dimensionless turbulent velocities near impeller	171
Table 7-6	power numbers - effect of draught tube and skirt upon total power consumption	172
Table 7-7	dimensionless turbulent velocities near impeller's blade illustration of effects of draught tube baffles on local turbulence structure	173
Table 7-8	dimensionless turbulent velocities near impeller's blade illustration of effect of orifice opening on local turbulence structure	175
Table 7-9	maximum observed dimensionless dissipation rates near impeller illustration of the effect of orifice opening on local turbulent dissipation rate	175
Table 7-10	power numbers - trials A03, B03 & B06 illustration of the effect of orifice opening on total power consumption	176
Table 8-1	typical properties of full-scale impeller & flow (no tangential inflow)	197
Table 8-2	confined impeller (configuration 03) required model-scale angular velocities to match full-scale ϵ	198
Table 8-3	confined impeller (configuration 03) required model-scale parameters to maintain geometric similarity of floc sizes	202
Table 8-4	confined impeller (configuration 03) required model-scale parameters to maintain full-scale mass-transfer rate	204
Table 8-5	confined impeller (configuration 03) required model-scale parameters to maintain full-scale energy-based quantities	207
Table 8-6	confined impeller (configuration 03) effects of various scale-up mechanisms on resultant maximum floc-size	209
Table 8-7	confined impeller (configuration 03) effects of various scale-up mechanisms on resultant turbulent dissipation rate	209
Table 8-8	confined impeller (configuration 03) effects of various scale-up mechanisms on required angular velocities	210
Table 9-1	1:10 scale model with tangential inflow, final model settings	213
Table 9-2	1:10 scale model with tangential inflow measured maximum dimensionless velocities near impeller	214
Table 9-3	flow numbers for various tangential inflows NHC model, 1:10 scale, $d=0.4262$ m, $\nu = 9.85 \times 10^{-7}$ m ² /s	219

Table 9-4	the relation between flow number and recycle ratio for various tangential inflows NHC model, 1:10 scale, $d=0.4262$ m. $\nu = 9.85 \times 10^{-7}$ m ² /s	221
Table 9-5	flow numbers and recycle ratios - full-scale & 1:10 scale, with tangential inflow	224

List of Figures

Figure 3-1	impeller details	43
Figure 3-2	draught tube details	44
Figure 3-3	configuration 01 - trials A01 & B01 unconfined impeller	45
Figure 3-4	configuration 02 - trials A02 & B02 no skirt	45
Figure 3-5	configuration 03 - trials A03 & B03 & nhc model originally constructed	46
Figure 3-6	configuration 04 - trial A04 only nhc's as-modelled skirt opening	46
Figure 3-7	configuration 05 - trial A05 only draught tube baffles	47
Figure 3-8	configuration 06 - trial B06 only enlarged orifice	47
Figure 4-1a	trial A01 - 1:55-scale vector plot of resultant average velocity in radial/axial plane, not normalized by tip speed, 50 rpm	57
Figure 4-1an	trial A01 - 1:55-scale vector plot of resultant average velocity in radial/axial plane, normalized by tip speed, 50 rpm	57
Figure 4-1b	trial A01 - 1:55-scale, vector plot of resultant average velocity in radial/axial plane, not normalized by tip speed, 100 rpm	58
Figure 4-1bn	trial A01 - 1:55-scale, vector plot of resultant average velocity in radial/axial plane, normalized by tip speed, 100 rpm	58
Figure 4-1c	trial A01 - 1:55-scale, vector plot of resultant average velocity in radial/axial plane, not normalized by tip speed, 200 rpm	59
Figure 4-1cn	trial A01 - 1:55-scale, vector plot of resultant average velocity in radial/axial plane, normalized by tip speed, 200 rpm	59
Figure 4-2a	trial A02 - 1:55-scale, vector plot of resultant average velocity in radial/axial plane, not normalized by tip speed, 50 rpm	60
Figure 4-2an	trial A02 - 1:55-scale, vector plot of resultant average velocity in radial/axial plane, normalized by tip speed, 50 rpm	60
Figure 4-2b	trial A02 - 1:55-scale, vector plot of resultant average velocity in radial/axial plane, not normalized by tip speed, 100 rpm	61
Figure 4-2bn	trial A02 - 1:55-scale, vector plot of resultant average velocity in radial/axial plane, normalized by tip speed, 100 rpm	61
Figure 4-2c	trial A02 - 1:55-scale, vector plot of resultant average velocity in radial/axial plane, not normalized by tip speed, 200 rpm	62

Figure 4-2cn	trial A02 - 1:55-scale, vector plot of resultant average velocity in radial/axial plane, normalized by tip speed, 200 rpm	62
Figure 4-3a	trial A03 - 1:55-scale, vector plot of resultant average velocity in radial/axial plane, not normalized by tip speed, 50 rpm	63
Figure 4-3an	trial A03 - 1:55-scale, vector plot of resultant average velocity in radial/axial plane, normalized by tip speed, 50 rpm	63
Figure 4-3b	trial A03 - 1:55-scale, vector plot of resultant average velocity in radial/axial plane, not normalized by tip speed, 100 rpm	64
Figure 4-3bn	trial A03 - 1:55-scale, vector plot of resultant average velocity in radial/axial plane, normalized by tip speed, 100 rpm	64
Figure 4-4a	trial A01 - 1:55-scale, vertical variation of radial average velocities near impeller, not normalized by tip speed, $2r/d = 1.044$	65
Figure 4-4an	trial A01 - 1:55-scale, vertical variation of radial average velocities near impeller, normalized by tip speed, $2r/d = 1.044$	65
Figure 4-4b	trial A01 - 1:55-scale, vertical variation of radial average velocities near impeller, not normalized by tip speed, $2r/d = 1.175$	66
Figure 4-4bn	trial A01 - 1:55-scale, vertical variation of radial average velocities near impeller, normalized by tip speed, $2r/d = 1.175$	66
Figure 4-4c	trial A01 - 1:55-scale, vertical variation of radial average velocities near impeller, not normalized by tip speed, $2r/d = 1.305$	67
Figure 4-4cn	trial A01 - 1:55-scale, vertical variation of radial average velocities near impeller, normalized by tip speed, $2r/d = 1.305$	67
Figure 4-4d	trial A01 - 1:55-scale, vertical variation of tangential average velocities near impeller, not normalized by tip speed, $2r/d = 1.044$	68
Figure 4-4dn	trial A01 - 1:55-scale, vertical variation of tangential average velocities near impeller, normalized by tip speed, $2r/d = 1.044$	68
Figure 4-4e	trial A01 - 1:55-scale, vertical variation of axial average velocities near impeller, not normalized by tip speed, $2r/d = 1.044$	69
Figure 4-4en	trial A01 - 1:55-scale, vertical variation of axial average velocities near impeller, normalized by tip speed, $2r/d = 1.044$	69
Figure 4-4f	trial A01 - 1:55-scale, vertical variation of average velocities along axis of swirling radial jet, not normalized by tip speed, $2r/d = 1.044$	70
Figure 4-4fn	trial A01 - 1:55-scale, vertical variation of average velocities along axis of swirling radial jet, normalized by tip speed, $2r/d = 1.044$	70
Figure 4-4g	trial A01 - 1:55-scale, vertical variation of radial turbulent velocities near impeller, not normalized by tip speed, $2r/d = 1.044$	71

Figure 4-4gn	trial A01 - 1:55-scale, vertical variation of radial turbulent velocities near impeller, normalized by tip speed, $2r/d = 1.044$	71
Figure 4-4h	trial A01 - 1:55-scale, vertical variation of tangential turbulent velocities near impeller, not normalized by tip speed, $2r/d = 1.044$	72
Figure 4-4hn	trial A01 - 1:55-scale, vertical variation of tangential turbulent velocities near impeller, normalized by tip speed, $2r/d = 1.044$	72
Figure 4-4i	trial A01 - 1:55-scale, vertical variation of axial turbulent velocities near impeller, not normalized by tip speed, $2r/d = 1.044$	73
Figure 4-4in	trial A01 - 1:55-scale, vertical variation of axial turbulent velocities near impeller, normalized by tip speed, $2r/d = 1.044$	73
Figure 4-4j	trial A01 - 1:55-scale, vertical variation of turbulent velocities along axis of swirling radial jet, not normalized by tip speed, $2r/d = 1.044$	74
Figure 4-4jn	trial A01 - 1:55-scale, vertical variation of turbulent velocities along axis of swirling radial jet, normalized by tip speed, $2r/d = 1.044$	74
Figure 4-4k	trial A01 - 1:55-scale, radial decay of maximum radial average velocity, not normalized by tip speed	75
Figure 4-4kn	trial A01 - 1:55-scale, radial decay of maximum radial average velocity, normalized by tip speed	75
Figure 4-4l	trial A01 - 1:55-scale, radial decay of maximum tangential average velocity, not normalized by tip speed	76
Figure 4-4ln	trial A01 - Ecodyne impeller, 1:55-scale, radial decay of maximum tangential average velocity, normalized by tip speed	76
Figure 4-4m	trial A01 - Ecodyne impeller, 1:55-scale, radial variation of maximum average velocities along axis of swirling radial jet, not normalized by tip speed	77
Figure 4-4mn	trial A01 - Ecodyne impeller, 1:55-scale, radial variation of maximum average velocities along axis of swirling radial jet, normalized by tip speed	77
Figure 4-4n	trial A01 - Ecodyne impeller, 1:55-scale, ξ -based variation of maximum average velocities along axis of swirling radial jet, not normalized by tip speed	78
Figure 4-4nn	trial A01 - Ecodyne impeller, 1:55-scale, ξ -based variation of maximum average velocities along axis of swirling radial jet, normalized by tip speed	78
Figure 4-5	Ecodyne impeller, 1:55-scale, tangential average velocities near orifice, illustration of reverse flow	79
Figure 4-6	measured power consumption, Ecodyne impeller, 1:55-scale and 1:41-scale models, all configurations	80

Figure 5-1a	power numbers, 1:55-scale impeller, all configurations	89
Figure 5-1b	power numbers, 1:41-scale impeller, all configurations	90
Figure 5-1c	power numbers, 1:55-scale and 1:41-scale impeller, unconfined impeller only	91
Figure 5-1d	power numbers, 1:55-scale and 1:41-scale impeller, configuration 02 only	92
Figure 5-1e	power numbers, 1:55-scale and 1:41-scale impeller, configuration 03 only	93
Figure 6-1-1n	configuration 01, all scales - radial average velocities near impeller, normalized by tip speed, $2r/d = 1.044$	109
Figure 6-1-2n	configuration 01, all scales - tangential average velocities near impeller, normalized by tip speed, $2r/d = 1.044$	110
Figure 6-1-3n	configuration 01, all scales - axial average velocities near impeller, normalized by tip speed, $2r/d = 1.044$	111
Figure 6-1-4n	configuration 01, all scales - average velocities along swirling radial jet, normalized by tip speed, $2r/d = 1.044$	112
Figure 6-1-5n	configuration 01, all scales - radial turbulent velocities near impeller, normalized by tip speed, $2r/d = 1.044$	113
Figure 6-1-6n	configuration 01, all scales - tangential turbulent velocities near impeller, normalized by tip speed, $2r/d = 1.044$	114
Figure 6-1-7n	configuration 01, all scales - axial turbulent velocities near impeller, normalized by tip speed, $2r/d = 1.044$	115
Figure 6-1-8n	configuration 01, all scales - turbulent velocities along swirling radial jet, normalized by tip speed, $2r/d = 1.044$	116
Figure 6-1-9n	configuration 01, all scales - radial decay of average radial velocity, normalized by tip speed	117
Figure 6-1-10n	configuration 01, all scales - radial decay of average tangential velocity, normalized by tip speed	118
Figure 6-1-11n	configuration 01, all scales - radial decay of average velocity along swirling radial jet's axis, normalized by tip speed	119
Figure 6-2-1n	configuration 02, all scales - radial average velocities near impeller, normalized by tip speed, $2r/d = 1.044$	120
Figure 6-2-2n	configuration 02, all scales - tangential average velocities near impeller, normalized by tip speed, $2r/d = 1.044$	121
Figure 6-2-3n	configuration 02, all scales - axial average velocities near impeller, normalized by tip speed, $2r/d = 1.044$	122
Figure 6-2-4n	configuration 02, all scales - average velocities along swirling radial jet, normalized by tip speed, $2r/d = 1.044$	123
Figure 6-2-5n	configuration 02, all scales - radial turbulent velocities near impeller, normalized by tip speed, $2r/d = 1.044$	124

Figure 6-2-6n	configuration 02, all scales - tangential turbulent velocities near impeller, normalized by tip speed, $2r/d = 1.044$	125
Figure 6-2-7n	configuration 02, all scales - axial turbulent velocities near impeller, normalized by tip speed, $2r/d = 1.044$	126
Figure 6-2-8n	configuration 02, all scales - turbulent velocities along swirling radial jet, normalized by tip speed, $2r/d = 1.044$	127
Figure 6-2-9n	configuration 02, all scales - radial decay of average radial velocity, normalized by tip speed	128
Figure 6-2-10n	configuration 02, all scales - radial decay of average tangential velocity, normalized by tip speed	129
Figure 6-1-11n	configuration 02, all scales - radial decay of average velocity along swirling radial jet's axis, normalized by tip speed	130
Figure 6-3-1n	configuration 03, all scales - radial average velocities near impeller, normalized by tip speed, $2r/d = 1.044$	131
Figure 6-3-2n	configuration 03, all scales - tangential average velocities near impeller, normalized by tip speed, $2r/d = 1.044$	132
Figure 6-3-3n	configuration 03, all scales - axial average velocities near impeller, normalized by tip speed, $2r/d = 1.044$	133
Figure 6-3-4n	configuration 03, all scales - average velocities along swirling radial jet, normalized by tip speed, $2r/d = 1.044$	134
Figure 6-3-5n	configuration 03, all scales - radial turbulent velocities near impeller, normalized by tip speed, $2r/d = 1.044$	135
Figure 6-3-6n	configuration 03, all scales - tangential turbulent velocities near impeller, normalized by tip speed, $2r/d = 1.044$	136
Figure 6-3-7n	configuration 03, all scales - axial turbulent velocities near impeller, normalized by tip speed, $2r/d = 1.044$	137
Figure 6-3-8n	configuration 03, all scales - turbulent velocities along axis swirling radial jet, normalized by tip speed, $2r/d = 1.044$	138
Figure 6-3-9n	configuration 03, all scales - radial decay of average radial velocity, normalized by tip speed	139
Figure 6-3-10n	configuration 03, all scales - radial decay of average tangential velocity, normalized by tip speed	140
Figure 6-3-11n	configuration 03, all scales - radial decay of average velocity along swirling radial jet's axis, normalized by tip speed	141
Figure 6-4	confined impeller, all scales, radial variation of maximum turbulence intensity	142
Figure 6-5a-1	trial A01 - dissipation rates near impeller, not normalized, $2r/d = 1.044$	143
Figure 6-5b-1	trial A01 - dimensionless dissipation rates near impeller, normalized by impeller diameter, $2r/d = 1.044$	143

Figure 6-5c-1	trial A01 - dimensionless dissipation rates near impeller, normalized by blade height, $2r/d = 1.044$	143
Figure 6-5a-2	trial A01 - dissipation rates near impeller, not normalized, $2r/d = 1.175$	144
Figure 6-5b-2	trial A01 - dimensionless dissipation rates near impeller, normalized by impeller's diameter, $2r/d = 1.175$	144
Figure 6-5c-2	trial A01 - dimensionless dissipation rates near impeller, normalized by blade height, $2r/d = 1.175$	144
Figure 6-6a	trial A02 - calculated dissipation rates near impeller, not normalized, $2r/d = 1.044$	145
Figure 6-6b	trial A02 - dimensionless dissipation rates near impeller, normalized by impeller's diameter, $2r/d = 1.044$	145
Figure 6-6c	trial A02 - dimensionless dissipation rates near impeller, normalized by blade height, $2r/d = 1.044$	145
Figure 6-7a	trial A03 - dissipation rates near impeller, not normalized, $2r/d = 1.044$	146
Figure 6-7b	trial A03 - dimensionless dissipation rates near impeller, normalized by impeller's diameter, $2r/d = 1.044$	146
Figure 6-7c	trial A03 - dimensionless dissipation rates near impeller, normalized by blade height, $2r/d = 1.044$	146
Figure 6-8a	trial A04 - calculated dissipation rates near impeller, not normalized, $2r/d = 1.044$	147
Figure 6-8b	trial A04 - dimensionless dissipation rates near impeller, normalized by impeller's diameter, $2r/d = 1.044$	147
Figure 6-8c	trial A04 - dimensionless dissipation rates near impeller, normalized by blade height, $2r/d = 1.044$	147
Figure 6-9a	trial A05 - dissipation rates near impeller, not normalized, $2r/d = 1.044$	148
Figure 6-9b	trial A05 - dimensionless dissipation rates near impeller, normalized by impeller's diameter, $2r/d = 1.044$	148
Figure 6-9c	trial A05 - dimensionless dissipation rates near impeller, normalized by blade height, $2r/d = 1.044$	148
Figure 6-10a-1	trial B01 - dissipation rates near impeller, not normalized, $2r/d = 1.044$	149
Figure 6-10b-1	trial B01 - dimensionless dissipation rates near impeller, normalized by impeller's diameter, $2r/d = 1.044$	149
Figure 6-10c-1	trial B01 - dimensionless dissipation rates near impeller, normalized by blade height, $2r/d = 1.044$	149
Figure 6-10a-2	trial B01 - dissipation rates near impeller, not normalized, $2r/d = 1.175$	150

Figure 6-10b-2	trial B01 - dimensionless dissipation rates near impeller, normalized by impeller's diameter, $2r/d = 1.175$	150
Figure 6-10c-2	trial B01 - dimensionless dissipation rates near impeller, normalized by blade height, $2r/d = 1.175$	150
Figure 6-11a	trial B02 - dissipation rates near impeller, not normalized, $2r/d = 1.044$	151
Figure 6-11b	trial B02 - dimensionless dissipation rates near impeller, normalized by impeller's diameter, $2r/d = 1.044$	151
Figure 6-11c	trial B02 - dimensionless dissipation rates near impeller, normalized by blade height, $2r/d = 1.044$	151
Figure 6-12a	trial B03 - calculated dissipation rates near impeller, not normalized, $2r/d = 1.044$	152
Figure 6-12b	trial B03 - dissipation rates near impeller, normalized by impeller's diameter, $2r/d = 1.044$	152
Figure 6-12c	trial B03 - dimensionless dissipation rates near impeller, normalized by blade height, $2r/d = 1.044$	152
Figure 6-13a	trial B06 - dissipation rates near impeller, not normalized, $2r/d = 1.044$	153
Figure 6-13b	trial B06 - dimensionless dissipation rates near impeller, normalized by impeller's diameter, $2r/d = 1.044$	153
Figure 6-13c	trial B06 - dimensionless dissipation rates near impeller, normalized by blade height, $2r/d = 1.044$	153
Figure 6-14a	trial A01 - radial variation of maximum dissipation rate, not normalized	154
Figure 6-14b	trial A01 - radial variation of maximum dimensionless dissipation rate, normalized by impeller's diameter	154
Figure 6-14c	trial A01 - radial variation of maximum dimensionless dissipation rate, normalized by blade height	154
Figure 6-15a	trial B01 - radial variation of maximum dissipation rate, not normalized	155
Figure 6-15b	trial B01 - radial variation of maximum dimensionless dissipation rate, normalized by impeller's diameter	155
Figure 6-15c	trial B01 - radial variation of maximum dimensionless dissipation rate, normalized by blade height	155
Figure 6-16a	trial A01 - variation of maximum dissipation rate along axis of swirling radial jet, not normalized	156
Figure 6-16b	trial A01 - variation of maximum dissipation rate along axis of swirling radial jet, normalized by impeller's diameter	156
Figure 6-16c	trial A01 - variation of maximum dissipation rate along axis of swirling radial jet, normalized by blade height	156

Figure 6-17a	trial B01 - variation of maximum dissipation rate along axis of swirling radial jet, not normalized	157
Figure 6-17b	trial B01 - variation of maximum dissipation rate along axis of swirling radial jet, normalized by impeller's diameter	157
Figure 6-17c	trial B01 - variation of maximum dissipation rate along axis of swirling radial jet, normalized by blade height	157
Figure 6-18-1a	configuration 01, all scales, vertical variation of dimensionless dissipation rate near impeller (normalized by impeller's diameter)	158
Figure 6-18-2a	configuration 01, all scales, vertical variation of dimensionless dissipation rate near impeller (normalized by impeller's blade height)	159
Figure 6-18-3a	configuration 02, all scales, vertical variation of dimensionless dissipation rate near impeller (normalized by impeller's diameter)	160
Figure 6-18-4a	configuration 02, all scales, vertical variation of dimensionless dissipation rate near impeller (normalized by impeller's blade height)	161
Figure 6-18-5a	configuration 03, all scales, vertical variation of dimensionless dissipation rate near impeller (normalized by impeller's diameter)	162
Figure 6-18-6a	configuration 03, all scales, vertical variation of dimensionless dissipation rate near impeller (normalized by impeller's blade height)	163
Figure 6-18-7a	configuration 01, all scales, radial variation of maximum dimensionless dissipation rate (normalized by impeller's blade height)	164
Figure 7-1a	radial average velocities near impeller, illustrating effect of skirt opening on flow-through	178
Figure 7-1b	radial average velocities near impeller, illustrating effect of baffles on flow-through	179
Figure 7-1c	radial average velocities near impeller, illustrating effect of enlarged orifice on flow-through	180
Figure 7-2a	radial turbulent velocities near impeller, illustrating effect of skirt opening on turbulence	181
Figure 7-2b	dimensionless dissipation rates near impeller, illustrating effect of skirt opening on local dissipation rate	182
Figure 7-3a	radial turbulent velocities near impeller, illustrating effect of baffles on turbulence	183
Figure 7-3b	dimensionless dissipation rates near impeller, illustrating effect of baffles on local dissipation rate	184
Figure 7-3c	calculated power numbers, illustrating effect of baffles on total power consumption	185
Figure 7-4a	radial turbulent velocities near impeller, illustrating effect of enlarged orifice on turbulence	186

Figure 7-4b	dimensionless dissipation rates near impeller, illustrating effect of enlarged orifice on local dissipation rate	187
Figure 7-4c	calculated power numbers, illustrating effect of enlarged orifice on total power consumption	188
Figure 9-1-1	NHC model, trial 1 - radial average velocities near impeller, not normalized by tip speed $2r/d = 1.07$, $Q_i = 0 \text{ l/s}$	228
Figure 9-1-1n	NHC model, trial 1 - radial average velocities near impeller, normalized by tip speed $2r/d = 1.07$, $Q_i = 0 \text{ l/s}$	228
Figure 9-1-2	NHC model, trial 1 - tangential average velocities near impeller, not normalized by tip speed $2r/d = 1.07$, $Q_i = 0 \text{ l/s}$	229
Figure 9-1-2n	NHC model, trial 1 - tangential average velocities near impeller, normalized by tip speed $2r/d = 1.07$, $Q_i = 0 \text{ l/s}$	229
Figure 9-1-3	NHC model, trial 1 - average velocities along axis of swirling radial jet, not normalized by tip speed $2r/d = 1.07$, $Q_i = 0 \text{ l/s}$	230
Figure 9-1-3n	NHC model, trial 1 - average velocities along axis of swirling radial jet, normalized by tip speed $2r/d = 1.07$, $Q_i = 0 \text{ l/s}$	230
Figure 9-1-4	NHC model, trial 1 - radial variation of maximum radial velocity, not normalized by tip speed $Q_i = 0 \text{ l/s}$	231
Figure 9-1-4n	NHC model, trial 1 - radial variation of maximum radial velocity, normalized by tip speed $Q_i = 0 \text{ l/s}$	231
Figure 9-1-5	NHC model, trial 1 - radial variation of maximum tangential velocity, not normalized by tip speed $Q_i = 0 \text{ l/s}$	232
Figure 9-1-5n	NHC model, trial 1 - radial variation of maximum tangential velocity, normalized by tip speed $Q_i = 0 \text{ l/s}$	232
Figure 9-1-6	NHC model, trial 1 - radial variation of maximum velocity along axis of swirling radial jet, not normalized by tip speed $Q_i = 0 \text{ l/s}$	233
Figure 9-1-6n	NHC model, trial 1 - radial variation of maximum velocity along axis of swirling radial jet, normalized by tip speed $Q_i = 0 \text{ l/s}$	233
Figure 9-2-1	NHC model, trial 2 - radial average velocities near impeller, not normalized by tip speed $2r/d = 1.07$, $Q_i = 7.9 \text{ l/s}$	234

Figure 9-2-1n	NHC model, trial 2 - radial average velocities near impeller, normalized by tip speed $2r/d = 1.07$, $Q_i = 7.9 \text{ l/s}$	234
Figure 9-2-2	NHC model, trial 2 - tangential average velocities near impeller, not normalized by tip speed $2r/d = 1.07$, $Q_i = 7.9 \text{ l/s}$	235
Figure 9-2-2n	NHC model, trial 2 - tangential average velocities near impeller, normalized by tip speed $2r/d = 1.07$, $Q_i = 7.9 \text{ l/s}$	235
Figure 9-2-3	NHC model, trial 2 - average velocities along axis of swirling radial jet, not normalized by tip speed $2r/d = 1.07$, $Q_i = 7.9 \text{ l/s}$	236
Figure 9-2-3n	NHC model, trial 2 - average velocities along axis of swirling radial jet, normalized by tip speed $2r/d = 1.07$, $Q_i = 7.9 \text{ l/s}$	236
Figure 9-2-4	NHC model, trial 2 - radial variation of maximum radial velocity, not normalized by tip speed $Q_i = 7.9 \text{ l/s}$	237
Figure 9-2-4n	NHC model, trial 2 - radial variation of maximum radial velocity, normalized by tip speed $Q_i = 7.9 \text{ l/s}$	237
Figure 9-2-5	NHC model, trial 2 - radial variation of maximum tangential velocity, not normalized by tip speed $Q_i = 7.9 \text{ l/s}$	238
Figure 9-2-5n	NHC model, trial 2 - radial variation of maximum tangential velocity, normalized by tip speed $Q_i = 7.9 \text{ l/s}$	238
Figure 9-2-6	NHC model, trial 2 - radial variation of maximum velocity along axis of swirling radial jet, not normalized by tip speed $Q_i = 7.9 \text{ l/s}$	239
Figure 9-2-6n	NHC model, trial 2 - radial variation of maximum velocity along axis of swirling radial jet, normalized by tip speed $Q_i = 7.9 \text{ l/s}$	239
Figure 9-3-1	NHC model, trial 3 - radial average velocities near impeller, not normalized by tip speed $2r/d = 1.07$, $Q_i = 3 \text{ l/s}$	240
Figure 9-3-1n	NHC model, trial 3 - radial average velocities near impeller, normalized by tip speed $2r/d = 1.07$, $Q_i = 4 \text{ l/s}$	240
Figure 9-3-2	NHC model, trial 3 - tangential average velocities near impeller, not normalized by tip speed $2r/d = 1.07$, $Q_i = 4 \text{ l/s}$	241
Figure 9-3-2n	NHC model, trial 3 - tangential average velocities near impeller, normalized by tip speed $2r/d = 1.07$, $Q_i = 4 \text{ l/s}$	241

Figure 9-3-3	NHC model, trial 3 - average velocities along axis of swirling radial jet, not normalized by tip speed $2r/d = 1.07$, $Q_i = 4 \text{ l/s}$	242
Figure 9-3-3n	NHC model, trial 3 - average velocities along axis of swirling radial jet, normalized by tip speed $2r/d = 1.07$, $Q_i = 4 \text{ l/s}$	242
Figure 9-3-4	NHC model, trial 3 - radial variation of maximum radial velocity, not normalized by tip speed $Q_i = 4 \text{ l/s}$	243
Figure 9-3-4n	NHC model, trial 3 - radial variation of maximum radial velocity, normalized by tip speed $Q_i = 4 \text{ l/s}$	243
Figure 9-3-5	NHC model, trial 3 - radial variation of maximum tangential velocity, not normalized by tip speed $Q_i = 4 \text{ l/s}$	244
Figure 9-3-5n	NHC model, trial 3 - radial variation of maximum tangential velocity, normalized by tip speed $Q_i = 4 \text{ l/s}$	244
Figure 9-3-6	NHC model, trial 3 - radial variation of maximum velocity along axis of swirling radial jet, not normalized by tip speed $Q_i = 4 \text{ l/s}$	245
Figure 9-3-6n	NHC model, trial 3 - radial variation of maximum velocity along axis of swirling radial jet, normalized by tip speed $Q_i = 4 \text{ l/s}$	245
Figure 9-4-1	NHC model - radial average velocities near impeller, normalized by tip speed $2r/d = 1.07$, $Q_i = 4.0 \text{ l/s}$ & 7.9 l/s	246
Figure 9-4-2	NHC model - tangential average velocities near impeller, normalized by tip speed $2r/d = 1.07$, $Q_i = 4.0 \text{ l/s}$ & 7.9 l/s	247
Figure 9-4-3	NHC model - radial variation of maximum radial velocity, normalized by tip speed $Q_i = 4.0 \text{ l/s}$ & 7.9 l/s	248
Figure 9-4-4	NHC model - radial variation of maximum tangential velocity, normalized by tip speed $Q_i = 4.0 \text{ l/s}$ & 7.9 l/s	249
Figure 9-5a	NHC model - assumed skirt-influx distribution function $Q_i = 7.9 \text{ l/s}$	250
Figure 9-5b	NHC model - assumed surface-efflux distribution function $Q_i = 7.9 \text{ l/s}$	250
Figure 9-6a	NHC model - assumed skirt-influx distribution function $Q_i = 4 \text{ l/s}$	251
Figure 9-6b	NHC model - assumed surface-efflux distribution function $Q_i = 4 \text{ l/s}$	251

Figure 9-6c	NHC model - general illustration of flow-through & recirculation	252
Figure 9-7a	NHC model - variation of recycle ratio with angular velocity $Q_i = 7.9 \text{ l/s}$	253
Figure 9-7b	NHC model - variation of recycle ratio with angular velocity $Q_i = 4 \text{ l/s}$	253
Figure 9-7c	NHC model - comparison of recycle ratios $Q_i = 4 \text{ l/s}$ & 7.9 l/s	254
Figure 9-7d	NHC model - comparison of recycle ratios to HNC's results $Q_i = 4 \text{ l/s}$ & 7.9 l/s	254

List of Photographs

Photograph 1-1	full-scale clarifier C-3	5
Photograph 1-2	full-scale clarifier C-3	5
Photograph 3-1	experimental apparatus, 1:41-scale & 1:55-scale models	48
Photograph 3-2	experimental apparatus, 1:41-scale & 1:55-scale models	48
Photograph 3-3	1:41-scale model in operation, configuration 03	49
Photograph 3-4	experimental apparatus, 1:41-scale & 1:55-scale models	49
Photograph 3-5	1:10-scale NHC model	50
Photograph 3-6	1:10-scale NHC model	50
Photograph 9-1	1:10-scale NHC model - flow patterns	255
Photograph 9-2	1:10-scale NHC model - flow patterns	255

List of Symbols

English:

A	an area (generic) (m^2)
b	impeller's blade-height (m)
D	width or diameter of tank (m)
d	diameter of impeller (m) (usually), or diameter of floc (m) (rarely)
d_f	diameter of floc (m)
D_m	molecular diffusivity
E_k	kinetic energy per unit mass (m^2/s^2)
c	swirl parameter (m)
F	shear force on flocculant particles (N)
G	velocity gradient ($1/s$)
g	gravitational acceleration (N/kg)
h	depth of fluid above weir (m)
L	a turbulent length-scale (m)
M_r	radial flux of radial momentum ($kg \cdot m/s^2$)
N	impeller's angular velocity (rpm) (usually), or radial flux of angular momentum ($kg \cdot m^2/s^2$) (rarely), or number of collisions in flocculation (rarely)
n	impeller's angular velocity (rps), or wavenumber ($1/m$)
P	power (J/s)
p	piezometric pressure head (m)
Q	volumetric flow rate (m^3/s)
Q_i	influent volumetric flow rate (m^3/s)
Q_r	recycled volumetric flow rate (m^3/s)
q	average velocity along swirling radial jet's axis (m/s), or total kinetic energy per unit mass (m^2/s^2)
q'	turbulent velocity along swirling radial jet's axis (m/s)
r	radius of impeller (m)
t	time (s)
U	average vector resultant velocity (m/s)
U'	turbulent vector resultant velocity (m/s)
u	radial average velocity (m/s)

u'	radial turbulent velocity (m/s)
V	a volume (m ³)
V_{tank}	volume of tank (m ³)
v	tangential average velocity (m/s)
v_{tip}	impeller's tip-speed (m/s)
v_{bulk}	a bulk velocity (generic) (m/s)
v'	tangential turbulent velocity (m/s)
w	axial average velocity (m/s)
w'	axial turbulent velocity (m/s)
z	axial coordinate (m)
(r, θ, z)	cylindrical coordinate system
(x, y, z)	Cartesian coordinate system

Greek:

β	jet's angle of deflection
γ	elemental mass of fluid
δ	turbulence length-scale (m) Kolmogorov length-scale (m)
ϵ	local turbulent dissipation rate (m ² /s ³ or W/kg)
$\bar{\epsilon}$	vessel-averaged turbulent dissipation rate (m ² /s ³ or W/kg)
ξ	turbulence velocity-scale (m/s) Kolmogorov velocity-scale (m/s)
η	efficiency term
\cdot	constant of proportionality
θ	tangential coordinate (radians)
κ	kinetic energy per unit mass (m ² /s ²)
Λ	width of turbulent jet (m)
ν	kinematic viscosity (m ² /s)
ξ	distance along swirling radial jet (m)
μ	dynamic viscosity (Pa·s)
ρ	density (kg/m ³)
τ	turbulence time-scale (s) or, Kolmogorov time-scale (s) or, torque (N·m)

ω impeller's angular velocity (1/s)

dimensionless parameters:

C_d	a drag coefficient
Ca	Camp parameter
Eu	Euler (power) number
F	Froude number
R	Reynolds number
N_h	head number
N_i	agitation intensity
N_p	power number
N_q	flow (or pumping) number
λ	model's geometrical scale
χ	similarity variable describing distance across the jet

other symbols:

l	turbulence length-scale
\mathfrak{R}	recirculation ratio

1.0 Introduction

1.1 Coagulation and Flocculation in Water Treatment

Often, water drawn directly from rivers, lakes and other natural watercourses is characterized by certain physical and chemical properties which render it unsuitable for public consumption until it may be subjected to treatment and conditioning. This is certainly true of the North Saskatchewan River, from which the City of Edmonton draws its water, and this contention is equally applicable to hundreds of other public water utilities throughout Canada. Such surface waters nearly always contain high concentrations of suspended colloidal materials, silts and sediments, and they contain potentially troublesome chemical and microbial contaminants. The removal of such undesirable constituent materials is, in general terms, the goal of water treatment.

Coagulation and flocculation are two processes which are of critical importance in the treatment of such surface waters for public consumption. Together, these terms designate the intended effect of any chemical or physical process whereby the agglomeration of suspended particles is promoted, leading to the ultimate clarification of the water. Though such terms are often used interchangeably, they do have fairly definite and distinctive meanings. Coagulation is an attempt to overcome the repulsive electrostatic forces which exist between suspended particles through the simultaneous application of chemical agents and mixing, thereby initiating interparticle contact and prompting the formation of ever larger agglomerations. Once agglomeration is initiated, the suspended particles continue to agglomerate into ever larger aggregations called flocs, which eventually settle out of the flow - this process is called flocculation, and it may be thought to represent the second stage in the overall process of coagulation.

There is an important correspondence among the turbulence-generating characteristics of the impeller, the resultant hydrodynamic conditions in the water and the progress of coagulation. Invariably, coagulation requires the addition of chemical agents called coagulants (*e.g.* alum, FeSO_4), and coagulation is initiated by molecular-scale interactions between the suspended colloidal particles and the chemical coagulant in order to effect the destabilization of the electrostatically repulsive particles. In order to favour the occurrence of such interactions, a physical impulse is applied to the flow via some device such as an impeller, or a turbulent jet, or an in-line mixer so that the flow may attain a state of turbulence. Eventually, the turbulent eddies become exceedingly small, prompting direct interactions between the chemical coagulant and the suspended particles, thereby initiating aggregation into flocs. By agitating or mixing the water at an ever increasing rate, molecular-scale or colloidal-scale turbulent forces would increase, and the rate of charge destabilization would increase accordingly. In this manner, the importance of *rapid mixing* to the successful initiation of flocculation is clear.

It is also clear, however, that there is an important process limitation concerning the unbounded application of turbulent energy to the water. Although agitation through externally applied turbulence can increase the efficiency of the coagulation process, a practical limit to the degree of agitation exists. Flocculation impellers in full-scale water treatment plants are generally not operated at high speeds. Too much externally applied agitation can actually shear the flocs apart, thereby hindering both the settleability of the flocs and the consequent clarificational effects upon the water. In practice, flocculation is usually favoured by agitating the flow by slow stirring so that the colloidal particles are subjected to the convective, impeller-generated currents, but the ambient hydraulic conditions are still conducive to continued agglomeration. In this sense, the importance of *slow mixing* to the successful completion of flocculation is clear. There is therefore a balance that must be struck between the rate of coagulation and the rate of flocculation.

Given the delicate nature of the alum flocs together with the incumbent responsibility upon the operators of the plant to produce a high-quality product, in practice rapid mixing and

slow mixing are typically performed separately. Rapid mixing is usually performed at a location upstream of the clarifier, so that chemical coagulant is already well mixed by the time the flow arrives at the clarifier, and only slow mixing is required to promote flocculation. In this manner, it is most correct to view the related processes of coagulation and flocculation as applied to the treatment of drinking water as slow-mixing phenomena.

Regardless of the actual operational definition that is used to describe the mixing process, it is clear that what is most important to the successful operation of a flocculation clarifier is the energy itself. Only by controlling the manner in which energy is consumed by the flocculation system can the desired result be attained, that being an efficient, effective rate of clarification. As the subsequent contents of this report will demonstrate, the application of energy and its consequent effects upon the hydrodynamic conditions present in the mixing vessel is of universal significance in the quantitative analysis of all types impeller-agitated flows.

1.2 Background

1.2.1 General Operation

The E.L. Smith Water Treatment Plant current has three circular upflow solids contact clarifiers. Both alum clarification and lime/soda-ash hardness removal are employed. The design capacity of each clarifier is 200 megalitres per day (Mℓ/d), although the design flow for the plant as a whole is also 200 Mℓ/d. The clarifiers are configured such that the influent raw water is introduced directly into a circular draught tube via a tangential entry. The raw water influent is then forced upward and out of the draught tube due to the presence of an impeller-generated recirculated flow which simultaneously being introduced into the draught tube. After exiting the draught tube, the flow may either be recycled back in, or it may exit the clarifier altogether through a system of tube settlers and perforated effluent launders lying peripheral to the draught tube. Illustrative photographs of the full-scale system are presented in photographs 1-1 and 1-2. Usually, alum treatment is performed in parallel in two clarifiers, and the third is used for hardness removal, although other operational combinations are possible.

In the alum clarifiers, the chemical coagulant is introduced to the flow at a point just upstream of the two clarifiers. Rapid mixing of the chemical coagulant occurs in an in-line mixer in the raw water supply line, ensuring that the coagulant is already well mixed upon entry into the draught tube. Once in the draught tube, slow mixing is performed by means of a rotating 10-bladed impeller. The existing impellers and clarifiers at EL Smith are a proprietary design of Ecodyne Ltd. and are commonly referred to as Ecodyne impellers. These impellers have been in place since the plant was commissioned in 1976, and they are typically operated at speeds of 4 to 10 revolutions per minute depending upon the conditions necessary to produce an acceptable degree of flocculation. As the flocculating particles become larger and begin to settle out of the flow, they are either drawn back into the draught tube as seed flocs by the recirculating flow, or they enter a sludge trap in the floor at the base of the impeller's support shaft drain, where they are removed for treatment and disposal.

1.2.2 Previous Studies

Although the impellers themselves have never been modified in all the time that the plant has been operational, the draught tubes have been subjected to various modifications, all in an attempt to improve the efficiency of the treatment process. Specifically, whereas the original design of the draught tube specified only a suspended cylindrical draught tube with a circular orifice floor, subsequent modifications to this configuration have included the installation of a skirt along the base of the draught tube, installation of baffles in the draught tube, construction of the so-called "rocket cone" in the lime clarifiers, and relocation of the chemical feed line. Written information concerning these modifications is to be found in a number of internal City of Edmonton design studies.

In the 1980's, the City of Edmonton began to plan the future expansion of the E.L. Smith plant. As part of the expansion planning, the City of Edmonton commissioned Northwest Hydraulic Consultants Ltd. of Edmonton in 1992 to construct a 1:10-scale working model of the entire alum clarifier in order to investigate a number of structural modifications which had been proposed for inclusion in the new clarifiers. Their study produced much interesting information concerning the general operations of these clarifiers and defined the effects of a variety of structural modifications upon the flow. A reference to their study is provided in the list of references at the end of this report.

Finally, the University of Alberta performed a series of tracer tests on the full-scale clarifiers in 1993 in order to define the hydraulic performance of the full-scale facility under a variety of operating conditions. The details of these studies may be found in a report by Stanley, Smith & Prince (1993).

1.2.3 Impetus for the Current Study

A discrepancy was identified between Northwest Hydraulic's observed value of the recycle ratio^{*} and that which was claimed by the manufacturer. The University of Alberta's tracer studies did not resolve this problem but instead seemed to emphasize this discrepancy further. At the present time, the concern of the civic authorities is that they would like a better comprehension of the hydraulic and mechanical processes occurring within their clarifiers in order to improve operational procedures and to plan future modifications. Consequently, in order to clarify the nature of this apparent discrepancy, the City of Edmonton contracted the University of Alberta to conduct further testing of the 1:10-scale clarifier model.

1.3 Objectives of the Current Study

In addition to a simple consideration of the discrepancy in recycle ratio, it was further decided that the University of Alberta would continue to investigate the effects of structural modifications to the impeller-draught tube system, specifically with respect to identifying means whereby the impeller-generated recirculated flow could be increased. Both of these tasks were to be performed in accordance with an overall consideration of the effects of scale. As well, it was decided that instead of testing only one model-scale, the 1:10-scale model, two additional scale models of the impeller would be constructed at a much smaller size so that the dynamics of such impeller-agitated flows could be analyzed in great detail by means of laser-doppler velocimetry, thereby providing a more firm basis for the development of scaling factors.

In general terms, the objectives of this project may be stated as:

- 1. to define the manner in which the local average and turbulent velocity fields are defined by the action of the impeller**
- 2. to define the manner in which the local and vessel-averaged turbulent dissipation rates are defined by the action of the impeller**
- 3. to define the manner in which both the local velocity fields and the local turbulence fields in the draught tube, near the impeller are affected by the imposition of structural modifications upon the system**

^{*} a dimensionless parameter representing the ratio of the measured recirculated flow rate to the rate of raw water inflow through the tangential entry, Q_r/Q_i .

4. to define the manner in which the tangential inflow affects both the local velocity fields and the local turbulence fields

This study represents an attempt to quantify the nature of impeller-agitated mixing from the perspective of bulk-flow hydraulics and turbulence-based dynamical properties by means of a series of tests conducted for different structural configurations, over a wide range of impeller speeds, and at three different geometrical scales. By comparison of the resultant model-based data to measured full-scale data, and also in light of the significant elements of analytical theory (as embodied by both published research and relevant textbooks), it is hoped that the fluid dynamical properties of the Ecodyne impeller may be described better than has before been possible. Such knowledge is expected to be useful both to the City of Edmonton, with regards to process modification, improvement and future expansion, and in some small manner to the scientific community in general, for whom further information concerning the hydraulics of mixing, especially with respect to such an uncommon type of impeller, would presumably be of interest.

2.0 Review of Literature

2.1 Introduction

Presented hereunder is a review of relevant literature in the area of impeller-agitated vessels. The review is presented in three separate sections: the quantification of observable effects (independent of scale), the hydromechanics of impeller-agitated vessels, and the attainment of a practical scale-up mechanism. Such a division reflects what are perceived to be the three most common approaches to the study of impeller-agitated mixing problems that are applied in practice.

Although very few references can be found which deal specifically with the study of water treatment problems, any studies that address the general phenomenon of mixing are fundamentally useful in that the principles of analysis contained may be applied to the hydraulic analysis of a flocculation clarifier. Even though certain specific properties such as reaction rates and mass concentration distributions are not of primary interest here given that this study is primarily an investigation of the hydraulics of mixer-agitated systems, as a primary concern of water treatment lies in the mechanics of chemical coagulation and flocculation, and as such occurrences depend strongly upon the hydraulic conditions in the mixing vessel, the chemical-engineering-based articles may be seen to be immediately useful. Historically, most of the detailed, quantitative studies of the mixing phenomenon do not appear until well into the twentieth century. Since then, the work in this area has gradually become more detailed with the advance of analytical technology.

2.2 Dimensionless Parameters and Bulk Quantities

Considering a typical mixing apparatus comprising an impeller and mixing tank, a number of geometric parameters corresponding to the apparatus could immediately be thought to be of importance. For example, a typical velocity v and rotation speed ω may be assumed to represent the action of inertial forces within the tank. Similarly, one may also assume that viscous forces as represented by μ (N/m²) or ν (m²/s) could be important, as well as the fluid's density ρ (kg/m³). The effect of geometry could be represented by a number of relevant dimensions such as the tank's diameter D , the impeller diameter d and the depth of liquid h . In addition, the fundamental principle of energy conservation demands that energy applied in turning the impeller's shaft and thus motivating the opposing fluid be included via the consumed power P (W or J/s). The ubiquitous gravitational acceleration g (N/kg) is again included here.

One may then arrange these quantities into a number of dimensionless groups according to the well-established principles of dimensional analysis*. After combination of these variables, it may be shown that:

$$f \left(\frac{d^2 \omega}{\nu}, \frac{d \omega^2}{g}, \frac{P}{\rho d^5 \omega^3}, \frac{d}{D}, \frac{d}{h} \right) = 0$$

which provides a relatively simple means of describing a highly complicated flow state. One may consult Rushton (1951) ; Rushton, Costich & Everett (1952-1) ; Van de Vusse (1955) ; Holland (1962) ; and Leentvaar & Ywema (1980) for good general presentations concerning the application of the Π -theorem to such problems. Alternatively, as illustrated by Rushton (1952-1), Burghardt & Lipowska (1972), and Pawinski & Ruskowski (1985), one may also derive such dimensionless parameters directly from the simplified Navier-Stokes equations, thereby according a hydromechanical justification to the use of such dimensionless parameters.

* for instance, Buckingham's Π -theorem or its simplified analogue Rayleigh decomposition

Upon examination, it is apparent that the terms in this equation actually represent a number of well known fluid-mechanical parameters:

$$\frac{d^2 \omega}{\nu} = R$$

$$\frac{d \omega^2}{g} = F$$

$$\frac{P}{\rho d^5 \omega^3} = N_p$$

where F is a Froude number (representing the ratio of inertial to gravitational forces), R is a Reynolds number (inertial to viscous forces) and N_p is the power number* (dimensionally analogous to a drag coefficient). Therefore, assuming invariant impeller-tank geometry, this expression may be stated more conveniently as:

$$f(R, F, N_p) = 0$$

or, isolating the parameter which contains the power consumption:

$$N_p \propto R^a F^b$$

Finally, as the installation of baffles in impeller-agitated mixers effectively eliminates the presence of vortices, it is usually assumed for such cases that the effect of the Froude number would be effectively suppressed**, thereby allowing the equation to be simplified further:

$$N_p = f(R)$$

where geometric invariance is again assumed. This equation has traditionally been a favourite of many researchers - possibly owing to its simplicity - and has been applied to a large number of impeller-agitated mixing problems.

Considering further the pumping capacity, if a *relevant**** impeller-generated flow rate be represented by Q (m³/s), then one may define the flow number or the pumping number:

$$N_q = \frac{Q}{\omega d^3}$$

It has been found that N_q is approximately constant for turbulent flow, and numerous impellers of various design have approximately equal flow numbers of the order of 0.75. However, as with the power number N_p , geometric considerations are of ultimate determinative importance as there is no necessary correspondence between any two impellers' flow numbers.

* frequently called the Newton number Ne or the Euler number Eu in the European literature

** *vid.* Gray, Treyball & Barnett (1982) *e.g.*, as well as numerous others

*** This discharge could be either axial, radial, tangential, some combination of these or a different discharge altogether such as a bulk inflow or outflow.

Holland (1962) assumed the concept of agitation to be important in many mixing operations and presented a means whereby the degree of agitation in a stirred tank could be classified as low, medium or high based upon impeller's tip speed and overall size. He suggested corresponding ranges of ω . Expanding upon this, Bowen (1985) examined axial flow turbines with respect to N_i , a dimensionless agitation intensity number which expresses degree to which an impeller-generated bulk velocity in a tank causes the contents to be circulated relative to the velocity required for a single circulation in a tank:

$$N_i = \frac{v_{bulk}}{v} = \frac{v_{bulk}}{6A}$$

where the number 6 represents 6 ft/s, a characteristic, arbitrary and relevant velocity scale based upon the bulk velocity in the tank, and A represents the area through which the flow is active. He suggested that N_i could be related to N_p and N_q so that N_i may be used for scale-up, although he did not attempt to define exactly how this may be done in practice.

Another number, N_h , the head number is also useful in the description of impellers, particularly in drawing an analogy between mixing impellers and pumps. N_h is related to pressure, where p. is the pressure head produced in the region of the impeller. Consideration of pressure head is important for certain situations such as dispersions and when large density differences exist. Applying dimensional analysis, one may show that

$$N_h = \frac{gP.}{\omega^2 d^2}$$

and for a particular value of pumping flow, Q, it may also be shown, Amirtharajah & Tambo (1991) that:

$$N_p = \eta N_h N_q$$

which expresses that energy input via the impeller is consumed both in generating kinetic energy and in generating pressure energy.

If temporal effects are important, a commonly used dimensionless parameter is of the form $\omega\theta$, where ω is the impeller's angular velocity (1/s) and θ is some appropriate unit of time such as blend time, the time to achieve a certain degree of dispersion in the tank or a residence time. Finally, the Weber number, Cauchy number, Schmidt number, Peclet number, Prandtl number, Archimedes number, Sherwood number and Rossby number have all been applied in some manner to the investigation of impeller-agitated mixing. For example, using the temporal variation of sodium chloride concentration in a mixer, Burghardt & Lipowska (1972) attempted to quantify the state of ideal mixing with respect to mixing time, according to a function defined by separate Reynolds numbers for the impeller and the tank.

2.3 Power & Energy Consumption

2.3.1 General

Despite the rather large set of dimensionless parameters that is available, two of these parameters have traditionally received the greatest attention in the literature, namely the power number, N_p , and the Reynolds number, R_i . As such, the general nature of such curves is very well known. A typical N_p - R_i correlation comprises three regions:

- in the low- R laminar range ($R \leq 10000$), it appears that N_p is inversely proportional to R_i ; furthermore, given that conditions would be decidedly non-turbulent at such values of R , it is implied that the Froude number, F , would not be important in this region:

$$N_p \propto \frac{1}{R_i}$$

- for high values of R_i ($R_i \geq 10^4$), if the effect of F were effectively suppressed through the use of baffles to control swirl, N_p would be approximately constant^{**} or may exhibit a *slight* variation^{***} with R_i

$$N_p \approx \text{const}$$

- in the intermediate- R_i transition range, the relationship follows a curved line, thus indicating both F and R_i to be important

$$N_p \propto R_i^a F^b$$

In this sense, the N_p - R_i correlation is similar both in appearance and function to the well-known Moody diagram (both curves attempt to relate energy consumption to some predominant hydraulic condition), perhaps giving further justification to the application of dimensionless parameters to the hydraulic analysis of impeller-agitated mixers. In general, it will soon be made clear that the concepts of power and energy consumption, even via a bulk parameter like N_p , is intimately related to the concept of turbulence and turbulent dissipation, topics which will be addressed further in this report.

2.3.2 Historical Review

White & Brenner (1931) recognized that a dimensionless group combining P , d^3 , ω and ρ is well suited to the description of impeller-agitated systems, but they never explicitly assigned to it the name *power number*. Mack & Marriner (1949) provided one of the earliest applications of N_p to the analysis of impeller-agitated mixing vessels; although they did not apply a strictly non-dimensional approach, they were able to correlate the impeller's angular speed (rpm) with

* Numerous constituents will combine to form the Reynolds number, representing any number of velocities and dimensions that could potentially be of interest. From hereon, and following standard practice, the *impeller-based* statement of the Reynolds number, which includes only the diameter and angular velocity of the impeller will be used. In order to indicate the impeller-based Reynolds number, the subscript "i" is used.

** Traditionally, specification of a **single** power number has been used as a means of classifying impeller performance in industrial catalogues and technical manuals.

*** v.s. Bujalski, Nienow, Chatwin & Cooke (1987) for further explication

a quantity $N_p \omega d^2$ (which is actually a form of $N_p R$) to describe the progress of solid-liquid mass transfer. In a well known study, Rushton, Costich & Everett (1950-1&2) applied the concepts of dimensionless analysis to the study of a variety of impeller types and geometries in order to quantify the behaviour thereof ; their results were generally of the form:

$$N_p = R_i^m \left(\frac{a}{b}\right) \left(\frac{b}{c}\right) \left(\frac{c}{d}\right) \dots$$

where in addition to the N_p and R terms, the system's geometry is included through the use of a number of geometrical simplexes. A number of other early studies, (*e.g.* Rushton, 1951 ; Rushton, 1952-1 ; Holland, 1962) applied a similar analytical approach. Papastefanos & Stamatoudis (1989) examined the N_p - R characteristics of a number of different types of impellers in both baffled and unbaffled square and round tanks, in the high- R and transition ranges. Metzner & Otto (1957) studied the hydraulic properties of non-Newtonian liquids by means of a N_p - R analysis. Assuming that the shear rate was proportional to the impeller's tip speed, they found that an N_p - R correlation was still valid, but that generally more power was required at a given R , and that the laminar zone lasted over a greater range of R .

In an extensive study of a wide range of Rushton disc turbines in the high- R range, Bujalski, Nienow, Chatwin & Cooke (1987) questioned the validity of the traditionally held assumption that N_p is approximately constant for high values of R . They suggested that due to convenience, the impracticality of measuring N_p and variant impeller geometries, accurate power numbers had not been defined in the past, and that actually, there exists a slight peak in the N_p - R curve that was seldom if ever identified in past work, and whose genesis remained virtually unexplained. Speculating that the disc thickness was a factor, especially at smaller scales, they tested a number of dimensionless geometrical factors in order to incorporate such structural parameters. They proposed that the blade of a Rushton turbine acts somewhat like an airfoil, and that the slight peak in N_p is related to the formation of separation zones behind the blades. Given the effects of both form drag and skin friction, they argued that there could be no fundamental, fluid-mechanical reason why N_p should remain constant with increasing R . Conversely, one may infer from their work that two geometrically similar impellers at two different geometric scales that are being operated at the same R would be subject to different drag forces, different torques and hence different values of power and N_p . Pursuant to such consideration of drag force and energy consumption, rational parameters of drag and lift upon mixing blades are presented, for instance, in Shulyak & Zapara (1989).

Van de Vusse (1955) studied a variety of agitators (paddle stirrers, turbomixers) by applying dimensionless parameters to the case of blending of miscible liquids. Using mixing time as a criterion, he quantified the effects of geometrical properties such as the impeller's location, the vessel's diameter relative to that of the impeller, various clearance distances, the location and size of baffles and the number of blades. He proposed a number of empirical equations which attempted to combine these variables into a single expression - for example, for a paddle stirrer:

$$N_p \propto R_i^{-0.15} \left(\frac{d}{p}\right)^{-1.3} \left(\frac{h}{p}\right)^{0.6} \left(\frac{w}{d}\right)^{0.4}$$

where p represents the paddle's height and w represents the blade width. Although his results were not much different from those of earlier researchers, he included an analysis of the flow mechanics of mixing impellers and suggested that they could be treated as turbulent jets, thereby

It seems reasonable that one could extend their proposal to any type of impeller, as well as the Rushton type.

establishing a basis for future analysis. Furthermore, he recognized that the pumping capacity of the stirrer exerts considerable influence upon the turbulent mixing operation.

Combining the expressions for N_p and N_h , the following expression results for average power consumption per unit volume:

$$\frac{Q}{P} = \frac{1}{\rho \omega^2 d^2 \eta N_h}$$

where η is a specific, particular constant, dependent upon geometry and probably not universal. The dimensions of the latter expression may be seen to be related to

$$\left(\frac{Q}{P}\right)^{-1} \rightarrow \frac{W}{m^3/s} \rightarrow \frac{Ws}{m^3} \rightarrow \frac{J}{m^3}$$

which thus implies the relevance of an ergometric approach to the analysis of impeller-agitated mixing, an idea whose importance will be revealed more fully later on.

Ryon, Daley & Lowrie (1959) studied the power consumption of impeller mixers. By measuring the rate of extraction of uranium by an organic solvent in an impeller-agitated system, they found that the impeller's performance could be expressed by:

$$rate = k = f\left(\frac{P}{V}\right)$$

where V represents the bulk volume of the tank. Furthermore, they suggested that this relationship is independent of scale.

Hoogendorn & DenHartog (1967) studied a number of impellers of various types and sizes in the low- R_i range and found that the required power per unit volume to achieve a given state of mixedness is independent of the vessel's size for some types of mixers. For other types, they found that the parameter:

$$\frac{\theta^2 P}{\eta d^3} = f\left(\frac{\rho D^2}{\theta \eta}\right)$$

where η is a constant and θ is the observed mixing time, is a useful means of comparison. Similarly, in an examination of the mechanics of mixing within stirred tanks, Schwartzberg & Treyball (1968) suggested a general relation of the form:

$$\frac{P}{Q} = \frac{\rho u^3}{L} \Phi(R)$$

where u is a significant velocity, L is an appropriate length scale, and Φ is an R_i -dependent constant of proportionality. More specifically, they suggested that for a Rushton turbine, this relation may be expressed as:

$$\frac{P}{Q} = 7.9 \frac{\rho \omega^3 d^5}{D^2 h}$$

which, by inspection, is seen to be dimensionally similar to the expression for N_p . This indicates that the quantity $\Phi(R_i)$ is actually the power number as given by the N_p - R curve, and that this power number has the approximately constant value of 7.9, further indicating that this relation

is only correct in the turbulent, high-R range.

Building upon the earlier work of Van de Vusse (1955), Sano & Usui (1985) described the mechanics of mixing near an impeller by studying N_p , N_q and $\omega\theta$ at sufficiently high values of R to render these three parameters essentially invariant with R. They found that:

$$N_p \propto N_q^{1.34}$$

and they contended that their data support the predominance of macro-mixing in the mixing process, and hence that analysis via such bulk-quantity-based dimensionless parameters is appropriate.

Of course, in any analysis of energy consumption in a stirred tank, the familiar G-value of Camp & Stein (1943) must be recognized. Although in practice it has attained the attributes of a rather simple bulk parameter, G may be derived explicitly from first principles through a rearrangement of the Navier-Stokes equations. Their expression for G may be seen to express the sum of work done by fluid shear in three directions. Specifically, they showed that:

$$G = \sqrt{\left(\frac{\partial u}{\partial y} + \frac{\partial v}{\partial x}\right)^2 + \left(\frac{\partial u}{\partial z} + \frac{\partial w}{\partial x}\right)^2 + \left(\frac{\partial v}{\partial z} + \frac{\partial w}{\partial y}\right)^2}$$

which is actually a form of a dissipation function, described as the absolute velocity gradient at a point. Dimensionally, G has the units of 1/s and is thus readily comparable to the expression for velocity gradient in the familiar one-dimensional expression of viscous shear of a Newtonian liquid:

$$\tau = \mu \frac{\partial u}{\partial y}$$

Furthermore, for the simplified case of a spherical particle, they describe how G may be expressed by means of C_d , a drag coefficient - a concept which is, at least intuitively, applicable to the analysis of a mixing impeller.

Although their expression G is theoretically sound in the form given above, in practice, G has been greatly oversimplified to:

$$G = \sqrt{\frac{P}{\mu V}} = \sqrt{\frac{\bar{\epsilon}}{\nu}}$$

where the quantity $\bar{\epsilon}$ represents the average rate of energy dissipation per unit mass in the tank:

$$\bar{\epsilon} = \frac{P}{\rho V}$$

Such an expression for G has received great acceptance in the environmental engineering field and is now well entrenched as a design method for mixers. Unfortunately, practical, full-scale applications of G to the design of full-scale systems are often based upon small-scale laboratory mixing data - data which are usually scale-variant, thereby requiring the use of empirical scale-up factors. Furthermore, use of such a simplified form of G is clearly open to criticism given that the presence of a highly complicated, spatially and temporally variant flow state within an impeller-agitated mixer is completely obscured by the use of such a simple, bulk-quantity-based parameter. Clearly, this practical definition of G retains neither the original multi-dimensionality

nor the implied spatial variance of its original derivation.

Nonetheless, the resemblance between G and the afore-described expressions for P/V and P/Q is obvious. Moreover, there is an implied similarity between G and N_r given that N_r is itself expressible via some type of drag coefficient, which again suggests the appropriateness of ergonomic analysis to the case of impeller-agitated mixing. For example, using a pilot-scale dynamometer to measure torque, Leentvaar & Ywema (1980) correlated energy-based dimensionless parameter N_r to G in the analysis of several types of impellers.

In a study of flow-through mixers, Seichter (1975) modelled the tank-blades as separate compartments or flocculation chambers, and through the use of tracer-test mixing time data proposed the use of the Camp parameter Ca :

$$Ca = G \bar{\tau}$$

where

$$\bar{\tau} = \frac{V}{Q} = t_d = \text{detention time}$$

Based upon his results, he related the temporal parameter Ca to other common dimensionless parameters and geometric simplexes:

$$Ca = \omega \bar{\tau} \sqrt{R} \sqrt{\left(\frac{4}{\pi}\right) Eu \left(\frac{h_s}{D}\right) \left(\frac{D}{d}\right)^{-3}}$$

where subscript s refers to local values of the various parameters, within a specific sub-section, thereby implying that the local G -value may be related to the power consumption via the Euler (*i.e.* power) number.

Camp & Stein recognized that G is in essence very influential in the description of flocculation for it attempts to quantify the local velocity field, something which is of great determinative potential with respect to such properties as settling rate, floc size and floc strength. Their early work is fundamental to more complicated theories of flocculation kinetics which are in use today. Although use of the simplified parameter that G has now become is perhaps somewhat misguided, it is nonetheless still useful in that at least dimensionally, it seems to indicate that the secret to describing impeller-agitated mixing problems lies in an examination of the kinetics of flow and the mechanics of energy dissipation. In this sense, the continued use of the traditional N_r - R correlation as a tool for analysis is somewhat justified. Furthermore, the apparent relevance of parameters such as N_r and G strongly adduces that if the process of dissipation could be studied in still more detail, the very essence of impeller-agitated mixing would be known. Consequently, it appears that an analysis of turbulence in impeller-agitated mixers is in order.

2.4 Turbulence

2.4.1 Introduction

The use of bulk parameters and dimensionless groups often allows a relatively complicated process to be described adequately well by a few easily obtained values. As well, the use of such parameters may allow a better appreciation of any forces which are dominant in a particular study. Unfortunately, although the principle of dimensionless groups is in theory applicable to any situation, its application is limited by the scale of the observed quantities. For instance, an average, bulk velocity says nothing concerning local or fluctuating variations in

velocity and thus cannot be used to describe something like micro-scale dissipation. Clearly, there can be very little progress toward addressing the concept of energy dissipation within stirred tanks without first understanding the mechanisms of the micro-scale processes that are present. Such an understanding would allow a better assessment of mixing and agitation in general and would assumedly provide a rational basis for the operation of physical models, specifically with respect to the selection of relevant and appropriate scale-up parameters. The concept of energy and the dissipation thereof is of fundamental significance to any process, and, as has already been illustrated, is strongly implied in the use of such well known parameters as N_p and Camp & Stein's G . In its simplified form, G requires the use of a vessel-averaged ϵ , which expresses the average rate of energy that is dissipated per unit-mass of fluid, averaged over the entire tank. As such, the analysis of turbulence - which demands a concentrated examination of the flow field within the tank - would presumably allow a more refined re-specification of those parameters whose preeminence seems to be indicated by the bulk-quantity-based dimensionless parameters.

Considering mixing, Oldshue (1981) stated "what ultimately controls the process is shear stress." As shear stress is intimately related to shear rate, one must then recognize the existence of both micro- and macro-scale effects. He suggested that fluid shear at a point can either be based upon the average velocity at a given point or on the magnitude of the velocity fluctuations. Furthermore, of many shear rates that are present in an impeller-agitated mixing tank, only four were said to be usually of prime importance: the maximum shear rate in the impeller stream ; the average shear rate in the impeller stream ; the average shear rate in the bulk of the tank ; and the minimum shear rate in the bulk of the tank. Finally, he qualitatively stressed the connection that exists among the root-mean-square (rms) velocity fluctuations, the length scale of turbulent dissipation and the minimum scale whereat all energy have been dissipated.

Similarly, Sano & Usui (1985) state that mixing time in the turbulent region of a mixing vessel is determined by the following factors:

- i) direct shear action between liquid and impeller
- ii) macro-mixing due to circulation flow in a vessel by the discharge action of the impeller
- iii) mixing due to turbulent diffusion during the liquid's circulation, and
- iv) mixing due to molecular diffusion

Of these, the first three are thought to be of primary determinative importance with respect to the turbulent mixing process within a stirred tank.

The collection of turbulence data requires the use of very sensitive instruments due to the high degree of variability that could be present in a typical turbulent flow. Historically, turbulence data within impeller-agitated mixers have been collected via a variety of courses: there have been intrusive probes such as the hot-wire anemometer and hot-film anemometer, *e.g.* Gunkel & Webb (1975) ; photographic techniques *e.g.* Cutter (1966), Schwartzberg & Treyball (1968), Van't Riet & Smith (1975) ; and most recently, laser-doppler velocimetry or LDV, *e.g.* Chen, Wang & Hajduk (1988).

2.4.2 General Principles of Turbulent Flow

The analysis of turbulent flow is a difficult field. For the purposes of this study, only a few general principles concerning the structure and analysis of turbulent flows need to be discussed here. For further information, Tennekes & Lumley's *A First Course in Turbulence* (1972) can be consulted.

In general, one may consider turbulence to be the presence of a disordered flow-field

where turbulence is manifested as a random series velocity fluctuations superposed upon a more or less temporally invariant spatial bulk-flow regime. This concept is represented by the traditional Reynolds decomposition scheme, where the total velocity is decomposed into its average and fluctuating components:

$$u = \bar{u} + u'$$

The velocity fluctuations may be thought to be caused by eddies in the flow. The eddies themselves represent a three-dimensional vorticity structure that is imposed upon the bulk flow. As these continually rotating eddies are conveyed by the bulk flow, they induce local fluctuations throughout the flow field, all the while succumbing to the forces of viscous shear and the dynamic forces exerted by a multitude of other eddies. Eventually, they gradually decay into a geometrically expanding series of eddies of ever-decreasing size until eddies of the molecular scale are reached.

Such a description of turbulence conveys very strongly an image of motion - a regime of vigorous random kinetic movements. For an eddy to be established, for the resultant series of turbulent fluctuations to be developed, and for the eddies to propagate in a series of ever smaller eddies, it is obvious that energy must be applied. In an impeller-agitated system, the impeller acts as the source of energy. The kinetic energy of the impeller is transferred to the fluid, and this energy fuels the continuous propagation of ever smaller eddies until eddies of an exceedingly small size are developed, whereupon the kinetic energy of the impeller is ultimately dissipated as heat.

The discussion of energy dissipation through propagation along a series of ever smaller eddies thus accords importance to the descriptive concepts of length, time and velocity-scales. It is a reasonable assumption that the large eddies are initially responsible for most of the transport of momentum to the smaller scales, and that the large eddies are initially as large as the width of the flow, which in turn could be defined by the turbulence-generant device, whether it be a nozzle, an orifice or an impeller's blade. As the eddy is shorn into smaller and smaller eddies, the length scale, which is a general representation of the eddy's size at a particular point in time, must decrease. As the length-scale decreases, it may be assumed that the time-scale, a general indication of an eddy's vorticity, should be dependent only upon the rate of momentum transfer from the larger scales in accordance with the local viscosity. The velocity scale, which is expressed as the ratio of length-scale to velocity-scale, and which may be understood to represent the eddy's kinetic energy, therefore depends upon both the local length-scale and the local time-scale.

By the principle of conservation of energy, it would be expected that the energy that is originally applied to the system via the impeller must equal the energy that is ultimately dissipated by the turbulent flow. It has already been shown that the total energy that is introduced to the system may be expressed by the average impeller power, P , which expresses the impeller's rate of energy consumption ; more specifically, it has been shown that the average rate of energy consumption *per unit mass* has been accorded much attention in the literature. Because the impeller-supplied energy is distributed down a continuum of ever smaller eddies, intuition would lead one to suspect that the local rate of energy consumption - that being the rate at which a single eddy expends energy - is some fraction of the average rate of energy consumption, P . Extending this assumption further, it may be argued that the local rate of energy consumption *per unit mass* is some fraction of the vessel-averaged rate of energy consumption per unit mass, $P/\rho V$. In practice, the rate at which the impeller-generated kinetic energy per unit mass is dissipated by the turbulent flow is given by the local turbulent dissipation rate, ϵ , which may be seen to have the following dimensions:

$$\epsilon \rightarrow \frac{m^2}{s^3} \rightarrow \frac{\frac{J}{kg}}{s} \rightarrow \frac{W}{kg}$$

In general terms, it may be speculated that the sum of all local dissipation rates, ϵ , throughout the entire tank must equal the average power per unit mass that is initially applied. That is:

$$P = \int_V \epsilon(V) \rho dV$$

or, expressed slightly differently:

$$\frac{P}{\rho V} = \oint_V d\epsilon$$

If a given eddy's energy is assumed to be entirely kinetic, the local rate at which the kinetic energy is consumed may be estimated from first principles: assuming a length-scale, δ , a turbulent velocity-scale, ζ , a time-scale, τ , and a mass, γ , an expression of a turbulent-velocity-induced eddy's rate of consumption of kinetic energy per unit time may be devised:

$$\epsilon \sim \frac{\left(\frac{E_k}{\gamma}\right)}{\tau} = \frac{\frac{1/2 \gamma \zeta^2}{\gamma}}{\tau} = \frac{1/2 \zeta^2}{\tau} = \frac{1/2 \zeta^2}{\frac{\delta}{\zeta}} \propto \frac{\zeta^3}{\delta}$$

This expression is dimensionally consistent with both ϵ and $P/\rho V$, a correspondence that will eventually be shown to be significant with respect to the analysis of impeller agitated mixing. Thus, in order to calculate ϵ , it remains only to determine the quantities ζ and δ - exactly what values these quantities should have though demands further discussion.

At the smallest scales, where ϵ is governed only by ν , it has been shown that ϵ may be related to ν in order to estimate the length, time and velocity scales. Specifically:

$$\begin{aligned}\delta &= \left(\frac{\nu^3}{\epsilon}\right)^{\frac{1}{4}} \\ \tau &= \left(\frac{\nu}{\epsilon}\right)^{\frac{1}{2}} \\ \zeta &= (\nu \epsilon)^{\frac{1}{4}}\end{aligned}$$

These are called the Kolmogorov microscales, Tennekes & Lumley (1972). They describe theoretically the characteristics of the smallest eddies that a given flow can maintain. It is interesting to note the corresponding Reynolds number at the Kolmogorov microscales:

$$R = \frac{\zeta \delta}{\nu} = \frac{(\nu \epsilon)^{\frac{1}{4}} \left(\frac{\nu^3}{\epsilon}\right)^{\frac{1}{4}}}{\nu} = \frac{\nu \left(\frac{\epsilon}{\nu}\right)^{\frac{1}{4}}}{\nu} = 1$$

Recalling the physical definition of R that was given earlier, it is shown that at the molecular scale, the inertial forces acting upon the flow are of exactly of the same order as the viscous forces, thus allowing one to view viscous dissipation as the direct transmutation of kinetic energy into heat. In practice, estimates of ϵ are variant, ranging from Camp & Stein's G -value to Prandtl's first and second hypotheses to κ - ϵ computer modelling. Such variance is consequent to the inherent mathematical complexity in turbulence analysis and description as embodied by the classic Reynolds closure-problem - they are all attempts to "close" the system of Reynolds equations.

However, given that what is ultimately dissipated by the system must originally have been added to the system, one may examine the opposite end of the turbulence system. Assuming now that at the largest scales, the turbulent motions are of some relevant length-scale, ℓ , with some appropriate turbulent velocity, u' , and time-scale τ , the so-called "inviscid" estimate of ϵ may be made. As before, if all of the energy is initially assumed to be kinetic, and assuming that this largest eddy expends a significant portion of its energy during one rotation, then the kinetic energy per unit mass of the largest eddy may be *approximately* estimated by:

$$\epsilon \approx \frac{E_k}{\tau} \propto \frac{(u')^2}{\frac{\ell}{u'}} = \frac{u'^3}{\ell}$$

where the constant of proportionality would be spatially, directionally and dynamically variant depending upon the degree of isotropy in the flow. For non-isotropic flows, this expression may be re-stated as:

$$\epsilon \propto \frac{(u'^2 + v'^2 + w'^2)^{\frac{3}{2}}}{\ell}$$

where u' , v' and w' represent the turbulent velocities in three dimensions.

It may be seen that as the Reynolds number, R , increases, the difference in magnitude between the small and large scales increases. Generally, the small-scale eddy is much more vigorous than its large-scale progenitor ; conversely, there is significantly more energy present in the large-scale eddies. This quality is recognized by Tennekes & Lumley (1972):

This is typical of all turbulence: most of the energy is associated with large-scale motions, most of the vorticity is associated with small-scale motions.

The general expression for ϵ presented here is extremely common. This same type of expression, a cubed turbulent velocity divided by a length-scale, has been shown to result regardless of the means of derivation, whether based upon simple dimensional arguments or more sophisticated derivations directly from the Reynolds equations. This type of expression historically has been very well studied in the literature, where a series of historical investigations has generally confirmed its appropriateness

2.4.3 Historical Review

Rosensweig (1964) provided one of the earliest applications of the principles of turbulent flow analysis to the case of impeller-agitated mixing. Limiting his study to the high-R range in order to facilitate application of Kolmogorov's principle of universal equilibrium, he performed his study based upon the assumption that "knowledge of the cascade rate is equivalent to knowledge of the dissipation rate," using unmixedness or fluctuation of concentration as the relevant analytical parameter. Beginning with an expression for the conservation of unmixedness:

$$\gamma^2 = (1 - \bar{\Gamma}) \bar{\Gamma} - \epsilon_\gamma \tau$$

where, by Reynolds time-averaging, $\bar{\Gamma}$ represents the average concentration, γ^1 represents the rms value of measured concentration fluctuations, and $\Gamma(\cdot)$ is the well known gamma function. Applying the results of previous researchers, an estimate of the concentration energy dissipation rate in turbulent mixing was presented:

$$\epsilon_\gamma = \frac{2 \Gamma(\frac{5}{6})}{\sqrt{\pi} \Gamma(\frac{1}{2})} \frac{\gamma k_o^{\frac{2}{3}} \epsilon^{\frac{1}{3}}}{c_\gamma}$$

where k_o is a wave number and c_γ is an experimental constant.

Recognizing that power per unit volume had long been a favourite criterion in the design and scale-up of mixing vessels, Cutter (1966) applied the concept of turbulent flow analysis via the Reynolds equations to the case of impeller-agitated mixing in order that the local mechanisms of energy dissipation throughout the tank might be better described. Assuming the predominance of turbulence and a state of approximate isotropy, the Reynolds equations may be simplified to integral expressions of conservation of angular momentum per unit mass and local rate of energy dissipation respectively:

$$r^2 \int_0^\infty (\overline{uv} + \overline{u'v'}) dy = \text{constant}$$

$$2\pi r \int_{-\infty}^\infty \epsilon dy = \frac{dr}{dr} 2\pi \int_0^\infty (k^2 \overline{u} + 2\overline{v} \overline{u'v'}) dy$$

His assumptions were investigated by a photographic streak technique wherefrom he found that all angular momentum is accounted for in the impeller stream except near the wall, where torque is lost to the baffles. From an Eulerian correlation scheme, appropriate turbulence scales were presented for the radial and tangential directions in the impeller stream, and it was suggested that the radial turbulence length scale can be correlated to the impeller's blade size. His results indicated that an assumption of isotropy is not particularly valid, especially far from the blades, and that the length scales generally varied as the square root of the radius except at the wall. He also concluded that the local mean velocities could be correlated to the tip speed, and that the nature of this correlation varied only with the location within the tank. The rms turbulent velocities were also seen to correlate with the tip speed, though the turbulence in the immediate vicinity of the impeller contained a higher proportion of small eddies which decay faster.

His results indicated that about 20 percent of the total input energy was dissipated in the impeller itself (presumably due to frictional losses to the blades), about 50 percent is dissipated in the impeller stream (turbulent dissipation in the jet-like flow), and about 30 percent is

dissipated in the bulk of the tank (turbulent dissipation and drag losses to the walls). For the radial velocity, it was confirmed that the local rate of dissipation could be expressed by:

$$\epsilon \propto \frac{3}{2} \frac{(\overline{u'})^3}{L}$$

where L represents an Eulerian length scale, which again was seen to correlate to the impeller blade size. Dimensionally, this expression has the same units as:

$$\overline{\epsilon} = \frac{P}{V} \approx \omega^3 d^2$$

Finally, in the impeller stream, he found that the quantity $\epsilon/\overline{\epsilon}$ decays rapidly with distance, and that this ratio may range from 70 to 3.5 - far greater than the same ratio outside the impeller stream (~ 0.25) - and that significant inhomogeneities may occur in the flow.

In a study of turbine impellers in baffled tanks, Schwartzberg & Treyball (1968) applied streak photography in order to quantify the average and rms fluctuating velocities, and to allow correlation of the various hydrodynamic factors that are present. In agreement with other researchers, they also accepted the apparent governance of the following type expression for the dissipation rate:

$$\frac{P}{Q} = \frac{\rho U^3}{L} \cdot \Phi(R_i)$$

where U and L represent a significant velocity (average or fluctuating) and length scales. For the high- R_i range, assuming N_r to be constant and assuming that the length scale is proportional to the impeller's blade height, they proposed the use of the following parameter in the quantification of local velocities:

$$\overline{u'} \propto \frac{\omega d^2}{(Dh)^{\frac{1}{3}}}$$

and confirmed that such a parameter may be used to correlate both average and fluctuating velocities reasonably well at a given location, although the use of

$$\frac{1}{3} (\overline{u'}^3 + \overline{v'}^3 + \overline{w'}^3)^{\frac{1}{3}}$$

is suggested for the definition of an appropriate velocity scale given the almost certain non-isotropy of such tanks. Further speculation is expressed that such parameters may be universal in nature, thus implying their possible use as scale-up similarity criteria - speculation that will be treated more fully later.

Gunkel & Weber (1975) mounted a probe on a spinning disk-type impeller, and, with the use of hot-wire anemometry, were able to measure the impeller-generated flows accurately (in contrast to many of the earlier studies) allowing quantification of the mean and fluctuating velocities, one-dimensional energy spectra and Eulerian autocorrelation functions in the impeller stream. By placing their probe behind the blades, they were able to show that four vortices may be associated with each blade: two on the blade's leading-edge (one above the impeller disk-plane

and one below it), and two on its trailing-edge (again, one above the impeller disk-plane and one below it). They described the impeller stream as having jet-like behaviour, including entrainment of the surrounding fluid. Consistent, similar one-dimensional energy spectra were determined in the impeller stream and were found to be the same for all operating conditions, with the spectra closest to the impeller showing a variation indicative of the presence of periodically passing impeller blades and a second smaller variation due to the vortices generated by such blades. They found that most of the input energy to be dissipated outside the impeller stream where the turbulence intensity is high : in the high-wave number range, turbulence was seen to be isotropic, thereby indicating the Kolmogorov length scale to be suitable for describing the degree of turbulence.

Considering the hydrodynamics of the generated flow, a large radial outflow was observed behind the leading blade, with a smaller radial velocity being observed ahead of the trailing blade. In order to isolate the truly random (turbulent) and periodic (impeller-generated) components of the fluctuating velocity, they applied an autocorrelation scheme whereby the total fluctuations were decomposed into their two components:

$$\overline{u'_{res}}^2 = \overline{u'_{turb}}^2 + \overline{u'_{periodic}}^2$$

In this manner, a plot of the total and periodic turbulence intensities as functions of radial distance indicate that the periodic fluctuation is dominant near the impeller, but that random turbulence dominates rather rapidly with radial distance. Plots of total and random turbulence intensities as functions of radial distance were seen to collapse onto a single curve at a distance of approximately one-half of the impeller's radius from the blade tip. Similarly, plots of the one-dimensional energy spectrum were punctuated by two peaks which indicated the periodic passage of the blades and the passage of the four-vortex structure generated thereby ; however, plots of energy spectrum at successively greater radii indicated that the significance of these peaks lessened with greater distance from the impeller.

Based upon integration of the measured energy spectra, they confirmed that the majority of input energy is dissipated in the bulk of the tank, that the assumption of isotropy is acceptable and that the length scale is relatively invariant. As such, they expressed that their "most important conclusion ... was that the turbulence parameters are not directly related to the impeller tank geometry, but indirectly through the power input per unit mass" - *i.e.* $P/\rho V$. For the case of high- R , flows such that N_p was approximately constant, and assuming approximately isotropic turbulence, they found that

$$\begin{aligned} \overline{u'}^2 &\propto \epsilon^{\frac{2}{3}} \\ \lambda_g^2 &\propto \epsilon^{-\frac{1}{3}} \end{aligned}$$

which provides a practical means of defining the turbulent velocity and length scales at a point. Upon rearrangement, it may be shown that

$$\epsilon \propto \overline{u'}^3$$

or, more specifically

$$\epsilon = \frac{3}{2} A \frac{\overline{u'}^3}{l_c}$$

which was also recognized by Cutter (1966), and Schwartzberg & Treyball (1968).

Based upon this, for a variety of tank sizes and impeller types, they were able to calculate the length scale, which was found to be very small, leading them to speculate that the commonly held assumption that the turbulence length scale l_c is related to the scale of the turbulent generant device perhaps deserves further scrutiny, especially when considering locations that are relatively far removed from the impeller ; such a contention is possibly further supported given that the impeller-generated periodic fluctuations were seen to have become negligible long before the wall was reached. Nonetheless, rearranging the expression for local dissipation, they suggested that the following expression is suitable for defining the turbulence characteristics of an impeller-agitated vessel:

$$\overline{u'} = \left(\frac{1}{A}\right)^{\frac{1}{3}} \left(\frac{2}{3}\right)^{\frac{1}{3}} \epsilon^{\frac{1}{3}} (l_c)^{\frac{1}{3}}$$

an expression which was also shown to be expressible as:

$$\overline{u'} = 0.73 \left(\frac{\pi}{4 N_p}\right)^{\frac{1}{3}} \epsilon^{\frac{1}{3}} (d)^{\frac{1}{3}}$$

In contrast to some researchers' enthusiasm for the assumption of isotropic turbulence, Van't Reit, Bruijn & Smith (1976) warned that certain special features characterize the impeller discharge flow, and thus any attempt to analyze the prominent characteristics thereof must recognize such features and incorporate them into the analysis. Building upon the earlier concept of the trailing vortex as presented by Van't Reit & Smith (1975), they also advised that the periodic turbulent fluctuations due to the passage of the impeller's blades be separated from the purely turbulent fluctuations. When the observed fluctuations are not decomposed, they suggested that most of the measured fluctuations should actually be described as pseudo-turbulence. Confirming the results of many others, they too observed peaks on the energy spectra plots corresponding to ω and 2ω , but that these effects diminished with increasing distance from the impeller stream.

More importantly though, given the influence of the impeller-generated trailing vortices, they felt that one could not justifiably assume isotropic conditions in any analysis of the undecomposed turbulence fluctuation measurements, thereby rendering any use of the typical concepts of turbulent length and velocity scales to be invalid anywhere that the periodic fluctuations be significant. In this sense, they suggested that true turbulence could only be observed when the turbulence probe is allowed to rotate with the impeller. In practice, the effects of periodic motion manifested in mixing-time studies may be seen in several studies, including Hoogendorn & DenHartog's (1967) decolorization studies, Khang & Levenspiel's (1976) mixing studies, and Sohn & Bajpai's (1987) two-compartment mixing-time model.

Bin (1984) provided a good general introduction to the application of turbulence characteristics to the study of stirred vessels with respect to liquid-gas mass-transfer. In this article, he presented the following commonly accepted expression for an rms fluctuating turbulent velocity:

$$\overline{u'} = c_6 \frac{\omega d^2}{\sqrt[3]{D^2 h}} \propto \omega d$$

where the value of the constant c_6 depends upon the location and direction of the rms velocity component of interest. Such an expression is similar to another generally accepted contention that the *average* velocity in the impeller flow stream is also proportional to ωd . By incorporating an expression for the integral length scale into the above expression for u' , he showed that

$$\epsilon_{corr} = k \frac{\omega^3 d^5}{D^2 h} = k_1 \frac{\bar{\epsilon}}{N_p} \Rightarrow \bar{\epsilon} \propto \frac{N_p d^5 \omega^3}{V} \propto \frac{v_{tip}^3}{d}$$

where the coefficient of proportionality can be determined by experiment. Thus, by his analysis, the ratio of the local dissipation rate ϵ_{corr} (corrected for anisotropy of turbulence and measured at any point of interest in the tank - Bin seemed to consider the gas-liquid interface) to the average rate of dissipation depends only upon N_p , which itself depends upon the geometry of the vessel and impeller.

Laufhaute & Mersmann (1985) applied the principles of laser-Doppler velocimetry from the perspective of turbulence analysis to a Rushton-turbine-agitated tank. For high R_i , such that the N_p - R_i curve could be assumed to be approximately invariant, they also assumed the average dissipation rate per unit mass to be proportional to $\omega^3 d^2$, but they warned that because any measured velocity in the vicinity of the stirrer would be subject both to true turbulent fluctuations and to periodic fluctuations due to the drag of stirrer-induced vortices, the actual measured fluctuating velocity should be partitioned into two components:

$$u'_{total} = u'_{turbulent} + u'_{periodic}$$

In accordance with a Taylor-type turbulence analysis, they assumed the local rate of turbulent dissipation to be expressible as

$$\epsilon = 15 \frac{v u'^2}{\lambda^2}$$

where the quantity λ represents a Taylor vortex length, the length of eddies that are primarily involved in dissipation. Assuming further that

$$\lambda \propto \sqrt{\frac{\ell v}{u'}} \quad \rightarrow \quad \lambda^2 \propto \frac{\ell v}{u'}$$

where ℓ is assumed to be a typical length of the turbulence-generant device (e.g. the blade width of the impeller), it was shown that

$$\epsilon = k \frac{u'^3}{d}$$

where, according to a thorough survey of previous results, the constant k was stated to have a value of 6.0 to 6.6. Assuming further that the local rate of dissipation measured at a given point

in the tank would be directly proportional to the average rate of dissipation for the entire tank, it was shown that for the turbulent flow regime

$$\begin{aligned} u'_{turb} &\propto \omega d \left(\frac{d}{D} \right) \\ &\propto \omega d \quad (\text{constant geometry}) \end{aligned}$$

In summary, they proposed that for conditions of high impeller R , the resultant significant velocity in the impeller stream may be characterized by:

$$u = (\bar{u} + u') \propto \omega d$$

a result which poses serious implications with respect to the scale-up of model stirrers, specifically that the degree of turbulence present at a specific point in the tank is constant, in spite of the scale - this however will be considered more fully below. In a later study, Mersmann & Laufhutte (1985) stated that for a *constant* mean power input per unit volume, it may be shown that:

$$u' \propto d^{\frac{1}{3}}$$

where the ratio $\epsilon / \bar{\epsilon}$ varies spatially in the tank, attaining a maximum of about 15 in the impeller stream.

By employing Van't Reit & Smith's (1975) concept of the trailing vortex together with the data of Gunkel & Weber (1975), Placek & Tavlarides (1985) evaluated the mean velocity and fluctuation intensity in a turbine impeller discharge flow. After presenting the salient features of the earlier trailing vortex model and quantifying the properties of such flows, based upon correlations of others' data in accordance with their own new interpretations, they proposed a means whereby the spatial variations of a vortex's coordinates and velocities could be defined. Starting from an integral expression for the total kinetic energy per unit mass of the velocity fluctuations and speculating (via a dimensional argument) that

$$\epsilon \propto \frac{k^{\frac{3}{2}}}{\Lambda}$$

where Λ represents an appropriate length scale, and accepting the correlation of Schwartzberg & Treyball (1968) which can be stated as

$$\frac{P}{\rho V} = 7.9 \frac{\omega^3 d^5}{D^2 h}$$

they proposed that the local value of ϵ may be estimated from:

$$\epsilon = \frac{0.8 (\omega^2 d^2)^{\frac{3}{2}}}{0.14 d} = 5.1 \omega^3 d^2$$

which immediately invites comparison to Bin (1984) and Laufhutte & Mersmann (1985).

Furthermore, if the tank geometry remain geometrically similar among models of various scales, upon combination of the above expressions for $P/\rho V$ and ϵ , it is seen that

$$\frac{\epsilon}{\epsilon} = 5.16$$

which lies within the range identified by Laufhütte & Mersmann (1985). However, they qualified the use of their model by stating that its use is most appropriate where a trailing vortex regime is in existence, a limit which was seen to extend to a radius of approximately 0.7 d.

Wu & Patterson (1989) applied laser-Doppler velocimetry to a baffled vessel agitated by a Rushton turbine. Along with a presentation of N_q data (representing a simpler non-dimensional, bulk-parameter approach) they examined most of the significant turbulent flow parameters. In defining turbulence, they also suggested that the fluctuating velocity must be partitioned into two parts, a random part (due to turbulence) and a periodic part (velocities induced by the passing impeller blades):

$$u'_{total}(t) = u'_{turbulent}(t) + u'_{periodic}(t)$$

and, for turbulence intensity

$$\overline{u'^2_{total}} = \overline{u'^2_{turbulent}} + \overline{u'^2_{periodic}}$$

where the bars indicate the application of a time-averaging scheme. By approximating the periodic part of the velocity fluctuations by a Fourier series and then analyzing their results by an autocorrelation function in order to decompose the measured fluctuations into their separate components, they found that both the total velocity fluctuations and the purely random velocity fluctuations near the impeller are proportional to the impeller's tip speed as expressed by ωd . Once the effect of the periodic velocity fluctuations was removed, the resultant velocity profiles exhibited two distinct maxima, both above and below the impeller-disk centreline - an property that was noted both by Van't Reit & Smith (1975) and Gunkel & Weber (1975). Specifically, they found that for radial velocities, the periodic, impeller-induced velocity fluctuation can be as much as 85 percent of the observed turbulence near the impeller's tip, but that such turbulence decreases rapidly, attaining only 20 percent at a distance of 1.5 r and approximately 0 percent at approximately 1.9 r. For axial velocities, it was seen that the periodic, impeller-induced turbulence is much less, on the order of 18 percent near the impeller; generally, the axial, radial and angular turbulence *intensities** are approximately equal in the region of the impeller. Interestingly, they suggested that the work of earlier researchers - Cutter (1966) *e.g.* - reported incorrect turbulence intensities near the impeller because those researchers did not identify the necessity of decomposing the measured fluctuations into random and periodic components. Such

* These percentages express the ratio of periodic turbulent velocity fluctuation to total velocity fluctuation; turbulence intensity itself is the ratio of the turbulent velocity fluctuation to the time-averaged mean velocity in a particular direction.

a decomposition routine facilitated Wu & Patterson's later calculation of the energy spectrum function

$$\int_0^{\infty} E_1(n) dn = \overline{u'^2}$$

In the same manner, the energy spectrum was also decomposed into random and periodic components ; had it not been decomposed, they indicated that the resultant plot of the energy spectrum would have retained the same shape as a typical curve but would have been punctuated by numerous maxima corresponding to the frequencies of periodic fluctuation. Depending upon the frequency of data collection, the energy-frequency spectrum diagram was seen to exhibit such peaks well into the high frequency range. Again employing only the statistically random part of the velocity fluctuations, they illustrated how Eulerian turbulence and length macro- and microscales may be estimated from the turbulence data, although they had difficulties in determining the microscales since their equipment was unable to collect noise-free data. Finally, they performed a kinetic energy balance around the impeller (neglecting pressure energy and viscous dissipation) in order to estimate the local values of the turbulence energy dissipation rate.

Incorporating the work of a number of earlier researchers together with a fair amount of judgement, they decided that the local dissipation rate may be expressed by:

$$\epsilon = k \frac{q^{\frac{3}{2}}}{L_{res}}$$

where the constant k is approximately 0.85, and where

$$q = \frac{1}{2} (\overline{u'^2} + \overline{v'^2} + \overline{w'^2})$$

and

$$L_{res} = \sqrt{L_1^2 + L_2^2 + L_3^2}$$

which is very similar to the results of Placek & Tavlarides (1986). According to this analysis, approximately 60 percent of the total energy input via the impeller is dissipated at or near the impeller, with the remainder being dissipated in the bulk of the tank.

2.4.4 Length-Scale

Accepting the general formula

$$\epsilon \propto \frac{u'^3}{\ell}$$

to be a valid expression of the local turbulent dissipation rate, and assuming that the turbulent velocities are known, it remains only to define a suitable estimate of the length-scale, ℓ . In practice, there are several means by which this may be done.

ℓ could be determined directly from integration of an energy spectrum: the energy spectrum attempts to present the mechanics of the continuum as a single mathematical function,

where the eddies' rotations are replaced by wave numbers. Energy is transferred from low wave number to high wave numbers via a complex, three-dimensional mechanism of fluid shear and eddy strain. The spectrum is calculated via a Fourier transform of the autocorrelation function, a function which itself is rooted in the statistical theory of turbulence and is a means whereby the degree of statistical independence of two particular measurements separated by continuously increasing intervals of sample time. Following Bin (1984), Tennekes & Lumley (1972), Stanley & Smith (1994) and numerous others, an estimate of the turbulent length-scale may also be made by integrating the autocorrelation function. Both the energy spectrum and the autocorrelation function are very site-specific, though ; it is generally necessary to perform such analyses at numerous locations throughout the region of turbulent flow in order to define the degree of spatial variation in l .

In general, the roster of possible length-scales is very large, and there is often considerable difficulty (if not outright impossibility) in calculating them. For this study, highly mathematical approaches were generally rejected in favour of a much simpler yet valid approach whereby l could be related conveniently to the physical dimensions of the experimental apparatus.

However, before presenting this simplified approach, it is important not to reject turbulence theory without first noting a few important points:

- the energy spectrum aptly depicts the phenomenon of turbulence as a continuous devolution of energy to eddies of ever decreasing size ; the very fact that only a single estimate of the length-scale is usually applied in a typical attempt to define the local turbulence state indicates how imprecise (in one sense) a science the study of turbulent flows is.
- the autocorrelation function finds great usefulness in allowing the effects of purely random turbulence to be separated from some externally imposed turbulence, such as that applied by the passage of the impeller's blade

Although some researchers' have attempted to extract this purely random component of turbulence from their velocity measurements, there are other factors to consider, such as measurement location and the type of impeller. In certain cases, there may be shown to be very little use in performing such an analysis. In this study, autocorrelations were performed periodically in the vicinity of the blade in order to determine whether or not the passage of the blade was artificially influencing the local turbulent state. Generally, it was found that the Ecodyne impeller produces a negligible amount of periodic turbulent fluctuation, even immediately adjacent to the impeller's blades, thereby precluding the need for decomposition of the measured turbulent velocities into their random and periodic components. It is speculated that because this impeller has ten blades, there is simply insufficient time between passages of the blade for the turbulent velocity to be affected. In contrast, for a two-blade paddle stirrer, *e.g.* Stanley & Smith (1994), there can exist a significant difference between the total and purely random turbulence, a difference that becomes greatly accentuated as the velocity measurement point is moved closer to the impeller's blade.

For impeller-agitated flows, given that it is reasonable to describe the flow as a succession of ever smaller eddies, and recognizing further that the impeller is in fact the starting

* *e.g.* Gunkel & Weber (1975), Wu & Patterson (1989)

point of this succession of eddies, intuition seems to implicate a close connection between the dimensions of the impeller and the size of the largest eddies in the turbulent flow. If the turbulent length-scale, ℓ , could be correlated satisfactorily to some relevant dimension of the impeller, such as d or b , the analysis of the local dissipation rate would be greatly simplified. Actually, the correlation of ℓ to the impeller's blade height, b , is well established in the literature.

In a summary of the results of numerous other researchers in defining the turbulent length-scale, Wu & Patterson (1989) stated that:

*the three components of the scales [the r , θ and z directions]
have about the same order of magnitude, ranging from about
0.25 to 0.50 b throughout the impeller stream*

From Laufhutte & Mersmann (1985), it is assumed that the length of a Taylor eddy, λ , may be related to "a typical length of the turbulence-generating device", so that

$$\lambda \propto \sqrt{\frac{r v}{u'}}$$

where

$$\ell \propto d_{\text{impeller}}$$

Similarly, Bin (1984) stated that the scale of the energy containing eddies, L_e , may be related to an integral, turbulence-based length-scale:

$$L_e \propto \frac{\Lambda_f}{0.75}$$

where Λ_f , the integral length-scale "can be assumed to be proportional to the impeller diameter". Furthermore, Placek & Tavlarides (1985) assumed that $\ell \approx 0.14 d$ for a Rushton turbine, which translates to $\ell \approx 0.7 b$ for the typical geometry of such turbines. Finally, based upon an extensive review of numerous other researchers' data, Kresta & Wood (1991) concluded that the width of the swirling radial jet is practically equal to b at the impeller's periphery.

Since a turbulent jet, by its very nature, represents a means of turbulence production at a source (the nozzle), and a subsequent means of turbulent dissipation, then presumably there should exist some relationship between the properties of the impeller and the resultant dissipation rate in the jet, somewhere downstream of the nozzle. In principle, this should hold true regardless of whether the turbulent jet is impeller-generated or free. Perhaps the clues to such a connexion may be found in Antonia, Satyaprakash & Hussain (1980), who studied the production of energy dissipation in freely discharging circular and plane jets. Given the apparent appropriateness of the expression

$$\epsilon = k \frac{u'^3}{\ell}$$

they set about defining some relationship between the overall dimensions of the jet (as defined both by initial conditions and local fluid-mechanical exertions).

At the core of their approach was the fact that the ratio of the measured local turbulent velocity to the measured local average velocity was observed to be constant everywhere along the axis of the jet, i.e.:

$$\frac{u'}{u} = \text{constant}$$

If the fluctuating turbulent velocities may be shown to be constant in the longitudinal direction, then it may also be shown that the local turbulent velocity fluctuations, expressed by a turbulence-based Reynolds number, R_t , may theoretically be related to some local average-velocity-based Reynolds number, R_{local} , in the following manner:

$$R_t = A_1^2 \left(\frac{15}{A_2^2} \right)^{1/2} R_{local}^{1/2}$$

where A_1 and A_2 are experimental constants, and where

$$R_t = \frac{u' \ell}{\nu}$$

$$R_{local} = \frac{u \Lambda}{\nu}$$

However, since jet-width Λ and local average velocity u may be shown to vary along the axis of the turbulent jet as

$$\Lambda \propto \left(\frac{x}{d} \right)^1$$

$$u \propto \left(\frac{x}{d} \right)^{-1}$$

and since u'/u is approximately constant, the local turbulence-based Reynolds number, R_t , may be related to a source Reynolds number, R_o . R_o is defined only by the momentum flux through the nozzle, in the following manner:

$$R_t \propto \sqrt{R_o} \left[A_1^2 \left(\frac{15}{A_2^2} \right)^{1/2} \left(\frac{k_1}{k_2} \right)^{1/2} \right]$$

$$\propto \sqrt{R_o} \propto \sqrt{k_{local}}$$

Decomposing these Reynolds numbers, the ratio between ℓ and Λ may now be shown:

$$R_t \propto R_{local}$$

$$\frac{u' \ell}{\nu} \propto \frac{u \Lambda}{\nu}$$

$$k u \ell \propto \sqrt{c_1 u_o \left(\frac{x}{d} \right)^{-1} c_2 d \left(\frac{x}{d} \right)^1}$$

$$k u_o \left(\frac{x}{d} \right)^{-1} \ell \propto \sqrt{c_1 c_2 u_o d}$$

But, as k , c_1 , and c_2 are physical constants, and as d and u_o are invariant source parameters, this expression may be simplified to:

$$\ell \propto \left(\frac{x}{d}\right)^1$$

This expression is immediately comparable to the spread of the total jet-width, Λ :

$$\Lambda \propto \left(\frac{x}{d}\right)^1$$

so that

$$\frac{\ell}{\Lambda} = \frac{c_3 \left(\frac{x}{d}\right)}{c_4 \left(\frac{x}{d}\right)} = \text{constant}$$

which shows that both the total jet-width, Λ , and the turbulence length-scale, ℓ , are found to depend only upon the dimension of the initial turbulence-generating device.

Now, as it has been shown that near the impeller's blade

$$\Lambda \sim b$$

and recognizing further that the size of the largest turbulent eddies that are created by the impeller must be of the order of

$$\ell \sim 1/2 \, b$$

it may be concluded that the **turbulent length-scale anywhere within the free turbulent jet may be approximated by 1/2 of the total jet-width.**

Indeed, the analysis presented by Antonia, Satyaprakash & Hussain (1980) provides sufficient justification to replace the local turbulence microscale, ℓ , with the easily measured local parameter $1/2\Lambda$, the jet's $1/2$ -width. Although it cannot be stated without doubt that a similar relation must exist for the analogous case of the swirling radial jet, intuitively there seems to be reason to expect that the same correspondence would indeed hold. This should be especially true near the impeller, since the dynamic analysis of turbulent jets in general relies on the fact that a number of specific functional relationships which describe them seem to hold true for numerous types of jets, and at any scale. As such, for the purposes of this project, it will be assumed that the turbulent length-scale will vary in much the same manner. Throughout this project, the local turbulent dissipation rate, ϵ , will be estimated by the following expression:

$$\epsilon = \frac{[1/2 (u'^2 + v'^2 + w'^2)]^{3/2}}{\ell}$$

where

$$\ell = \frac{1}{2} b$$

at (or very close to) the impeller's periphery, and where

$$\ell = \frac{1}{2} \Lambda$$

throughout the region characterized by the impeller-generated jet-like flow.

Correlation of the turbulent length-scale to the overall dimensions of the turbulence-generating device is a cornerstone of ϵ -based analysis in the literature. It allows a relatively straightforward estimate of the local turbulent dissipation rate to be made, and it provides a reasonable justification therefor. Although the experimental data which were collected during this project will be presented and discussed later in this document, inspection of figure 6-4 is appropriate, as this figure illustrates that the observed variation of u'/u is indeed approximately constant in this project, for a number of structural configurations, for various scales, and for a decidedly different experimental apparatus altogether from that studied by Antonia, Satyaprakash & Hussain (1980). This would tend to support the assumed correlation of the turbulent length-scale to the impeller's blade height.

2.5 Physical and Numerical Analyses

2.5.1 Introduction

In an effort to quantify the mechanics of flow in impeller-agitated mixers, it appears that the bulk of the research has been directed toward analytical collection of laboratory data in order to express and identify what appear to be the most significant properties of the fluid's behaviour such as turbulence parameters and energy consumption data. The flow state within an impeller-agitated vessel is a highly complicated mix, where swirl, turbulence and rotation occur simultaneously in three dimensions; given this complexity, to attempt a numerical analysis would certainly be very difficult, especially in comparison with the prospect of simply collecting laboratory data. Nonetheless, given the assumed universality of the Navier-Stokes and Reynolds equations, a numerical solution must remain possible, with the only impediments to its attainment being computational ability, boundary layer specification and of course the Reynolds equations closure problem. Given an adequate closure scheme (of which many have been proposed), boundary conditions which describe observable and observed behaviour, and justifiable simplifications of the governing equations, numerical description seems to be increasing in viability.

There have been numerous attempts to predict the behaviour of impeller-agitated systems via numerical analyses, mostly within the last decade. In this project, such numerical routines were not applied directly - only certain elements of such mathematical approaches were extracted for application to this study. In this manner, such mathematical approaches, even when not used in their entirety, are still extremely useful. Moreover, because the various energy-based phenomena and physical characteristics of the flow that are expected and ultimately observed are often contained explicitly in the various formulae, such mathematical approaches can serve as very useful tools of prediction. This can help the researcher to anticipate the behaviour of the particular system of concern. An analysis of a number of such attempts follows.

2.5.2 Historical Review

Representing a further application of the fundamental nature of the Navier-Stokes equations to the agitation problem, the description of impeller-generated flow as jet flow has received considerable attention. DeSouza & Pike (1972), in an early study, attempted to apply the concept of a swirling tangential jet to the problem of impeller-agitated mixing. They believed that such a complicated flow condition could not be described as a single region, thereby precluding the derivation of a single, closed solution. Instead, they proposed that a typical tank be subdivided into several regions wherein appropriate solutions could be obtained through the

application of different concepts of fluid mechanical analysis as necessary.

Of these, three zones within the tank can be identified as most significant. Firstly, they suggested that the flow at the impeller be modelled as a tangential jet. Under slightly idealized conditions, for the analysis of the tangential jet, the Navier-Stokes equations can be reduced to

$$\begin{aligned} \frac{\partial}{\partial r} r v_r + r \frac{\partial}{\partial z} v_z &= 0 \\ v_r \frac{\partial v_r}{\partial r} + v_z \frac{\partial v_r}{\partial z} - \frac{a^2}{r(r^2 - a^2)} v_r^2 &= -\frac{1}{\beta} \frac{\sqrt{r^2 - a^2}}{r} \frac{\partial}{\partial z} |\tau| \end{aligned}$$

Combining these equations with Prandtl's second hypothesis, and together with certain boundary conditions, one may perform a similarity solution such that the jet's velocity profile may be described completely:

$$\begin{aligned} v_r &= v_{r \max} \left[1 - \tanh \frac{\eta}{2} \right] \\ v_z &= \frac{-v_{r \max}}{\sigma} \left[\frac{2r^2 + a^2}{r^2 - a^2} \tanh \eta - \eta \left(1 - \tanh^2 \frac{\eta}{2} \right) \right] \\ v_{r \max} &= \frac{1}{2} A \left(\frac{\sigma}{r^3} \right)^{\frac{1}{2}} (r^2 - a^2)^{\frac{1}{4}} \\ \eta &= \sigma \frac{z}{r} \end{aligned}$$

The details of the derivation and solution may be found in, *e.g.* Rajaratnam (1975). Thus, the impeller discharge field is described by three parameters, σ - a jet width similarity parameter, A - a volumetric flow rate parameter that depends upon influent momentum, and a - the radius of the source. Geometrically, the impeller's discharge may be expressed as

$$Q = 4 \pi A \left(\frac{\sigma}{r^3} \right)^{\frac{1}{2}} (r^2 - a^2)^{\frac{1}{4}}$$

Secondly, they suggested that the return flow along the centre of the impeller's axis be modelled as a turbulent circular jet, for which numerous solutions have been developed, *e.g.* Rajaratnam (1975). Thirdly, they identified the presence of doughnut-shaped dead zones which represent stagnant zones between the impeller flow and the return (vertical) flow. Although these zones are not stagnant *per se* as the actual impeller would impart a peripheral velocity in the θ direction, insofar as their steady-state model is concerned, they are stagnant. Using a three-dimensional Pitot tube, velocities were collected in order to confirm their assumed model. They found that their two-dimensional tangential jet model accurately described the flow in the impeller stream, and that the resultant discharge could be correlated with the quantity ωd^3 , thus indicating that the tangential jet model and bulk-parameter N_{js} , though fundamentally different, are both somehow related, thereby conferring some degree of legitimacy upon the flow number. In the bulk of the tank, their model was observed to be less representative, probably because the predicated assumption of a dominant turbulent jet is violated. This, however, relates directly to the concepts of isotropy and turbulent dissipation, concepts that are of decidedly fundamental importance in describing the dynamics of impeller-agitated mixing.

Hiraoka & Ito (1975) treated the impeller flow as a jet and presented simplified forms of the Reynolds equations in an effort to prove analytically the relationship between input power and jet-flow rate. According to their analysis, without large error, it may be approximated that

$$\rho \int_0^h | r^2 u w |_r dz = \int_0^h | r^2 \tau_{r\theta} |_R dz$$

Upon examination, it may be seen that the left hand side represents the angular momentum transferred from the jet to the peripheral direction, and that the right hand side represents the torque from the sidewall of the vessel. Assuming that the peripheral velocity v would equal the speed at the edge of the impeller, this is further simplified to

$$\frac{\pi}{2} D^2 h \overline{\tau_{wall}} = \rho r (r\omega - v_d) Q$$

where v_d represents the angular velocity at the point where the radial velocity is just less than zero. Introducing from their own work the experimental result that $(r\omega - v_d)$ is proportional to the square root of the wall stress, one may isolate an expression for Q , the impeller jet-flow

$$Q = \frac{\pi}{10} \frac{D^2 h}{d} \sqrt{\frac{\tau_{wall}}{\rho}}$$

Now, assuming that all the input power is dissipated in wall friction, one could very approximately state that

$$\frac{\tau_{wall} \pi d^2 h r \omega}{\rho \omega^2 d^5} = N_p$$

in order to show that

$$N_q \propto \sqrt{\frac{D^2 h}{d^3}} \sqrt{N_p}$$

where the constant of proportionality depends upon the geometry of the system being studied. Although their equations are very simplified with respect to local dissipation and three-dimensional flows, they nonetheless seem to justify the use of dimensionless parameters such as the power number in the hydromechanical analysis of impeller-agitated systems, further implying the relevance of energy and power in any analysis.

Pursuing a more purely mathematical course, Curev (1980) analysed turbine-impeller-agitated flows by treating them as submerged cylindrical tangential jets. By applying Prandtl's second hypothesis

$$\bar{\tau} = \rho k s(r) |\bar{v}_{\max}| \frac{\partial \bar{v}}{\partial z}$$

and streamline theory, he was able to collapse the set of simplified Reynolds equations down to a single ordinary differential equation which was amenable to a similarity solution. Specifically, for a dimensionless similarity variable χ which describes the distance across the jet, he determined that the velocity profile across the jet for a particular radial location may be defined by

$$f(\chi) = 1 - \frac{\chi^2}{2} + \frac{\chi^4}{12} - \frac{\chi^6}{72} + \frac{\chi^8}{504} - \frac{5\chi^{10}}{18144}$$

For the spatial variation of the jet-velocities, by assuming similarity of velocity profiles, it was also shown that:

$$\begin{aligned} v_r &= v_{r\max} f(\chi) \\ v_{r\max} &= \frac{1}{s(r)} \end{aligned}$$

where $s(r)$ is a function that defines the $1/2$ jet width, and which thus indicates the consideration of streamline theory in this solution.

Kolar, Filip & Curev (1982), in a study of a swirling radial jet with swirl, presented a solution that is similar to that of DeSouza & Pike (1972), but without the assumption of specific shapes of flow geometries that had been assumed by earlier researchers. Applying a Goertler-type solution together with Prandtl's second hypotheses, they derived the following description of the swirling radial jet's velocity field:

$$\begin{aligned} u &= \sqrt{\frac{3M_\infty}{4k\rho}} \frac{1}{x} \sqrt{\frac{x^2 - e^2}{x^2 - R^2}} [1 - \tanh^2 \eta(x,y)] \\ w &= \frac{e}{\sqrt{x^2 - e^2}} u \\ \eta &= \frac{1}{2k} \sqrt{x^2 - e^2} (x^2 - R^2)^{-1/2} y \\ M_\infty &= \int_0^\infty \rho x u^2 dy \\ N &= \int_0^\infty \rho x^2 u w dy \\ e &= \frac{N}{M_\infty} \end{aligned}$$

where η is a similarity parameter and k is a spreading rate parameter. The expressions for M_∞ and N represent the conservation of radial flux of radial momentum and the conservation of radial flux of angular momentum respectively, and the parameter e is called the swirl parameter.

Similarly, Kolar, Filip & Curev (1984) critically examined a tangential jet model to describe the high-speed turbine impeller stream in an agitated, baffled vessel. Specifically, the swirling radial jet model attempts to replace the impeller with an equivalent point source of

momentum flux whose important physical qualities - location, radius, direction, discharge and resultant momentum flux - attempt to relate the impeller's geometry to the generated jet flow. Specifically, they showed that the momentum at the source could be expressed by

$$M_w \approx (\text{const.}) \rho N_p \omega^2 d^5 \frac{1}{e}$$

which, upon introduction into a specific space-flow geometry as-defined by the governing Navier-Stokes equations, allowed them to derive:

$$q = \sqrt{\frac{c_{d/D} \omega^2 d^5}{k e}} \frac{1}{\sqrt{x^2 - R^2}} \left[1 - \tanh^2 \left(\frac{1}{2k} \frac{\sqrt{x^2 - e^2}}{x^2 - R^2} (y - r_R) - \eta_o \right) \right]$$

where q is the velocity component in the ξ direction, ξ is a tangential coordinate, and the properties of the impeller are represented by various constants in this model. This solution was expected to be an improvement over earlier models such as DeSouza & Pike (1972) as it is expressed in terms of vessel parameters and thus lacks the parametrical uncertainty that was implied by the apparent physical irrelevance of some earlier parameters, especially in the specification of a virtual origin. Experimental velocity profiles were collected for a variety of radially discharging impeller streams through the use of a five-hole Pitot tube. Generally, they observed good agreement between their experimental results and their model. However, this model's applicability was seen to be limited to the region proximate to the maximum velocity in the impeller stream, and not immediately adjacent to the impeller itself. Such a limitation strongly indicates that the influence of fluctuating velocities therein precludes any analytical method that assumes the predominance of average velocities, especially since turbulent effects were not incorporated into their swirling radial jet model. Furthermore, such a limitation also seems to indicate the fundamental importance of turbulent mixing and dissipation in any analysis of impeller-agitated mixing.

Further application of numerical theory is given by Kolar, Filip & Curev (1985), who presented a refinement of their earlier work, including the analysis of multiple swirling jets and antisymmetric (or contrarotational) swirling jets. In Filip, Kolar & Curev (1985-1), Filip, Kolar & Curev (1985-2) and Filip, Kolar & Curev (1986), the swirling radial jet analysis is expanded to include swirling wall jets and multiple jets, but with different closure techniques such as Reichardt's hypothesis and Prandtl's second hypothesis.

Kresta & Wood (1991) incorporated a number of previous studies together with numerical analysis in an attempt to model flow patterns in a tank that is agitated by a Rushton turbine. Proceeding again from a simplified set of Reynolds equations, and assuming that the flow would exhibit the qualities of a swirling radial jet, they extended Kolar *et al.*'s (1982) original model by means of κ - ϵ modelling in order to obtain direct estimates of κ and ϵ on the impeller volume's periphery, in addition to predicting the mean velocities therein as did earlier models. Their entire approach is of course based upon the assumption that the impeller stream behaves as a radial turbulent jet. Given that earlier solutions such as DeSouza & Pike (1972) and Kolar, Filip & Curev (1982) did not allow a means of estimating the local turbulence parameters, their work may be seen to represent a significant improvement. They based their selection of boundary conditions upon twenty years of previously collected data to estimate the necessary parameters for deconvolution of the similarity solution to the physical quantities of interest. In comparison to experimental data, their model was seen to predict the decay of ϵ and the local variation of κ very well.

Assuming that N_r would be constant and equal to 5, and following an energy balance around the impeller, they found that 54 percent of the input energy would be dissipated in the impeller itself, 35 percent in the impeller stream and only 11 percent within the bulk of the tank - values which demand immediate comparison to those of Cutter (1966), Gunkel & Weber (1975) and Wu & Patterson (1989) among others. The fact that approximately ninety percent of the total energy was seen to be dissipated at or near the impeller presents certain implications concerning the effects of geometry and clearances within the vessel upon the average dissipation rate therein since dissipation within the impeller zone would assumedly be near 50 percent regardless of the tank's external geometry. Specifically, they suggested that the local decay of kinetic energy κ and the local dissipation rate ϵ may be normalized as

$$\frac{\kappa}{(\pi \omega d)^2}$$

$$\frac{\epsilon}{(\pi \omega d)^3/d}$$

as opposed to the traditional practice of expressing local energy dissipation as the ratio of ϵ to the rather simple vessel-averaged quantity $P/\rho V$. In accordance with others' results, ϵ is seen to decay exponentially from the impeller, but their model seems to describe the region near the impeller faithfully given the assumed boundary conditions that were predicted by the similarity analysis.

To describe the spatial variation of the swirling radial jet, their similarity solution employed a new geometric variable, ξ , originally described by Kolar, Filip & Curev (1982), to represent the distance along the axis of the swirling radial jet.

$$\xi = \sqrt{r^2 - e^2}$$

where quantity e is described as:

$$e = \frac{\int_{-\infty}^{\infty} \rho \, 2 \, \pi \, r \, u^2 \, dz}{\int_{-\infty}^{\infty} \rho \, 2 \, \pi \, r^2 \, u \, v \, dz}$$

which may be seen to represent the ratio of the radial momentum to the angular momentum within the swirling radial jet. In this sense, e was named the "swirl parameter" by Kolar, Filip & Curev (1984). In practice, e may be fully defined for a given set of conditions from a single measurement of the radial and tangential velocities at the impeller's periphery:

$$\beta_o = \tan^{-1} \left(\frac{v_o}{u_o} \right)$$

so that e may be determined directly, from

$$e = r_o \sin \beta_o$$

which then allows coordinate ξ to be determined for any radius, r . Finally, knowing u and v (and neglecting the axial velocity, w), a vector sum of these may be made in order to define a new velocity, q , which is the local velocity along the axis of the swirling radial jet:

$$q = \sqrt{u^2 + v^2}$$

With the jet-referenced axial coordinate ξ defined, the shape of the swirling radial jet may be defined. Considering the length-scale, the width of the jet may be described by:

$$\delta(\xi) = k_1 \xi$$

and the variation of maximum jet velocity, q , may be expressed as:

$$q_{\max} = \frac{K_2}{\xi}$$

thereby predicting a *linear* growth of the length-scale, and a hyperbolic decrease in maximum velocity. Such behaviour is again found to be analogous to the case of the circular free jet proposed by Antonia, Satyaprakash & Hussain (1980).

In effect, β defines the deflection of the jet from a purely tangential flow. Although the reduction of the problem from two dimensions to a single dimension, ξ , provides a convenient descriptive framework, it is somewhat difficult to visualize exactly what ξ is. In practice, given the variability of initial conditions at the impeller's periphery (depending upon such factors as impeller type, size and rotation), depending upon the swirl parameter, e , a single impeller produces jets having entirely different values of the location parameter ξ . Therefore, ξ should not be assumed to be an absolute expression of the path of the jet, but instead should only be understood as an analytical tool, based upon an idealized situation.

In this project, certain elements of such one-dimensional, ξ -based modelling will be employed, specifically ξ and q , but only to assess the nature of the flow at the impeller's periphery with respect to swirl, and then again only for a few selected cases. An absolute definition of the impeller-generated jet's path throughout the tank is neither practical nor possible given the numerous differences that exist between the idealized situation for which such mathematical models are derived and the actual situation that was tested here.

3.0 Experimentation

3.1 Introduction

The purposes of this project are, in broad terms, twofold. Firstly, it was desired to define the general state of flow with respect to velocities and turbulence that is present within the impeller-agitated system. Secondly, it was desired to assess the effects of certain structural modifications to the draught tube - impeller system via a number of representative parameters. Both of these investigations we performed in light of an attempt to assess the overall amenability of the system to scale-up via a number of methods. In this regard, experimental investigation was undertaken at a number of different geometric scales.

3.2 Apparatus

3.2.1 Dimensions, Scaling & Structure

Experimentation in this project may be divided into four distinct components. The first three components correspond to testing that was performed on models of three different geometric scales for the case of no tangential inflow to the draught tube. The fourth component represents one of the same geometric scales from before, but it includes the effect of a non-zero tangential inflow. In the first two of these components, the experimental apparatus was constructed to enable a great amount of flexibility in defining the geometric properties of the tube -impeller system.

There were three model-scales that were tested in this project: 1:55.647, 1:41.130 and 1:10. The first two scales have non-integral values because it was necessary to employ commonly available materials of standard sizes, invariably measured in British units, and which obviously have no necessary relation to the dimensions of the full-scale impeller -for convenience, these scales are referred to as 1:55 and 1:41 throughout this report. The 1:55 and 1:41-scale models were constructed specifically for this study. Whereas these two smaller-scale models are representations of the impeller and draught tube only, with no externally applied inflow, the 1:10-scale model represents a faithful reproduction of the entire clarifier, complete with a tangential inflow pipe, flocculation zone, settling zone and perforated launders. This model resides in the hydraulic laboratory of Northwest Hydraulic Consultants Ltd. (NHC) in Edmonton, and it is the same one that was studied by NHC in 1993 - NHC (1993). Considering the three scales, it is found that a common element exists only in the draught tube, the skirt and the impeller itself. At all three scales, these features of the clarifier were reproduced from the full-scale under the tenets of the maintenance of 100 % geometric similarity insofar as possible. Table 3-1 summarizes the general features of the three models that were examined in this study.

Table 3-1
general properties of the scale-models

nominal scale	actual scale	general properties
1:55	1:55.647	flat-bottomed tank, no tangential inflow pipe, removable skirt & draught tube, removable floor of draught tube, baffles were installed later
1:41	1:41.130	flat-bottomed tank of the same size as that for 1:55 model, no tangential inflow pipe, removable skirt & draught tube, removable floor of draught tube, no baffles

NHC	1:10	sloping floor, operational tangential inflow pipe, removable skirt and draught tube, removable floor of draught tube, no baffles, flocculation zone, inclined tube settlers, perforated launders
-----	------	--

The relevant dimensions for the full-scale impeller and draught tube were obtained from a variety of sources including firsthand inspection of the full-scale facility while it was temporarily inoperational for maintenance purposes, original design drawings, NHC's 1993 report and NHC's project file. For illustrative purposes, a number of photographs of the full-scale system have already been presented - see Photographs 1-1 through 1-3. After considering these numerous sources together with the limitations implied by the available materials (*e.g.* it was impossible to scale certain thicknesses exactly using acrylic pipe at such small scales), a final set of dimensions was defined for the impeller, draught tube and skirt - these dimensions are summarized on Figures 3-1 and 3-2. The placement of the impeller off the floor, the placement of the draught tube, and the height of the skirt were deliberately maintained throughout this project at the specific locations defined by the full-scale structural data.

The models themselves were constructed from a variety of materials: for the 1:55-scale model, the impeller was constructed from stainless steel, and the draught tube and skirt were constructed from transparent acrylic or polycarbonate; for the 1:41-scale model, the impeller was a hybrid of a stainless steel impeller and an acrylic shaft, and the draught tube and skirt were again constructed of transparent acrylic or polycarbonate; the 1:10-scale NHC model was constructed slightly differently - details may be found in NHC's 1993 report. Whereas the 1:10-scale model was housed in geometrically accurate full-sized tank, the 1:55 and 1:41-scale models were housed, due to spatial limitations, in plexiglass tanks of similar dimension, each approximately 0.345 m by 0.340 m - it may be seen that this size actually represents a geometrically consistent reduction of the full-scale baffle walls when scaled by $\lambda = 55.647$. For all scales, the skirt and draught tube could be removed or adjusted easily, thereby enabling numerous combinations of the of the structural system, including a free impeller, variant skirt heights, and variable orifice openings. The impellers in the 1:55 and 1:41-scales were turned by a variable-speed motor controlled by an adjustable-voltage power supply, enabling angular velocities anywhere from 1 to 1000 revolutions per minute (rpm) to be maintained. Angular velocities were measured by means of a hand-held Digitach tachometer. The 1:10-scale impeller was also turned by a variable-speed motor, which allowed angular velocities over 100 rpm to be attained. All connections of the impeller's shaft to the motor were via flexible couplings to eliminate the effects of eccentricity in the smaller-scale models. Finally, the entire tank, draught tube and impeller system for the 1:55-scale and 1:41-scale could be mounted on a milling machine table so that the convergence point of the laser doppler measurement system could be moved in any direction, radially, vertically or laterally. A number of illustrative photographs describing the models are presented in Photographs 3-1 through 3-6.

3.3 Measurement

3.3.1 General

For the 1:55 and 1:41-scales, two-dimensional velocity measurements were performed with a 300 mW argon laser manufactured by Ion Laser Technology. The laser beams were passed through a Dantec LDA Laser Doppler Anemometry system of prisms, and the signal was connected to a Dantec PDA Particle Dynamics Analyzer receiving optics system. Each of the two beams was split through a Bragg cell where the frequency of one of the resultant beams was shifted by 40 MHz in order to determine direction of the flow. Operation of the entire system was governed via interactive computer software also provided by Dantec. Software which allowed the

rapid assessment of a variety of parameters, including average and turbulent velocities, energy spectra and Eulerian autocorrelation functions. Moments were calculated by means of a residence-time weighting scheme to eliminate velocity bias.

Although the laser was capable of measuring only in two dimensions (specifically, in a horizontal plane and in an orthogonal vertical plane), accurate three-dimensional velocity measurements could be fabricated given the fact that the convergence point of the two laser beams could be moved to any point within the tank. Under the assumption of a tangentially invariant flow field within the draught tube, by collecting data at any two points lying on the same horizontal plane, at the same radius, and separated by an angle of 90° , it may be shown that from every two sets of two-dimensional velocity data that are collected, one can obtain two measurements of axial velocities w and w' , and one measurement each of radial velocities u and u' and tangential velocities v and v' .

To measure velocities in the 1:10 NHC model, a Nixon propeller meter attached to a Novonic StreamFlow processor was used. Given the spatial limitations present in the NHC model, only the radial (u) and tangential (v) velocities could be measured. This current meter was calibrated by means of a velocity measurement across a rectangular flume under the conditions of steady flow. Consistent vertical location of the current meter was ensured by mounting the meter to a movable point gauge, and radial locations were maintained by referencing the radial position to a fixed reference point.

Finally, to measure the impeller's power consumption at the 1:55 and 1:41 scales, torque was measured with a model TRPA5 Rotary Parallel Shaft torque transducer manufactured by Industrial Measurements Ltd. of Melbourne, Derby England. This device was connected to a special conditioning unit which gives readout in N·m directly. The manner in which the measured torques were converted to power consumption is addressed in detail in section 4.3 of this document.

3.3.2 Location

In order to preserve a geometrically consistent means of spatial location both within and among the various scales, it was necessary to devise a system of dimensionless locational parameters whereby a particular radial (r) or axial (z) location could be duplicated at any scale. This relatively simple task was performed for the radial location by normalizing a given radial coordinate by the impeller's diameter. For the axial location, the particular vertical coordinate was first referenced to the top of the impeller, which was assigned a location of $z = 0$, and it was assumed that all elevations above the top of the impeller were positive ($+z$) and that those below were negative ($-z$). These z -values were then normalized by the impeller's blade height, b . Consequently, all dimensionless locations are specified throughout this study by the following parameters:

$$\begin{aligned} \text{radial:} & \quad \frac{2r}{d} \\ \text{axial:} & \quad \frac{z}{b} \end{aligned}$$

whereby maintenance of $2r/d$ and z/b at constant values among the various scales guarantees consistent maintained spatial locations. It was not necessary to define a similar system for the tangential (or angular) location, θ , since θ is already dimensionless. θ -invariance was assumed for every trial except the 1:10-scale NHC trials, where θ was assigned a value of 0 at a point lying near the tangential entrance on a line running parallel to the centreline of this tangential entrance ; θ is defined as increasing in a counterclockwise direction when viewed from above.

The consistently maintained radial locations that were employed in this study are presented in Table 3-2, and the orientation of the tangential location system is depicted in Figure 3-2.

Table 3-2
Summary of dimensionless radial locations used in the various trials
 (✓ denotes point where velocity measurements were performed)

2r/d	configurations:							comments
	01	02	03	04	05	06	NHC	
1.000								edge of impeller's blade
1.044	✓	✓	✓	✓	✓	✓		nearest measurement point to impeller
1.070							✓	nearest point to impeller - NHC only
1.175	✓	✓	✓	✓	✓	✓	✓	-
1.304	✓	✓	✓	✓	✓	✓	✓	final location within draught tube
1.409								inside wall of draught tube
1.567								free impeller only
2.089	✓							free impeller only
2.611	✓							free impeller only

3.3.3 Model Configurations & Operational Parameters

Data collection proceeded according to a fixed schedule of trials. Each trial was intended to allow some aspect of the apparatus on the resultant hydraulic condition to be investigated. Each trial was run at anywhere from one to five separate angular velocities, with three-dimensional flow being determined in each trial. In total, through the various trials, six different configurations were studied in this project, many at two different scales. The various configurations are depicted in Figures 3-3 through 3-8. In addition, a series of trials was performed for the 1:41-scale model where, beginning with configuration 03, the depth in the tank and the size of the orifice opening were varied simultaneously - collectively, this trial was called B-ANN. For the 1:55-scale and 1:41-scale models, individual trials are identified by prefixing the number of the configuration by either A or B, where A refers to the 1:55-scale model and B refers to the 1:41-scale model. In general, the effect of scale between the 1:55 and 1:41-scale models is immediately available by comparing the results of any two trials having the same suffix, *e.g.* A02 and B02. For the 1:10-scale NHC model, a slightly different numbering system was employed. Although the NHC model may be seen to represent configuration 03, the individual trials are referred to as NHC trial 1, NHC trial 2 and NHC trial 3, reflecting the fact that the NHC model was run at three different discharges.

The relevant features of each trial may be expressed by the following table, Table 3-3.

Table 3-3
Summary of experimental conditions - all configurations & all scales

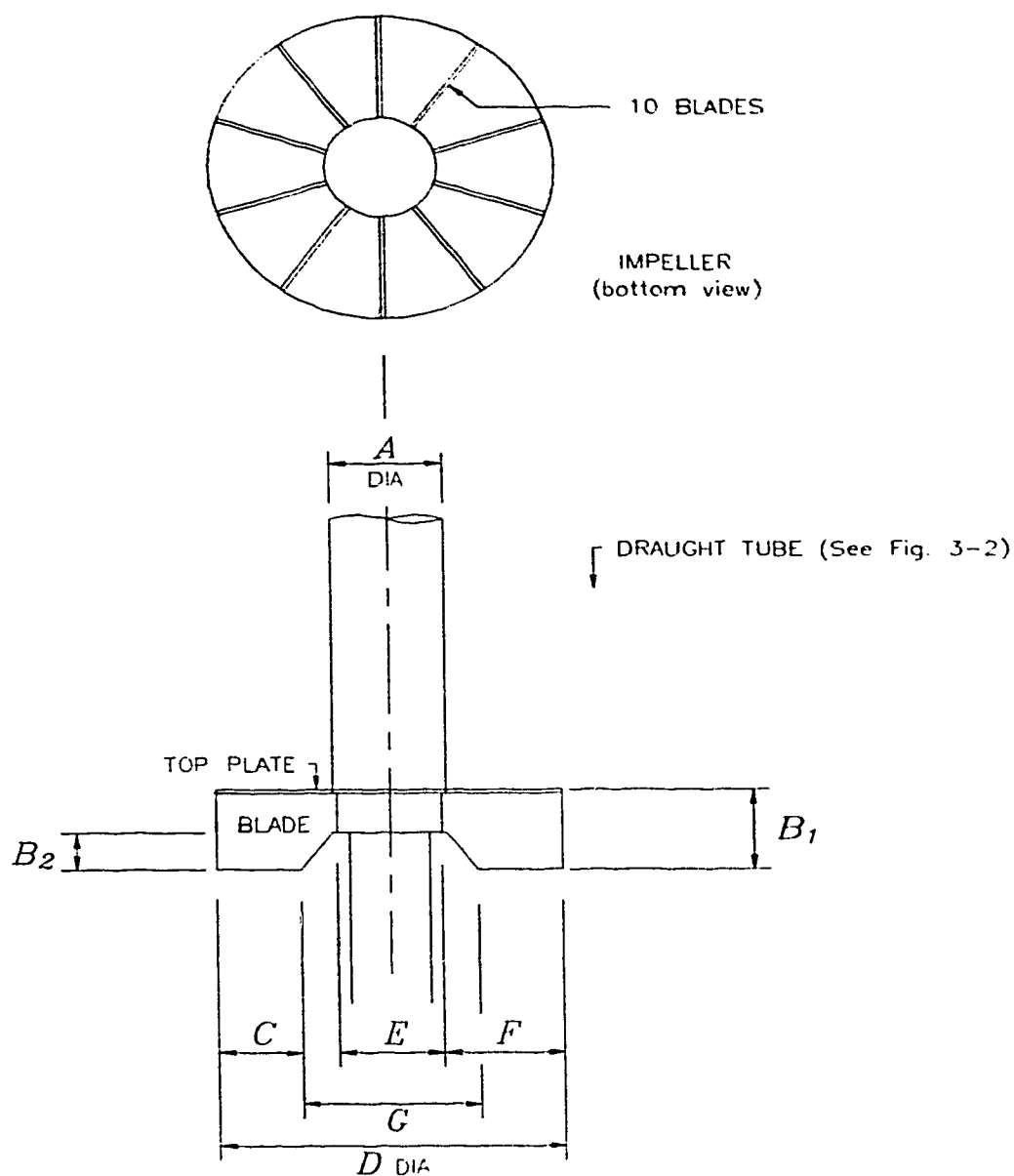
scale	configuration	trial	depth (m)	influent Q (l/s)	free impeller	draught tube	as-built skirt	lowered skirt	buffer	as-built outlet	large outlet
1:55	01	A01	0.127	-	✓						
1:55	02	A02	0.127	-		✓				✓	
1:55	03	A03	0.127	-		✓	✓			✓	
1:55	04	A04	0.127	-		✓		✓		✓	
1:55	05	A05	0.127	-		✓	✓		✓	✓	
1:41	02	B01	0.172	-	✓						
1:41	02	B02	0.172	-		✓				✓	
1:41	03	B03	0.172	-		✓	✓			✓	
1:41	06	B06	0.172	-		✓					✓
1:10	03	trial 1	0.71	-		✓	✓			✓	
1:10	03	trial 2	0.71	7.9		✓	✓			✓	
1:10	03	trial 3	0.62	4.0		✓	✓			✓	

The operational depths and associated inflow discharges, Q_i , for NHC trials 2 and 3 were scaled directly from the depths employed by NHC (1993). These depths correspond to full-scale inflows of 200 Mℓ/d and 100 Mℓ/d, which represent the relevant design conditions for the full-scale facility. Generally, the operational depths for all trials A and B, and NHC trials 1 and 2 were set at the depth corresponding to 200 Mℓ/d (with appropriate scaling, of course). Only trial 3 was run at a different depth, the depth corresponding to the case of $Q_i = 100$ Mℓ/d. Given that the full-scale tank and NHC 1:10-scale models had sloping floors, but that the 1:55-scale and 1:41-scale models had flat-bottomed tanks, the reported depths represent the depth above the floor at the edge of the skirt ; in the case of the free impeller (configuration 01), or the case where no skirt was installed (configuration 02), this depth was nonetheless maintained in the interest of consistency.

The intended purposes of all trials may now be summarized:

Table 3-4
intended effects of configurational and operational changes

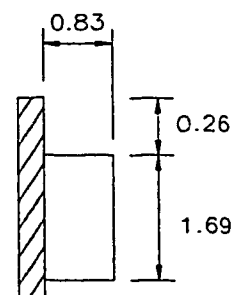
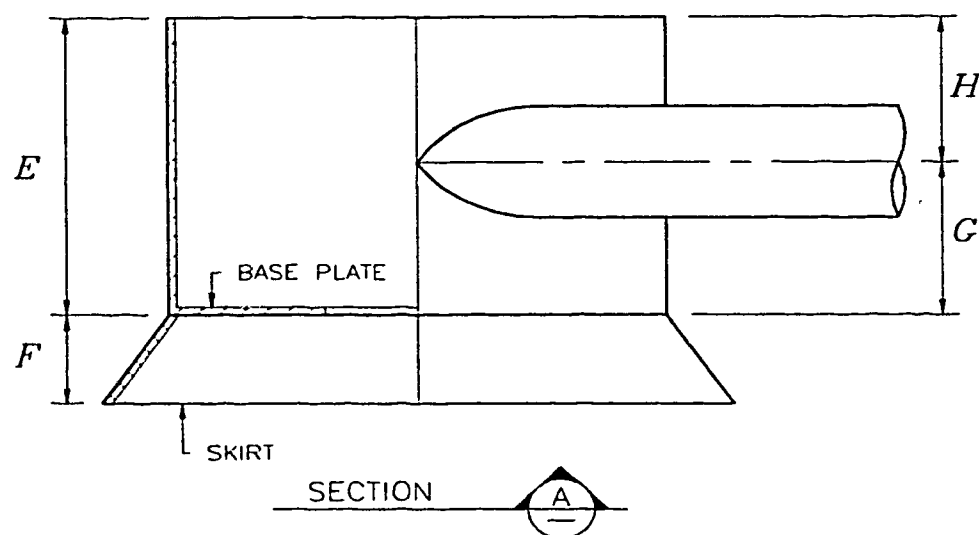
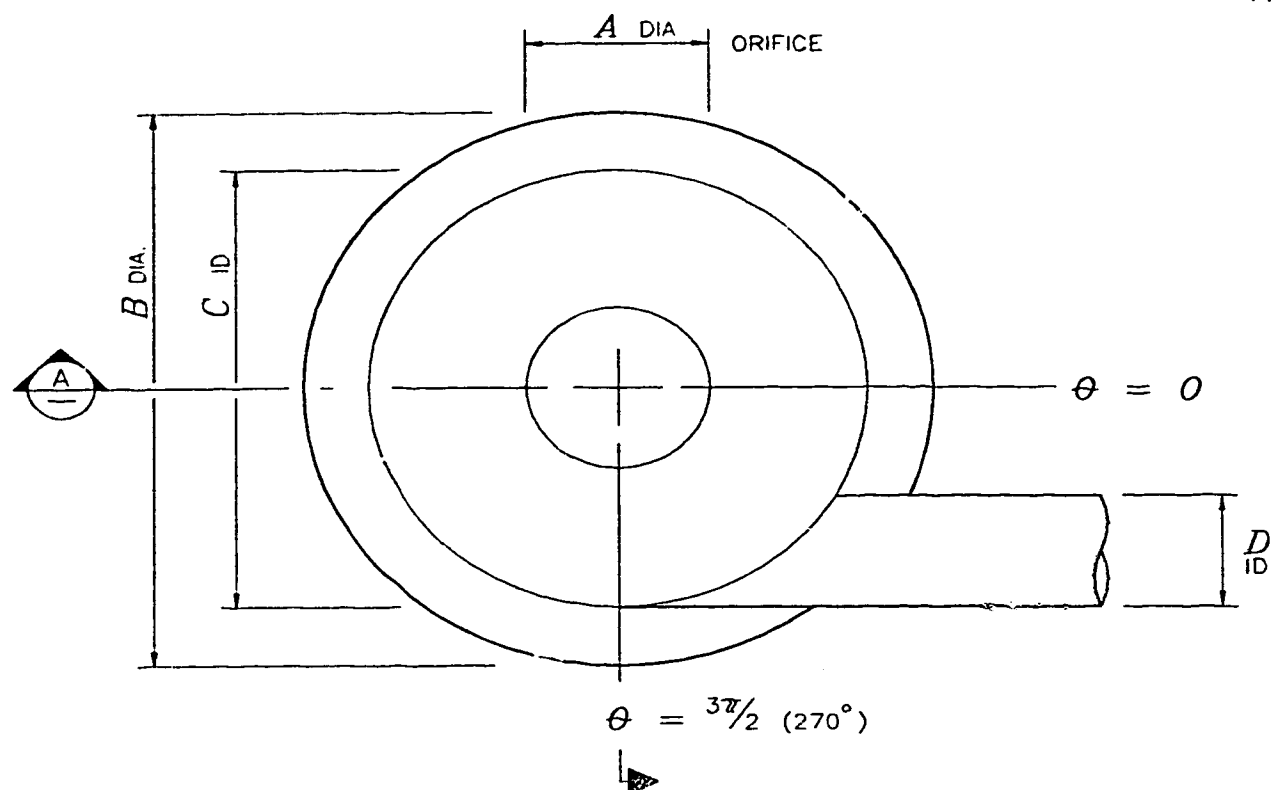
configuration	intended effect or distinctive feature
01	free impeller
02	illustrates effect of draught tube
03	illustrates effect of as-built skirt
04	illustrates effect of lowered skirt opening
05	illustrates effect of draught tube baffles
06	illustrates effect of enlarged orifice
B-ANN	illustrates effect of depth and enlarged orifice together
NHC trial 1	illustrates effect of zero tangential inflow
NHC trial 2	illustrates effect of 200 Ml/d tangential inflow
NHC trial 3	illustrates effect of 100 Ml/d tangential inflow



Dimension	1:55.647	1:41.13	1:10	full-scale
A	2.46	3.33	14.0	136.9
B_1	1.94	2.63	10.8	108.3
B_2	0.94	1.27	5.30	53.35
C	1.85	2.50	10.3	102.9
D	7.66	10.37	42.7	426.7
E	1.95	2.64	10.7	106.7
F	2.86	3.87	16.0	160.0
G	3.97	5.37	22.1	221.0
FLOOR * OPENING	0.82	1.11	4.6	45.72

* For trial A04 only, floor opening is 0.55cm

FIGURE 3-1
IMPELLER DETAILS
All dimensions in centimetres



BAFFLES
(Trial AO5 only)

Dimension	1:55.647	1:41.13	1:10	full-scale
A*	4.000	5.37	22.10	221.0
B	13.700	18.50	76.00	760.0
C	10.795	14.60	60.10	600.7
D	-	-	15.20	152.0
E	7.300	9.88	40.60	406.4
F	1.910	2.61	10.65	106.5
G	-	-	20.80	208.3
H	-	-	19.80	198.1

* For trial B06 only, $A \approx 7.9\text{cm}$

FIGURE 3-2
DRAUGHT TUBE DETAILS
All dimensions in centimetres

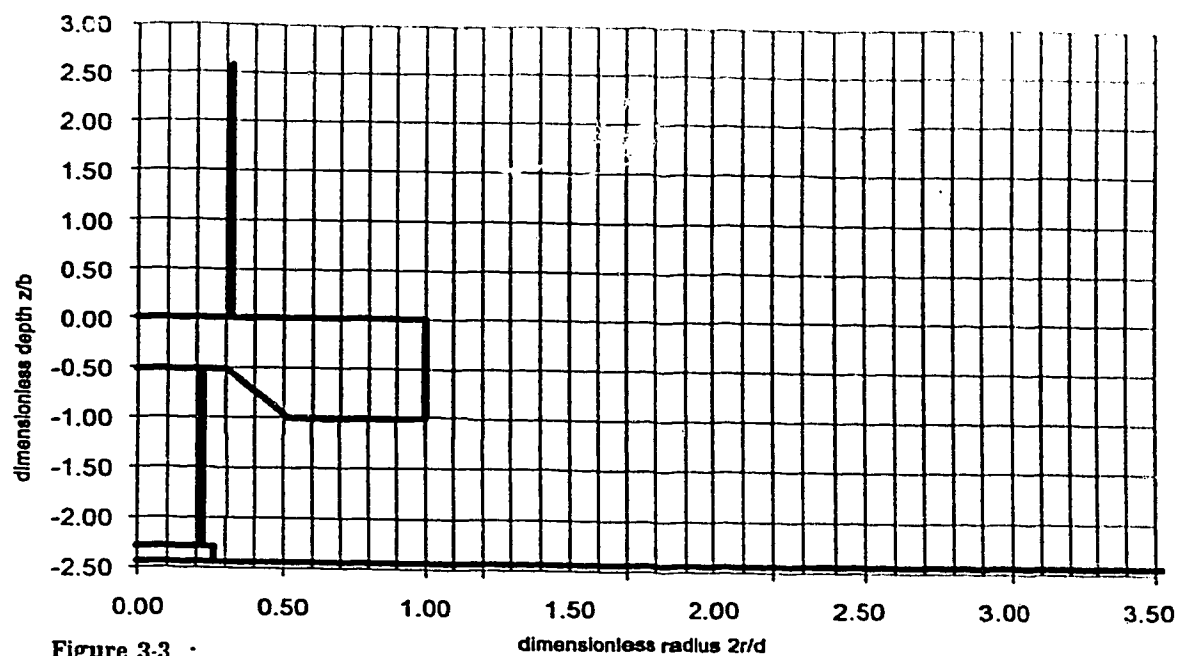


Figure 3-3 :

configuration 01 - trials A01 & B01
unconfined impeller
 $d=7.66 \text{ cm} \text{ \& } 10.37 \text{ cm}$; $b=1.94 \text{ cm} \text{ \& } 2.63 \text{ cm}$

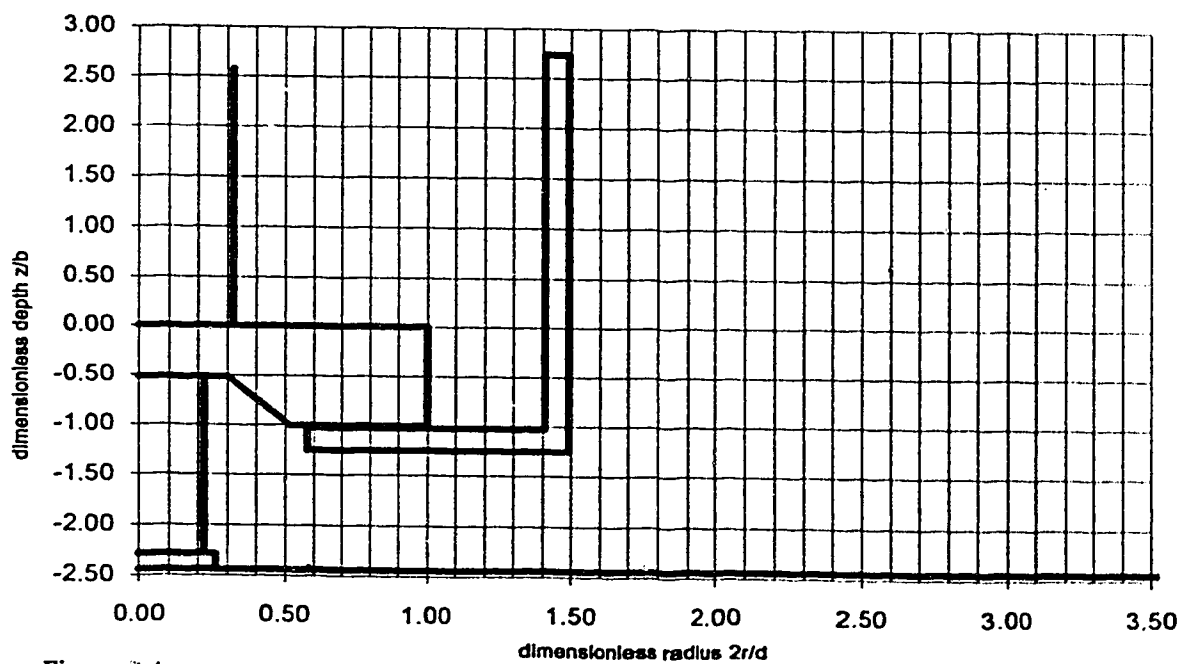


Figure 3-4 :

configuration 02 - trials A02 & B02
no skirt
 $d=7.66 \text{ cm} \text{ \& } 10.37 \text{ cm}$; $b=1.94 \text{ cm} \text{ \& } 2.63 \text{ cm}$

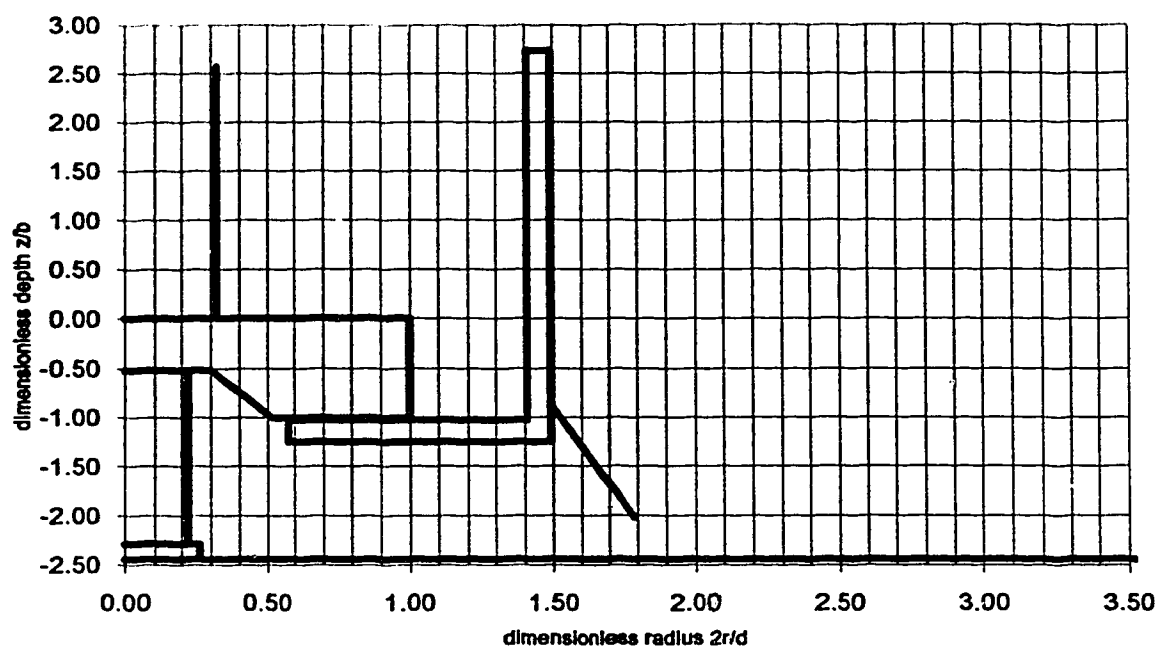


Figure 3-5 :

configuration 03 - trials A03 & B03 & nhc model
originally constructed
 $d=7.66$ cm, 10.37 cm & 42.62 cm ; $b=1.94$ cm, 2.63 cm & 10.8 cm

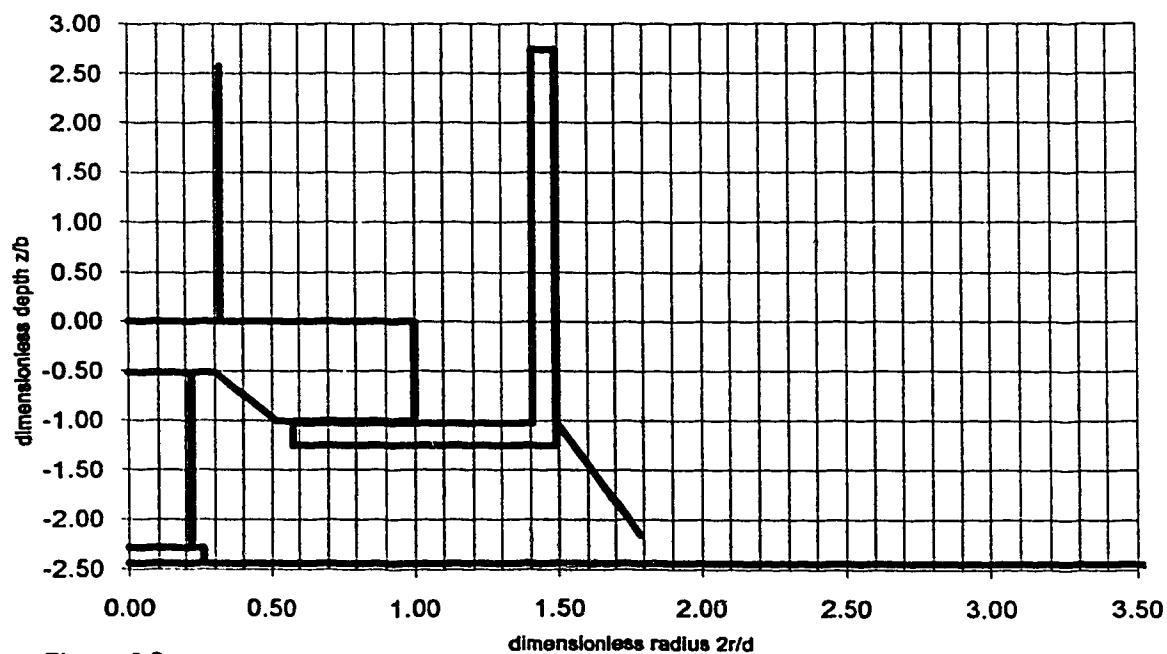


Figure 3-6 :

configuration 04 - trial A04 only
nhc's as-modelled skirt opening
 $d=7.66$ cm ; $b=1.94$ cm

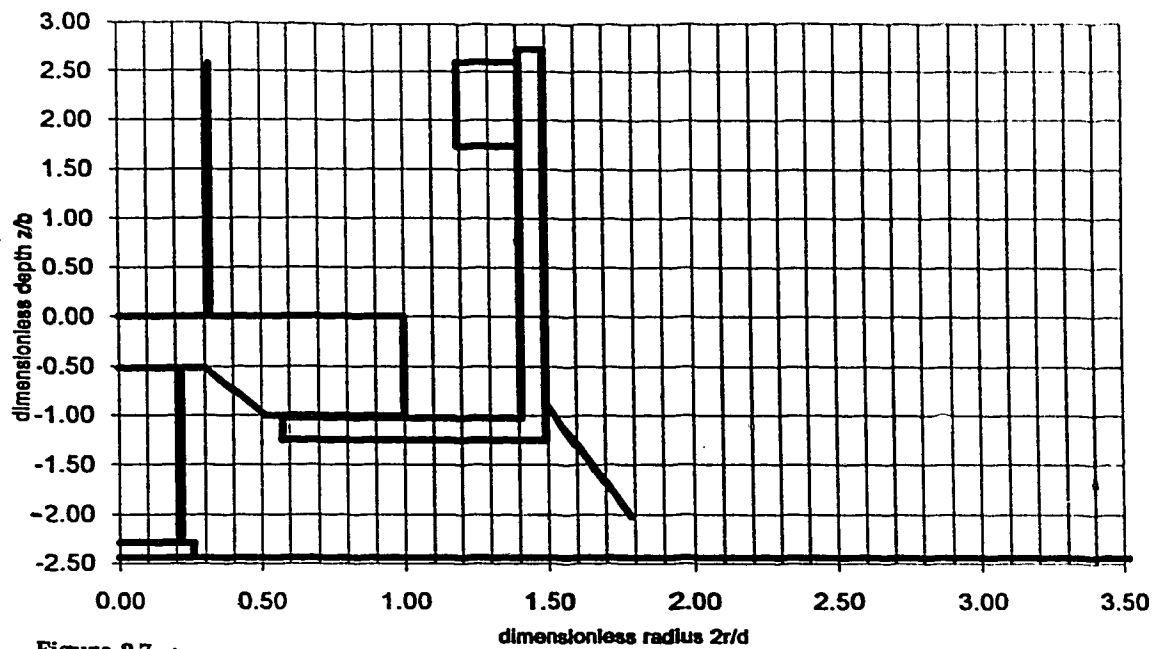


Figure 3-7 :

configuration 05 - trial A05 only
draught-tube baffles
 $d=7.66$ cm ; $b=1.84$ cm

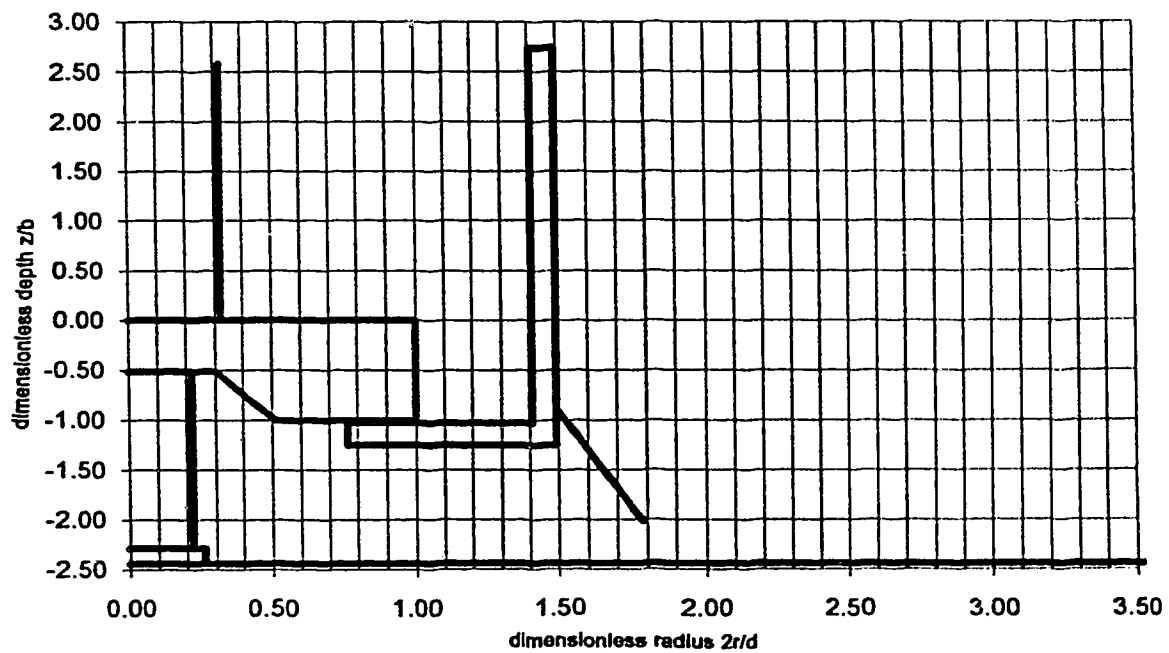


Figure 3-8 :

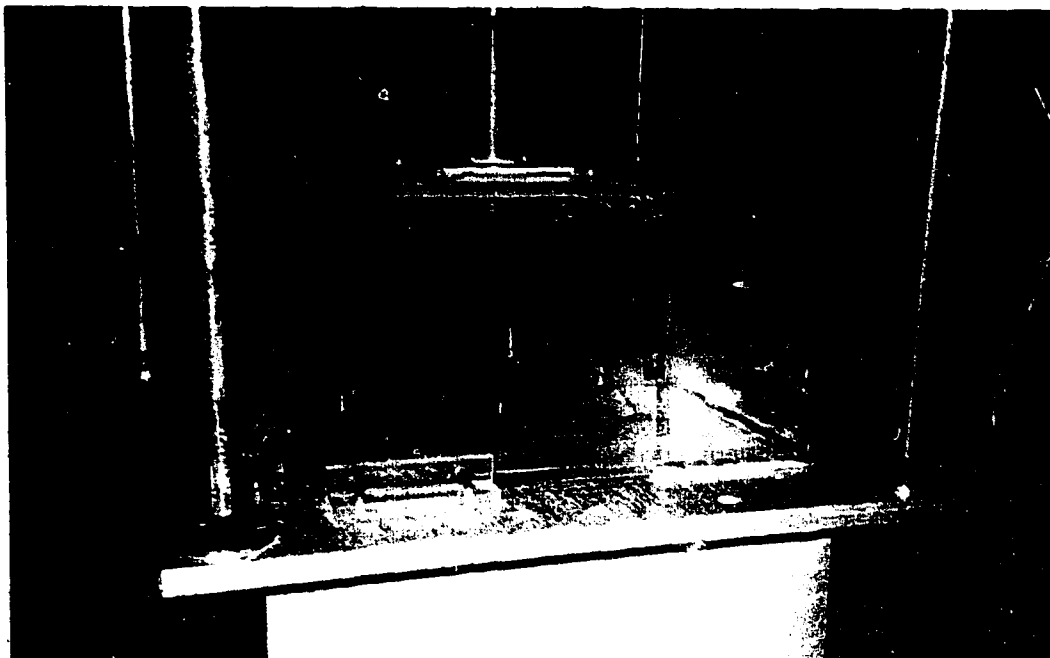
configuration 06 - trial B06 only
enlarged orifice
 $d=10.37$ cm ; $b=2.63$ cm



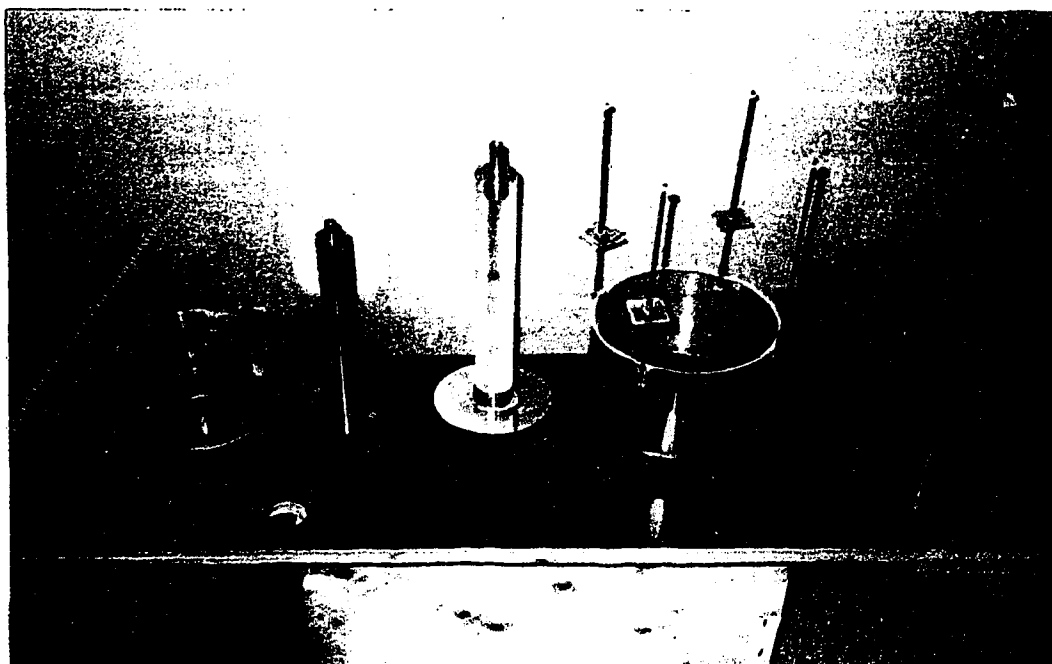
Photograph 3-1
laser-doppler system & scale-model, University of Alberta
(note laser-doppler output on computer screen)



Photograph 3-2
laser, prisms, Bragg cell, variable-speed motor & scale-model
University of Alberta



Photograph 3-3
1:41-scale model - configuration 03, trial B03
angular velocity = 100 rpm
(note path of laser beams)



Photograph 3-4
experimental apparatus: 1:41-scale & 1:55-scale models
both existing & enlarged orifices shown for the 1:41-scale model

4.0 Results: Measured Quantities (no tangential inflow)

4.1 Introduction

In this project, only three quantities were measured directly, velocity, torque and impeller speed. These three quantities formed the foundation upon which numerous additional descriptive quantities were later based, such as flow numbers, power numbers and turbulent dissipation rates. A program of data collection was implemented which comprised laser-doppler velocity measurements for both laboratory-scale models and current-meter velocity measurements for three settings of the 1:10 scale NHC model. In hopes that the data would exhibit certain consistent behavioral trends both at a particular model-scale and among the various model scales, and in hopes that any observed behaviour could be well documented, the testing was performed for numerous combinations of angular velocity (ω) and geometric scale (λ) under various combinations of the external structural geometry.

The following discussion is intended only as a presentation of the raw, observed data. Although nearly every figure that is presented in this chapter is presented both in a dimensional form and in an equivalent dimensionless form, any consideration of re-expressing such results in a dimensionless manner is deliberately suppressed until later, in the **Similarity** chapter of this document.

4.2 Velocities - General Properties of the Flow Field

4.2.1 Free Impeller - 1:55 & 1:41-Scale Models

The case of the free impeller was represented by series A01 and B01, in which three-dimensional velocities were determined at five angular velocities (1:55-scale) and three angular velocities (1:41-scale). The general nature of the flow is presented in Figures 4-1a through 4-1cn, a series of vector plots from trial A01 showing the resultant velocities in the r - z plane for the various impeller speeds that were studied*. These plots are assumed to be θ -invariant, and they may be seen to illustrate a number of important structural properties of the flow:

- the impeller-generated flow is primarily a recirculation ring with suction of the flow through the bottom of the impeller and ejection of the flow via a clearly identifiable swirling jet-like zone of high velocity
- there is a second large recirculation ring lying above the jet and between the wall of the tank
- generally, the impeller-generated flow has a downward orientation toward the floor

Comparison of these vector with respect to angular velocity indicates further that as the angular velocity is increased, the width of the impeller-generated jet seems to decrease, thereby indicating that the jet's virtual origin (*i.e.* the theoretical point-source of the jet) moves closer to the edge of the impeller. The nature of this variation will be examined in some detail with respect to the turbulent length-scale later.

Velocities were measured at five geometrically consistent dimensionless radii for the 1:55 scale model, but at only three such locations for the 1:41 scale because the walls of the tank (the tank was actually the same size as that used for the 1:55 scale trials) were suspected to be able to influence the behaviour of the jet near the walls. Plots of the vertical variation of the observed average and turbulent velocities at various dimensionless radii are presented in Figure 4-4a

* Though the concept of non-dimensionality is addressed later in the **Similarity** chapter of this report, these vector plots are also included in a dimensionless form, where the local velocities are normalized by the impeller's tip-speed, which illustrates immediately how the kinetic properties of the impeller-generated velocity field over a wide range of angular velocity may be quantified via consistent dimensionless values at a given location.

through 4-4jn. Three important observations may be made from these plots. Firstly, the magnitude of the velocity (any velocity) is greatest in the range $-1 \leq z/b \leq 0$, *i.e.* in the vertical plane along the blade of the impeller, thereby illustrating the predominance of the impeller-generated jet-like flow in this region. Secondly, as the angular velocity is increased, the magnitude of the developed local velocity increases. Thirdly, the magnitude of the velocity (any velocity) is generally greatest near the impeller, thus implying that velocity decreases with increasing distance from the impeller.

Quantification of the radial variation in velocity is deserving of special attention here given that the case of the free impeller enables the impeller-generated flow to be approximated as a free, unrestrained swirling radial jet, an approach not possible with the other configurations, where the draught tube confines the flow. The swirling radial jet has been fairly well described, and a number of mathematical solutions have been proposed whereby the path and spatial velocity variation of the jet may be predicted. In order to define the path of the jet in trials A01 and B01, a location parameter, ξ , which is actually an adaption of the formulae of Kolar, Filip & Curev (1985) by Kresta & Wood (1991). As described in the **Review of Literature**, the quantity ξ is a locational parameter which describes the distance along the axis of the swirling radial jet, and its value depends only upon radial distance from the impeller together with the flow's angle of deflection from a purely radial direction at the impeller's tip. Plots of the radial and ξ -based variations of the major velocity components are presented in Figures 4-4k through 4-4nn.

Figures 4-4k through 4-4nn, representing the radial variations in velocity, exhibit a distinct non-linearity in the decay of the particular velocities of interest. The ξ -based plot, Figure 4-4nn, possibly exhibits more of a linearity with respect to location. Such behaviour would validate the use of the swirling radial jet model since the similarity solutions inherent in such models do predict a linear variation of the major velocities with ξ . Though the fit is not perfect, and although the wall effects likely begin to exert some influence upon the jet-like flows at the outer measurement locations, the swirling radial jet model is probably fairly descriptive and useful as a comparative device between the case of the free jet and its swirling analogue.

Finally, it should be noted that the series of Figures numbered 4-4 represents plots of the *complete set* of measured radial, tangential, vertical and ξ -referenced average and turbulent velocities for the case of the 1:55-scale free impeller only, trial 01. Such a large set of plots is presented simply as an illustration of the extent to which data collection was performed for nearly every trial in this project, even though practical limitations prevent all of these plots from being shown.

4.2.2 Confined Impeller - 1:55 & 1:41-Scale Models

The case of the confined impeller is described by series A02 & B02 (draught tube only), A03 & B03 (draught tube with skirt), A05 (draught tube, skirt and baffles). The general nature of the confined flow is again presented via a series of vector plots for all configurations: Figures 4-2a-1 through 4-2cn (representing configuration 02) and figures 4-3a through 4-3bn (representing configuration 03), with θ -invariance again being assumed in all cases. These vector plots illustrate a number of significant properties of the confined flow:

- firstly, a counterclockwise recirculation ring is found to be present between the wall of the draught tube and the axis of the impeller, compelling one to recall the mathematical modelling of DeSouza & Pike (1972) who generally assumed such a recirculation ring to be of little significance with respect to the temporal effects of turbulence and mixing

- secondly, the predominance of the jet-like flow in the region near the impeller's blade is again evident ; again, the height of the region of jet-like flow is approximately equal to the impeller's blade height ; with the presence of the floor of the draught tube, a slight downward orientation in the flow is no longer observed, being replaced by a slight upward progression of the jet as it approaches the wall
- there is a zone of collision near the wall of the draught tube where the direction of the impeller-generated jet-like flow (lying primarily in the $r-\theta$ plane) changes drastically to flow in a predominantly $\theta-z$ plane ; the zone of re-direction is punctuated by a second zone of large-scale recirculation eddies in the corner formed by the wall and floor of the draught tube
- finally, after the flow is redirected by the wall to flow vertically out of the draught tube, it appears that the flow is not unlike a vertical wall-jet, which again demands comparison to DeSouza & Pike (1972)

As described above, plots of the as-measured velocities for configurations 02 and 03 are not provided here for any trial other than trial A01. However, the measured velocities from these trials are presented as a series of *dimensionless* velocity profiles in the **Similarity** chapter of this report: the radial variation of these dimensionless velocities is illustrated by Figures 6-2-1n through 6-2-8n (configuration 02), and by Figures 6-3-1n through 6-3-8n (configuration 03). The tangential variation is illustrated by Figures 6-2-9n through 6-2-11n (configuration 02), and by Figures 6-3-9n through 6-3-11n (configuration 03). Again, the significance of such dimensionless velocity distributions will be discussed more fully in the **Similarity** chapter.

Examination of these Figures again indicates that the jet is approximately the height of the impeller's blade. With the presence of the draught tube, swirling radial jet analysis of the type performed in trials A01 and B01, it was found that the wall of the draught tube, residing very close to the impeller, was able to exert significant influence upon the flow. As such, it was possible to calculate ξ for the case of the confined impeller, but such an analysis was found to be of only limited use. Consequently, except for the case of the free impeller (configuration 01), all plots of the lateral variation of the relevant velocities are presented with respect to the radial coordinate, $2r/d$, only, and not with respect to ξ .

Drawdown near the impeller's shaft was observed to be more significant for the case of the confined impeller than it was for the free impeller. However the observed drawdown was not found to be excessive until relatively high angular velocities were attained, of the order of 150 rpm for the 1:41-scale impeller and 200 rpm for the 1:55-scale impeller. The fact that the observed drawdown is accentuated upon installation of the draught tube is ascribed to the action of entrainment, whereby the expanding vertical wall jet draws in the surrounding fluid. In this case, the surrounding fluid is constrained by the draught tube to be the fluid surrounding the shaft of the impeller, thereby resulting in the increased drawdown.

No velocity measurements were taken between the skirt and floor of the tank because the skirt was too low to enable the laser beams to converge there.

4.2.3 Northwest Hydraulic Consultants Model - no tangential inflow

Testing of the 1:10-scale NHC model for the case of zero inflow was defined as NHC trial 1. Structurally, it was assumed that the configuration of the NHC model was equivalent to configuration 03 from the small-scale models, and thus that the flow would exhibit similar behaviour to that observed in trials A03 and B03, at least in the immediate vicinity of the draught tube. Data for trial 1 were collected at three different angular velocities, along three vertical traverses within the draught tube, and at approximately the same dimensionless geometric locations as for the 1:55-scale and 1:41-scale trials. By means of a downstream control weir, the water level in the model was maintained at the same relative height above the draught tube as in trials A03 and B03.

Plots of the observed vertical variation of radial (u) and tangential (v) velocities are presented in Figures 9-1-1 through 9-1-4, and plots of the observed radial variation are presented in Figures 9-1-4 through 9-1-6, in the **Implications of Tangential Inflow** chapter of this document. Because of spatial and practical limitations, it was not possible to determine vertical (w) velocities for any of the NHC trials, thereby precluding definition of the type of vector plots that were presented for the smaller-scale models. The u and v velocities were measured at the same tangential location, $\theta = 0$, and were assumed to be θ -invariant given the absence of any imposed tangential flow regime for this particular NHC trial.

4.2.4 Reverse-Flow

While observing data collection for trial A02, the first trial in which the draught tube was installed, an interesting phenomenon was observed. When the traverse points along the base of the orifice were examined for the case of $N = 200$ rpm, it was found that the v -velocities there were actually negative (*i.e.* in opposition to the motion of the impeller) when both intuition and experience led one to expect positive values of v there. Curiously, v is seen to be positive everywhere within the draught tube and throughout most of the space between the draught tube's floor and the tank's floor - only in one narrow layer did the v -velocities appear to be reversed, in a direction opposing the motion of the impeller. Interestingly, in this same layer, u and w appeared to behave as expected for all angular velocities, bearing toward the shaft and up into the draught tube.

In order to examine this curious reverse flow phenomenon more closely, a special series of runs was performed (in addition to the regular test runs), wherein the angular velocity was varied from 25 rpm to 250 rpm so that the point of incipient reversal could be defined, and so that any spatial variation in the zone of reversal might also be defined. The resultant velocities, measured near the orifice, are presented in Figure 4-5. This testing indeed confirmed that what would be expected to be a predominantly pro-impeller* flow field is (for a very brief instant, only in the immediate vicinity of the orifice) flow field contra-impeller as successively higher angular velocities be attained. This phenomenon was also observed with the skirt in place, although no quantitative study was performed.

The rapidity with which the tangential v -velocity is reversed and reversed again implies the action of a very localized aberration in what is otherwise a visibly smooth flow regime. It is speculated that such a rapid reversal is caused by a rapid drop in the pressure that is incurred by the flow upon entering the orifice. This pressure drop may result from the area of low-pressure residing immediately behind the blades and below the top of the impeller. Such zones of low pressure have been well described by numerous researchers such as Van't Reit & Smith (1975),

* Here, the term pro-impeller means that the local tangential velocity and the impeller's tip are moving in the same direction. In contrast, the term contra-impeller means that the local tangential velocity and the impeller's tip are moving in opposite directions.

and Gunkel & Weber (1975). Alternatively, it is speculated that a significant amount of vortexing around the impeller's shaft could have established some sort of reverse pressure gradient near the orifice.

Regardless of the true cause of this curious behaviour, although such an observation may be interesting, its application to the study of the full-scale facility is unknown. Certainly, this phenomenon indicates that all flow velocities below the floor of the draught tube probably cannot be normalized by the tip-speed (as is the common practice), so that quantities such as flow numbers, N_q , and local dissipation rate may not necessarily vary with increases in angular velocity just outside the draught tube in the same manner as they do inside the draught tube. Because (as will be demonstrated) the general mechanical and dissipative structure is fairly well consolidated inside the draught tube, the effect of this phenomenon upon such turbulence-related processes such as flocculation may not be significant in the full-scale.

4.3 Torque and Power Consumption

4.3.1 General

Power consumption is traditionally expressed by the power number, N_p , in the study of impeller-agitated mixing. N_p is traditionally the parameter of choice because it is a relatively simple and straightforward expression of the ultimate vessel-averaged power consumption. However, definition of N_p is often difficult as it requires a means of measuring power. Furthermore, in measuring power, it is implied that only the power applied in resisting the drag force of the water (and which is therefore ultimately dissipated by turbulent dissipation) must be known in order for N_p to be relevant. Most often, the approach that is employed is to measure the torque on the impeller's shaft and then to convert this torque to power via the following fundamental expression:

$$P = \tau \omega$$

where the angular velocity, ω , is expressed in units of radians per second, and the torque, τ , is expressed in N·m or any other consistent SI unit. The relevant units would be expressed as follows:

$$\frac{\text{N}\cdot\text{m}}{\text{s}} \rightarrow \frac{\text{J}}{\text{s}} \rightarrow \text{W}$$

In this study, τ was measured with a rotary parallel shaft torque transducer that was mounted directly in the shaft between the variable-speed motor and the impeller. For a given structural configuration, the impeller was run first in air and then in water, where the difference between the wet and dry torques was assumed to represent the torque applied agitating the water only, without the inclusion of any mechanical losses to the apparatus. Torque measurements were performed from 5 rpm up to 300 rpm for nearly every structural combination of impeller, draught tube, skirt and baffles that was investigated during the velocity measurements. Although the torque measurements at extremely low angular velocities are most prone to error given the relatively low torques incurred there, the data seem to exhibit a consistent behaviour. The variation of the measured values of P with ω (as represented by N) are presented graphically in Figure 4-6.

Certain important characteristics of these $P-R_i$ curves are immediately apparent:

- firstly, power seems to increase non-linearly, which is consistent with dimensional analysis (or with the power number itself) which states that:

$$P \propto \rho \omega^3 d^5 \propto \rho n^3 d^5 \propto \rho N^3 d^5$$

and thus demands a cubic increase with angular velocity for a given diameter, d , not a linear one.

- secondly, it is clear that P consumption is much greater for the cases where the impeller is confined than for when it is not.
- finally, it is seen that for a given R , or ω , P consumption is consistently higher for the 1:41-scale impeller than for the 1:55 scale impeller - a consequence of a greater area being available for drag losses.

The relevance of such observations will be discussed in relative detail in subsequent chapters of this report, especially with respect to N_p and the local turbulent dissipation rate.

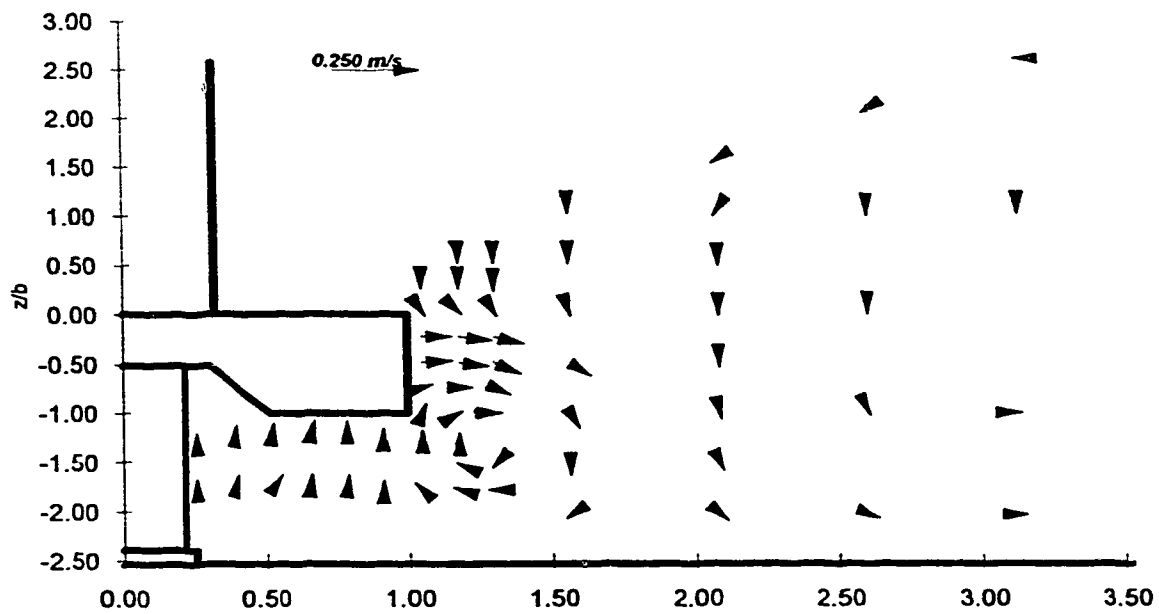


Figure 4-1a : trial A01 - ecodyne impeller ; 1:55 scale
radial and axial resultant average velocities - not normalized by tip speed
 $d=7.66$ cm ; $b=1.94$ cm ; 50 rpm

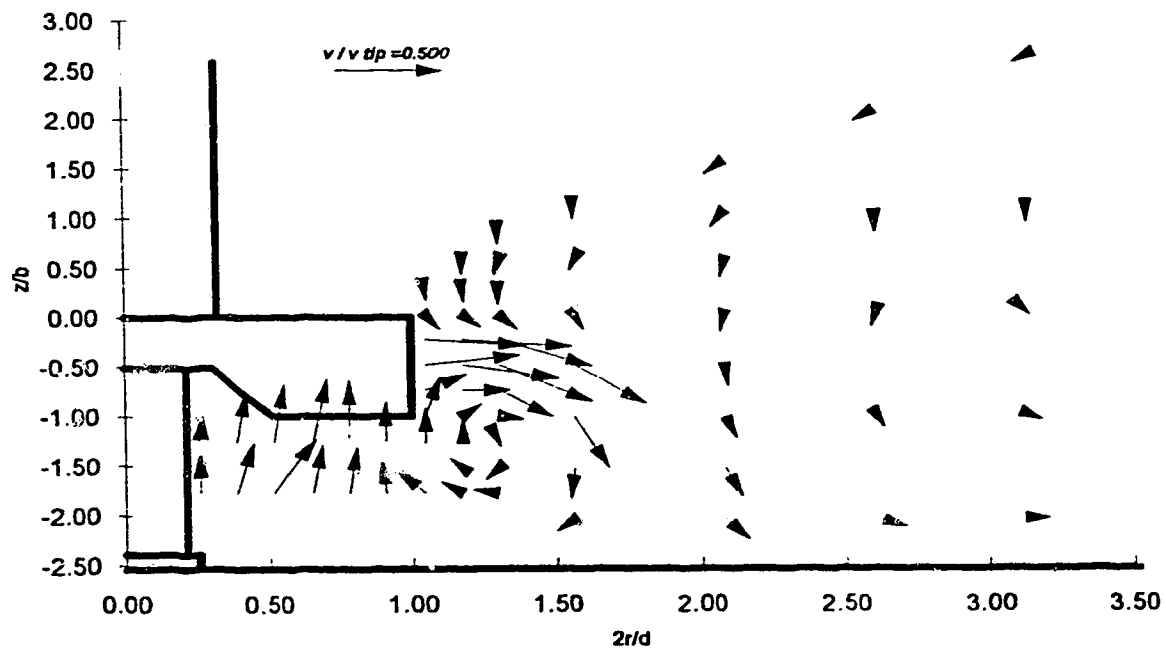


Figure 4-1an : trial A01 - ecodyne impeller ; 1:55 scale
radial and axial resultant average velocities - normalized by tip speed
 $d=7.66$ cm ; $b=1.94$ cm ; 50 rpm

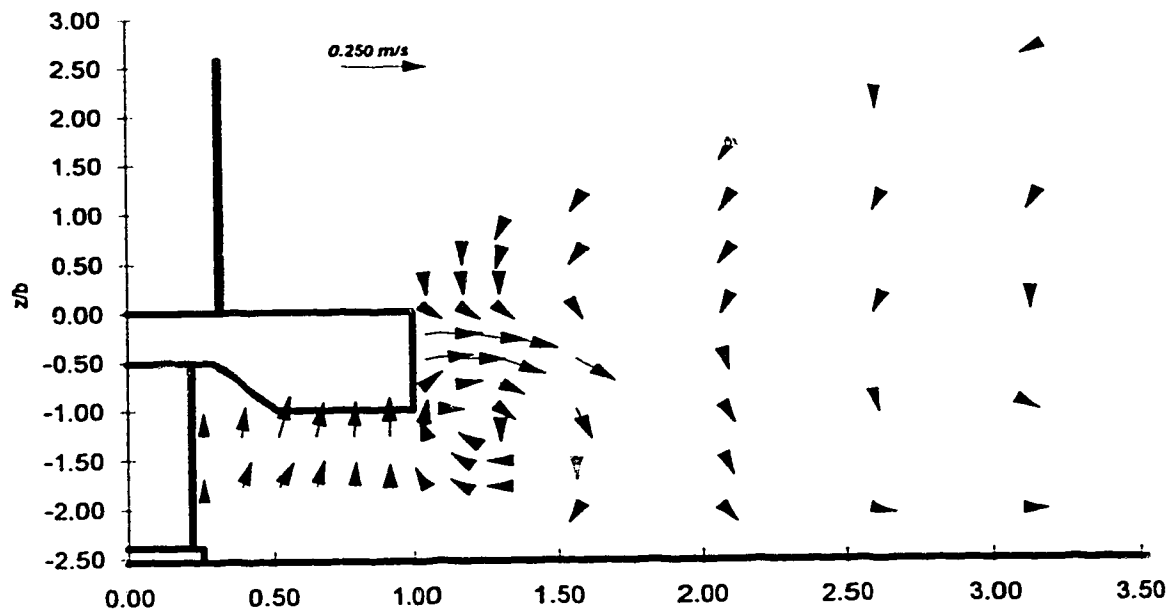


Figure 4-1b : trial A01 - ecodyne impeller ; 1:55 scale
radial and axial resultant average velocities - not normalized by tip speed
 $d=7.66$ cm ; $b=1.94$ cm ; 100 rpm

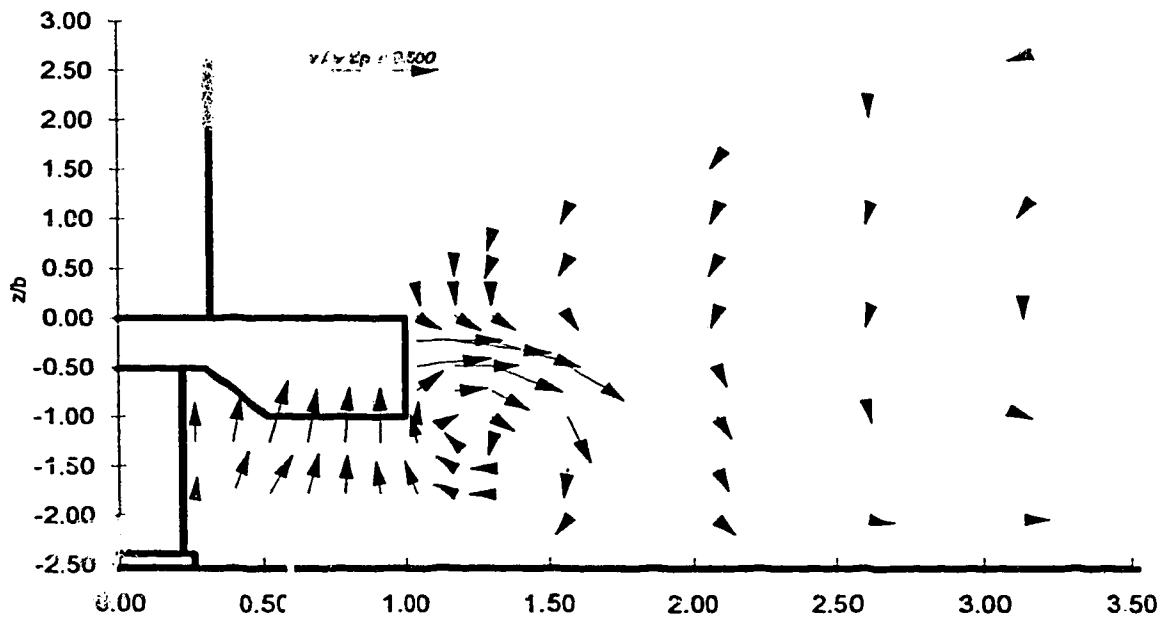


Figure 4-1bn : trial A01 - ecodyne impeller ; 1:55 scale
radial and axial resultant average velocities - normalized by tip speed
 $d=7.66$ cm ; $b=1.94$ cm ; 100 rpm

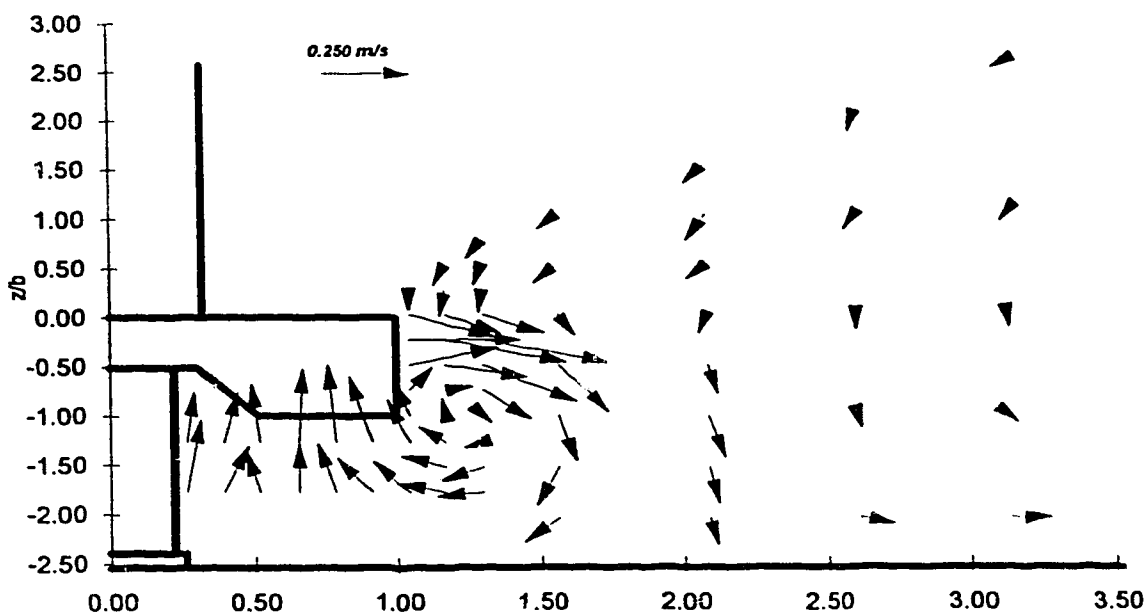


Figure 4-1c : trial A01 - ecodeyne impeller ; 1:55 scale
radial and axial resultant average velocities - not normalized by tip speed
 $d=7.66$ cm ; $b=1.94$ cm ; 200 rpm

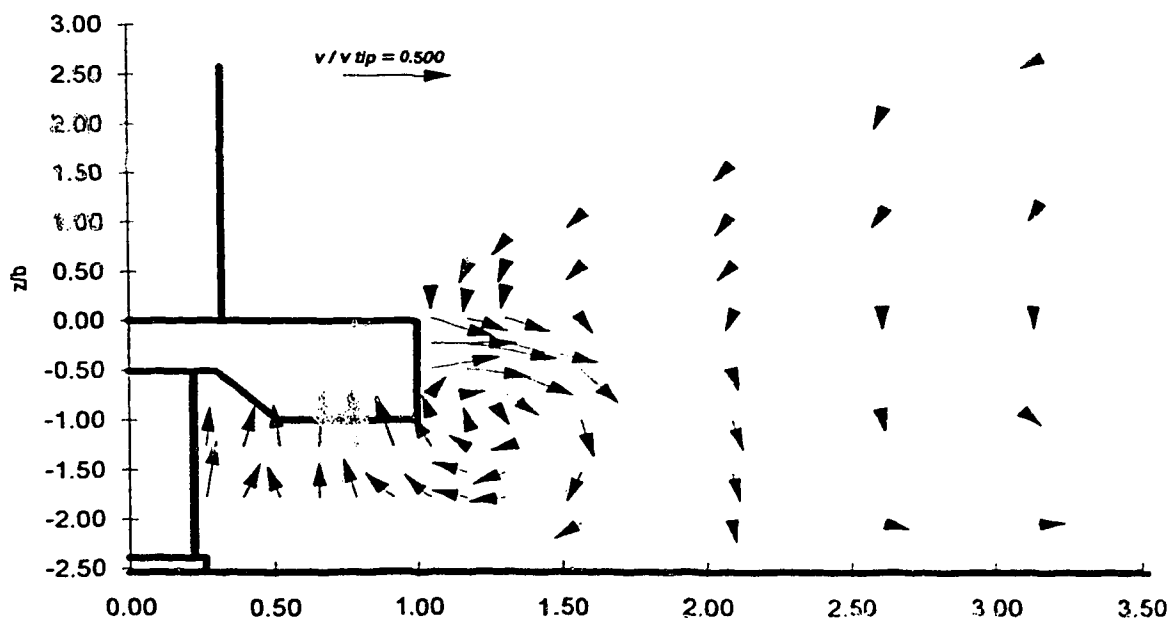


Figure 4-1cn : trial A01 - ecodeyne impeller ; 1:55 scale
radial and axial resultant average velocities - normalized by tip speed
 $d=7.66$ cm ; $b=1.94$ cm ; 200 rpm

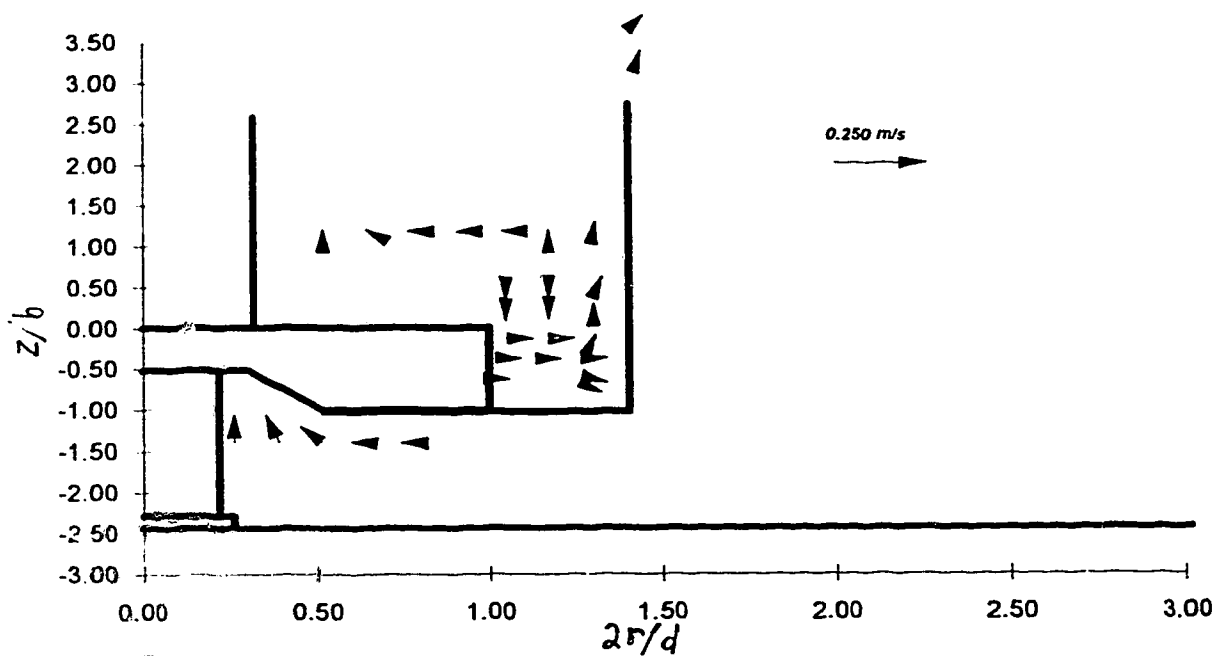


Figure 4-2a : trial A02 - ecodyne impeller ; 1:55 scale
radial and axial resultant average velocities - not normalized by tip speed
 $d=7.66$ cm ; $b=1.94$ cm ; 50 rpm

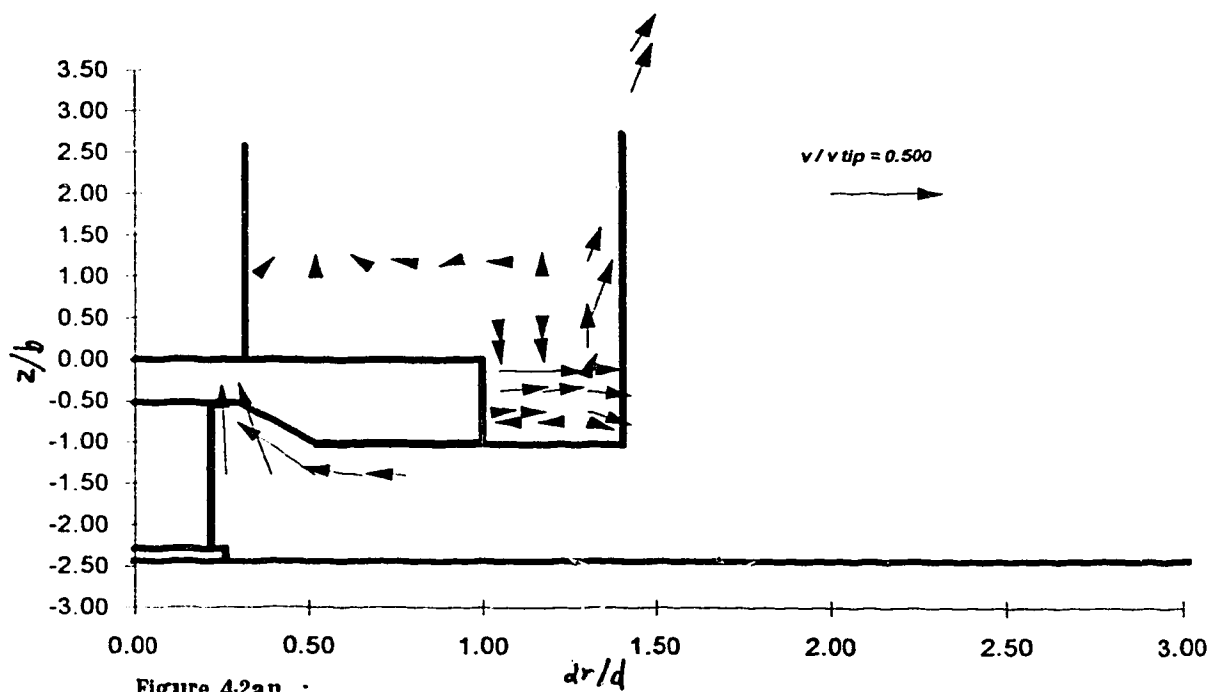


Figure 4-2an : trial A02 - ecodyne impeller ; 1:55 scale
radial and axial resultant average velocities - normalized by tip speed
 $d=7.66$ cm ; $b=1.94$ cm ; 50 rpm

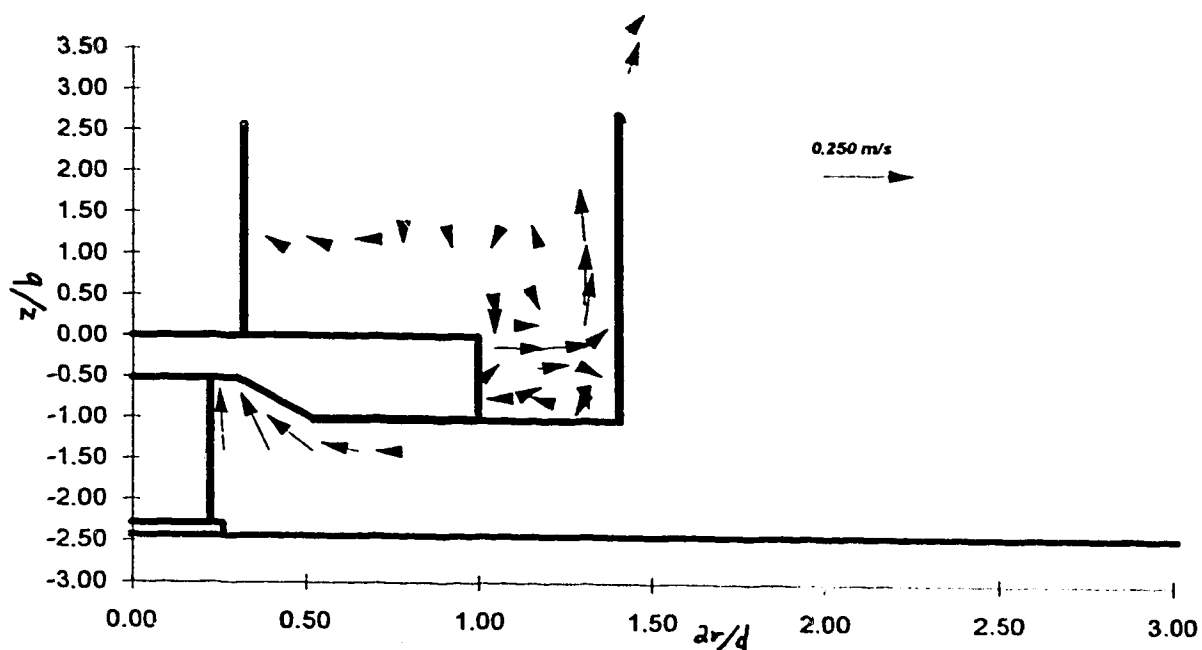


Figure 4-2b : trial A02 - ecodyne impeller ; 1:55 scale
radial and axial resultant average velocities - not normalized by tip speed
 $d=7.66$ cm ; $b=1.94$ cm ; 100 rpm

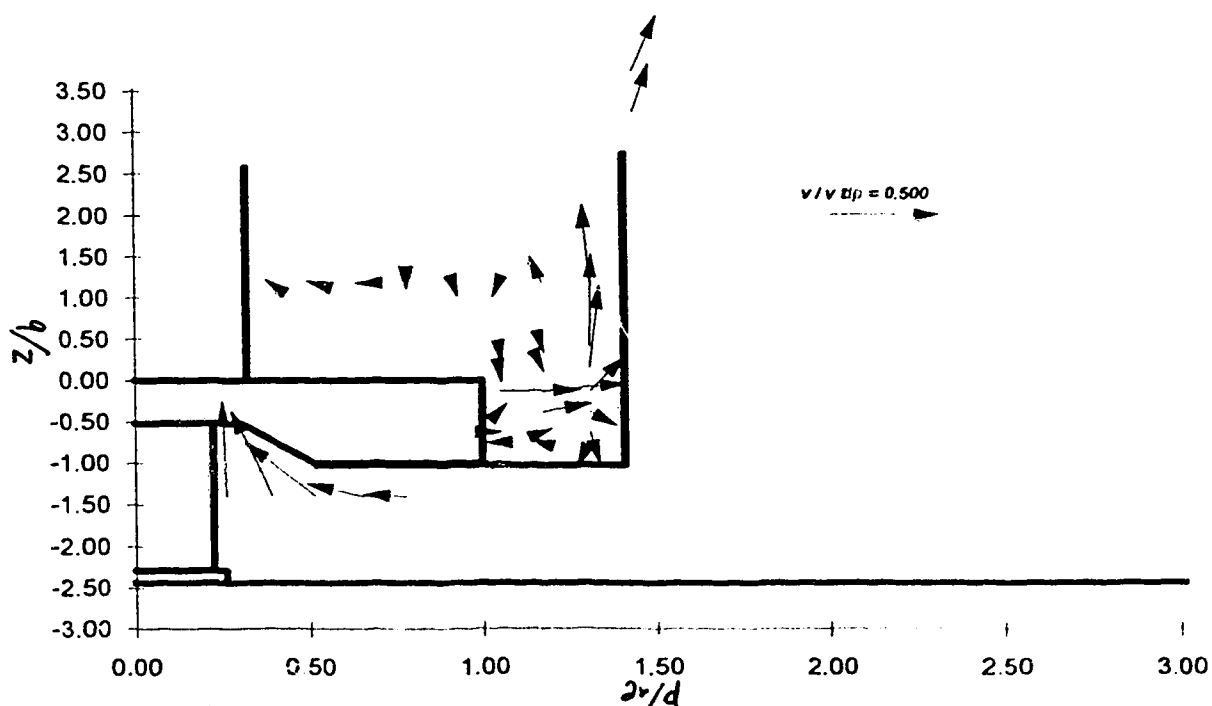


Figure 4-2bn : trial A02 - ecodyne impeller ; 1:55 scale
radial and axial resultant average velocities - normalized by tip speed
 $d=7.66$ cm ; $b=1.94$ cm ; 100 rpm

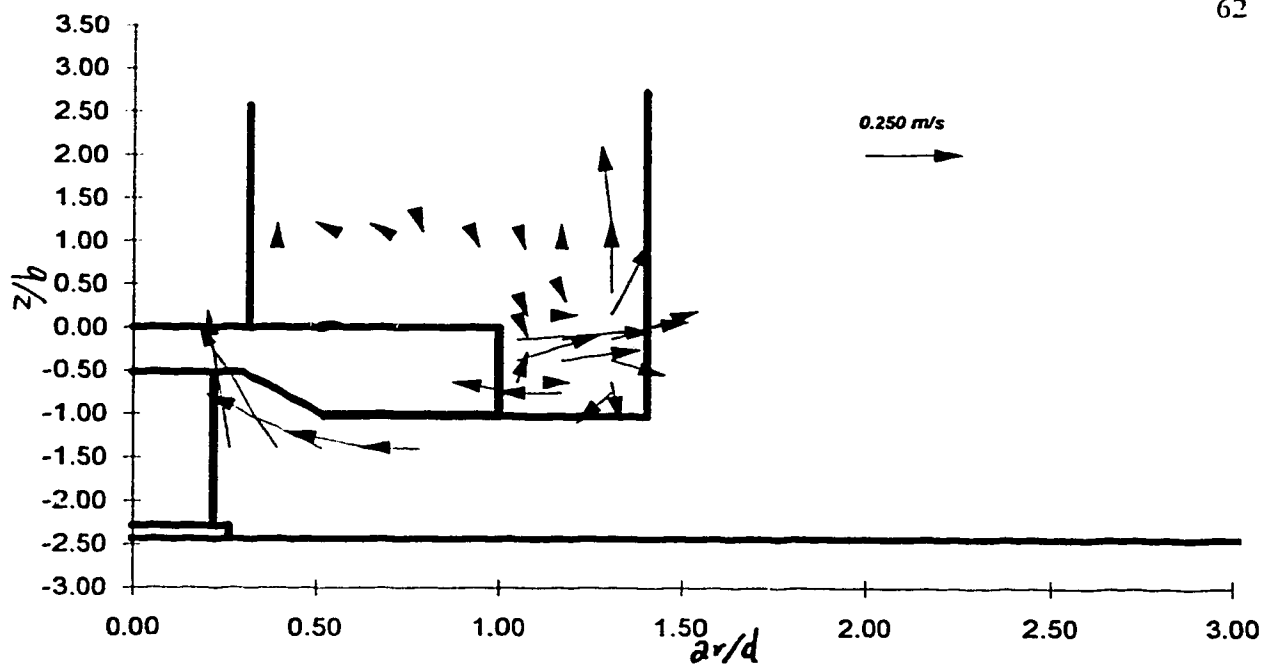


Figure 4-2c : trial A02 - ecodyne impeller ; 1:55 scale
radial and axial resultant average velocities - not normalized by tip speed
 $d=7.66$ cm ; $b=1.94$ cm ; 200 rpm

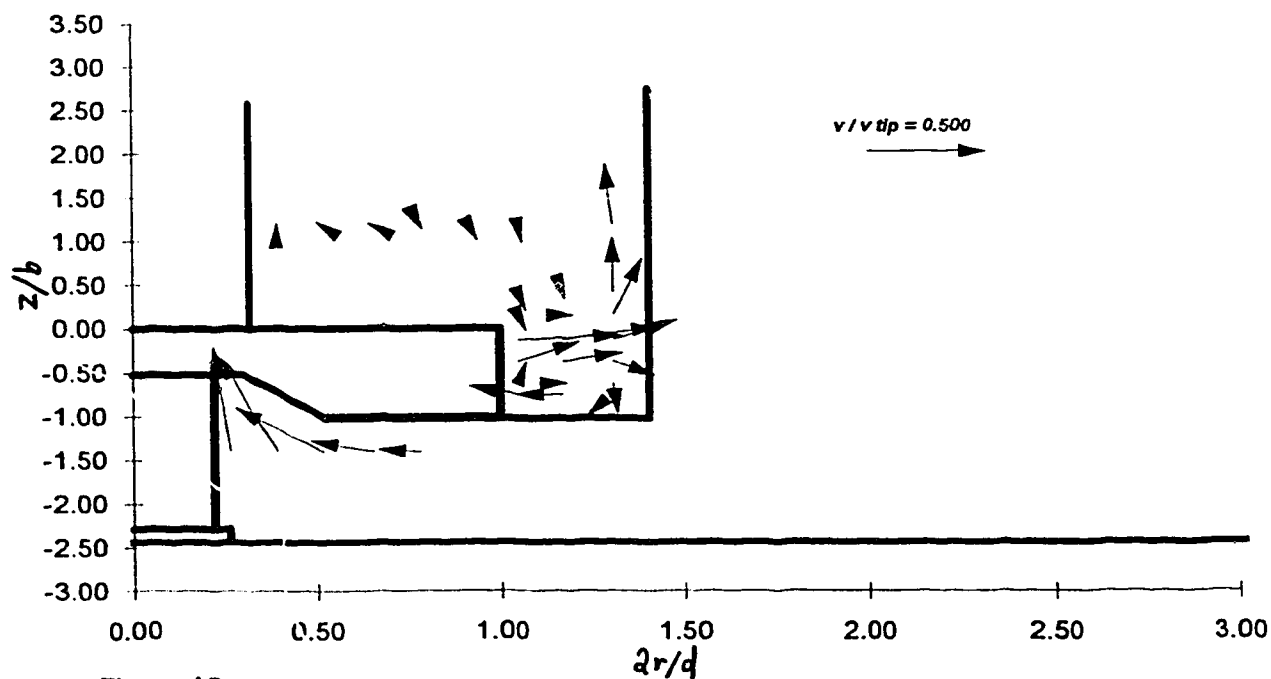


Figure 4-2cn : trial A02 - ecodyne impeller ; 1:55 scale
radial and axial resultant average velocities - normalized by tip speed
 $d=7.66$ cm ; $b=1.94$ cm ; 200 rpm

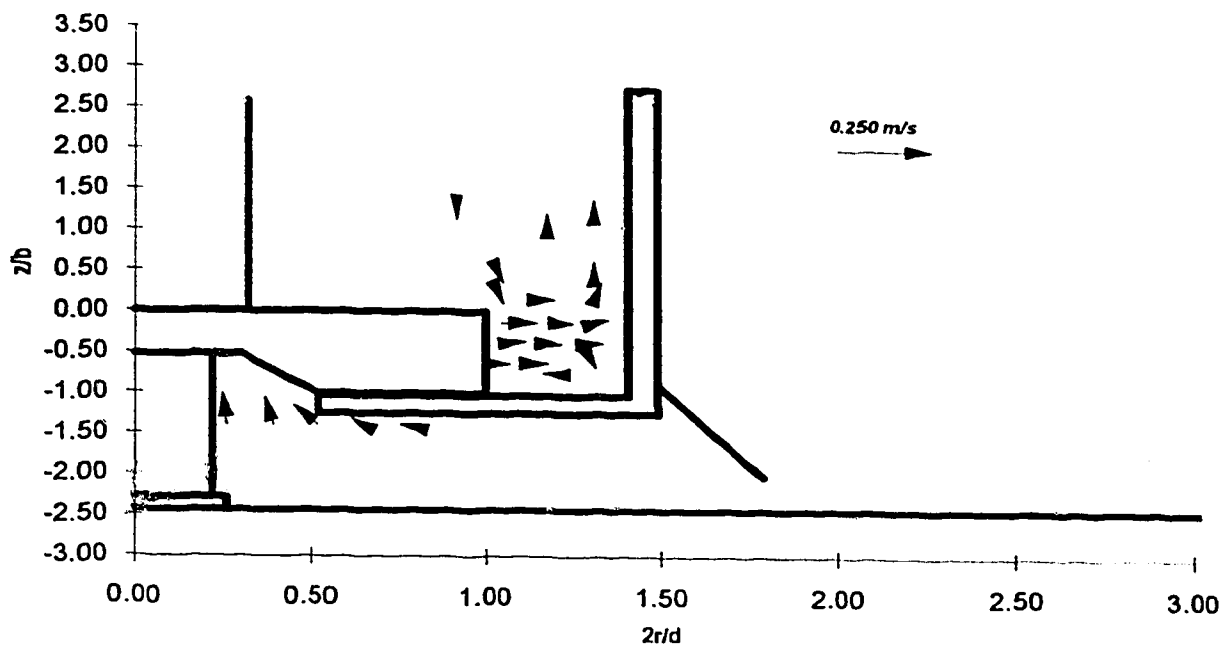


Figure 4-3a :

trial A03 - ecodyne impeller ; 1:55 scale
radial and axial resultant average velocities - not normalized by tip speed
 $d=7.66$ cm ; $b=1.94$ cm ; 50 rpm

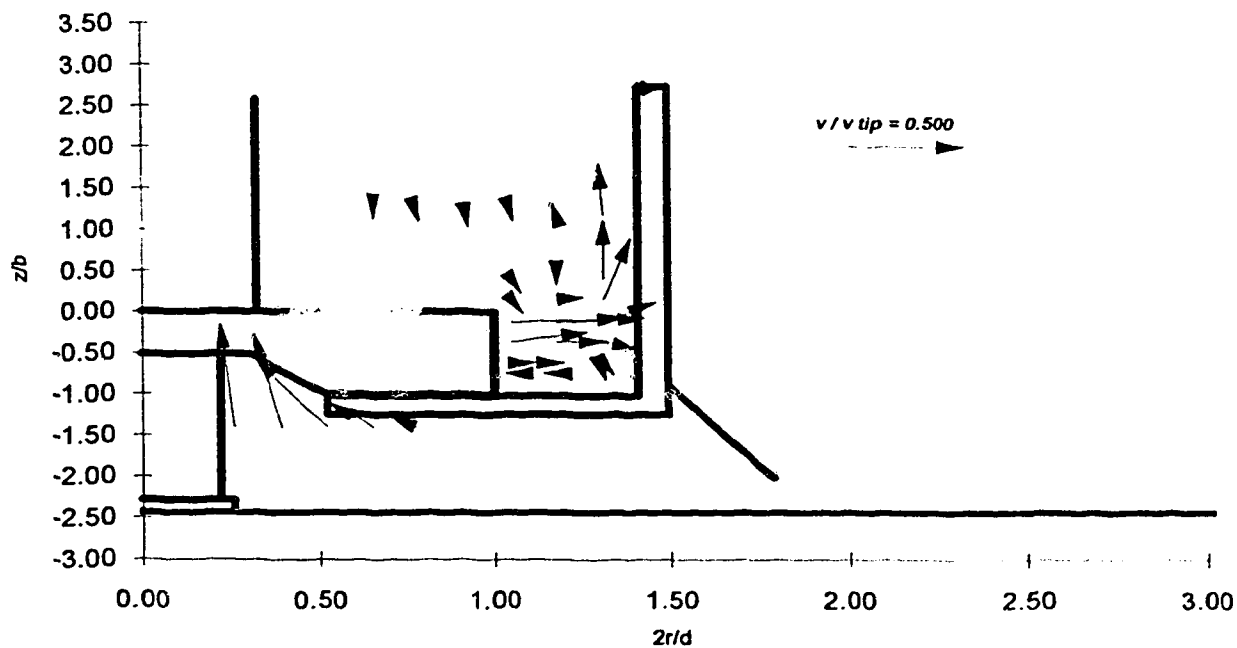


Figure 4-3an :

trial A03 - ecodyne impeller ; 1:55 scale
radial and axial resultant average velocities - normalized by tip speed
 $d=7.66$ cm ; $b=1.94$ cm ; 50 rpm

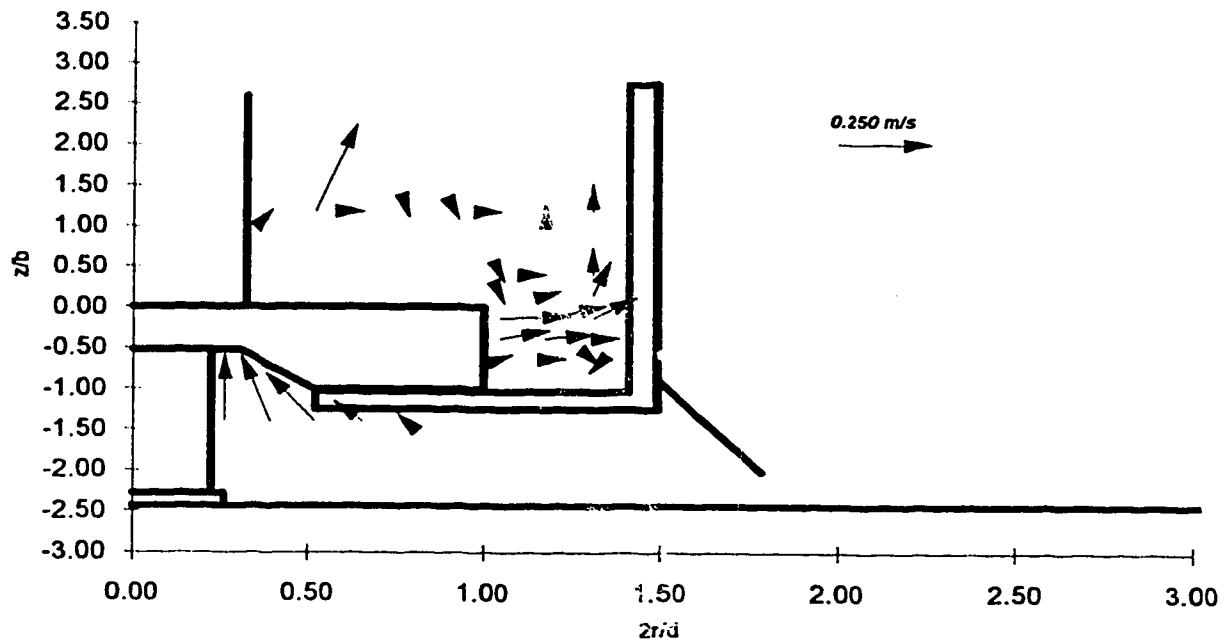


Figure 4-3b : trial A03 - ecodyne Impeller ; 1:55 scale
radial and axial resultant average velocities - not normalized by tip speed
 $d=7.66 \text{ cm}$; $b=1.94 \text{ cm}$; 100 rpm

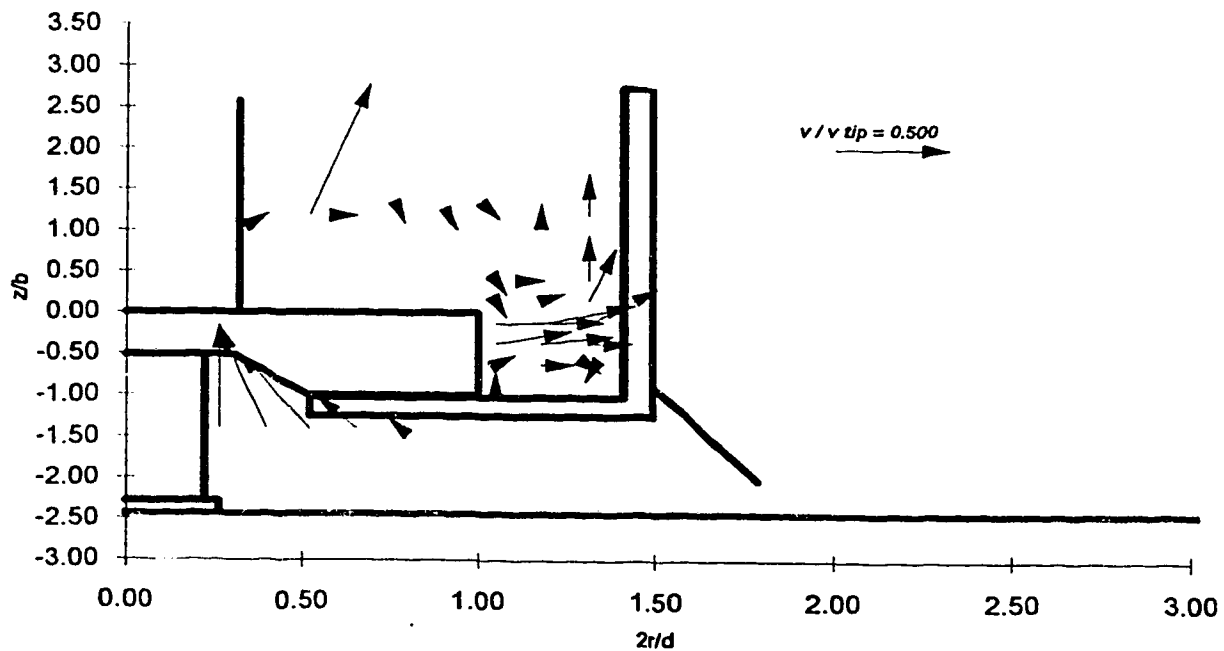


Figure 4-3bn : trial A03 - ecodyne Impeller ; 1:55 scale
radial and axial resultant average velocities - normalized by tip speed
 $d=7.66 \text{ cm}$; $b=1.94 \text{ cm}$; 100 rpm

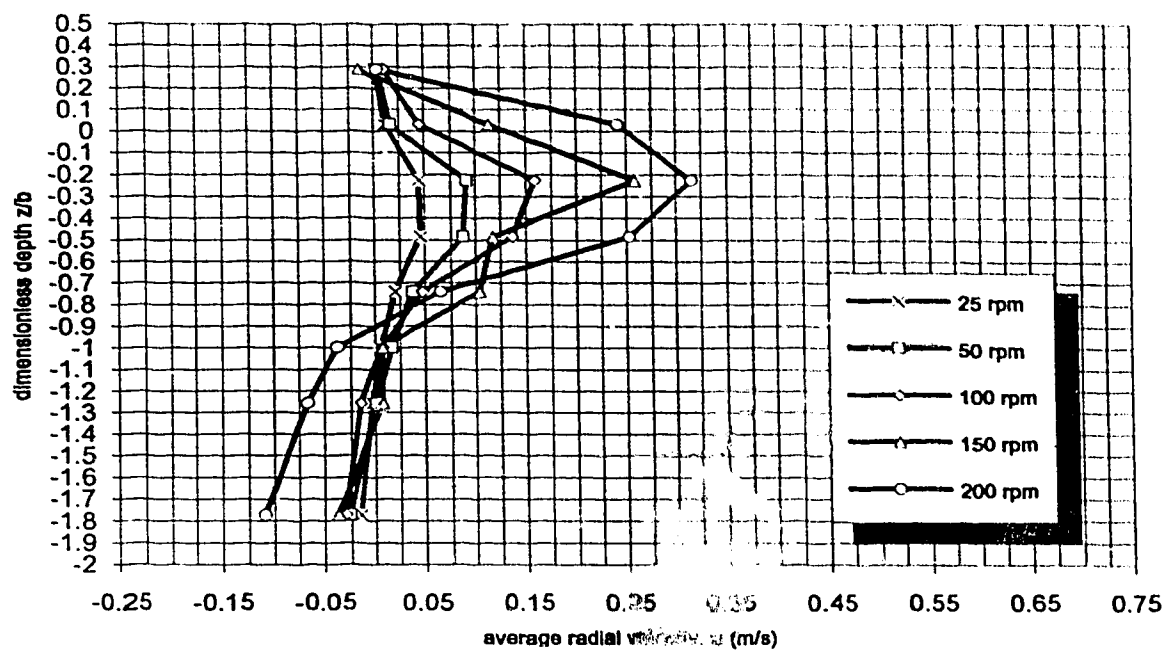


Figure 4-4a :

trial A01 - ecodyne impeller ; 1:55 scale
radial average velocities near impeller - not normalized by tip speed
 $d=7.66$ cm ; $b=1.94$ cm ; $2r/d=1.044$

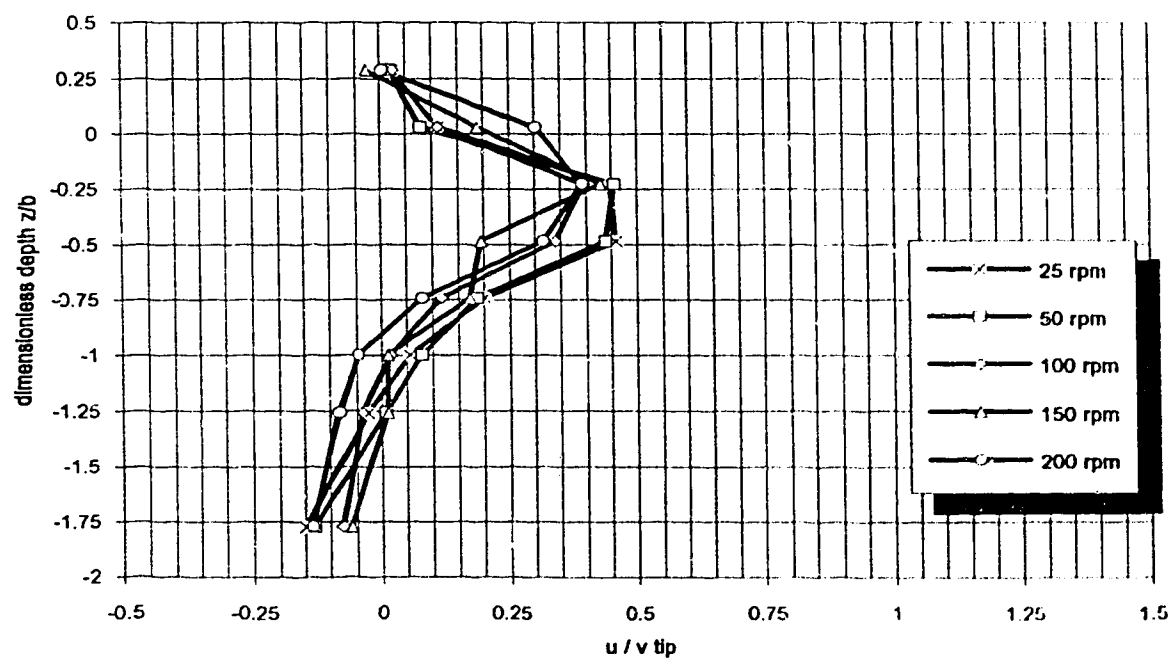


Figure 4-4an :

trial A01 - ecodyne impeller ; 1:55 scale
radial average velocities near impeller - normalized by tip speed
 $d=7.66$ cm ; $b=1.94$ cm ; $2r/d=1.044$

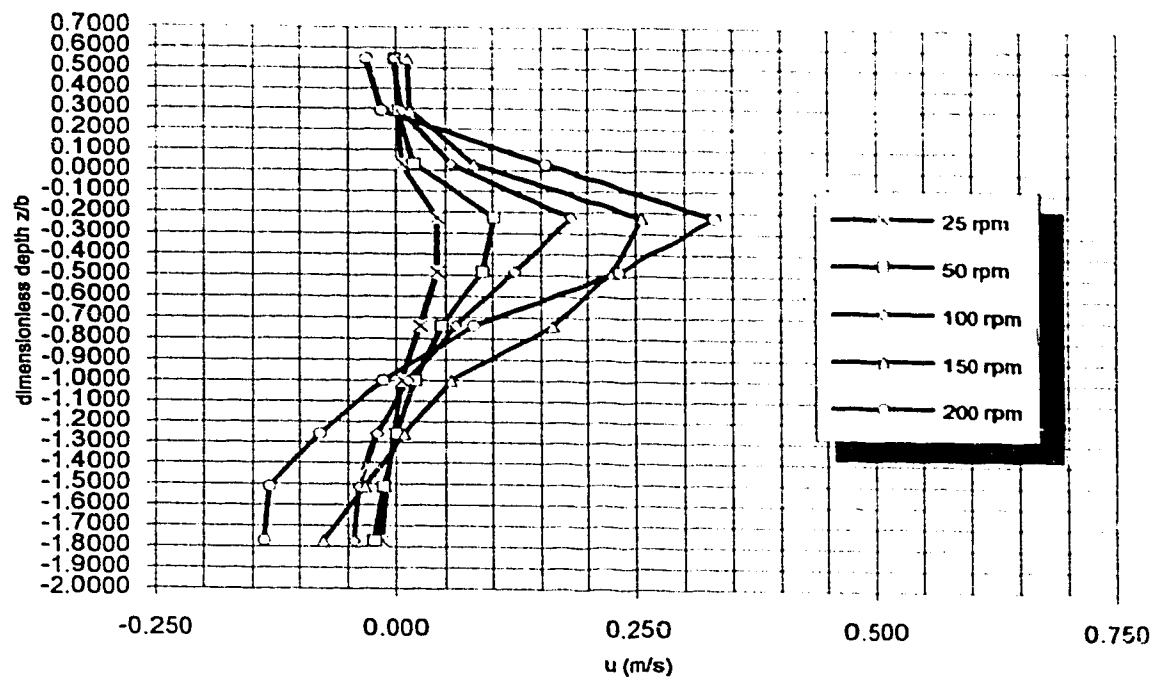


Figure 4-4b : trial A01 - ecodyne Impeller ; 1:55 scale
radial average velocities near impeller - not normalized by tip speed
 $d=7.66$ cm ; $b=1.94$ cm ; $2r/d=1.175$

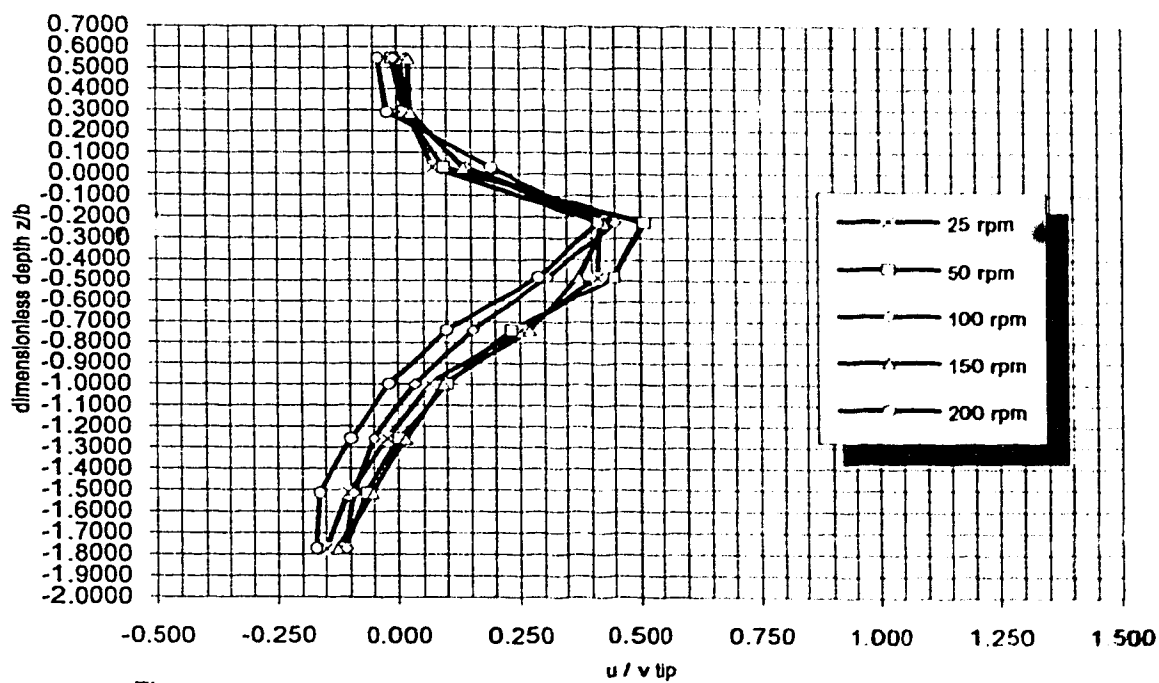


Figure 4-4bn : trial A01 - ecodyne Impeller ; 1:55 scale
radial average velocities near impeller - normalized by tip speed
 $d=7.66$ cm ; $b=1.94$ cm ; $2r/d=1.175$

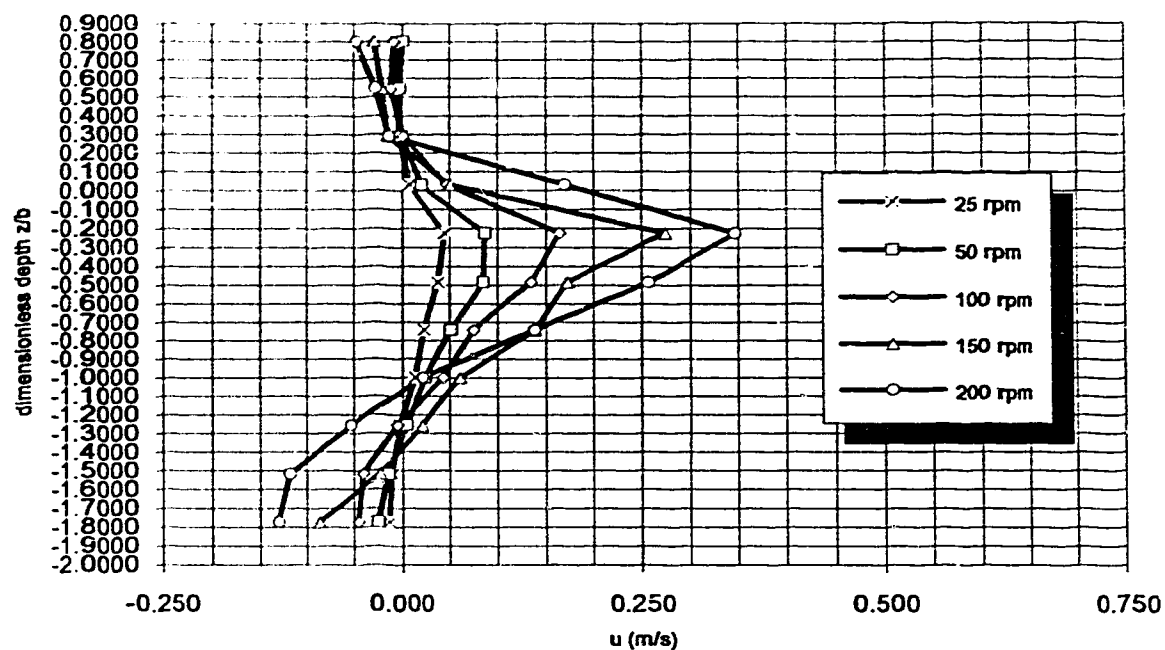


Figure 4-4c :

trial A01 - ecodyne impeller ; 1:55 scale
radial average velocities near impeller - not normalized by tip speed
 $d=7.66$ cm ; $b=1.94$ cm ; $2r/d=1.305$

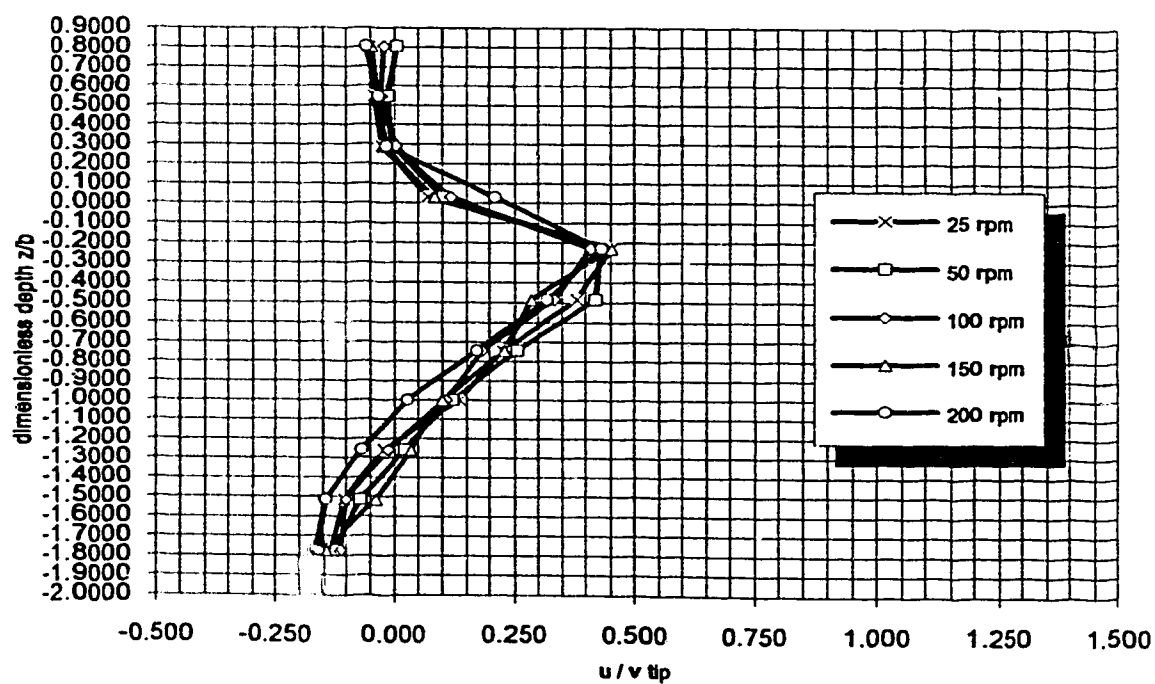


Figure 4-4cn :

trial A01 - ecodyne impeller ; 1:55 scale
radial average velocities near impeller - normalized by tip speed
 $d=7.66$ cm ; $b=1.94$ cm ; $2r/d=1.305$

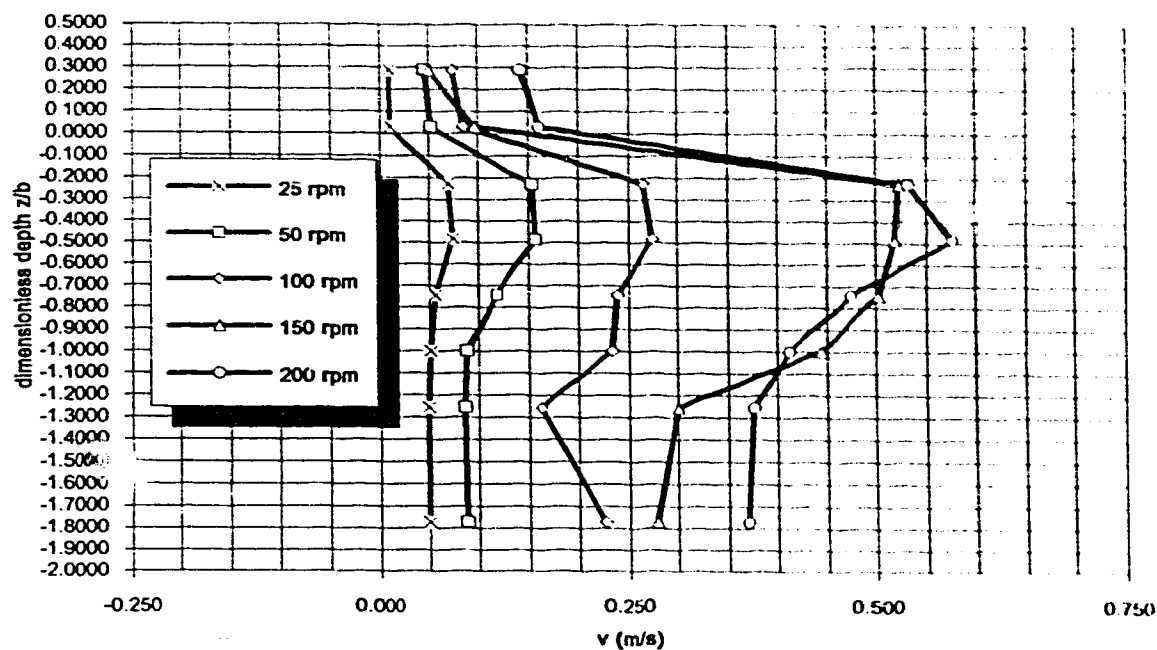


Figure 4-4d :

trial A01 - ecodyne impeller ; 1:55 scale
 tangential average velocities near impeller - not normalized by tip speed
 $d=7.66$ cm ; $b=1.94$ cm ; $2r/d=1.044$

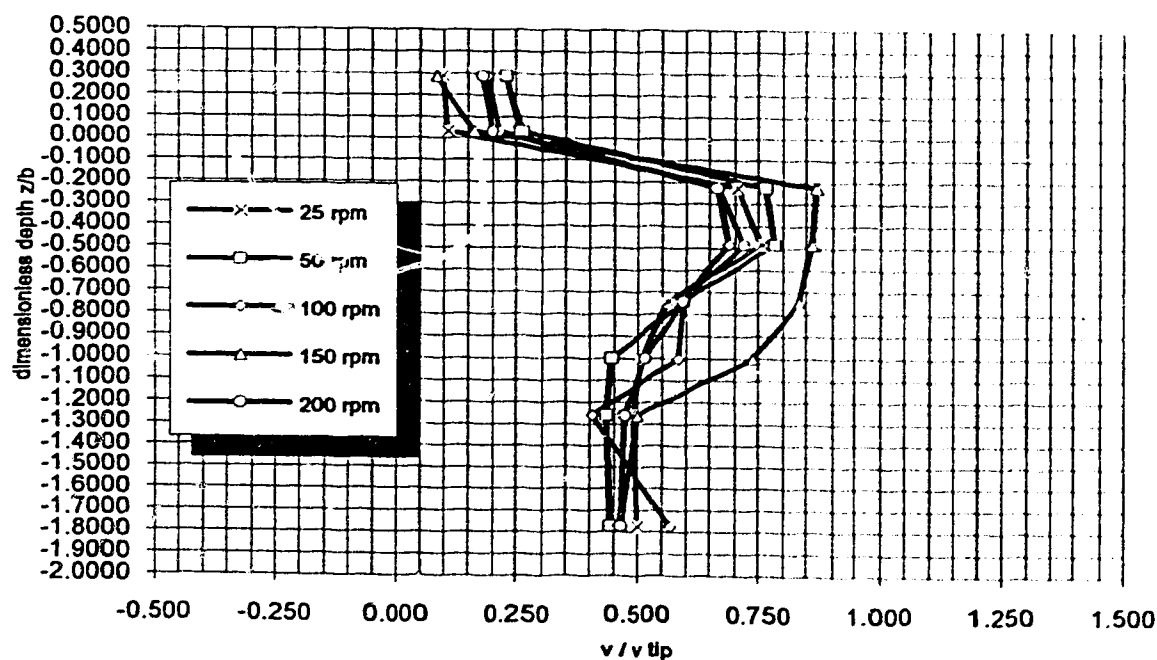


Figure 4-4dn :

trial A01 - ecodyne impeller ; 1:55 scale
 tangential average velocities near impeller - normalized by tip speed
 $d=7.66$ cm ; $b=1.94$ cm ; $2r/d=1.044$

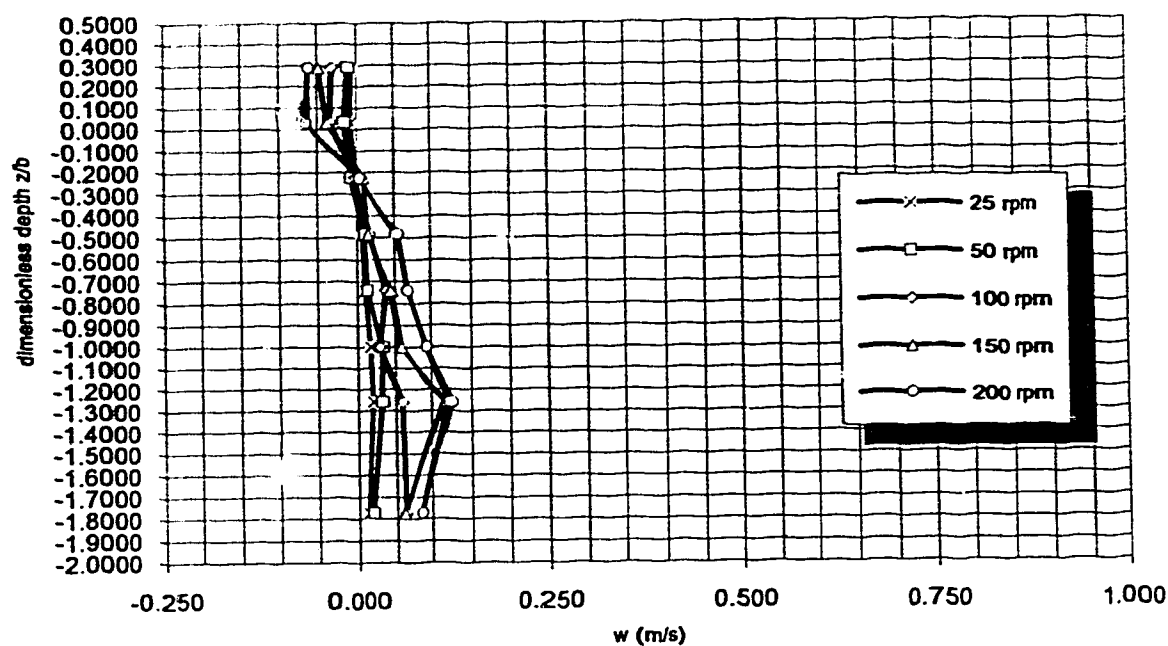


Figure 4-4e : trial A01 - ecodyne impeller ; 1:55 scale
axial average velocities near impeller - not normalized by tip speed
 $d=7.66$ cm ; $b=1.94$ cm ; $2r/d=1.044$

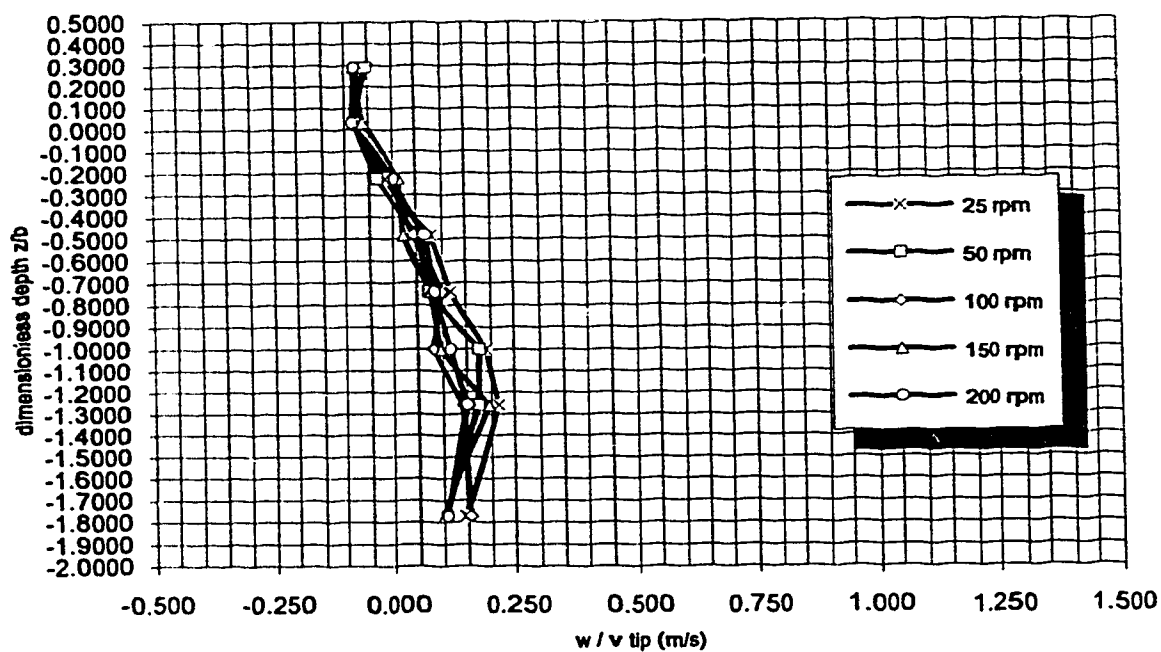


Figure 4-4en : trial A01 - ecodyne impeller ; 1:55 scale
axial average velocities near impeller - normalized by tip speed
 $d=7.66$ cm ; $b=1.94$ cm ; $2r/d=1.044$

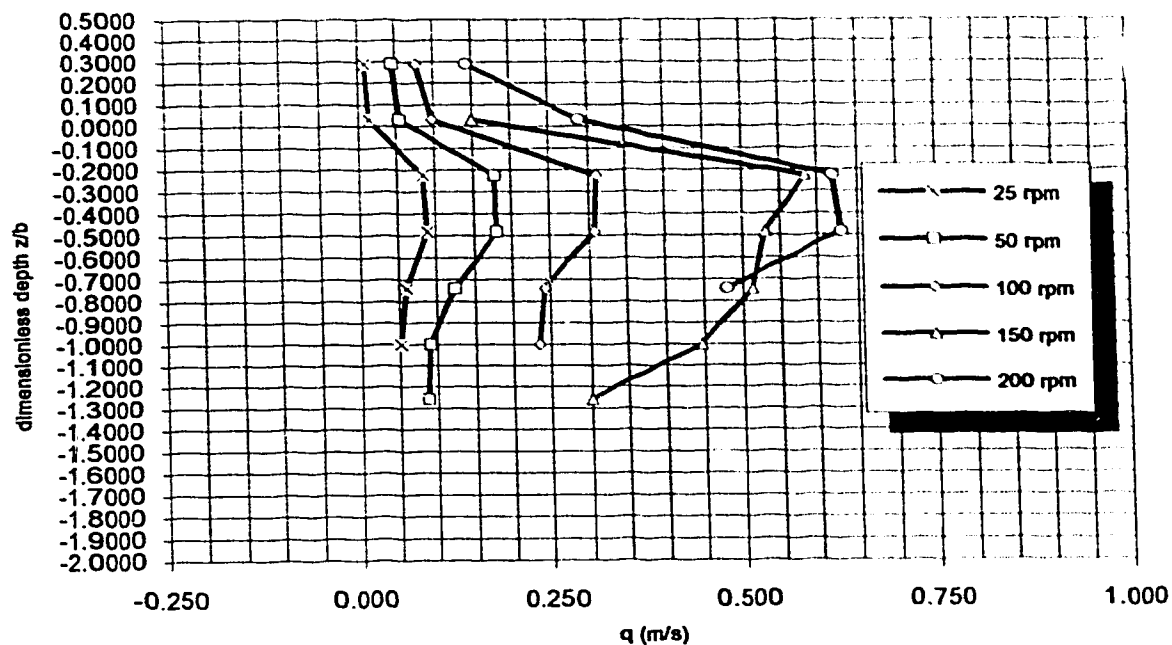


Figure 4-4f : trial A01 - ecodyne Impeller ; 1:55 scale
average velocities along axis of swirling radial jet - not normalized by tip speed
 $d=7.66$ cm ; $b=1.94$ cm ; $2r/d=1.044$

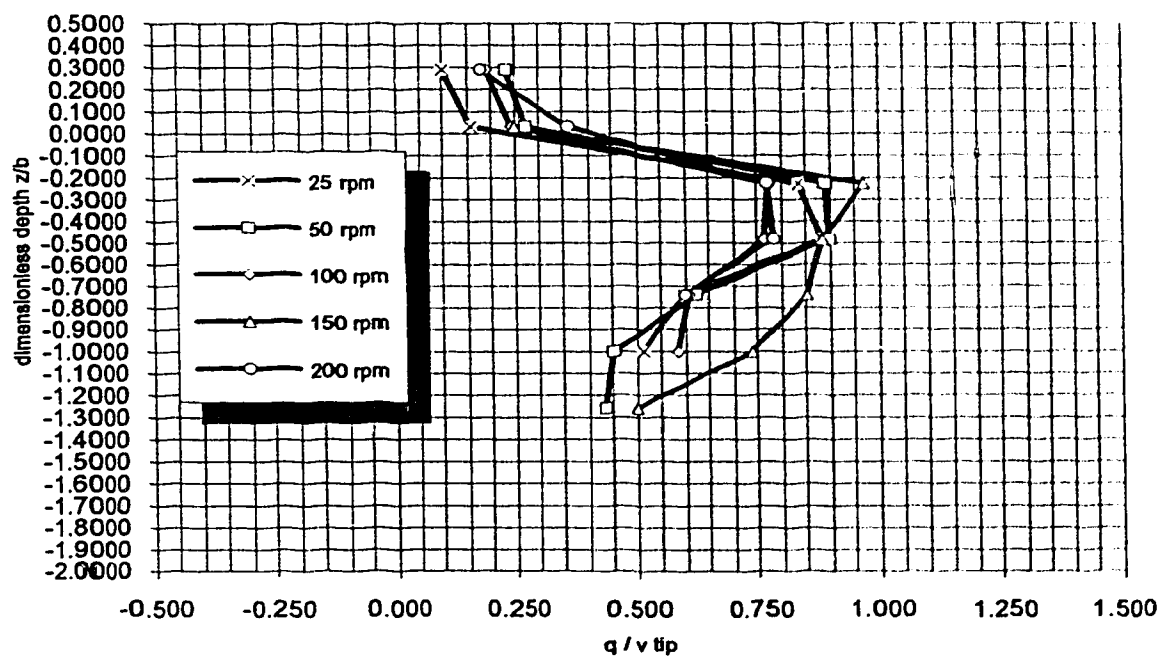


Figure 4-4fn : trial A01 - ecodyne Impeller ; 1:55 scale
average velocities along axis of swirling radial jet - normalized by tip speed
 $d=7.66$ cm ; $b=1.94$ cm ; $2r/d=1.044$

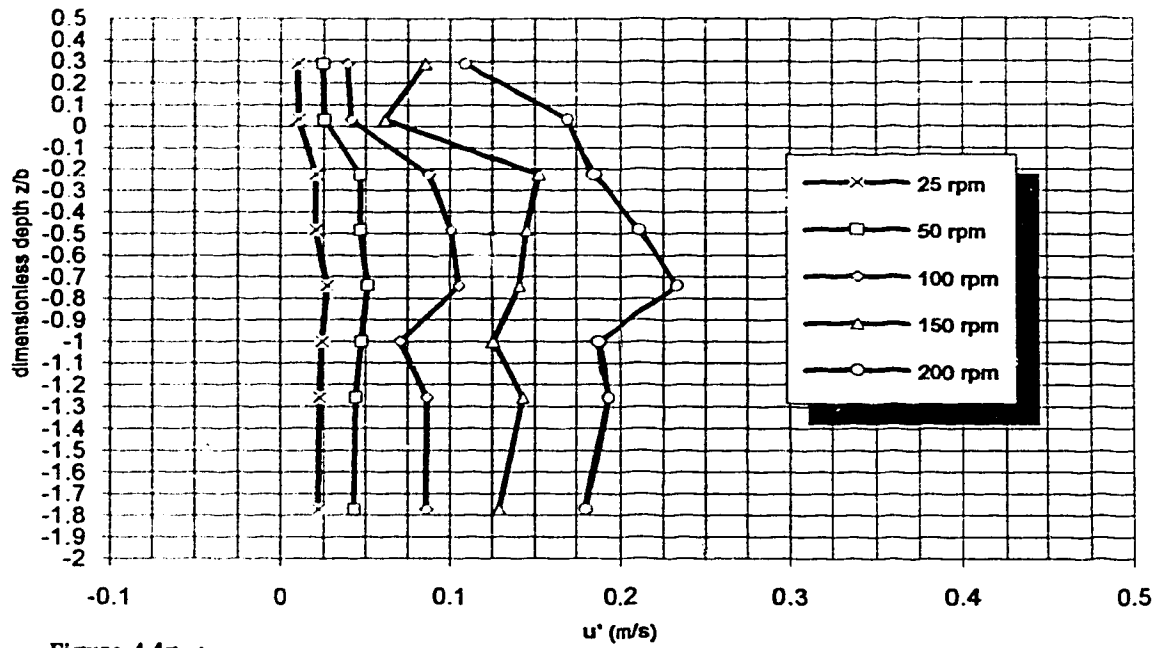


Figure 4-4g :

trial A01 - ecodyne impeller ; 1:55 scale
radial turbulent velocities near impeller - not normalized by tip speed
 $d=7.66$ cm ; $b=1.94$ cm ; $2r/d=1.044$

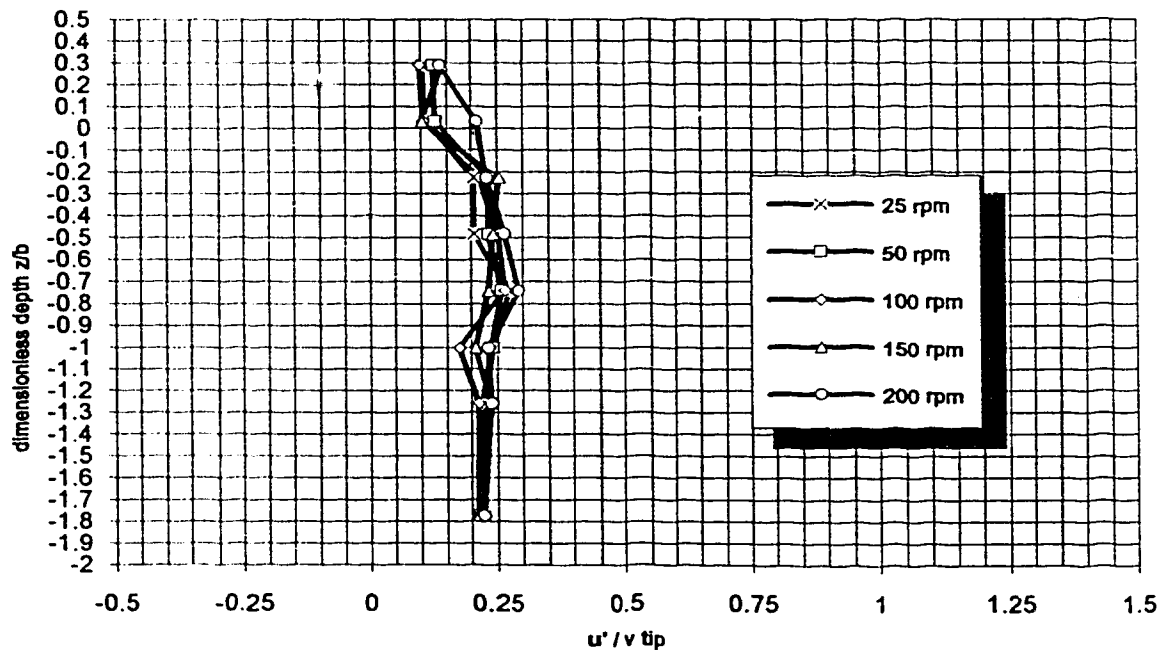


Figure 4-4gn :

trial A01 - ecodyne impeller ; 1:55 scale
radial turbulent velocities near impeller - normalized by tip speed
 $d=7.66$ cm ; $b=1.94$ cm ; $2r/d=1.044$

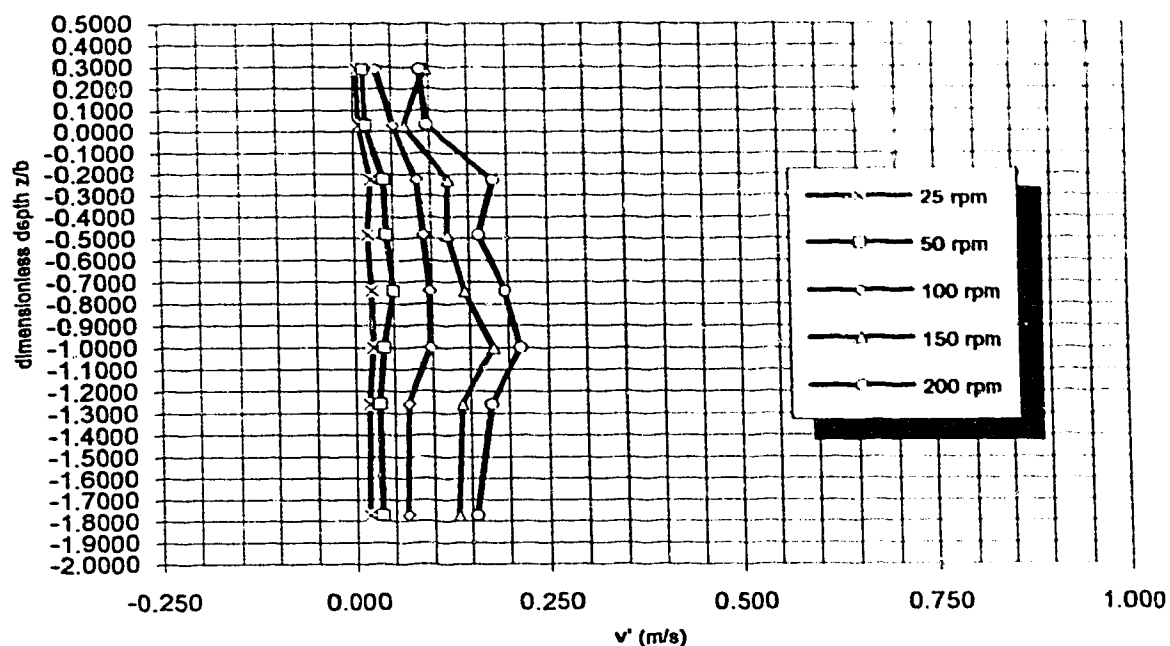


Figure 4-4h :

trial A01 - ecodyne Impeller ; 1:55 scale
 tangential turbulent velocities near Impeller - not normalized by tip speed
 $d=7.66$ cm ; $b=1.94$ cm ; $2r/d=1.044$

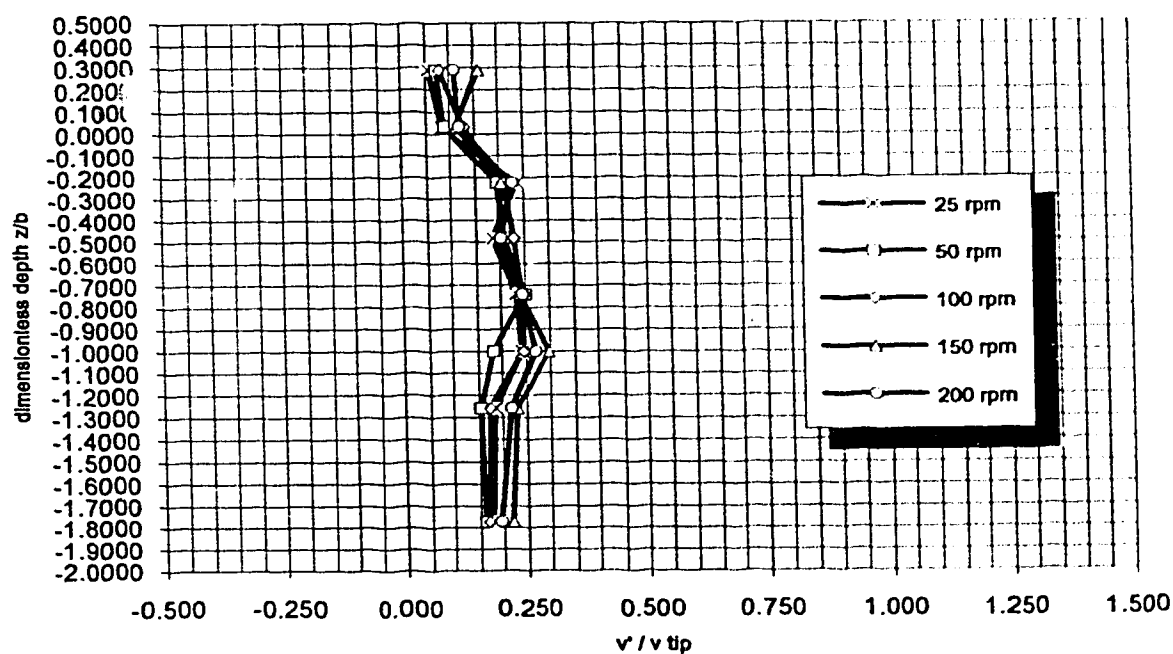


Figure 4-4hn :

trial A01 - ecodyne Impeller ; 1:55 scale
 tangential turbulent velocities near Impeller - normalized by tip speed
 $d=7.66$ cm ; $b=1.94$ cm ; $2r/d=1.044$

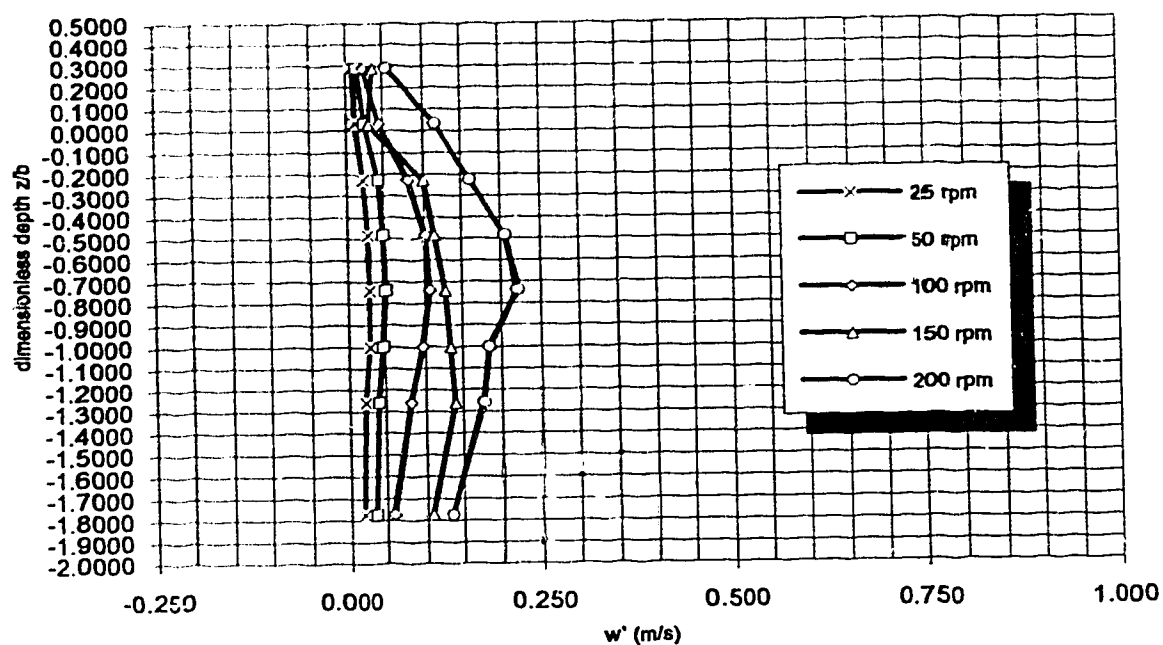


Figure 4-4i :

trial A01 - ecodyne impeller ; 1:55 scale
axial turbulent velocities near impeller - not normalized by tip speed
 $d=7.66$ cm ; $b=1.94$ cm ; $2r/d=1.044$

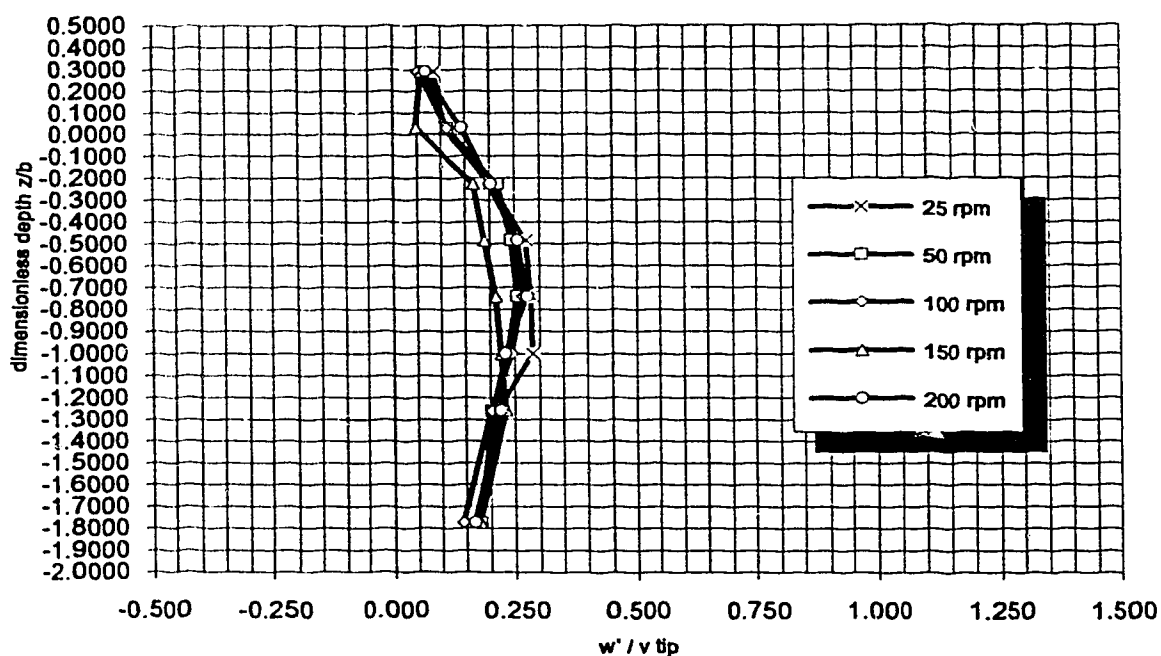


Figure 4-4in :

trial A01 - ecodyne impeller ; 1:55 scale
axial turbulent velocities near impeller - normalized by tip speed
 $d=7.66$ cm ; $b=1.94$ cm ; $2r/d=1.044$

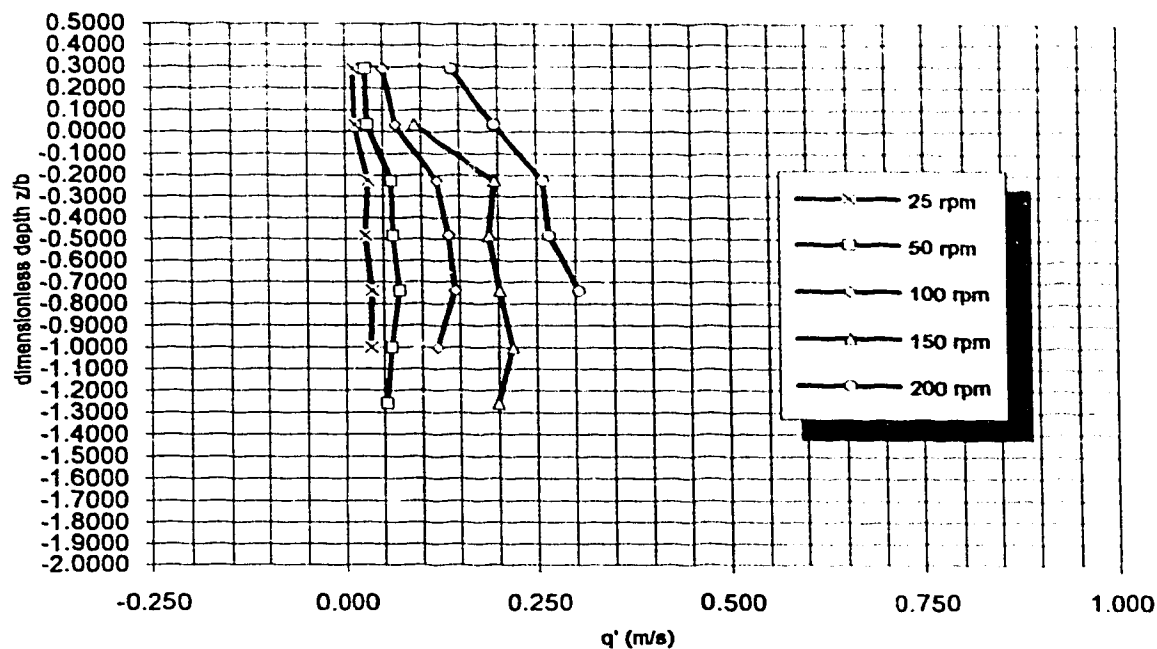


Figure 4-4j : trial A01 - ecodyne impeller ; 1:55 scale
turbulent velocities along axis of swirling radial jet - not normalized by tip speed
 $d=7.66 \text{ cm}$; $b=1.94 \text{ cm}$; $2r/d=1.044$

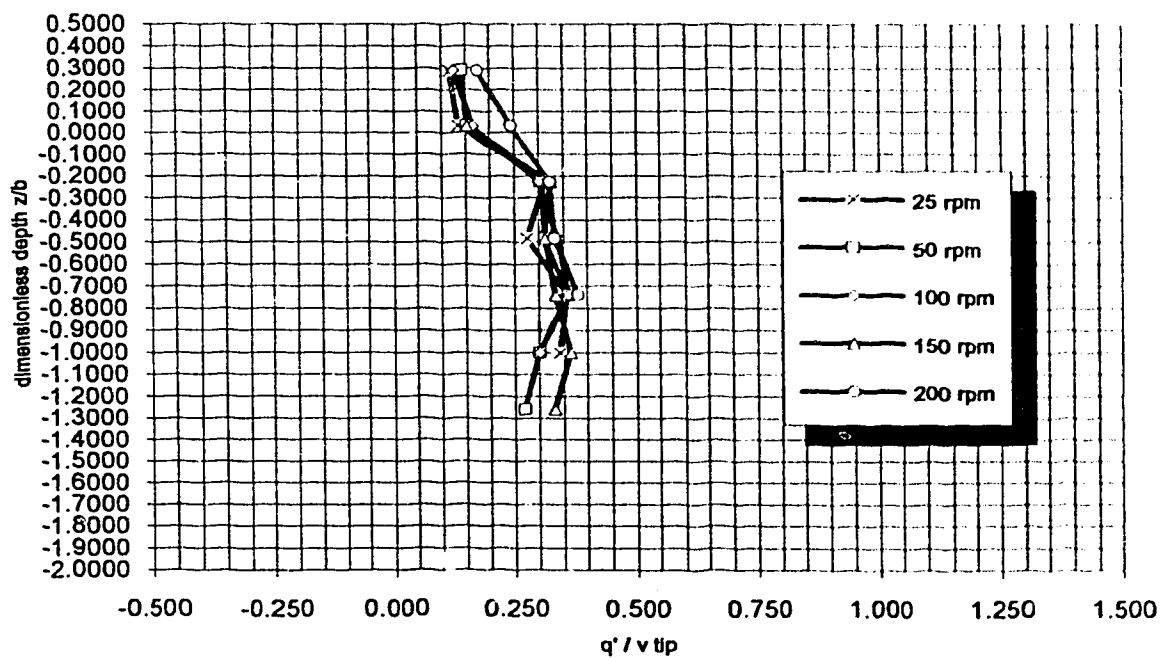


Figure 4-4jn : trial A01 - ecodyne impeller ; 1:55 scale
turbulent velocities along axis of swirling radial jet - normalized by tip speed
 $d=7.66 \text{ cm}$; $b=1.94 \text{ cm}$; $2r/d=1.044$

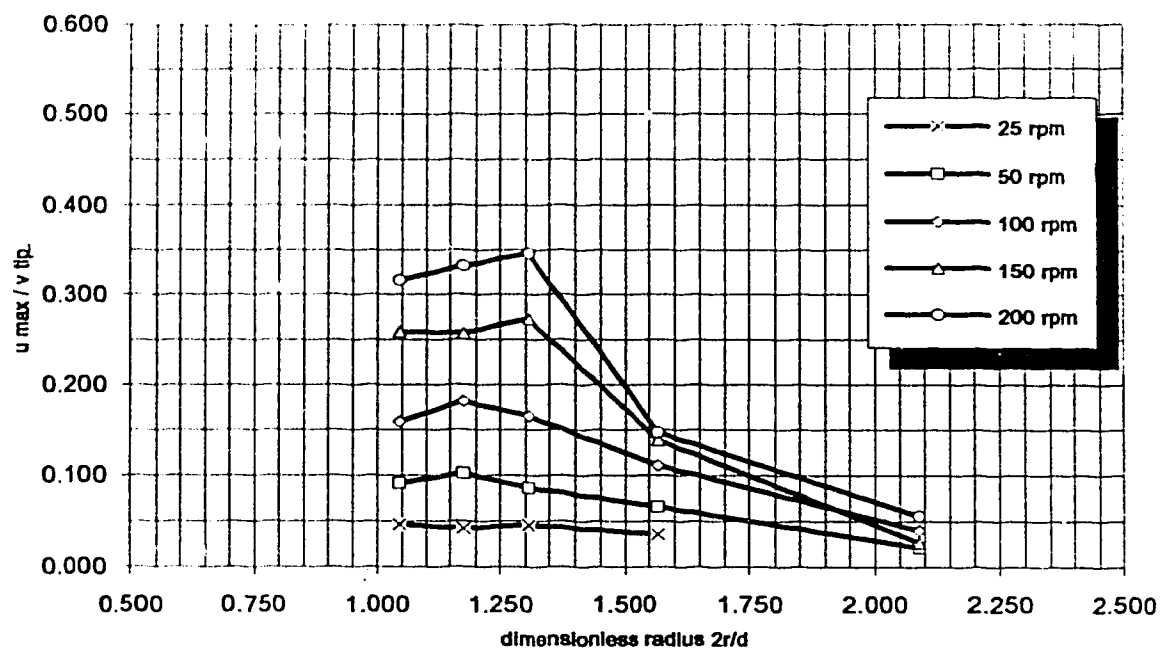


Figure 4-4k : trial A01- ecodyne Impeller ; 1:55 scale
radial decay of maximum radial average velocity - not normalized by tip speed
 $d=7.66$ cm ; $z/b=1.94$ cm

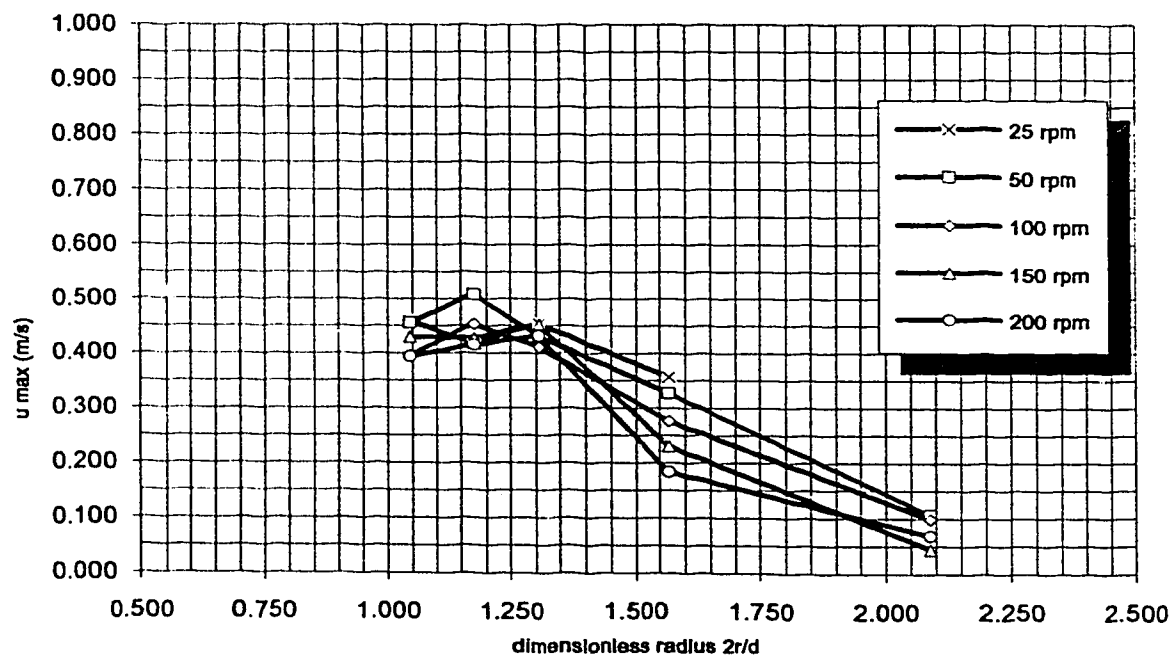


Figure 4-4kn : trial A01- ecodyne Impeller ; 1:55 scale
radial decay of maximum radial average velocity - normalized by tip speed
 $d=7.66$ cm ; $z/b=1.94$ cm

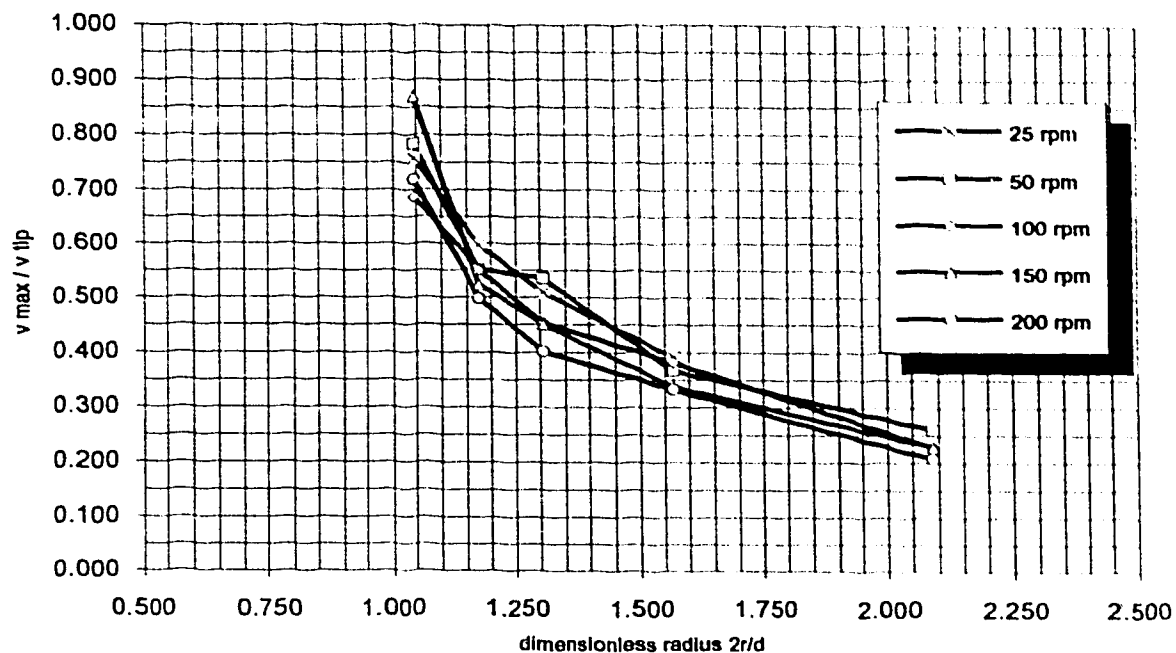


Figure 4-4l :

trial A01- ecodyne Impeller ; 1:55 scale
radial decay of maximum tangential average velocity - not normalized by tip speed
 $d=7.66$ cm ; $z/b=1.94$ cm

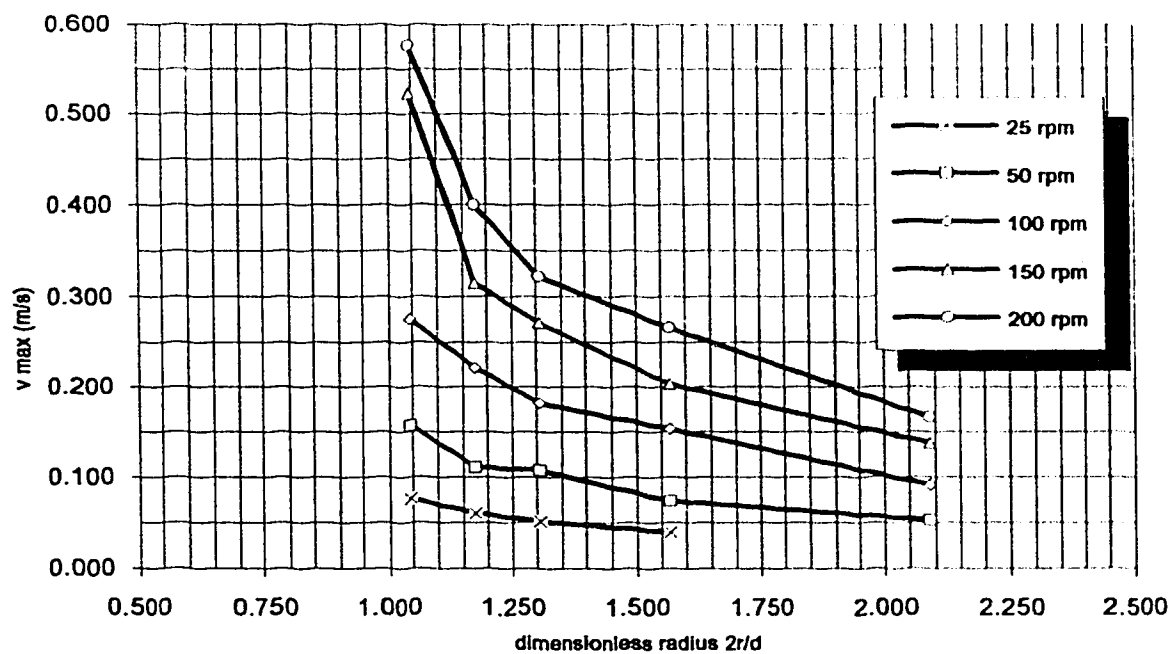


Figure 4-4ln :

trial A01- ecodyne Impeller ; 1:55 scale
radial decay of maximum tangential average velocity - not normalized by tip speed
 $d=7.66$ cm ; $z/b=1.94$ cm

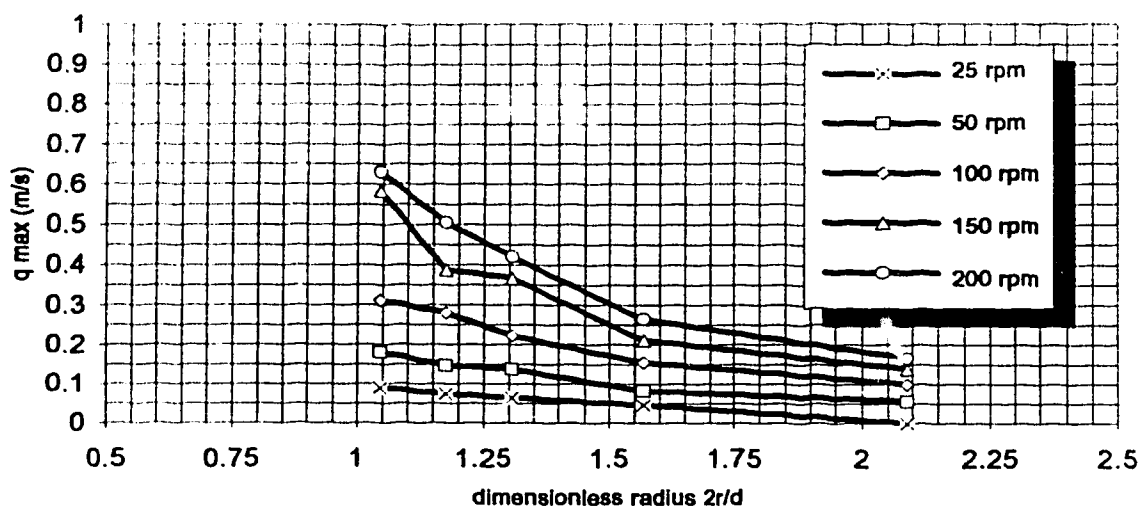


Figure 4-4m
trial A01- ecodyne impeller ; 1:55 scale
radial variation of maximum average velocities along axis of swirling radial jet - not
normalized by tip speed
 $d=7.66$ cm ; $b=1.94$ cm

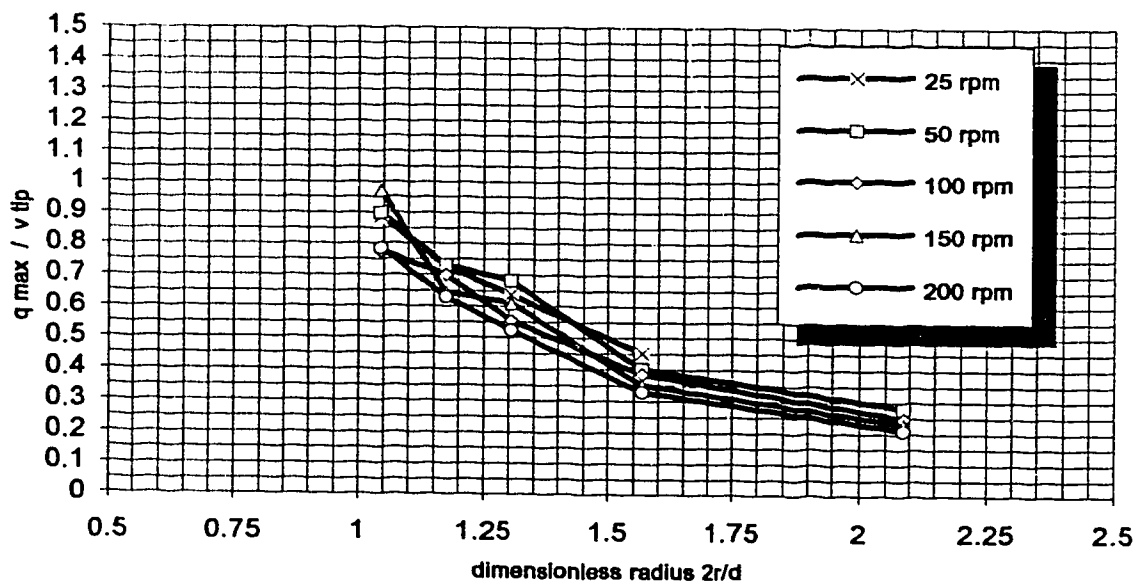


Figure 4-4mn
trial A01- ecodyne impeller ; 1:55 scale
radial variation of maximum average velocities along axis of swirling radial jet -
normalized by tip speed
 $d=7.66$ cm ; $b=1.94$ cm

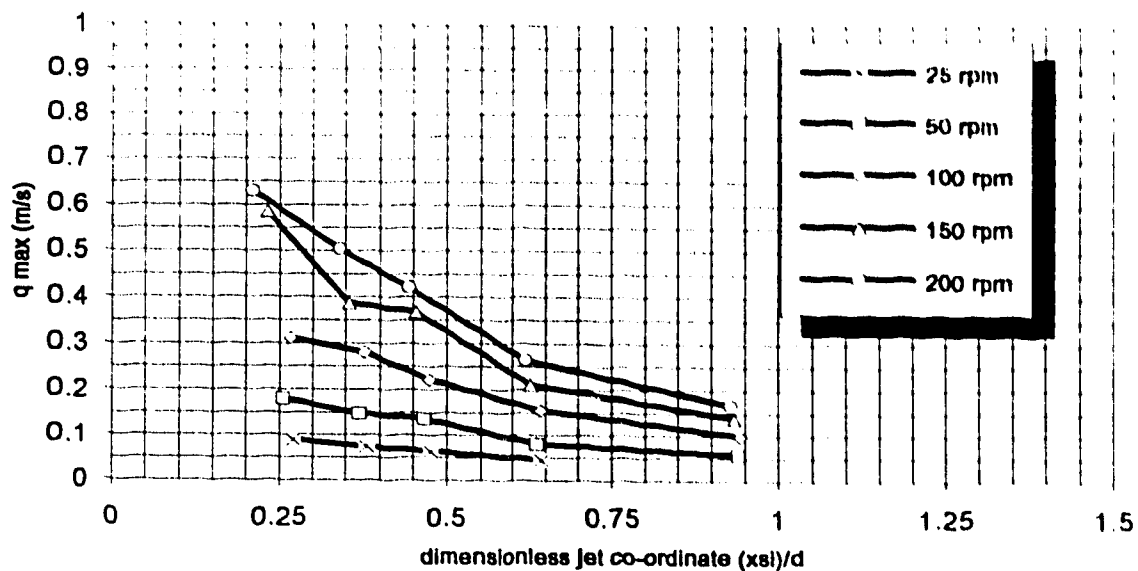


Figure 4-4n
 trial A01- ecodyne Impeller ; 1:55 scale
 xsi-based variation of maximum average velocities along axis of jet - not normalized
 by tip speed
 $d=7.66$ cm ; $b=1.94$ cm

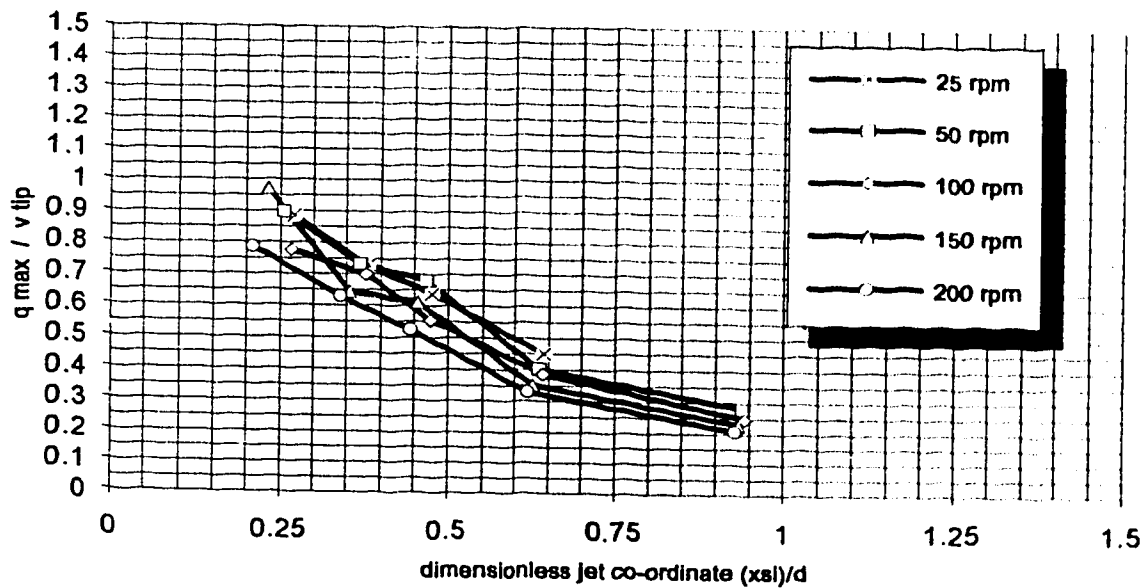
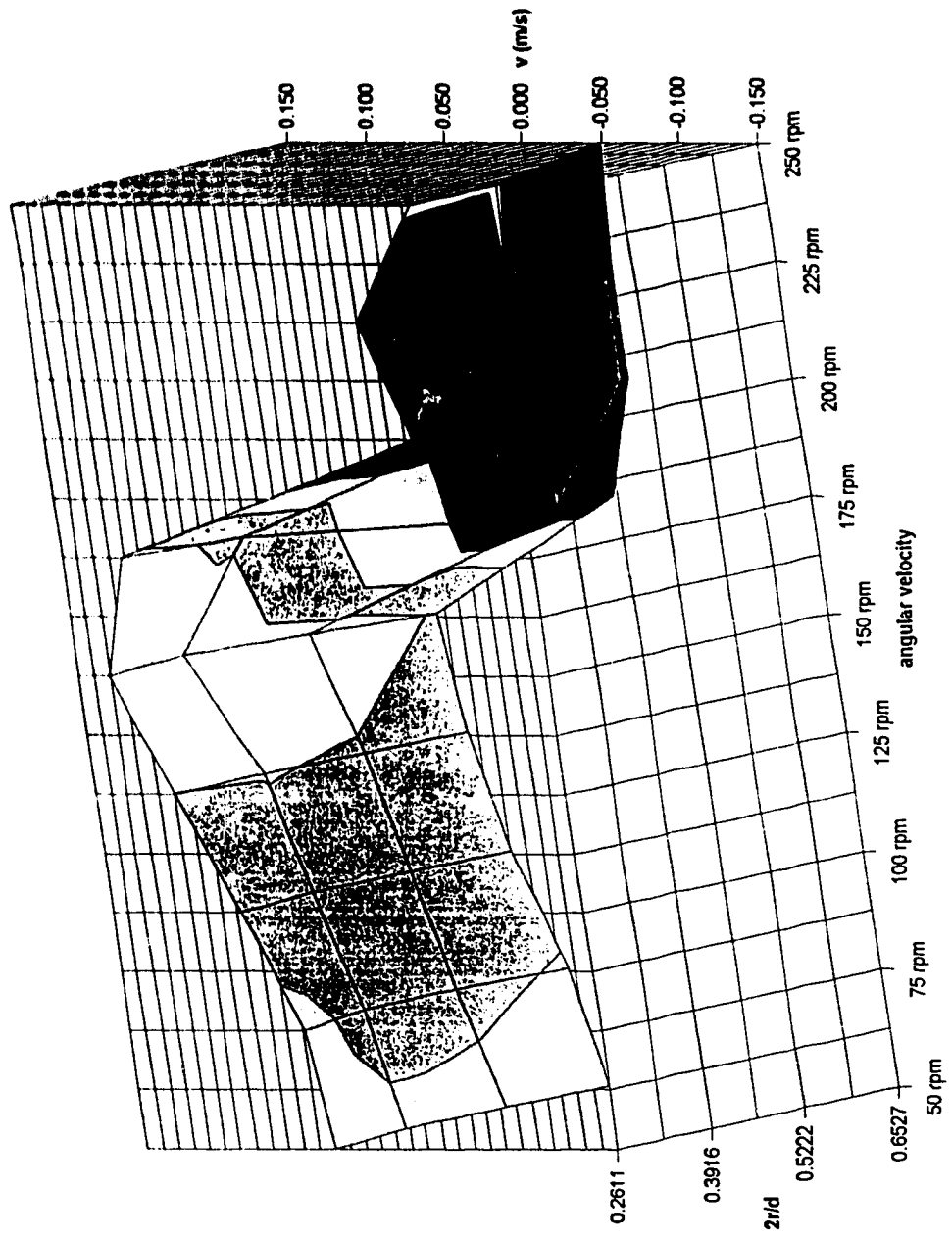


Figure 4-4nn
 trial A01- ecodyne Impeller ; 1:55 scale
 xsi-based variation of maximum average velocities along axis of jet - normalized by tip
 speed
 $d=7.66$ cm ; $b=1.94$ cm

Figure 4.5 :
ecodyne impeller, 1:55 scale
tangential average velocities near orifice - illustration of reverse flow



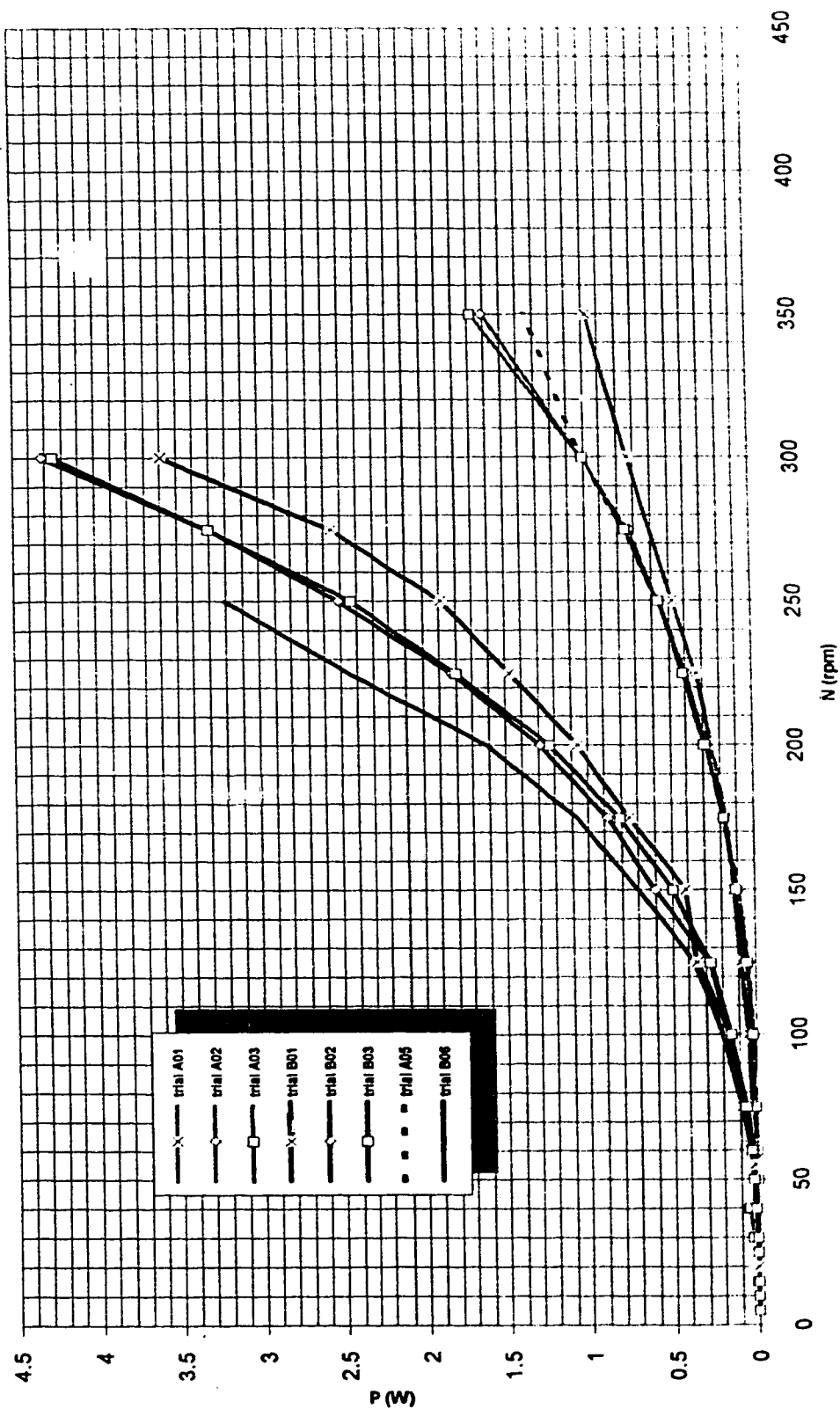


Figure 4-6 : measured power consumption
ecodyne impeller, 1:85-scale and 1:41-scale models - all configurations
impeller in water at approximately 20° C

5.0 Results: Derived Quantities (no tangential inflow)

5.1 Pumping Capacities

5.1.1 General

To recall, a dimensionless expression of an impeller's pumping capacity is expressed by the flow number, N_q . The relevant discharge is determined by defining a control volume around the impeller for the case of the free-impeller, and by defining and summing a rough incremental velocity flux both through the orifice and along the vertical face of the impeller's blade for the confined cases. These flow (or pumping) numbers may then be applied as a basis for defining the operational effects of various structural changes to the system, and for assessing the effect of scale-up upon the impeller's effectiveness. In order to render the most immediate comparison, the various impellers' resultant flow numbers at the different scales are compared not via angular velocity but via R_{i1} , the dimensionless impeller Reynolds number.

For the free impeller, *i.e.* trials A01 and B01 only, it was assumed that because the influx would be drawn up predominantly through the impeller's bottom, and because the efflux would be total via a swirling radial jet-like flow from the impeller, the total axial influx was roughly assumed to equal the total radial efflux. For the confined impeller, for the 1:55 and 1:41-scale models only, the total influx through the orifice was compared to three separate effluxes, calculated along the vertical face of the impeller's blade, radially across the interior of the draught tube, and vertically between the top of the draught tube and the water surface. The four resultant estimates of flow-through were often found not to correlate well with one another, so a certain amount of discretion was usually applied in averaging these values. For this reason, the calculated values of N_q are reported in a tabular format, not a graphical one. Finally, for the 1:10-scale NHC model, with no tangential inflow, as operational limitations precluded the collection of axial w-velocities, flow numbers were determined by measuring the influx velocities between the skirt and the floor, and by measuring the efflux velocities between the water surface and the top of the draught tube, thereby providing two estimates of flow-through^{*}.

In principle, the flow number, N_q , may be expressed by three separate expressions depending upon the units in which the angular velocity is expressed:

$$N_q = \frac{Q}{\omega d^3} \propto \frac{Q}{nd^3} \propto \frac{Q}{Nd^3}$$

The first represents flow numbers based upon the angular velocity in radians per second, the second represents the angular velocity given in revolutions per second (rps) and the third represents the angular velocity in revolutions per minute (rpm). Each of these expressions is dimensionally consistent, but tradition dictates that angular velocity in the calculation of N_q be expressed in units of rps instead of rad/s. As a result, N_q was consistently based upon angular velocity, n (rps), throughout this study. The various forms of N_q can easily be expressed in terms of the n -based expression that was used here:

$$N_q = \frac{Q}{nd^3} = \frac{Q}{\frac{1}{2\pi} \omega d^3} = \frac{Q}{\frac{1}{60} Nd^3}$$

* Note that for the case where tangential inflow Q_t is nonzero (NHC trials 2 and 3), the estimate of efflux discharge over the top of the draught tube is necessarily larger than the estimate of influx through the skirt opening. The case of nonzero Q_t is addressed in great detail in the **Implications of Tangential Inflow** chapter of this report.

Similarly, for the impeller Reynolds number R_i , it may be shown that:

$$R_i = \frac{nd^2}{\nu} = \frac{\frac{1}{2\pi} \omega d^2}{\nu} = \frac{\frac{1}{60} Nd^2}{\nu}$$

Where again only the n -based expression of R_i was employed.

5.1.2 Results

For the free impeller, represented by trials A01 and B01, the calculated flow numbers are presented in the following table, Table 5-1:

Table 5-1
flow numbers - trials A01 and B01
free impeller

scale	N (rpm)	R_i	N_q (influx - orifice)	N_q (efflux - jet)	N_q (average)
1:55	25	2.5×10^3	0.754	0.817	0.790
1:55	50	5.0×10^3	0.622	0.817	0.720
1:55	100	9.9×10^3	0.635	0.609	0.622
1:55	150	1.49×10^4	0.666	0.603	0.630
1:55	200	1.99×10^4	0.591	0.553	0.572
1:41	55	1.00×10^4	0.565	0.603	0.572
1:41	100	1.82×10^4	0.496	0.352	0.421

For the case with the draught tube only, trials A02 and B02 should be comparable. The results are summarized in Table 5-2:

Table 5-2
flow numbers - trials A02 and B02
confined impeller: draught tube only

scale	N (rpm)	R_i	N_q (influx - orifice)	N_q (efflux - jet)	N_q (average)
1:55	50	5.0×10^3	0.308	0.402	0.402
1:55	100	9.9×10^3	0.320	-	-
1:55	200	1.99×10^4	0.302	0.276	0.276
1:41	55	1.00×10^4	0.339	0.377	0.377
1:41	100	1.82×10^4	0.358	0.459	0.459

Trials A03, B03 and NHC trial 1 represent the case of the confined impeller with the as-built orifice and a 0.457 m opening between the skirt and floor, with no tangential influent, in an unbaffled tank. This configuration represents most closely the clarifier as it was just after the installation of the skirt in the early 1980's. The resultant flow numbers are presented in the following table, Table 5-3:

Table 5-3
flow numbers - trials A03, B03 & NHC trial 1
confined impeller: draught tube and skirt only

scale	N (rpm)	R_i	N_q (influx - orifice)	N_q (efflux - jet)	N_q (average)
1:55	50	5.0×10^3	0.364	0.465	0.547
1:55	100	9.9×10^3	0.383	0.452	0.540
1:55	200	1.99×10^4	0.364	0.471	0.490
1:41	55	1.00×10^4	0.333	0.383	0.553
1:41	100	1.82×10^4	0.383	0.379	0.471
1:10	10	3.10×10^3	0.628	-	-
1:10	30	9.22×10^3	0.521	-	-
1:10	50	1.54×10^4	0.496	-	-
1:10	70	2.15×10^4	0.440	-	-

Trial A04 represents a special case where the height of the skirt was lowered to a full-scale equivalent of 0.3048 m from the observed height of 0.457 m. Such an opening corresponds to the opening that NHC modelled in its original report (*q.v.*). The results of this single-N trial are presented in Table 5-4:

Table 5-4
flow numbers - trial A04
confined impeller: draught tube and constricted skirt opening

scale	N (rpm)	R_i	N_q (influx - orifice)	N_q (efflux - jet)	N_q (average)
1:55	100	9.9×10^3	0.333	0.534	0.427

The results of trial A05 are presented in Table 5-5. Configuration A05 is identical to that of trials A03 and B03 except that baffles are present in the upper portion of the draught tube. This configuration was again tested at only one angular velocity.

Table 5-5
flow numbers - trial A05
confined impeller: draught tube, skirt & baffles

scale	N (rpm)	R,	N_q (influx - orifice)	N_q (efflux - jet)	N_q (average)
1:55	100	9.9×10^4	0.276	0.333	0.339

The results of trial B06, which incorporated an enlarged orifice opening, are presented in Table 5-6. Again, only one angular velocity was tested.

Table 5-6
flow numbers - trial B06
confined impeller: draught tube, skirt & enlarged orifice

scale	N (rpm)	R,	N_q (influx - orifice)	N_q (efflux - jet)	N_q (average)
1:41	100	1.82×10^4	0.415	0.672	0.478

Finally, the results of a special trial, B-ANN are presented. As the purpose of this trial was to assess simultaneously the effects of increasing the orifice size while decreasing the depth in the tank, a full set of data collection points was not run for each set-up. The flow numbers were not collected along the orifice and along the vertical face of the impeller's blade as they were for all other trials. Instead, axial flow numbers were determined by means of a set of data collection points lying along the radius of the draught tube, between the impeller's shaft and the wall of the draught tube. The results are presented in Table 5-7.

Table 5-7
flow numbers - trial B06
confined impeller: draught tube & skirt, with variable orifice opening and variable depth
equivalent full-scale depth above draught tube = 1.482 m

scale	N (rpm)	R,	full-scale depth above draught tube (m)	fraction of full- scale depth above draught tube	orifice	N_q (average)
1:41	100	1.82×10^4	1.482	1.000		0.333
1:41	100	1.82×10^4	1.0	0.675	as-built	0.371
1:41	100	1.82×10^4	0.5	0.337		0.364
1:41	100	1.82×10^4	1.482	1.000		0.415
1:41	100	1.82×10^4	1.0	0.675	enlarged	0.459
1:41	100	1.82×10^4	0.5	0.337		0.509

5.2 Power Numbers

As with the flow number, N_q , and impeller Reynolds number, R_i , the power number may also be expressed in terms of N , n and ω . Again, tradition dictates that the power number be expressed in the following form:

$$N_p = \frac{P}{\rho n^3 d^5}$$

where the various forms of the power number can be related by simple constants:

$$N_p = \frac{P}{\rho n^3 d^5} = \frac{P}{\frac{1}{(2\pi)^3} \omega^3 d^5} = \frac{P}{\frac{1}{60^3} N^3 d^5}$$

According to custom, the calculated power numbers were plotted with respect to R_i , the (n-based) impeller Reynolds number, for every configuration that was investigated - the resultant plots are presented in Figures 5-1a through 5-1e. It must be recalled that these power numbers represent the case of an unbaffled tank, with a draught tube that is unbaffled for every trial except one.

Traditionally, the convention has been to express the power number as a single parameter in handbooks of technical specifications, manuals and the like. Such an approach enables one to attain an immediate appreciation for the capabilities of the impeller, especially if that impeller is to be run in the high- R_i flow regime. Although the laser-doppler velocity measurements were not run past $R_i \approx 2 \times 10^4$, torque (and hence power) measurements were performed at angular velocities well beyond those that were investigated in the velocity measurements. According to Figures 5-1a through 5-1e, whereas the calculated power numbers all seem to follow some form of curved path in the low- R_i range, they indeed do seem to approach a state of constancy once sufficiently high values of R_i are achieved, thereby exhibiting the inception of the so-called turbulent flow regime. In order to facilitate comparison, the approximately constant, high- R_i , turbulent power numbers are presented in Table 5-8:

Table 5-8
constant high- R_i power numbers - all trials & configurations

trial	description	"constant" N_p
A01	free impeller	2.3
B01	free impeller	2.3
A02	draught tube only	3.0
B02	draught tube only	3.0
A03	draught tube & skirt	3.0
B03	draught tube & skirt	3.0
A04	decreased skirt opening	-
A05	draught tube, skirt, baffles	3.1
B06	enlarged orifice	3.6

5.3 Turbulent Dissipation Rates

5.3.1 General

Analysis of the structure of turbulent flow in impeller-agitated mixing is at present probably the most intensive field of study with respect to the impeller-agitated mixing. Much of the impetus behind the study of turbulence lies in the definition of appropriate boundary conditions for computer modelling of impeller-generated mixing phenomena. As previously explained, turbulence encompasses a wide variety of length scales and time scales, with any number of turbulent eddies being present within a spatially and temporally variant flow structure that is changing with great rapidity. As well, practical limitations ensure difficulty in the collection of turbulence data in anything but the lowest frequencies of energy transmission. One only has to recall the Reynolds equations and the classic Reynolds closure problem to realize the difficulties in analyzing turbulent flow. Consequently, this study is concerned with the concepts of turbulence and energy dissipation only insofar as a fairly simple yet generally well accepted expression of the local turbulent energy dissipation rate permits.

5.3.2 Dissipation Rate

In the **Review of Literature**, it was shown that for the case of isotropic turbulence, the local turbulent dissipation rate may be estimated as:

$$\epsilon \propto \frac{u'^3}{\ell}$$

However, for the more general case where the turbulent velocities are known in all three directions, the following formula can be used:

$$\epsilon = \frac{U'^3}{\ell} = \frac{[\frac{1}{2} (u^2 + v^2 + w^2)]^{\frac{3}{2}}}{\ell}$$

It was shown that the turbulent length scale, ℓ , is generally thought to be of the order of the swirling radial jet's $\frac{1}{2}$ -width, which in turn can be directly related to the impeller's blade height, b . For this study, it was generally assumed for all calculations of the local turbulent dissipation rate that

$$\ell \approx \frac{1}{2} b$$

except for the case of the free impeller, where a slightly different estimate of ℓ was examined.

5.3.3 Estimation & Confirmation of the Turbulent Length Scale

In order to assess these assumptions, the radial variations of the resultant velocity profiles for trials A01 and B01 were examined in the radial jet for the various angular velocities. As Figure 4-4a (among others) illustrates, the radial jet appears as a clearly defined zone of comparably high velocity with respect to the other points in the tank. The linear variation of the total width of the radial jet, Λ , was estimated through manual measurement of the height of the positive portion of the u -velocity profile for a given dimensionless radial location $2r/d$. The fact that the impeller was unconfined in these trials allowed a much more thorough analysis of the spreading rate to be made than for the cases of the confined impeller as velocity measurements were taken at five different dimensionless radii, not three.

Since the radial decay of the velocities in the case of a swirling radial jet is decidedly non-linear (see Figure 4-4m, *e.g.*), it was difficult to isolate any functional dependency of the length scale upon radial coordinate $2r/d$. However, according to swirling radial jet analysis as presented by Kolar, Filip & Curev (1985), or Kresta & Wood (1991), the variation of the jet-width, when referenced along a new coordinate, ξ , which expresses the distance along the axis of the swirling radial jet, should presumably be linear. Thus, coordinate ξ was defined for each particular dimensionless radius $2r/d$, and the measured jet-width was then simultaneously examined with respect to *both* ξ *as well as* N by means of multiparameter linear regression analysis. Specifically, variation of the jet-width with ξ and N was assumed to be of the form:

$$\beta_0 + \beta_1 \xi + \beta_2 N + \beta_3 \xi N = \Lambda$$

After solution of this equation, it was found that the jet-width, Λ , may be expressed for trials A01 and B01 by the following expressions:

$$\begin{aligned} \text{trial A01:} \quad \frac{\Lambda}{b} &= 1.2559 - 0.00191 N + 0.13351 \xi + 0.0026 \xi N \\ \text{trial B01:} \quad \frac{\Lambda}{b} &= 1.0015 - 0.00268 N + 0.09679 \xi + 0.00010 \xi N \end{aligned}$$

Obviously, this approach is limited by the relatively small sample size available (five dimensionless radii at five N 's for the 1:55-scale ; three dimensionless radii at two N 's for the 1:41-scale). These best-fit lines appeared to fit the data reasonably well, especially near the impeller, but there was still a fair amount of scatter.

These relations cannot therefore be thought to define absolutely the variation of jet-width for this type of impeller. What is useful in this analysis is that several expected, fundamental properties of the jet's behaviour are indicated. Specifically, these resultant linear regression models indicate a negative dependence of jet-width Λ upon N : as the angular velocity is increased, the width of the jet appears to decrease, behaviour which may be seen clearly in the series of vector plots, Figures 4-1a through 4-1c. Secondly, although a dependence of Λ upon ξ exists, it is seen to be only a fraction of the calculated dependence of Λ upon ξ , implying that the mechanics of turbulent dissipation along the jet's axis are ultimately most responsible for the variation in the jet-width. Thirdly, it is seen that the dependence of Λ upon ξ is approximately of the order of 0.10, thus indicating that the width of the swirling radial jet increases approximately as one-tenth of the distance travelled. This result is comparable to the work of Antonia, Satyaprakash & Hussain (1980) who found that the width of the circular free jet increases at a similar rate ; unfortunately, no explicit values of the spreading rate of the swirling radial jet were found in the literature. Finally and most importantly, setting $\xi = 0$, it is seen that the dimensionless jet-width is of the order of unity near the impeller. In other words, near the impeller:

$$\frac{\Lambda}{b} \approx 1.0$$

which, when taken together with the assumption that

$$\Lambda \approx b \approx 2 \ell$$

yields the following expression for the turbulent length-scale at the impeller's blade:

$$l = \frac{1}{2} b$$

5.3.4 Results

Given that the linear regression analysis apparently confirmed that the width of the turbulent jet is approximately equal to the height of the impeller's blade in the vicinity of the impeller, thereby allowing the further confirmation that the turbulent length-scale is approximately equal to the blade-height, b , it was decided that for trials A01 and B01, ϵ would be defined with the value of the turbulent length-scale being estimated by $\frac{1}{2}$ of the of the best-fit value of Δ . For all other trials, ϵ was estimated only in the immediate vicinity of the impeller's blade (*i.e.* $2r/d = 1.044$ & $2r/d = 1.175$ only), under the assumptions that $l = \frac{1}{2} b$, and that the jet's width would increase by approximately ten percent between dimensionless radial locations $2r/d = 1.044$ and $2r/d = 1.175$.

In this manner, local estimates of the turbulent dissipation rate were calculated for all trials. The results of this analysis are presented graphically in Figures 6-5a through 6-13a as a series of plots of the variation of ϵ along the vertical face of the impeller's blade, and also in Figures 6-14a through 6-17a, which depict the lateral variation of ϵ (both with respect to $2r/d$ and to ξ/d) for trials A01 and B01 only. Each of these plots is presented together with two accompanying non-dimensionalized restatement of the same ϵ data. The significance of these dimensionless plots will be discussed more fully in the following chapter of this report.

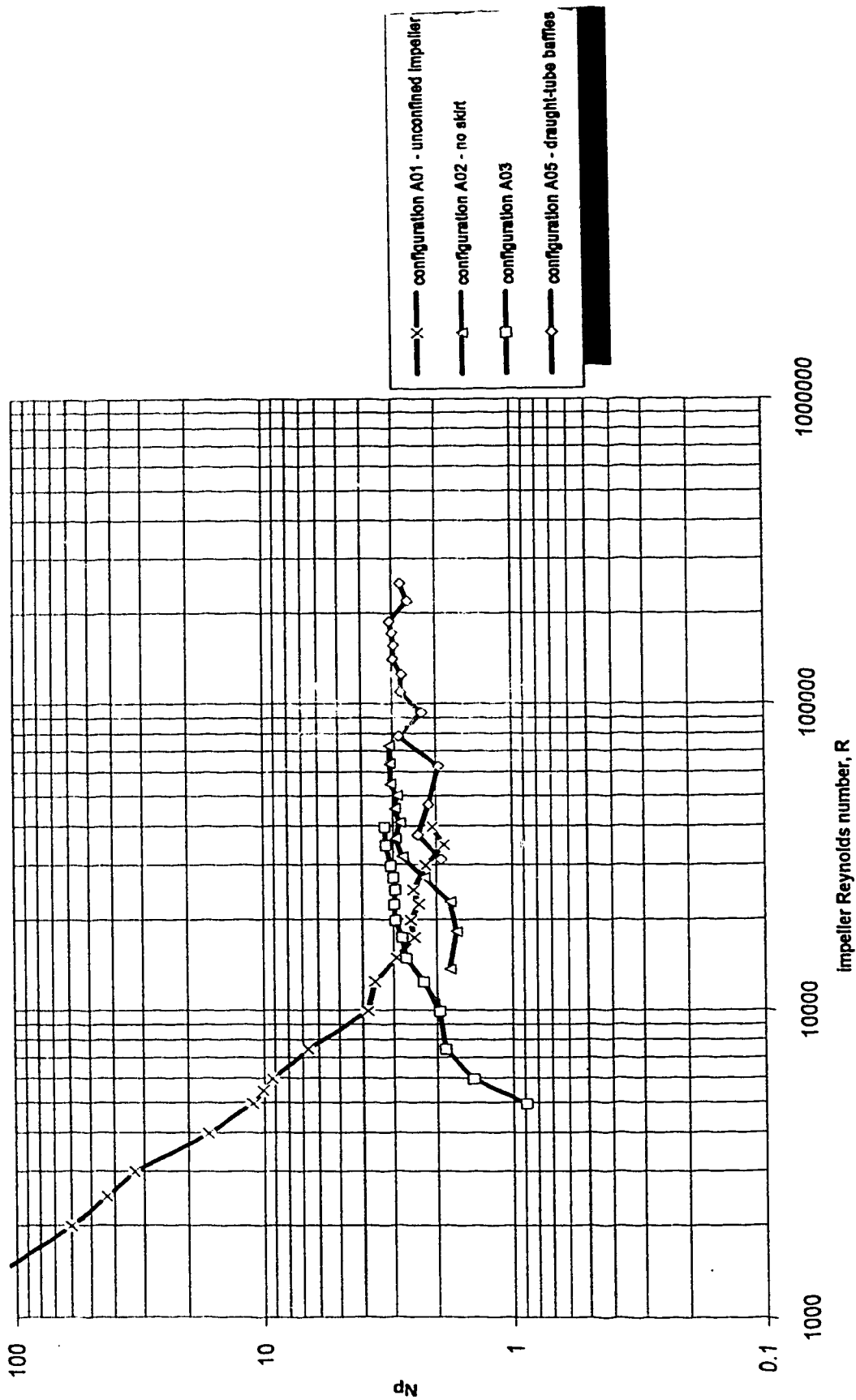


Figure 5-1a : ecodyne Impeller - 1:55 scale, trials A01 - A05
power numbers
 $d = 7.66 \text{ cm}$

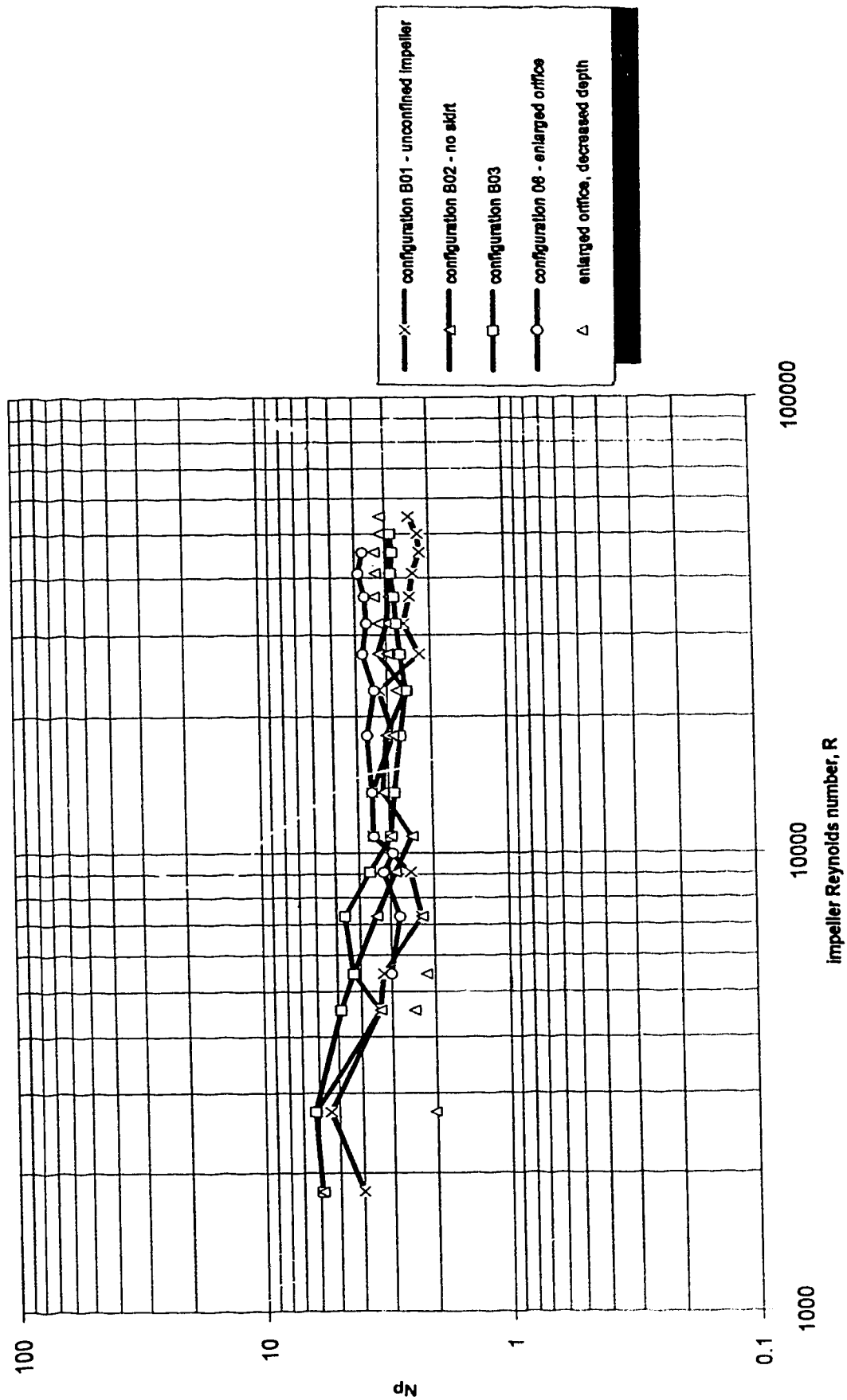


Figure 5.1b : ecodyne impeller - 1:55 scale, trials B01 - B05
power numbers
d=10.37 cm

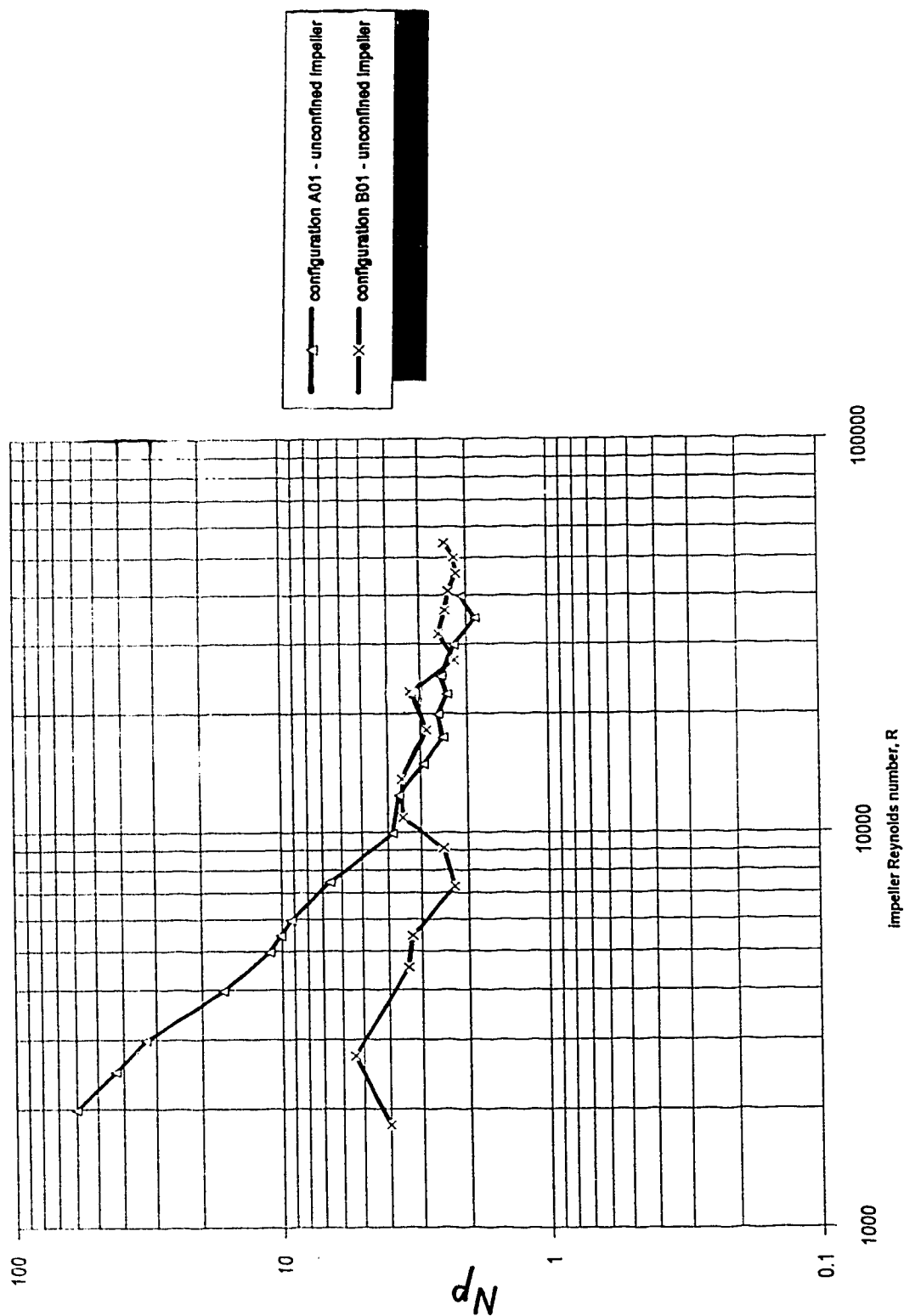


Figure 5-1c : ecodyne Impeller - 1:55 scale & 1:41 scale, configuration 01
power numbers
d=10.37 cm

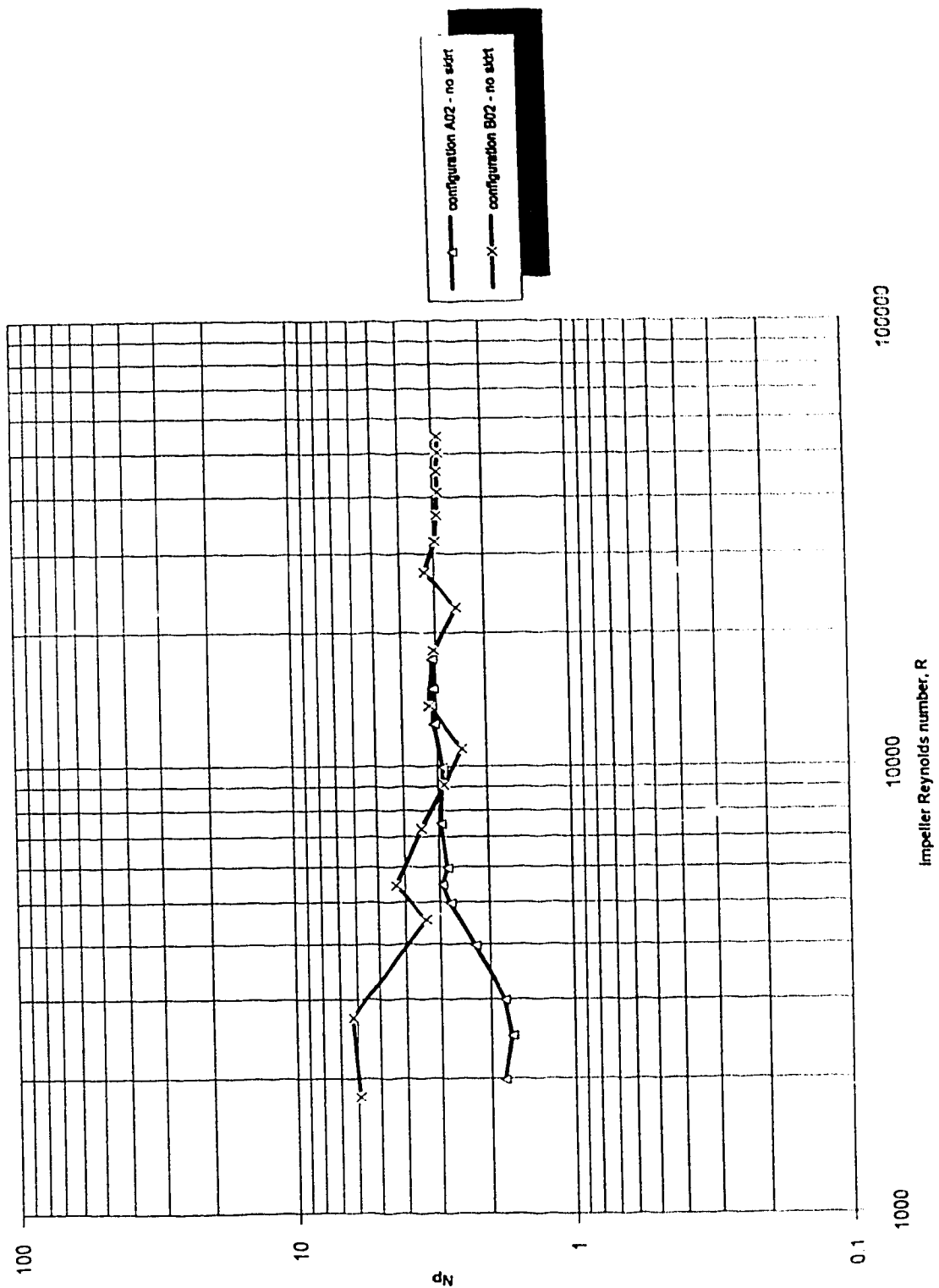


Figure 5-1d : ecodyna impeller - 1:55 scale & 1:41 scale, configuration 02
power numbers
d=10.37 cm

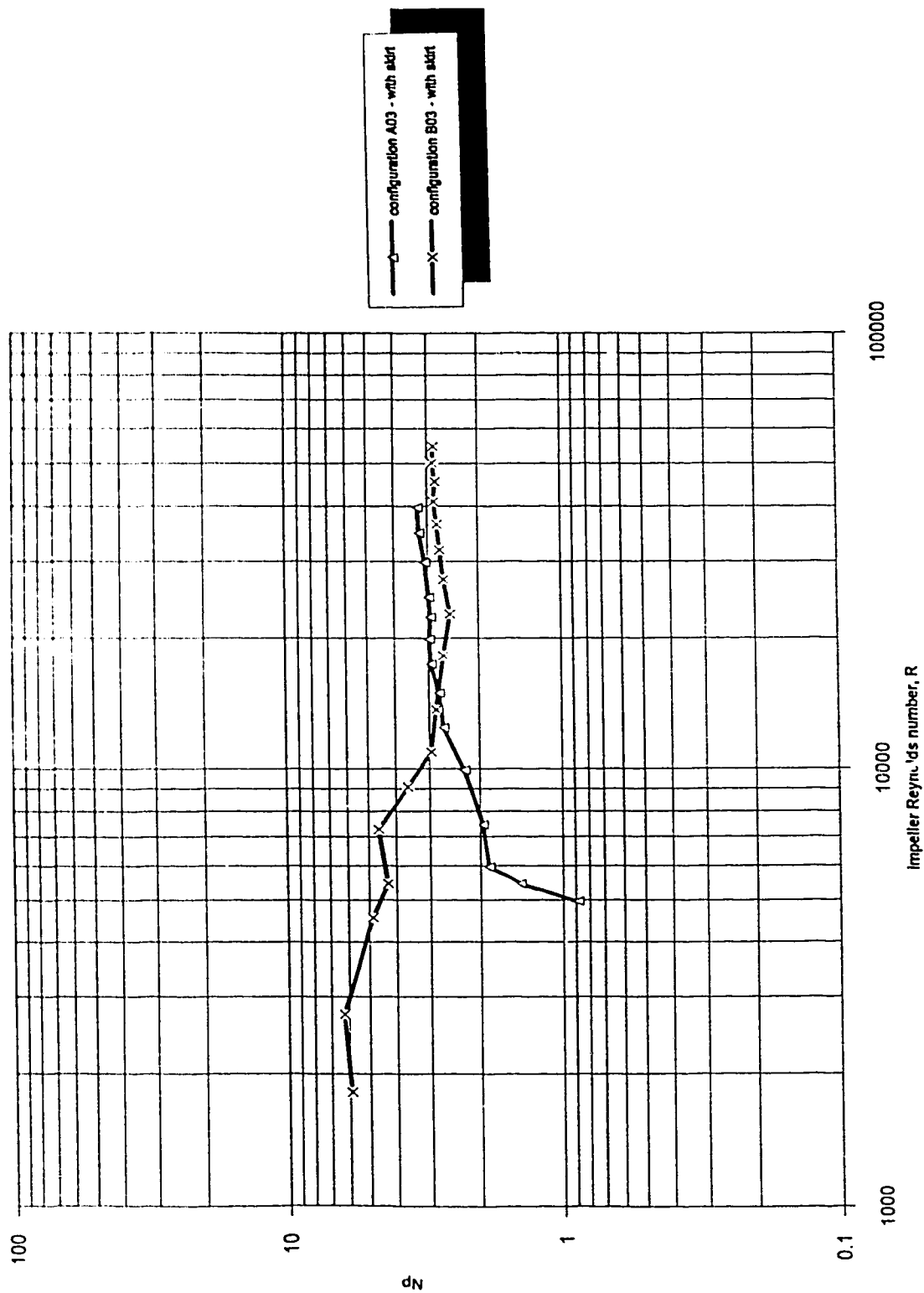


Figure 5-1e : acodyne Impeller - 1:55 scale & 1:41 scale, configuration 03
power numbers
 $d=10.37$ cm

6.0 Similarity (no tangential inflow)

6.1 General

Because the Ecodyne impeller is decidedly uncommon, it is desired to compare it to numerous other types of impellers that have been studied more extensively in the literature. Such a comparison may be made most conveniently by the use of dimensionless parameters. In addition, the use of dimensionless parameters presents a straightforward, relevant means by which the effect of scale, if any, on the impeller's characteristic behaviour may be recognized. Thus, a number of calculated dimensionless parameters for the Ecodyne impeller will now be presented along with comparable values from the literature for other types of impellers so that the relative behaviour of the Ecodyne impeller may be appreciated.

6.2 Velocities

The practice of normalizing velocities via tip speed of the impeller is probably the most common means of comparison. In order to illustrate the practice on non-dimensionalization of velocities, consider the series of vector plots, Figures 4-1a through 4-3b, which express the as-measured average velocities for a particular configuration. By dividing all of the as-measured velocities by the tip speed of the impeller, $\frac{1}{2}\omega d$, the resultant flows are normalized. Such normalized flow-pattern vector-plots are presented in Figures 4-1an to 4-3bn and are presented on the same page as the non-normalized vector-plots to emphasize similarity. Comparison of these plots illustrates that generally, for a specific configuration, the scaled velocity-vectors are approximately the same length, regardless of angular velocity, thereby indicating that the velocity profiles are similar. As such, the angles of the vectors do not change greatly upon normalization, and it continues to appear that flow near the impeller is the most vigorous.

To illustrate this concept further, the vertical variations of the various measured velocities for any given trial may also be divided by the tip speed. In this case, however, both average and turbulent velocities are subjected to the non-dimensionalization process. The resultant series of plots is presented (again for trial A01 only) in Figures 4-4an through 4-4jn. In this project, as there are far too many plots required to describe every test in such great detail, the results of only one particular test are presented here (trial A01) for illustrative purposes. As before, the as-measured and normalized velocity plots are presented adjacent to one another for emphasis. The series of normalized velocities seems to indicate that the measured velocities at any particular value of ω and at any spatial location collapse onto a single curve. Similarly, one may normalize the radial variation of velocities, such as in Figures 4-4fn through 4-4mn, although presumably such quantities must be treated with caution with increasing distance from the impeller since wall effects could begin to affect the jet-like flow from the impeller. Therefore, in practical terms, both the time-averaged and turbulent velocity fields in any given configuration at a particular scale are seen to be expressible as a simple proportion of the impeller's tip speed.

The occurrence of kinetic similarity is observable in every configuration that was studied. Actually, the concept of kinetic similarity is one of the tenets of the analysis of turbulent jets. For ideally symmetrical cases, mathematical similarity analysis has allowed the definition of specific mathematical functions to describe the measured velocity profiles: consider the approximation of the velocity profile in a circular jet by the gaussian distribution, Rajaratnam (1975), or Curev's (1980) characterization of the swirling radial jet via a Taylor-series similarity function. In this study, there is a distinct lack of symmetry of the jet about its own axis because the presence of a cap or plate over the impeller's blades allows flow from the bottom only to be pumped in, resulting in a velocity profile that is unbalanced or skewed about the blade's mid-height.

* This is identical to the traditional statement of V_{tip} as $\pi\omega d$.

Conceivably, an appropriate velocity distribution could be developed for insertion into a mathematical similarity analysis, but the usefulness of such an analytical tool to this study is limited - it is much more useful simply to report the velocities and velocity profiles in a clear dimensionless manner.

In the spirit of mathematical similarity analysis, as it is generally known, *e.g.* Rajaratnam (1975), that the behaviour of a jet with respect to spreading depends upon the conservation of momentum flux, and that the initial momentum flux depends only upon the discharge at the source and the dimensions of the nozzle, there exists then by necessity a direct means of predicting similar behaviour at two different scales for the same geometrical configuration. Conversely, since the properties of the jet depend only upon initial conditions, the superposition of dimensionless velocity profiles from geometrically similar models should collapse upon a single line if inter-scale similarity indeed be proven. To this end, representative dimensionless velocity profiles are presented in Figures 6-1-1n through 6-3-11n, showing superposition of typical non-dimensionalized velocity profiles for configurations 01 to 03, and for all scales. Again, the series of dimensionless velocity-profile plots seems to indicate fairly conclusively that the measured velocities, both average and turbulent, ostensibly everywhere in the impeller-agitated flow but most appropriately in the jet itself, at any value of ω , at the same spatial location, and regardless of scale collapse onto a single curve.

Mathematically, the existence of such similarity may be expressed in the following manner.

Both average and turbulent velocities may be expressed via scale-invariant and ω -invariant constant fractions of the tip speed:

$$\frac{u}{v_{tip}} = k$$

$$\frac{u'}{v_{tip}} = k'$$

Now, since $v_{tip} = \frac{1}{2}\omega d$, it may be shown that

$$\frac{u'}{u} = \frac{k_u' v_{tip}}{k_u v_{tip}} = \text{constant} = B$$

Thus the turbulent velocity may be expressed as a specific fraction of the average velocity:

$$u' = B u$$

a result which demands comparison to the work of Antonia *et al.* (1980), who defined a similar result for the case of the free circular jet.

The significant features of the dimensionless velocity profiles, Figures 6-1-1n through 6-3-11n, may now be summarized in Table 6-1 by tabulation of the relevant maxima at a common, dimensionally consistent radial location together with the implied assumption that the corresponding complete velocity profiles are similar.

Table 6-1
dimensionless characteristics of velocity near impeller's blade
Ecodyne impeller, all scales, all observed ω 's - no tangential inflow

trial	scale	2r/d	maxima:							
			u/v_{up}	v/v_{up}	w/v_{up}	U/v_{up}	u'/v_{up}	v'/v_{up}	w'/v_{up}	U'/v_{up}
A01	1:55	1.044	0.44	0.73	0.18	0.85	0.26	0.25	0.25	0.439
B01	1:41	1.044								
A02	1:55	1.044	0.43	0.88	0.06	0.98	0.26	0.20	0.18	0.374
B02	1:41	1.044								
A03	1:55	1.044								
B03	1:41	1.044	0.48	0.88	0.07	1.00	0.25	0.20	0.18	0.367
nhc-1	1:10	1.070								
A04	1:55	1.044	0.46	0.91	0.08	1.02	0.23	0.19	0.18	0.348
A05	1:55	1.044	0.35	0.89	0.06	0.96	0.20	0.18	0.16	0.313
B06	1:41	1.044	0.85	0.90	0.15	1.25	0.25	0.20	0.18	0.367

Immediately, a number of conclusions may be drawn from Table 6-1:

- the turbulent velocities are of the same order and are approximately scale-invariant
- the presence of the draught tube apparently causes the average tangential (v) velocities to increase but causes the average axial (w) velocities to decrease, and
- it would appear that the turbulent velocities may be ranked in order of magnitude as $u' > v' > w'$

Such a observations lead to a number of inferences with respect to the effects of structural modifications on the flow - a topic that will be addressed in greater detail later in this document.

Accepting then that the similarity of velocity profiles is indeed scale-invariant, one may now set out to compare the observed characteristics of the Ecodyne impeller to equivalent dimensionless characteristics of various other types of impellers, as collected from the literature. In researching the literature, no studies dealing specifically with the Ecodyne impeller have yet been found, so it is not possible to compare the results determined here directly to those for a similar type of impeller. The results of this study are still of great interest though because they enable the Ecodyne impeller and the velocities induced thereby (both average and turbulent) to be compared among impellers of entirely different design and intended usage as represented by a number of articles from the last thirty years.

A tabular presentation, Table 6-2, provides the most immediate means of comparison. Again, as it is difficult to plot the entire vertical variation of the measured dimensionless velocity profiles, and given the variety of types of impeller, the resultant variety in flow patterns, and the lack of consistency in spatial location, comparison is again most directly possible by choosing locations in the immediate vicinity of the stirrer and selecting the significant dimensionless-velocity maxima there. The values extracted from the literature represent a number of relevant articles covering the last thirty years.

Table 6-2
dimensionless characteristics of velocity near impeller's blade
various impellers, various scales - historical comparison

author or source	u/u_{ip}	v/v_{ip}	w/v_{ip}	U/v_{ip}	u'/v_{ip}	v'/v_{ip}	w'/v_{ip}	U'/v_{ip}	type of impeller
Chen, Wang & Hajduk (1988)	0.31	0.40	0.10	-	0.10	0.10	0.07	-	6-blade Rushton
Chen, Wang & Hajduk (1988)	0.14	0.54	0.22	-	0.35	0.22	0.15	-	inclined paddle
Laufhutte & Mersmann (1985)	0.64	-	-	-	0.40	-	-	-	6-blade Rushton
Wu & Patterson (1989)	0.75	0.68	variable	1.03	0.15	0.13	0.15	0.25	6-blade Rushton
Stanley & Smith (1994)	0.32	-	-	-	-	-	-	-	2-blade paddle
Cutter (1966)	0.58	0.62	-	-	0.39	0.33	0.35	0.45	6-blade Rushton
Gunkel & Weber (1975)	0.86	0.86	-	1.25	-	-	-	0.33	6-blade Rushton
Oldshue (1966)	-	-	-	0.95	-	-	-	0.40	6-blade Rushton
Schwartzberg & Treybal (1968)	-	-	-	1.70	-	-	-	0.50	6-blade Rushton

Comparison of velocities is still not straightforward, even with such tabular reductions because there is such a marked difference between the confined impeller studied here and what invariably is a free impeller in a comparatively large tank in the literature. However, it would appear that a number of conclusions based upon this table seem plausible:

- Radial velocities are generally of the same order for Rushton-type and Ecodyne-type impellers - though there is a fair amount of scatter in the literature. As well, tangential velocities are generally higher in the Ecodyne-type impeller, but it must be kept in mind that the tank was unbaffled for most of the tests performed in this project.
- In all cases, the turbulent velocities are all of the same order, regardless of scale and regardless of impeller type. Such a conclusion holds significant implications with respect to the use of variant impellers to control the level of turbulence at a given point while allowing other factors such as discharge and velocity to vary.

For the purposes of this study, it is required simply to recognize the difficulties inherent in the comparison of impeller-induced velocity fields. Such a comparison would probably be easier with a greater quantity of comparative data, but at this point, it is most useful and most important to recognize that the flow field induced by the Ecodyne impeller may be satisfactorily quantified via a number of apparently constant coefficients in terms of the impeller's tip speed, regardless of what that speed may be.

6.3 Pumping Discharges

The flow number, N_q , has been shown to be a simple, concise means of quantifying an impeller's behaviour with respect to hydraulic performance. The N_q 's that were determined in this study are tabulated in Tables 5-1 through 5-7. If pumping were important to a given process, the flow-through discharge would be of interest. Since N_q represents the impeller's capacity to develop a flow-through discharge, impellers may easily be compared on the basis of their flow numbers. The pumping abilities of the Ecodyne impeller will now be classified with respect to a number of impellers in Table 6-3. As an impeller's dynamic state is traditionally expressed via an impeller Reynolds number, the relevant dimensions are reported along with the particular operating conditions.

Table 6-3
historical review of flow numbers

author or source	d (m) or (-)	N (rpm)	R_i	N_q	type of impeller
Connolly & Winter (1969)	-	-	-	0.31	4-blade downthrusting turbine
Gunkel & Weber (1975)	0.228	> 950	> 10^4	1.00	6-blade disk turbine
Sano & Usui (1985)	various	various	> 10^4	1.00	6-blade Rushton
Sano & Usui (1985)	various	various	> 10^4	0.81	6-blade Rushton
Bowen (1985)	$\frac{1}{2}$ T	various	> 10^4	0.87	2-blade paddle
Bowen (1985)	$\frac{1}{4}$ T	various	> 10^4	0.6	6-blade Rushton
Bowen (1986)	$\frac{1}{4}$ T	various	> 10^4	0.76	6-blade Rushton
Wu & Patterson (1989)	$\frac{1}{8}$ T	various	> 10^4	0.87	6-blade Rushton
Weetman & Oldshue (1988)	-	-	> 10^4	0.79	6-blade Rushton
Weetman & Oldshue (1988)	-	-	> 10^4	0.56	6-blade Rushton
Weetman & Oldshue (1988)	-	-	> 10^4	0.72	6-blade Rushton
Weetman & Oldshue (1988)	-	-	> 10^4	0.56	6-blade Rushton

And in general, Godfrey & Amirtharajah (1991) suggest that the flow numbers of a large number of impellers acting in baffled tanks of various configurations may be described by the expression

$$N_q = 0.75 \pm 0.15$$

Clearly, there is a great variation in the reported values of N_q . This variation is certainly due in part to the variety of impellers available, but it is also due to the variety of conditions in which the impellers were studied, as numerous authors have reported that the position of the impeller with respect to the wall or floor of the tank affects the efficiency of pumping. Every N_q shown above assumes fully turbulent conditions (roughly corresponding to $R_i \geq 1 \times 10^4$) since N_q , like N_p , may be assumed to be approximately constant under turbulent conditions. In this regard, only a few of the tests that were performed for this project were in performed for $R_i \geq 1 \times 10^4$, and of these, only the trials with the 1:10 scale NHC impeller were well into this turbulent range. Despite this fact, it appears that the values of N_q that were calculated for the Ecodyne impeller are of approximately *of the same order* as those calculated in the literature ; the fact that the flow numbers calculated here generally appear to be *smaller* than those in Table 6-3 is likely due to the fact that only one side of the Ecodyne impeller is available for drawing in the surrounding fluid (the top is covered by a circular plate), yet most in the literature are open both at the top and the bottom. Finally, whereas the measured flow numbers appear to *decrease* with increasing R_i , the flow numbers in the literature are usually seen to *increase* with R_i toward the so-called "constant" turbulent N_q that may be predicted from a consideration of the observed scale-invariant presence of kinetic similarity. Although the cause of this behavioral difference is unknown, it is speculated that it results from the presence of the impeller's plate: the development of significant pressures within the impeller zone is suspected to be much more efficient at lower ω 's, and to be increasingly ineffective, possibly as the flow in the impeller comes under the influence of ever

increasing drag forces acting on the blade. Unfortunately, angular velocities required to establish impeller Reynolds numbers higher than approximately 1×10^4 in both the 1:41-scale and 1:55 scale models caused an unreasonable amount of drawdown and agitation in the tank, an obvious change to the fluid's kinematic properties (air entrainment increased drastically), and violent vibrations of the impeller as the presence of slight imbalances and eccentricities in the alignment became greatly accentuated.

6.4 Power Numbers

Traditionally, the power number, N_p , is reported with respect to the impeller Reynolds number R_i . As discussed earlier, the variation of N_p with R_i usually has three sections which are analogous to zones of laminar, transitional and turbulent flow around the impeller. In turbulent (*i.e.* high- R_i) flow for the so-called "standard" arrangement of Rushton-type impellers, the power numbers have been found to be approximately constant, especially in fully baffled tanks where the effects of swirl are suppressed. In the literature, most studies appear to have been performed in baffled tanks, thereby minimizing the influence of swirl on power consumption; indeed, the full-scale clarifiers do in fact have draught-tube baffles*. Thus, the results of this study probably would have been more immediately relevant if draught-tube baffles had been present in every trial, but because the NHC model had no draught-tube baffles, and given that a comparison to and analysis of the NHC model was one of the primary motives in commissioning this project, nearly all of the trials were performed in this study without draught-tube baffles (trial A05 being the only exception). Nonetheless, as the range of impeller speeds that was investigated here appeared to cause significant drawdown only at the highest tip speeds, it was concluded that such vortexing and drawdown caused only negligible effects. This contention is supported by the fact that the various N_p - R_i curves that were developed during the various tests all exhibited an approximate constancy of N_p in the high- R_i range for all configurations, and at both scales - such constancy implies relatively little influence of swirl.

The power numbers measured in this study were presented earlier, in chapter 5.0, as a number of plots (Figures 5-1a through 5-1e). It is appropriate now to restate the salient features of those plots, namely the so-called "constant" high- R_i power numbers, for the purposes of comparison. This comparison is presented in Table 6-4.

* The dimensions of said baffles are presented in Figure 3-2. It should be mentioned that these baffles were not included on the original design drawings of these clarifiers.

Table 6-4
calculated high- R , approximately constant power numbers
all trials & configurations

trial	description	N_p
A01	free impeller	2.3
B01	free impeller	2.3
A02	draught-tube only	3.0
B02	draught-tube only	3.0
A03	draught-tube & skirt	3.0
B03	draught-tube & skirt	3.0
A04	decreased skirt height	not taken
A05	draught-tube baffles	3.0-3.1
B06	enlarged orifice	3.6

As expected, regardless of configuration, the measured power numbers seem to verge upon a single value for a given structural configuration. It is interesting to recognize that the power numbers behave in such a manner in light of the flow numbers' hesitancy to collapse onto a single, constant and scale-invariant value at high values of the impeller Reynolds number. Apparently, N_p approaches this approximately "asymptotic" value more quickly than N_q , possibly because whereas the power numbers were defined from a set of directly measured quantities, the flow numbers, which are defined via an approximate calculation of velocity flux through a control surface are subject to considerable more error, especially since the flow numbers that were calculated at the various locations within the draught-tube showed considerable inconsistency at times.

At this point, the power numbers presented in Table 6-4 can now be compared to those found in the literature via a tabulated and representative survey of literature values, Table 6-5. Table 6-5 illustrates that the power numbers found in this study are of the same order as those found in the literature. More specific comparisons based upon the actual magnitudes of N_p derived here versus those in the literature as a basis of turbulence analysis are also possible, though such an endeavour is not pursued here.

Table 6-5
historical review of power numbers

source	type of impeller	N_p (turbulent flows)	conditions
Mack & Marriner (1949)	2-blade flat blade impeller	≈ 1.75	fully baffled
Rushton, Costich & Everett (1950-2)	flat-blade turbine	4.0 - 7.0	depending upon degree of baffling
Rushton, Costich & Everett (1950-2)	flat-blade turbine (no baffles)	≈ 1.0	-
Metzner & Otto (1957)	6-blade flat blade disk turbine	3.7	non-Newtonian fluid
Leentvar & Ywema (1980)	small propeller	0.5	no baffles - cylindrical vessel
Leentvar & Ywema (1980)	small propeller	1.0	baffled - cylindrical vessel
Leentvar & Ywema (1980)	paddle	0.7	no baffles - cylindrical vessel
Leentvar & Ywema (1980)	paddle	2.6	baffled - cylindrical vessel
Leentvar & Ywema (1980)	paddle	2.0	square tank
Gray, Treyball & Barnett (1982)	paddle	5.2	fully baffled : large off-bottom height
Bujalski, Nienow, Charwin & Cooke (1987)	6-blade Rushton	4.0 - 6.0	various configurations within tank
Papastefanos & Stamatoudis (1989)	6-blade Rushton	3.0 - 7.0	unbaffled & baffled, square & cylindrical vessels
Papastefanos & Stamatoudis (1989)	6-blade open impeller	3.5 - 5.0	unbaffled & baffled, square & cylindrical vessels
Papastefanos & Stamatoudis (1989)	45° pitched 6-blade open impeller	1.25 - 1.75	unbaffled & baffled, square & cylindrical vessels
Kamienski (1980)	45° pitched 6-blade disk impeller	1.5	fully baffled
Kamienski (1980)	135° pitched 6-blade disk impeller	1.8	fully baffled
Kamienski (1980)	6-blade disk	2.0	fully baffled
Weetman & Oldshue (1988)	Rushton turbine	1.25	-

6.5 Dimensionless Rate of Turbulent Dissipation

6.5.1 Theoretical

Based upon the previous comparative presentations of power numbers and flow numbers, it appears that the Ecodyne impeller studied here may be characterized by power numbers and flow numbers of the same order of those found in the literature. In practice, the various types of impellers operate within a variety of hydraulic flow regimes, yielding numerous combinations of flow generation and power consumption. Although there is no obvious mathematical connection between the flow numbers and power numbers, it may be shown that there is a strong link between the two. In one sense, the flow number may be thought to represent a particular impeller's ability to impart kinetic (and pressure) energy to the flow ; similarly, the power number may be considered to be a compact statement of the total energy imparted to the flow. As the total power consumption in the impeller-tank system must be inherently linked both to the initially supplied kinetic energy of the bulk-flow and to the turbulent dissipation therein, it is therefore necessary that the power number be inherently linked to the statement of local turbulent dissipation rate in the tank. Whereas the power number states the total, vessel-wide power consumption, the turbulent dissipation rate serves as a more locally specific expression of energy consumption in terms of a turbulent transfer of kinetic energy input via a chain of ever smaller eddies.

The previous presentation and historical review of power numbers clearly demonstrates that there is a wide range power numbers that is possible. Furthermore, given the dynamical property of the impeller-tank system that all velocities seem to scale with tip-speed, it is obvious that a multitude of turbulent dissipation rates is possible for any given impeller. If one wished to compare any two impellers' abilities to impart energy to the fluid (*e.g.* for a mixing study where the reaction rate or mass-transfer or any other turbulence-dependent quantity were of interest) it would be exceptionally difficult to make such a comparison by considering only the as-measured ω -dependent variation of the local turbulent dissipation rate given the variegated properties of the various impellers. Moreover, even in comparing the same type of impeller, either at the same scale at different speeds, or for different scales at different speeds, a comparison of any two ϵ 's means nothing unless punctuated by knowledge of the properties of the impeller such as d , b , ω and R_p .

Fortunately, there is a very effective means of comparison of ϵ , based upon the dimensional similarity that exists between ϵ and N_p . Intuitively, since N_p may be interpreted as a rough indication of an impeller's power consumption, as N_p increases, so too does the overall rate at which the energy is consumed. Now, pursuant to the earlier definition of ϵ in the **Review of Literature**, ϵ may be interpreted either as the rate of ultimate energy dissipation at the molecular level, or as the rate of energy originally applied to the system - an obvious consequence of the principle of conservation of energy. Because all energy is initially applied to the system via the impeller only, one would expect some sort of mathematical relationship to exist between the bulk power consumption, as expressed by N_p , and the rate of energy *transfer*, as expressed by ϵ . The existence of such a mathematical relationship between ϵ and N_p will be seen to enable the definition of a convenient dimensionless form of ϵ , which serves as an extremely useful means of comparison of ϵ among an number of impellers. Such a relationship may be derived in the following manner.

Firstly, by rewriting the general expression of the power number in a slightly different form:

$$N_p = \frac{P}{\rho \omega^3 d^5} = \frac{P}{\rho (2 v_{np})^3 d^3 \frac{1}{d}} = \frac{P}{\frac{(2 v_{np})^3}{d} \rho d^3} \propto \frac{P}{\frac{(v_{np})^3}{b} \rho V}$$

it may be shown that

$$N_p \frac{v_{tip}^3}{b} \propto \frac{P}{\rho V} = \frac{v_{tip}^3}{b} \propto \bar{\epsilon}$$

where the constant of proportionality depends solely upon geometry and is constant for the case where N_p is approximately constant. Now, given the previously postulated universality of the dimensionless dissipation rate (see Review of Literature):

$$\epsilon = k \frac{v_{tip}^3}{b}$$

a general expression for observable ϵ immediately follows:

$$\epsilon \propto \frac{v_{tip}^3}{b} \propto \bar{\epsilon} \propto \frac{d^3 \omega^3}{b}$$

where each expression is seen to be in units of W/kg or m²/s³.

In other words, the concept of a constant power number N_p is analogous to the existence of a constant, scale-invariant, ω -invariant value of the dimensionless dissipation rate. The various constants of proportionality in this expression primarily depend upon the impeller's geometry and the various hydromechanical effects resulting thereby. This expression is immediately comparable to the work of Bin (1984), who stated that

$$\epsilon_{corr} = \left(\frac{c_6}{c_{14}}\right)^3 \frac{\pi \bar{\epsilon}}{4 N_p}$$

and to the work of Rice & Baud (1990), who stated that

$$\epsilon = \bar{\epsilon} \phi = \frac{\phi N_p \omega^3 d^3}{V_{tank}}$$

and also to Antonia, Satyaprakash & Hussain (1980) who derived a similar expression for the case of the free jet discharging into a stagnant medium.

In this manner, it is seen that the traditional practice of scaling-up via the maintenance of a constant value of the volume-averaged dissipation rate, $P/\rho V$, is analogous to the maintenance of a constant value of ϵ upon scale-up. Conversely, it is seen that an inherent dependence upon the condition of local similarity (as expressed by a b -based or d -based normalization of ϵ) is assumed whenever the traditional approach of scale-up based upon power-per-unit-volume is applied. However, it is also required that 100% geometric similarity be maintained among the various scales for these expressions to be correct.

At this point, although it is seen that one may now express energy dissipation in various forms, there is still a practical consideration to be made with respect to the quantity V , the volume of the tank. Because of the great variability in V , the explicit use of P/V can potentially lead to great confusion - for instance, in studying the draught-tube-confined Ecodyne impeller, should V be taken as the volume of the tank, the volume of the draught-tube, or perhaps the volume occupied by the impeller's blades? Certainly, for the case of the unconfined Rushton turbine in so-called "standard" conditions, the relevant volume is obviously the volume of the tank, but given the ambiguity present in this study, the selection of volume is not so straightforward. Therefore, in this study, the measured power values were used for the calculation of power numbers only, not in the estimation of some volume-based expression of the vessel-averaged power consumption. In contrast, the fact that ϵ was estimated via an approximate expression depending only upon turbulent velocities (which were shown to be functions of only ω and the impeller's geometry as expressed by b or d) and some fraction of the impeller's blade height implies that non-dimensionalization of ϵ by impeller-specific properties provides a practical, immediately meaningful means of quantifying the observed behaviour. It now remains to illustrate this means of non-dimensionalization via the measured data.

6.5.2 the Non-Dimensionalization of ϵ

For the purposes of this study, a practical form of the dimensionless dissipation rate was assumed to be:

$$\frac{\epsilon}{\frac{v_{np}^3}{b}}$$

which, given the maintenance of 100% geometric similarity of the impeller, is equivalent to:

$$\frac{\epsilon}{\frac{v_{np}^3}{d}}$$

Although the d -based means of normalization is more common in the literature, for this study, the b -based normalization is preferred as it reflects the blade's height directly - and is thus felt to be more immediately practical since b and not d is used in the original expression for ϵ . In effect, such a normalization is a manifestation of the fact that both u and u' are proportional to the impeller's tip-speed (see Figures 6-1-1n through 6-3-11n) so that what is a complicated local phenomenon may be conveniently quantified in terms of the initial conditions.

The resultant ϵ -data for all trials are presented in Figures 6-5a through 6-13c, where plots of the vertical variation of the calculated local dissipation rate ϵ , the d -based dimensionless dissipation rate, and the b -based dimensionless dissipation rate at the blade's tip are presented for each configuration in adjacent positions in order to illustrate the effectiveness of the normalization procedure. The data do indeed appear to collapse upon a single curve - actually, such a correspondence is all the more remarkable given that ϵ is based upon a measured turbulent quantity that is *cubed*, and thus is subject to great magnification of any measurement errors in the original velocities.

In addition, the variation of maximum ϵ , both in dimensional and non-dimensional forms, with respect to distance from the impeller is presented in Figures 6-14a through 6-17c, but for configuration 01 only; these maxima were measured with respect to both the dimensionless radial coordinate, $2r/d$, and with respect to ξ , a coordinate which expresses the distance along the axis

of a swirling radial jet'. However, despite the fact that the turbulent length scale, ℓ , was observed to expand linearly with $2r/d$ for the case of the free impeller, the non-dimensionalized plots of maximum ϵ with $2r/d$ for configurations 02 through 06 (all representing a confined impeller) were not seen to be as well correlated farther from the blade, likely indicating the effects of confinement upon ℓ 's spreading rate, and thus such graphs are not presented.

Finally, carrying the concept of non-dimensionality further, the plots of dimensionless ϵ at different scales are were then plotted together, on the same axes, for the particular configurations 01 through 03 ; these plots are presented in Figures 6-18-1n through 6-18-7n. Remarkably, the dimensionless dissipation rate appears to be constant *regardless of scale* for a given configuration, and at a given spatial location. Again, the radial variation (Figure 6-18-7) is shown only for configuration 01, the free impeller.

Considering the analysis of turbulent energy dissipation, it is clear that by such a non-dimensionalization scheme, ϵ may be expressed concisely for any scale. Given this, it is now possible to compare the various dimensionless dissipation rates determined here to those of other impellers in the literature. In performing such a comparison however, because the plots of dimensionless ϵ for the Ecodyne impeller are decidedly unsymmetrical, it was felt to be impractical to fit a curve, *i.e.* some type of similarity function, to the plots of the vertical (z/b) variation of dimensionless ϵ . Instead, it is predicated upon the principle of kinetic similarity that a specification of the dimensionless ϵ at only one point, such as the point of maximum dimensionless ϵ , is a valid means of expressing the entire vertical distribution of ϵ since kinetic similarity would ensure that the ratio of the maximum dimensionless ϵ to the dimensionless ϵ at all other locations should remain constant. Therefore, the maximal values of the dimensionless local turbulent energy dissipation rate near the impeller's blade were extracted from Figures 6-3-1n through 6-3-11n, and the results are tabulated hereunder, in Table 6-6:

Table 6-6
maximum observed dimensionless dissipation rates near the impeller's blade

configuration	maximum b-based dimensionless dissipation rate	maximum d-based dimensionless dissipation rate
	$\epsilon/[v_{up}^3 / b]$	$\epsilon/[v_{up}^3 / d]$
01	0.032	0.140
02	0.032	0.140
03	0.032	0.140

Although values of the dimensionless dissipation rates are also available for trials A04, A05 & B06, these numbers are withheld until later, when the effects of structural and configurational changes upon ϵ are discussed. For comparison, a table of similarly-normalized dimensionless dissipation rates from various authors in the literature allows immediate assessment of the turbulence-generant qualities of the Ecodyne impeller.

See the **Review of Literature** for definitions of ξ and q .

Table 6-7
historical review of maximum dimensionless dissipation rates near the impeller's blade

source or author	type of impeller	$\epsilon / [v_{tp}^3 / b]$	$\epsilon / [v_{tp}^3 / d]$
Chen, Wang & Hajduk (1988)	6-blade Rushton	0.003	0.140
Wu & Patterson* (1989)	6-blade Rushton	0.088	0.442
Wu & Patterson** (1989)	6-blade Rushton	0.011	0.054
Kresta & Wood (1991)	6-blade Rushton	-	~ 0.65
Gunkel & Weber (1975)	6-blade Rushton	0.009	0.043
Cutter (1966)	6-blade Rushton	0.168	0.839
Stanley & Smith (1994)	general survey	-	0.2 - 0.7

Unfortunately, there is a considerable amount of scatter present in the literature data. This is because the tabulated dimensionless ϵ 's - except for Kresta & Wood (1991) - were all estimated using values obtained from the plots presented in the various articles, so that there is opportunity to interpret which turbulent velocities should be used in the calculation of the dimensionless ϵ . The value of ϵ determined by Kresta & Wood (1991) is not necessarily comparable to those determined in this study because they determined ϵ via computer modelling, not by the simpler velocity-based approach employed here. The two values given for Wu & Patterson (1989) reflect values of ϵ which are determined firstly from the total turbulent velocity, and then from the random turbulent velocity. Perhaps the most significant conclusion that this type of comparison allows is that the concept of ϵ is at best only an approximation - one cannot not treat any single value of ϵ as if it were an absolutely known, incontrovertible quantity.

6.6 Conclusions

In the analysis of both measured and derived quantities in this experiment, certain consistent properties of the flow were concisely illustrated by a number of dimensionless parameters. Such an analysis is significant both as a description of the general nature of the hydraulic and dynamic conditions in the flow, and also as a means of scale-up. The most significant conclusions which may be drawn from this analysis are summarized below:

1. **All velocities, both average and turbulent, may be normalized by the tip-speed, such that at any scale, the local velocities in any direction may be expressed as a definite fraction of the impeller's tip-speed.**
2. **At any scale, as the angular velocity is increased, the flow numbers, N_q , for a given configuration appear to converge upon a constant, ω -invariant value.**

* based upon both the random and periodic components of turbulent velocity

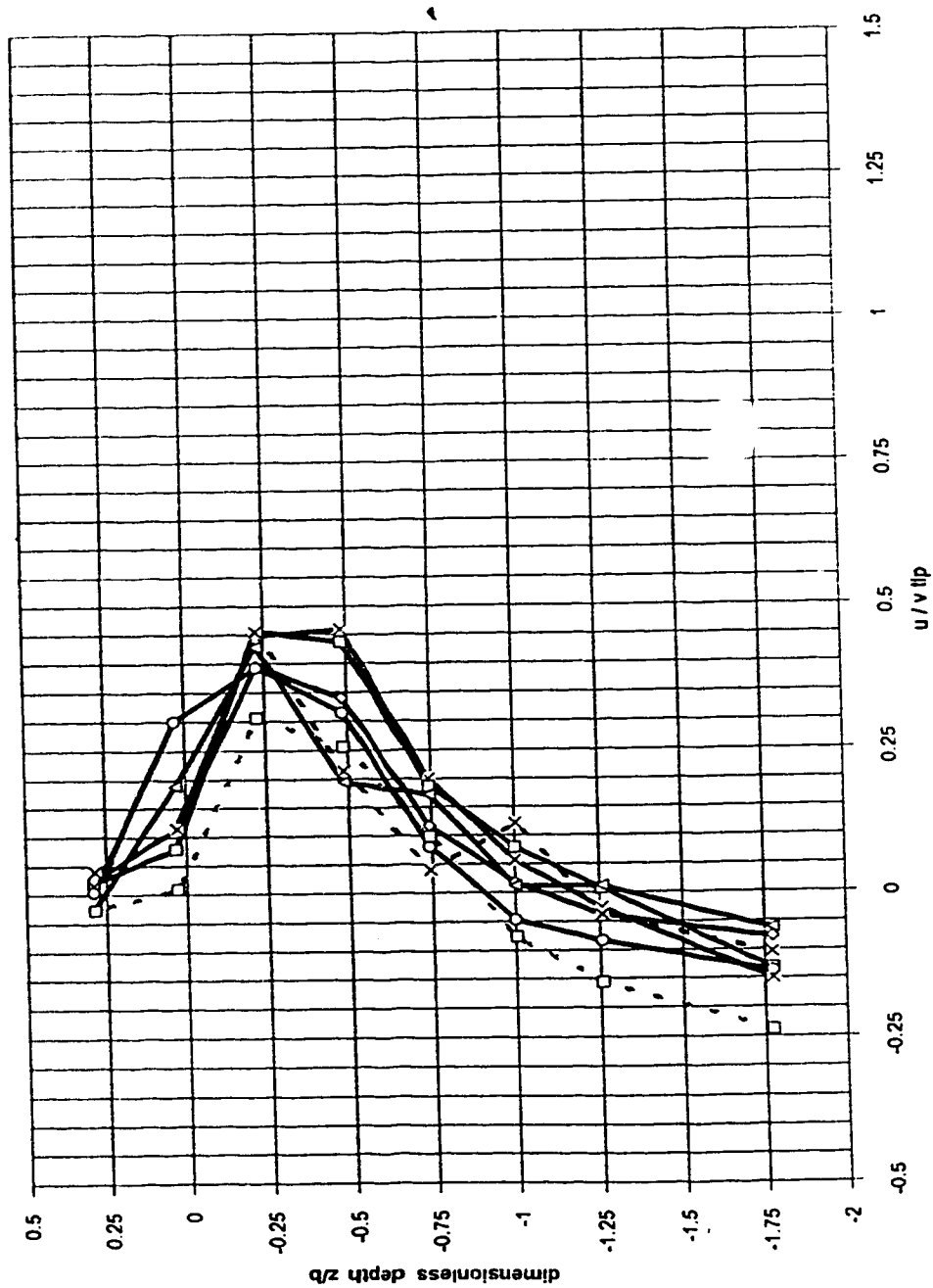
** based upon only the random component of turbulent velocity

3. **For all configurations, for all angular velocities, and for all geometric scales, the quantity defined by**

$$\frac{v_{np}^3}{\ell}$$

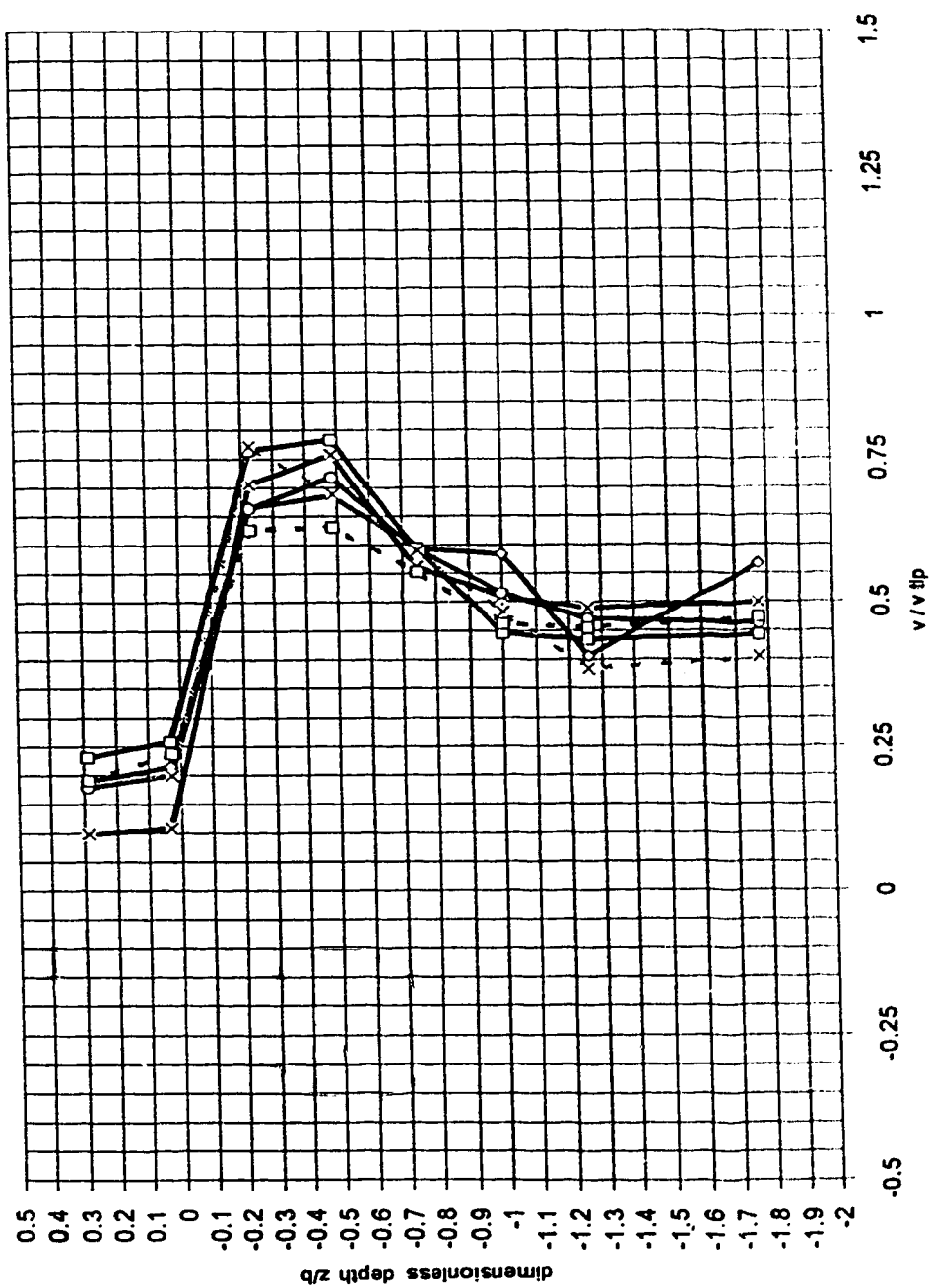
appears to be a constant anywhere in the impeller-generated flow.

As such, the speculations of numerous researchers of a spatially invariant distribution of the ratio ϵ to average ϵ is apparently confirmed. Such a constancy allows immediate, straightforward scale-up based upon duplication of a particular turbulent dissipation rate anywhere in the impeller stream.



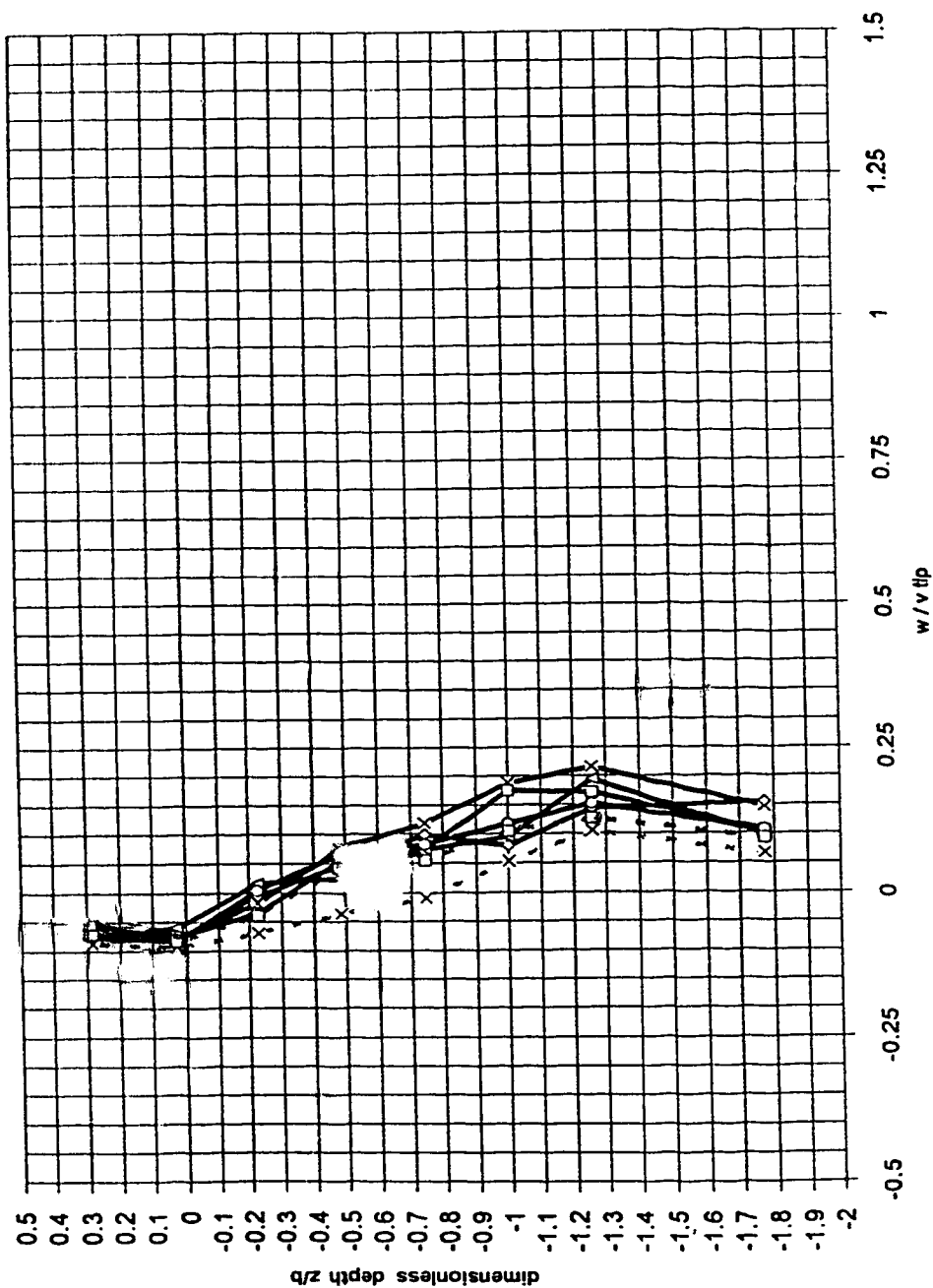
configuration 01 - ecdyne impeller; 1:55 and 1:41 scales
radial average velocities near impeller - normalized by tip speed
 $d=7.68 \text{ cm}$ & 10.37 cm ; $b = 1.94 \text{ cm}$ & 2.63 cm ; $2\pi r/d=1.044$

Figure 6-1-1n :



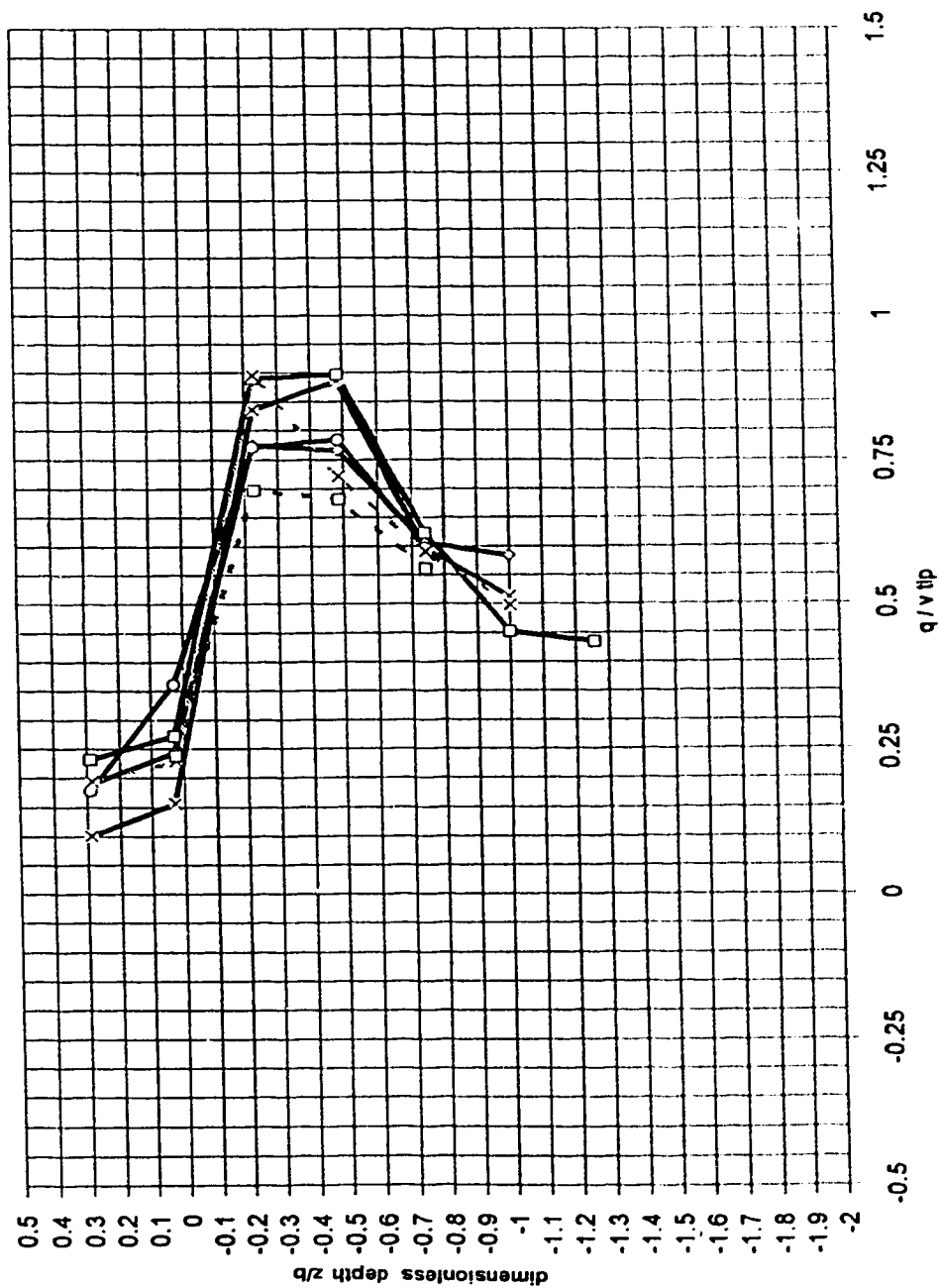
configuration 01 - eco-dyna impeller : 1:55 scale & 1:41 scale
 tangential average velocities near impeller - normalized by tip speed
 $d=7.66$ cm & 10.37 cm ; $b=1.94$ cm & 2.63 cm ; $2r/d=1.044$

Figure 6-1.2n :



configuration 01 - ecdyme impeller : 1:55 scale & 1:41 scale
axial average velocities near impeller - normalized by tip speed
 $d=7.66$ cm & 10.37 cm ; $b=1.94$ cm & 2.63 cm ; $2r/d=1.044$

Figure 6.1.3n :



configuration 01 - eodyne impeller ; 1:55 scale & 1:41 scale
average velocities along swirling radial jet's axis - normalized by tip speed
 $q=7.66 \text{ cm \& } 10.37 \text{ cm}$; $b=1.94 \text{ cm \& } 2.63 \text{ cm}$; $2/d=1.044$

Figure 6-1-4n :

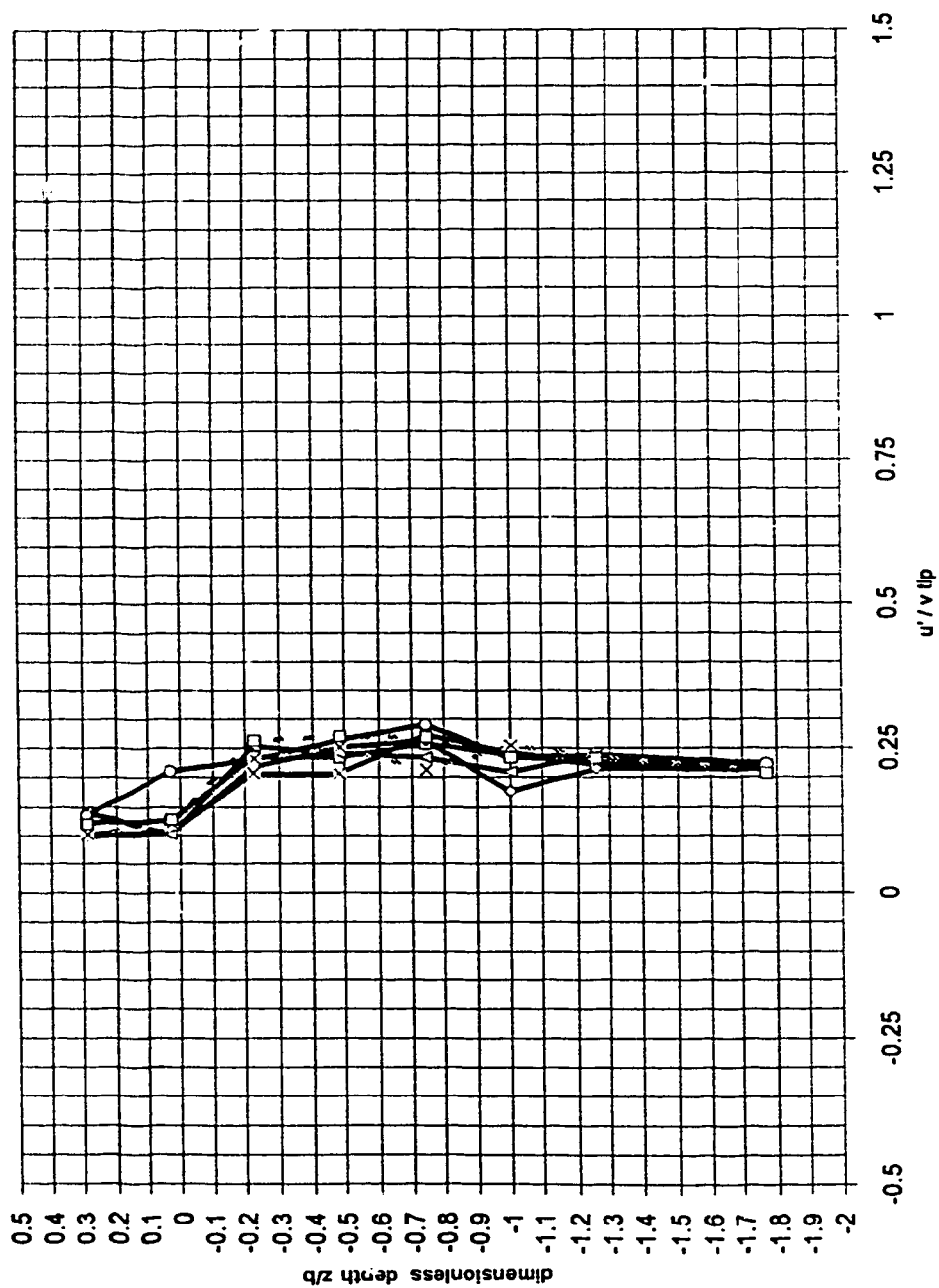
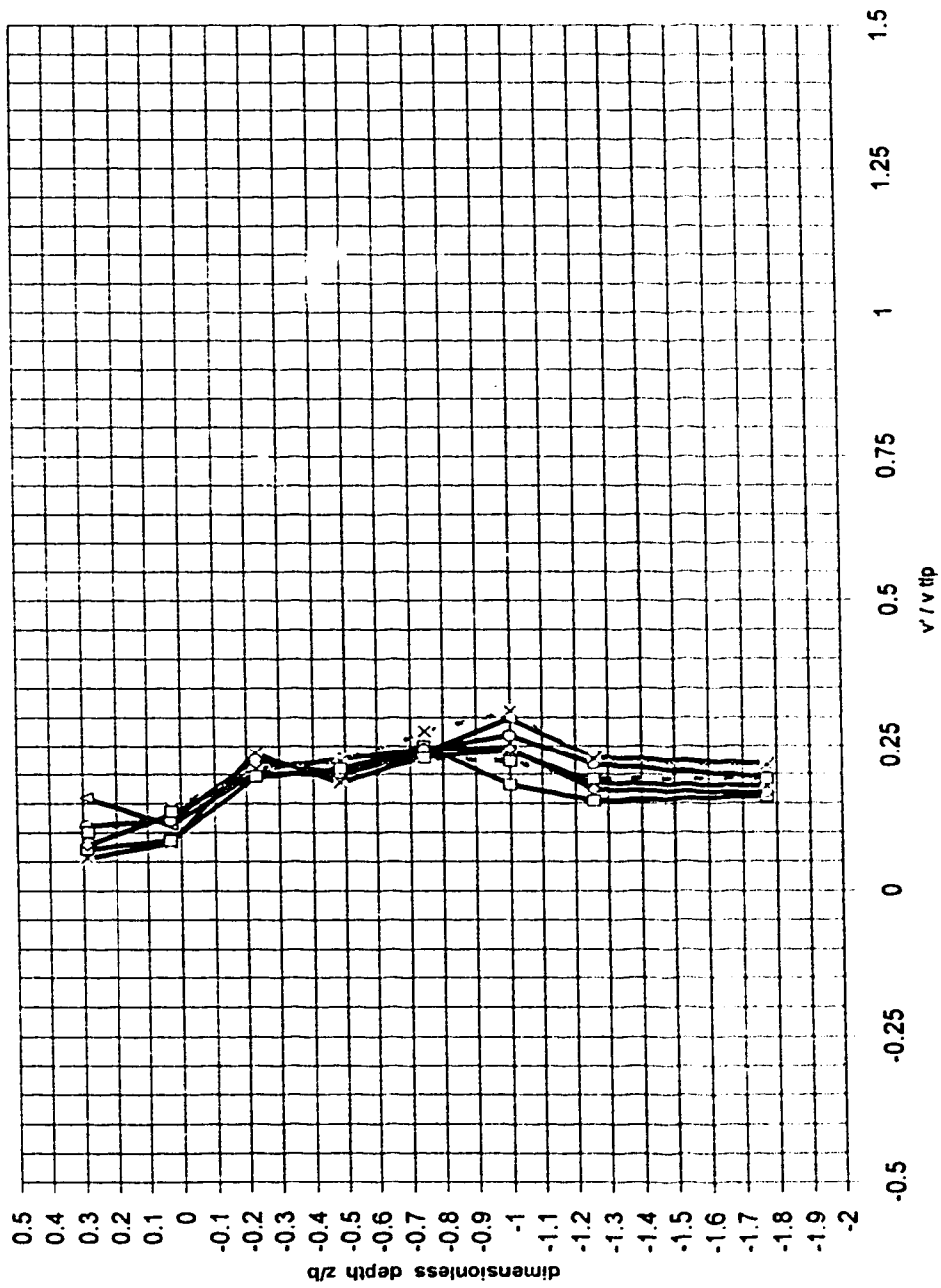


Figure 6-1-5n :
radial turbulent velocities near impeller - normalized by tip speed
 $d=7.66 \text{ cm}$ & 10.37 cm ; $b=1.94 \text{ cm}$ & 2.63 cm ; $2/d=1.044$



configuration 01 ecodyne impeller : 1:55 scale & 1:41 scale
 tangential turbulent velocities near 'tipeller - normalized by tip speed
 $q=7.66 \text{ cm \& 10.37 cm ; } b=1.94 \text{ cm \& 2.63 cm ; } 2r/d=1.044$

Figure 6.1.6n :

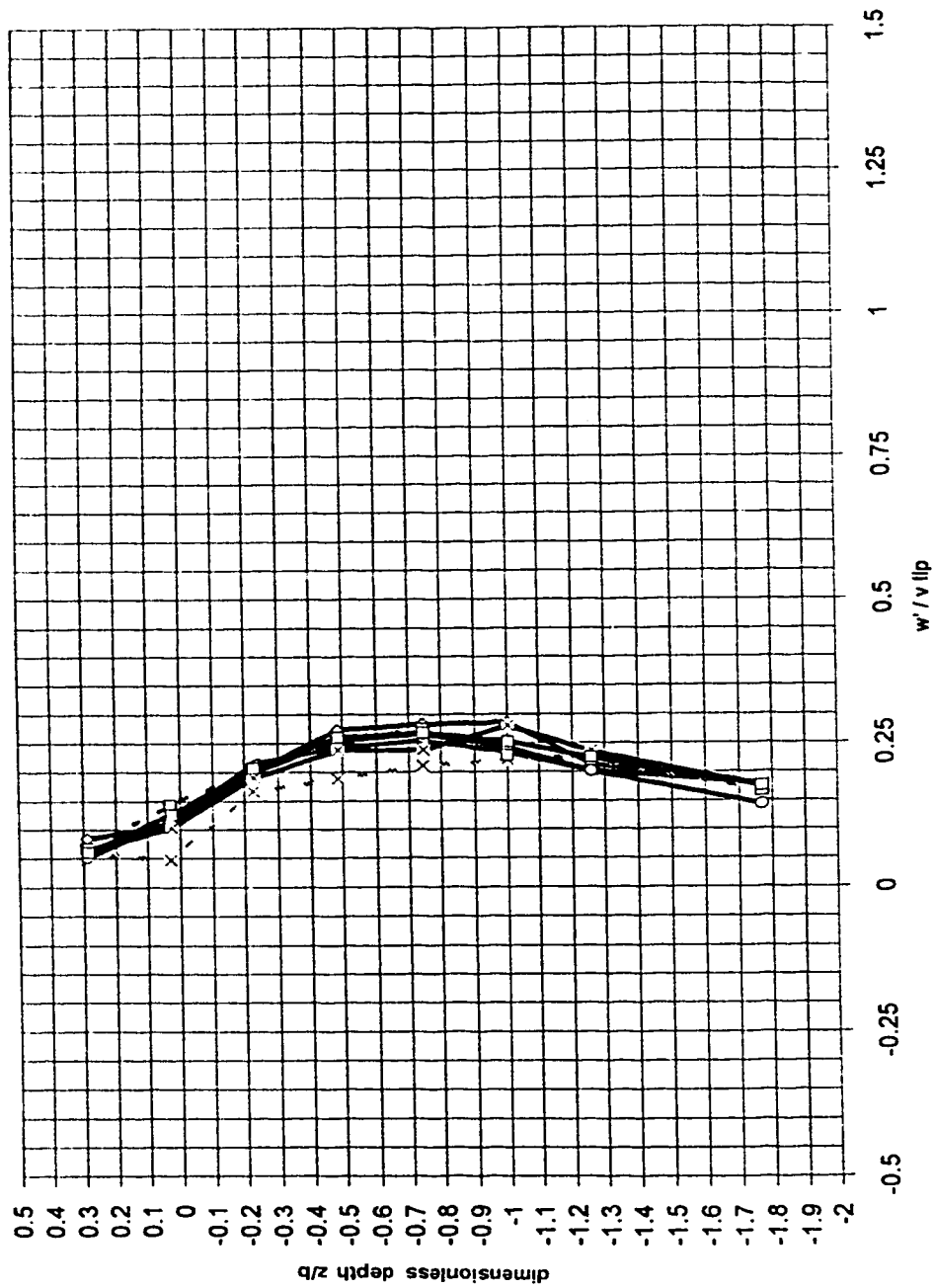
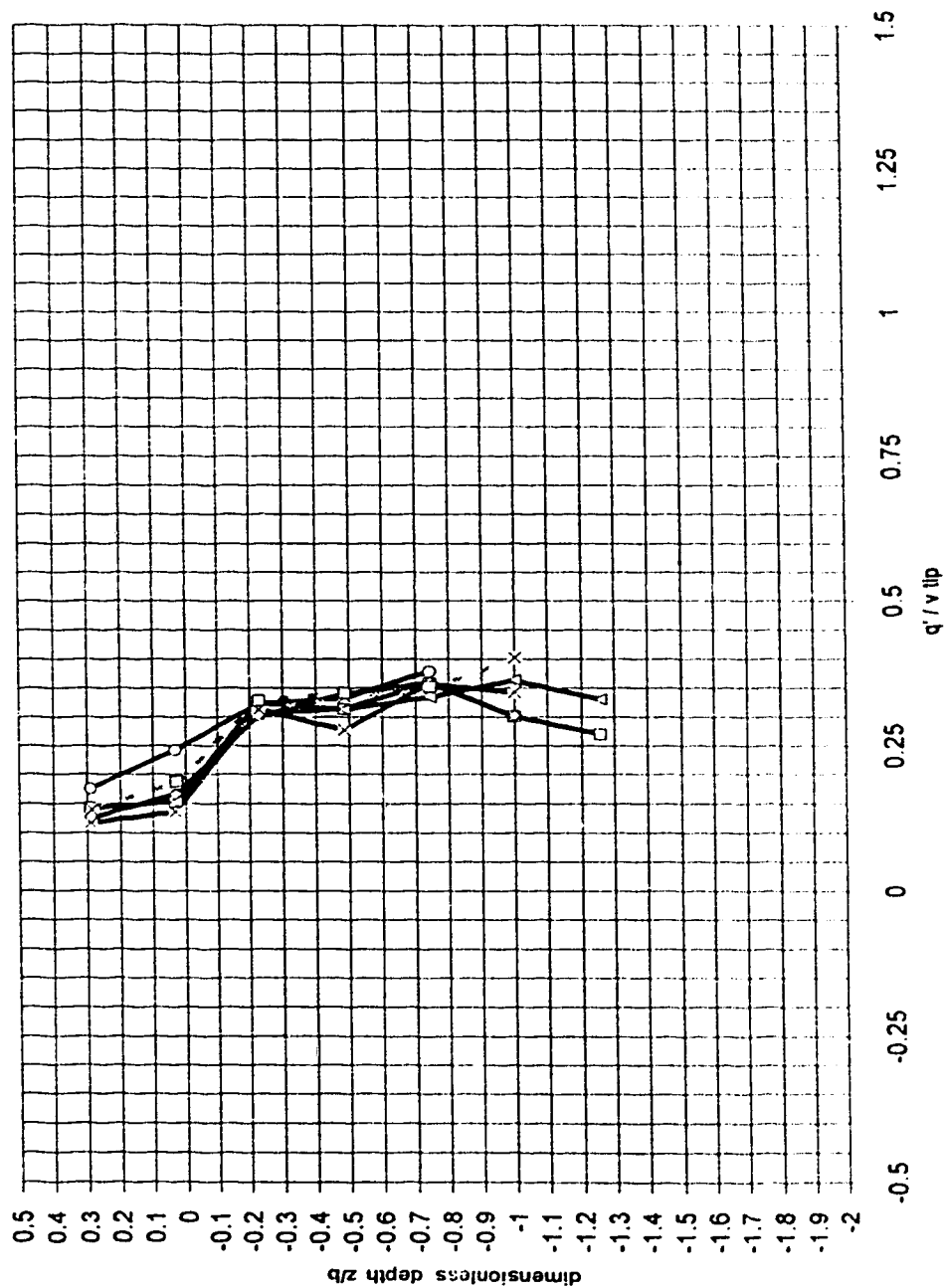


Figure 6.1.7n :
 configuration 01 - ecodyne Impeller ; 1:55 scale & 1:41 scale
 axial turbulent velocities near Impeller - normalized by tip speed
 $d=7.66$ cm & 10.37 cm ; $b=1.94$ cm & 2.63 cm ; $2r/d=1.044$



configuration 01 - ecodyne impeller ; 1:55 scale & 1:41 scale
 turbulent velocities along axis of swirling radial jet - normalized by tip speed
 $d=7.66$ cm & 10.37 cm ; $b=1.94$ cm & 2.63 cm ; $2r/d=1.044$

Figure 6-13m :

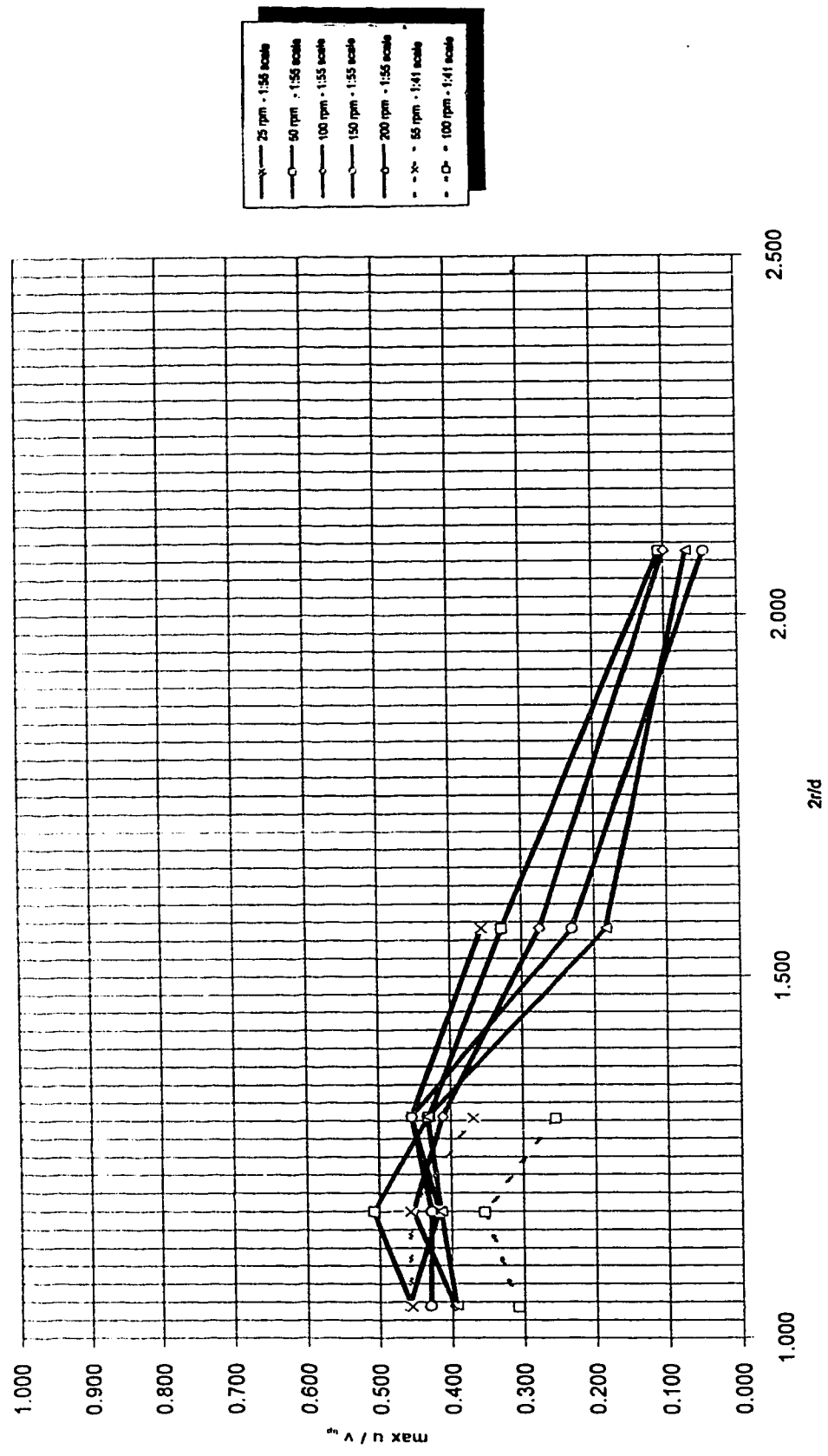


Figure 6.1.9n : configuration 01 - ecdyne impeller ; 1:55 scale & 1:41 scale
radial decay of average radial velocity - normalized by tip speed
 $\alpha=7.66$ cm & 10.37 cm ; $b=1.94$ cm & 2.63 cm ; $2r/d=1.044$

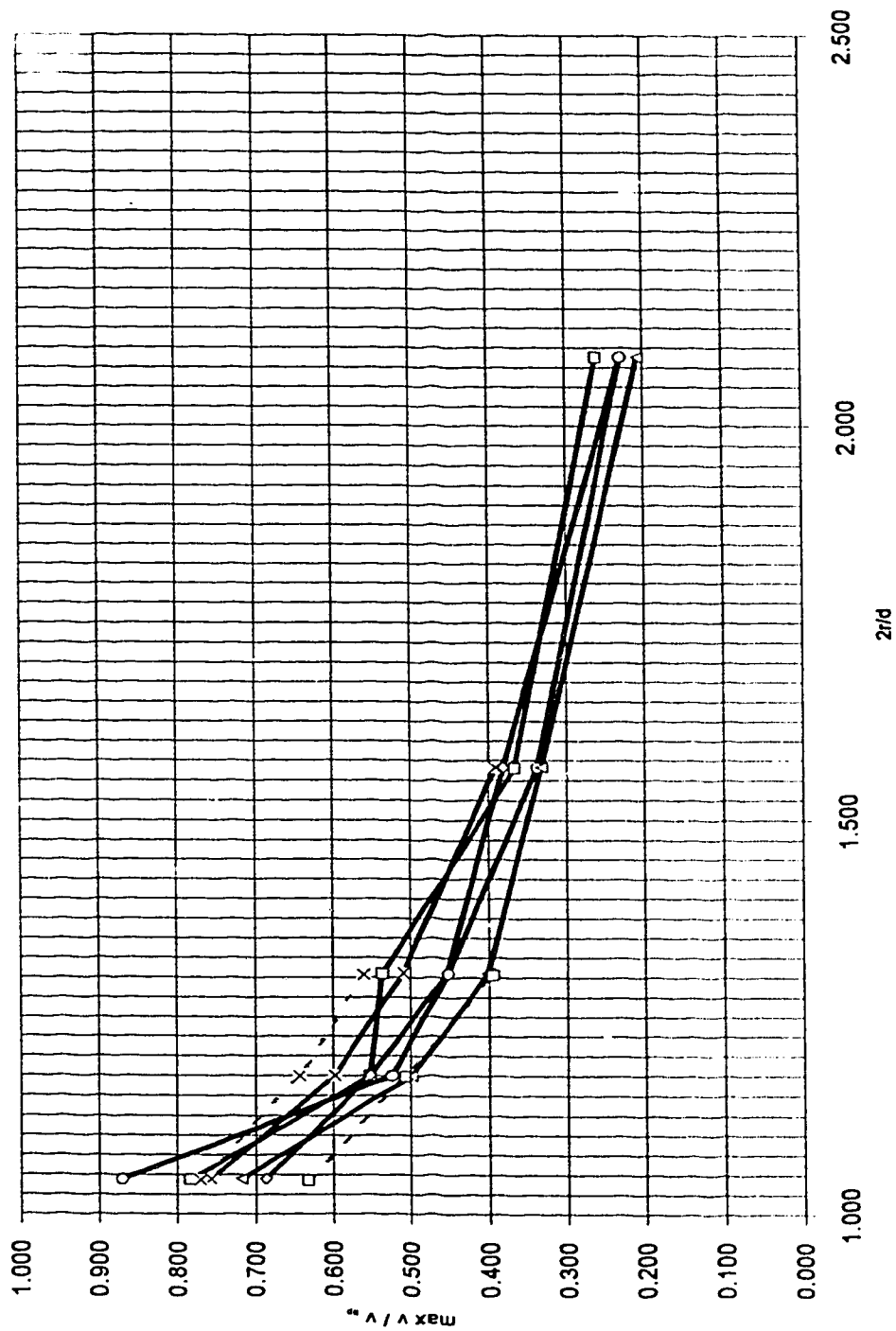


Figure 6.1.10n :
configuration 01 - ecdyne impeller ; 1:55 scale & 1:41 scale
radial decay of average tangential velocity - normalized by tip speed
d=7.66 cm & 10.37 cm ; b= 1.94 cm & 2.63 cm ; 2r/d=1.044

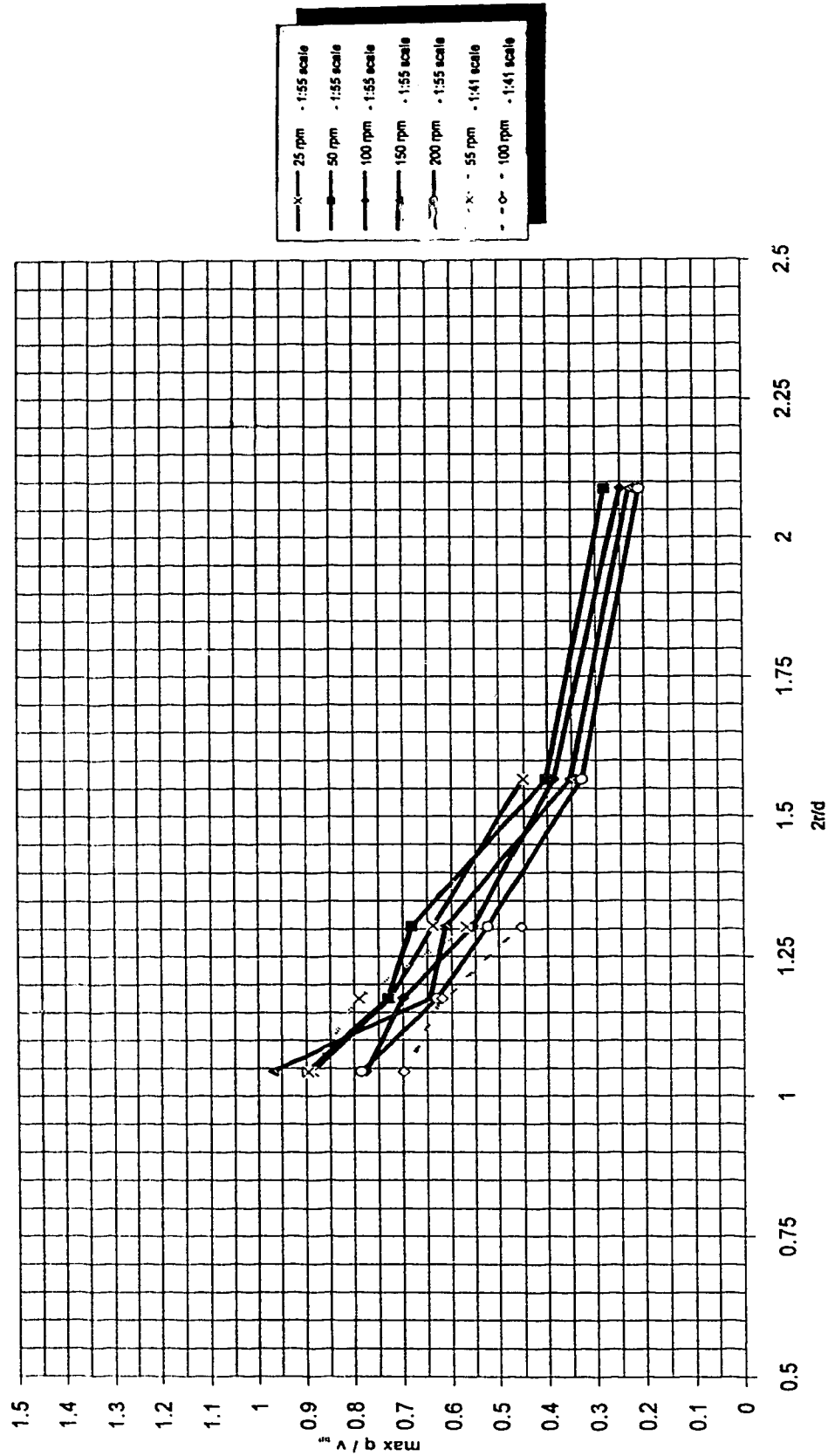


Figure 6-1-11n : configuration 01- ecdodyne impeller ; 1:55 scale & 1:41 scale
 maximum average velocities along axis of jet - normalized by tip speed
 $d=7.66 \text{ cm}$ & 10.37 cm ; $b=1.94 \text{ cm}$ & 2.63 cm

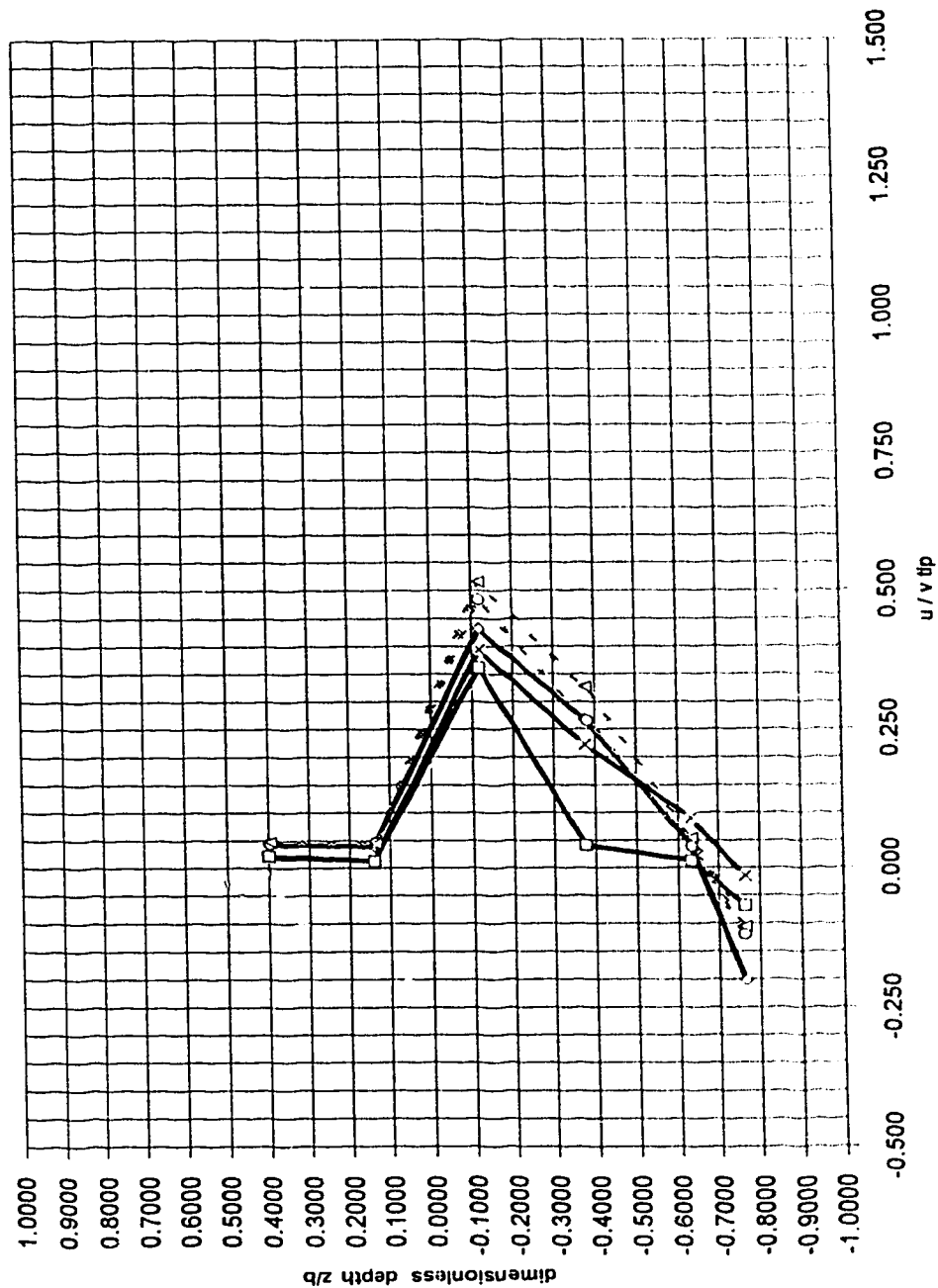


Figure 6-2.1a : configuration 02 - ecodyne impeller ; 1:55 scale & 1:41 scale
radial average velocities near impeller - normalized by tip speed
 $d=7.66$ cm & 10.37 cm ; $b=1.94$ cm & 2.63 cm ; $2\pi/d=1.044$

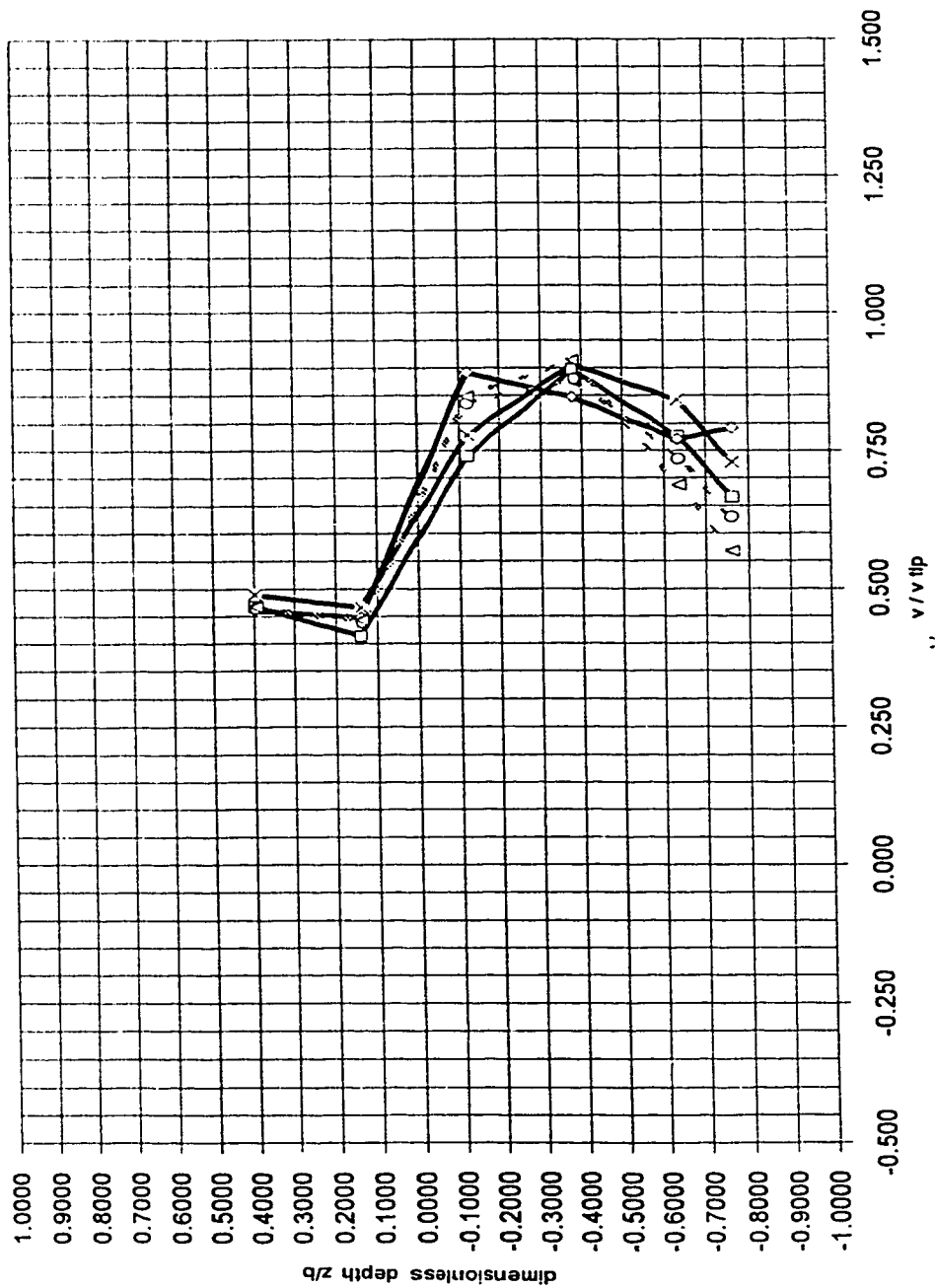
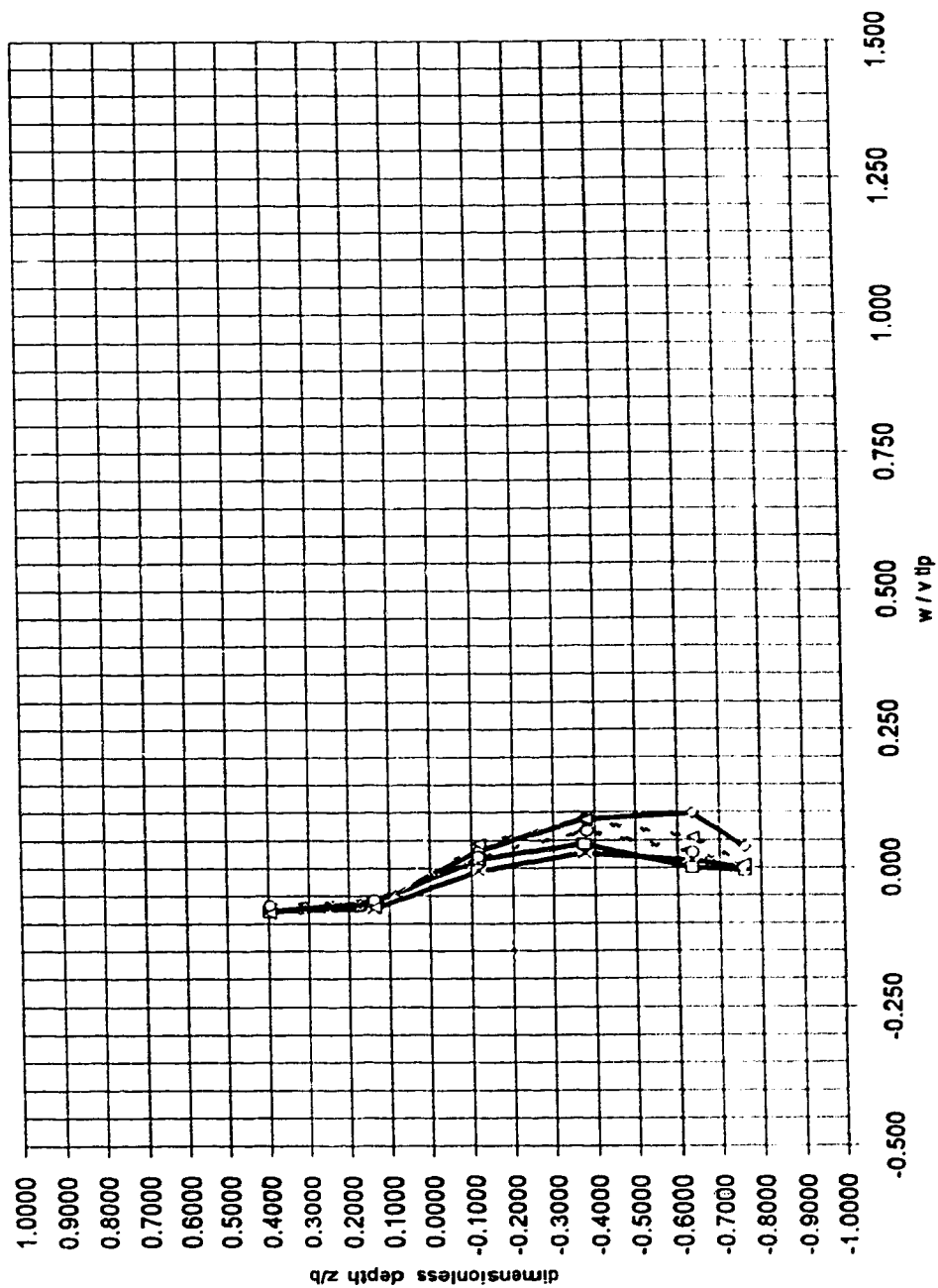


Figure 6-2-2n :



configuration 02 - eco-dyne Impeller ; 1:55 scale & 1:41 scale
axial average velocities near impeller - normalized by tip speed
 $d=7.66$ cm & 10.37 cm ; $b=1.94$ cm & 2.63 cm ; $2r/d=1.044$

Figure 6-2-3n :

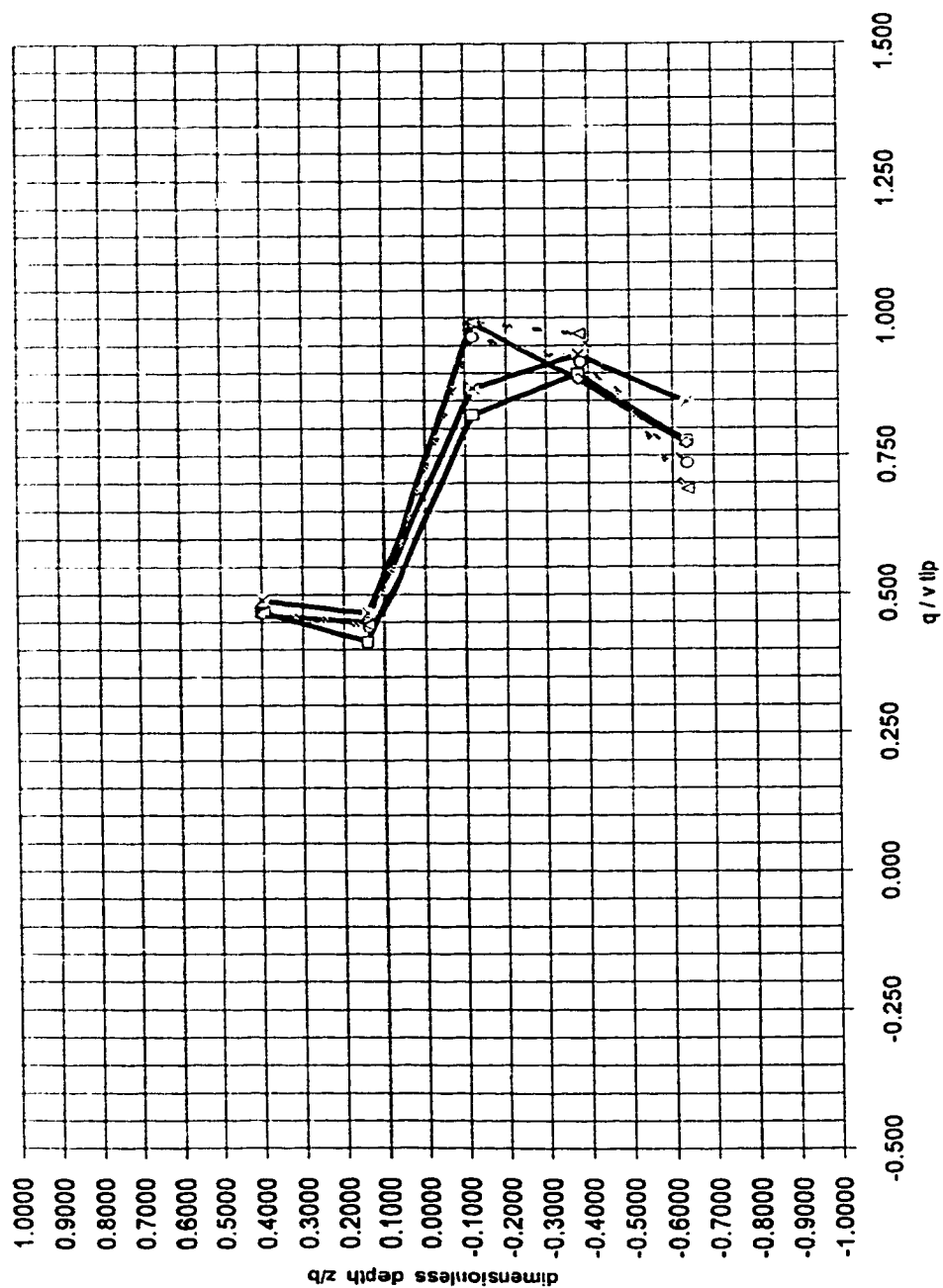


Figure 6-2-4n :
 configuration 02 - ecooyne impeller ; 1:55 scale & 1:41 scale
 average velocities along swirling radial jet's axis - normalized by tip speed
 $d=7.66 \text{ cm}$ & 10.37 cm ; $b=1.94 \text{ cm}$ & 2.63 cm ; $2r/d=1.044$

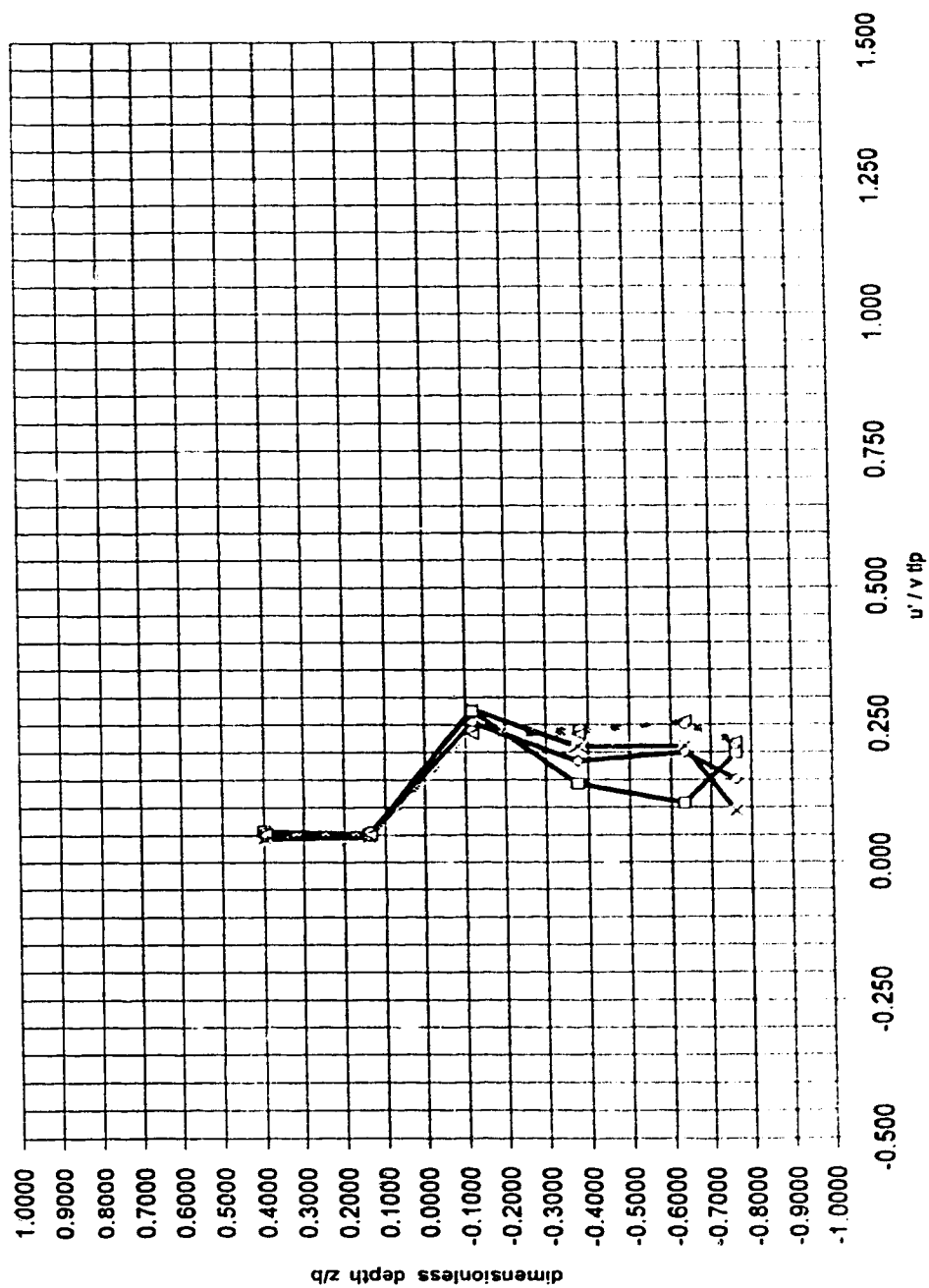


Figure 6-2.5n :
 configuration 02 - eodyne impeller ; 1:55 scale & 1:41 scale
 radial turbulent velocities near impeller - normalized by tip speed
 $q=7.66$ cm & 10.37 cm ; $b=1.94$ cm & 2.63 cm ; $2r/d=1.044$

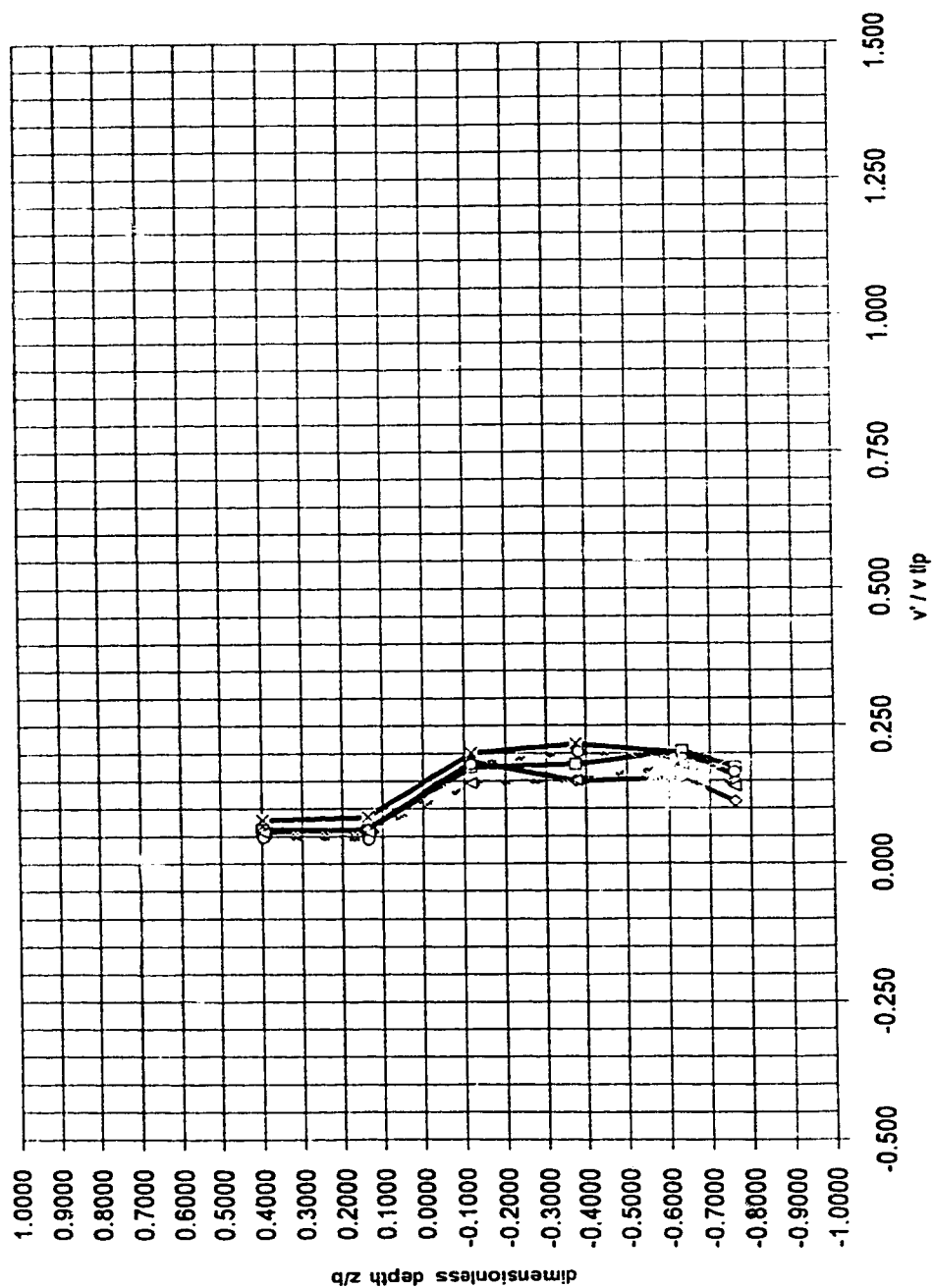


Figure 6-2-6n :
 configuration 02 - eodyne impeller ; 1:55 scale & 1:41 scale
 tangential turbulent velocities near impeller - normalized by tip speed
 $d=7.66$ cm & 10.37 cm ; $b=1.94$ cm & 2.63 cm ; $2r/d=1.044$

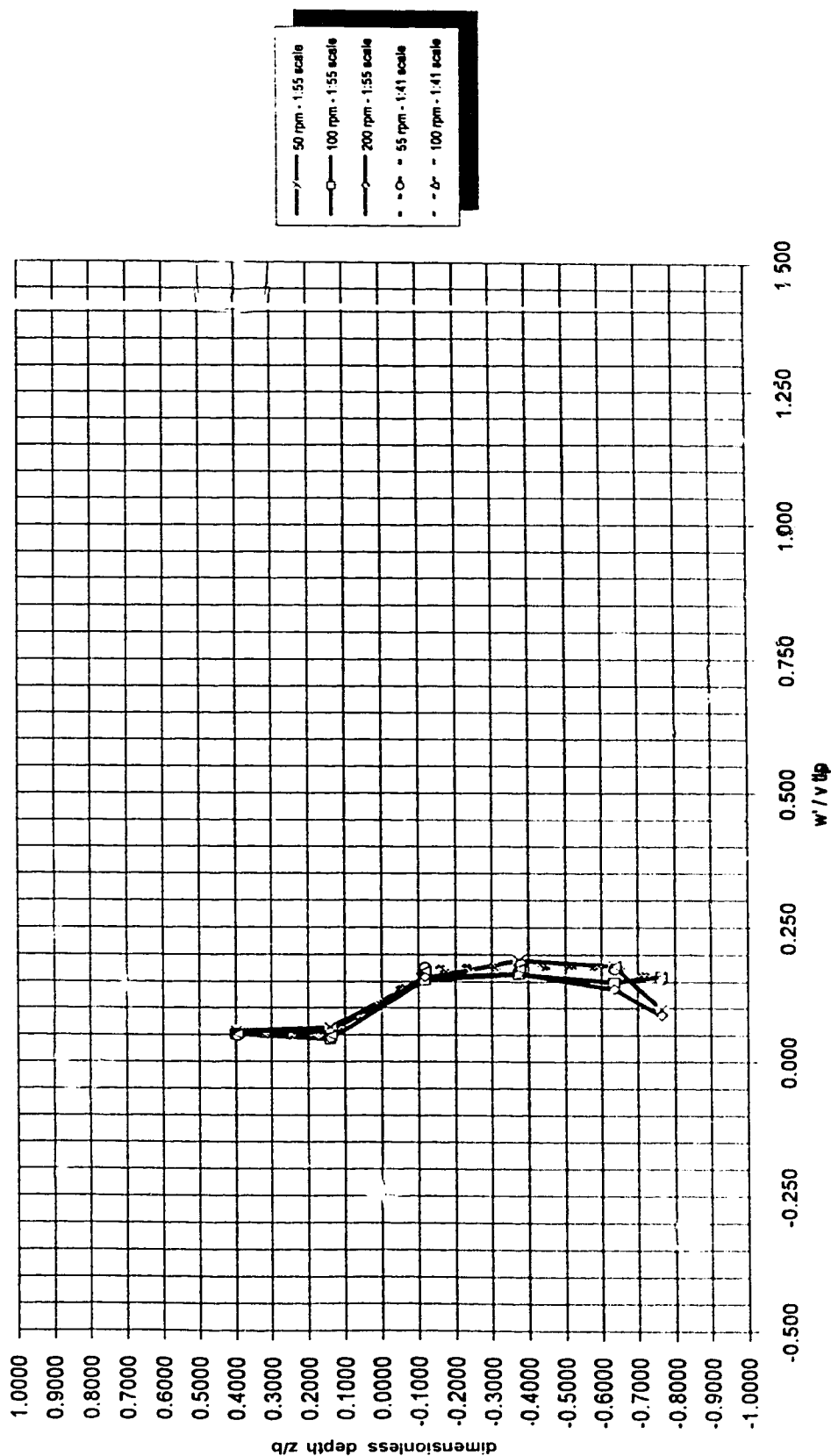
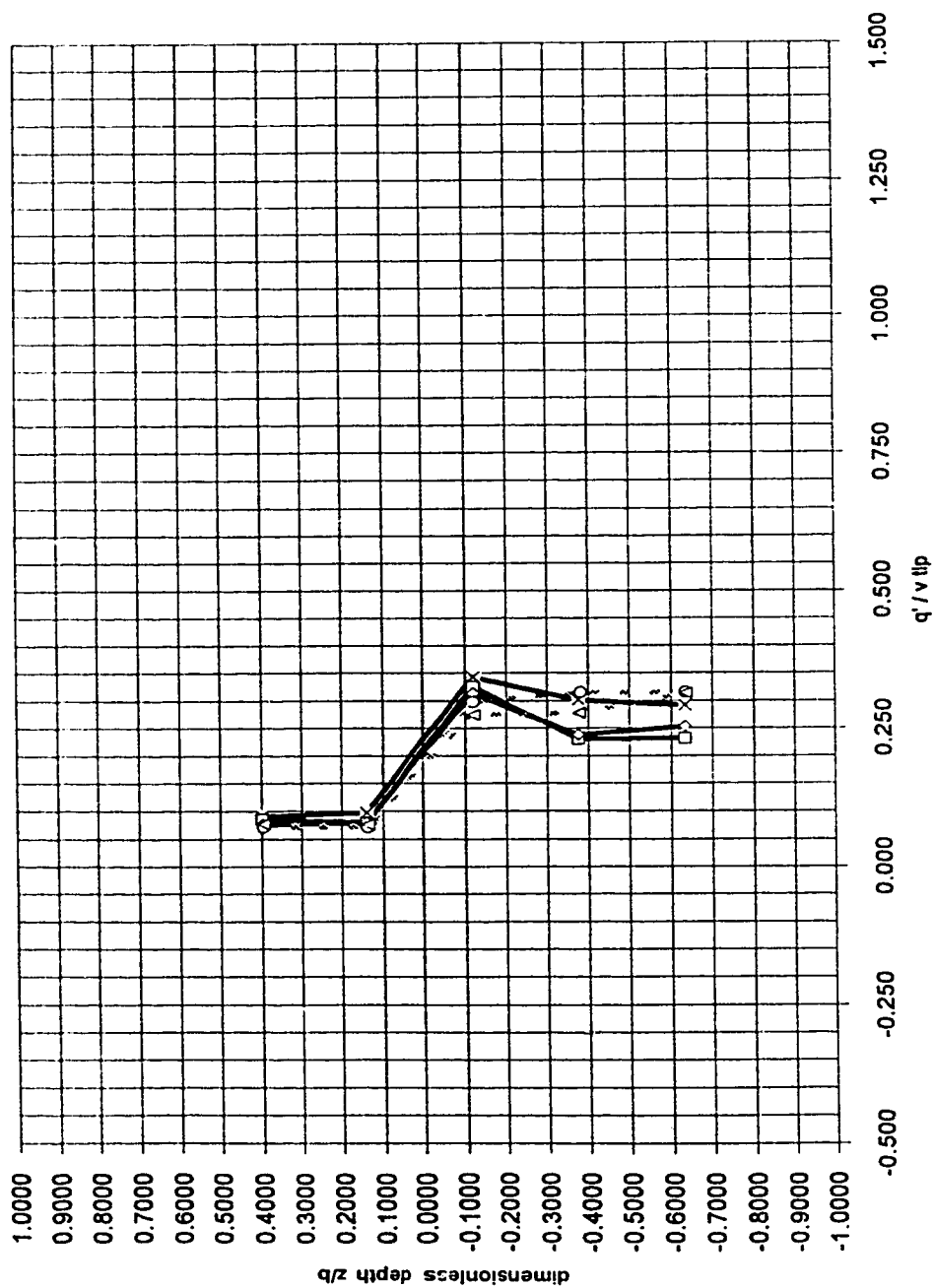
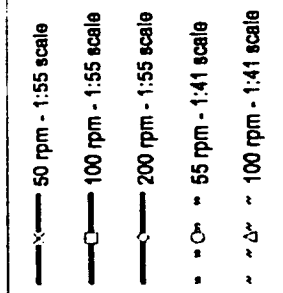


Figure 6-2-7n :
 configuration 02 - ecdyne impeller ; 1:55 scale & 1:41 scale
 axial turbulent velocities near impeller - normalized by tip speed
 $d=7.66$ cm & 10.37 cm ; $b=1.94$ cm & 2.63 cm ; $2r/d=1.044$



configuration 02 - eodyne Impeller ; 1:55 scale & 1:41 scale
 turbulent velocities along swirling radial jet's axis - normalized by tip speed
 $d=7.66 \text{ cm}$ & 10.37 cm ; $b=1.94 \text{ cm}$ & 2.63 cm ; $2r/d=1.044$

Figure 6-2-8n :



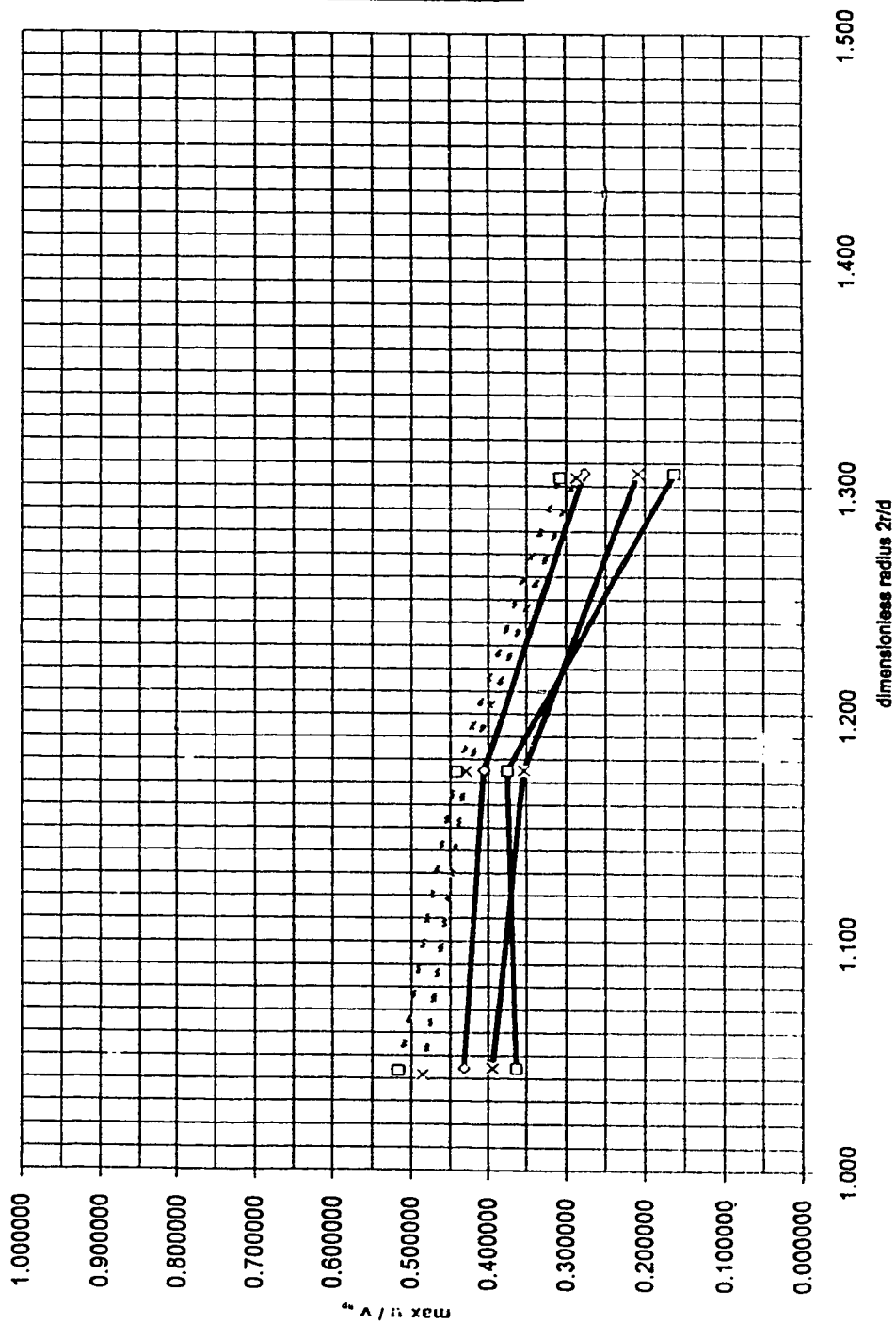


Figure 6-2-9n :
 configuration 02- ecodyne impeller ; 1:55 scale
 radial decay of maximum radial average velocity - normalized by tip speed
 $d=7.66$ cm & 10.37 cm ; $Z/b=1.94$ cm & 2.63 cm

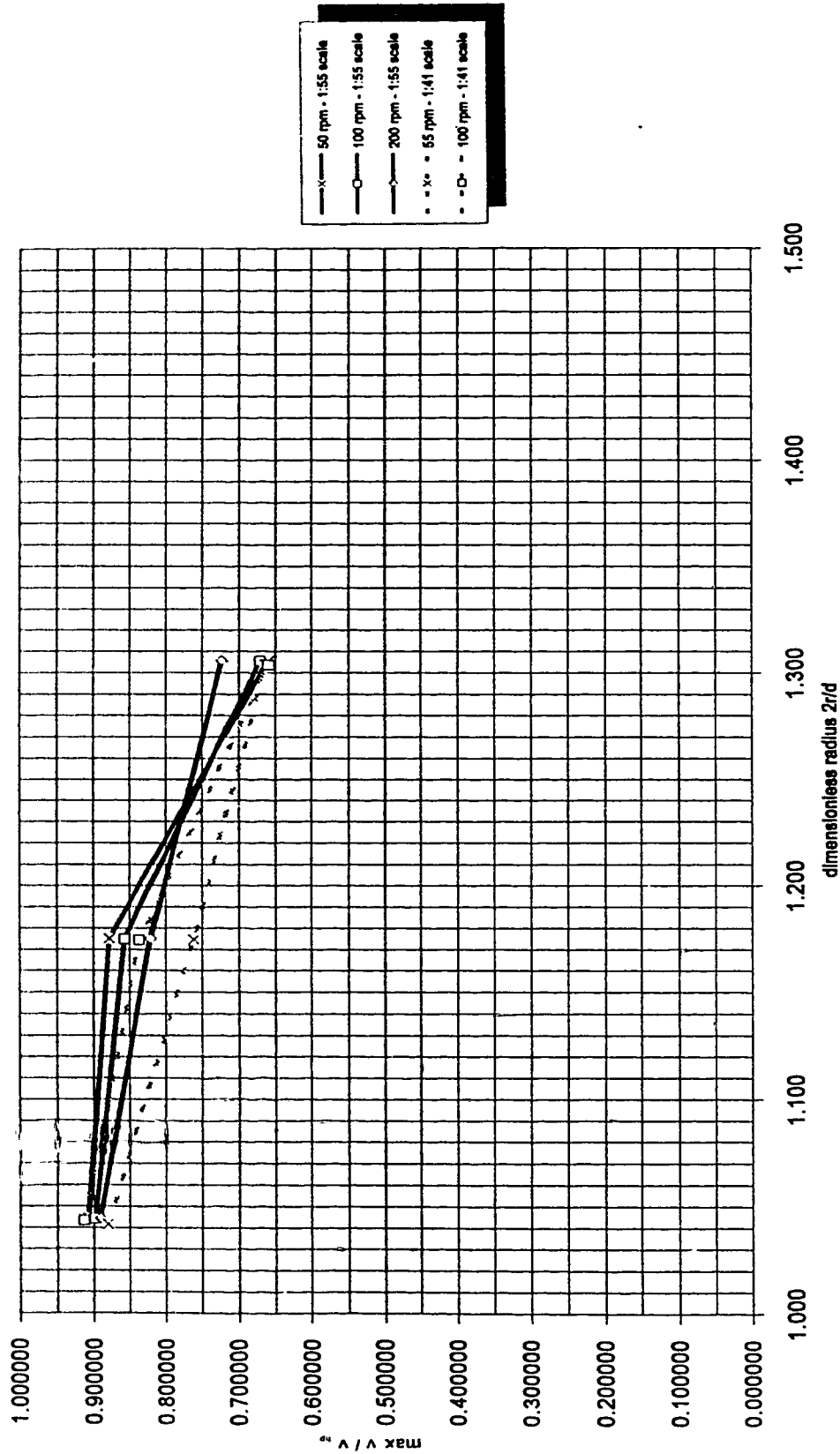


Figure 6-2-10n : configuration O2- ecodyne impeller ; 1:55 scale
radial decay of maximum tangential average velocity - normalized by tip speed
d=7.66 cm & 10.37 cm ; z/b=1.94 cm & 2.63 cm

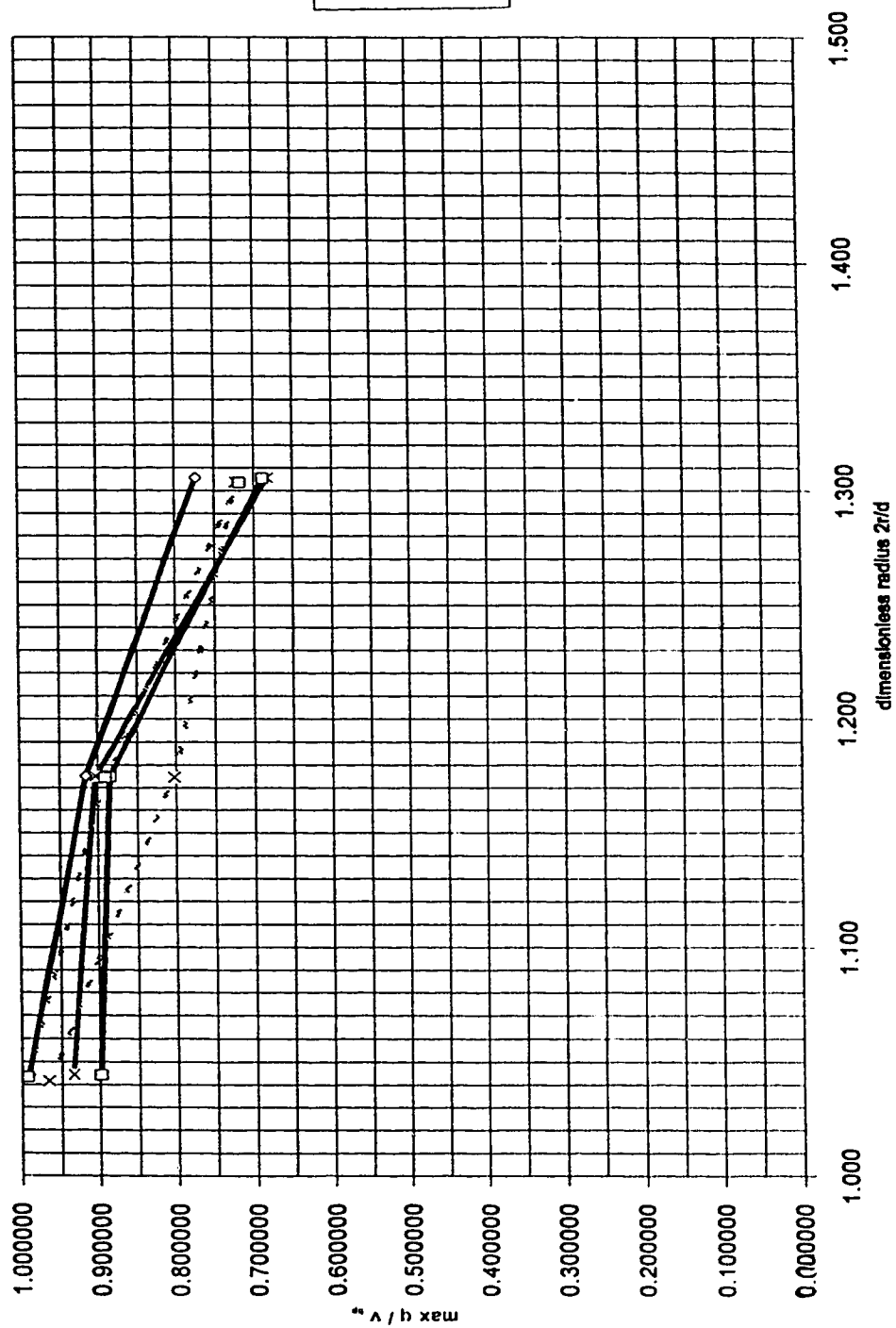
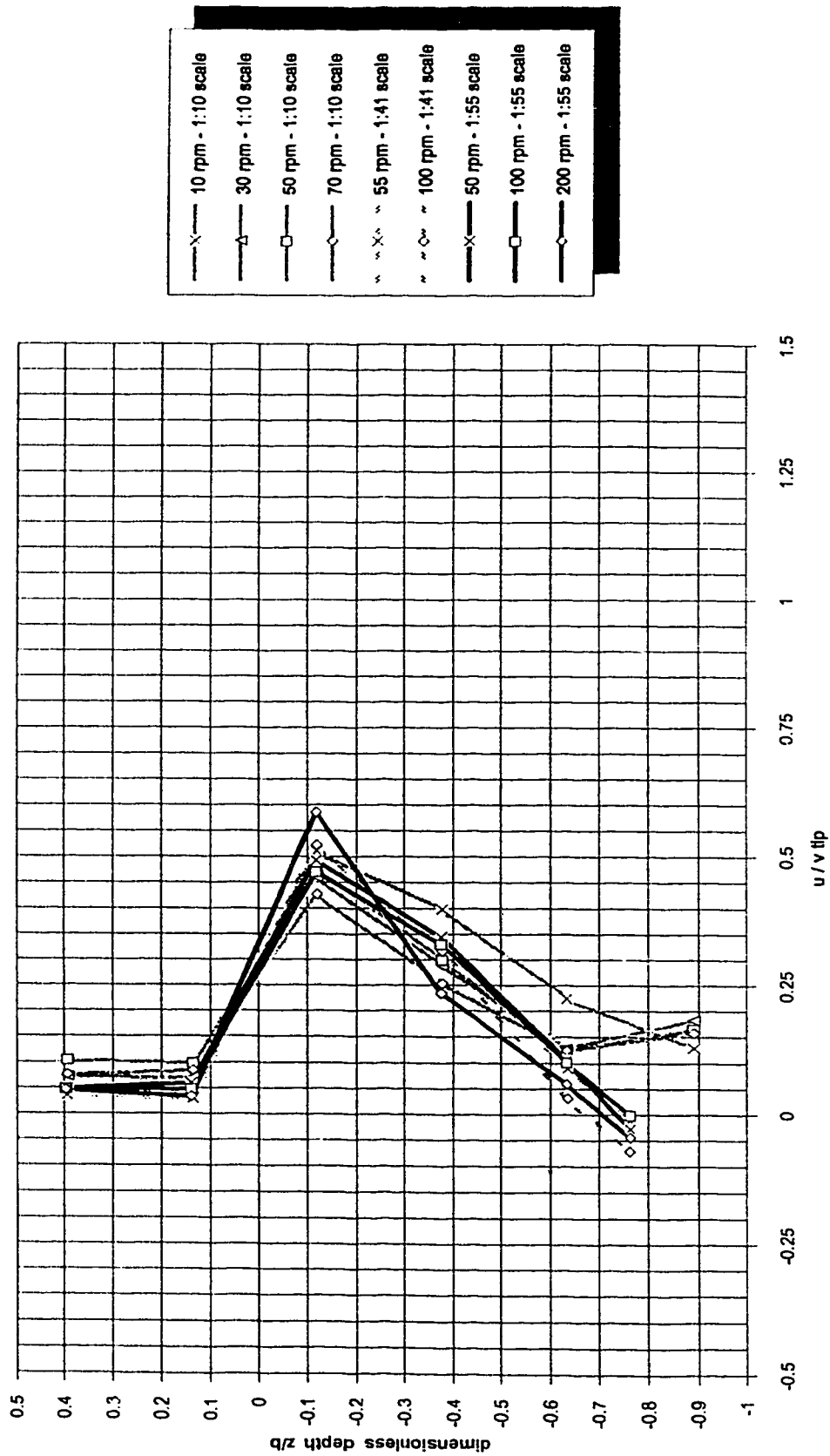


Figure 6-211a : configuration 02- ecodyne impeller ; 1:55 scale
 maximum average velocities along swirling radial jet's axis - normalized by tip speed
 $d=7.66$ cm & 10.37 cm ; $z/b=1.84$ cm & 2.63 cm



configuration 03 - ecodyne impeller ; 1:55 scale, 1:41 scale & 1:10 scale
 radial average velocities near impeller - normalized by tip speed
 $d=7.66 \text{ cm}$, 10.37 cm & 42.62 cm ; $b=1.94 \text{ cm}$, 2.63 cm & 10.8 cm ; $2r/d=1.044$

Figure 6-3.1n :

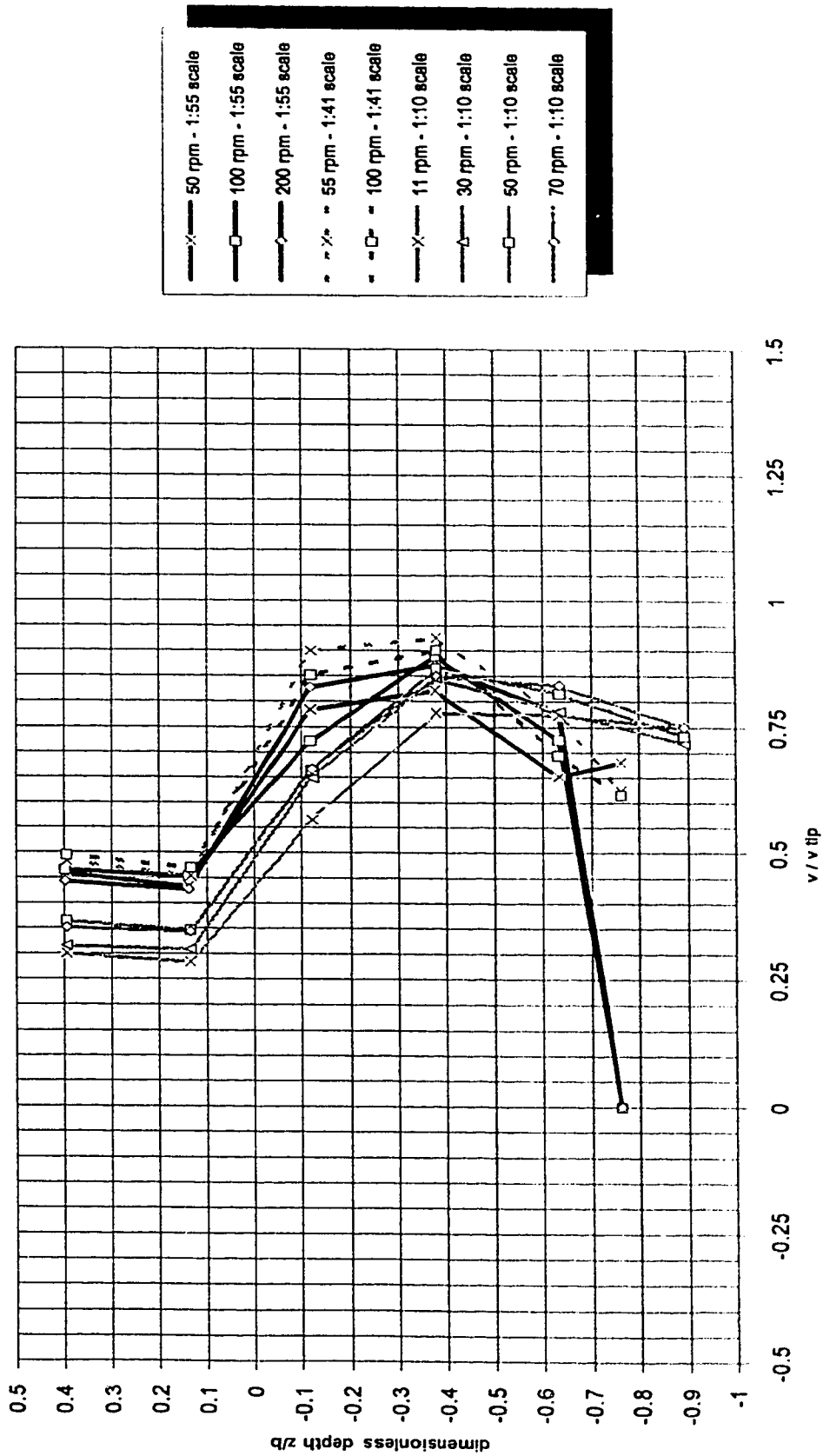


Figure 6-3-2n :
 configuration 03 - ecdyne impeller, all scales
 tangential average velocities near impeller - normalized by tip speed
 $d=7.66$ cm, 10.37 cm & 42.62 cm ; $b=1.84$ cm, 2.63 cm & 10.83 cm ; $2r/d=1.044$

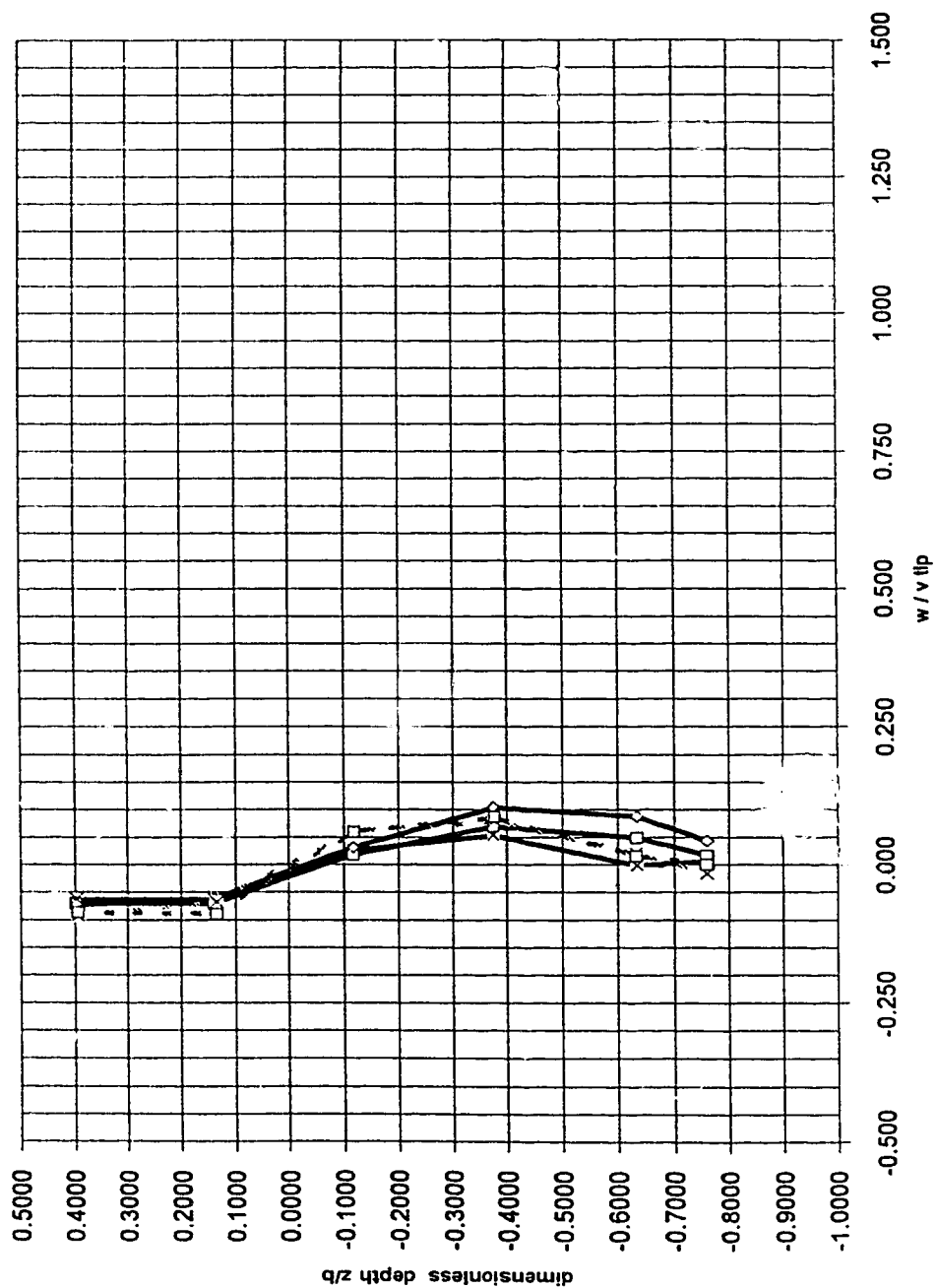


Figure 6-3-3n :

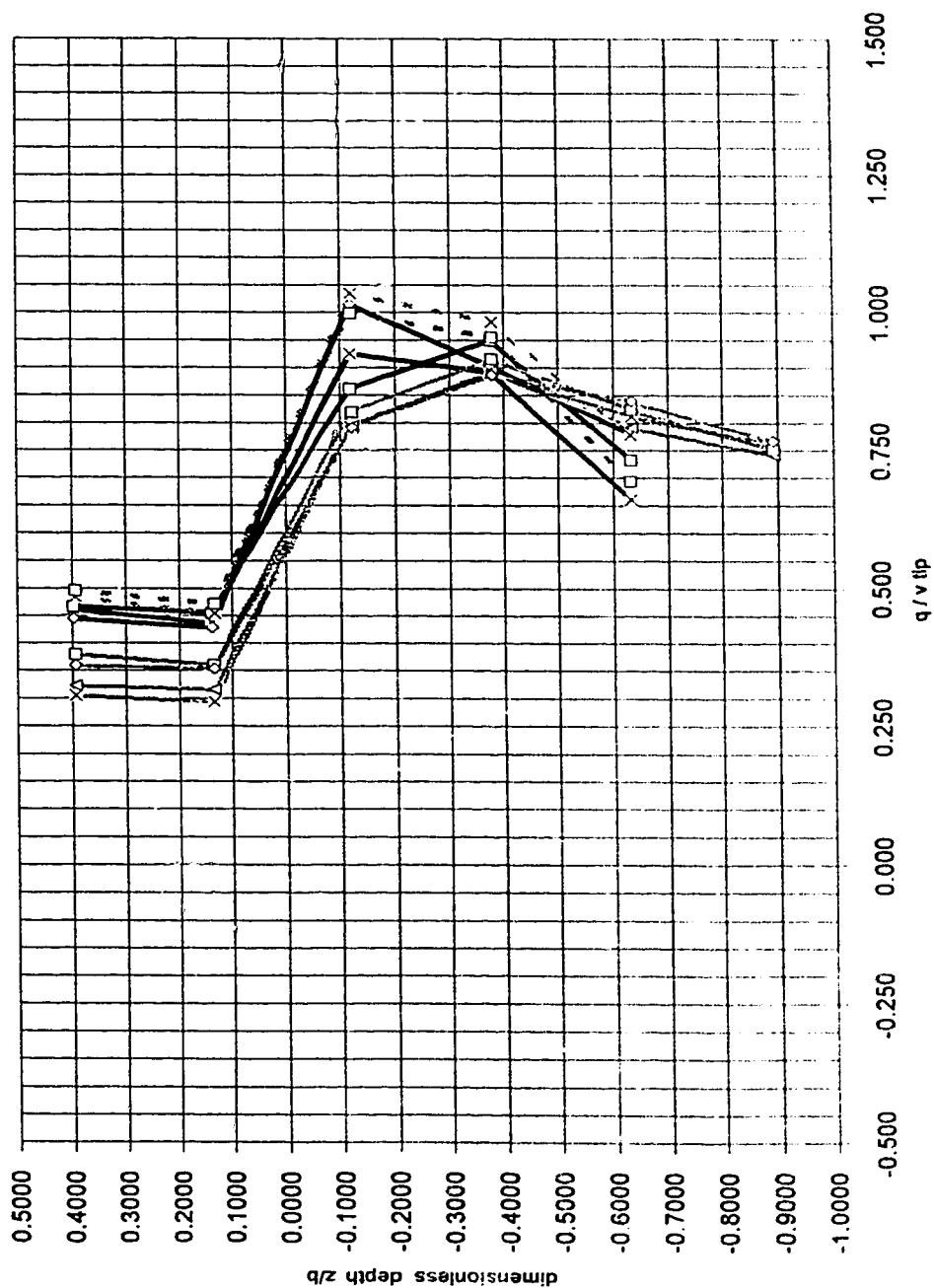


Figure 6-3-4n :
 configuration O3 - eodyne Impeller, all scales
 average velocities along swirling radial jet's axis - normalized by tip speed
 $d=7.66 \text{ cm}$, 10.37 cm & 42.62 cm ; $b=1.94 \text{ cm}$, 2.63 cm & 10.8 cm ; $2r/d=1.044$

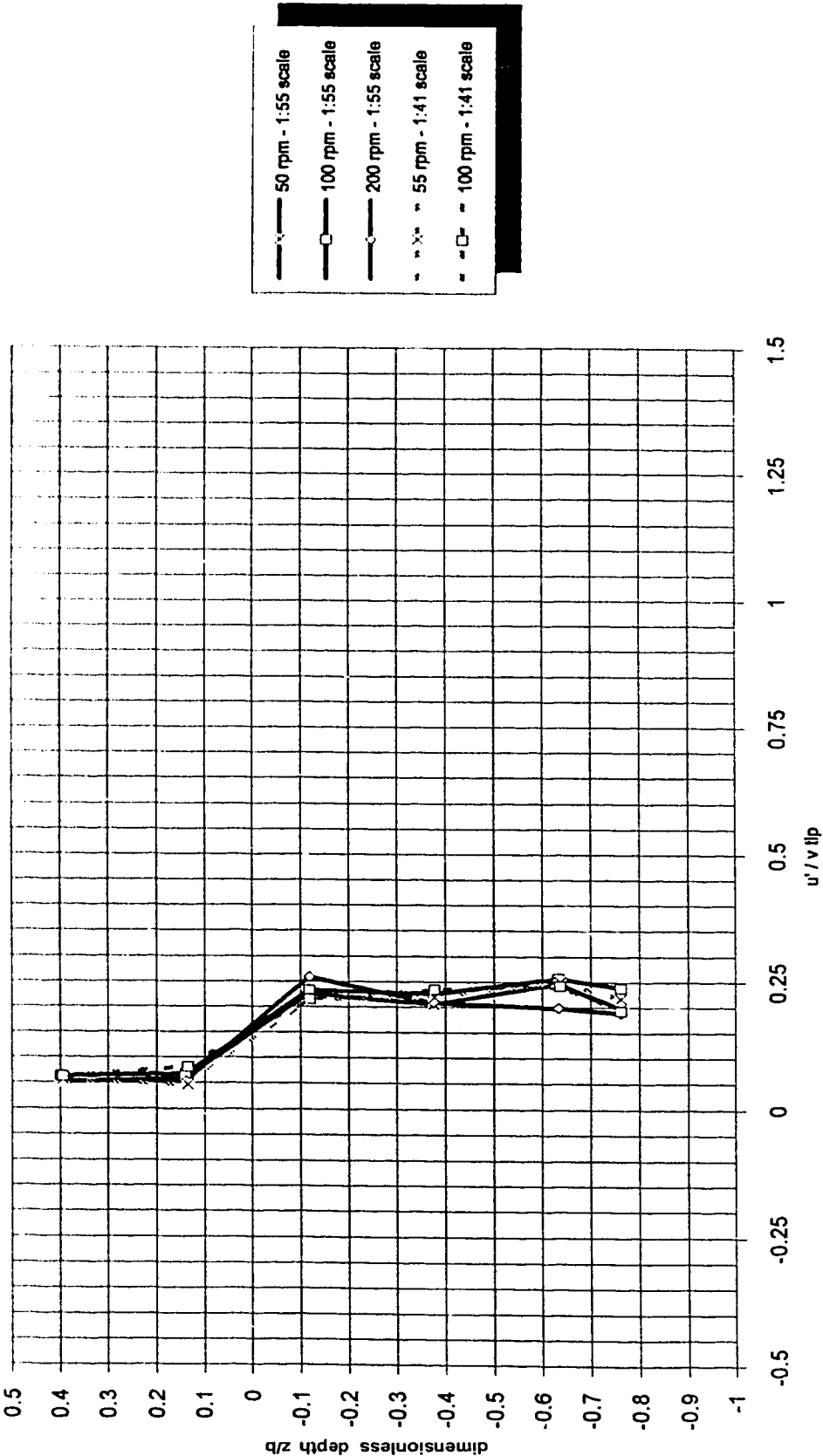


Figure 6-3-5n : configuration 03 - eodyne Impeller, 1:55 scale & 1:41 scale
radial turbulent velocities near impeller - normalized by tip speed
 $d=7.66$ cm, 10.37 cm & 42.62 cm ; $b=1.94$ cm, 2.63 cm & 10.83 cm ; $2r/d=1.044$

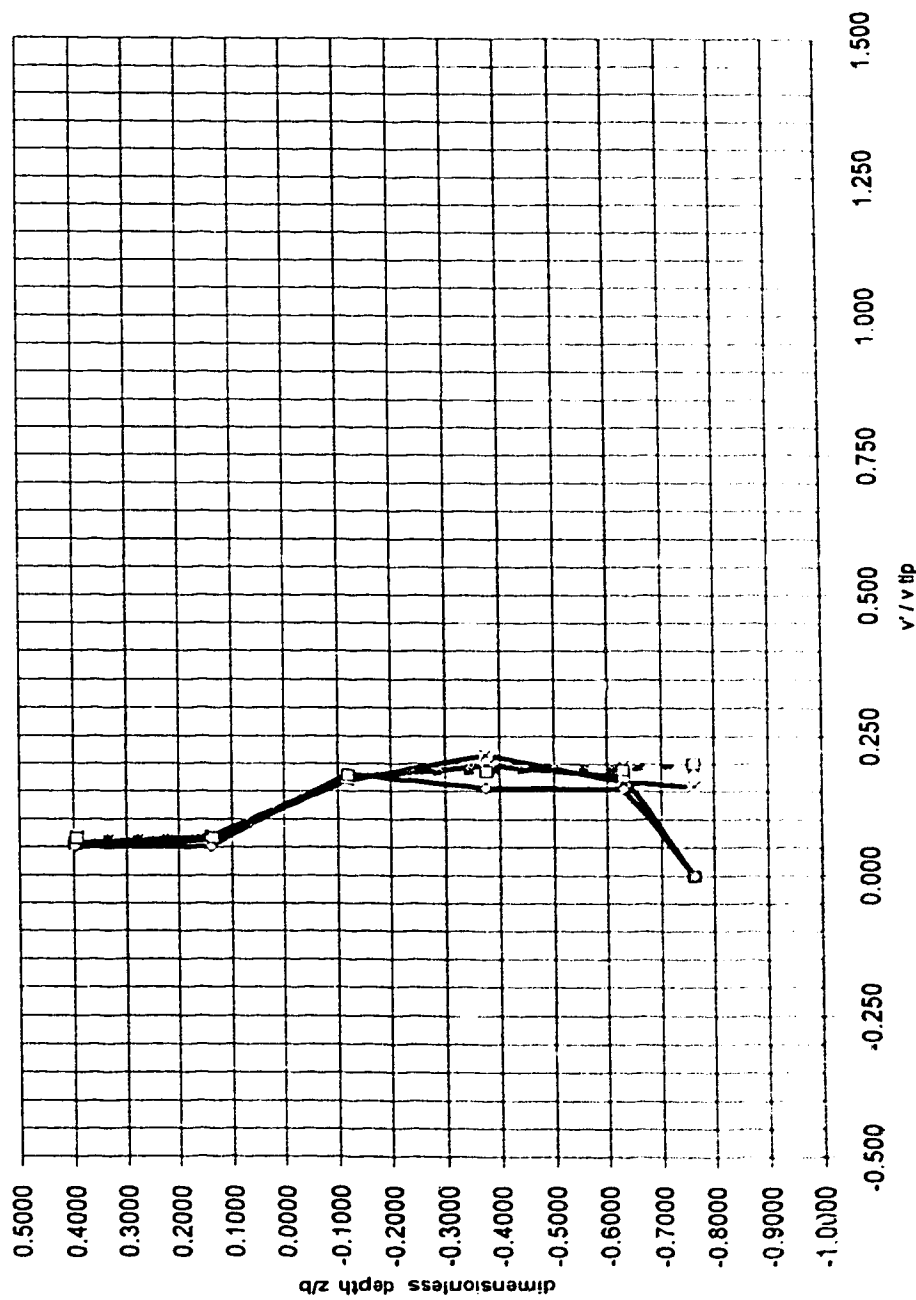
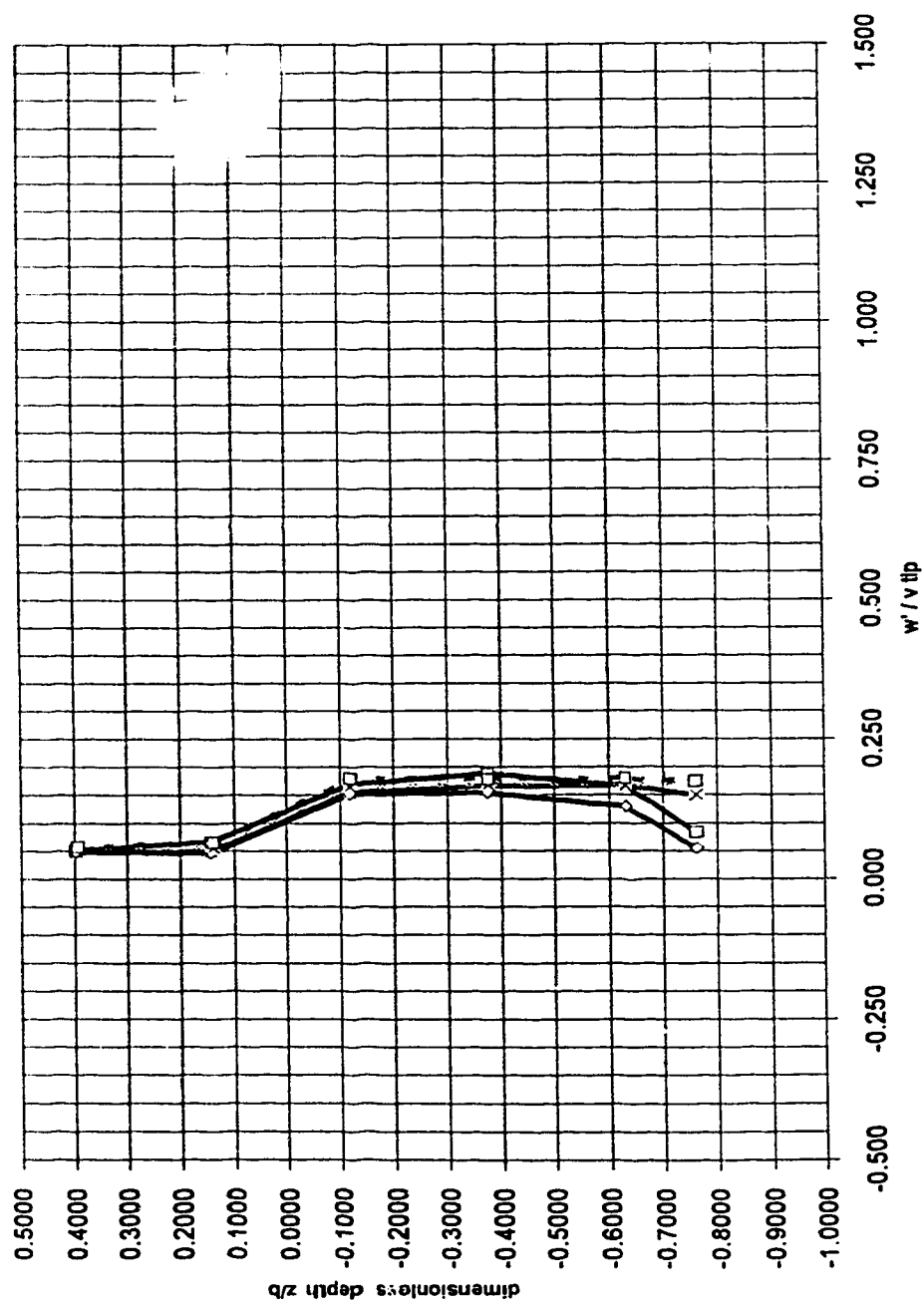


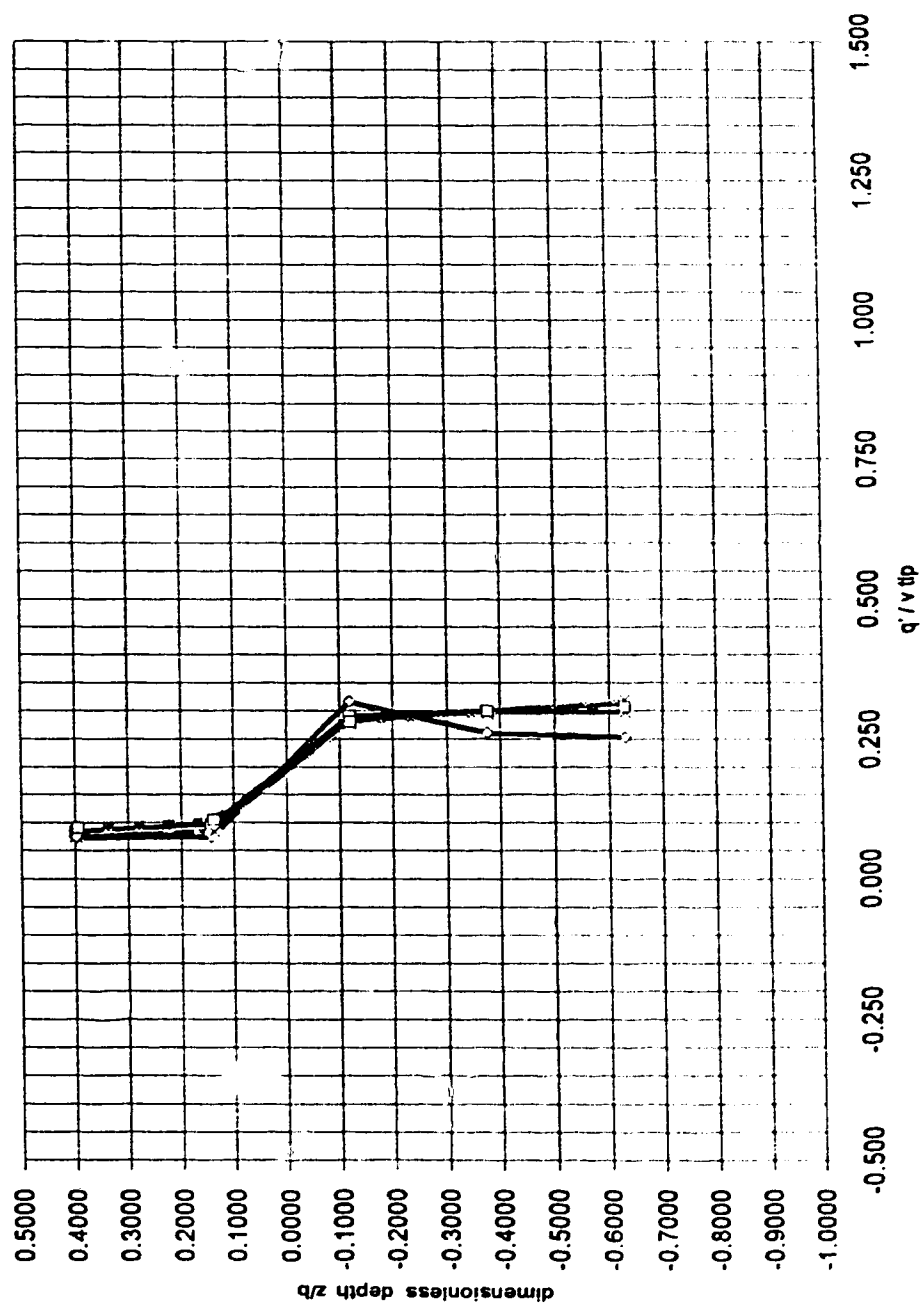
Figure 6-3-5a : configuration 03 - eodyne Impeller ; 1:55 scale & 1:41 scale
tangential turbulent velocities near impeller - normalized by tip speed
 $d=7.66$ cm & 10.37 cm ; $b=1.94$ cm & 2.63 cm ; $2r/d=1.044$

50 rpm - 1:55 scale
100 rpm - 1:55 scale
200 rpm - 1:55 scale
55 rpm - 1:41 scale
100 rpm - 1:41 scale



configuration 03 - eodyne impeller ; 1:55 scale & 1:41 scale
axial turbulent velocities near impeller - normalized by tip speed
 $d=7.66$ cm & 10.37 cm ; $b=1.94$ cm & 2.63 cm ; $2r/d=1.044$

Figure 6-3-7n :



configuration 03 - ecdyne impeller ; 1:55 scale & 1:41 scale
 turbulent velocities along axis of swirling radial jet - normalized by tip speed
 $d=7.66$ cm & 10.37 cm ; $b=1.94$ cm & 2.63 cm ; $2\pi d=1.044$

Figure 6-3-8n :

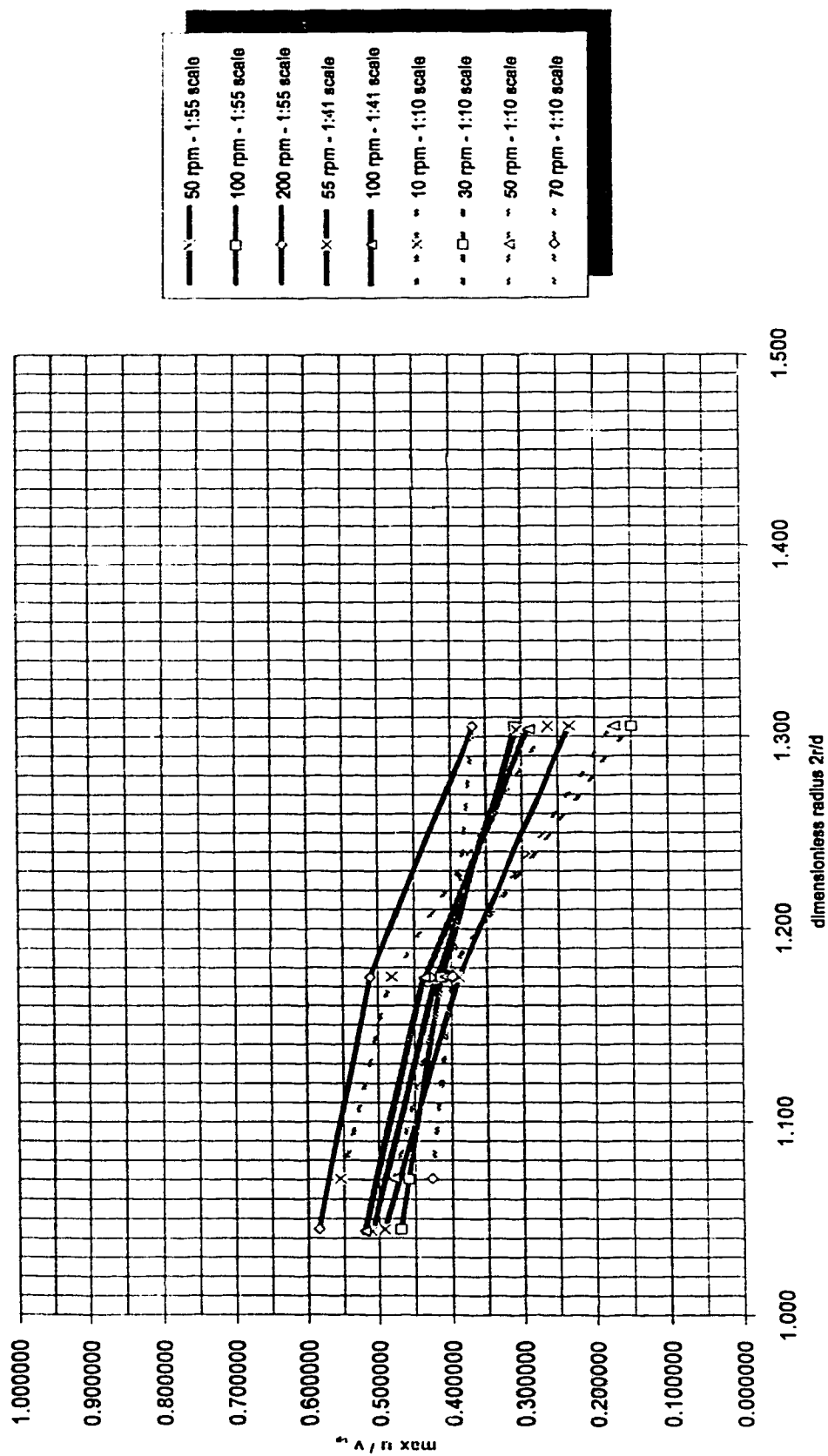


Figure 6-3-9n :
 AO3-ecodyne impeller ; 1:55 scale
 radial decay of radial average velocity - normalized by tip speed
 $d=7.66 \text{ cm}$; $z/b=1.94 \text{ cm}$

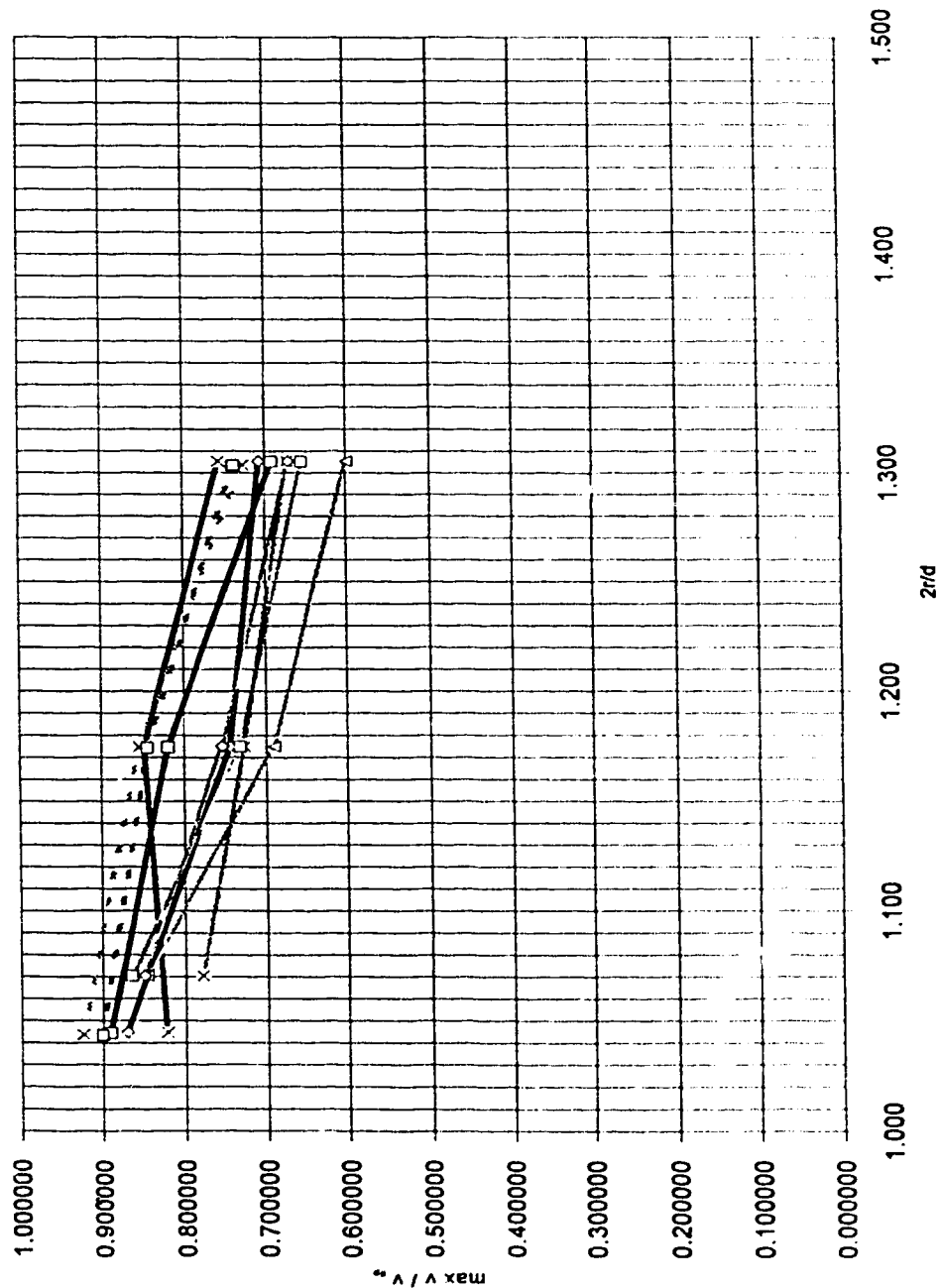


Figure 6-3-10n : configuration 03 - ecodyne Impeller, 1:55 scale, 1:41 scale & 1:10 scale
radial variation of maximum tangential velocities - normalized by tip speed
 $d=7.66$ cm & 10.37 cm ; $b=1.94$ cm & 2.63 cm ; $2r/d=1.044$

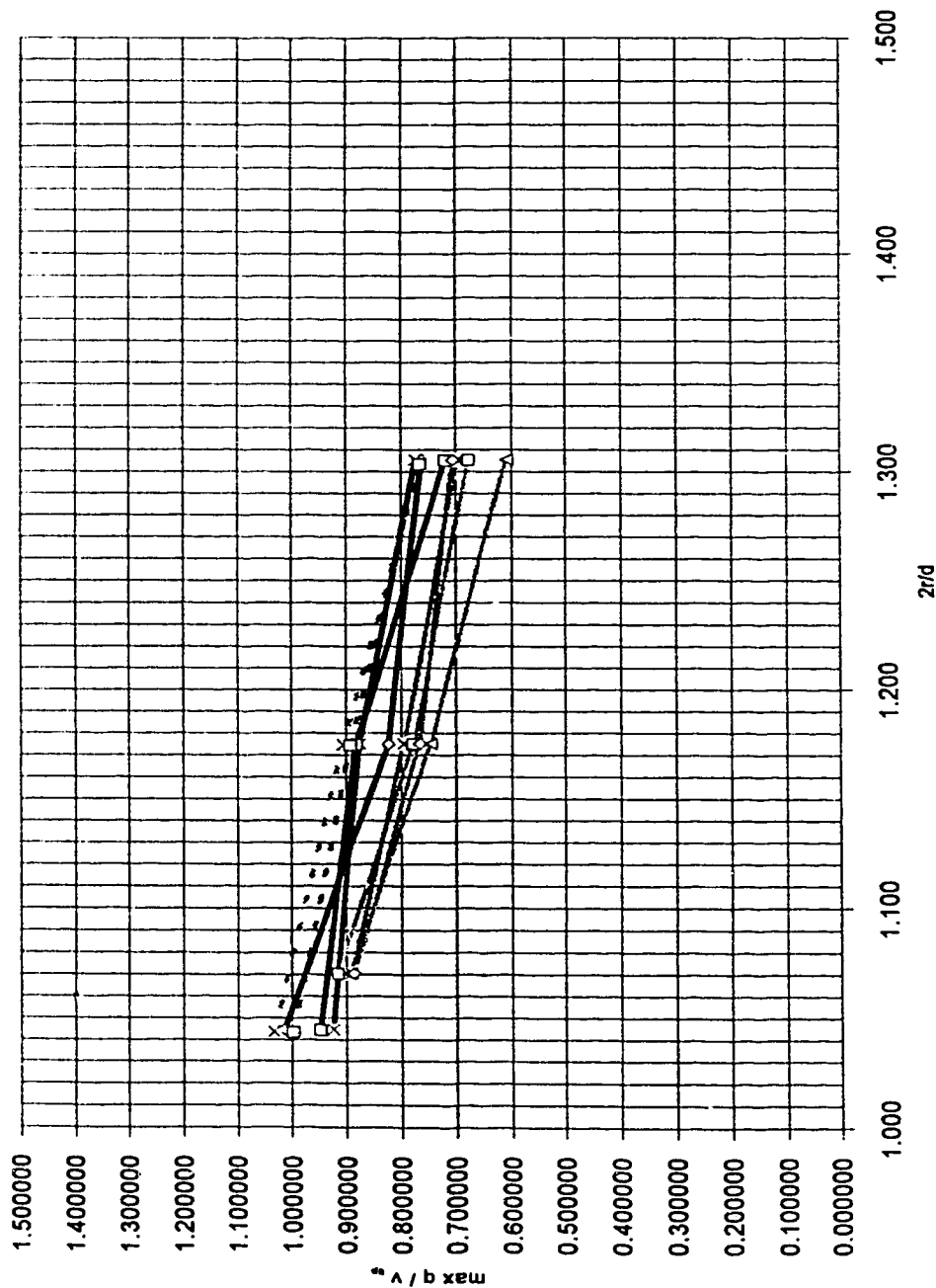
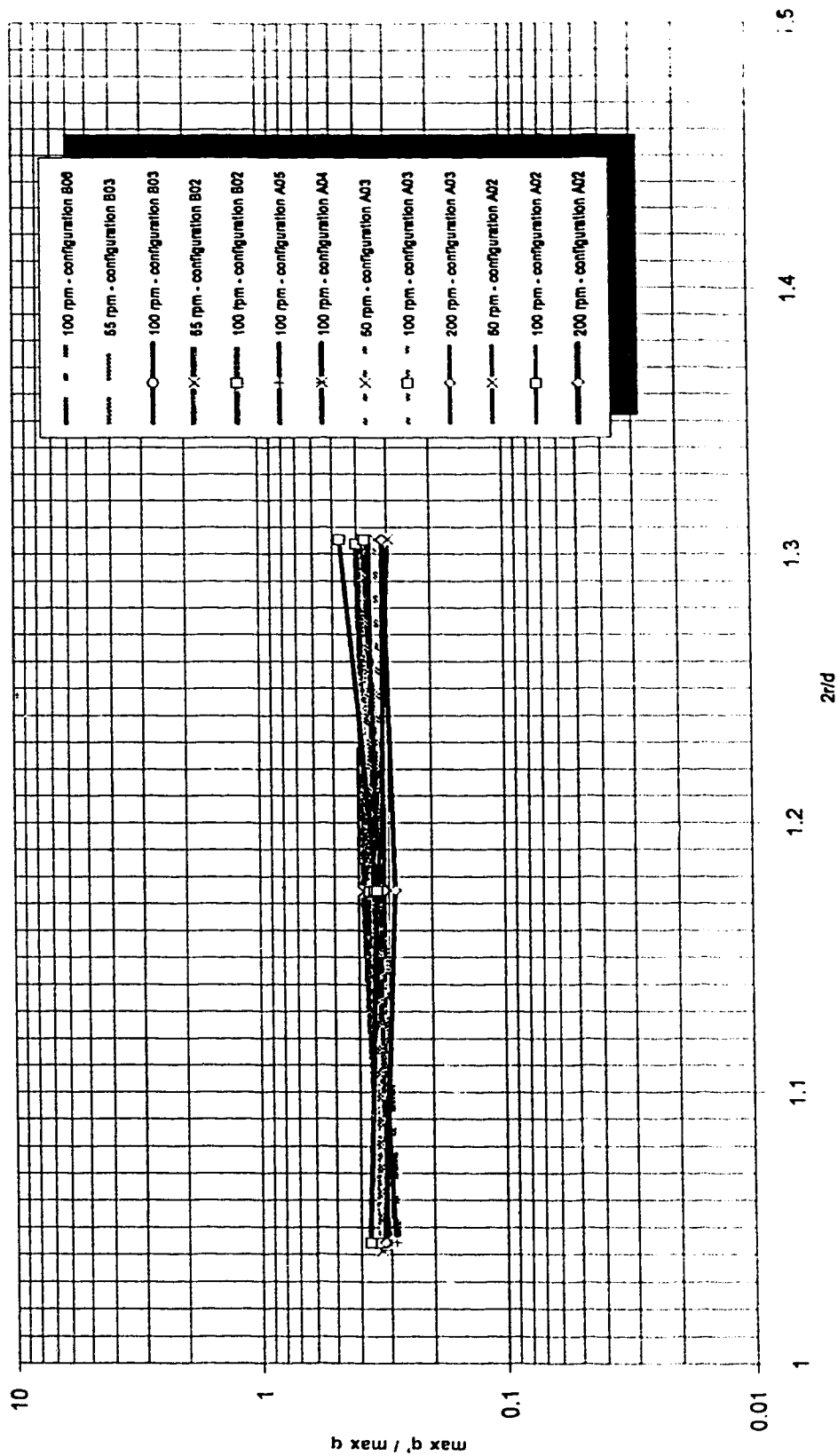


Figure 6-3-11a :
 configuration 03 - ecodyne impeller, all scales
 maximum average velocities along swirling radial jet's axis - normalized by tip speed
 $d=7.66$ cm, 10.37 cm & 42.62 cm ; $b=1.94$ cm, 2.63 cm & 10.8 cm ; $2r/d=1.044$



ecodyne impeller - confined impeller, all scales
radial variation of maximum turbulence intensity
d=7.66 cm & 10.37 cm ; b=1.94 cm & 2.63 cm

Figure 6-4 :

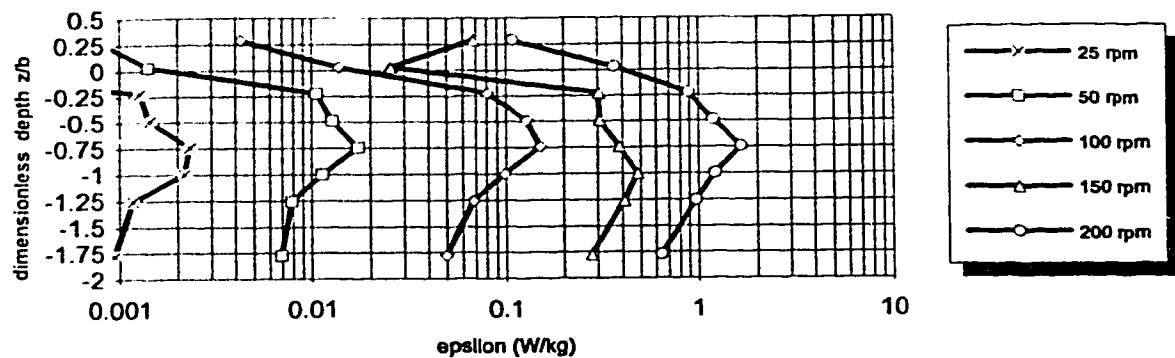


Figure 6-5a-1 : trial A01 - ecodyne impeller ; 1:55 scale
dissipation rates near impeller
 $d=7.66$ cm ; $b=1.94$ cm ; $2r/d=1.044$

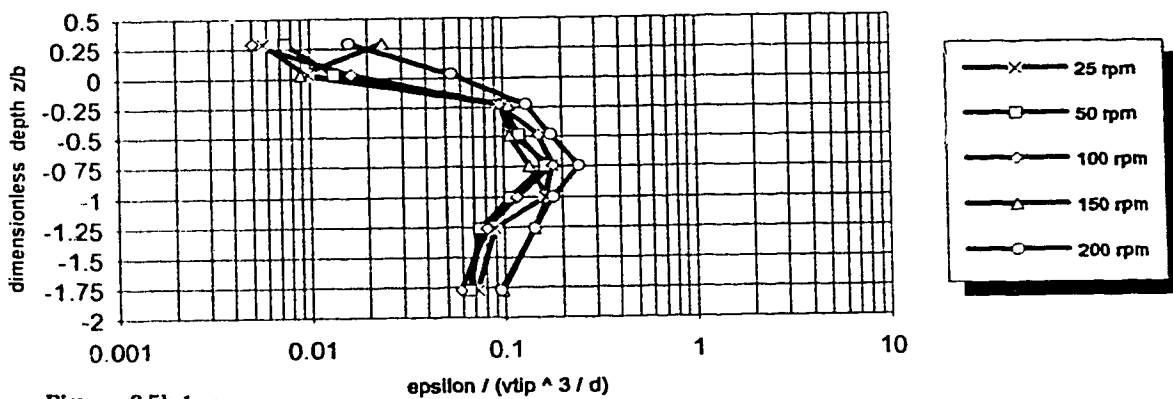


Figure 6-5b-1 : trial A01 - ecodyne impeller ; 1:55 scale
dimensionless dissipation rates near impeller - normalized by impeller's diameter
 $d=7.66$ cm ; $b=1.94$ cm ; $2r/d=1.044$

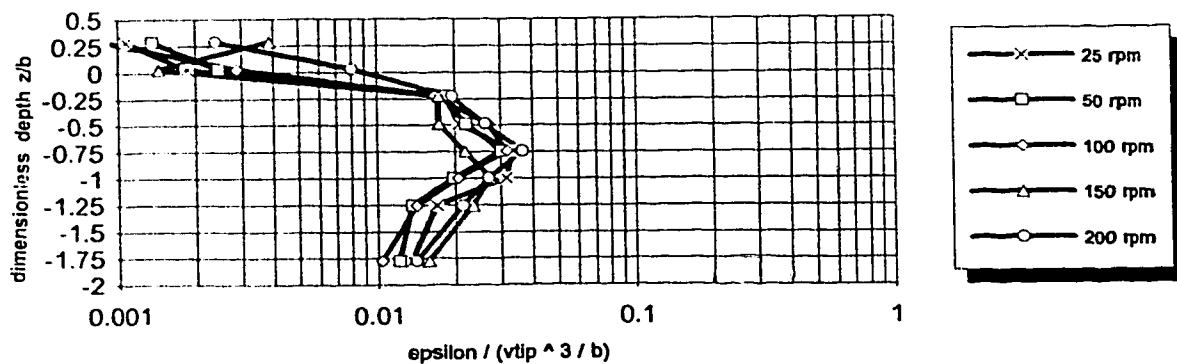
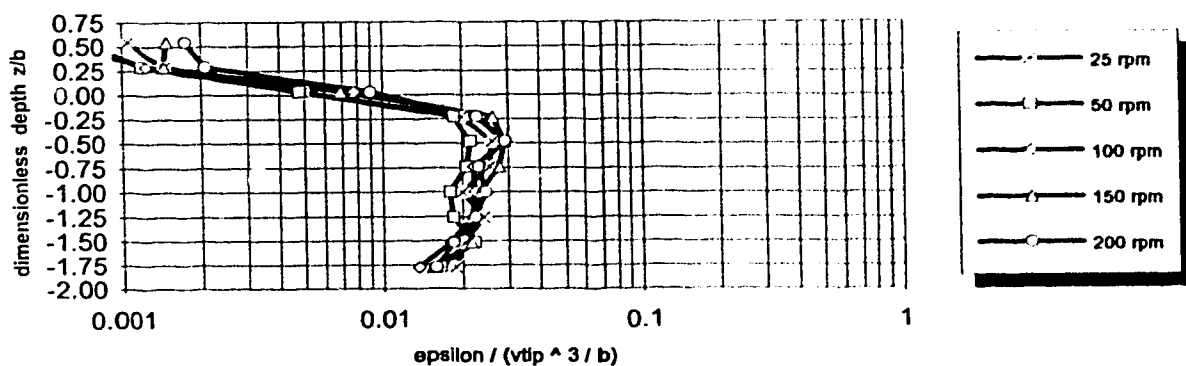
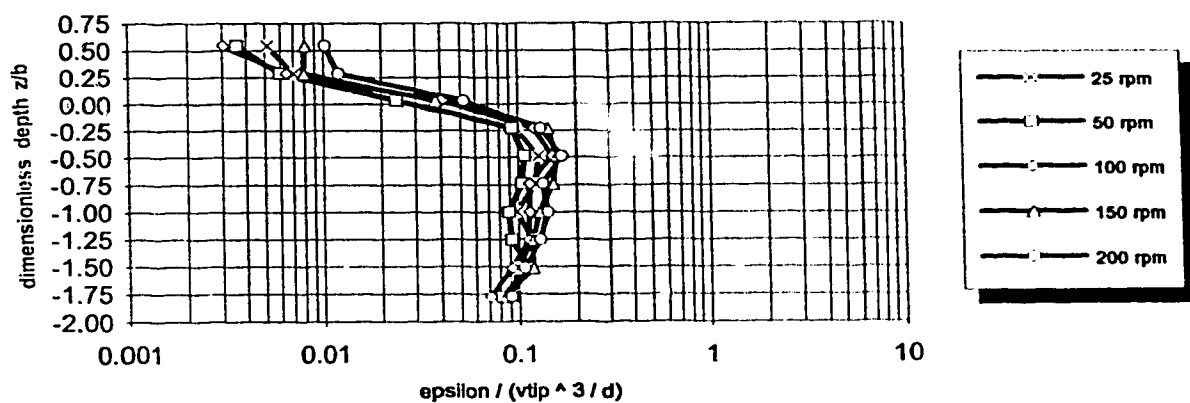
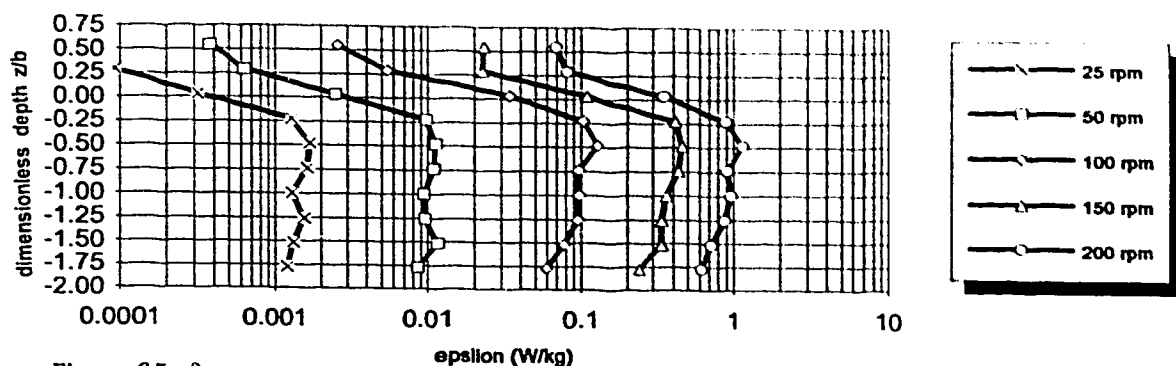


Figure 6-5c-1 : trial A01 - ecodyne impeller ; 1:55 scale
dimensionless dissipation rates near impeller - normalized by blade height
 $d=7.66$ cm ; $b=1.94$ cm ; $2r/d=1.044$



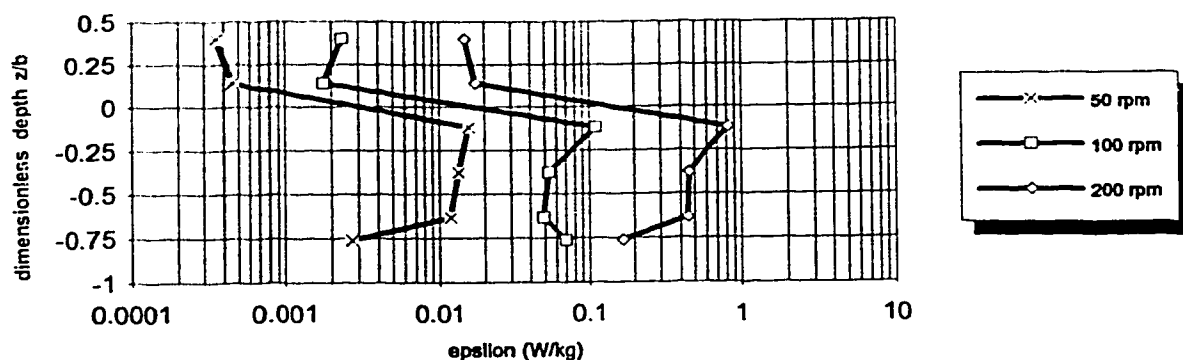


Figure 6-6a :
trial A02 - ecodyne Impeller ; 1:55 scale
dimensionless dissipation rates near impeller
 $d=7.66$ cm ; $b=1.94$ cm ; $2r/d=1.044$

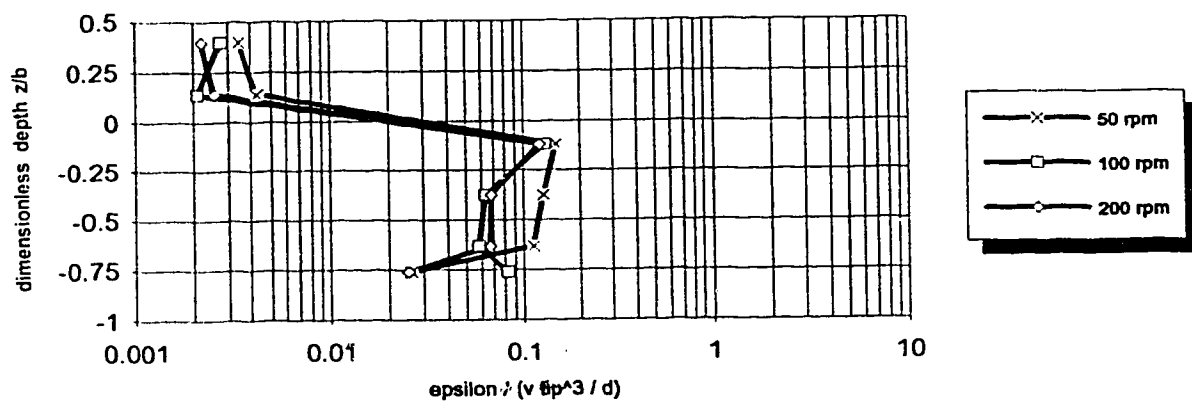


Figure 6-6b :
trial A02 - ecodyne Impeller ; 1:55 scale
dimensionless dissipation rates near impeller - normalized by impeller's diameter
 $d=7.66$ cm ; $b=1.94$ cm ; $2r/d=1.044$

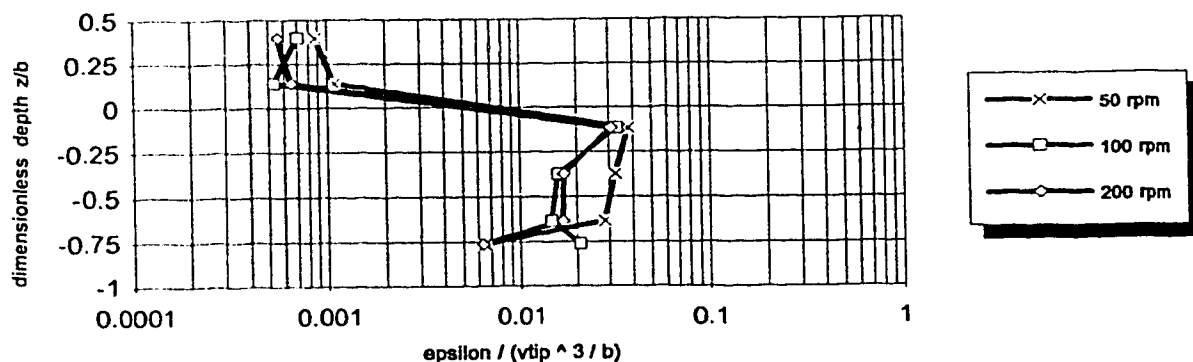


Figure 6-6c :
trial A02 - ecodyne Impeller ; 1:55 scale
dimensionless dissipation rates near impeller - normalized by blade height
 $d=7.66$ cm ; $b=1.94$ cm ; $2r/d=1.044$

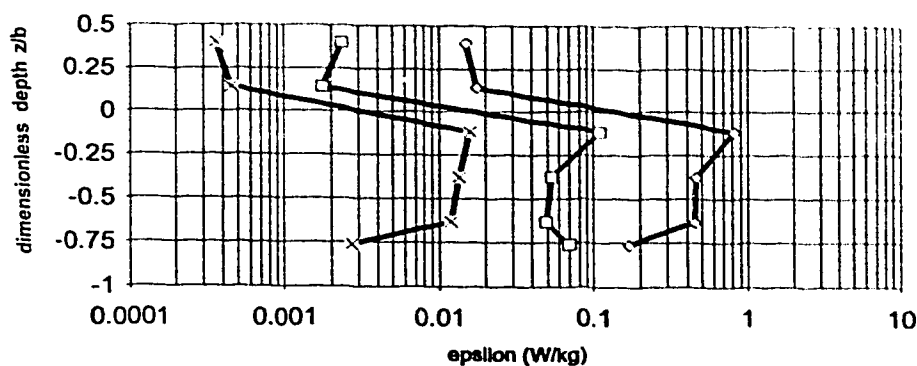


Figure 6-7a :
trial A03 - ecodyne impeller ; 1:55 scale
dissipation rates near Impeller
 $d=7.66$ cm ; $b=1.94$ cm ; $2r/d=1.044$

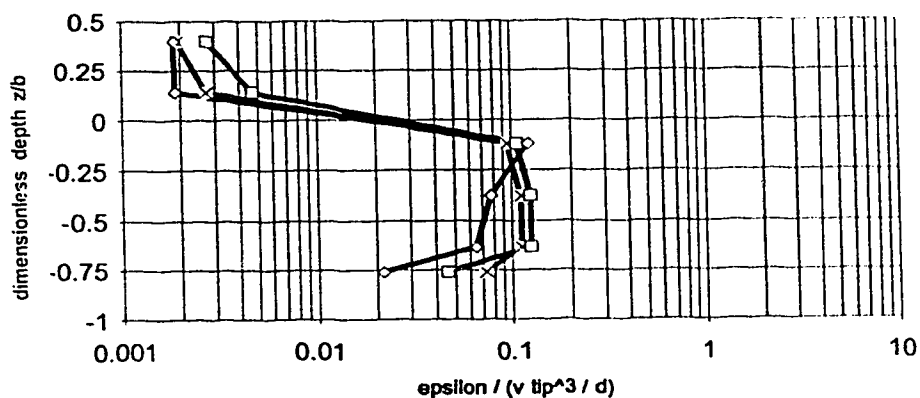


Figure 6-7b :
trial A03 - ecodyne impeller ; 1:55 scale
dimensionless dissipation rates near Impeller - normalized by Impeller's diameter
 $d=7.66$ cm ; $b=1.94$ cm ; $2r/d=1.044$

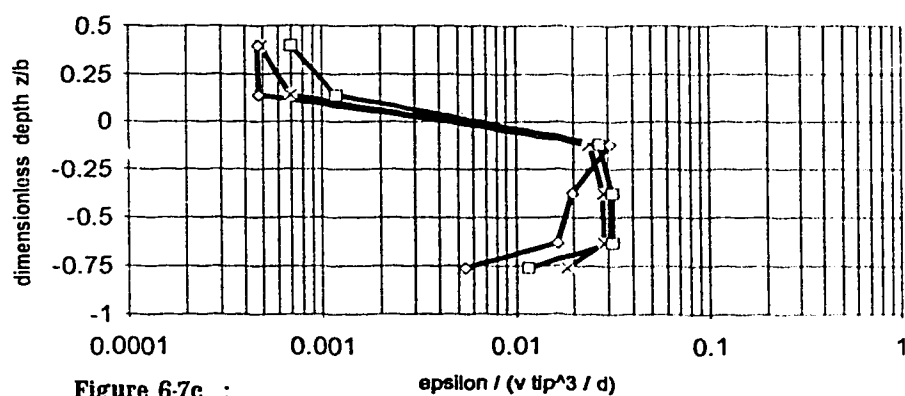


Figure 6-7c :
trial A03 - ecodyne impeller ; 1:55 scale
dimensionless dissipation rates near Impeller - normalized by blade height
 $d=7.66$ cm ; $b=1.94$ cm ; $2r/d=1.044$

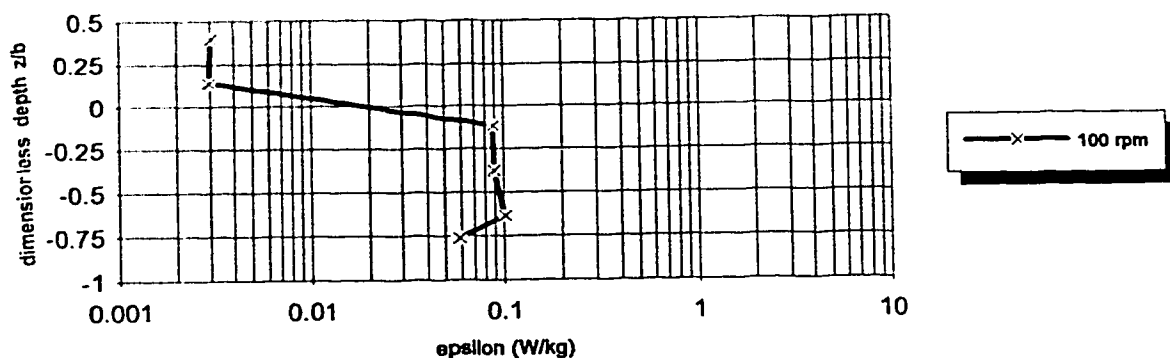


Figure 6-8a : trial A04 - ecodyne Impeller ; 1:55 scale ; decreased skirt opening
dissipation rates near impeller
 $d=7.66$ cm ; $b=1.94$ cm ; $2r/d=1.044$

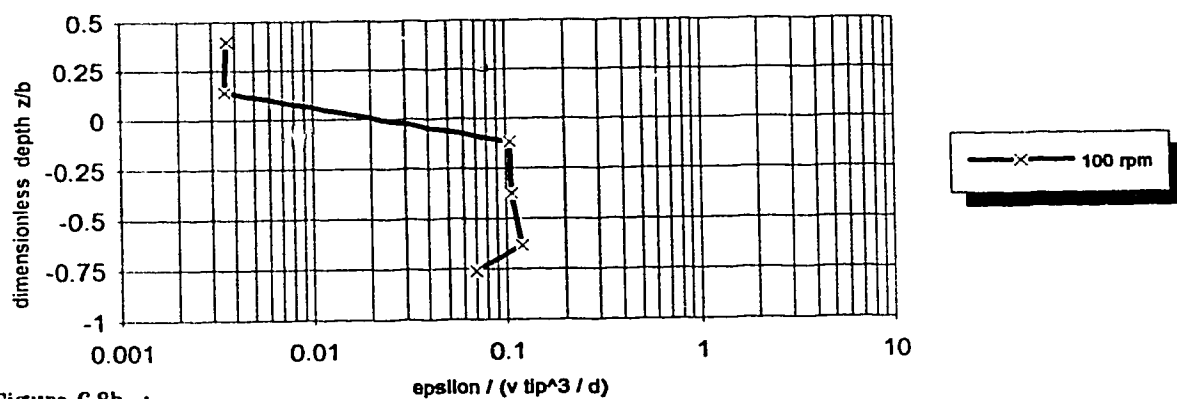


Figure 6-8b : trial A04 - ecodyne Impeller ; 1:55 scale ; decreased skirt opening
dimensionless dissipation rates near impeller - normalized by impeller's diameter
 $d=7.66$ cm ; $b=1.94$ cm ; $2r/d=1.044$

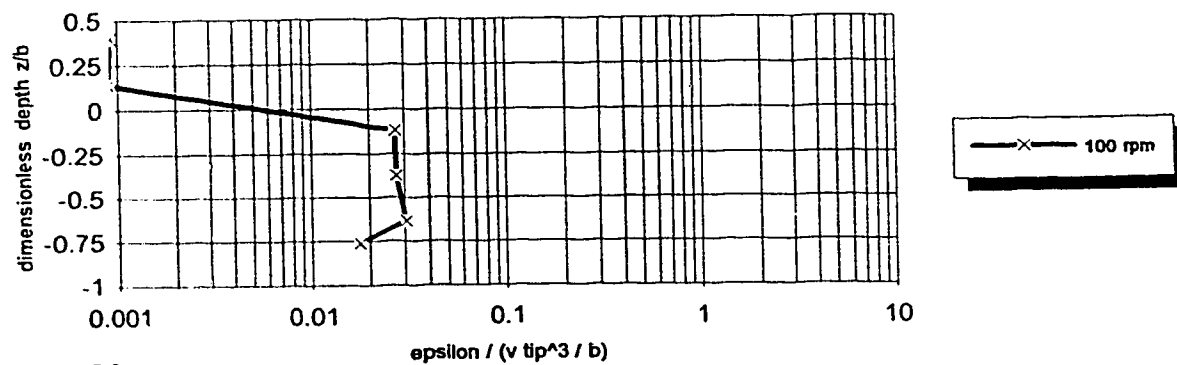


Figure 6-8c : trial A04 - ecodyne Impeller ; 1:55 scale ; decreased skirt opening
dimensionless dissipation rates near impeller - normalized by blade height
 $d=7.66$ cm ; $b=1.94$ cm ; $2r/d=1.044$

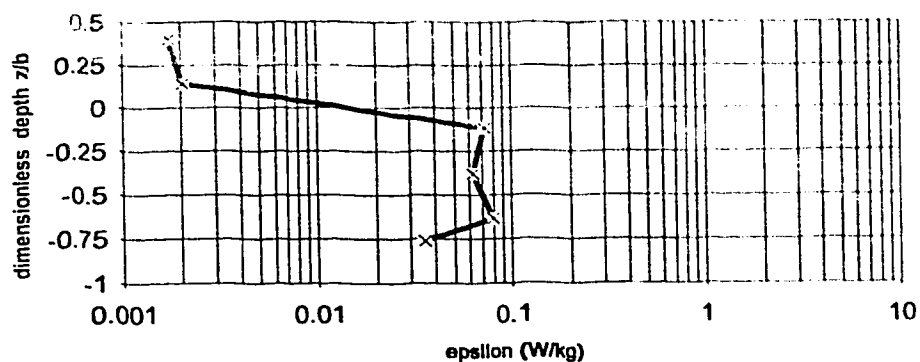


Figure 6-9a : trial A05 - ecodyne Impeller ; 1:55 scale ; draught-tube baffles
dissipation rates near Impeller
 $d=7.66$ cm ; $b=1.94$ cm ; $2r/d=1.044$

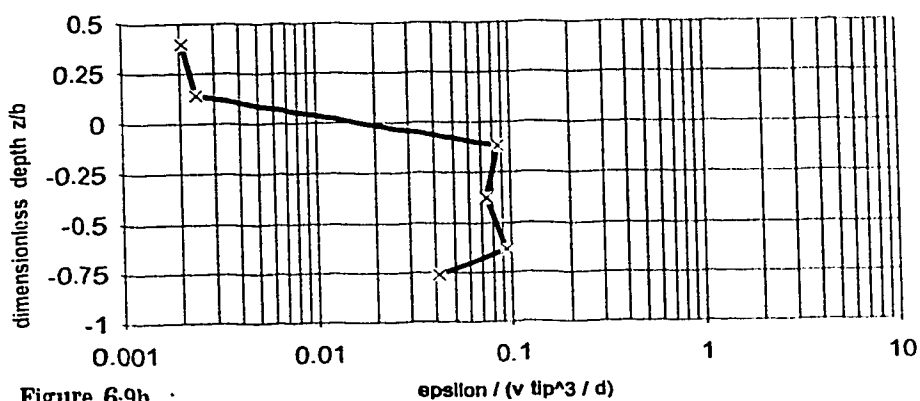


Figure 6-9b : trial A05 - ecodyne Impeller ; 1:55 scale ; draught-tube baffles
dimensionless dissipation rates near Impeller - normalized by Impeller's diameter
 $d=7.66$ cm ; $b=1.94$ cm ; $2r/d=1.044$

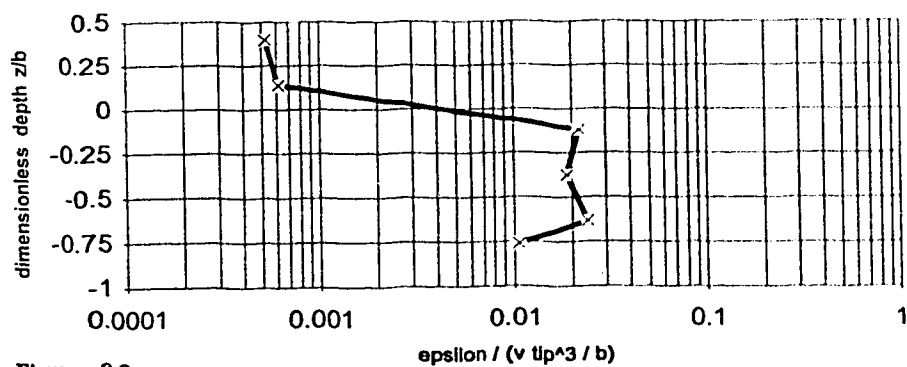


Figure 6-9c : trial A05 - ecodyne Impeller ; 1:55 scale ; draught-tube baffles
dimensionless dissipation rates near Impeller - normalized by blade height
 $d=7.66$ cm ; $b=1.94$ cm ; $2r/d=1.044$

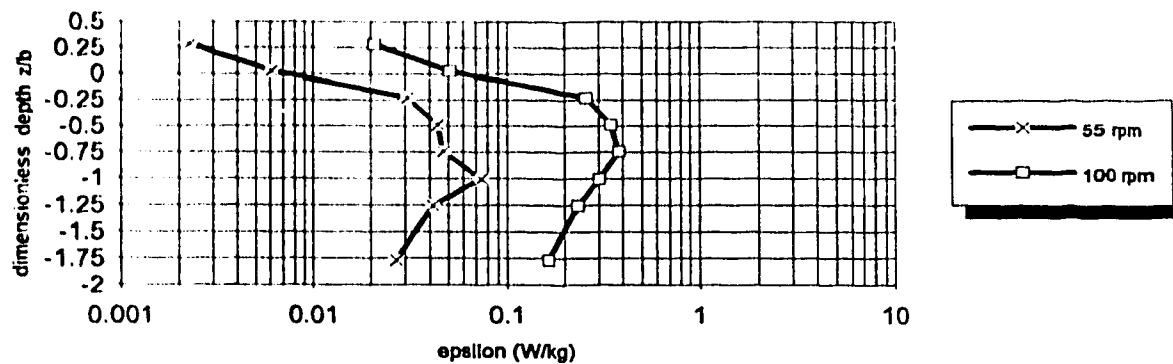


Figure 6-10a-1 : trial B01 - ecodyne impeller ; 1:41 scale
dissipation rates near impeller
 $d=10.37$ cm ; $b=2.63$ cm ; $2r/d=1.044$

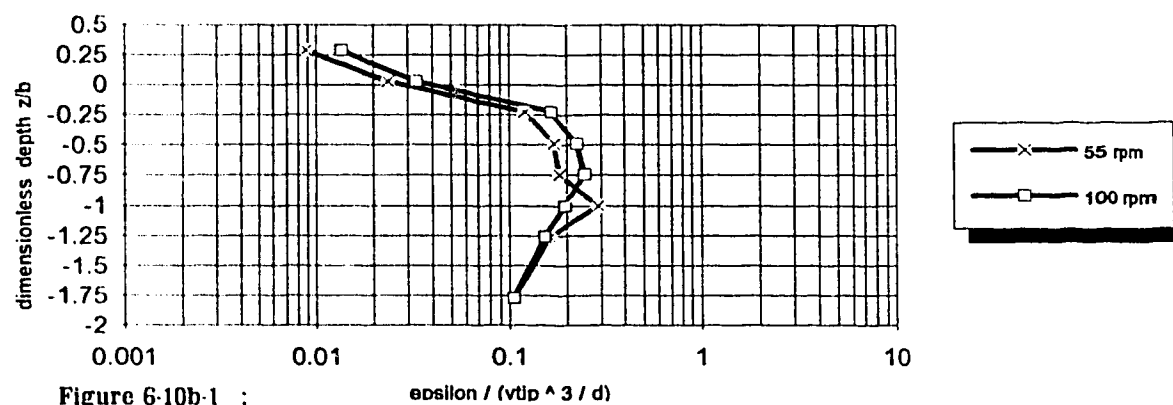


Figure 6-10b-1 : trial B01 - ecodyne impeller ; 1:41 scale
dimensionless dissipation rates near impeller - normalized by impeller's diameter
 $d=10.37$ cm ; $b=2.63$ cm ; $2r/d=1.044$

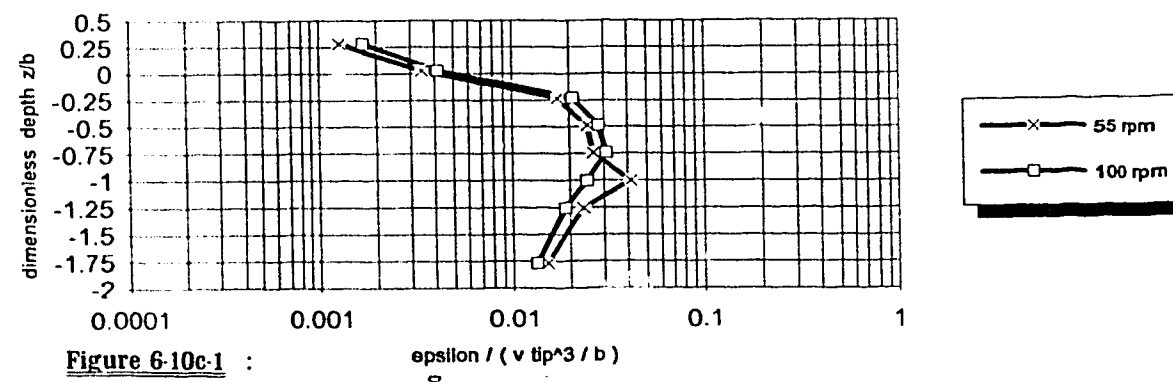


Figure 6-10c-1 : trial B01 - ecodyne impeller ; 1:41 scale
dimensionless dissipation rates near impeller - normalized by length scale
 $d=10.37$ cm ; $b=2.63$ cm ; $2r/d=1.044$

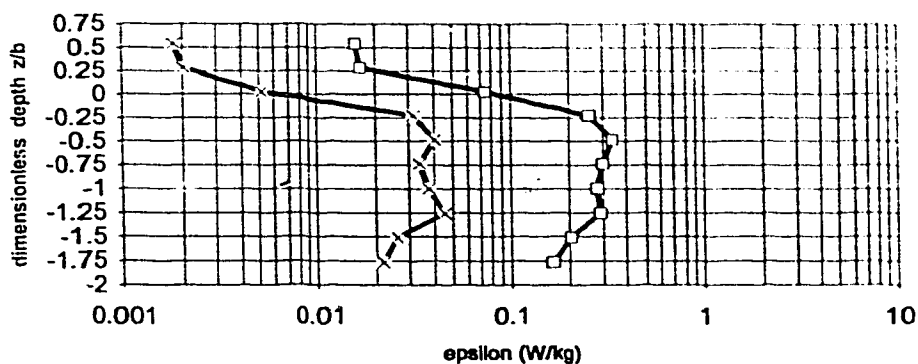


Figure 6-10a-2 :

trial B01 - ecodyne Impeller ; 1:41 scale
dissipation rates near Impeller
 $d=10.37$ cm ; $b=2.63$ cm ; $2r/d=1.175$

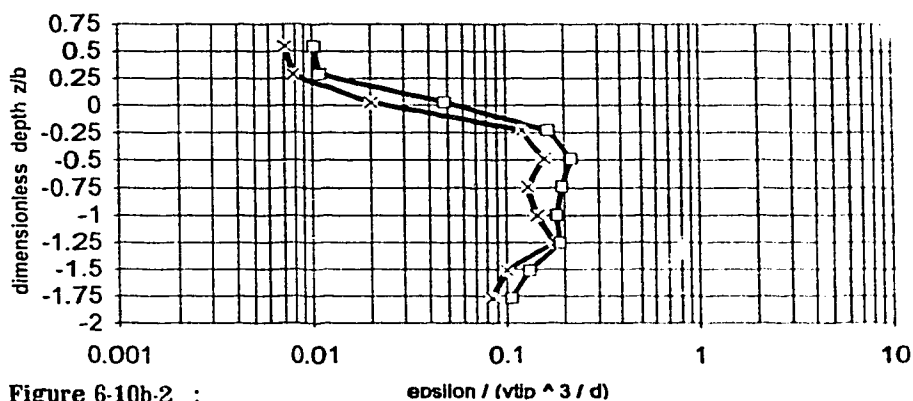


Figure 6-10b-2 :

trial B01 - ecodyne Impeller ; 1:41 scale
dimensionless dissipation rates near Impeller - normalized by Impeller's diameter
 $d=10.37$ cm ; $b=2.63$ cm ; $2r/d=1.175$

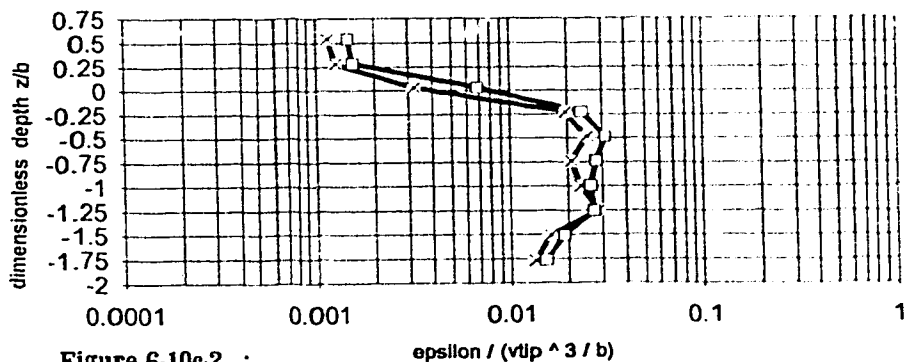
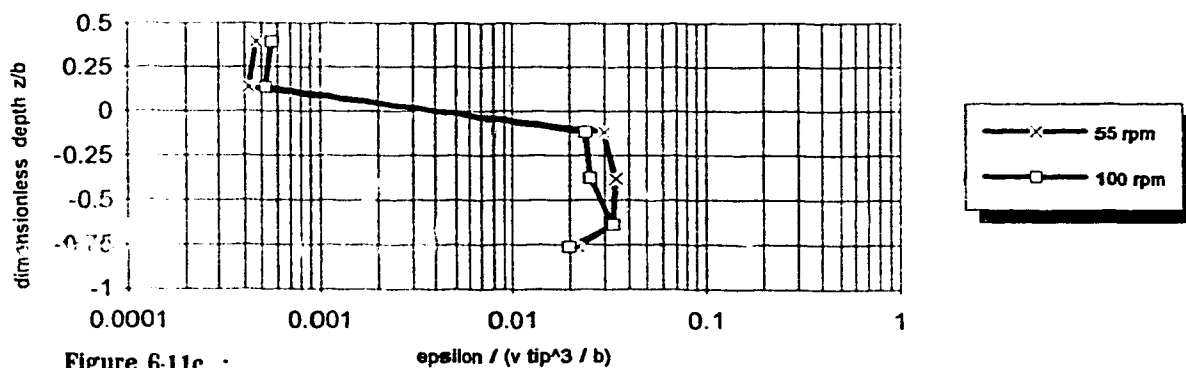
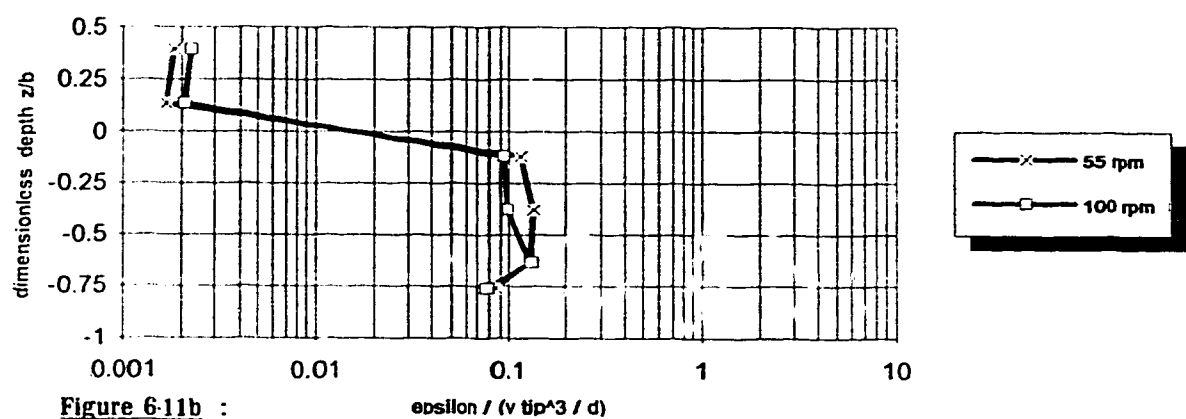
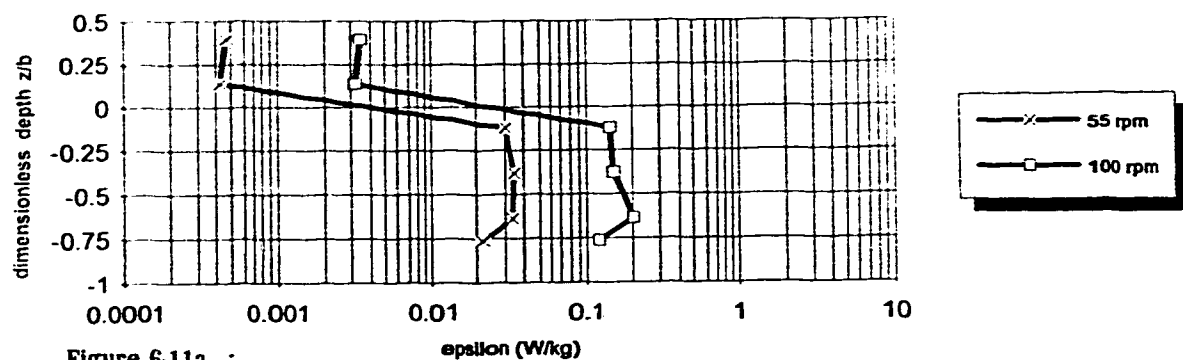


Figure 6-10c-2 :

trial B01 - ecodyne Impeller ; 1:41 scale
dimensionless dissipation rates near Impeller - normalized by length scale
 $d=10.37$ cm ; $b=2.63$ cm ; $2r/d=1.175$



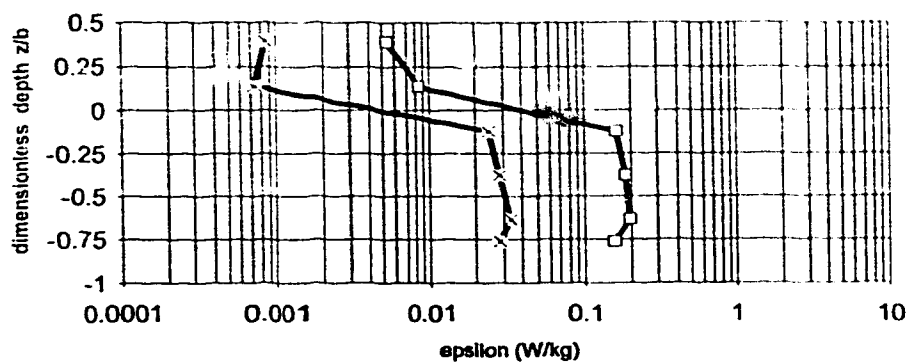


Figure 6-12a :

trial B03 - ecodyne Impeller ; 1:41 scale
dissipation rates near Impeller
 $d=10.37$ cm ; $b=2.63$ cm ; $2r/d=1.044$

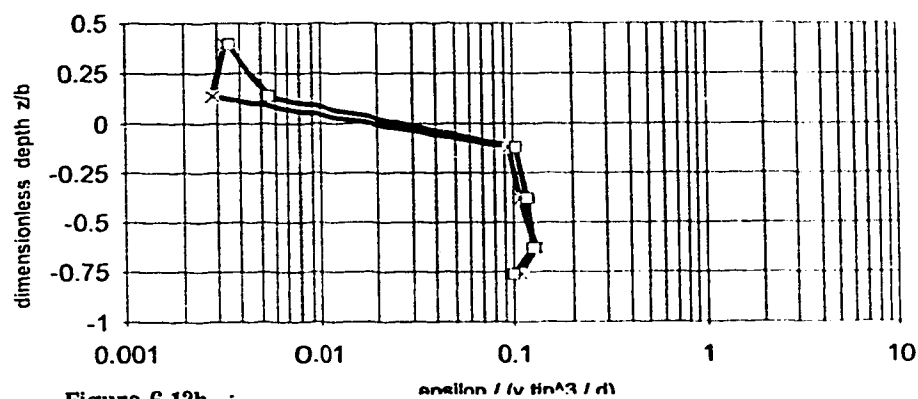


Figure 6-12b :

trial B03 - ecodyne Impeller ; 1:41 scale
dimensionless dissipation rates near Impeller - normalized by Impeller's diameter
 $d=10.37$ cm ; $b=2.63$ cm ; $2r/d=1.044$

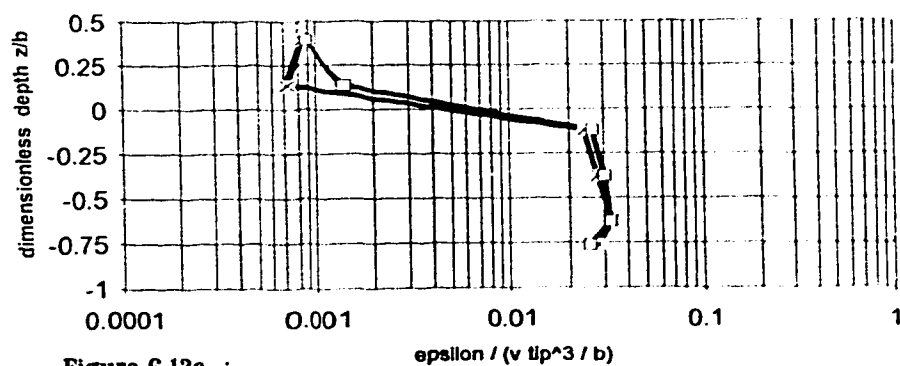


Figure 6-12c :

trial B03 - ecodyne Impeller ; 1:41 scale
dimensionless dissipation rates near Impeller - normalized by blade height
 $d=10.37$ cm ; $b=2.63$ cm ; $2r/d=1.044$

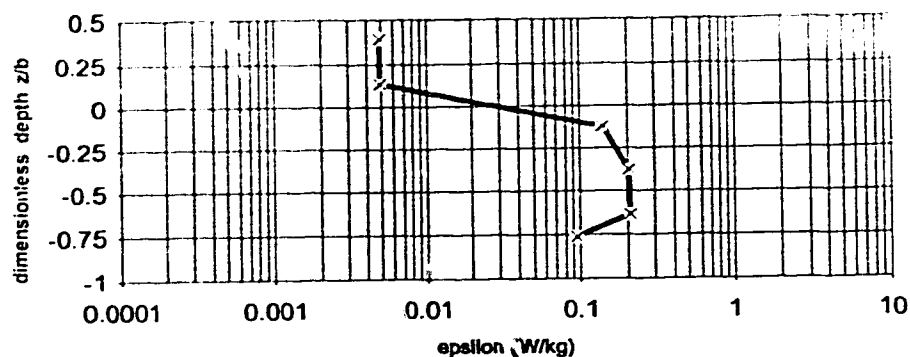


Figure 6-13a : trial B06 - ecodyne impeller ; 1:41 scale ; enlarged orifice
dissipation rates near impeller
 $d=10.37$ cm ; $b=2.63$ cm ; $2r/d=1.044$

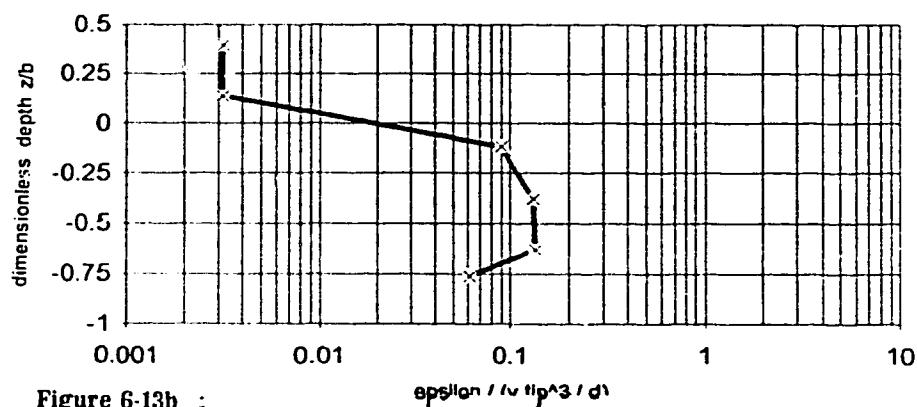


Figure 6-13b : trial B06 - ecodyne impeller ; 1:41 scale ; enlarged orifice
dimensionless dissipation rates near impeller - normalized by impeller's diameter
 $d=10.37$ cm ; $b=2.63$ cm ; $2r/d=1.044$

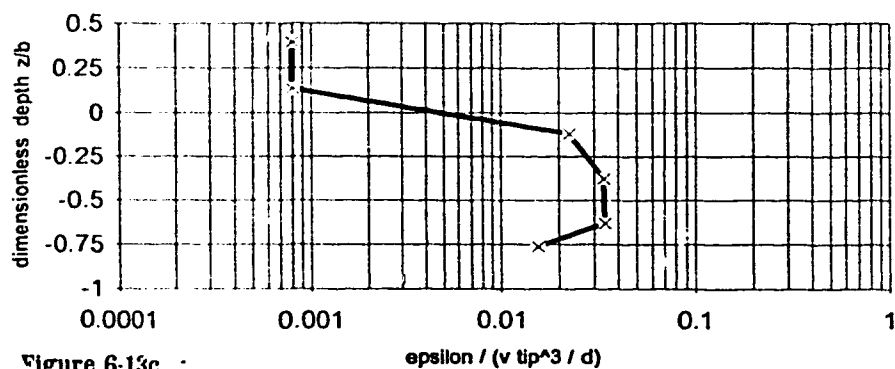


Figure 6-13c : trial B06 - ecodyne impeller ; 1:41 scale ; enlarged orifice
dimensionless dissipation rates near impeller - normalized by impeller's diameter
 $d=10.37$ cm ; $b=2.63$ cm ; $2r/d=1.044$

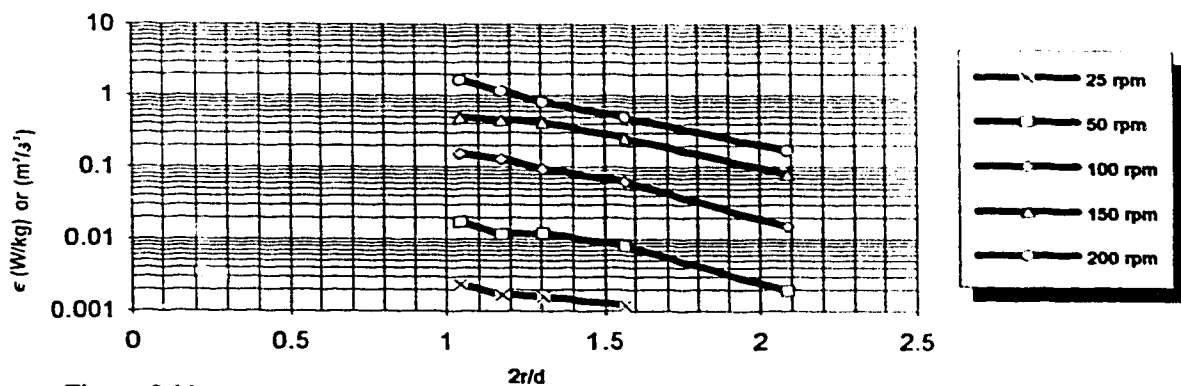


Figure 6-14a :
trial A01 - ecodyne impeller ; 1:55 scale
radial variation of maximum dissipation rate
 $d=7.66$ cm ; $b=1.94$ cm

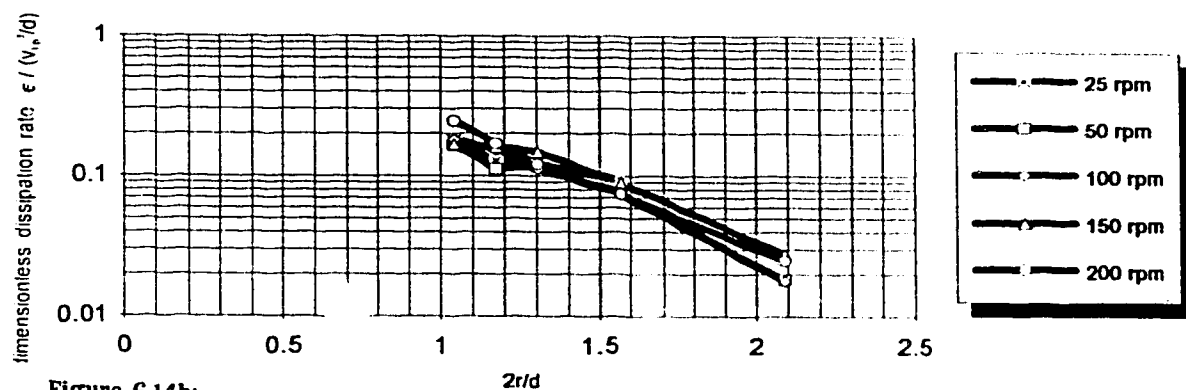


Figure 6-14b:
trial A01 - ecodyne impeller
radial variation of maximum dimensionless dissipation rate
normalized by impeller's diameter
 $d=7.66$ cm ; $b = 1.94$ cm

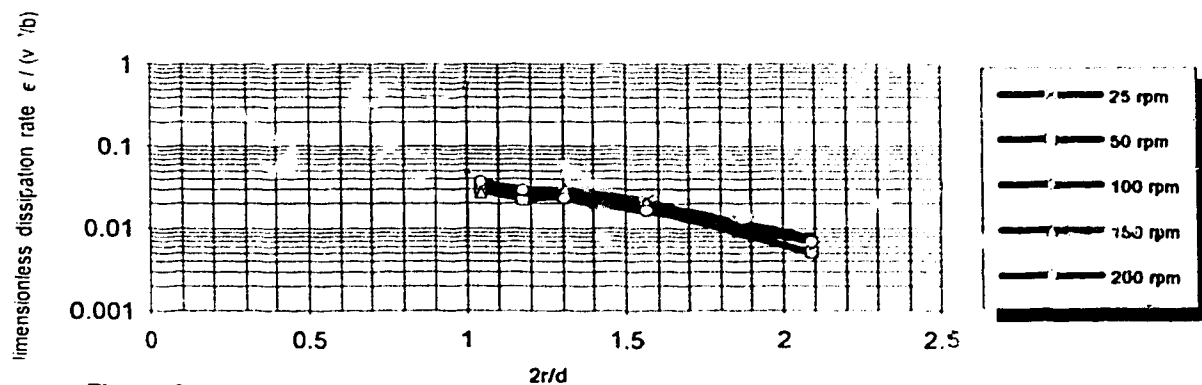
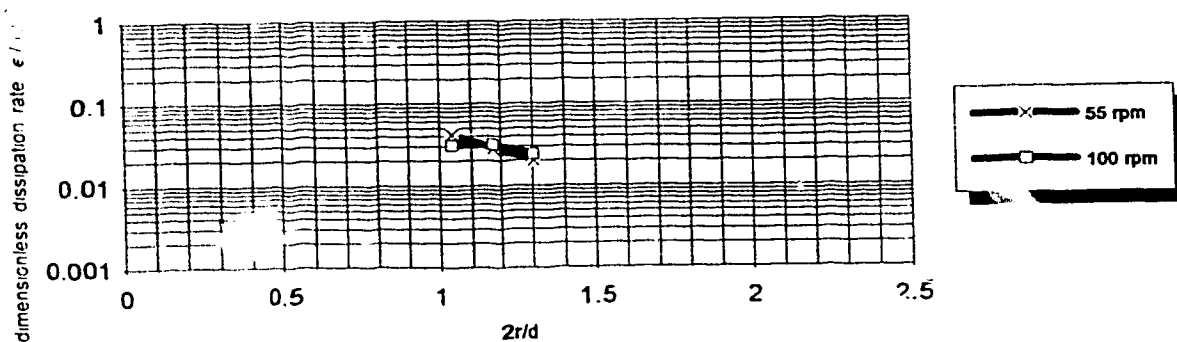
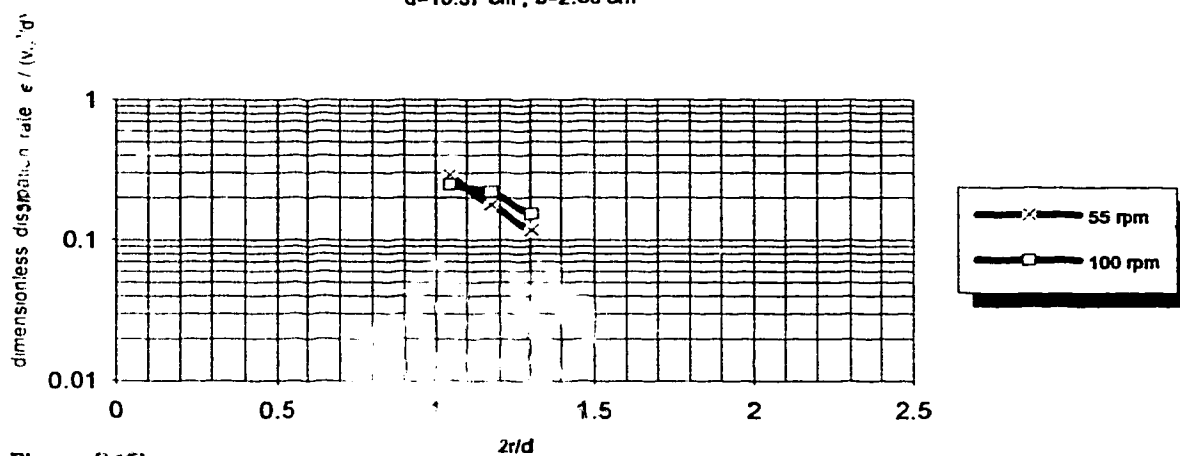
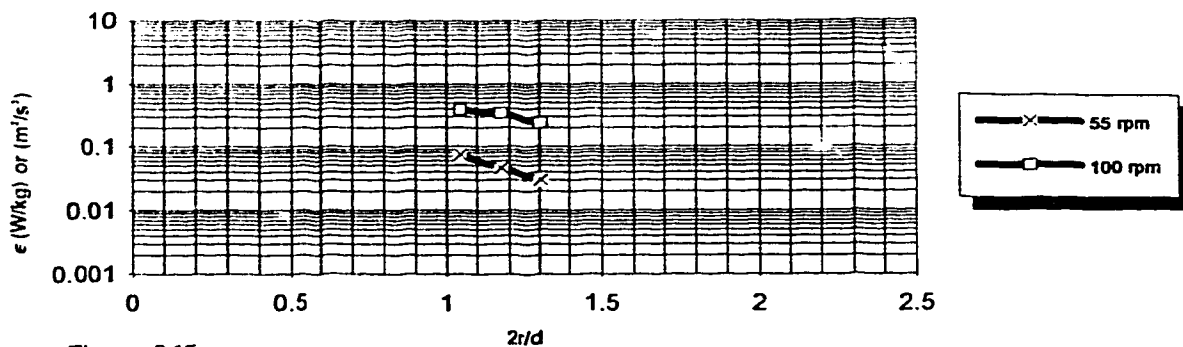
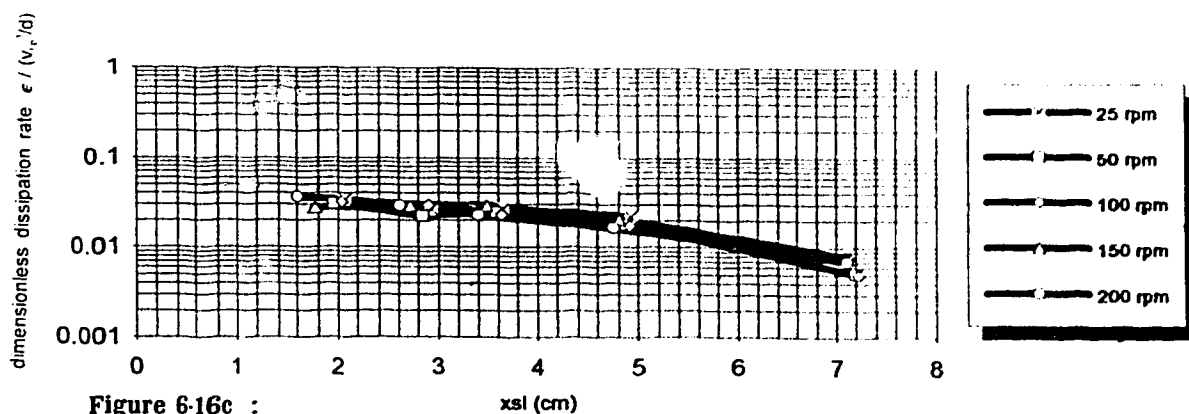
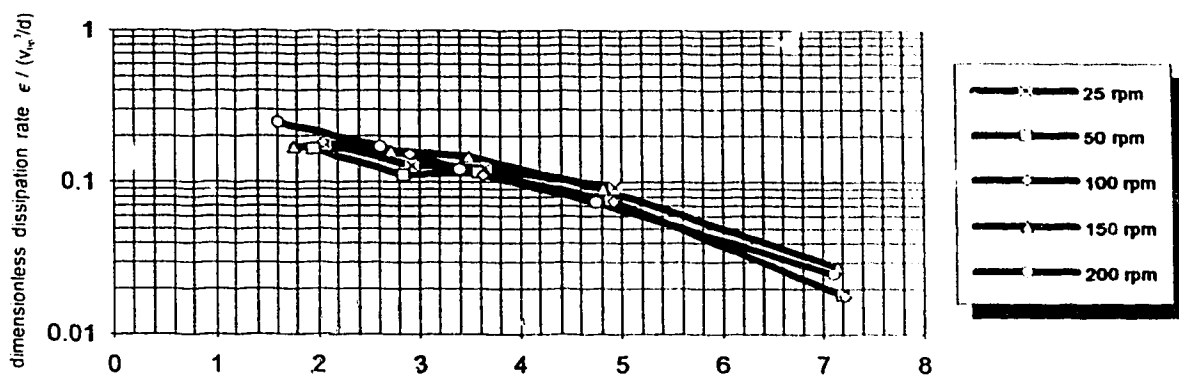
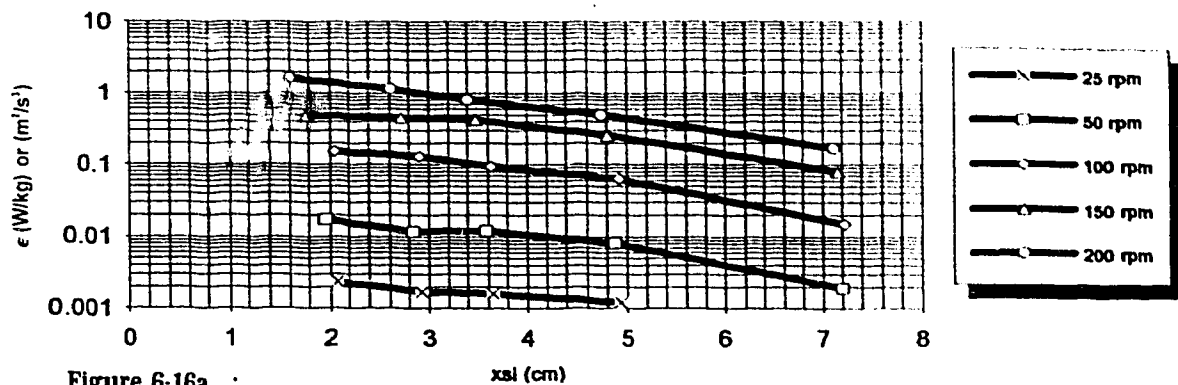
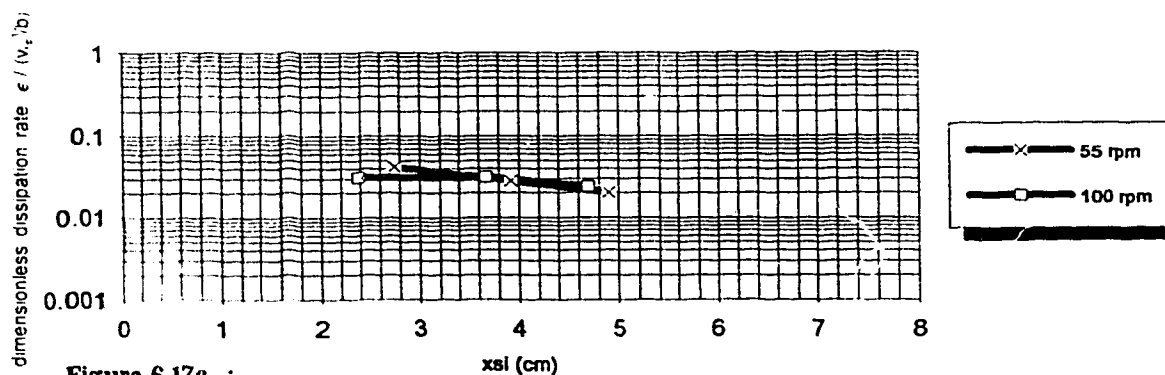
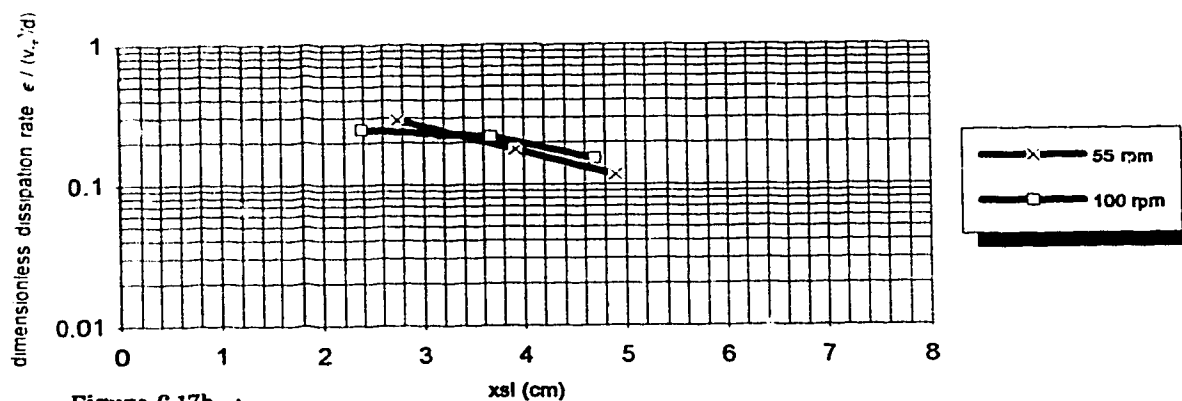
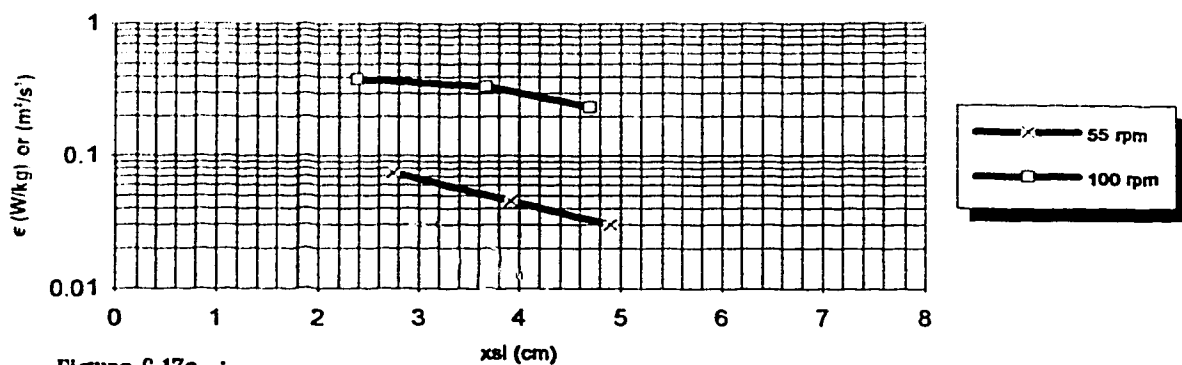


Figure 6-14c :
trial A01 - ecodyne impeller
radial variation of maximum dimensionless dissipation rate
normalized by length scale
 $d=7.66$ cm ; $b = 1.94$ cm







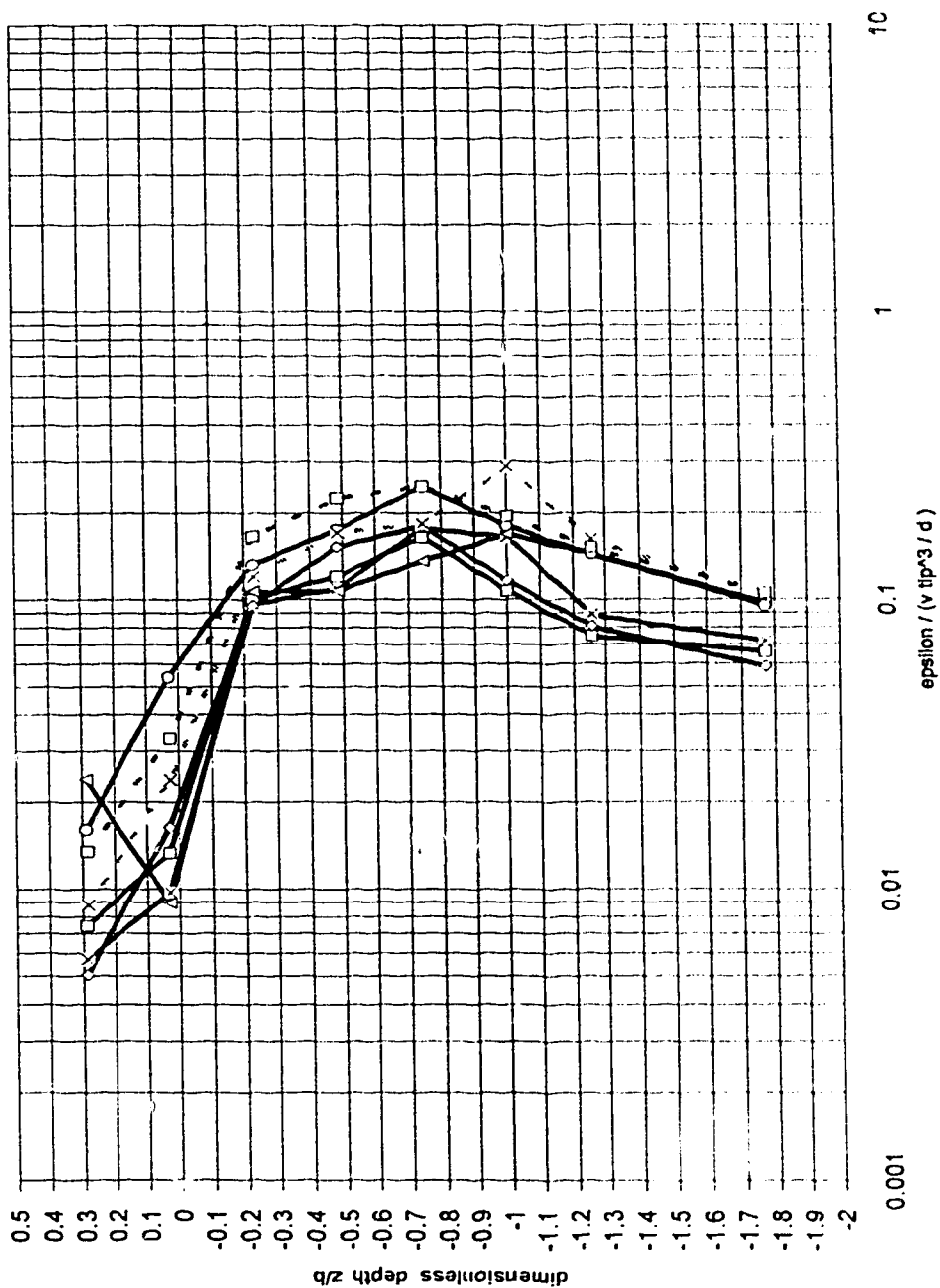


Figure 6-18-1n :
 configuration 01 - ecdyne impeller ; 1:55 scale & 1:41 scale
 dimensionless dissipation rates near impeller - normalized by impeller's diameter
 $d = 7.66 \text{ cm}$ & 10.37 cm ; $b = 1.94 \text{ cm}$ & 2.63 cm ; $2r/d = 1.044$

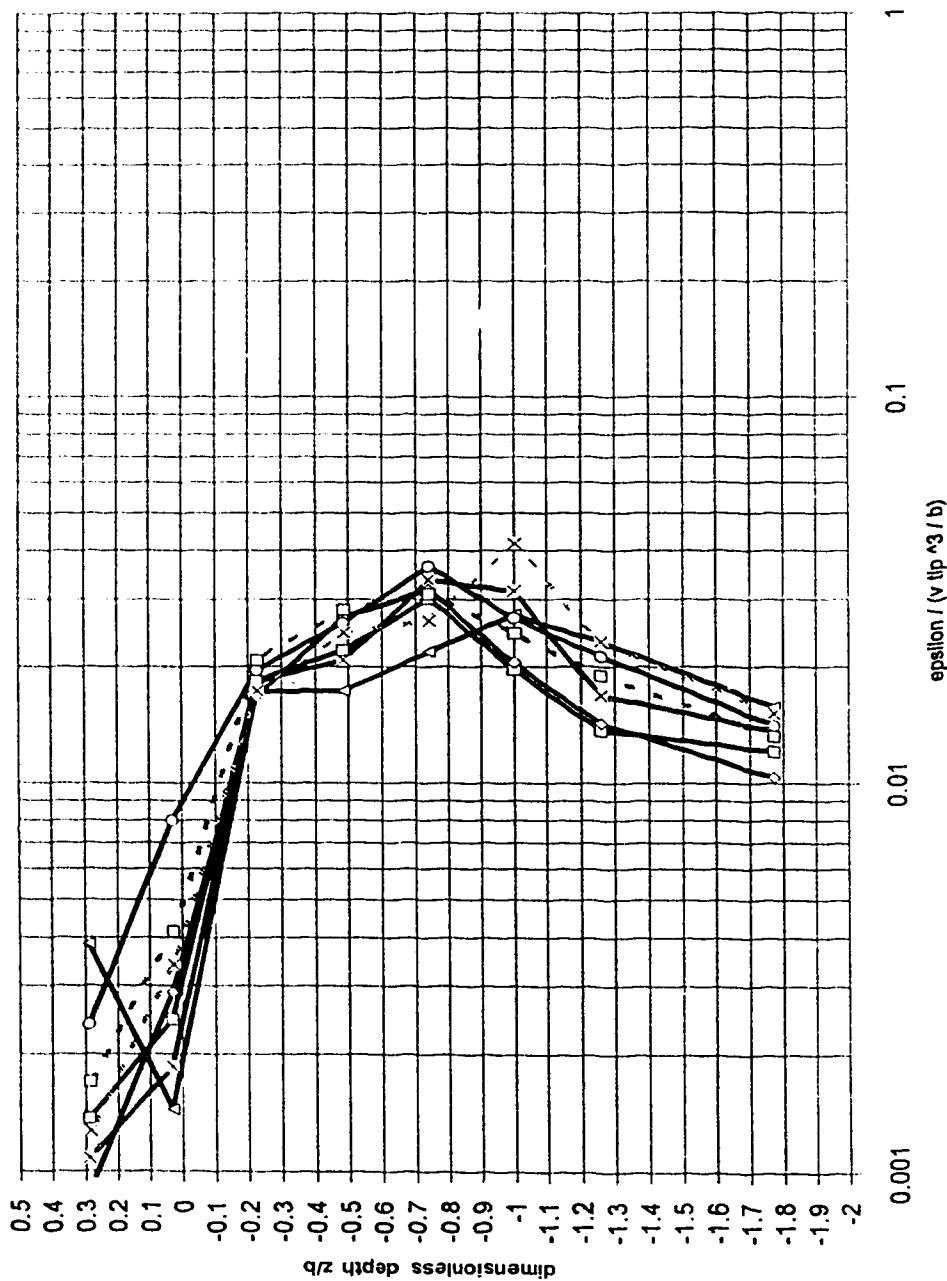


Figure 6-18-2n : dimensionless dissipation rates near impeller - normalized by length scale (blade height)
 configuration 01 - ecdyne impeller ; 1:55 scale & 1:41 scale
 $d=7.66$ cm & 10.37 cm ; $b=1.94$ cm & 2.63 cm ; $2r/d=1.044$

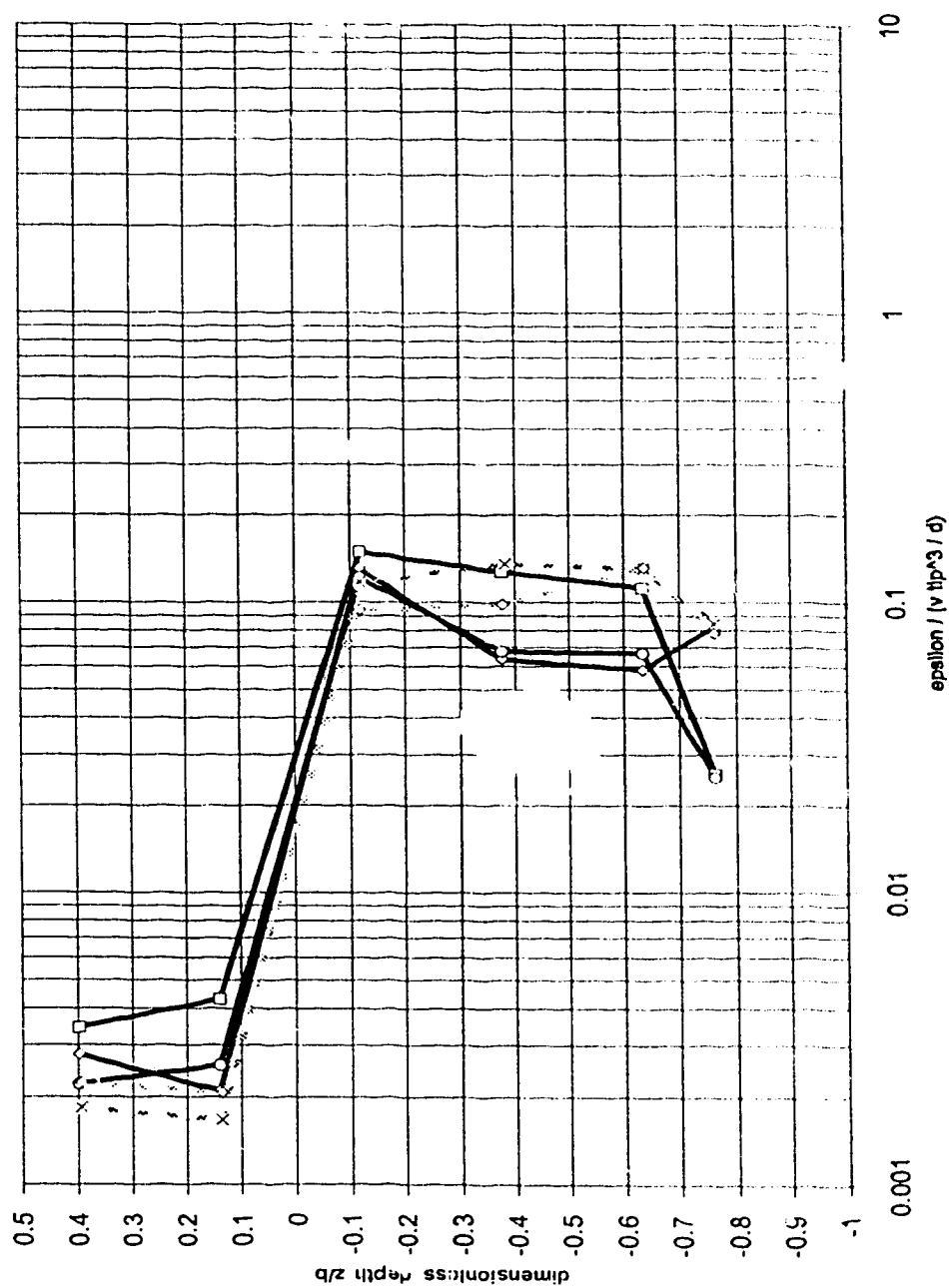


Figure 6.18.3n :
 configuration 02 - ecodyne impeller : 1:55 scale & 1:41 scale
 dimensionless dissipation rates near impeller - normalized by impeller's diameter
 $d=7.66$ cm & 10.37 cm ; $b=1.94$ cm & 2.63 cm ; $2r/d=1.044$

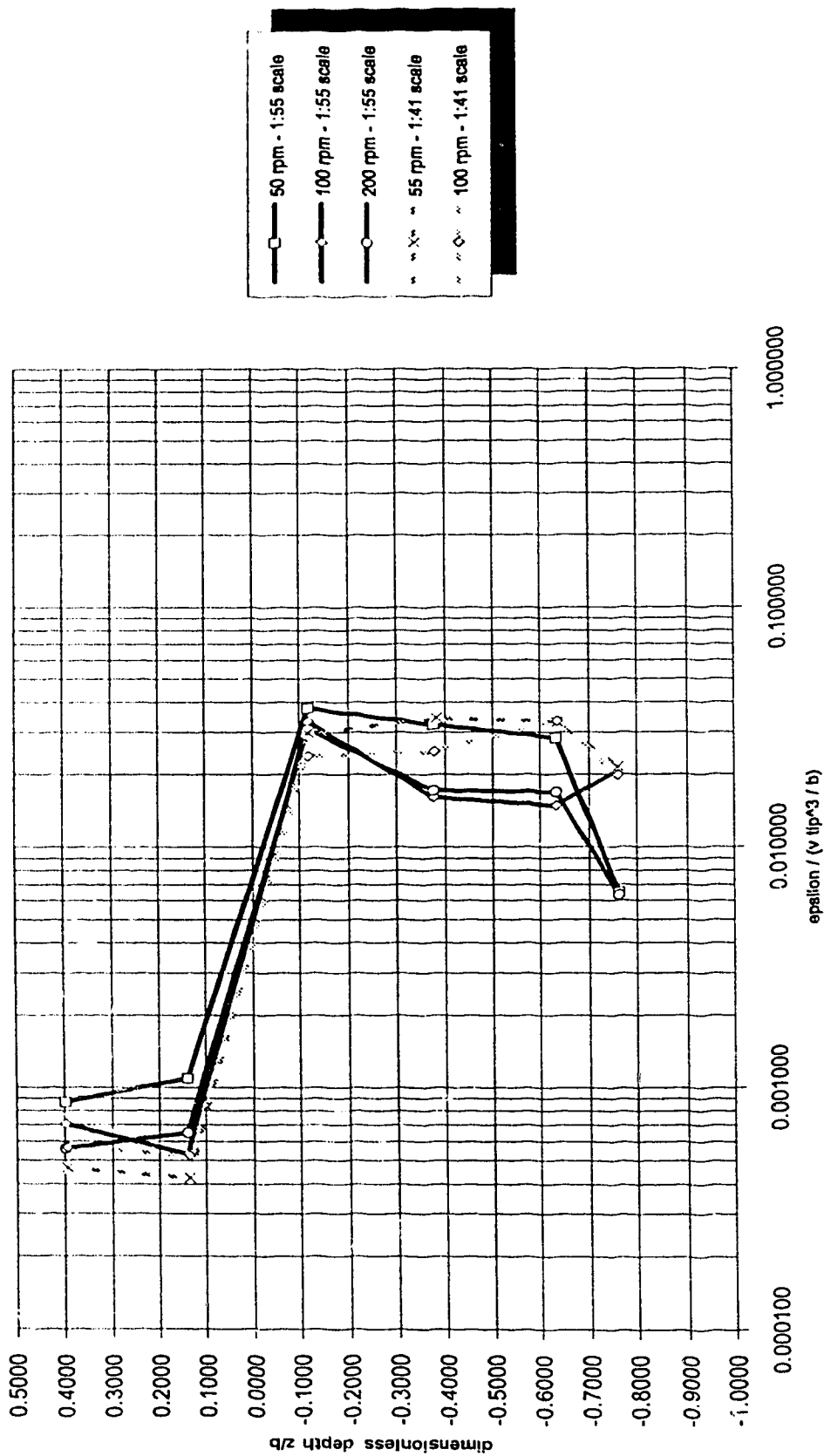
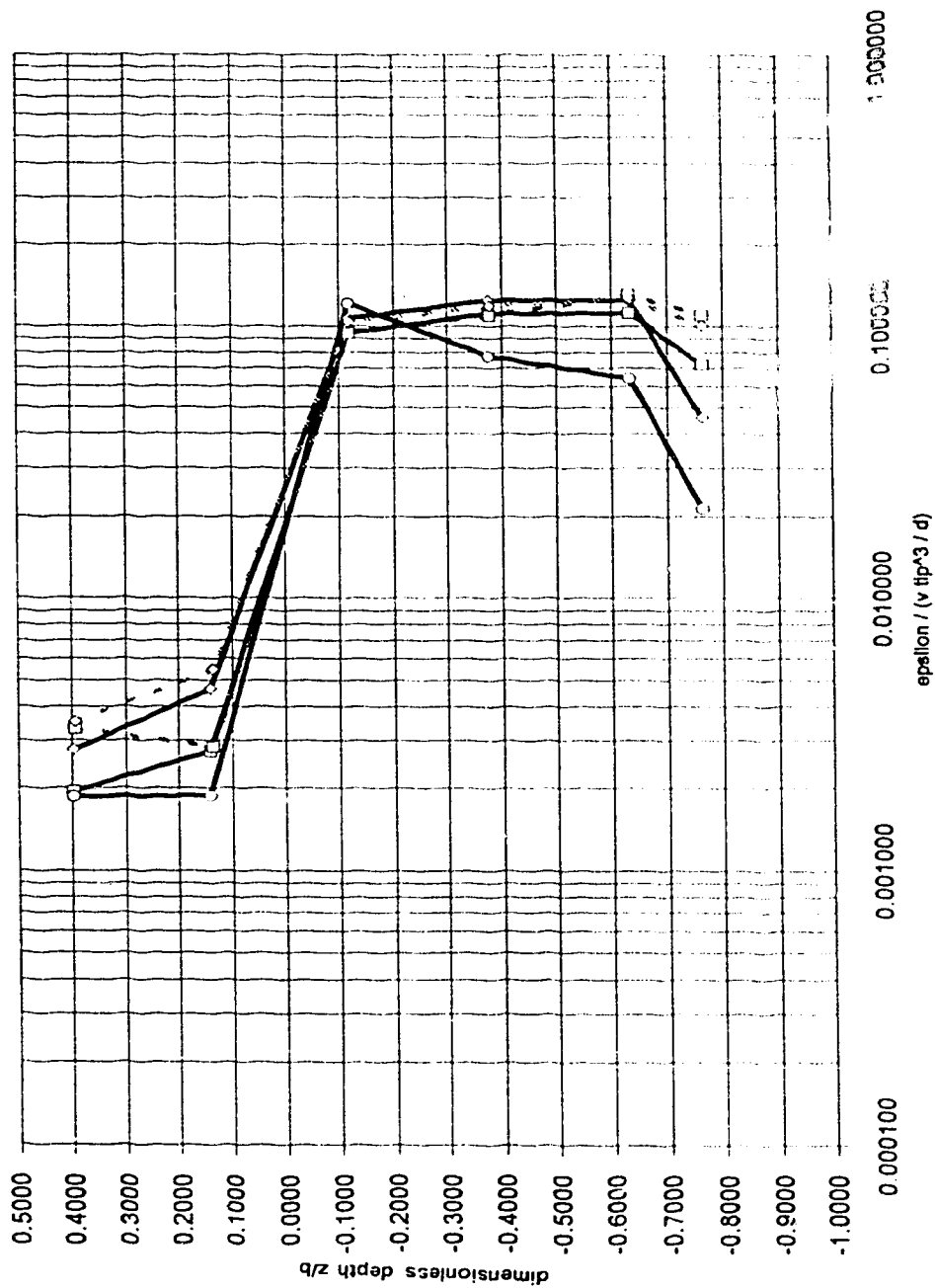
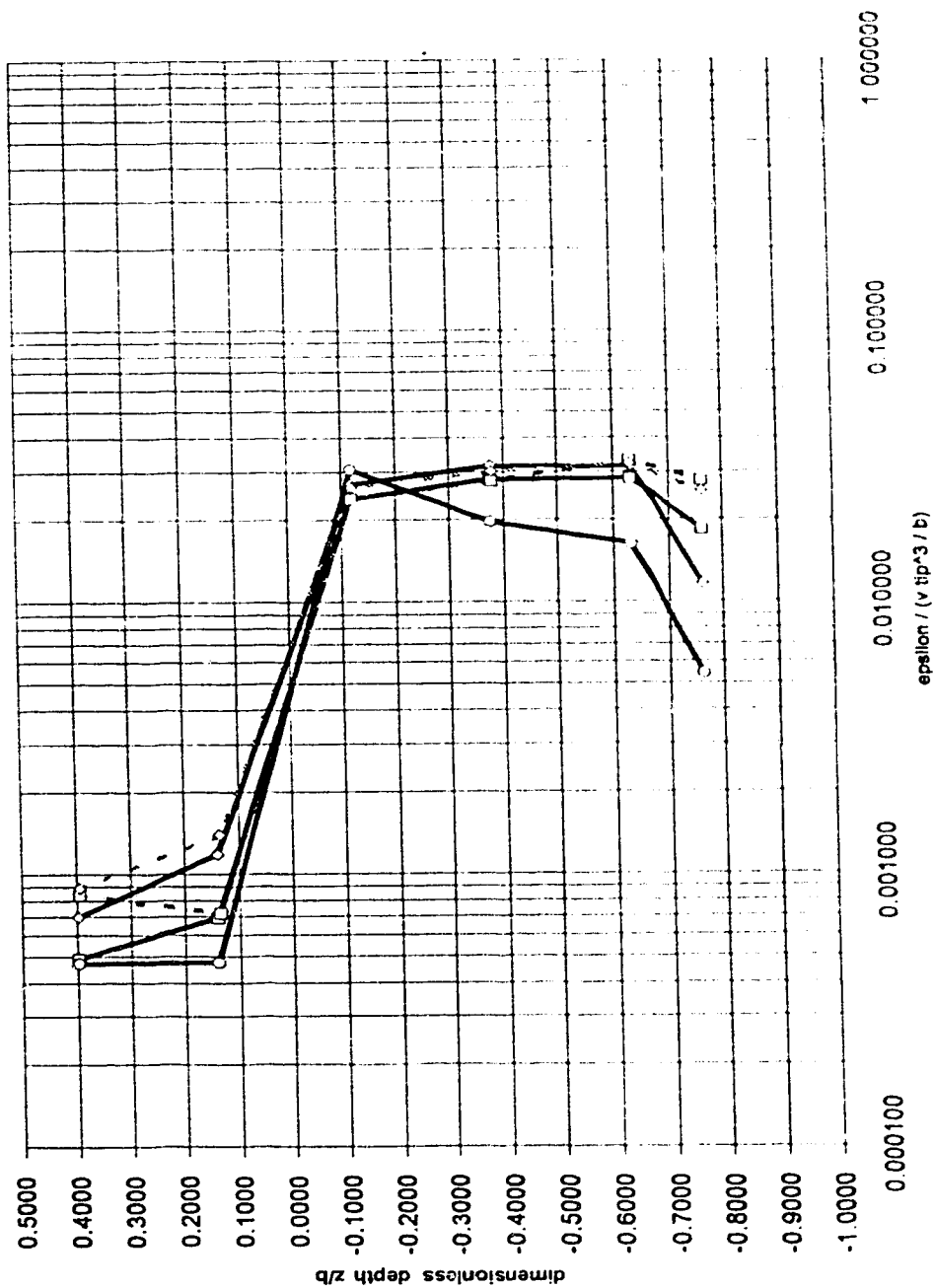


Figure 6-18-4n :
 configuration: 02 - ecdyme impeller ; 1:55 scale & 1:41 scale
 dimensionless dissipation rates near impeller - normalized by blade height
 $d=7.66$ cm & 10.37 cm ; $b=1.84$ cm & 2.63 cm ; $2r/d=1.044$



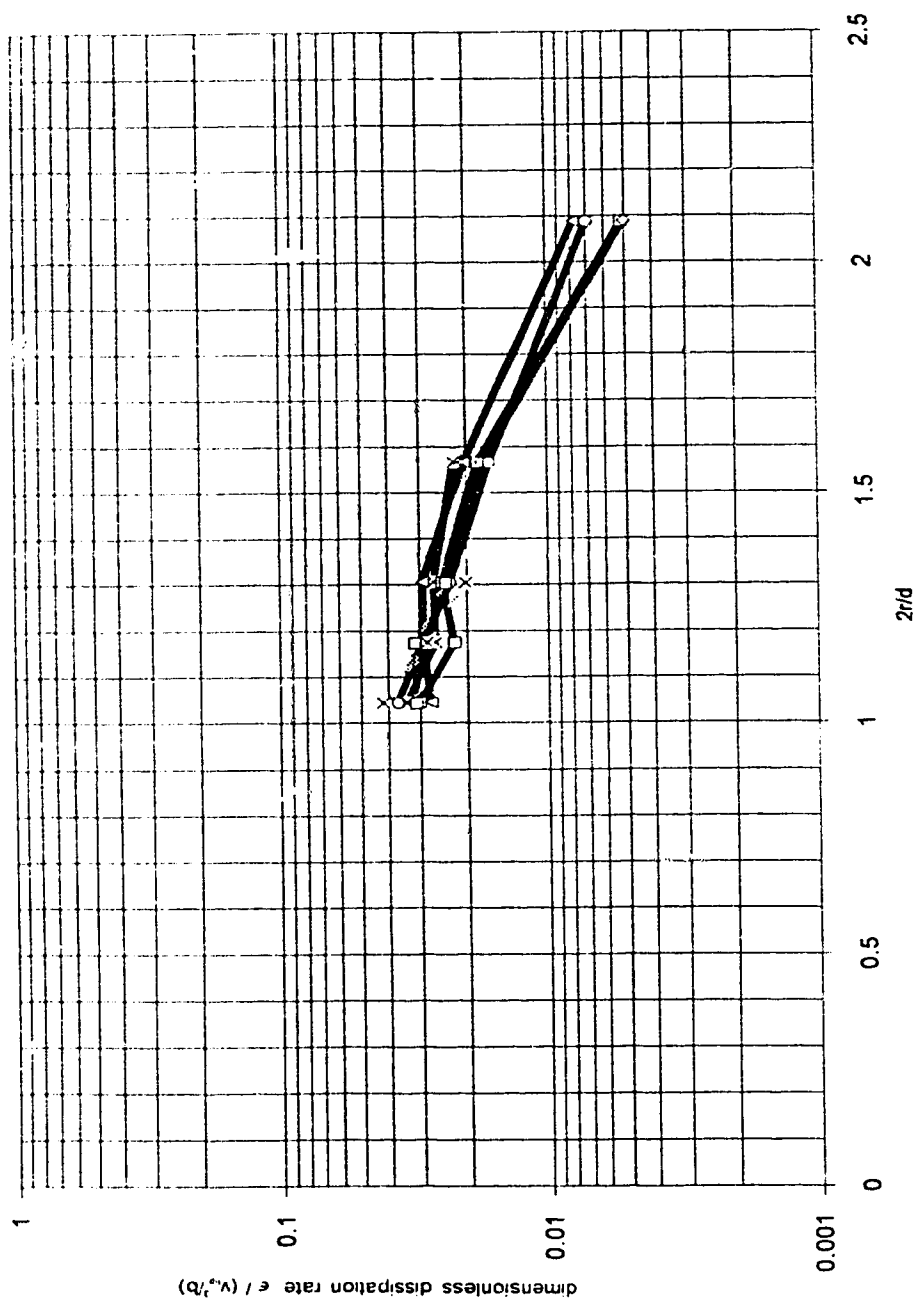
configuration 03 - ecdyne Impeller ; 1:55 scale & 1:41 scale
dissipation rates near impeller - normalized with diameter
 $d=7.66 \text{ cm}$ & 10.37 cm ; $b=1.94 \text{ cm}$ & 2.63 cm ; $2r/d=1.044$

Figure 6.18.5h :



configuration 03 - ecodeyne impeller : 1:55 scale & 1:41 scale
dissipation rates near impeller - normalized with blade height
d=7.66 cm & 10.37 cm ; b=1.94 cm & 2.63 cm ; 2r/d=1.044

Figure 6-18-6n :



configuration 01 - eodyne impeller ; 1:41 scale & 1:55 scale
radial variation of maximum dimensionless dissipation rate
normalized by length scale (blade height)
d=7.66 cm & 10.37 cm ; b=1.94 cm & 2.63 cm

Figure 6-18-7n :

7.0 Effects of Configurational Changes (no tangential inflow)

7.1 Introduction

During the performance of this project, it became apparent that there are two aspects to the information that was being obtained. The first was seen to encompass matters dealing with a purely scientific principles of impeller analysis, specifically with the calculation of turbulence-based and dynamical quantities such as N , and purely kinematic quantities such as N_q . Such things are indeed useful, as the ability to quantify the nature of the flow thoroughly allows one to assess the effects of imposing certain configurational changes upon the impeller-draught tube system in a non-arbitrary, technically sound manner. In doing so, the second aspect of this project became apparent, that being process improvement through structural modification.

In this manner, a number of elements were systematically varied during the testing of the models in order to illustrate, by comparison, the resultant effects of imposed changes in geometry upon the system's behaviour. For instance, it is seen that by comparing the resultant hydraulic state present in configuration 03 to that in configurations 01 and 02 can illustrate the effects of imposed confinement upon the free impeller and the effects of constricting the recirculation flow area by means of the skirt. Additionally, as configuration 04 presents a situation closer to that of NHC's 1:10 scale model as it was originally constructed^{*}, further assessment of the effects of skirt opening is possible. Configuration 05 is actually closest to the existing clarifiers since it includes draught tube baffles, so that the effects of draught tube baffles on the hydraulic conditions near the impeller may be assessed. Configuration 06 represents the effect of increasing the orifice opening over that which currently exists in the clarifier, specifically from a 2.210 m full-scale diameter to a 3.265 m full-scale diameter. Finally, a special series of trial was run, where both the existing orifice (configuration 03) and the enlarged orifice (configuration 06) were tested together, but with variable depth of water in the tank.

Ideally, a full factorial design incorporating every possible combination of these factors would have been desirable, but as this would have required an extensive amount of testing, it was chosen instead to vary specific configurational parameters selectively, thereby furnishing a general illustration of the relevant effects.

7.2 Effects upon Flow-Through

7.2.1 Draught Tube and Skirt

Starting with the free impeller, the flow numbers there provide a first basis of comparison for assessment of the effects of structural alterations upon pumping capacity. As explained above, though the calculated flow numbers for trial A and trial B counterparts (*i.e.* the same structural configuration surrounding the impeller) cannot be compared directly between scales since, it is speculated, neither scale of model was run at sufficiently high values of R , to produce an approximately constant value of N_q , the N_q data still yield sufficient information to enable a useful analysis. Consider now the following table, Table 7-1, formed by recombining certain elements of Tables 5-1 through 5-7. It is important to note that the flow numbers determined from the impeller's efflux are often greater than those determined at the orifice. This possibly illustrates entrainment of the ambient fluid by the swirling radial jet over the very small distance between the data collection point and the edge of the impeller. Entrainment is not surprising given that there are significant negative pressures developed within the impeller. Figure 4-4a illustrates this nicely, where radial velocity u is found to be < 0 along the vertical face of the impeller at high

^{*} In accordance with recommendations from the City of Edmonton, NHC assumed a full-scale equivalent skirt opening of approximately 30 cm for their testing. For this project, the skirt-height was readjusted to a full-scale equivalent of 45.7 cm, a number which more accurately reflects the conditions in the clarifier that were found during a personal inspection in September, 1993.

angular velocities. Despite the suspected influence of entrainment upon the local value of N_q , it is felt that these flow numbers are nonetheless illustrative of a general and significant trend.

Table 7-1
flow numbers - illustration of the effect of the skirt and draught tube on flow-through

configuration	trial	N (rpm)	R_i	influx-based N_q	efflux-based N_q	average N_q
01	A01	50	4.96×10^1	0.622	0.817	0.720
02	A02	50	4.96×10^1	0.308	0.402	0.352
03	A03	50	4.96×10^1	0.364	0.547	0.465
01	A01	100	9.93×10^1	0.635	0.609	0.622
02	A02	100	9.93×10^1	0.320	-	0.333
03	A03	100	9.93×10^1	0.383	0.540	0.452
04	A04	100	9.93×10^1	0.333	0.534	0.427
01	B01	55	1.00×10^1	0.565	0.603	0.572
02	B02	55	1.00×10^1	0.339	0.377	0.352
03	B03	55	1.00×10^1	0.333	0.553	0.383
01	B01	100	1.82×10^1	0.496	0.352	0.421
02	B02	100	1.82×10^1	0.358	0.459	0.371
03	B03	100	1.82×10^1	0.377	0.471	0.377

A number of conclusions may be drawn from this table:

1. **As the draught tube is added, circulation decreases**
This is clear in all cases., and such a supposition is strongly supportive of intuition in that the draught tube should severely restrict the available flow area. This is supported by the traditionally observed fact that an impeller's capacity to circulate the fluid is observed to decrease as the impeller is moved closer to a wall or any other solid boundary - *e.g.*, Bowen (1986) and Van de Vusse (1955) illustrate this effect quantitatively.
2. **Installing the skirt to an equivalent full-scale opening of 45.7 cm actually increases the flow-through as represented by the flow number, N_q .**
Despite the fact that adding the skirt restricts the available flow area, it appears that the skirt somehow improves the hydraulic performance of the impeller. It seems reasonable to assume that the skirt improves the entrance conditions in somewhat a similar manner to the influence of a culvert's entrance conditions on the resultant discharge. This could allow a more energetic and

defined influx which could then provide greater potential for a stronger, faster turbulent jet from the impeller. It is interesting to recognize the increase in flow-through in light of the fact that the skirt was initially installed to improve the circulation of solids:

The presence of the skirt forced the recycling water deeper into the clarifier and through a narrow opening at the top of the sludge pit. The upwardly flowing water was therefore able to lift larger quantities of heavier and better formed floc into the draft tube directly from the sludge pit... (Kellendonk, ca. 1989 ?)

3. Further decreasing the skirt to an equivalent full-scale opening of 30.5 cm (1 foot) provides a marginal impediment to flow-through.

Based upon analysis of flow analysis only, it is clear that N_q appears to have decreased in trial A04 in comparison to trial A03. However, because trial A04 comprised testing at only one angular velocity, it was felt that there was insufficient cause to conclude on the basis of flow numbers alone that decreasing the skirt opening would indeed decrease flow-through. Alternatively, the radial velocity profiles for trial A04 were examined with respect to those of configuration 03 (three different model scales) - the relevant comparative plot is presented in Figure 7-1a. What this comparison shows is that the radial velocity from the impeller is not distinguishable from the other local radial velocities, thereby indicating that lowering the skirt by roughly $\frac{1}{3}$ has at best only a marginal effect on flow through. Of course, there must be a point where decreasing the skirt opening eventually does affect the recirculated discharge adversely, but what this height is remains unknown. There is some further evidence that N_q does in fact decrease as the skirt is lowered, but this deserves to be discussed later in this report, where the effects of tangential inflow are assessed with respect to the NHC model.

7.2.2 Draught Tube Baffles

In addition to the variation in flow caused by the draught tube and skirt, the effect of baffles on flow-through and recirculation was also investigated. Starting with the draught tube from trial A03, four geometrically scaled baffles were installed at the appropriate locations (based again upon measurements made during inspection of the clarifiers in September, 1993) thereby defining a new configuration, configuration 05. Trial A05 consisted of a run at a single impeller speed, $N=100$ rpm, so that immediate comparison was possible between it and the 100 rpm run of trial A03 based upon flow numbers. Comparison via a table, Table 7-2, is again most effective:

Table 7-2
flow numbers - illustration of the effect of draught tube baffles on flow-through

configuration	trial	N (rpm)	R_i	influx-based N_q	efflux-based N_q	average N_q
03	A03	100	9.93×10^1	0.383	0.540	0.452
05	A05	100	9.93×10^1	0.333	0.534	0.427

From this table, it appears that flow-through is generally lower with the baffles in place. These flow numbers are presented in a slightly different manner in Figure 7-1b, a plot of the resultant radial velocity distributions - distributions which, when integrated, yield the radial discharge. This figure illustrates a similar decrease in radial velocities with the installation of baffles. From these two sources, a number of conclusions with respect to the effect of baffles on flow-through may be drawn.

4. The presence of baffles in the draught tube decreases the pumping performance of the impeller.

Perhaps it is best to consider the baffles to be analogous to an increase in surface roughness. As the impeller may be thought of as an energy source, any energy received by the flow from the impeller defines the flow's subsequent motion. In general terms, in order for the effluent swirling radial jet to rise to an ultimate height above the draught tube, it must have enough kinetic energy from the impeller both in order to overcome the force of gravity and to absorb frictional losses to the draught tube and form-drag losses to the baffles. Since the baffles increase the form-drag losses, the flow cannot circulate through the draught tube as effectively, and consequently the more slowly moving bulk of fluid acts as an impediment to further flows being pumped into the draught tube from below. Conversely, in order for the same flow-through to occur, more energy (*i.e.* a faster impeller rotation) must be added. This effect has been observed in the literature: Bowen (1986) - Figure 9 illustrates this effect.

7.2.3 Size of Orifice

Earlier, though it was shown that the draught tube seemed to restrict flow-through severely, the skirt's effect was apparently ameliorative with respect to flow-through, and it was only a minor impediment when placed at a lower height. Thus, aside from a consideration of flow-through discharge alone, the interaction of the draught tube and skirt implies further the relevance of the action of a *control point*. That is, the fact that observed flow-through did not decrease significantly in trial A04 relative to trial A03 nearly as much as it did in trial A02 relative to trial A01 was thought to imply that the draught tube (or more specifically the orifice in the floor of the draught tube) acted as more of a controlling element upon the flow than did the skirt. To test this theory, an enlarged orifice, approximately $\frac{1}{3}$ larger than the existing orifice, was inserted into the 1:41 scale model, and the flow-through was determined at 100 rpm - this trial was called trial B06. As before, the resultant flow numbers were compared to those from a comparable case without the enlarged orifice, that being trial B03, and the resultant radial velocity profiles were compared to those for configuration 03 (which encompassed nine different

trials at three scales). The resultant N_q 's are presented in the following table, Table 7-3, and the corresponding radial velocity profiles are presented in Figure 7-1c.

Table 7-3
flow numbers - illustration of the effect of enlarged orifice on flow-through

configuration	trial	N (rpm)	R_i	influx-based N_q
03	B03	100	1.82×10^3	0.383
06	B06	100	1.82×10^3	0.415
01	B01	100	1.82×10^3	0.496

Clearly, these flow numbers seem to illustrate a definite trend that flow-through decreases as the opening in the floor of the draught tube is decreased. Examination of the resultant plots of radial velocity profiles in Figure 7-1c further supports this trend since the velocity profile for trial B06 attains noticeably higher values of radial velocity, u_r , than do the other two profiles on that plot. Furthermore, specific results of trial B-ANN may be consulted; these results have already been presented in Table 5-7, from which it is evident that regardless of depth of water in the tank, the enlarged orifice admitted significantly more flow than did the smaller, as-built orifice. Therefore, it seems reasonable to conclude that:

5. **The size of the orifice ultimately controls the amount of recirculation through the draught tube provided that the skirt not be installed at an unreasonably low height.**

This result may also be viewed in light of NHC's finding that in general, the recirculated flow increased when the draught tube's floor was removed altogether (NHC, 1993) although their result was determined for the case of a non-zero tangential inflow.

7.2.4 Depth in Tank

Finally, the effect of depth on flow-through should also be considered. Although altering the depth in the clarifier does not represent a structural change *per se*, a variant depth is still extremely significant to the operation of the plant since in practice the water level does not remain static over time. As stated above, the results of this test are presented in Table 5-7, and they seem to indicate that regardless of orifice size, N_q increases as the depth of water above the impeller decreases for a given angular velocity. Thus:

6. **The impeller's pumping efficiency improves when the depth in the clarifier is lowered**

This is a simple consequence of gravity and potential energy. At large depth, there is a greater overlying mass of water to be displaced, so that the recirculating flow must have a higher amount of kinetic energy initially, upon being discharged through the impeller, in order to maintain the same flow as depth is increased; conversely, if the angular velocity is constant (*i.e.* the rate of kinetic energy input remains constant) then the flow becomes successively less able to displace the overlying mass of

water as depth is increased. This same phenomenon was observed during testing of the 1:55 and 1:41 scale models when, upon draining the tank for cleaning, previously unsuspended particles of titanic oxide would suddenly be drawn off the floor as the water level became lower.

7.3 Effects upon Turbulence, Turbulent Dissipation & Energy Consumption

7.3.1 Draught Tube and Skirt

Beginning again with the free impeller, examination of the dimensionless dissipation rate (normalized by either b or d) allows comparison of the effects of imposed structural changes upon the resultant local turbulent dissipation rate, ϵ , near the impeller's blade. As before, given the problems in estimating the radial variation of ϵ in the jet and the spatial variation of ϵ throughout the remainder of the draught tube, the comparison of dimensionless estimates of ϵ in such a manner is thought to be most practical and most useful near the impeller's blade. That the structure of turbulence in the remainder of the draught tube would more or less continue to exhibit similarity at all other geometrically consistent locations therein is assumed based upon the evidence that the turbulent velocities would continue to be expressible in terms of the impeller's tip-speed throughout the draught tube.

Firstly, considering the calculated values of dimensionless ϵ , a table of the b -based and d -based normalizations of ϵ for configurations 01 through 03 should be consulted. This table has already been presented (*vid.* Table 6-6), but for the purposes of illustration, it will be presented again here as Table 7-4. As well, the plots from which these maxima were extracted, Figures 6-5a, 6-6a and 6-7a should also be consulted.

Table 7-4
maximum observed dimensionless dissipation rates near the impeller's blade

configuration	maximum b -based dimensionless dissipation rate $\epsilon/[v_{tip}^3 / b]$	maximum d -based dimensionless dissipation rate $\epsilon/[v_{tip}^3 / d]$
01	0.032	0.140
02	0.032	0.140
03	0.032	0.140

Based upon this results, it would appear that the resultant local maximum dimensionless dissipation rate is unaffected by the installation of the draught tube and skirt. Theoretically, this may be explained if the turbulent velocity structure could be shown to be dependent only upon the tip-speed and the turbulent length scale (here assumed to be of the order of $\frac{1}{2} b$) and not any imposed structural modifications. The apparent constancy of dimensionless ϵ implies that the local turbulent velocities are unaffected by the presence of the draught tube and skirt, whereas the bulk average velocities were shown above to be greatly affected by the presence of the draught tube and skirt. In order to assess the effects of the draught tube and skirt upon the turbulent velocities directly, the vertical variation of the local dimensionless turbulent velocity along the impeller's blade should be examined. In order to do so, certain relevant dimensionless turbulent velocities were extracted from Table 6-1 and restated here, as Table 7-5:

Table 7-5
maximum dimensionless turbulent velocities near the impeller's blade

configuration	maximum u' / v_{up}	maximum v' / v_{up}	maximum w' / v_{up}	maximum U' / v_{up}
01	0.26	0.25	0.25	0.439
02	0.26	0.20	0.18	0.374
03	0.25	0.20	0.18	0.367

In this regard, it appears that the installation of the draught tube and skirt does in fact affect the local turbulence structure. Specifically, it appears that the magnitudes of the local turbulent velocities decrease upon installation of the draught tube and skirt, where the tangential and axial components of turbulent velocity are affected much more strongly than is the radial component. As such, it may be concluded that:

7. Installation of the draught tube and of the skirt decreases the resultant local dimensionless turbulent velocities near the impeller's blade.

A consequence of this is that the turbulent flows that are generated by the confined impeller are decidedly less isotropic than those generated by the free impeller. By implication, it is expected that the magnitude of the turbulent velocities throughout the remainder of the draught tube should also be slightly less than should be the velocities in a similarly sized volume surrounding the free impeller.

Furthermore, the fact that ϵ depends directly upon the cube of the resultant turbulent velocity together with the apparent decrease in turbulent velocities indicates that:

8. Installation of the draught tube and of the skirt decreases the resultant local turbulent dissipation rate near the impeller's blade.

The fact that there is only a slight difference among the turbulent velocities u', v', \dots is probably responsible for the fact that the curves of dimensionless ϵ are generally indistinguishable, a fact which renders such an approach inconclusive with respect to quantifying the nature of the turbulent flows in the draught tube. Direct examination of the constituent turbulent velocities in this manner allows the consequent effects of imposed geometrical changes to be assessed directly.

However, neither a comparison of the dimensionless dissipation rate near the impeller's blade nor a comparison of the magnitude of the resultant turbulent velocity near the impeller's blade allows the effect of confinement upon the turbulent dissipation rates either throughout the rest of the draught tube or anywhere else in the fluid to be assessed. Although a thorough definition of the variation of turbulent velocities could, presumably, be integrated to yield the gross turbulent energy consumption throughout the entire draught tube, such an effort is well beyond the purposes of this study. Fortunately, an examination of the calculated power numbers

allows this quantity to be expressed directly since N_p is an expression of the total energy input to the system. As such, by tabulating the observed power numbers for both the free impeller (configuration 01) and the confined impeller (configuration 03) the effect of the draught tube and skirt upon total energy consumption is apparent. This comparison is now presented in Table 7-6.

Table 7-6
power numbers - the effect of draught tube and skirt upon total power consumption

configuration	trial	maximum N_p
01	A01	2.3
02	A02	3.0
03	A03	3.0
01	B01	2.3
02	B02	3.0
03	B03	3.0

These power numbers seem to illustrate conclusively that N_p increases upon confinement of the impeller. Since N_p increases, the total power imparted to the fluid in turning the impeller must also increase if a given angular velocity be maintained, indicating that the confined cases ultimately consume more energy. As such, it is concluded that:

9. The confined impeller consumes significantly more energy than the free impeller for a given angular velocity.

Logically, the increase in total energy consumption over that of the free impeller may be viewed as a direct consequence of the greatly increased drag losses to the walls and floor of the draught tube. Clearly, the impeller is extremely closely confined by the draught tube. In terms of the total breadth of the draught tube, it is seen that the Ecodyne impeller occupies almost eighty percent of the diameter of the draught tube (*i.e.* $d/D \approx 0.80$). Generally, for Rushton turbines, it is found that the diameter of the impeller is only $\frac{1}{3}$ to $\frac{1}{2}$ of the tank's diameter. Thus, it is speculated that the draught tube's proximity to the impeller allows the walls to impart a stabilizing drag-force on the local velocity field. The influence of this wall-induced drag force is also believed to enable the observed power numbers in this study to attain approximately constant values in the high- R , range, despite decades' worth of studies which consistently show that the power number in unbaffled vessels is generally not constant.

However, the fact that the **total** energy consumption increases does not ensure that the **local** energy consumption in the draught tube, as represented by ϵ , also increases. Actually, the effect of confinement upon the local dissipation rate may be thought to depend upon some sort of complex energy balance in which the frictional losses to the walls and floor of the draught tube and the internal losses to turbulent dissipation are intimately related to local geometry and the resultant magnitude of the bulk flow through the draught tube. The fact that the total energy consumption increases upon confinement is most correctly a result of increased frictional losses to the walls and floor of the draught tube and **not** primarily the result of an increase in the turbulent dissipation rate. In this regard, recalling the earlier conclusion that the local dissipation rate near the impeller's blade was found to decrease upon installation of the draught tube and skirt, and taking this conclusion together with the presence of surface drag within the draught tube and the suspected agency of such drag forces in damping or otherwise altering the magnitude

of the turbulent velocities therein, it seems reasonable to conclude that:

- 10. The installation of the draught tube decreases the local turbulent dissipation rate throughout the draught tube but increases the total power consumed in turning the impeller.**

Noting further that the power numbers for configurations 02 and 03 are not significantly different regardless of scale, and recalling the earlier statement that the installation of the skirt does not appear to affect the magnitude of the local turbulent velocities in comparison to the case where the impeller is confined by the draught tube alone, it may also be reasonably concluded that:

- 11. The further installation of the skirt to the draught tube affects neither the total energy consumption nor the local turbulent velocity structure in the draught tube**

This conclusion is evidently related to the earlier conclusion that the installation of the skirt does not adversely affect the impeller-generated flow-through in the draught-tube.

Finally, it is implied that decreasing the skirt opening still further, *i.e.* trial A04, should result in similar values of the local turbulent dissipation rate to those found in configuration 03. Although power numbers were not determined for trial A04, the fact that both the radial turbulent velocities (Figure 7-2a) and the dimensionless dissipation rates (Figure 7-2b) are not significantly different from those which were determined for configuration 03 seems to confirm this.

7.3.2 Draught Tube Baffles

In considering the effects of draught tube baffles on flow-through, the previously noted connection between the flow and wall-drag forces may again be implicated. Intuitively, it could be believed that the case where baffles are installed in the draught tube should affect the estimated local value of ϵ due to the extra potential for form drag losses to the baffles. As before, this effect may be assessed by several means. Figure 7-3a presents the dimensionless turbulent radial velocity profile near the impeller for configuration 03 (which represents five runs at two scales) together with the dimensionless radial turbulent velocity profile for trial A05 (which represents only a single angular velocity). In this manner, it appears that the dimensionless turbulent velocity for trial A05 attains noticeably lower values. Quantitatively, the relevant elements of the generalized dimensionless turbulent velocities that were expressed in Table 6-1 may be combined as shown in Table 7-7 to illustrate this difference:

Table 7-7
dimensionless turbulent velocities near impeller's blade
illustration of effects of draught tube baffles on local turbulence structure

trial	N (rpm)	R_i	maximum u'/v_{up}	maximum v'/v_{up}	maximum w' / v_{up}	maximum U' / v_{up}
A03	100	1.82×10^4	0.25	0.20	0.18	0.367
A05	100	1.82×10^4	0.20	0.18	0.16	0.313

Thus, it appears that the presence of draught-tube baffles both decreases the magnitude of the local turbulent velocity structure and introduces a further degree of non-isotropy to the flow. Given that the local dimensionless turbulent dissipation rate is dependent (at least near the

impeller's blade) only upon ω and d (or b), a consequence of lower local turbulent velocities should be a decrease in the local observed value of ϵ . In this manner, a plot of the resultant local b -based dimensionless ϵ , which compares the calculated values of ϵ from configuration 03 to the calculated value of ϵ from trial A05, is presented in Figure 7-3b. The presence of lower turbulent velocities is indeed confirmed since Figure 7-3b seems to indicate that the local estimate of ϵ does indeed decrease upon installation of draught tube baffles. Thus, one may (with some confidence) assume that:

12. The installation of draught tube baffles serves to decrease the local dissipation rate still further.

Again, just as the local dissipation rate near the impeller's blades is found to be attenuated by the presence of the draught tube baffles in trial A05, it is a necessary consequence of similarity that so too must the turbulent dissipation rate throughout the remainder of the draught-tube also be attenuated.

To assess the total amount of energy consumed, a comparison of measured power numbers from trials A03 and A05 is in order - this plot is presented in Figure 7-3c. In this case, it appears that the installation of baffles actually very slightly *increases* the total energy that is imparted to the fluid via the impeller. Such behaviour is to be expected given the evidence in the literature which shows overwhelmingly that the presence of baffles tends to increase power consumption over the unbaffled condition. For instance, Rushton (1950-1) provided an extensive series of N_p measurements on both baffled and unbaffled tanks, and Papastefanos & Stamatoudis (1989) compared N_p in baffled cylindrical vessels, square vessels and unbaffled vessels - these studies both indicate that N_p is greatest in baffled circular vessels and least in unbaffled circular vessels, with N_p in square vessels usually falling amid these two limits; Mhaisalkar, Paramasivam & Bhole (1986) found that G , a close relative to N_p , is greatest in baffled square vessels and least in unbaffled circular vessels.

In the same manner as before, the apparent paradox that local turbulent dissipation rate decreases while the total amount of energy applied increases may be explained by the presence of increased frictional drag. In adding baffles to the walls of the draught tube, the effective ratio of the impeller's diameter to that of the containing vessel increases still further, imparting even more of a damping effect on the local turbulent velocities. Again, this effect is likely accentuated by the baffles' impediment to the bulk flow-through, as-discussed earlier, whereby the overlying mass of flowing water seems to affect the vigour of the upwardly moving flow below it.

7.3.3 Size of Orifice

The analysis of the effect of the orifice upon ϵ proceeds in an identical manner to the previous analyses of the draught tube, skirt and baffles' effects upon ϵ . Again, using configuration 03 as a basis*, the effects of an enlarged orifice upon the local turbulent dissipation rate in the draught tube may be determined through direct comparison between the turbulent velocities, power numbers and dimensionless dissipation rates of trial B06 to those of trials A03 and B03.

Beginning with the turbulent velocities, a comparison of the local dimensionless turbulent velocities at a geometrically consistent point illustrates the relative magnitudes of the local turbulent velocities. Appropriate values of these velocities were extracted from Table 6-1 and

* This configuration may be thought to represent the impeller-draught-tube system in its as-designed form: that is, the existing full-scale orifice opening, a full-scale skirt height of 45.7 cm, and no baffles.

compared directly in Table 7-8:

Table 7-8
dimensionless turbulent velocities near impeller's blade
illustration of effect of orifice opening on local turbulence structure

trial	N (rpm)	R,	maximum u'/v_{up}	maximum v'/v_{up}	maximum w'/v_{up}	maximum U'/v_{up}
A03	various	various	0.25	0.20	0.18	0.367
B03	various	various	0.25	0.20	0.18	0.367
B06	100	1.8×10^4	0.25	0.20	0.18	0.367

According to this table, it appears that the orifice has no significant effect upon the local turbulent velocities. This lack of noticeable effect is further illustrated in Figure 7-4a, which represents a graphical statement of the above table.

Considering the estimated local turbulent dissipation rate, a comparison of the local b-based maximum dimensionless dissipation rates may be made for the same three trials:

Table 7-9
maximum observed dimensionless dissipation rates near the impeller's blade
illustration of the effect of orifice opening on local turbulent dissipation rate

trial	maximum b-based dimensionless dissipation rate $\epsilon/[v_{up}^3/b]$	maximum d-based dimensionless dissipation rate $\epsilon/[v_{up}^3/d]$
A03	0.032	0.140
B03	0.032	0.140
B06	0.032	0.140

This table, or a graphical comparison of the ϵ -distributions (Figure 7-4b) also indicate that a larger orifice has no effect upon the local dissipation rate, either near the impeller or throughout the entire draught tube.

Considering such kinetic behaviour together with the earlier result that flow-through may be increased significantly by a larger orifice, it may further be concluded that:

13. **Enlarging the orifice allows the flow through the draught tube to be increased without changing the turbulent structure of the flow.**

This result together with the fact that such relevant physical and chemical processes as rate of flocculation and rate of chemical reaction have generally been shown to be dependent upon the local rate of turbulent dissipation implies further that:

14. **Enlarging the orifice should allow the flow-through to be increased without affecting the kinetics of the chemical and physical processes which occur in the draught tube.**
 This in turn would presumably allow increased process efficiency

since more of the flow could be exposed to highly agitated, impeller-generated flow in a given length of time yet still emerge from the reaction zone with an acceptable level of quality.

In contrast to the apparent constancy of the dimensionless turbulent dissipation rate, an examination of the resultant power numbers again seems to exhibit the paradoxical behaviour that whereas local the dissipation rate is found to be either unchanged or lower upon installation of a larger orifice, the total rate of energy consumption in the draught tube actually increases. According to Figure 7-4c, the approximately constant high- R , power numbers for trials A03 and B03 are actually found to be *lower* than those of trial B06. Specifically, these power numbers may be tabulated as presented in Table 7-10:

Table 7-10
power numbers - trials A03, B03 & B06
illustration of the effect of orifice opening on total power consumption

trial	equivalent diameter of full-scale orifice (m)	approximately constant N_p
A03	2.210	3.0
B03	2.210	3.0
B06	3.265	3.6 to 3.7

Possible explanations for the increase in total power consumption are elusive. It is somewhat surprising that the total area available for flow should increase while the annular surface area available for development of frictional drag should decrease, yet the total power consumed should increase. It is speculated that a larger orifice exposes the flow below the floor of the draught tube to the impeller's developed suction sooner, before this flow may penetrate closer to the shaft of the impeller where the suction is thought to be greatest, thereby causing less energy-efficient pumping through the impeller. Perhaps a more credible speculation is that the higher-velocity flow develops more boundary shear on the walls of the draught tube. In retrospect, it seems that a trial where the impeller is confined by a draught tube without a floor would have been a useful illustrative endeavour, as would have been trials with other orifice openings. As a consequence, it is probably should not be stated conclusively that increasing the orifice opening does in fact cause the total power consumption to increase.

The fact that N_p for trial B06 is much greater than those for configuration 03 whereas intuition may have caused one to expect it to lie somewhere *in between* those of configurations 01 and 03 provides further indication that the nature of the flow in such a situation is indeed complex. Admittedly, testing at more angular velocities would have been useful in trial B06, but the fact that the turbulent velocities were invariably well correlated with the tip speed in every test performed in this study provides considerable evidence that trial B06's degree of kinetic similarity with respect to turbulent velocities should not be any different.

7.3.4 Depth in Tank

The effect of depth upon ϵ and turbulence was not investigated directly. It is speculated, however, that the mass of overlying water together with the fact that the draught tube constrains the flow to flow in a specific direction, *i.e.* vertically, would again establish some sort of impediment to the development of turbulence in the draught tube. In such a manner, it is speculated that by increasing the depth, the local development of turbulence would be lessened.

thereby adducing the concomitant effect that local reaction rate, turbulent diffusion, heat transfer and any other process that is turbulence-dependent would be adversely affected.

7.4 Conclusions

It is clear that the nature of flow in such an impeller-agitated, confined system is very complex, depending upon numerous factors such as ω , h and the degree of confinement. It must be recalled that these tests were performed under somewhat idealized conditions: there was no tangential inflow, a flat-bottomed tank, and no scraper mechanism, factors which could be thought to exert some influence upon the flow in the full-scale facility. As well, this analysis employed power numbers that were only approximately constant (and only in the high- R_i range) which may or may not be appropriate at the full-scale. Nonetheless, the observed general trends and consequences of the imposed structural modifications should still be apparent at the full scale, though probably not necessarily exhibiting exactly the same behaviour, in terms of some relevant dimensionless parameters, as those which were observed at the model-scale.

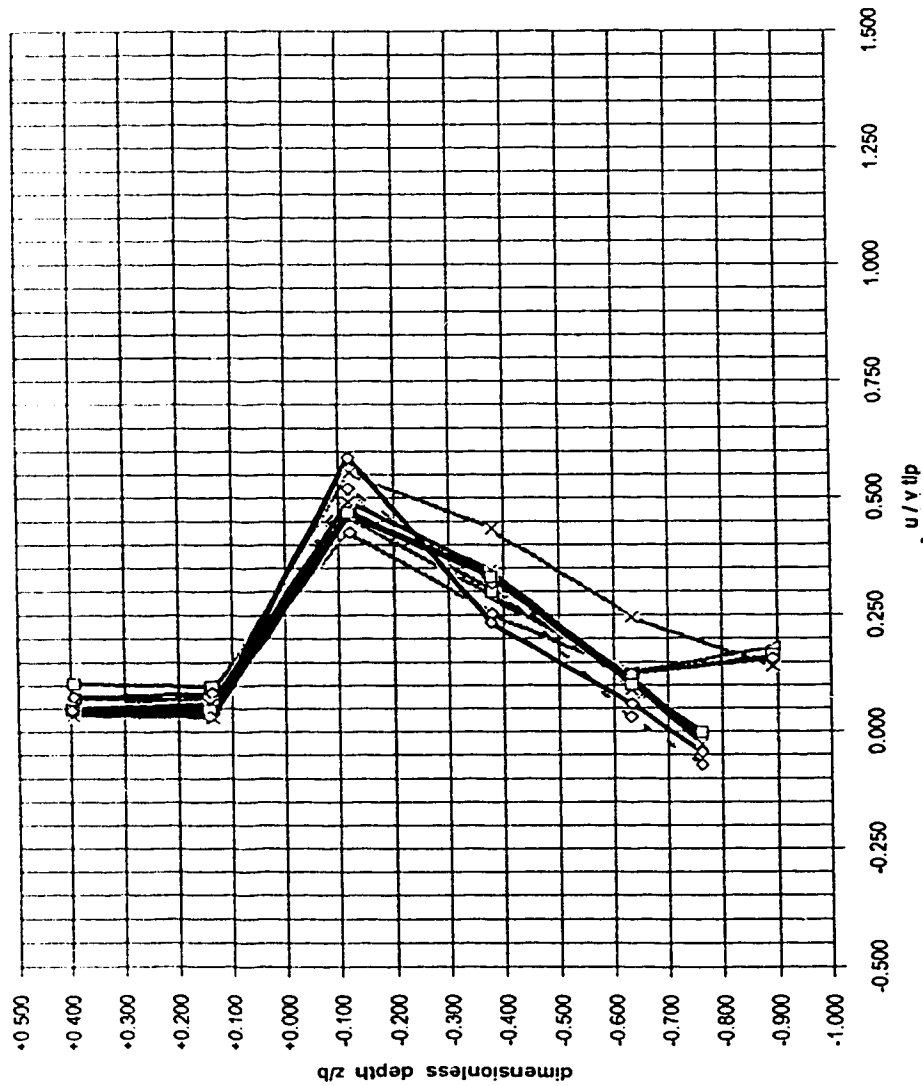
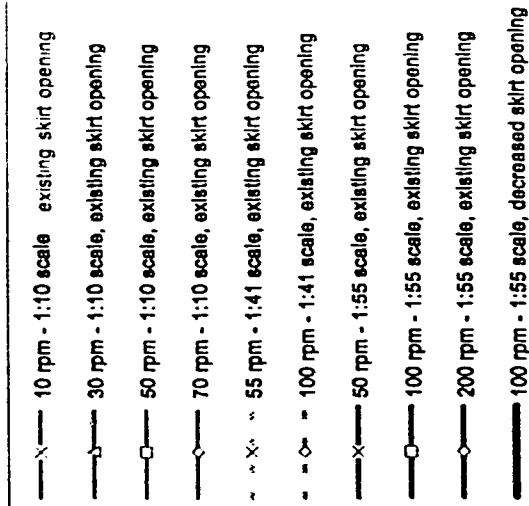


Figure 7.1a : ecodyne Impeller : 1:55 scale, 1:41 scale & 1:10 scale
 investigation of effect of reduced skirt opening on flow-through
 radial average velocities near Impeller - normalized by tip speed
 $d=7.66$ cm, 10.37 cm & 42.62 cm ; $b=1.94$ cm, 2.63 cm & 10.8 cm ; $2r/d=1.044$



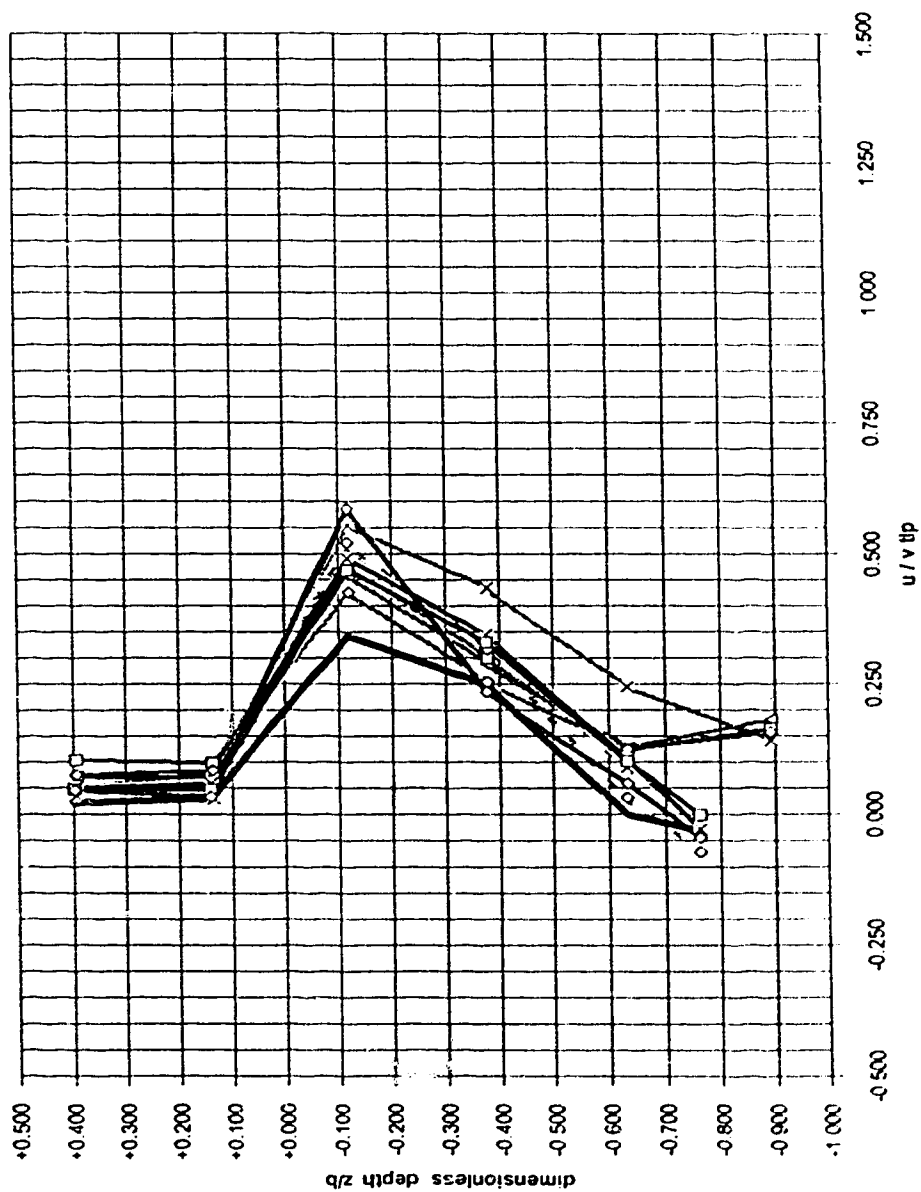


Figure 7.1b :
 ecdyne impeller ; 1:55 scale, 1:41 scale & 1:10 scale
 investigation of effect of draught tube baffles on flow-through
 radial average velocities near impeller - normalized by tip speed
 $d=7.66$ cm, 10.37 cm & 42.62 cm ; $b=1.94$ cm, 2.63 cm & 10.8 cm ; $2\pi r/d=1.044$

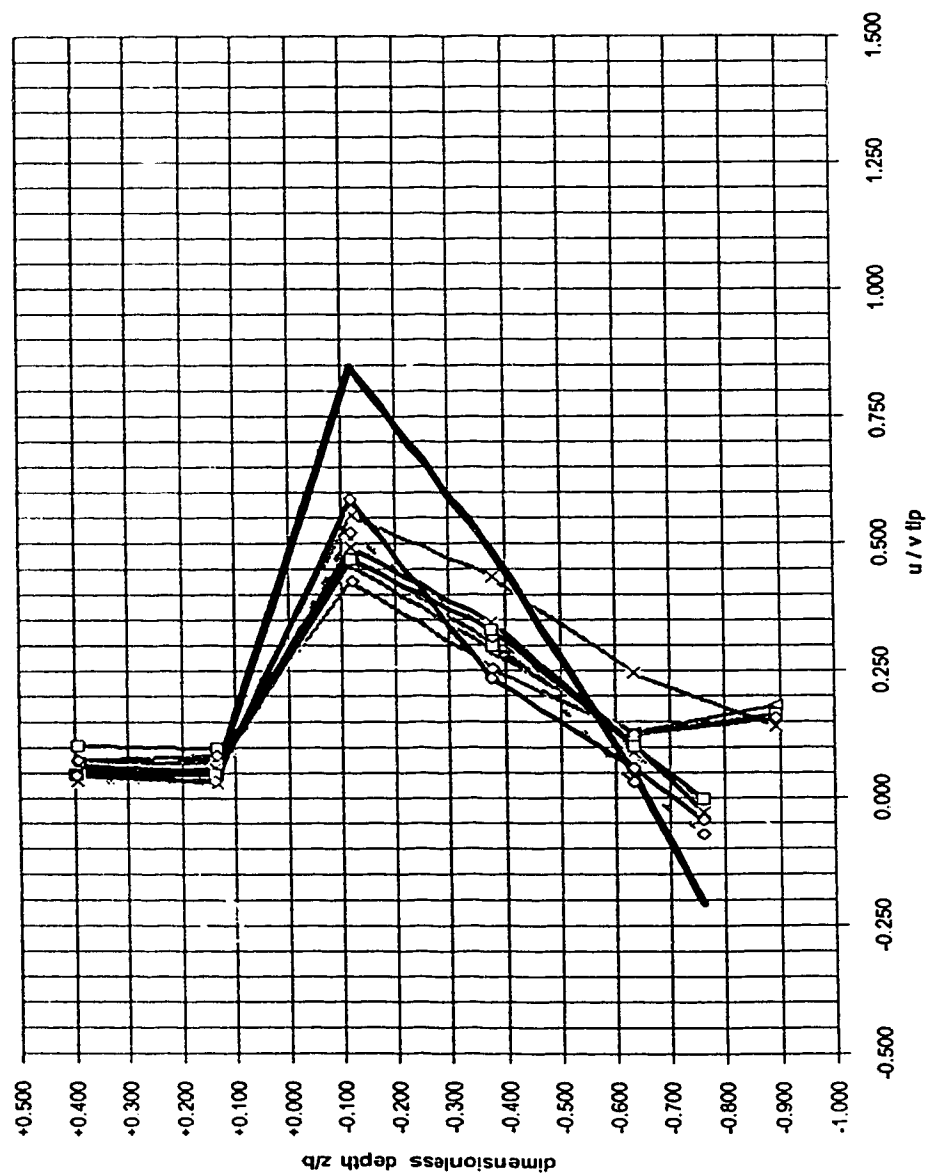


Figure 7-1c : ecdyne impeller : 1:55 scale, 1:41 scale & 1:10 scale
 investigation of effect of enlarged orifice on flow-through
 radial average velocities near impeller - normalized by tip speed
 $d=7.66$ cm, 10.37 cm & 42.62 cm ; $b=1.94$ cm, 2.63 cm & 10.8 cm ; $2/r/d=1.044$

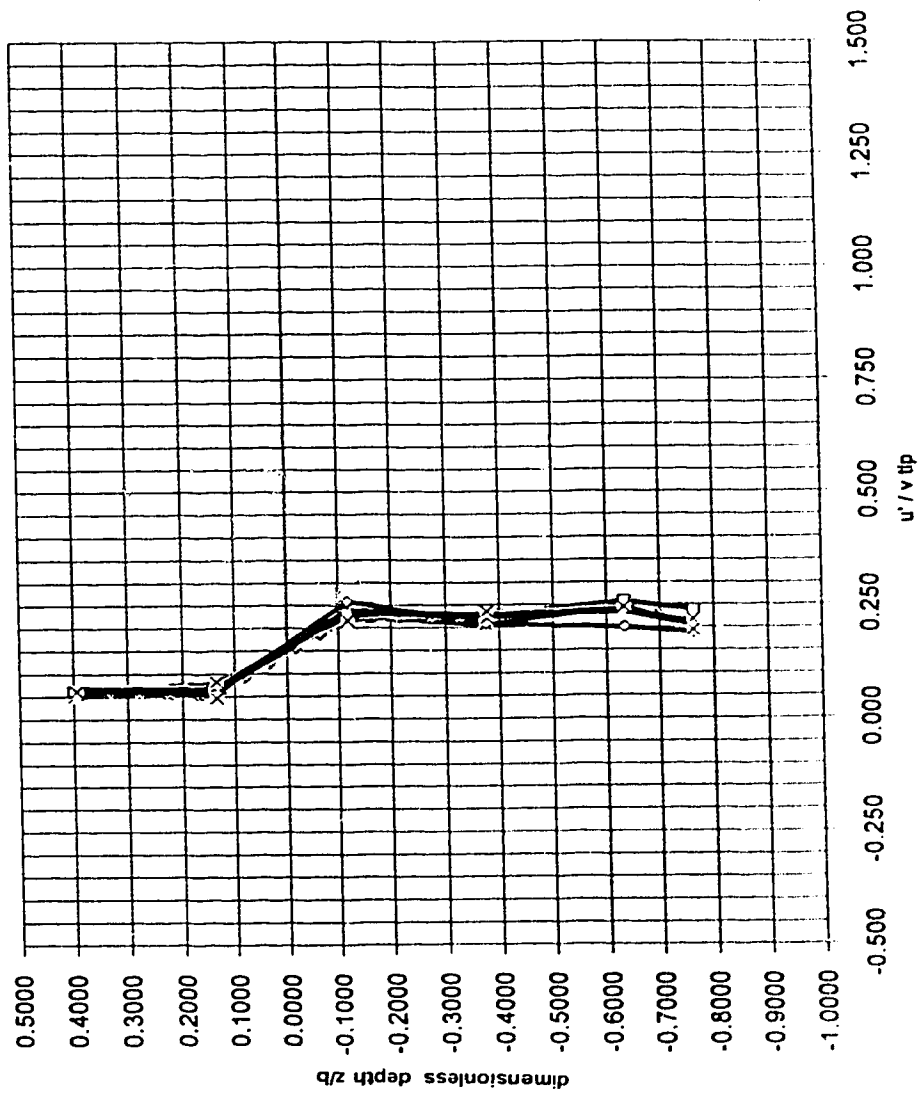


Figure 7-2a : ecodyne impeller, 1:55 scale & 1:41scale
 investigation of effect of reduced skirt opening on turbulence
 radial turbulent velocities near impeller - normalized by tip speed
 $d=7.66 \text{ cm}$, 10.37 cm & 42.62 cm ; $b=1.94 \text{ cm}$, 2.63 cm & 10.83 cm ; $2\pi d=1.044$

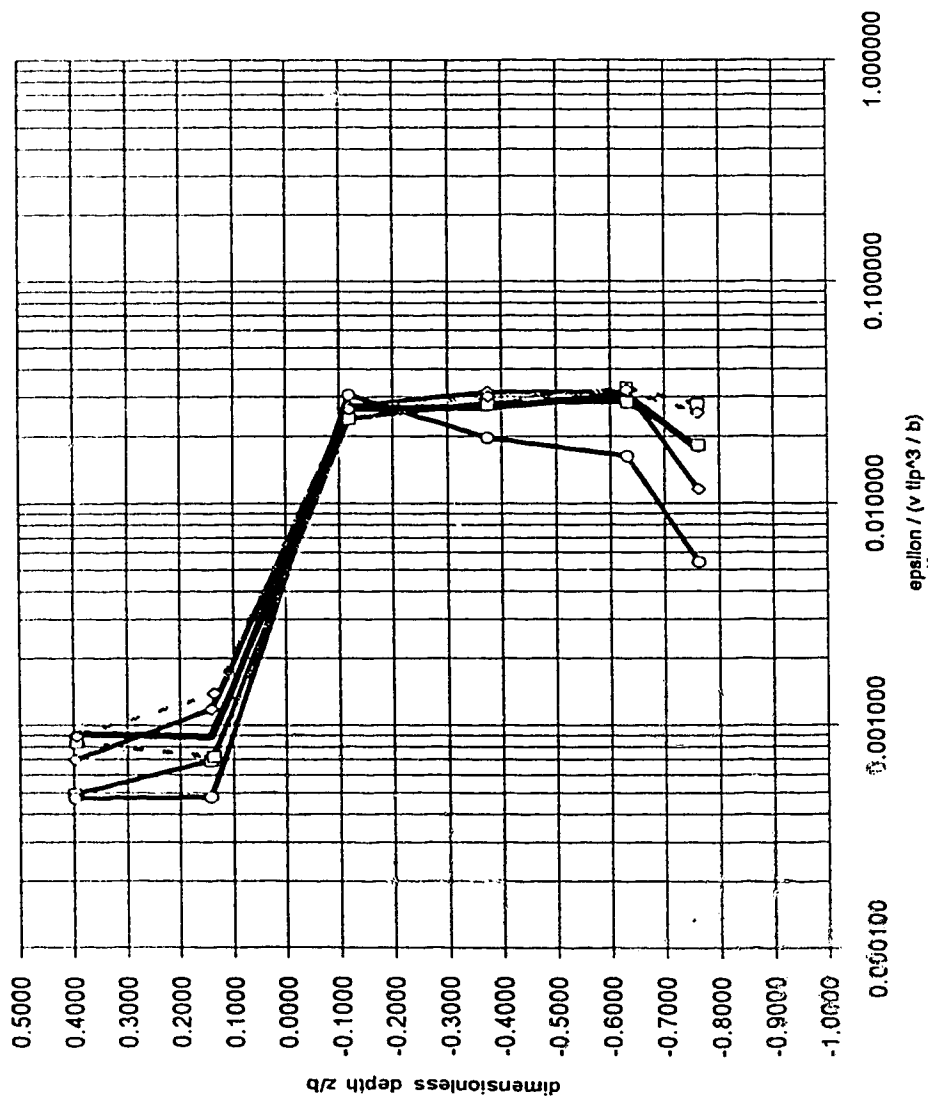


Figure 7-2b : ecdyne impeller : 1:55 scale & 1:41 scale
 investigation of effect of reduced skirt opening on local dissipation rate
 dissipation rates near impeller - normalized with blade height
 $d=7.66$ cm & 10.37 cm ; $b=1.94$ cm & 2.63 cm ; $2r/d=1.044$

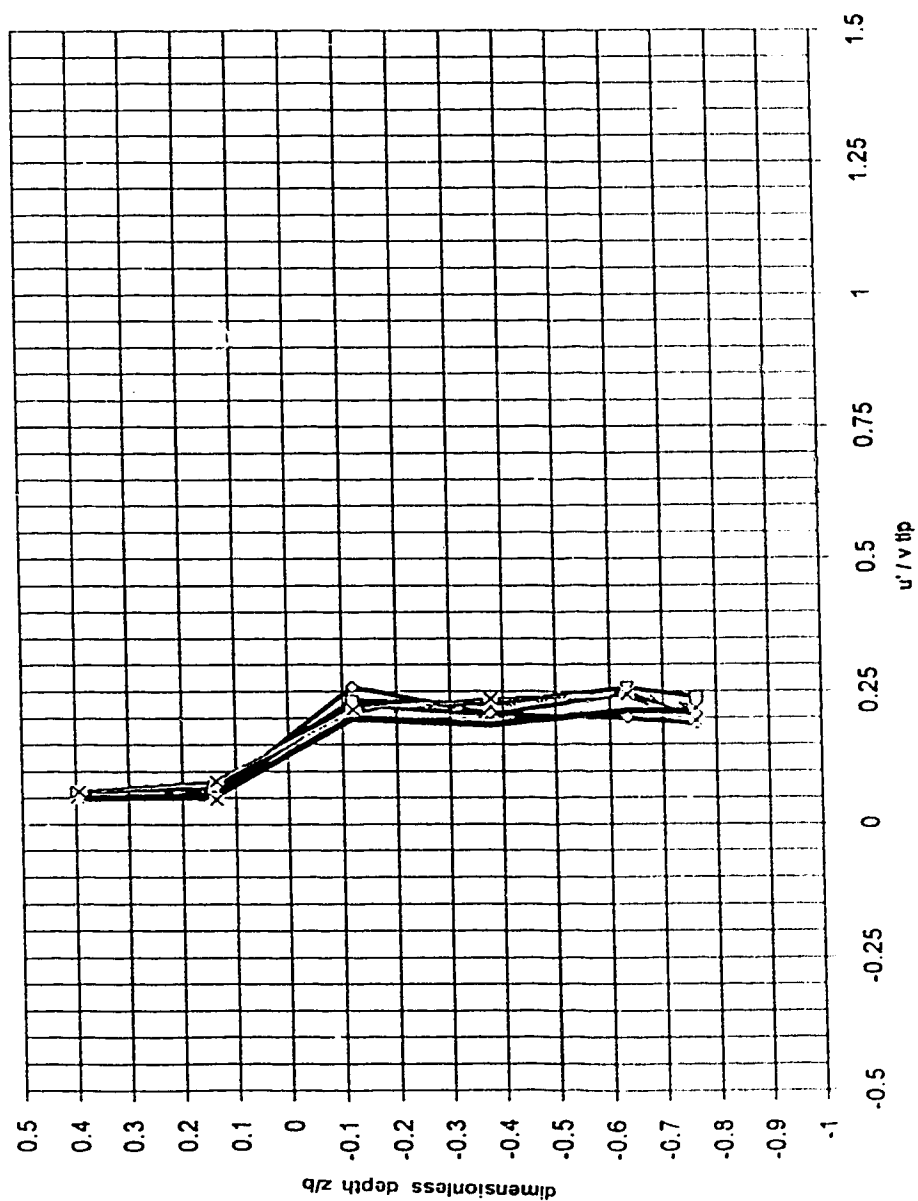


Figure 7.3a : ecdymer impeller, 1:55 scale & 1:41 scale
 investigation of effect of draught tube baffles on turbulence
 radial turbulent velocities near impeller - normalized by tip speed
 $d=7.66$ cm & 10.37 cm ; $b=1.94$ cm & 2.63 cm ; $2r/d=1.044$

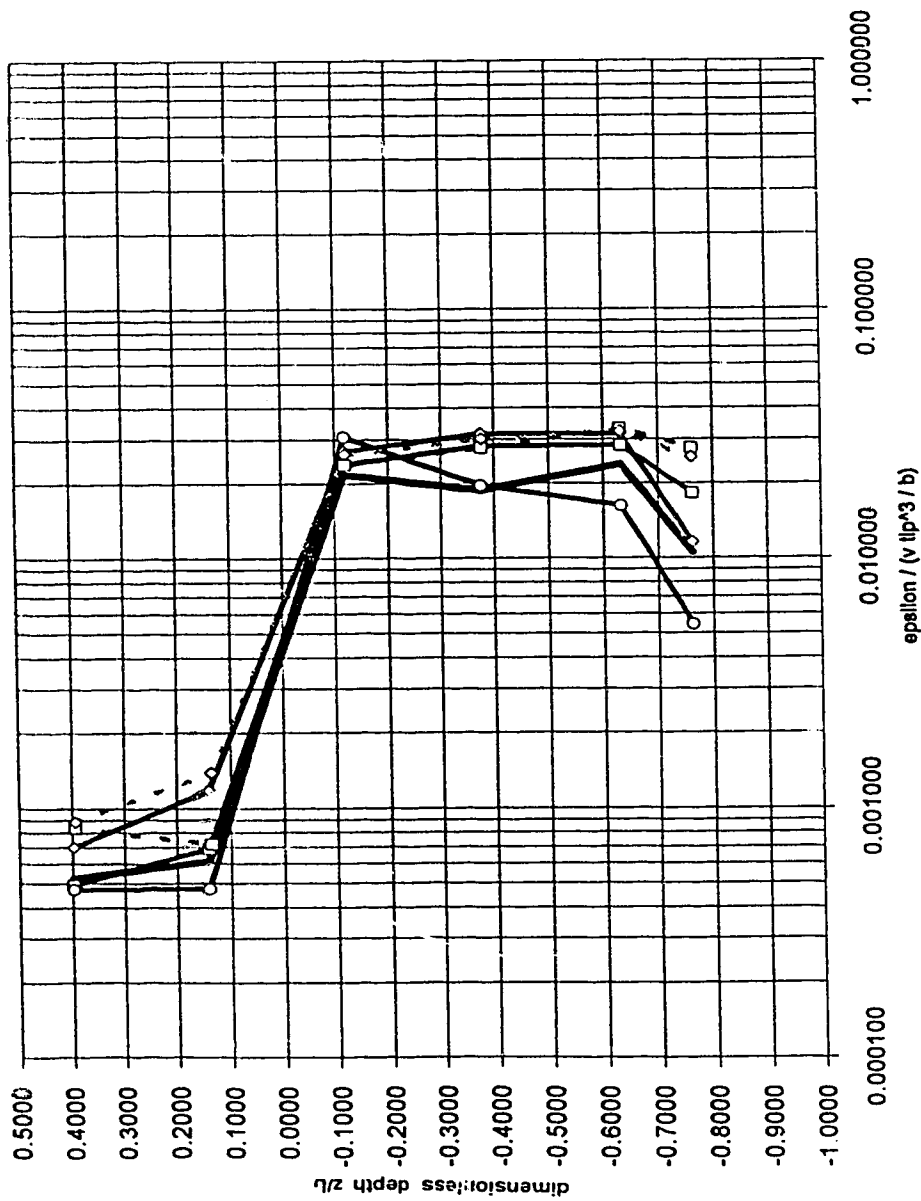
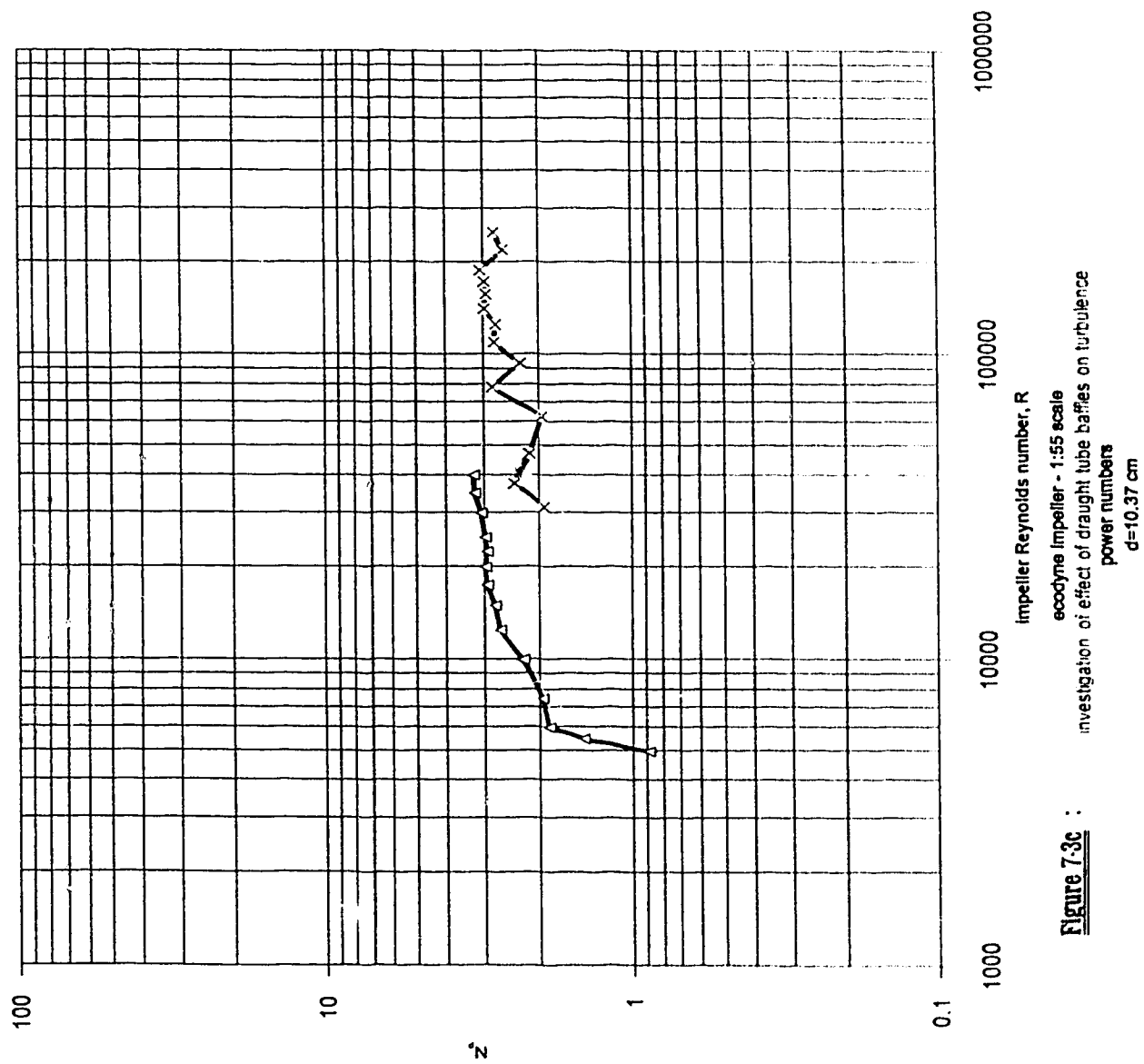


Figure 7.3b :
 ecodyne Impeller : 1:55 scale & 1:41 scale
 investigation of effect of draught tube baffles on local dissipation rate
 dissipation rates near Impeller - normalized with blade height
 $d=7.66$ cm & 10.37 cm ; $b=1.94$ cm & 2.63 cm ; $2r/d=1.044$



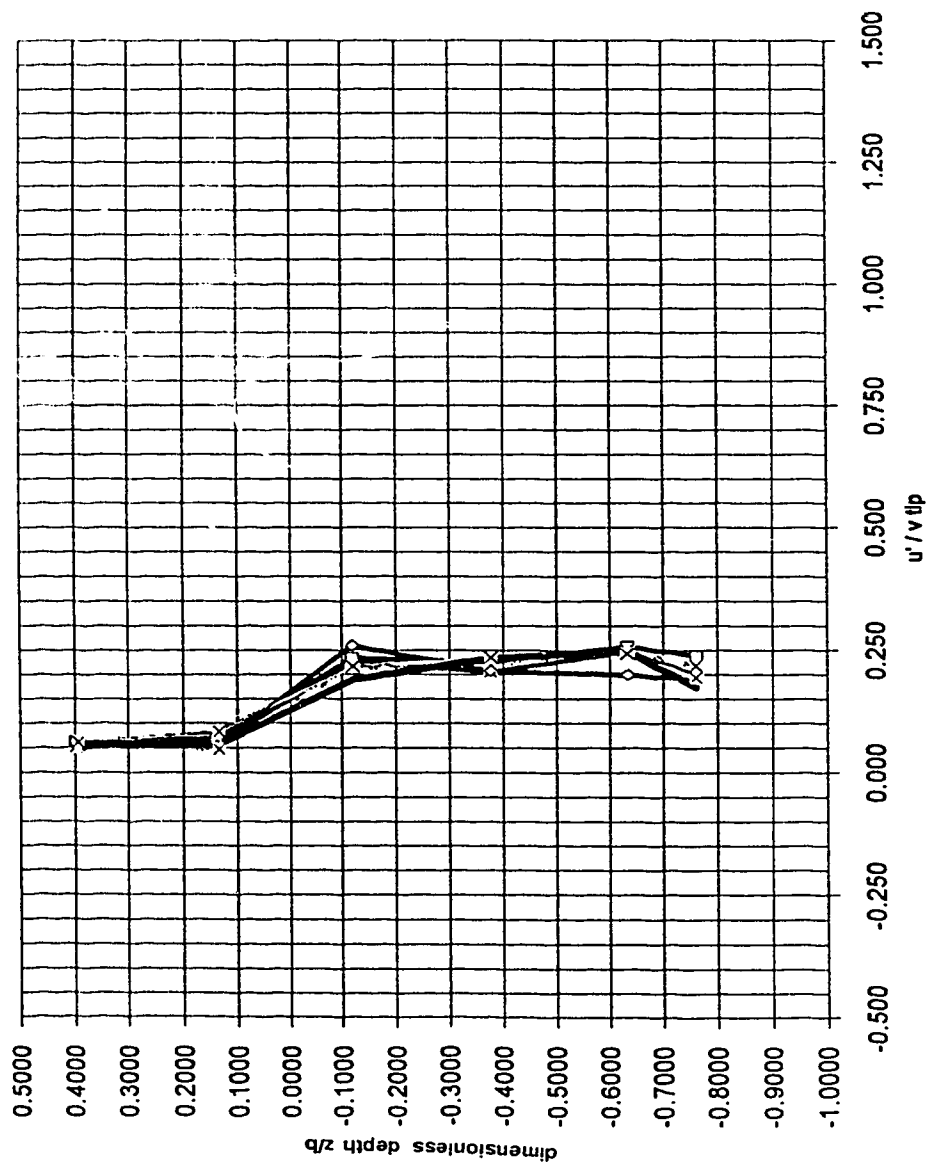


Figure 7.4a : ecodyne Impeller, 1:55 scale & 1:41 scale
 investigation of effect of enlarged orifice on turbulence
 radial turbulent velocities near Impeller - normalized by tip speed
 $d=7.66$ cm, 10.37 cm & 42.62 cm ; $b=1.84$ cm, 2.63 cm & 10.83 cm ; $2r/d=1.044$

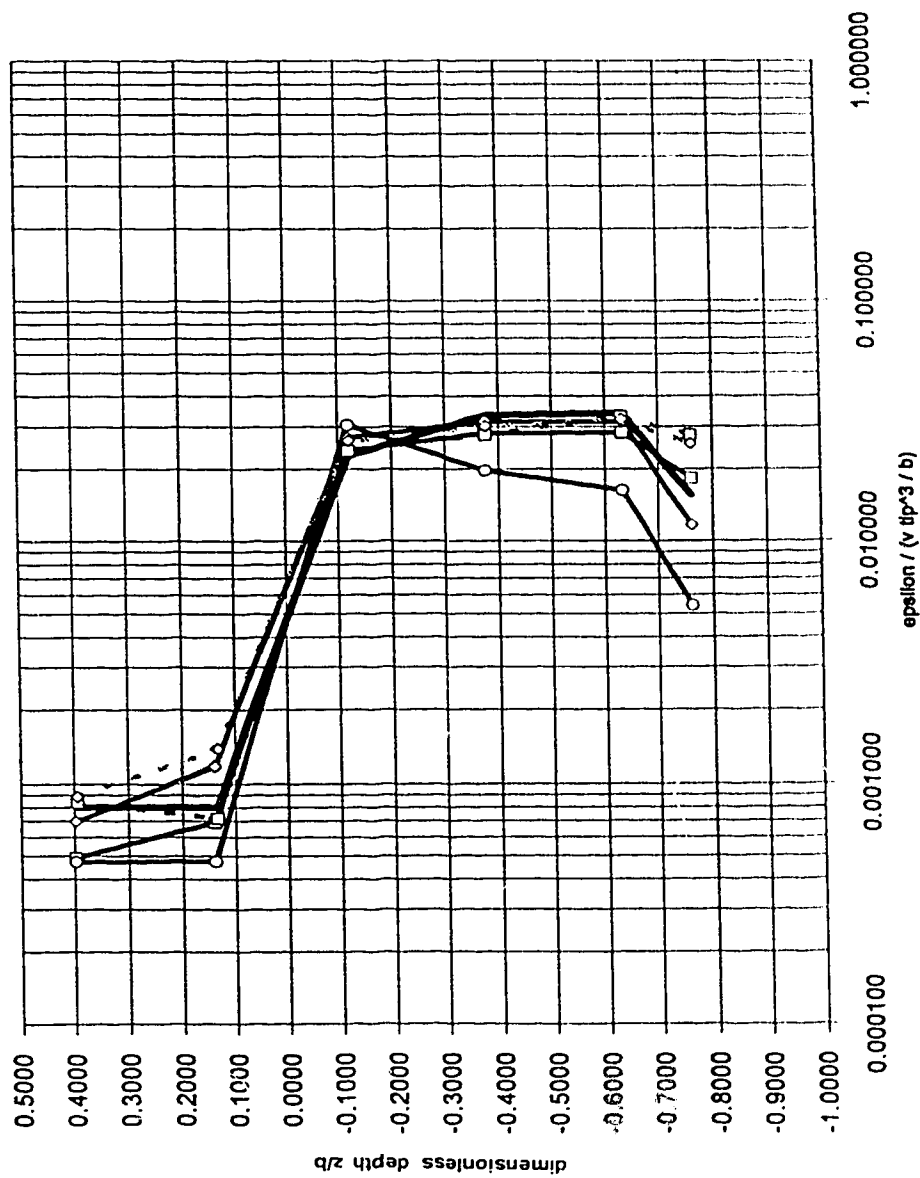


Figure 7-4b : eodyne impeller ; 1:55 scale & 1:41 scale
 investigation of effect of enlarged orifice on local dissipation rate
 dissipation rates near impeller - normalized wim blade height
 $d=7.66$ cm & 10.37 cm ; $b=1.94$ cm & 2.63 cm ; $2\pi/d=1.044$

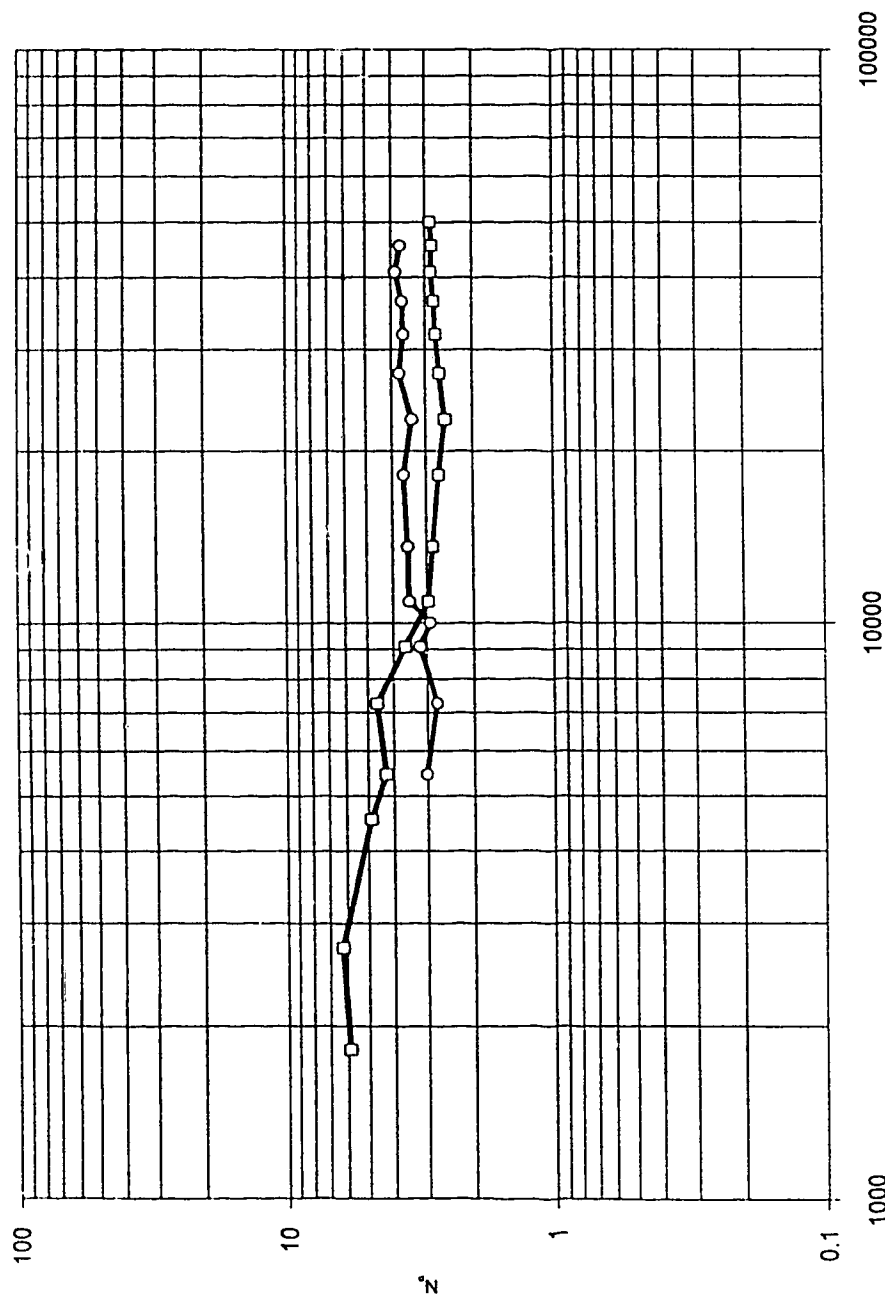


Figure 7.4c : investigation of effect of enlarged orifice power numbers
 $d=10.37$ cm
 ecodyne Impeller - 1:41 scale
 impeller Reynolds number, R

8.0 Inferences with Respect to Scale-Up (no Tangential Inflow)

8.1 Scaling and Similarity

8.1.1 General

Scale-up demands the establishment of a consistent, fundamentally sound procedure whereby the nature of an experimentally observed occurrence may be predicted at any other scale based upon the experimentally observed flow properties at another scale. Impeller-agitated mixing is a very complicated process wherein numerous physical properties could potentially be of interest such as local velocities and velocity distributions, bulk velocities, discharges, suspension of solids, temperature distribution, reaction rate, caloric production and power consumption, thus implying the necessity of observation of many or any criteria of importance upon scale-up. This in turn implies the necessity of maintenance of any number of relevant scale-up parameters depending upon what in particular is being studied.

Scale-up can be very complicated, demanding knowledge of any dynamical-physical process that may be present, or it can potentially be relatively simple should any specific aspect of the mixing-agitation be of concern. Moreover, depending upon the nature of the flow and the interrelations among the various physical-dynamic-chemical processes which may occur at a given scale, there appears to be no guarantee that the relative manifestations of any two such process should each scale up proportionally so that they would exist in the same ratio at two different scales - different aspects of mixing might demand totally different scale-up schemes: for instance, a representative velocity distribution may incur significantly higher shear forces upon scale-up, thereby causing the observed rates of some chemical processes to increase, or conversely, for the observed reaction rate to remain constant, a completely different velocity distribution may be required.

The major obstacle in the successful performance of model studies in defining a theoretically sound course whereby the results collected at a small scale may be duplicated in a geometrically similar unit at full-scale. Leentvar & Ywema (1980) recognized the difficulty of this task:

a number of other possible scale-up criteria are the following: constant Reynolds number, constant Froude number, constant Weber number, constant tip velocity, constant power per unit volume and constant volumetric flow per velocity head. None of this (sic.) scale-up criteria are compatible

Holland (1963) stated that if one dimensionless group did not dominate in a particular system, the fluid structure would be subject to a so-called "mixed regime" wherein it would be impossible to satisfy the maintenance of each dimensionless group simultaneously upon scale-up, and therefore any analysis would be subject to a great deal of uncertainty. With specific reference to chemical reactions, it is seen that the inclusion of additional variables introduces additional complications. One could seek to maintain, for instance, a constant reaction rate or heat transfer rate upon scale-up, but as these are usually subject to temporal variation, temperature variation and agitation, depending upon the particular regime that is of interest (*i.e.* either a fluid mechanical regime or a chemical regime is being studied), one could potentially scale-up according to a regime in which the aforementioned kinematic or dynamic similarity would no longer exist, even though a chemical-thermodynamic similarity would be maintained. Oldshue (1981) described scale-up of mixing as "mostly art and very little science" - not to be taken literally, his remark addresses both the difficulty of describing the intricacies of the mixing process, and the traditional predilection of many workers in the field to apply basic, simple rules of thumb to the interpretation, scale-up and application of laboratory-scale mixing data.

Scale-up is decidedly process-dependent. It appears that a consistent, universal scale-up

scheme still remains or must remain relatively elusive: in effect, scale-up analysis is a universe of apparently divergent theories punctuated by numerous traditional rules. Nonetheless, the question of scale-up of impeller-agitated mixing has been pursued by researchers for decades via several different paths, with specific intent of scaling-up any of numerous and variant qualities of the flow, and with an ever increasing degree of complexity. Given the historical review that was presented in the **Review of Literature**, where the relevance of concepts such as dimensionless analysis, energy, turbulence and mathematical modelling to the study of impeller-agitated mixing was addressed, an attempt can be made to link such analytical approaches together in order that a general illustration may be made concerning the practice of scale-up with respect to its appropriateness and feasibility in a variety of situations.

8.1.2 Hydraulic Parameters

Traditionally, the use of hydraulic scale models in engineering has been predicated upon the concept of dynamic similarity and the supposition that dynamic similarity necessitates a definite interrelation with geometric similarity. It is often assumed that dimensionless parameters are sufficient to describe a particular flow situation subject to the condition that a certain single parameter would exist in a state of primacy and thus would be sufficient to describe the situation. There are three dimensionless parameters which are most commonly applied in the study of hydraulics, representing the significant physical properties of the fluid: R , (the Reynolds number), F (the Froude number) and W (the Weber number). These may be seen to incorporate the effects of viscous forces, inertial forces and surface tension, and may also be seen to represent the ratios of two assumedly significant force regimes. As such, the usual approach is to assume the predominance of one of these parameters and to scale based upon an assumed similarity that would exist if the dynamic responses of small- and large-scale systems would be systematically and definitely conjoined provided that certain quantities' ratios were to remain the same upon scaling.

If it be assumed that one parameter should be kept constant upon scale up, then given a geometric length ratio λ , all the other relevant ratios could be defined rather conveniently. The analysis of hydraulic structures and pipe flow, as well as many other areas of study such as aeronautics and acoustics have been particularly amenable to such an analytical approach. The theory of similarity is well accepted and practiced in hydraulic engineering. Rushton (1952-3) capitulated by stating that

a pilot operation must be operated in such a way that not more than one fluid property force is predominant. These are the only conditions under which the fluid mechanics can be duplicated. If this can be achieved, it will be possible to predict large-scale power requirements and results. If this cannot be achieved, then scale-up cannot be made, and large scale results cannot be predicted.

8.1.3 Power & Vessel-Averaged Energy Consumption

The use of the N_p - R correlation is extremely common in the analysis of impeller-agitated systems. Such correlations are almost universally applied in the literature as a means of quantifying the behaviour of impeller-agitated systems, especially in the earlier studies. However, it is also known that the power number is only a fairly general consolidation of the combined effects of turbulent dissipation throughout the tank. Consequently, any application of the total vessel-averaged energy consumption, whether expressed by N_p , P/V or $P/\rho V$, as a description of the dynamical conditions in the impeller-agitated flow is necessarily and inherently linked to the actions of turbulence. Depending upon the particular process of interest that may be occurring within an impeller-agitated vessel, there may be numerous justifiable means whereby an observed dynamical condition at one scale may be scaled-up to some other scale, reflecting the particular

manner in which turbulence and bulk-flows influence that process. In practice, the analysis of energy consumption within impeller-agitated systems has been applied to numerous situations. For instance, chemical reaction rates, impeller-induced flocculation, heat transfer, mass transfer, solids-suspension and the general turbulence structure in impeller-agitated vessels have all been described by such general means as N_p - R correlations and vessel-averaged power consumption.

Holland (1962) recognized that two conditions are required for the scale-up of hydraulic features to be reliable: that one fluid regime dominate, and that the predominance of that regime not change as the scale be changed. This implies a deliberate suppression of certain dimensionless groups in favour of others in hydraulic modelling (e.g. operating in the high- R range or installing baffles to diminish the influence of F). His suggestion that

a N_p versus R curve for a particular geometrically similar system holds true whether the vessel size is five gallons or five-thousand gallons. The curve depends only on the geometrical configuration. This is the reason that experiments on very small models can be used to determine the power characteristics of large-scale plant mixing systems

is certainly a typical postulation of many of the early studies, although his later statement that constant tip velocity and constant P/V are also useful scale-up parameters seems to contradict this, as some simple algebra will confirm.

Zlokarnik (1987) studied a wide range of impeller types and sizes, applied to a number of mixing tasks, and found that if the homogenization of two liquids is being studied, the simultaneous maintenance of constant P/V and constant mixing time can also only occur over a narrow range of mixing times, such that P/V should only be thought to represent a condition of partial similarity. It is suggested that P/V is only a suitable criterion for scale-up when the impeller's power is to be dissipated as uniformly (isotropically) as is possible within the tank volume. In general, with respect to the suitability of P/V , he found that:

the complicated fluid-mechanical processes which determine the mass and heat transfer cannot generally be described adequately with the help of a simple criterion

Based upon a thorough presentation of turbulence characteristics, Gunkel & Weber (1975) suggested that:

since most of the energy is dissipated in the bulk of the tank, it is not surprising that correlations based upon the total power input per unit mass or per unit volume work so well for a number of processes in stirred tanks

An assumed corollary of their contention is that the spatial variation of turbulence and the relevant turbulence parameters should be similar for any two geometrically similar tanks, and thus should it be desired to scale-up (or scale-down) between them, P/V comparisons or the like provide a fairly reasonable means of comparison. Knowledge of the turbulence field would then presumably provide an exact means of comparison and scale-up, presuming that the spatial and dynamic variations were expressible in terms of bulk quantities such as P/V .

* Such a contention is disputed: many claim that the bulk of total dissipation occurs nearer the impeller and the impeller stream and not in the bulk of the tank.

8.1.4 Turbulence

In studying mass-transfer in a stirred tank, Bin (1984) stressed the importance of characterization of the basic turbulence parameters as fundamental to a comprehension of the links between mass transfer and hydrodynamics within stirred vessels and demonstrated that the spatial structure of turbulence within the tank could be described by:

$$\epsilon_{local} = \frac{1}{N_p} \bar{\epsilon}$$

Therefore, considering scale-up, if $P/\rho V$ be kept constant between any two model scales, it may be shown that:

$$\epsilon_{ratio} = \frac{1}{N_{p ratio}}$$

Conversely, if a constant value of N_p could be maintained between two scales (a reasonable expectation for high- R , flows), it may be speculated that:

$$\left| \frac{\epsilon}{\bar{\epsilon}} \right| = 1$$

By this derivation, the local proportional dissipation rate would depend only upon the geometry of the system (or more correctly, the resultant power consumption and dissipation caused by such geometry). As such, were complete geometric similarity maintained between two mixing units, then one could assume that at any two points located identically with respect to some dimensionless spatial location parameter, the maintenance of this parameter represents a reliable turbulence-based means of scale-up.

In a similar manner, Laufhutte & Mersmann (1985) addressed the quantification of flow-properties of the jet flow via turbulence characteristics. Following a general analysis of the theory of turbulence and turbulence dissipation, they described the manner in which such turbulence-based relations may be used for scale-up

the degree of turbulence, expressed as the ratio of the fluctuating velocity u' to the mean velocity u , is independent of the scale-up factor. This means that, in stirred vessels of different sizes, there will always be the same degree of turbulence which depends only on the geometry of and the location in the stirred vessel but not on the stirring speed or the tip velocity of the stirrer, as long as $R > 10'$ remain valid

In a later paper, Mersmann & Laufhutte (1985) contended that successful scale-up of processes wherein micromixing and diffusion are most important demand knowledge of the fluctuating velocity field in accordance with diffusivity as such parameters interact with the local dissipation rate ϵ . For such cases, they stated:

In scale-up procedures, the value of ϵ should remain constant at the point of inmission of the reactants.

It is assumed that one could substitute the term liquid-liquid mixing without any loss of general correctness ; such an assumption serves as the basis by which Bin's analysis is proposed to apply to scale-up.

Following Schwartzberg & Treyball (1968), together with the Kolmogorov theory of equilibrium, Placek & Tavlarides (1986) proposed that near the impeller disk plane:

$$\frac{\epsilon}{\epsilon} \propto \frac{D^2 h}{d^3}$$

a parameter which apparently must remain constant, *regardless of scale and independent of the impeller's speed*. The existence of a constant value of this ratio between two geometrically similar mixers of different scale was indeed observed in this study: as illustrated by Figures 6-18-1n through 6-18-7n, the b-based normalizations of the local dissipation rate all plotted upon the same curve for a given structural configuration, regardless of angular velocity. Finally, a scale-up mechanism is innate in any attempt to address the impeller-agitated turbulent flow field through the solution of the simplified Navier-Stokes or Reynolds equations. It seems that similarity solutions of the flow, based upon the number of such attempts that one may find in the literature^{*}, must be an appropriate course of action. By its very nature, a similarity solution should be applicable at any scale, with the only constraint being that the momentum, dimensions and relevant physical parameters conspire to establish a truly turbulent flow regime, thereby justifying the various simplifications of the governing equations that were required to enable the initial solution.

Kolar, Filip & Curev (1984), for example, proposed a model where the shape and dynamics of a tangential jet depend upon a number of constants (such as flux rate and swirl parameter) which, for a Rushton-type turbine, are dependent only upon geometrical conditions and thus would be applicable at any scale provided that geometrical similarity were maintained. If the model and prototype could both be operated in a state of turbulent flow, one could attempt to relate such quantities as the decay of centreline velocity u_{max} to the decay of ϵ , or perhaps even pursue a purely geometrical approach whereby complete similarity of velocity profiles would indicate complete similarity between two scales. In general, one should be able to correlate ϵ and energy concepts with the similarity present in the swirling radial jet. In this manner, after describing the hydraulic conditions in impeller-agitated mixers by a similarity solution, Kresta & Wood (1991) suggested that the axial decay of ϵ , once made dimensionless through division by v_{tip}^3/d

allows exact scale-up over the axisymmetric range

8.1.5 Other Processes

In contrast, different processes such as blending, dispersion and suspension seem to require the maintenance of slightly different power-based or turbulence-based scale-up parameters. For instance, Mamleev (1985) stated that:

for a field of local isotropic turbulence in which the similitude of mixing can be established regardless of the geometry of the mixing devices, it is proposed here that the decisive criterion of modelling should be the equality of the rms averages of the turbulent fluctuations in velocity

Based upon analysis of coalescence frequencies, he qualified this by stating that:

^{*} See, for example, Curev (1980), Dzaugashtin & Shelepov (1991), Kresta & Wood (1991), Kolar, Filip & Curev (1984), Kolar, Filip & Curev (1985), Filip, Kolar & Curev (1985-1), Filip, Kolar & Curev (1985-2), Rajaratnam (1975)

the modelling of turbulent mixing ... in a commercial mixer on the basis of equality of the average of the turbulent fluctuating velocity can be performed with adequate accuracy only for the mixing of a homogeneous liquid of a finely dispersed emulsion with drops smaller than the maximum size which is resistant to breakup

Considering blending of miscible liquids and considering the distinction between micro- and macro-mixing, Laufhütte & Mersmann (1985) suggested that:

it is therefore recommended to increase the tip velocity of the stirrer directly with d^n and thus to maintain the specific power input P/V constant

Mersmann & Laufhütte (1985) also discussed various other types of mixing such as homogenization, suspension and blending of various multi- and single-phase systems and stressed that depending upon the process that is being modelled in the vessel, different dynamic features of the flow can appear to be of significance. Specifically, they suggested that macro-mixing of inert systems and of suspensions should be described by means of average velocities.

Chudacek (1986) recognized that the most important elements of the flow are the fluid velocity, the resultant lift and drag effects, and the eddies produced by the impeller - thus also implying the importance of turbulence in such processes:

With increasing tank size, the distance between the source of eddies and the tank bottom also increases, so it is likely that in larger scale tanks, these eddies would decay more before reaching unsuspended solids. Therefore, hydrodynamic nonsimilarity of tanks of different scales would be further increased

In other words, the maintenance of constant P/V upon scale-up is likely not a valid scale-up approach for the case of impeller-induced solids suspension - an observation that is directly opposed to the traditional use of constant P/V ratio to scale-up those cases where solids suspension is not important. It does appear that the assumption of constant P/V becomes more valid and less responsive to changes in scale as the flow becomes more orderly, such as when draught tubes are present. In conclusion, the following caution is offered:

...an indiscriminate presentation of scale-up data without a full description of tank geometry, impeller geometry, solids concentration range, solids size range and tank size range is misleading and is mainly responsible for the lack of agreement of scale-up parameters reported by various workers. The current practice of using scale-up procedures based on linear extrapolation of scale-up exponents, often obtained on very small tanks, cannot be considered a correct practice and is certainly due for a review.

Similarly, Geisler, Burmann & Mersmann (1993) studied suspension criteria, and although they applied a novel approach to the theoretical analysis of such problems (including separation of the flow energy's dissipation into swirling and suspending components and incorporation of density differences), they were nonetheless forced to conclude that:

there is no simple and constant scale-up rule possible in order to describe the power input for a large range of suspension properties, tank size, particle size, geometric conditions or comparable suspension criteria. For more than five decades we have asked the wrong question, i.e. "What is the scale-up rule?"

Finally, in studies of liquid-liquid dispersions, Nishikawa, Mori, Fujieda & Kayama (1987) found that the maintenance of constant $P/\rho V$ is a valid scale-up factor, but that if scale-up is performed based upon constant $P/\rho V$, the contribution of middle-scale turbulent eddies to the energy spectrum increases, thereby causing smaller drop sizes in the emulsions. As such, a scale-invariant, completely similar flow condition is not seen to exist for such processes, a further illustration of the fact that most traditional scale-up rules are generally inconsistent with one another.

8.2 Application of Experimental Results to Scale-up Mechanisms

8.2.1 Introduction

The previous pages of this report have attempted to quantify the impeller's observed behaviour and the resultant flow state via a number of dimensionless parameters. Based upon this analysis, a number of general statements describing the state of flow may be made:

- first, it appears that the bulk average velocities are well normalized by the tip-speed, especially near the impeller's blade, but also throughout the region that may be described as swirling radial jet-like flow;
- second, it appears that the turbulent velocities are also well normalized by the tip-speed (perhaps even better than are the average velocities), and that the assumption of near-isotropy within the swirling radial jet-like flow is also valid;
- third, the observed maximum turbulent velocity anywhere along the axis of the impeller-generated jet seems to occur in a definite, radially invariant multiple of the local maximum average velocity, thereby validating the presupposition that the impeller-generated flow may be treated as an angular analogue to the free-jet^{*};
- fourth, considering linear dimension, it appears that the width of the impeller-generated jet is approximately equal to the blade's height, and that such a correspondence seems to exist regardless of scale, and;
- fifth, the occurrence of constant values of the power number, N_p , was found to be analogous to the existence of a λ -invariant, ω -invariant dimensionless dissipation rate:

$$\epsilon \propto \frac{v_{tip}^3}{b} \propto \bar{\epsilon}$$

Regardless of scale, and for each experimental configuration, such consistently similar behaviour was (to varying degrees of accuracy) inevitably observed.

Now that the dynamic and hydraulic state present in these tests may be well defined at numerous scales and for various structural configurations, a series of speculations may now be

^{*} specifically, cf. Antonia, Satyaprakash & Hussain (1980).

made concerning the manner in which the various scale-models should be operated in order to simulate certain dynamical aspects of the full-scale facility. In this manner, the relevant model-scale operational parameters will be presented and analyzed with respect to the concepts of dissipation, power, torque, circulation and flocculation in order to demonstrate quantitatively a constant theme in the study of impeller-agitated mixing, that there exists a variety of individually inconsistent scale-up mechanisms which preclude the existence of a universal scale-up law which addresses the totality of conditions which may be encountered in practice.

8.2.2 The Full-Scale

Given that one of the goals of a model test could be to duplicate those conditions present in the full-scale facility with respect to the dynamics of mixing therein, one must first determine exactly what conditions are to be duplicated.

Considering velocities, as it has been illustrated that normalization of both the average and turbulent velocities by the tip-speed allows definition of the local velocity field at any scale, the typical full-scale velocities may be estimated directly from the laboratory data together with a definition of the full-scale tip-speed. In practice, the angular velocity of the full-scale impeller is continually varied, reflecting changes in the influent water quality and flow rate. According to NHC (1993), the full-scale impeller is operated at angular velocities up to 10 rpm; for the sake of simplicity, a single representative angular velocity will be assumed, namely 8 rpm (or 0.838 rad/s). Taking this speed together with the full-scale impeller diameter, $d = 4.263$ m, a representative full-scale tip-speed may be defined.

Unfortunately, unlike the velocities, the turbulent dissipation rate is not something that can be easily measured at the full-scale. Instead, the results of the small-scale laser studies, specifically those representing configuration 03, will be applied here in an attempt to estimate a representative full-scale value of ϵ . For simplicity, only the maximum observed value of dimensionless ϵ at a point near the impeller will be considered. This quantity may be estimated from two different sets of data. Firstly, considering the laser analysis, it was demonstrated (*e.g.* Figures 6-1-5n through 6-1-8n) that at a point near the impeller's blade (that is $2r/d = 1.044$), and at any angular velocity, a typical maximum turbulent velocity is approximately $0.25 v_{tip}$. Assuming isotropy, and recalling the full-scale blade height, the maximum full-scale local turbulent dissipation rate near the impeller may be estimated as:

$$\epsilon_{full} \sim \frac{u'^3}{\frac{1}{2} b} = \frac{(k v_{tip})^3}{\frac{1}{2} b} = \frac{[0.25 (0.838 \frac{rad}{s})(\frac{1}{2})(4.263 m)]^3}{\frac{1}{2} (1.08 m)} = 0.165 \frac{m^2}{s^3}$$

Alternatively, from the plots of vertical variation of the b-based dimensionless dissipation rate (Figures 6-5 through 6-13), it is found that regardless of angular velocity, the maximum value occurs at approximately the $\frac{1}{2}$ -blade height, and that this value is approximately 0.032. In other words, the resultant energy dissipation rate at a specific point is fully defined by geometric quantities b and d for a given angular velocity ω or N . Therefore, a second estimate of the full-scale turbulent dissipation rate near the impeller is possible:

$$\begin{aligned}
 \epsilon &= \epsilon_{\text{dimensionless}} \frac{V_{\text{tip}}^3}{b} \\
 &= 0.032 \frac{(\frac{1}{2} \omega d)^3}{b} \\
 &= 0.032 \frac{[\frac{1}{2} (0.838 \frac{\text{rad}}{\text{s}}) (4.263 \text{ m})]^3}{1.08 \text{ m}} \\
 &= 0.169 \frac{\text{m}^2}{\text{s}^3}
 \end{aligned}$$

Actually, the close correspondence between these two estimates is remarkable considering that ϵ is defined by a cubed quantity. For the purposes of illustration, the average of these two estimates of ϵ will be used here.

Finally, these relevant full-scale representative estimates may now be tabulated in Table 8-1:

Table 8-1
typical properties of full-scale impeller & flow (no tangential inflow)

scale	d (m)	N (rpm)	v_{tip} (m/s)	b (m)	ϵ (m ² /s ³)
1:1	4.263	8	1.79	1.08	0.167

8.2.3 Turbulent Dissipation Rate

8.2.3.1 Maintenance of the Local Turbulent Dissipation Rate

If it were now required to duplicate the same state of local turbulent energy in a scale-model as that which exists at the full-scale, the required model-scale operational parameter (*i.e.* angular velocity, ω) could again be determined through the assumption of a scale-invariant dimensionless turbulence structure. A possible justification for maintenance of a constant local dissipation rate lies in Rice & Baud (1990) who examined the progress of coupled chemical reactions as indicators of the degree of mixing. They concluded that:

for turbulent mixing in geometrically similar vessels, equal micromixing ... will be obtained during scale-up if the value of energy dissipation in the reaction zone is held constant

Or, one may look to Laufhütte & Mersmann (1985), from which it is implied that because microscale eddies ultimately define the molecular-scale processes, the local dissipation rate, ϵ , is necessarily held constant if the size of the particles is unchanged.

By substituting the estimate of the full-scale maximum turbulent dissipation rate into the above expression for the maximum dimensionless dissipation rate, together with the appropriate *model-scale* dimensions, the required model-scale angular velocity follows directly. Firstly, considering the 1:10-scale model ($d = 0.4263 \text{ m}$, $b = 0.108 \text{ m}$), in order to reproduce the full-scale turbulent dissipation rate, it may be shown that:

$$\frac{\epsilon_{10}}{\epsilon} \approx \frac{c}{\frac{v_{tp}}{b}^3} \approx 0.032$$

$$\frac{0.167 \frac{m^2}{s^3}}{\frac{(\frac{1}{2} 0.4263 m \omega_{10})^3}{0.108 m}} = 0.032$$

$$\omega_{10} = 3.871 \frac{rad}{s}$$

$$\therefore N_{10} = 37 \text{ rpm}$$

For the 1:55-scale model ($d=10.37$ cm, $b=2.63$ cm) and 1:41-scale model ($d=7.66$ cm, $b=1.94$ cm), the required angular velocities may be defined in exactly the same manner. The results of this analysis are summarized in the following table, Table 8-2:

Table 8-2
confined impeller (configuration 03)
required model-scale angular velocities to match full-scale ϵ

scale	local ϵ (m^2/s^3)	required N (rpm)
full	0.167	8
1:10	0.167	37
1:41	0.167	95
1:55	0.167	116

Consequently, it appears that at sometime during the testing program, each of the three scale-models was operated at an angular velocity which enabled the full-scale local dissipation rate (that is, at least an estimate of it for the case of zero tangential inflow) to be duplicated at a point near the impeller's blade.

8.2.3.2 Flocculation

Considering the practical implications of the local dissipation rate, it is well established that the processes of destabilization, coagulation and flocculation depend primarily upon the local turbulent flow state. For instance, Camp & Stein (1943) found that the number of collisions, N (s^{-1}), between two flocculant particles, denoted 1 and 2, could be estimated as:

$$N = \frac{1}{6} N_1 N_2 \overline{G} (d_1 + d_2)^2$$

where

$$\overline{G} = \sqrt{\frac{\epsilon}{\nu}} = \sqrt{\frac{P}{\rho \nu}}$$

Similarly, the well known Smoluchowski rate expression^{*} states that the number of collisions, k , (and thus the rate of flocculation) depends directly upon the surrounding velocity field:

$$k = \frac{1}{6} (d_1 + d_2)^3 \left(\frac{du}{dz} \right)$$

All flocculation-rate expressions may be defined by the following general expression, wherein only the values of the constants and the nature of the coefficients differs, Amirtharajah & Tambo (1991):

$$k \propto (d_1 + d_2)^3 \left(\frac{\epsilon}{\nu} \right)^{1/2}$$

where the expression $(\epsilon/\nu)^{1/2}$ represents some form of a dissipation rate, be it local, average or otherwise. According to such formulations, it may be inferred that the rate of flocculation depends solely upon the ambient local turbulent flow structure, or, more generally, upon the manner in which the impeller-applied energy is dissipated.

Assuming the validity of such formulas, one can attempt to express the ratio^{**} of the rates of flocculation that would be observed at any two scales, and at the same point in geometrically-similar space:

$$\frac{N_2}{N_1} = \frac{k_2 (d_a + d_b)_2^3 \left(\frac{\epsilon_2}{\nu_2} \right)^{1/2}}{k_1 (d_a + d_b)_1^3 \left(\frac{\epsilon_1}{\nu_1} \right)^{1/2}} = \frac{(d_a + d_b)_2^3 \sqrt{\epsilon_2}}{(d_a + d_b)_1^3 \sqrt{\epsilon_1}}$$

It is interesting to recognize the dependence of the flocculation-rate ratio upon the square-root of ϵ . If the ratio

$$\frac{\epsilon}{\nu}$$

is indeed a scale-invariant, ω -invariant constant at any particular point in space, the maintenance of constant ϵ at a point demands the maintenance of constant power per unit volume for the overall system. In other words, it is implied that the flocculation rate would be the same at each scale (assuming of course that the sizes of the incipient flocs were λ -invariant) if power per unit volume (or $P/\rho V$) were held constant at each scale. Such a consideration seems to justify the traditional assertion that certain mixing process can be scaled-up by the maintenance of constant power per unit volume.

Returning now to the ratio of the rate of flocculation, one may re-state the governing expression as:

* e.g. Amirtharajah & Tambo (1991) as a general treatment of this expression

** where subscript 2 indicates the larger, and subscript 1 indicates the smaller of the two models

$$\frac{N_2}{N_1} = \frac{(d_a + d_b)_2^3}{(d_a + d_b)_1^3} \sqrt{\frac{r_2^3 \omega_2^3 b_1}{r_1^3 \omega_1^3 b_2}} = \frac{(d_a + d_b)_2^3}{(d_a + d_b)_1^3} \sqrt{\frac{\lambda_1^2 \omega_2^3}{\lambda_2^2 \omega_1^3}}$$

Since flocculation has been assumed to initiate by molecular-scale interactions between coagulant and colloidal particle, then it could be argued that the diameters of the flocculant particles (d_a and d_b) would, at least initially, be of the same order. In this manner, the ratio may now be simplified to:

$$\frac{N_2}{N_1} \approx \frac{\lambda_1}{\lambda_2} \sqrt{\frac{\omega_2^3}{\omega_1^3}}$$

If one again wished to maintain the same local ϵ at every scale, then the angular velocities from Table 8-1 should be inserted into this simplified expression in order to determine the resultant ratio of flocculation rate. In this manner it may be shown that:

$$\begin{aligned} \frac{N_{full}}{N_{10}} &\approx \frac{10}{1} \sqrt{\frac{(8rpm)^3}{(37rpm)^3}} = 1.00 \\ \frac{N_{full}}{N_{41}} &\approx \frac{41.130}{1} \sqrt{\frac{(8rpm)^3}{(95rpm)^3}} = 1.00 \\ \frac{N_{full}}{N_{55}} &\approx \frac{55.647}{1} \sqrt{\frac{(8rpm)^3}{(116rpm)^3}} = 1.00 \end{aligned}$$

which, of course, is the obvious result given the assumptions imposed upon this analysis.

8.2.3.3 Dynamic Force

Whereas certain assumptions were made in this analysis concerning the relative sizes of the flocculating particles, in reality, the floc's cohesive qualities would limit the maximum size of floc that could be maintained. Thus, it is not possible to increase the rate of flocculation (or, similarly, the rate of some chemical reaction which also depends upon the local turbulence) without bound, because eventually a floc of unacceptable quality would result. The maximum turbulence-induced force acting upon a floc of diameter d_f can be estimated (for the case where $d_f < \text{turbulent microscale}$) by a simple expression, Amirtharajah & Tambo (1991):

$$\Delta F \propto \rho \left(\frac{\epsilon}{\mu} \right) d_f^4$$

For a consideration of the so-called floc-strength, one may look to Tambo & Watanabe (1979), as presented in Amirtharajah & Tambo (1991):

$$\begin{aligned} d_{f_{max}} &\approx k \bar{\epsilon}^{-a} \\ &\approx 1.25 \bar{\epsilon}^{-0.3} \end{aligned}$$

By substituting the expression for maximum floc diameter into the expression for the hydraulic force, an estimate of the limiting maximum force may be expressed:

$$F_{\max} \propto \rho \left(\frac{\epsilon}{\nu} \right) k^4 (\bar{\epsilon})^{1.2}$$

Thus, there must be some limiting maximum value of ω beyond which floc-formation is impeded.

This expression may be used, together with the fact that the vessel-averaged dissipation rate is proportional to $(v_{ip})^3/b$, to define how this limiting value of angular velocity, ω , varies with geometric scale:

$$\frac{F_{\max_2}}{F_{\max_1}} = \frac{k \rho_2 \epsilon_2 k_f^4 \omega_2^{-12a} d_2^{-8a}}{k \rho_1 \epsilon_1 k_f^4 \omega_1^{-12a} d_1^{-8a}} = \frac{\epsilon_2 \omega_2^{-12a} d_2^{-8a}}{\epsilon_1 \omega_1^{-12a} d_1^{-8a}}$$

From Amirtharajah & Tambo (1991), exponent 'a' has been found to have a value of approximately 0.3. Thus, for the force ratio, it may be approximated that:

$$\frac{F_{\max_2}}{F_{\max_1}} = \frac{\epsilon_2 \omega_2^{-3.6} d_2^{-2.4}}{\epsilon_1 \omega_1^{-3.6} d_1^{-2.4}}$$

If the local dissipation rate be maintained at each scale, the angular velocities from Table 8-2 can again be applied. For the case of the 1:55-scale model, the resultant force ratio to the full-scale may be defined:

$$\frac{F_{\max_{full}}}{F_{\max_{55}}} = \frac{(0.167 \frac{m^2}{s^3}) (8rpm)}{(0.167 \frac{m^2}{s^3}) (116rpm) (\frac{1}{55.647})^{-2.4}} = 1$$

Similarly, it can be shown that for the 1:41 and 1:10 scales, the force ratio is unity provided that the same turbulent dissipation rate be maintained at each scale.

8.2.3.4 Floc Size

Alternatively, one can extend the concept of 100% geometric similarity to the floc sizes as well. In this manner, assuming that the model-scale floc sizes can be scaled as

$$\frac{d_f}{d_{f_1}} = \frac{\lambda_1}{\lambda_2}$$

a comparison of the maximum floc size may be used to define the angular velocities that are necessary to preserve such a ratio. Beginning with Tambo & Watanabe's expression for maximum floc size, it may be shown (for the comparison of the 1:10-scale to the full-scale) that:

$$\frac{d_{f_{full}}}{d_{f_{10}}} \propto \frac{1.25 \bar{\epsilon}_2^{-0.3}}{1.25 \bar{\epsilon}_1^{-0.3}} = \frac{\lambda_{10}}{\lambda_{full}} = \frac{10}{1}$$

This expression is seen to be equivalent to:

$$\epsilon_{full}^{-0.3} = 10 \epsilon_{10}^{-0.3}$$

$$\frac{v_{tip}^3}{b} \Big|_{full} = 10^{3.33} \frac{v_{tip}^3}{b} \Big|_{10}$$

After substituting $N_{full} = 8$ rpm (or $\omega_{full} = 0.838$ rad/s) and $b_{full} = 1.08$ m, and $b_{10} = 0.108$ m into this expression, it is found that the 1:10-scale model must be run at an angular velocity of 480 rpm in order to maintain geometric similarity of floc sizes. The corresponding value of ϵ , the local turbulent dissipation rate, may be defined for the 1:10-scale model after substitution of $N = 480$ rpm into:

$$\epsilon_{10} \propto \epsilon_{dimensionless} \frac{V_{tip}^3}{b} = 0.0320 \frac{\frac{1}{2} (4.263 \text{ m}) (50.237 \frac{\text{rad}}{\text{s}})^3}{1.08 \text{ m}} = 365 \frac{\text{m}^2}{\text{s}^3}$$

Corresponding values of N and ϵ may be defined in the same manner for the other model scales. The results are summarized in the following table, Table 8-3:

Table 8-3
confined impeller (configuration 03)
required model-scale parameters to maintain geometric similarity of floc sizes

scale	local ϵ (m^2/s^3)	required N (rpm)
full	0.167	8
1:10	365	480
1:41	40595	5929
1:55	249000000	132546

Obviously, such values are well beyond the capabilities of any model that was investigated in this study, and very likely any model that can be built at all.

8.2.3.5 Rates of Physical and Chemical Processes

Considering the rate of chemical reactions, because such reactions occur at the molecular level, and because microscale turbulent eddies provide the convective flow which gives rise to intermolecular collisions, there must be a definite link between the reaction rate and the impeller. This link is illustrated by the fact that the expression for chemical reaction rate in impeller-agitated vessels invariably contains some expression of energy input or dissipation rate. Numerous expressions have been developed to describe such molecular-scale processes, ranging from expressions of the kinetics of metal ion extraction to the kinetics of flocculation to the kinetics of mass-transfer.

Bin (1984) proposed that the kinetics of gas-liquid mass-transfer reactions may be defined by the expression

$$k_L d. = c_{26} \left(\frac{\bar{e}}{v} \right)^P$$

where exponent, P , is dependent upon the liquid medium (*e.g.* $P = 1/3$ for aqueous systems, $P = 1/4$ for organic systems), and where molecular diffusivity, $d.$, is assumed to be constant with respect to angular velocity and scale. Again, the energy applied via the impeller is the significant determinative element in such expressions - only the exponent is different.

Again, recalling the correspondence among ϵ , N_p and $P/\rho V$, this expression may be restated as:

$$k_L d. = c_{26} (r^3 \omega^3 b^{-1} v^{-1})^P$$

Thus, if it were wished to duplicate the kinetics of gas-liquid mass-transfer at any scale, the required model settings may be estimated by:

$$\frac{k_L d. |_2}{k_L d. |_1} = \frac{c_{26} (r_2^3 \omega_2^3 b_2^{-1} v^{-1})^P}{c_{26} (r_1^3 \omega_1^3 b_1^{-1} v^{-1})^P}$$

By assuming that $P = 1/3$ (aqueous systems), and assuming that the diffusivity, $d.$, is scale-invariant, this expression may be further simplified:

$$\frac{k_L |_2}{k_L |_1} = \frac{(r_2^3 \omega_2^3 b_2^{-1})^{\frac{1}{3}}}{(r_1^3 \omega_1^3 b_1^{-1})^{\frac{1}{3}}} = \frac{r_2 \omega_2}{r_1 \omega_1} \left(\frac{b_1}{b_2} \right)^{\frac{1}{3}}$$

In order to quantify the effect of scale, consider again the full-scale and the 1:10-scale. The ratio of mass-transfer rates takes the form

$$\frac{k_L |_{full}}{k_L |_{10}} = \frac{\lambda_{10} \omega_{full}}{\lambda_{full} \omega_{10}} \left(\frac{\lambda_{full}}{\lambda_{10}} \right)^{\frac{1}{3}} = \frac{\omega_{full}}{\omega_{10}} \left(\frac{\lambda_{10}}{\lambda_{full}} \right)^{\frac{2}{3}} = \frac{\omega_{full}}{\omega_{10}} 10^{\frac{2}{3}}$$

If it were required to establish the same rate of mass-transfer at the model scale as that which exists at the full-scale, by inserting the assumed full-scale angular velocity of $\omega = 0.838$ rad/s (8 rpm), the necessary angular velocity for the 1:10-scale model may be determined:

$$\frac{k_L |_{full}}{k_L |_{10}} = \frac{\omega_{full}}{\omega_{10}} 10^{\frac{2}{3}} = \frac{0.838 \frac{rad}{s}}{\omega_{10}} 10^{\frac{2}{3}} = 1.0$$

$$\omega_{10} = 3.8965 \frac{rad}{s} \rightarrow N_{10} \approx 37.1 \text{ rpm}$$

By applying a similar approach for the 1:55-scale and 1:41-scale models, the required angular velocities may easily be found for those scales. The results of such an analysis are presented in the following table, Table 8-4:

Table 8-4
confined impeller (configuration 03)
required model-scale parameters to maintain full-scale mass-transfer rate

scale	local ϵ (m ² /s ³)	required N (rpm)
full	0.167	8
1:10	0.167	37.1
1:41	0.167	95.4
1:55	0.167	116

These figures immediately demand comparison to those in Table 8-1, representing the case where ϵ_{full} is maintained at all scales. Therefore, it is clearly illustrated that the rate of reaction is also dependent upon ϵ . As a further illustration, the results of Ju, Chiu & Hoh (1991) exhibit similar behaviour. They found that exclusive of geometry and at several model-scales, the rate of a copper extraction reaction depended only upon P/V , the vessel-averaged dissipation rate:

$$k = -3.0 + 0.4 \log \frac{P}{V}$$

where the coefficient $\cdot P$, in Bin's equation is now 0.4 instead of $\frac{1}{3}$. Again, this result holds only for turbulent conditions.

8.2.3.6 Summary

If the goal of the maintenance of a constant turbulent dissipation rate is an appropriate modelling constraint, certain general trends are found to exist. Clearly, as λ increases (*i.e.* the model becomes smaller), successively higher values of ω , the impeller's angular velocity, are required. Accordingly, there appears to be sufficient justification of the contention that one cannot scale-up all aspects of a particular process by keeping ϵ constant. Although the maintenance of a constant ϵ guarantees that kinetic quantities such as reaction rates, mass-transfer rates and flocculation rates also remain constant, there is apparently no feasible manner in which anything other than liquid-liquid aqueous reactions and commixtures may be performed where both the geometric scale - specifically, with regard to floc sizes - and the reaction rate can be simultaneously equal to the full-scale, unless temperature or other properties of the liquids be altered, or unless the testing be done over a very limited range of λ .

8.2.4 Scaling Based upon G and Power per Unit-Volume

8.2.4.1 Derivation

The velocity gradient, G , has traditionally been treated in a very simple manner in the matter of scale-up. Whenever bench-scale velocity gradients are applied in the design of full-scale systems, the original meaning of Camp & Stein's original velocity gradient is often greatly abused. From Camp & Stein's (1943) original derivation:

$$G = \sqrt{\frac{P}{\mu V}} = \sqrt{\frac{P}{\rho \nu V}} = \sqrt{\frac{\epsilon}{\nu}}$$

it is the term V , the volume, that has been subject to the most misinterpretation in the design of large-scale tanks. Commonly, jar-tests have served as the means of analysis ; once a floc of

suitable quality is obtained, the power is measured, G is computed, and then it is assumed that G will remain constant at the full-scale. However, it is usually the case that the full-scale volume is, in relative terms, well beyond that which existed at lab-scale, thereby causing excessively powerful impeller systems to be specified at the full-scale. Such misapplications are unfortunate given that at the outset, Camp & Stein (1943) defined G such that:

Under steady conditions of work input, there is a mean velocity gradient which corresponds with the mean value of Φ [power per unit volume]

In other words, for a specific point within the mixing vessel or mixing tank, it is assumed that the local velocity gradient existing there must be some definite multiple of the vessel-averaged velocity gradient.

As the term "velocity gradient" actually represents something analogous to a Stokes-type dissipation function, it is appropriate to re-express G in terms of the overall, vessel-averaged dissipation rate. In this analysis, it is necessary that the power number (assumed to be based upon angular velocity, n , in rps) be divided by the factor 2π (thereby changing angular velocity from rps to radians per second) in order to maintain dimensional consistency:

$$G = \sqrt{\frac{P}{\mu V}} = \sqrt{\frac{N_p \rho \omega^3 d^5}{k(2\pi)^3 d^3 \nu}} = \sqrt{\frac{\rho}{k\nu(2\pi)^3}} \sqrt{N_p \omega^3 d^2} \propto \sqrt{N_p \omega^3 d^2}$$

Between any two scales, if 100% geometric similarity be assumed, and if the flow regimes at each scale be such that the power numbers are approximately constant and equal, the ratio between any two scale-models' G -values may be defined as:

$$\frac{G_2}{G_1} = \frac{k_2 \sqrt{N_{p2} \omega_2^3 d_2^2}}{k_1 \sqrt{N_{p1} \omega_1^3 d_1^2}} = \left(\frac{\omega_2}{\omega_1}\right)^{\frac{3}{2}} \left(\frac{d_2}{d_1}\right) = \left(\frac{\omega_2}{\omega_1}\right)^{\frac{3}{2}} \left(\frac{\lambda_1}{\lambda_2}\right)$$

where k simply represents a constant coefficient of proportionality. By comparison, the ratio of average power per unit mass may be expressed in the same manner:

$$\frac{\overline{\epsilon}_2}{\overline{\epsilon}_1} = \frac{N_{p2} \rho_2}{N_{p1} \rho_1} \left(\frac{\omega_2^3 d_2^5}{\omega_1^3 d_1^5}\right) \frac{k d_1^3}{k d_2^3} = \frac{\omega_2^3 d_2^2}{\omega_1^3 d_1^3} = \left(\frac{\omega_2}{\omega_1}\right)^3 \left(\frac{\lambda_1}{\lambda_2}\right)^2$$

And, for the local dissipation rate:

$$\frac{\epsilon_2}{\epsilon_1} = \frac{(k_{u2}^{1/2} \omega_2 d_2)^3 (1/2 b_1)}{(k_{u1}^{1/2} \omega_1 d_1)^3 (1/2 b_2)} = \left(\frac{\omega_2}{\omega_1}\right)^3 \left(\frac{\lambda_1}{\lambda_2}\right)^2$$

In this manner, it is immediately apparent that if the flow state be amenable to such non-dimensional normalization, if 100% geometric similarity be maintained at each scale, and if the flow numbers be both approximately constant and approximately identical, then these three terms may be related by:

$$\frac{\epsilon_2}{\epsilon_1} = \frac{\overline{\epsilon_2}}{\overline{\epsilon_1}} = \frac{G_2^2}{G_1^2}$$

It follows that whenever the velocity gradient, G , be maintained constant between any two scales, the concomitant result is that the ratios of dissipation rates (local and average) must also remain constant. Conversely, whenever the square root of power per volume be kept constant upon scale-up, it is implied that G is simultaneously being maintained constant. In other words, ϵ and G describe exactly the same quality of the flow, provided that the condition of 100% geometric similarity be maintained.

8.2.4.2 Duplication of the Full-Scale G and $P/\rho V$

As an illustration of this principle, if the full-scale values of G and $P/\rho V$ were known, and if the full-scale N_p would also be constant and equal to the values of N_p which were determined for the small-scale models, it would be possible to define appropriate model-scale settings of ω at which the full-scale values of G and $P/\rho V$ (or some fraction thereof) could be duplicated.

Firstly, considering $P/\rho V$, it may be assumed from Table 6-4 that the full-scale impeller would have a power number of 3.0. For the volume term, V , any combination of relevant linear dimensions is appropriate, so long as consistency be maintained at all scales - here, assume simply that V is proportional to d^3 . Thus:

$$\overline{\epsilon} \Big|_{full} = \frac{P}{\rho V} \Big|_{full} \approx \frac{N_p \rho \omega^3 d^5}{\rho d^3 (2\pi)^3} = \frac{N_p \omega^3 d^2}{(2\pi)^3} = \frac{1}{(2\pi)^3} (3.0) \left(0.838 \frac{rad}{s}\right)^3 (4.263 m)^2 = 0.129 \frac{m^2}{s^3}$$

It is worth noting that the assumed value of the maximum local ϵ is greater than the vessel-averaged value of ϵ ; the magnitude of this difference would be even greater if the entire volume of the clarifier were used here. To maintain this value of $P/\rho V$ at another scale, the required model-scale values of ω may now be found - here, consider the 1:10-scale model:

$$\omega_{10} = \sqrt[3]{\frac{\overline{\epsilon}}{N_p d^2}} = \sqrt[3]{\frac{(2\pi)^3 0.129 \frac{m^2}{s^3}}{(3.0)(0.4263 m)^2}} = 3.889 \frac{rad}{s}$$

This angular velocity is equivalent to $N_{10} = 37$ rpm. Similarly, it may be shown that $N_{41} = 95$ rpm, and $N_{ss} = 117$ rpm are the resultant angular velocities at the other scales.

Considering the full-scale again, G may be estimated by:

$$G_{full} \approx \sqrt{\frac{N_p \rho \omega^3 d^5}{\rho V d^3 (2\pi)^3}} = \sqrt{\frac{(3.0) \left(1000 \frac{kg}{m^3}\right) \left(0.838 \frac{1}{s}\right)^3 (4.263 m)^5}{\left(1000 \frac{kg}{m^3}\right) (9.85 \times 10^{-7} \frac{m^2}{s}) (0.4263 m)^3 (2\pi)^3}} = 361 \frac{1}{s}$$

By inserting the appropriate model-scale dimensions into this expression, and by assuming that the full-scale G -value needed to be duplicated at the other scales, it could again be shown that $N_{10} = 37$ rpm, $N_{41} = 95$ rpm, and $N_{ss} = 117$ rpm are the required angular velocities at the other scales.

The results of this analysis may be summarized in the following table, Table 8-5:

Table 8-5
confined impeller (configuration 03)
required model-scale parameters to maintain full-scale energy-based quantities

scale	G (1/s)	P/ρV (m ² /s ³)	local ε (m ² /s ³)	required N (rpm)
full	361	0.129	0.167	8
1:10	361	0.129	0.167	37
1:41	361	0.129	0.167	95
1:55	361	0.129	0.167	116

As such, it is proven that by maintaining one of these ϵ -dependent quantities, all of the others are simultaneously maintained. Of course, there are many assumptions in this analysis. It was assumed that the flows were completely turbulent in all cases, which may or may not be the case in the actual full-scale facility. It was also assumed that, *for whatever reason*, it was necessary to maintain a constant value of the dissipation rate and/or G - this may be a reasonable assumption for the case of liquid-liquid systems for duplicating the chemical kinetics, but over anything but the smallest range of model-scales, the usefulness of such a constancy becomes questionable given the increasing error that is incurred in the model-scale reaction times. Finally, this analysis assumed the lack of any tangential inflow whatsoever in the draught tube - an approach that will soon be seen to be invalid. However, despite these limitations, there is probably a certain amount of general truth present in such an analysis.

Finally, concerning the apparent correspondence among ϵ , P/ρV and G, it should be noted that whereas G and ϵ were determined from torque-transducer measurements of power, ϵ was determined from laser-doppler velocimetry and the relevant impeller geometry. The resultant correspondence in estimates of ω from two such different sources is encouraging.

8.2.5 Maintenance of Constant Velocities

In essence, the maintenance of constant velocities is intrinsically linked to the existence of a scale-invariant, ω -invariant flow-field throughout the impeller-draught tube system. If it is known that a velocity at a point in the impeller-agitated flow occurs as some definite fraction of the impeller's tip-speed, then in order to maintain such a velocity at a constant value at another scale implies that

$$\frac{1}{2} \omega_2 d_2 = \frac{1}{2} \omega_1 d_1$$

at any scale. In principle, the maintenance of a constant tip-speed finds its greatest popularity in the study of suspensions. Following Chudacek (1986), for example, it may be assumed that equivalent suspension homogeneity is maintained by the establishment of an equivalent upward velocity regime. This approach must be carefully considered with respect to scale. Whereas this "constant peripheral velocity criterion" is apparently based upon inert silicate suspensions of constant and invariant size, 100% similarity between scales is only maintained if the size of the particles may also be scaled accordingly.

A more general statement of the effect of a constant tip-speed lies in the application of drag-force analysis. Typically, if a particle is acted upon by a drag-force within a flow-field, then the local velocity must represent some fraction of the tip-speed, and the ratio of forces applied

to two geometrically scaled particles (where scale-2 represents the larger model and scale-1 represents the smaller model) may be described as follows:

$$\frac{F_2}{F_1} = \frac{\frac{1}{2} \rho_2 u_2^2 A_{P1}}{\frac{1}{2} \rho_1 u_1^2 A_{P1}} = \frac{(k_u \frac{1}{2} d_2 \omega_2)^2 k_A d_2^2}{(k_u \frac{1}{2} d_1 \omega_1)^2 k_A d_1^2} = \frac{d_2^4 \omega_2^2}{d_1^4 \omega_1^2}$$

But, given the constraint that the tip-speed must be the same at each scale, this expression is simplified to:

$$\frac{F_2}{F_1} = \frac{d_2^4 \omega_2^2}{d_1^4 \omega_1^2} = \frac{(d_2 \omega_2)^2}{(d_1 \omega_1)^2} \frac{d_2^2}{d_1^2} = 1.0 \frac{d_2^2}{d_1^2}$$

Apparently, this analysis shows that as the model becomes smaller (λ_2 increases), the resultant shearing force on a geometrically scaled particle would decrease if the impeller's tip-speed were maintained constant. However, if the floc-sizes do not scale geometrically, such an analysis is not so straightforward. Indeed, it has already been shown (Table 8-2) that the maintenance of geometric similarity of the maximum floc sizes requires nearly untenable angular velocities as the model becomes smaller.

Instead, the effects of constant-velocities on flocculant particles may also be analyzed by Tambo & Watanabe's general expression for the maximum floc-size. For the specific case of the 1:10-scale model versus the full-scale, the ratios of maximum size of the resultant flocculant particles could be estimated as:

$$\frac{d_{f_{max}}|_{full}}{d_{f_{max}}|_{1:10}} \approx \frac{1.25 \overline{\epsilon}_{full}^{-0.3}}{1.25 \overline{\epsilon}_{10}^{-0.3}} \approx \left[\frac{(\frac{1}{2})^3 d_{full}^3 \omega_{full}^3 b_{10}}{(\frac{1}{2})^3 d_{10}^3 \omega_{10}^3 b_{full}} \right]^{-0.3} \propto 1.0 \left(\frac{1}{\lambda_{10}} \right)^{-0.3} = 10^{0.3} \approx 2$$

This indicates that for the maintenance of constant tip-speed upon scale-down to the 1:10-scale, the maximum attainable floc size decreases.

However, this decrease is not a linear decrease: although the overall dimensions of the impeller are decreased by one-tenth, the resultant floc-size is decreased by only one-half. Similarly, for the other model scales, it may be shown that:

$$\begin{aligned} \frac{d_{f_{max}}|_{full}}{d_{f_{max}}|_{1:41}} &= (41.130)^{0.3} \approx 3.05 \\ \frac{d_{f_{max}}|_{full}}{d_{f_{max}}|_{1:55}} &= (55.647)^{0.3} \approx 3.40 \end{aligned}$$

At even smaller model-scales, this effect becomes more apparent: for a 1:100-scale model, while the model-scale impeller's diameter is 1/100 of its full-scale equivalent, the resultant model-scale flocs would be 1/4 of the full-scale flocs; for a 1:1000-scale model, the resultant flocs would have decreased to only 1/8 of full-scale.

The resultant maximum floc sizes for a number of scale-up mechanisms may be now be summarized:

Table 8-6
confined impeller (configuration 03)
effects of various scale-up mechanisms on resultant maximum floc-size

mechanism	<i>ratio of model-scale floc-size to full-scale-floc-size::</i>			
	full-scale	1:10-scale	1:41-scale	1:55-scale
constant ϵ	1.000	1.000	1.000	1.000
constant tip-speed	1.000	0.500	0.328	0.300
geometrically scaled d_i	1.000	0.100	0.024	0.018

Furthermore, in defining these floc-sizes according to the vessel-averaged dissipation rate, $P/\rho V$, the manner in which the local turbulent dissipation rate varies was already illustrated. Specifically, again for the 1:10-scale versus the full-scale, it may be shown that:

$$\frac{\epsilon_{full}}{\epsilon_{10}} = \frac{(v_{tip_{full}})^3 b_{10}}{(v_{tip_{10}})^3 b_{full}} = 1.0 \frac{b_{10}}{b_{full}} = \frac{1}{10}$$

After applying the same procedure to the other scales, the corresponding ratios of resultant model-scale dissipation rates may be tabulated:

Table 8-7
confined impeller (configuration 03)
effects of various scale-up mechanisms on resultant turbulent dissipation rate

mechanism	<i>ratio of model-scale ϵ to full-scale ϵ::</i>			
	full-scale	1:10-scale	1:41-scale	1:55-scale
constant ϵ	1.000	1.000	1.000	1.000
constant tip-speed	1.000	10.000	41.1	55.6
geometrically scaled d_i	1.000	2.19×10^4	2.43×10^5	1.5×10^6

Considering this analysis further, the angular velocities corresponding to these constant-tip-speed-based estimates of the local dissipation rate may easily be estimated by means of the assumption of a scale-invariant spatial variation of ϵ to $P/\rho V$. For example, for the 1:10-scale:

$$\frac{\epsilon}{\frac{v_{up}^3}{b}} = \text{const}$$

$$\frac{(1.67 \text{ m}^2/\text{s}^3) \cdot 0.108 \text{ m}}{(\frac{1}{2} \omega \cdot 0.4268 \text{ m})^3} = 0.032$$

$$\omega = 8.339 \frac{\text{rad}}{\text{s}}$$

$$N \approx 80 \text{ rpm}$$

The necessary angular velocities for each of assumed scale-up mechanisms, and for all scales may now be tabulated:

Table 8-8
confined impeller (configuration 03)
effects of various scale-up mechanisms on required angular velocities

mechanism	<u>required model-scale angular velocities (rpm):</u>			
	full-scale	1:10-scale	1:41-scale	1:55-scale
constant ϵ	8	37	95	116
constant tip-speed	8	80	329	445
geometrically scaled d_i	8	480	5930	1.32×10^4

Of course, a scale-variant ϵ implies that any ϵ -dependent process, be it flocculation, mass-transfer or a chemical reaction, must proceed at a scale-variant rate. Considering a physical process such as mass-transfer, Bin (1984) stated directly that:

$$\frac{K_{L2}}{K_{L1}} = \frac{\omega_2}{\omega_1} \frac{\lambda_1^{2/3}}{\lambda_2^{2/3}}$$

Thus, for the case of a constant tip-speed, and for any model-scale, the resultant ratios of the mass-transfer coefficient, k_L , may be defined by inserting the appropriate model scale constants, λ , into this expression together with the corresponding angular velocities from Table 8-7. For the case of the 1:10-scale model, it may be shown that:

$$\frac{K_{L2}}{K_{L1}} = \frac{8 \text{ rpm}}{80 \text{ rpm}} \frac{10^{2/3}}{1^{2/3}} = 0.466$$

or, in other words:

$$k_{L10} = 2.14 k_{L_{full}}$$

In a similar manner, it may be shown that

$$\begin{aligned} k_{L_{41}} &= 3.44 k_{L_{full}} \\ k_{L_{35}} &= 3.80 k_{L_{full}} \end{aligned}$$

8.2.6 Maintenance of Constant Torque per Unit Volume

Finally, considering briefly this traditional scale-up parameter, it may be shown that:

$$\frac{P}{\rho V} = \frac{\tau \omega}{\rho V} \propto N_p \omega^3 d^2$$

whence it may be shown

$$\frac{\tau}{\rho V} \propto N_p \omega^2 d^2 \propto (v_{tip})^2$$

Therefore, whenever the quantity torque per unit volume be maintained constant upon scale-up or scale-down, it may be shown that:

$$\frac{\frac{\tau}{\rho V} |}{\frac{\tau}{\rho V} |} = \frac{\omega_2^2 d_2^2}{\omega_1^2 d_1^2}$$

As such, it is immediately clear that the maintenance of constant torque per unit volume is analogous to the case where the tip-speed is constant. Accordingly, any inferences regarding the effects of scale on the various hydromechanical quantities that can be made for the case of constant tip-speeds are equally applicable to the case of constant torque per unit volume. The two cases are identical.

8.3 Concluding Remarks

As this analysis has shown, the variety of potential scale-up mechanisms that have traditionally been applied to the study of impeller-agitated mixing can yield numerous and different model-scale operational parameters. Hopefully it has been demonstrated that the search for a universal scale-up "law" must remain at least partially unfulfilled. Instead, one must apply the general principles of hydraulic modelling selectively to the analysis of impellers. Many of the various scale-up schemes are most appropriate only for certain specific aspects of the flow. The traditional rule-of-thumb scale-up mechanisms probably work best only when the difference between two models' scales is not very large. However, in scaling to the full-scale from models the size of those studied here, such potential differences among the various scale-up mechanisms are magnified considerably, demanding that one always be mindful of the implicit responsibilities in attempting to effect a meaningful scale-up.

9.0 Implications of Tangential Inflow

9.1 Introduction

Initially, work proceeded on the 1:10 scale NHC model under the expectation that the tangential inflow, Q_t , would not adversely affect the state of flow near the impeller in comparison to that observed in the laboratory-scale tests. Although the presence of a hydraulic imbalance in the clarifier has been amply illustrated: Stanley, Smith & Prince (1993), NHC (1993) ; and although such an imbalance is well known by the operators at the plant, it was hoped that the superposition of a tangential flow regime onto an impeller-generated tangential flow regime would be of little consequence given the apparent governance of the orifice opening on flow-through. With this "control point" in effect lying upstream of the impeller, and with the tangential inlet discharging its flow at a level effectively downstream of the impeller-generated jet-flow, it was thought that any disturbances caused by the inlet would, for the most part, be carried outside the draught tube, into the so-called flocculation zone, where dissipation would occur. This view was supported in part by a photographic analysis contained in NHC's report^{*} that seemed to indicate that the tangential inflow did not influence the impeller-generated flow beneath it. One such photograph, Photograph 9-1, is included in this document for illustrative purposes.

Once data collection began, it immediately became apparent however that the tangential inflow wields significant influence on the recirculation of fluid through the bottom of the draught tube. Specifically, it was found that the presence of the tangential inflow caused a tangential variation in the velocity distribution of the impeller-generated swirling radial jet, and that the interaction between the impeller-generated flow and the tangentially entering flow was likely responsible for the observed hydraulic imbalance in the clarifier. Moreover, the magnitude and spatial variation of this interaction was generally found to be dependent upon the velocity of the radial inflow (which in turn depends upon the angular velocity of the impeller) with respect to the velocity of the tangential inflow. Given the large variation that is possible in Q_t and ω , it is clear that numerous flow combinations are possible in the full-scale facility. As it is too impractical to attempt to quantify the resultant effects of every possible combination of Q_t and ω , the NHC model was tested for a number of specific tangential inflows in an attempt to illustrate the significant operational characteristics of the full-scale facility in a fairly general yet useful manner.

9.2 General Operation

For the case where Q_t is nonzero the situation becomes much more complicated since the somewhat idealized case of a velocity field that is dominated purely by something resembling a swirling radial jet has superposed upon it a potentially dominant tangentially variant flow regime. To examine the hydraulic conditions with the applied tangential discharge, two tests with a nonzero Q_t were performed on the 1:10 scale NHC model. These are defined as NHC trial 2 and NHC trial 3, and they complement NHC trial 1, in which $Q_t = 0$ (discussed earlier). Specifically trial 2 represents an equivalent full-scale influent discharge of 200 Mℓ/d, and trial 3 represents an equivalent full-scale discharge of 100 Mℓ/d, which represent the cases where both the design flow and twice the design flow are passed through the clarifier. In this study, Q_t was scaled by the Froude similarity criterion. Scaling by the Froude criterion is a typical practice for scaling overall bulk flows and velocities in free surface models, and it is the approach taken by NHC in their 1993 study. Following the practice of NHC further, the two discharges are referred to in a shorthand form as Q200 and Q100. Insofar as possible, it was attempted to maintain discharges

* specifically Photographs 7-11 through 7-13 on page B9 of NHC's 1993 report

and water surface elevations identical to those used by NHC in their study (*q.v.*).

Q, was controlled by a v-notch 90° weir. Although numerous equations are available to define the flow over such weirs, all can be shown to have the general form

$$Q = C \frac{8}{15} \sqrt{2g} h^{\frac{3}{2}}$$

where h is assumed to be the elevation of the flow's total energy line above the flow's zero-discharge elevation, and where the constant C can be selected from tabulated values. For NHC trials 2 and 3, a value of C of 0.58 (dimensionless) was selected from King (1954). Now, by the Froude criterion, it may be shown* that in order to maintain the same value of the discharge-based Froude number at any two scales, the discharges are scaled by the geometric length scale, λ , to the five-halves power. That is

$$Q_{model} = \frac{1}{\lambda^{\frac{5}{2}}} Q_{full-scale}$$

In this manner, Q200 and Q100 were scaled to appropriate values for the 1:10 scale model. Given scaled equivalents of Q200 and Q100, the necessary model-scale values of h were determined from the generalized weir equation, and applicable operational parameters were determined. Unfortunately, the target values of h were not duplicated exactly in this study - the process of fine-tuning the model to specific values of Q200 and Q100 (and their associated model depths) was very difficult since both the weir depth (controlled by a butterfly valve) and the model depth (controlled by a downstream weir) had to be adjusted simultaneously. The final operational parameters at which the model was run are presented in Table 9-1 along with those values originally used by NHC. The tabulated depths represent the depth of water in the clarifier *above the top of the draught tube* and were taken directly from NHC's report.

Table 9-1
1:10 scale model with tangential inflow
final model settings

trial	<u>full-scale:</u>		<u>1:10 scale (scaled by Froude criterion):</u>			
	Q (Ml/d)	depth (m)	Froude-based Q (l/s)	NHC Q (l/s)	this study Q (l/s)	depth (m)
1	0	1.48	0	0	0	0.148
2	200	1.48	7.32	7.32	7.9	0.148
3	100	1.39	3.66	3.66	4.0	0.139

The difference between the discharges run by NHC and those run in this study is only of the order of a few percent, which is certainly acceptable given the semi-empirical nature of the weir equation. This difference results primarily from slightly higher weir heads, h, used in this study. It should also be noted that the depth of water in NHC trial 1 (no inflow) was the same as that

* For instance, ASCE (1942), or any other suitable text.

for trial 2.

9.3 the Velocity Field - General Analysis

All velocities were measured with a Nixon propeller meter in the radial and tangential directions only, and the velocity measurements were taken at locations that were generally consistent with those from the lab-scale studies so that both axial and radial variations of the radial and tangential velocities could be compared directly. Resultant plots of all local and vertical variations of u and v for each of the NHC trials 1 through 3 are presented in a series of figures identified by the prefixes 9-1, 9-2 or 9-3. Whereas for NHC trial 1, the collection of data occurred at only one specific angular location, $\theta=0^\circ$, NHC trials 2 and 3 were each performed at two tangential locations^{*,**}, $\theta=0^\circ$, and $\theta=180^\circ$, in order to assess any tangential variation of the flow in the draught tube prompted by the presence of the tangential influent. Therefore, two curves are plotted for each particular angular velocity in these figures. Proceeding as before, the measured radial and tangential velocities were normalized via the tip-speed so that the resultant velocities at the various impeller speeds could be compared directly. These plots are also presented in Figures 9-1 through 9-3. In addition, by applying the concept of similarity of velocity profiles, it may be assumed that the maximum value of the dimensionless velocity represents a valid means of comparison of the various velocity profiles for trials 2 and 3. This comparison is presented here via a tabular format, along with the results of trial 1 for comparison:

Table 9-2
1:10 scale model with tangential inflow
measured maximum dimensionless velocities near impeller

description	$Q, (l/s)$	$2r/d$	<u>near side:</u>		<u>far side:</u>	
			u / v_{tip}	v / v_{tip}	u / v_{tip}	v / v_{tip}
Q200	7.9	1.070	0.42	0.80	0.33	0.88
Q100	4.9	1.070	0.45	0.88	0.40	0.84
no inflow	0	1.070	0.48	0.88	-	-

At this point, several important characteristics of the flow may be observed. Firstly, the local velocity field appears to vary tangentially: both the figures and Table 9-2 indicate that there are obvious differences in the magnitudes of the velocities at each location, which clearly implies that the assumption of θ -invariance, a critical assumption in those tests where $Q_i=0$, is no longer applicable here. Secondly, it would appear that the magnitude of the local dimensionless velocity field is related to the magnitude of the influent discharge. Finally, inspection of Figures 9-1 through 9-3 allows a third characteristic to be observed: the fact that the measured velocity profiles for the lowest values of N do not scale with the tip-speed indicates that the rate of angular rotation and the velocity of the tangentially entering flow somehow define some critical

* Again, geometric constraints demanded that the radial location nearest the impeller be $2r/d=1.070$ instead of $2r/d=1.044$.

** These two locations are referred to as near-side and far-side respectively. For review, the system of tangential location that was employed in this study is presented in greater detail in chapter 3, the Experimentation chapter of this report.

velocity within the draught tube below which the tangential inflow seems to dominate the flow regime. Actually, the interaction between the tangential influx and the radial efflux from the impeller is known. For example, photographs taken by NHC (1993) illustrate that the spreading of dye in the clarifier is decidedly unsymmetrical - one such illustrative photograph is provided here for illustration, Photograph 9-2. Similarly, tracer tests on the full-scale facility performed by Stanley, Smith & Prince (1993) indicated that the clarified water exits through the west launder sooner than it does through the east launder, with the west launder being located closer to the tangential entry.

9.4 Flow Distribution Within the Draught Tube

9.4.1 General

Because the efflux velocities through the impeller are directly affected by the tangential inflow, it is strongly implied that the efflux distribution over the top of the draught tube and into the ambient fluid surrounding the draught tube must also be decidedly non-symmetric. Similarly, intuition prompted the further supposition that the influent discharges, through the opening between the skirt and the floor, should also exhibit some degree of dependence upon the tangential inflow. Because it is certainly important with respect to the operation of full-scale clarifier to be able to express this perceived interaction between the tangential influent, Q_i , and the consequent nature of the spatial variation in the flow, it was decided to perform a series of velocity measurements, both above the draught tube and below the skirt, and for a variety of angular velocities, thereby allowing the hydraulic conditions that exist in the draught tube to be defined more clearly. Such measurements were performed toward the ultimate goal of defining a so-called velocity distribution "function" for the draught tube, whereby the interaction between Q_i , ω and the spatial variation of the magnitudes of the influent and effluent velocities could be quantified.

Definition of the distribution "functions" required the radial u-velocities to be measured perpendicular to an imaginary circular control volume, defined either by a vertical projection of the draught tube to the water surface (for the efflux velocities) or by a projection of a vertical surface between the skirt and the floor of the tank (for the influx velocities). Depending upon which particular trial was performed, these velocities were collected at anywhere from two to four different values of θ , and in vertical increments of approximately $\frac{1}{4}$ of the total height of the particular control volume. The incremental velocities were then vertically averaged in order to define general, average, radial velocities for the particular tangential increment. These average velocities were then normalized by some significant measured velocity (normally the average radial velocity at $\theta = 0^\circ$). The final form of the tangential variation of these dimensionless average radial velocities distribution was determined via comparison to a special complete tangential traverse wherein the radial velocities were determined at eight different angular locations (*i.e.* every 15°). A plot of the tangential variation of the dimensionless, vertically-averaged, radial velocities is assumed to represent the final distribution "function" for a particular location. This analysis was performed both for trial 2 (Q200) and trial 3 (Q100), but not for trial 1. The resultant velocity distribution "functions" that were determined for this study are presented in Figures 9-5 and 9-6. As these plots are presented in a form where the velocities are normalized by the measured velocity at $\theta = 0^\circ$, it is seen that the entire tangential velocity distribution may be determined knowing only the angular velocity of the impeller and the local average radial velocity at the point $\theta = 0^\circ$.

9.4.2 Surface Efflux - the Velocities across the Top of the Draught Tube

Considering the surface efflux, examination of Figures 9-5b through 9-6b indicates certain properties of the derived flow distribution "function" to be of interest. For Q200, Figure 9-5b, there consistently appears a maximum magnitude of efflux velocity somewhere along the draught

tube's perimeter. Usually, this point of maximum efflux is seen to occur at $\theta \cong 270^\circ$ (for $N=30$ rpm or above), but when $N = 10$ rpm, the location of maximum efflux shifts to a location directly across the draught tube from the previous location, $\theta \cong 90^\circ$. Finally, when Q_i is allowed to efflux on its own, without the impeller ($N = 0$ rpm), the observed point of maximum efflux again at approximately 270° .

It is speculated that because of the presence of both the tangential inlet flow and radial flow from the impeller, the tangentially entering flow is somehow deflected vertically by the impeller-generated jet-flow - this is why a peak is observed. However, considering the *location* of this peak, it becomes necessary to examine the magnitude of the tangential influent jet-like flow with respect to the magnitude of the impeller-generated jet-like flow (or, in equivalent terms, the velocity of the tangentially entering flow to the impeller's tip-speed). To this end, the velocity distribution across the tangential inlet was measured, and it was found that the maximum entrance velocities occur in a roughly reverse-L-shaped zone, with the transverse arm of this L lying along the bottom of the inlet pipe and the vertical lying along that part of the inlet pipe that merges into the wall of the draught tube. The flow here was found to have a significant velocity, approximately 0.75 m/s. With reference to the impeller's tip speed, it may be seen that only when the impeller is turning at angular velocities less than a certain minimum value is the velocity of the tangentially entering flow exceeded by the impeller's tip-speed. An estimate of this minimum angular velocity may be determined easily:

$$\begin{aligned} \max v_{tang.} &\geq v_{tip} \\ 0.75 \text{ m/s} &\geq (\omega)(\frac{1}{2})(0.4268 \text{ m}) \\ \omega &\leq 3.52 \text{ rad/s} \\ N &\leq 34 \text{ rpm} \end{aligned}$$

Thus, by this relatively crude approach, it may be speculated that for $N \geq 34$ rpm, the impeller-generated flow is dominant and is therefore able to deflect the tangentially entering flows out of the draught tube. Further support is accorded this supposition in that such a mechanism would explain how the location of maximum efflux seems to be invariant once N attain a certain value. Conversely, it is speculated that for $N = 0$ rpm, the inlet flow is free to circulate within the draught tube (held to the wall by centrifugal force) before rising to the surface - thus it is assumed to be coincidence that in Figure 9-5b, the point of maximum efflux for 0 rpm appears to coincide with those for the higher values of N . Finally, for $0 \text{ rpm} \leq N \leq 34 \text{ rpm}$, the presence of the impeller-generated influx likely offers a much smaller vertical impetus to the tangentially entering flow than is found at the higher angular velocities, so that the flow is eventually expelled, but not as quickly as would occur at higher values of N . This theory is *possibly* supported by the measured tangential velocity profiles, Figure 9-2-2n, which seems to indicate that the superposed tangential velocity regime due to Q_i is predominant over the impeller-induced regime for angular velocities less than approximately 30 rpm.

Considering now the surface efflux flow distribution for Q_{100} , a similar peak is found in Figure 9-6b, but as only a single angular velocity was tested for this inflow, the ω -based variation of this peak is unknown. Regardless, the same principles governing the location of the peak efflux for Q_{200} are certainly expected to be valid here.

9.4.3 Skirt Influx - Consideration of Velocities through the Skirt Opening

Considering now inflow through the opening between the skirt and the floor, definition of the skirt-influx distribution function was found to be much more straightforward since comparatively little impeller-inflow interaction appeared to be present. Instead, it was consistently observed that the skirt inflows were greatest at approximately $\theta \cong 215^\circ$, and that the location of the maximum inflow remained approximately unchanged regardless of inflow. Thus the portion

of the skirt lying just downstream* of the tangentially entering flow can be identified as generally having higher influent velocities. The resultant assumed skirt-influx velocity distributions are presented in Figure 9-5a and 9-6a.

For Q200, comparison of Figures 9-5a and 9-5b indicates that the location of the peak effluent surface flow across the draught tube and the location of the peak influent skirt flow occur very close to one another. This apparent close correspondence leads one intuitively to propose that the nature of the skirt-inflow distribution "function" is inextricably linked to the surface efflux distribution "function" by means of some sort of entrainment** phenomenon. That is, it is thought that the expansion of the tangentially entering, jet-like flow as it is able to draw in fluid from the ambient, that being the flow immediately below it, thereby establishing a pressure gradient which favours fluid being drawn in through the skirt at a location lying relatively close to the tangential inlet.

In contrast, for Q100, comparison of Figures 9-6a and 9-6b indicates that the point of peak inflow does not appear to coincide with the observed point of maximum outflow. This inconsistency is possibly explicable by comparison of the magnitude of the tangentially entering flow to the impeller's tip-speed. That is, for Q100, the volume occupied by the core of the tangentially entering jet-like flow must be less for the less vigorous for Q100 than it is for Q200, and it probably occupies a lower volume of the space between the impeller's tip and the draught tube. Moreover, it is known by implication (based upon the observed maximum velocity across the tangential inlet for Q200) that for $N = 30$ rpm and $Q_i = Q_{100}$, the impeller's tip speed must have been greater than the maximum velocity of the superposed tangential flow regime, thereby indicating that the impeller-generated swirling radial jet-like flow regime was dominant for the single angular velocity that was studied. Accordingly, the interaction between swirling radial jet from the impeller and the jet-like flow from the tangential inlet was probably of an entirely different nature in trial 3 from what existed in trial 2. In retrospect, it appears that measurement of skirt-influxes and surface-effluxes at lower angular velocities for Q100 would have been useful.

9.4.4 Velocity Profiles - Near-Side and Far-Side Measurements in Light of Flow Distribution

Given that the hydraulic conditions within the draught tube depend upon the simultaneous consideration of jet-like flows resulting from Q_i and V_{ip} , it is appropriate now to re-examine the measured velocities themselves. In order to illustrate the difference between the hydraulic properties of the flow on the near-side and the far-side, as well as the effects thereupon of Q_i directly, all of the Q_i -dependent vertical variations of the radial and tangential velocities from Figures 9-2 and 9-3 are presented in Figures 9-4-1 through 9-4-2. As well, the observed radial variations in u and v are presented in Figures 9-4-3 through 9-4-4.

Based upon inspection of these Figures, a number of interesting observations may be made. Firstly, it appears that the far-side radial efflux velocity u is actually **greater** for Q100 than for Q200, but that the Q100 near-side radial velocity is arguably **less** than its Q200 equivalent. Furthermore, considering the maximum values of these dimensionless u -velocities, it appears that the ratio of near-side-maximum to far-side-maximum u -velocities is greater for Q200, thereby indicating the existence of a greater θ -variation of the magnitude of the impeller-generated flow for Q200 than for Q100, *i.e.*

* *downstream* in the sense of being some distance from the source, along the path of the entrant tangential flow

** Rajaratnam (1975) *q.v.* for a general discussion and application of the concept of entrainment.

$$\frac{\max u_{\text{far-side}}}{\max u_{\text{near-side}}} \bigg|_{Q200} > \frac{\max u_{\text{far-side}}}{\max u_{\text{near-side}}} \bigg|_{Q100}$$

Both of these observations are thought to be linked to the suspected agency of entrainment into the tangentially entering jet-like flow.

Considering the tangential velocities, Figure 9-4-2 shows that *near the impeller's blade*, the maximum tangential velocity, v , for Q200 is on the far-side, possibly reflecting the dominance of the tangential inflow regime, but that for Q100, v is found on the near-side. However, notwithstanding whichever v -velocity be observed to be greatest near the impeller's blade, *away from the blade* the maximum tangential velocity is invariably found on the far-side - a direct consequence of the centrifugally flowing tangential flow along the draught tube. Finally, it must be remembered that the NHC model was tested without baffles - the local velocity structure, especially the tangential velocities nearest the draught tube, would certainly be affected were baffles present.

9.4.5 Conclusion

Based upon a graphical analysis of the measured velocity data, it is clearly demonstrated that there exists some kind of relationship between the rate of tangential influent, Q , and the rotation of the impeller, ω , and that this relationship defines the hydraulic conditions in the draught tube with respect to the nature of both the impeller-generated inflow and the total outflow. However, it is contended that an accurate and complete definition of the various velocity structures and interactions present in the draught tube should not be the ultimate goal of this study. Instead, it is considered to be far more practical simply to acknowledge that such a complex interaction exists - what is most useful is simply to be aware of the consequent general effects upon the resultant bulk flow-through and recirculation, regardless of the actual spatial distribution and mechanism that may be present.

9.5 Pumping Capacities: Flow Numbers and the Recirculation Ratio

9.5.1 General

The fact that the tangential influent renders the assumption of a θ -invariant flow field inappropriate holds significant implications with respect to the various physical quantities and dimensionless parameters which are usually used to characterize the impeller-generated flow. That is, because the impeller-generated flows into the draught tube seem to be affected by the tangential entry, it is strongly implied that the relevant descriptive parameters such as N_q and ϵ should also be affected. Unfortunately, as there was no available means of measuring turbulent velocities at this scale, it was not possible to analyze the flow in terms of the dissipation rate or any other turbulence-related parameter. However, given that the average radial velocities were measured both through the skirt and across the top of the draught tube in the examination of the tangential velocity distribution, it was possible to determine tangential variation of the discharge flowing through the impeller by determining the flux of these velocities in accordance with the previously defined concept of the so-called velocity distribution "function".

9.5.2 Flow Numbers

In this manner, flow numbers were defined for the NHC model by applying the distributed, incremental velocity flux to a series of incremental sub-areas over the both control volumes (*i.e.* in determining both influx through the skirt and efflux over the draught tube) according to the following scheme:

$$\begin{aligned}
 Q &= \sum Q_a \\
 &\approx 2 \frac{1}{8} \sum_a F_a \sum_j u_{aj} \pi r \Delta h_j \\
 &= 2 \pi r \frac{1}{8} \sum_{a=0,45,90}^{315} F_a \sum_{j=1}^n u_{aj} \pi r \Delta h_j
 \end{aligned}$$

where subscript a represents the particular sector of the circular control volume (22.5° or $\pi/4$ radians). h_j represents an incremental vertical height, and F_j represents the distribution "function".

Once the discharges were determined, they were normalized by nd^3 as before, thus giving the dimensionless flow number, N_q , and then the two flow numbers (influx-based and efflux-based) were averaged for each angular velocity. The final averaged flow numbers are presented for NHC trial 2 and trial 3 in the following table, Table 9-3, along with those for trial 1 ($Q_i = 0 \text{ m}^3/\text{s}$) which were extracted from Table 5-3:

Table 9-3
flow numbers for various tangential inflows
NHC model, 1:10 scale, $d=0.4262 \text{ m}$, $\nu = 9.85 \times 10^{-7} \text{ m}^2/\text{s}$

model Q_i (ℓ/s)	N (rpm)	n (rps)	R_i (-)	average N_q
7.3	10	0.167	3.1×10^1	0.502
7.3	30	0.500	9.2×10^1	0.471
7.3	50	0.833	1.5×10^2	0.452
7.3	70	1.167	2.2×10^2	0.465
7.3	90	1.500	2.8×10^2	0.471
4.0	10	0.167	3.1×10^1	0.509
4.0	30	0.500	9.2×10^1	0.427
4.0	50	0.833	1.5×10^2	0.465
4.0	70	1.167	2.2×10^2	0.440
4.0	90	1.500	2.8×10^2	0.402
0	10	0.167	3.1×10^1	0.628
0	30	0.500	9.2×10^1	0.521
0	50	0.833	1.5×10^2	0.496
0	70	1.167	2.2×10^2	0.440

In a manner consistent with the observed flow numbers for the 1:55 and 1:41 scale models, these N_q 's also appear not to be constant but instead appear to decrease with increasing angular velocity. As well, it appears that for a particular value of Q_i , the flow number N_q again seems to approach some limiting, constant value at high angular velocities. Although, as stated previously, a simple bulk parameter such as N_q cannot describe the complexities of the bulk flow within the draught tube, it is still extremely useful as an illustrative device when considering the effect of Q_i on the impeller's pumping capacity.

Despite a few inconsistencies, these flow numbers seem to illustrate that for a given impeller rotation, N , as the tangential inflow into the draught tube, Q_i , is increased, the magnitude of the impeller-generated recirculated flow decreases. Because the recirculated flow in the full-scale unit is required to contain a certain amount of chemical sludge and flocculated particles, it may be inferred that as Q_i be increased while the angular velocity remain constant, the recycled flow will decrease, thereby decreasing the rate of sludge transport, ultimately producing a floc of lower quality. Such a lessening in the water quality would presumably be aggravated by the higher water levels in the clarifier that would accompany a higher inflow Q_i . In order to compensate for the decreasing effectiveness of pumping and the expected loss of water quality, it seems reasonable that ω should be increased for higher inflows so that more recycled flow could be drawn into the draught tube. Therefore, by itself, such behaviour appears to hold significant implications with respect to the operation of the full-scale facility.

However, although the observed flow numbers (listed in Table 9-3) for NHC trials 2 and 3 are indeed different, it must be recognized that they are not *significantly* different for a given angular velocity, N . Regarding then the earlier contention that the interaction between the tangential inflow and the impeller-generated flows is of determinative importance in defining the spatial variation of the velocity field in the draught tube, it would appear that such an interaction primarily affects the *local characteristics* of the flow *within* the draught tube but does not necessarily affect the *magnitude* of the flow *through* the draught tube.

In this regard, a more detailed consideration of the impeller-generated flow with respect to the magnitude of the tangential inflow is now in order.

9.5.3 Recirculation Ratios

At this point, it is appropriate to discuss the concept of recirculation and the recirculation ratio. Recalling section 1.2.1 of the **Introduction**, it was shown that the flow exiting the top of the draught tube is actually a combination of both Q_r (impeller-generated flow into the draught tube) and Q_i (tangentially entering flow). Upon exiting the draught tube, this flow then separates into two component streams, one which recirculates back into the draught tube, and one which leaves the flocculation zone altogether. The general nature of the exiting and recirculating flows is illustrated in Figure 9-6c.

The recirculation ratio is a dimensionless parameter which expresses the pumping performance of the impeller for a given tangentially inflow discharge with respect to the subsequent flow distribution between the recirculated and non-recirculated flow streams:

$$\mathfrak{R} = \frac{Q_r}{Q_i}$$

Here, Q_r is the magnitude of the impeller-generated flow through the skirt opening and orifice, and Q_i is the magnitude of the tangentially entering flow.

This parameter generally has a high value for efficient flow-through (Q_r is high) and low values for deficient or ineffective pumping performance (Q_r is low). It has long been held by the City of Edmonton, in accordance with claims by the manufacturer, that the recirculation ratio should have a value of 4 or more.

The application of this parameter deserves careful analysis since its usage is and has been subject to great misinterpretation. For instance, in the above expression, attention is immediately drawn to the denominator, Q_i . If Q_i remains constant, then the use of \mathfrak{R} as a descriptor of pumping performance for a given structural configuration would indeed be legitimate, for \mathfrak{R} would simply be a convenient dimensionless parameter based upon two immediately accessible, dimensionally consistent quantities. However, as Q_i is extremely variable depending upon the time

of year, and because it has been demonstrated that there is some interaction between Q_r and Q_i , any attempt to characterize the pumping performance via such a simple parameter is inappropriate without an accompanying specification of the impeller's angular velocity ω , n or N . It is this angular velocity that defines both the magnitude of Q_r , and the degree of interaction between Q_r and Q_i . Furthermore, the claim that $\mathfrak{R} \approx 4$ for the impeller in the full-scale facility also demands a great deal of scrutiny: how was this value determined? where was it determined? under what conditions? was it determined in exactly the same geometrical structure as that which exists in the City of Edmonton's clarifiers?

Instead, it is suggested that the recycle ratio, \mathfrak{R} , be decomposed into its principal elements so that a more consistently descriptive parameter may be developed, namely the flow number N_q . Upon closer examination, because Q_r represents the recycled flow, Q_r is identical to the so-called pumping flow or flow-through that was discussed earlier. If Q_i is known, along with \mathfrak{R} , the recirculated flow may be determined directly; furthermore, if the angular velocity at which a particular Q_r is observed is also known, then there is sufficient information to allow the flow number to be calculated:

$$N_q = \frac{Q_r}{\omega d^3} = \frac{\mathfrak{R} Q_i}{\omega d^3} = \frac{60 \mathfrak{R} Q_i}{n d^3} = \frac{2 \pi 60 \mathfrak{R} Q_i}{N d^3}$$

Clearly, the incorporation of \mathfrak{R} with N_q is far more useful than \mathfrak{R} alone since it contains the influence of the flow-generant impeller via the inclusion of ω and d , and because it contains an implicit statement of pumping effectiveness via $\mathfrak{R}Q_i$ (or simply Q_r). As well, this expression allows the effects of scale to be incorporated into the recirculation analysis directly, via the diameter, d .

In this manner, all of the flow numbers which were determined for NHC trials 2 and 3, presented in Table 9-3 above, were converted into the corresponding \mathfrak{R} values and plotted with respect to angular velocity in order to illustrate the influence of both angular velocity and tangential inflow on this parameter. These flow numbers their and corresponding recycle ratios are presented in the following table, Table 9-4:

Table 9-4
the relation between flow number and recycle ratio for various tangential inflows
NHC model, 1:10 scale, $d=0.4262$ m, $\nu = 9.85 \times 10^{-7}$ m²/s

N (rpm)	model Q_i (l/s)	model Q_r (l/s)	$\mathfrak{R} = Q_r/Q_i$	average N_q
10	7.9	6.5	0.8	0.502
30	7.9	18.2	2.3	0.471
50	7.9	29.2	3.7	0.452
70	7.9	41.7	5.3	0.465
90	7.9	54.7	6.9	0.471
10	4.0	6.6	1.6	0.509
30	4.0	16.5	4.1	0.427
50	4.0	30.0	7.5	0.465
70	4.0	39.7	9.9	0.440
90	4.0	46.7	11.7	0.402

These calculated recycle ratios are presented individually in Figures 9-7a and 9-7b, and on the same set of axes (for comparison) on Figure 9-7c. These Figures can then be compared directly to NHC's results via Figure 9-7d, which is a reproduction of Figure 5 from NHC's 1993 report. Clearly, these plots indicate that for a given constant Q_i , the recirculation ratio \mathfrak{R} varies approximately linearly with N . Such linearity is a direct consequence of the definition of N_q as a function of Q_i (stated on page 221). In this expression, it is immediately apparent that for constant impeller geometry and the somewhat idealized case of a constant value of N_q , the expression can be reduced to:

$$\mathfrak{R} \propto N$$

wherein the linearity is immediately apparent. In other words, a recirculation ratio that varies directly with angular velocity implies the existence of an approximately constant value of the flow number N_q . However, as N_q was not observed to be constant with angular velocity (at least not at very low angular velocities), such a linearity may not be entirely correct except for operation at the highest angular velocities.

Despite this slight inconsistency, the observation of such linearly variant recycle ratios may now be used to illustrate some very significant points concerning the description of the operation of the full-scale clarifier:

- with reference to Figures 9-7a through 9-7c, the recycle ratio, \mathfrak{R} , for Q200 is observed to be *consistently smaller* than that for Q100 for a given angular velocity, N
- as illustrated in Tables 9-3 & 9-4 above, approximately equal flow numbers were found in both trial 2 and trial 3 for a given N , even though the corresponding tangential inflows were significantly different, clearly implying that *two impellers with approximately equal pumping performance can adduce vastly different values of the recycle ratio, \mathfrak{R}*
- consequently, the bulk of the decrease in \mathfrak{R} that would be observed in increasing the tangential inflow from, say, Q100 to Q200 should be ascribed primarily to the fact that there is a large change in the denominator, Q_i and **not** to the assumedly comparatively marginal change in numerator, Q_r

Hence, it is clear that the specification of a single, simple recycle ratio \mathfrak{R} , without further specification of the relevant dynamic and geometric parameters as an intended definition of the clarifier's performance is of **indeterminate use if of any use at all**.

In practice, this variation in \mathfrak{R} is equivalent to recognizing that as Q_i changes, the recirculation ratio cannot be assumed to be constant, and thus the impeller's rotation must be adjusted to maintain the same degree of turbulence (and thus the same chemical kinetics) in the draught tube. Actually, this quality of the impeller-draught-tube system is already recognized by operators of the full-scale facility in that the clarifier's performance is roughly gauged to influent conditions with respect to the spreading of a chemical "cloud" around the top of the draught tube. If this cloud spread too far beyond some local reference point that would be familiar to the operators, the impeller's angular velocity is reduced. Thus, the concept of a variable recirculation ratio is already understood, even if not recognized explicitly, in the operation of the full-scale facility.

9.5.4 Use of Recirculation Ratios for Scale-up

Accepting then the apparent relevance of a linearly variant, Q_i -dependent recirculation ratio, \mathcal{R} , this approach may now be used to determine the corresponding model-scale parameters (specifically ω , n or N) which would be required to duplicate some observed \mathcal{R} in the full-scale facility, were that required to be done. This can be done through employment of the results of a relevant study of the full-scale system. Firstly, in order to attempt to duplicate the full-scale \mathcal{R} , it is first necessary to know what that full-scale value of \mathcal{R} is. Unfortunately, information concerning the recycle of flow in the full-scale facility is generally very rare, so it is fortunate that a recent study by Stanley, Smith & Prince (1993) is available. In this study, it was determined that:

At the flow of 180 Mℓ/d and at a recirculation (sic.) speed of 6 rpm, it appears the recycle ratio varies somewhere between 1.4:1 to 4.2:1, with a best-fit value of 2.5:1

For the 1:10 scale NHC model, the full-scale discharge of 180 Mℓ/d translates to a model-scale tangential inflow of 6.6 ℓ/s when scaled by the Froude criterion:

$$Q_{\text{model}} = \frac{Q_{\text{full-scale}}}{\lambda^{\frac{5}{2}}} = \frac{180 \frac{\text{M}\ell}{\text{d}}}{10^{\frac{5}{2}}} = \frac{2.083 \frac{\text{m}^3}{\text{s}}}{10^{\frac{5}{2}}} = 6.6 \frac{\ell}{\text{s}}$$

To determine the required model settings, consider firstly the best-fit value of $\mathcal{R} = 2.5$, and refer this value to Figure 9-7c. In this manner, since 6.6 ℓ/s lies between the Q200 equivalent discharge of 7.9 ℓ/s that was run in trial 2 and the Q100 equivalent discharge of 4.0 ℓ/s that was run in trial 3, examination of Figure 9-7c indicates that the NHC model should be run at something slightly less than 32 rpm, perhaps 30 rpm. This compares to an angular velocity of 19 rpm that results from estimating the required model-scale angular velocity directly from the observed full-scale angular velocity of 6 rpm via the Froude criterion.

In contrast, by applying NHC's reported value of the recirculation ratio, NHC (1993), of $\mathcal{R} = 0.9$, to the same analytical approach (*i.e.* analysis with respect to Figure 9-7d), it is found that the necessary impeller speed should be approximately 11 rpm. This compares to 22.1 rpm, which was scaled directly from the Froude law, and which was the angular velocity that was employed by NHC in their study*. This difference implies that the recirculation discharge that was measured by NHC was much lower than that which would be measured in this study for a given angular velocity - a fact that is plainly obvious from a comparison of Figures 9-7c and 9-7d. Conversely, if this study had been run at NHC's assumed experimental conditions of $N = 22.1$ rpm and $Q_i = 7.32$ ℓ/s, Figure 9-7c indicates that the observed recycle ratio would have been $\mathcal{R} \approx 1.7$ instead of the $\mathcal{R} = 0.9$ that was reported by NHC in their report. In general, both the flow numbers and the recycle ratios that were determined by NHC in their 1993 study may seem a little low when compared to both the full-scale results and the results of this study. However, because their test employed a skirt opening that was approximately only ⅓ of that which was employed in this study, the reduced flow area ensured that their recirculated flows would be lower than those which were measured here.

Finally, beginning with the reported values of \mathcal{R} , Q_i , and N from both the full-scale test and NHC's original study, corresponding values of N_q may be derived. All of these results are

* NHC assumed a full-scale angular velocity of 7 rpm, not the 8 rpm that was observed in Stanley, Smith & Prince (1993).

presented in the following table, Table 9-5.

Table 9-5
flow numbers and recycle ratios - full-scale & 1:10 scale, with tangential inflow

description	scale	Q_i (l/s)	Q_r (l/s)	\mathcal{R}	N (rpm)	d (m)	R_i	N_i
full-scale 93	1:1	2083	5218	2.5	6	4.262	1.107×10^4	0.672
NHC original	1:10	7.32	6.6	0.9	22.1	0.426	4.08×10^4	0.231
U of A 94 (estimated)	1:10	7.9	19.8	2.5	30	0.426	4.08×10^4	0.484
U of A 94 (estimated)	1:10	7.32	12.4	1.7	22.1	0.426	4.08×10^4	0.435

It is important to recognize the limitations that are present in this analysis. Firstly, in attempting to duplicate the observed full-scale recirculation ratio, the best-fit value of $\mathcal{R} = 2.5$ was assumed. Obviously, as there is a considerable amount of uncertainty present in this number, it must be recognized that even if \mathcal{R} were only slightly different, the resultant operational parameters required to duplicate \mathcal{R} would be different. As well, before attempting to scale-down to model scale based upon the maintenance of any parameter, not just \mathcal{R} , there must first be sufficient justification to do so. It is entirely possible that by maintaining \mathcal{R} constant at the model-scale, numerous other aspects of the flow would not be duplicated. This is the nature of the scale-up problem - impeller-generated flow is simply too complicated to be characterized completely by a single parameter. The fact that the bulk tangential inflow Q_i was scaled by the Froude criterion, yet other quantities like ϵ were shown to scale by an entirely different mechanism is further illustration of problem.

9.6 Effects of Tangential Inflow on Turbulence and Turbulent Dissipation

Regardless of what the flow-through and recycle ratio may be, it is a consistent truth that turbulent dissipation depends only upon the local turbulent velocity. Unfortunately, as it was simply not possible to measure the turbulent velocities in the 1:10-scale model, any discussion of the effects of Q_i on the local turbulent velocity structure must be of a purely speculative nature. Conceivably, one could analyze the impeller-draught-tube system mathematically as the case of a non-uniform tangential macro-flow superposed over the case of a swirling radial jet, together with the appropriate rigid-boundary constraints required by the presence of the draught tube. Unfortunately, as the differential equations governing the swirling radial jet are not linear (and probably those for the tangential flow also), it is impossible to superpose the two solutions for the two cases. In general terms, although the flow within the draught tube could be described as a swirling radial jet with an imposed radial swirl, no such analysis was found in the literature, which is not surprising given the complexity of this situation. By default, then, it is probably most useful to examine the dimensionless plots of velocity from the 1:10 scale model in an approximate manner only, together with a number of results from the literature, with the intention of developing a simplified general means whereby this complicated situation may be analyzed.

In a crude sense, examination of the velocity data allows the flows within the draught tube to be separated into two zones of analysis. In the region of the draught tube lying a fair distance downstream of the tangential entry, roughly between $\theta \approx 0^\circ$ and $\theta \approx 180^\circ$, Figure 9-4-4 seems to indicate that for all trials, *i.e.* regardless of Q_i , the magnitude of the dimensionless tangential velocity, v/v_{tm} , at a point nearest the wall of the draught tube appears to be approximately Q_i -invariant, possibly indicating that the superposed tangential flow regime is no

longer dominant in this part of the draught tube. Thus, to a fair approximation, it could be assumed that the local dissipation rate in that portion of the draught tube would also be approximately Q_i -invariant, such that ϵ could be estimated via the b-based or d-based non-dimensionalizations which were determined for the 1:55 and 1:41 scale models. However, considering the region immediately downstream of the tangential entry, *i.e.* $\theta = 270^\circ \pm 45^\circ$, this approach may not be valid any longer since the impeller-generated flow would not be the dominant feature of the local velocity structure therein.

Instead, it is felt that turbulent dissipation in this region could be analyzed - at least to a first approximation - by applying the free-jet analysis of Antonia, Satyaprakash & Hussain (1980) to the general velocity measurements across the tangential entry. In trial 2, it was found that the flow in the tangential entry had a maximum velocity along the wall, and that this velocity was approximately 0.75 m/s. In dimensionless terms, this corresponds to

$$3.4 \geq \frac{v}{v_{tip}} \geq 0.48$$

depending upon the impeller's angular velocity. In the analysis of a free circular jet discharging into a stagnant ambient, Antonia, Satyaprakash & Hussain (1980) found that the turbulence intensity expressed in terms of the nozzle velocity had an approximately constant value of $u'/u_n = 0.2$ along the jet's axis. Although the tangentially entering flow regime is more correctly described as a wall-jet, not a free-jet, if it be assumed that this ratio would nonetheless still be approximately constant and applicable there, then it may be estimated that in the region where the tangential inflow dominates, typical turbulent velocities would be of the order of

$$0.68 > \frac{u'}{v_{tip}} > 0.10$$

depending upon the impeller's tip speed. And, from the laser analyses of the 1:55 and 1:41 scale models, it was found that for the swirling radial jet acting alone, *i.e.* $Q_i = 0$, a typical value of the turbulent velocity near the wall of the draught tube is given by

$$\frac{u'}{v_{tip}} \approx 0.2$$

In comparing this result with the estimated magnitude of the Q_i -generated turbulent velocity, several important inferences may be drawn. Firstly, the interaction between tip-speed and Q_i is again found to be important. At low angular velocities, it appears that in the region near the tangential entry, the impeller-generated turbulent velocities would be smaller than the Q_i -generated turbulent velocities. However, as angular velocity is increased, it appears that the significance of the Q_i -generated turbulent velocities would be diminished as the impeller-generated flow became more vigorous. Accordingly, it is implied that as the angular velocity were decreased, the *extent* of the region in which the tangential flow regime is dominant would become larger. Quantitatively, when the tangential inflow is not dominant (either because of location within the draught tube or because the impeller is operated at a high angular velocity) the structure of turbulence can probably be estimated reasonably well by plots of dimensionless ϵ that were defined for the 1:55 and 1:41 scale tests; in other words, the influence of the tangentially entering flow upon the local turbulent flows becomes suppressed as impeller is operated at ever higher angular velocities. In contrast, in the region near the tangential inlet, especially at comparatively low angular velocities, it may be estimated that a typical turbulent velocity could

be of the order of three times greater than a typical turbulent velocity at a point located diametrically from the tangential inlet. Assuming that the turbulent length scale would be approximately constant throughout the draught tube, it is implied that ϵ can be up to twenty-seven times greater near the tangential inlet than it would be elsewhere in the draught tube. The manner in which ϵ varies just beyond this maximum, however, can only remain a matter of speculation since such an analysis would be complicated by the additional factor that the Q-generated jet-like inflow decays with distance from the inlet.

Admittedly, this is only a very approximate analysis, but it is still believed to be useful in illustrating the general effects of the tangential inflow on turbulence. If this analysis is to be believed, even on the most general level, it is seen that there is considerable potential for an imbalance in the chemical properties of the treated water given the increased reaction rates that would be implied by the higher ϵ there. Although it is only speculation, it may be surmised that depending upon the impeller's angular velocity, the floc sizes issuing from one side of the clarifier could be significantly larger than those issuing from the other side. This turbulence-prompted chemical asymmetry would represent a further imbalance in the clarifier, in addition to the previously recognized hydraulic asymmetry.

9.7 General Consideration of Angular Velocity at the Full-Scale

Consistently, the influence of N , the impeller's angular velocity, is recognized. As described above, depending upon the magnitude of the impeller's angular velocity with respect to the magnitude of the tangential inflow, the hydraulic conditions in the reactor can vary considerably. As a consequence, the turbulent flows and their concomitant effects upon reaction rate and water quality would be variable. Considering bulk flows, it was demonstrated earlier, in a very general sense, that there exists some minimum angular velocity below which the flow in the draught tube would be dominated by the tangential inflow. This contention may now be extended further: it is assumed that in addition to defining some operational boundary between two different flow regimes, such a minimum angular velocity also defines the point at which the chemical processes occurring within the draught tube would be affected. Therefore, considering N at the full-scale, it would be very useful to establish some sort of guideline whereby this operational limit could be defined, thereby allowing the typical operational conditions in the full-scale facility to be designated with respect to the relative dominance of the impeller-generated and tangential flow regimes that are present therein.

An expression for this operational limit for the full-scale for the case of the Q200 inflow will now be attempted. Firstly, considering the maximum observed efflux velocity across the tangential inlet that was observed in NHC trial 2, 0.75 m/s, it may be assumed that this value would remain proportional to the full-scale *average* tangential inlet velocity. That is

$$\frac{\text{inlet } v_{\text{maximum}}}{\text{inlet } v_{\text{average}}} = \frac{\text{inlet } v_{\text{maximum}}}{\frac{Q_t}{\pi r_t^2}} = \frac{0.75 \text{ m/s}}{\frac{0.0079 \text{ m}^3/\text{s}}{\pi (\frac{1}{2} 0.158 \text{ m})^2}} = 1.89$$

Assuming that this same ratio would be found in the full-scale facility for Q200, it may be estimated that the maximum local inlet velocity in the full-scale would be approximately 2.38 m/s. Previously, it was found that by referring the maximum inlet velocity to the impeller's tip-speed, the resultant angular velocity (when compared to the observed velocity profiles) seemed to define the angular velocity below which the observed velocities could not be normalized by the tip-speed, and was thus taken to be the angular velocity above which the impeller-generated flow regime would begin to predominate. By applying this same procedure to the full-scale for the case of Q200, it may be shown that:

$$\begin{aligned}
 \max v_{tang.} &\geq v_{tip} \\
 2.381 \text{ m/s} &\geq (\omega)(\frac{1}{2})(4.263 \text{ m}) \\
 \omega &\leq 1.1175 \text{ rad/s} \\
 N &\leq 10.7 \text{ rpm}
 \end{aligned}$$

In practice, the full-scale impeller is generally not run at angular velocities over 10 rpm. As such, this analysis seems to indicate that the tangential flow regime is predominant during typical operation of the full-scale clarifier. However, because the influent raw water is actually split into two equal streams at a point lying upstream of the two alum clarifiers, a more practical estimate of the typical full-scale discharge is Q100, not Q200. Applying Q100 to this same analysis, it is found that the corresponding minimum angular velocity is found to be $N \leq 5.4$ rpm, one-half of that calculated for Q200. As the full-scale impeller is usually run at speeds greater than 5 rpm, it would appear that the impeller-generated flow regime is predominant for the typical, full-scale operating conditions.

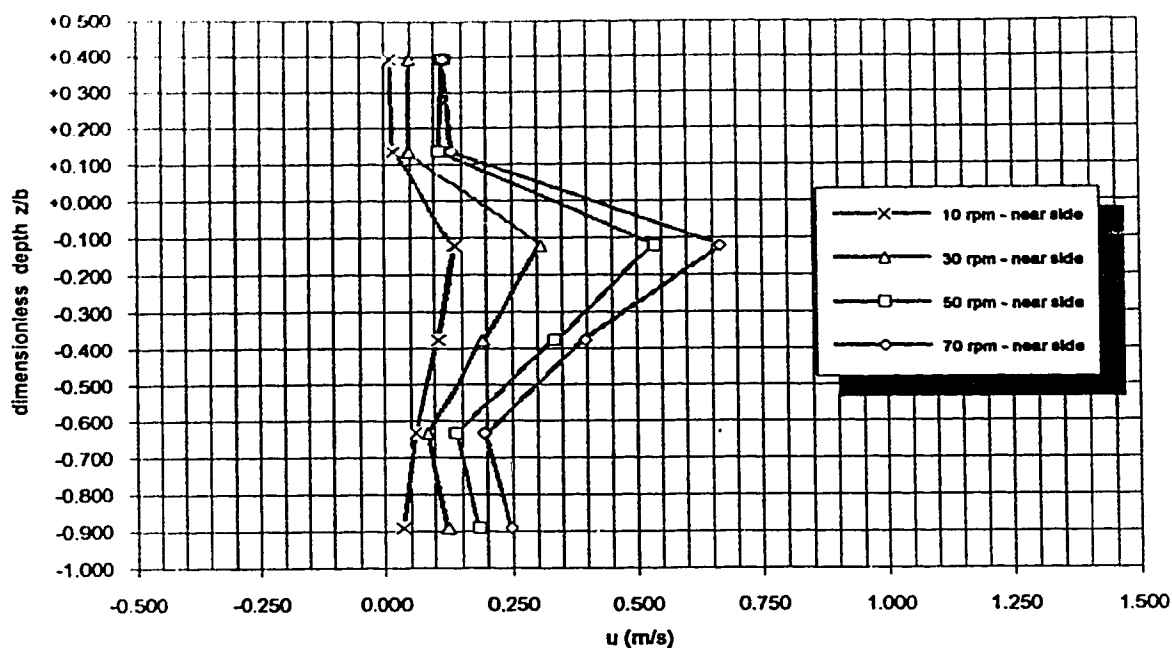


Figure 9-1-1 : trial 1 ; nhc model ; 1:10 scale ; Influent $Q = 0$ L/s
radial average velocities near impeller - not normalized by tip speed
 $d=42.62$ cm ; $b=10.8$ cm ; $2r/d=1.070$

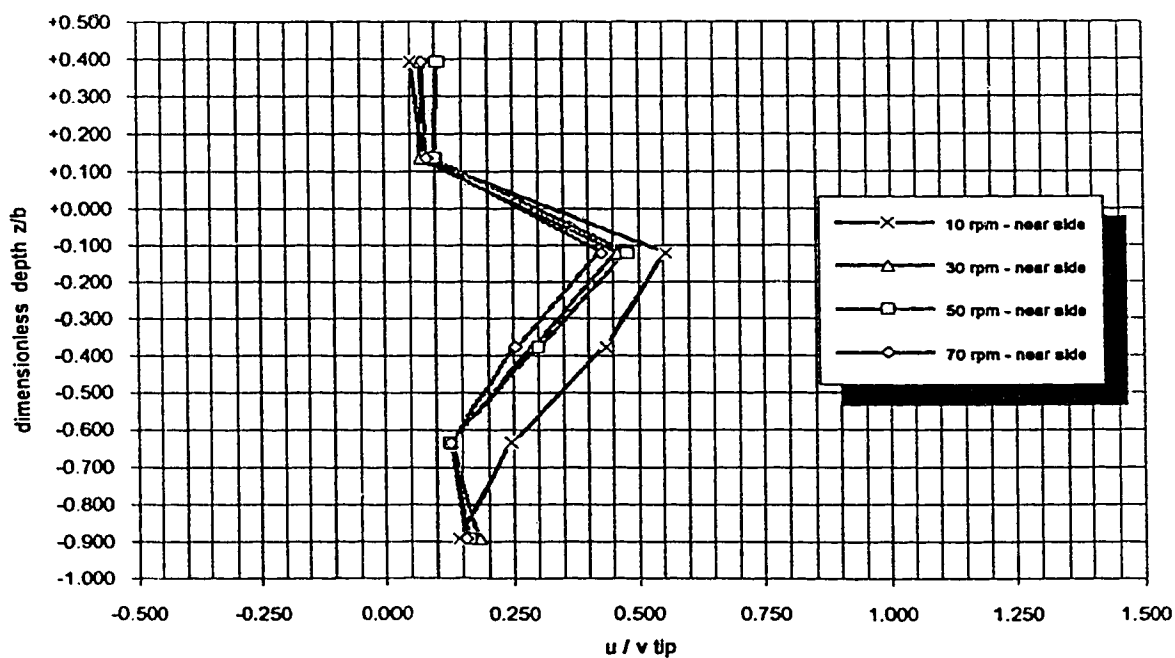


Figure 9-1-1n : trial 1 ; nhc model ; 1:10 scale ; Influent $Q = 0$ L/s
radial average velocities near impeller - normalized by tip speed
 $d=42.62$ cm ; $b=10.8$ cm ; $2r/d=1.070$

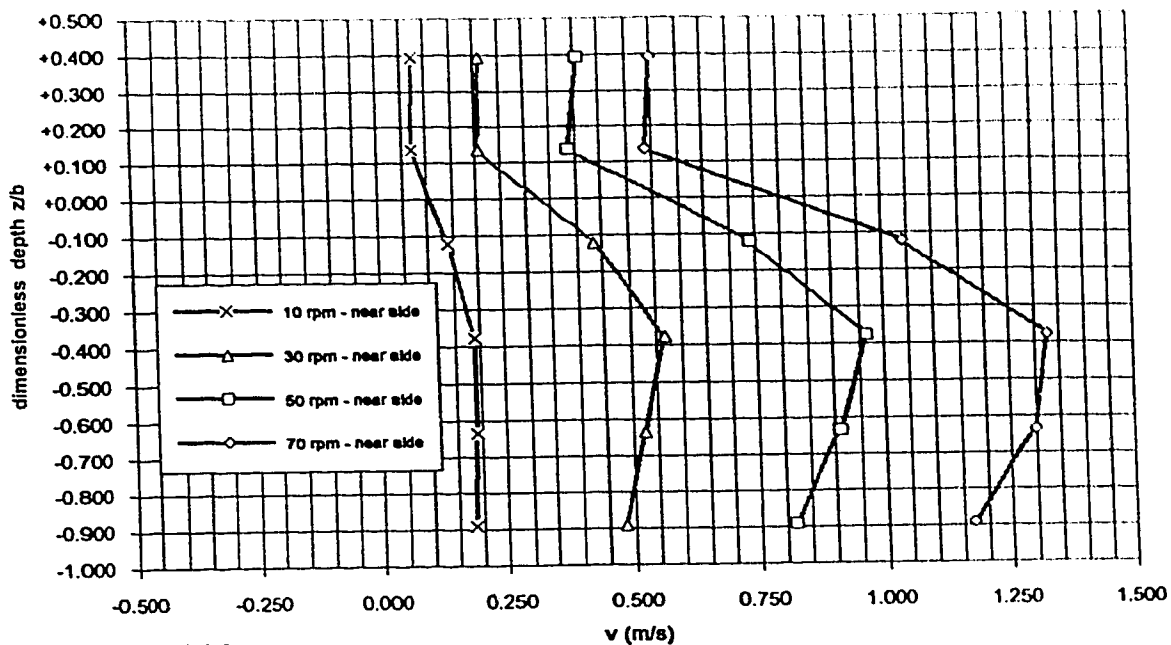


Figure 9-1-2 : trial 1 ; nbc model ; 1:10 scale ; Influent $Q = 0$ L/s
 tangential average velocities near impeller - not normalized by tip speed
 $d=42.62$ cm ; $b=10.8$ cm ; $2r/d=1.070$

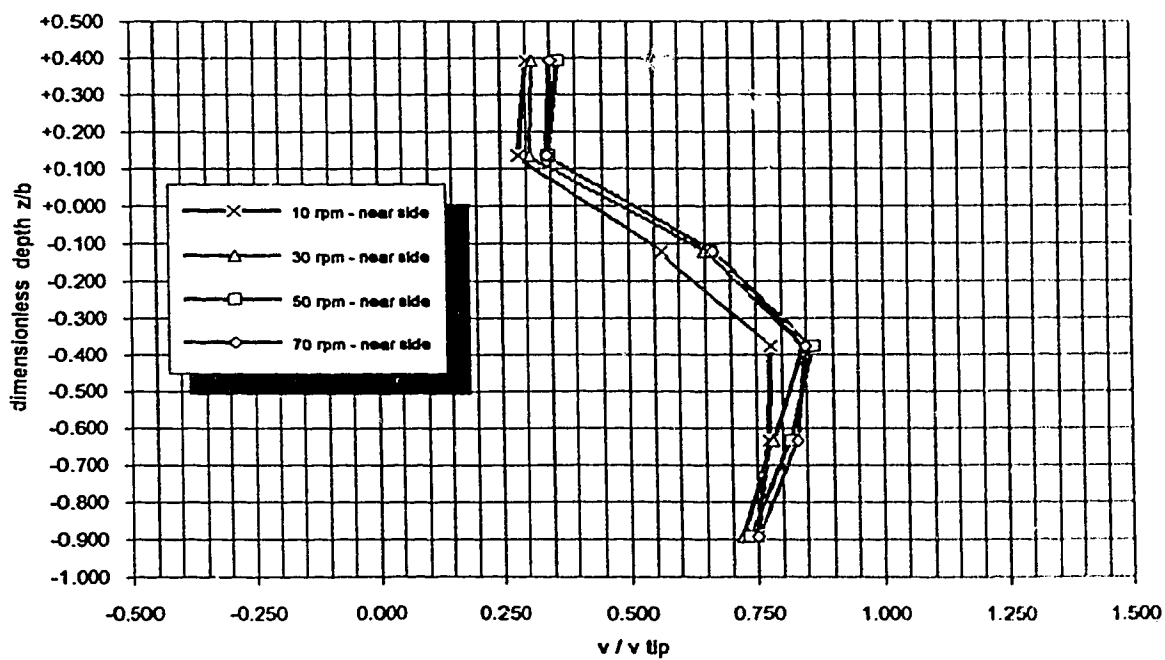


Figure 9-1-2n : trial 1 ; nbc model ; 1:10 scale ; Influent $Q = 0$ L/s
 tangential average velocities near impeller - normalized by tip speed
 $d=42.62$ cm ; $b=10.8$ cm ; $2r/d=1.070$

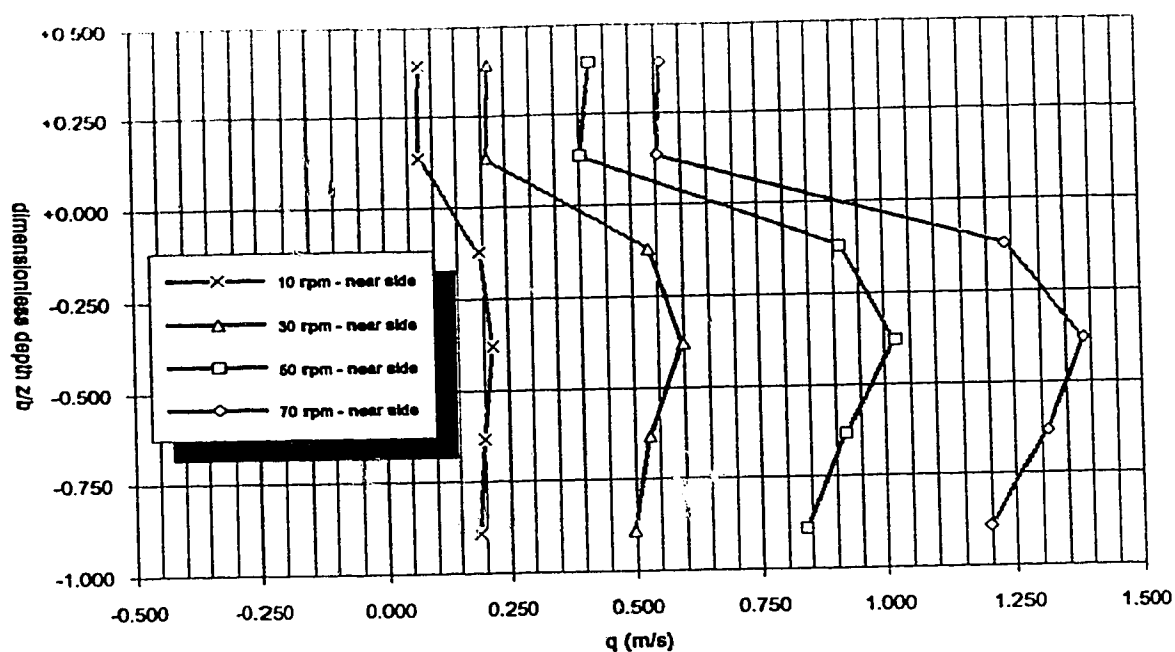


Figure 9-1-3 : trial 1 ; nhc model ; 1:10 scale ; Influent $Q = 0$ L/s
average velocities along axis of jet - not normalized by tip speed
 $d=42.62$ cm ; $b=10.8$ cm ; $2r/d=1.070$

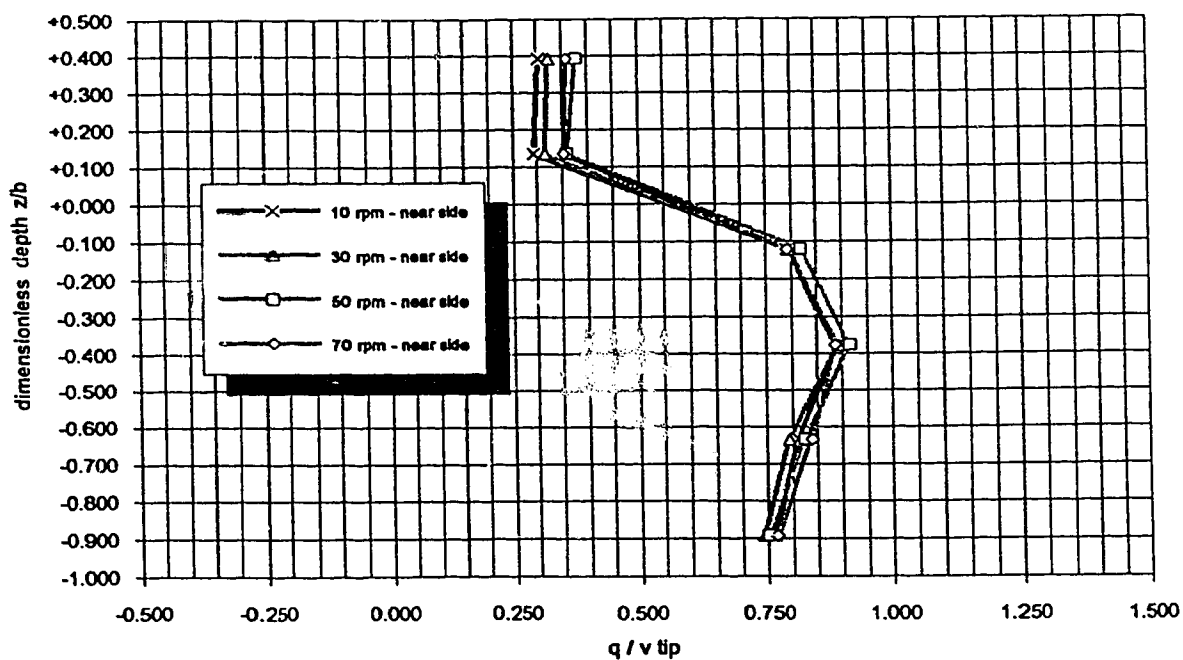


Figure 9-1-3n : trial 1 ; nhc model ; 1:10 scale ; Influent $Q = 0$ L/s
average velocity along axis of jet - normalized by tip speed
 $d=42.62$ cm ; $b=10.8$ cm ; $2r/d=1.070$

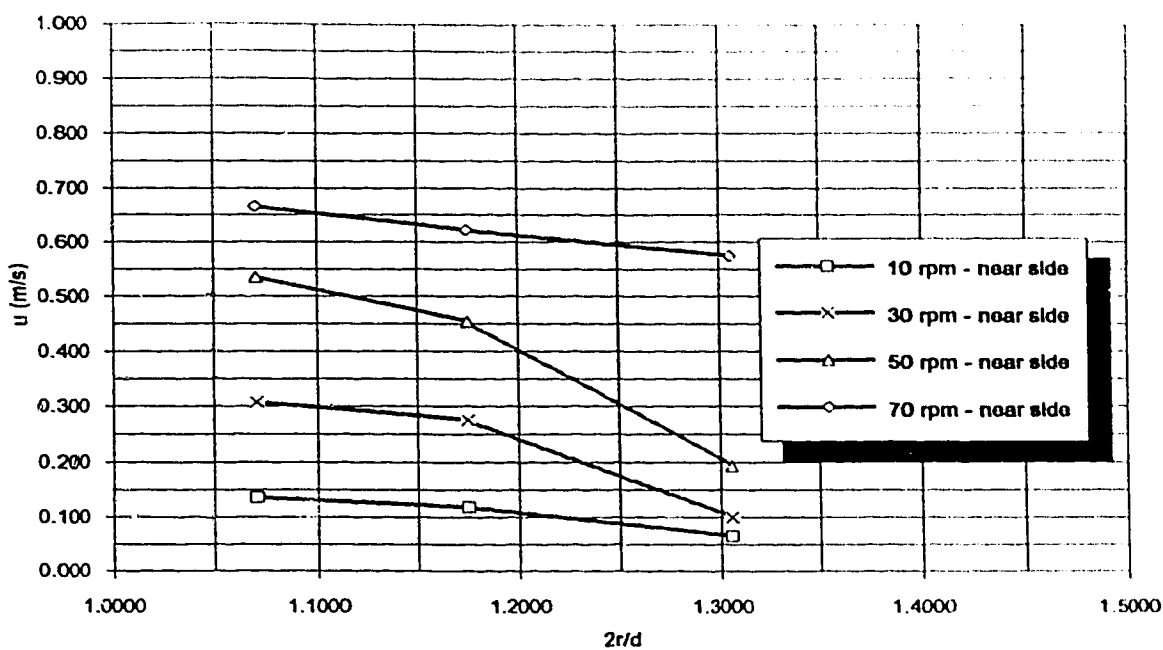


Figure 9-1-4 : trial 1 - ecodyne Impeller ; 1:10 scale
radial variation of maximum radial velocity - not normalized by tip speed
 $d=42.62$ cm ; $b=10.83$ cm ; Influent $Q = 0$ L/s

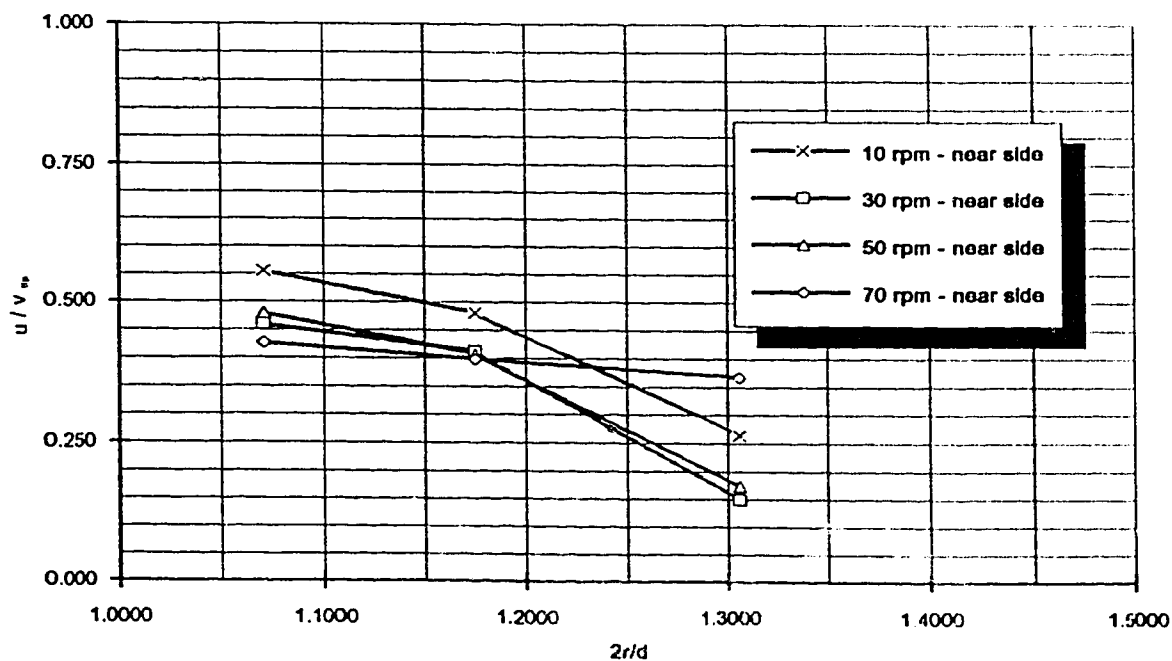


Figure 9-1-4n : trial 1 - ecodyne Impeller ; 1:10 scale
radial variation of maximum radial velocity - normalized by tip speed
 $d=42.62$ cm ; $b=10.83$ cm ; Influent $Q = 0$ L/s

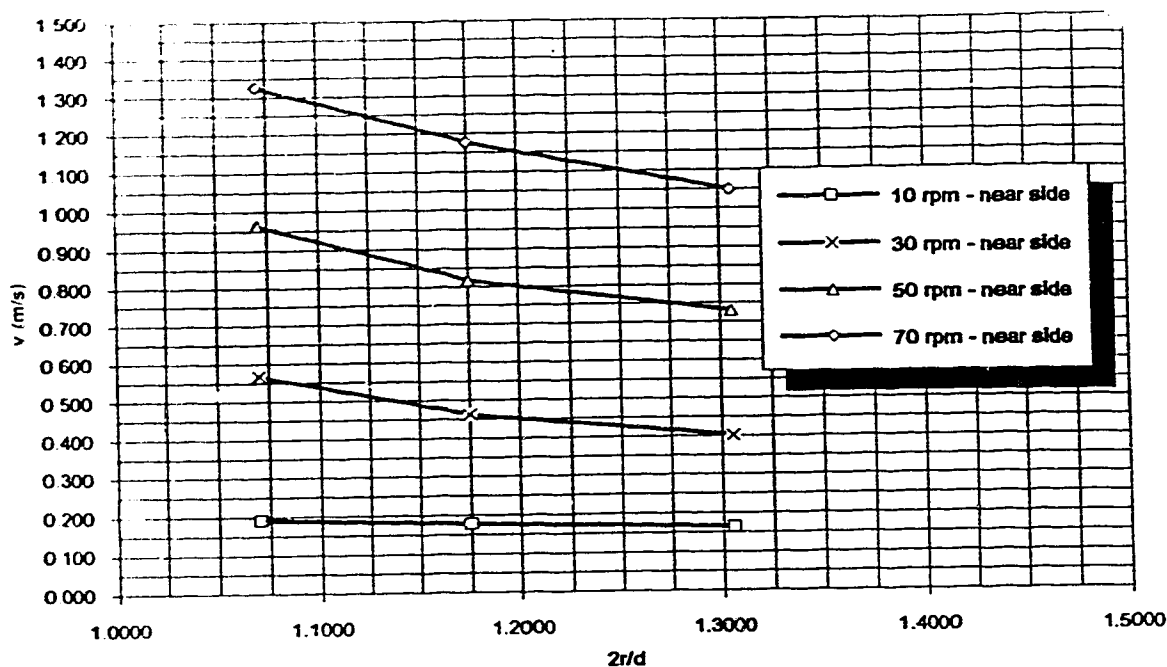


Figure 9-1-5 : nhc model - 1:10 scale
radial variation of maximum tangential velocity - not normalized by tip speed
 $d=42.62$ cm ; $b=10.83$ cm ; Influent $Q = 0$ L/s

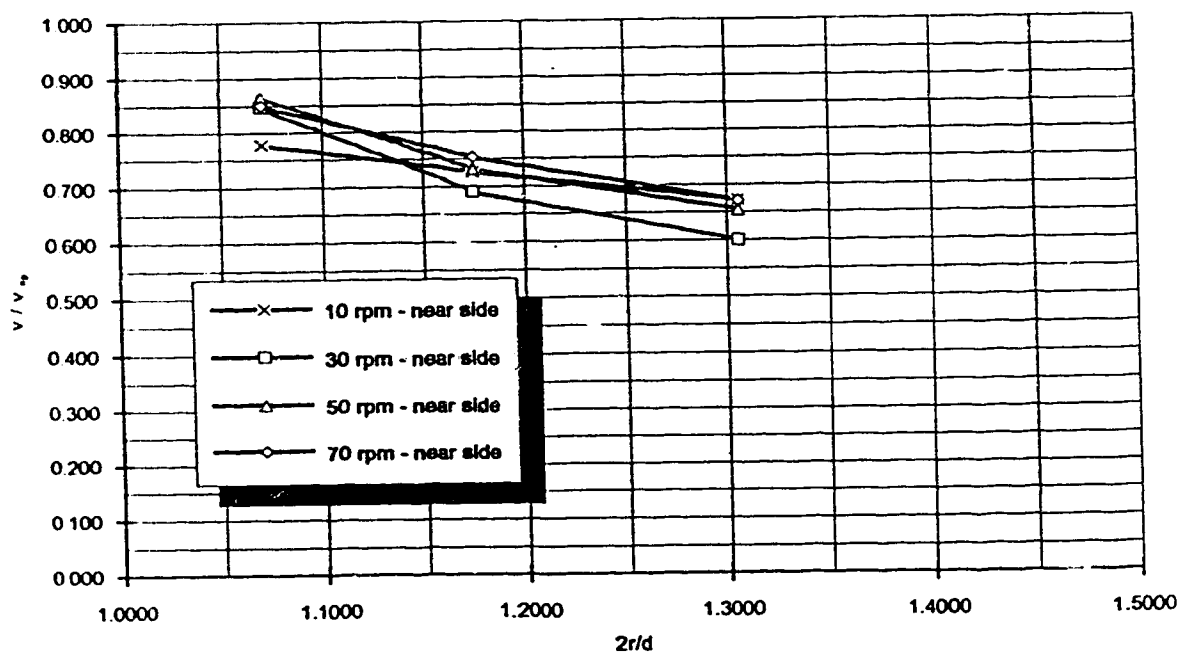


Figure 9-1-5n : trial 1 - ecodyne impeller ; 1:10 scale
radial variation of maximum tangential velocity - normalized by tip speed
 $d=42.62$ cm ; $b=10.83$ cm ; Influent $Q = 0$ L/s

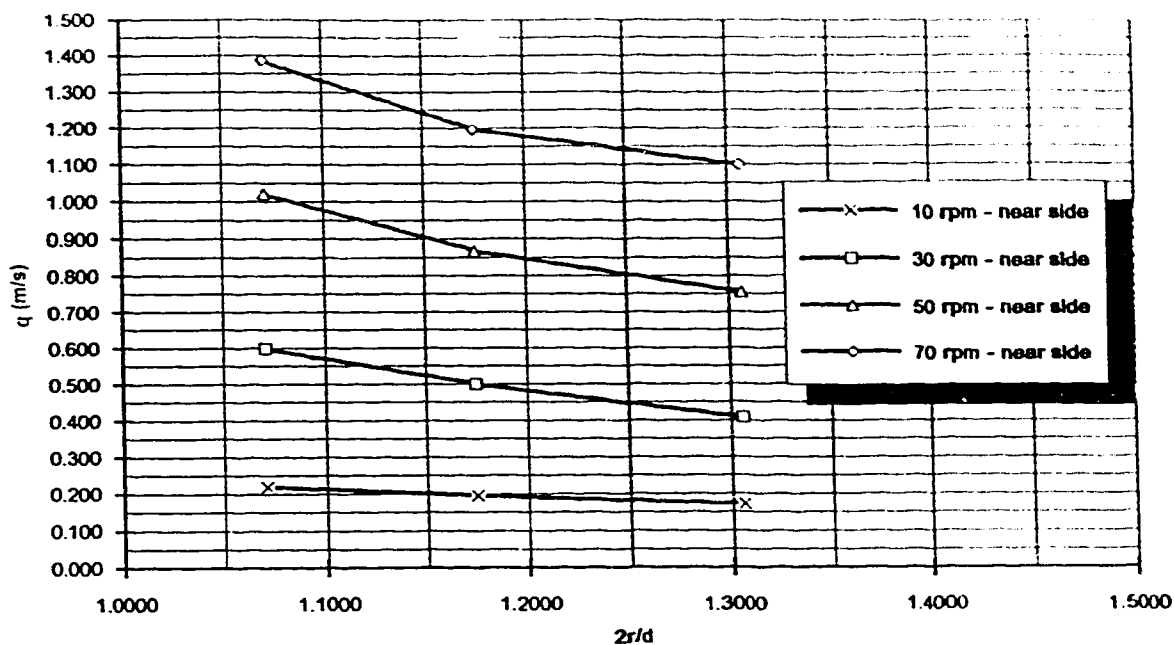


Figure 9-1-6 : trial 1 - ecodyne impeller ; 1:10 scale
radial variation of maximum velocity along axis of jet - not normalized by tip speed
 $d=42.62$ cm ; $b=10.83$ cm ; Influent $Q = 0$ L/s

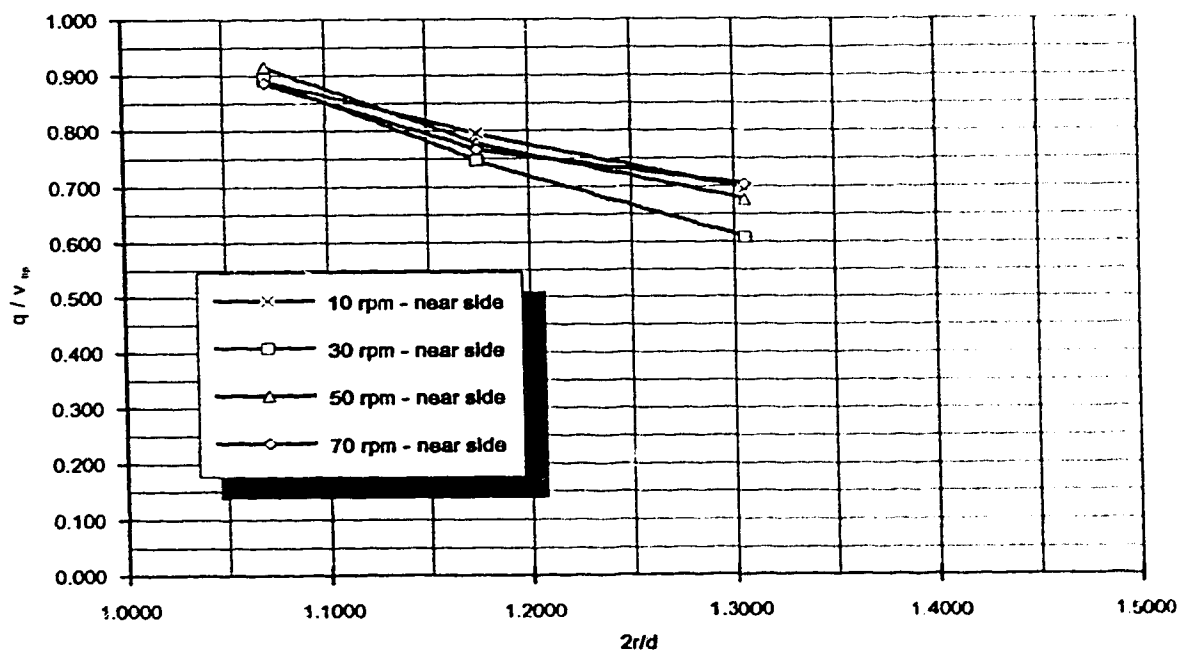


Figure 9-1-6n : trial 1 - ecodyne impeller ; 1:10 scale
radial variation of maximum velocity along axis of jet - normalized by tip speed
 $d=42.62$ cm ; $b=10.83$ cm ; Influent $Q = 0$ L/s

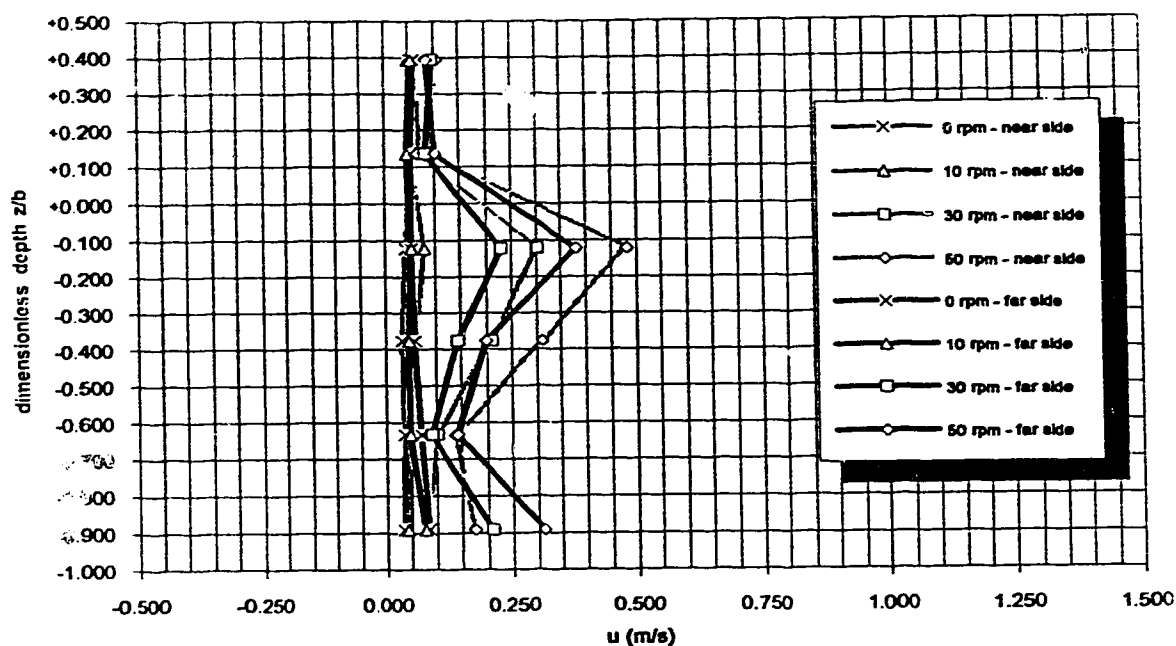


Figure 9-2-1 : trial 2 ; nbc model ; 1:10 scale ; influent $Q = 7.9$ L/s (Q200)
radial average velocities near impeller - not normalized by tip speed
 $d=42.62$ cm ; $b=10.8$ cm ; $2r/d=1.070$

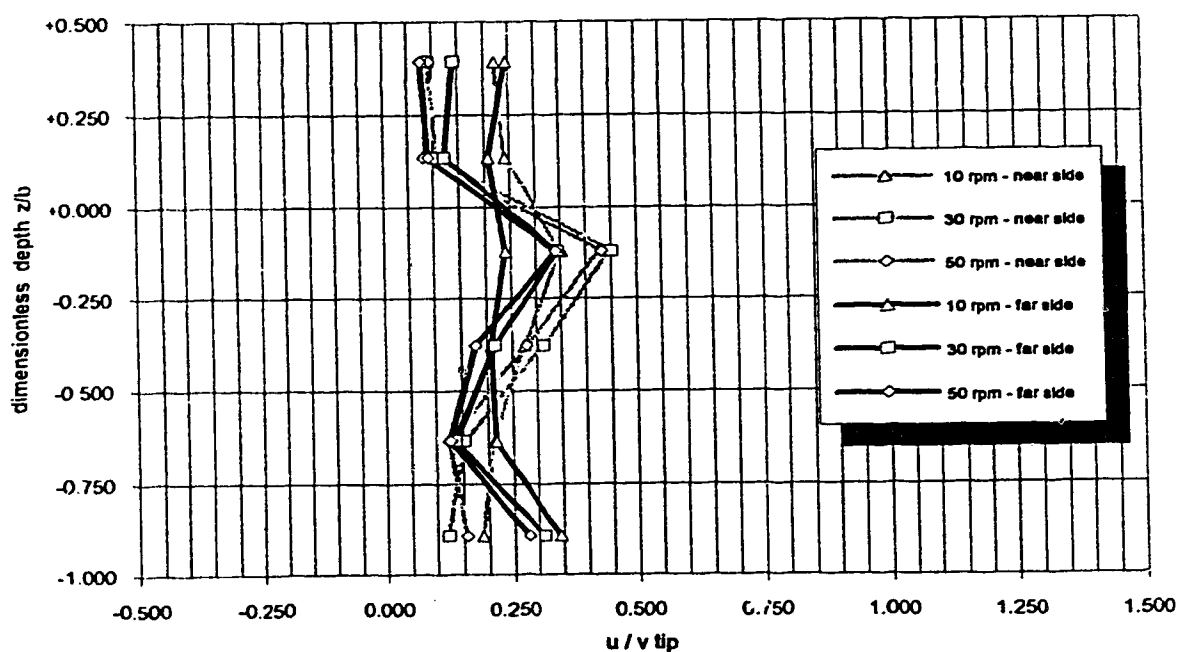


Figure 9-2-1n : trial 2 ; nbc model ; 1:10 scale ; influent $Q = 7.9$ L/s (Q200)
radial average velocities near impeller - normalized by tip speed
 $d=42.62$ cm ; $b=10.8$ cm ; $2r/d=1.070$

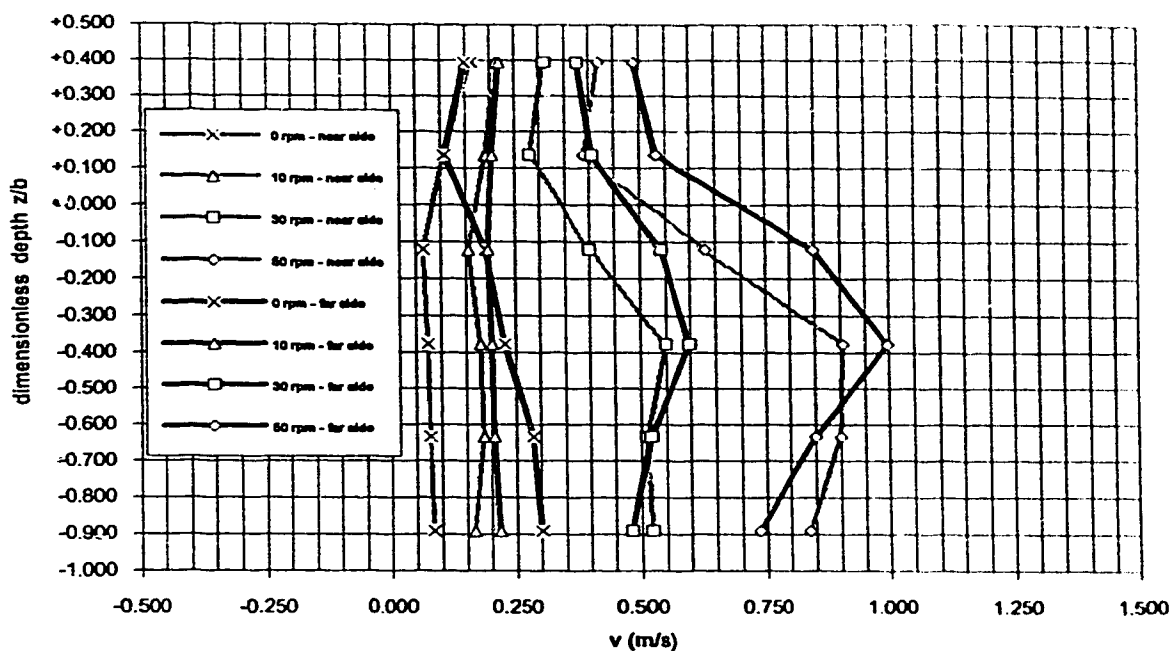


Figure 9-2-2 : trial 2 ; nhc model ; 1:10 scale ; influent $Q = 7.9$ L/s (Q200)
tangential average velocities near impeller - not normalized by tip speed
 $d=42.62$ cm ; $b=10.8$ cm ; $2r/d=1.070$

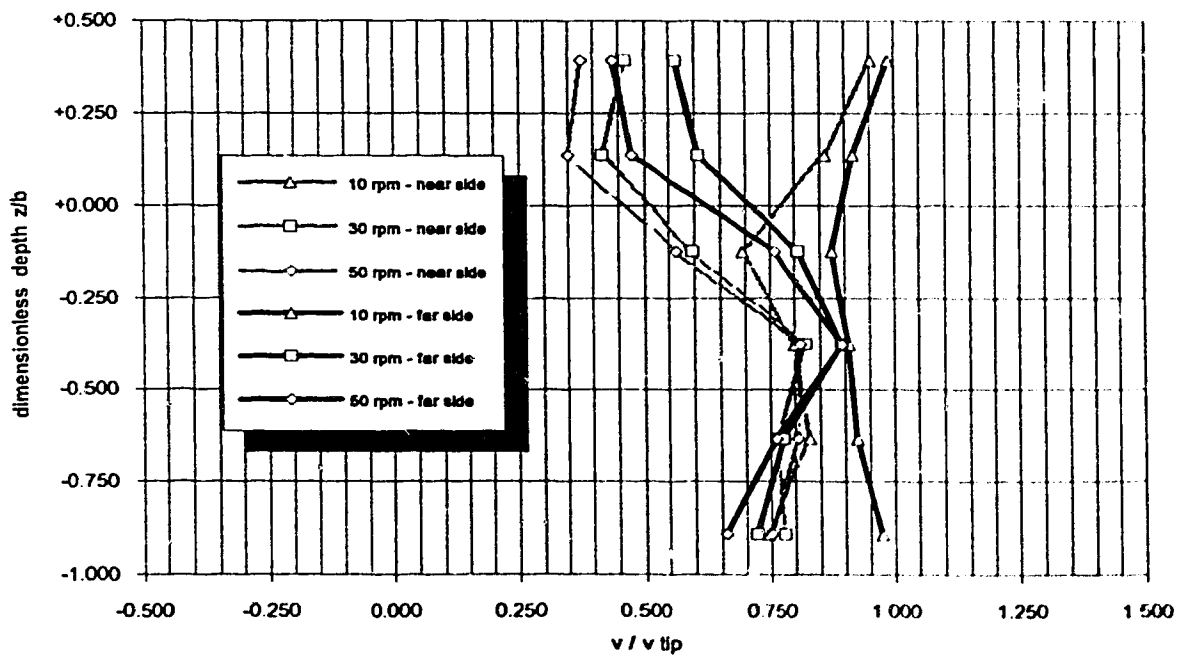


Figure 9-2-2n : trial 2 ; nhc model ; 1:10 scale ; influent $Q = 7.9$ L/s (Q200)
tangential average velocities near impeller - normalized by tip speed
 $d=42.62$ cm ; $b=10.8$ cm ; $2r/d=1.070$

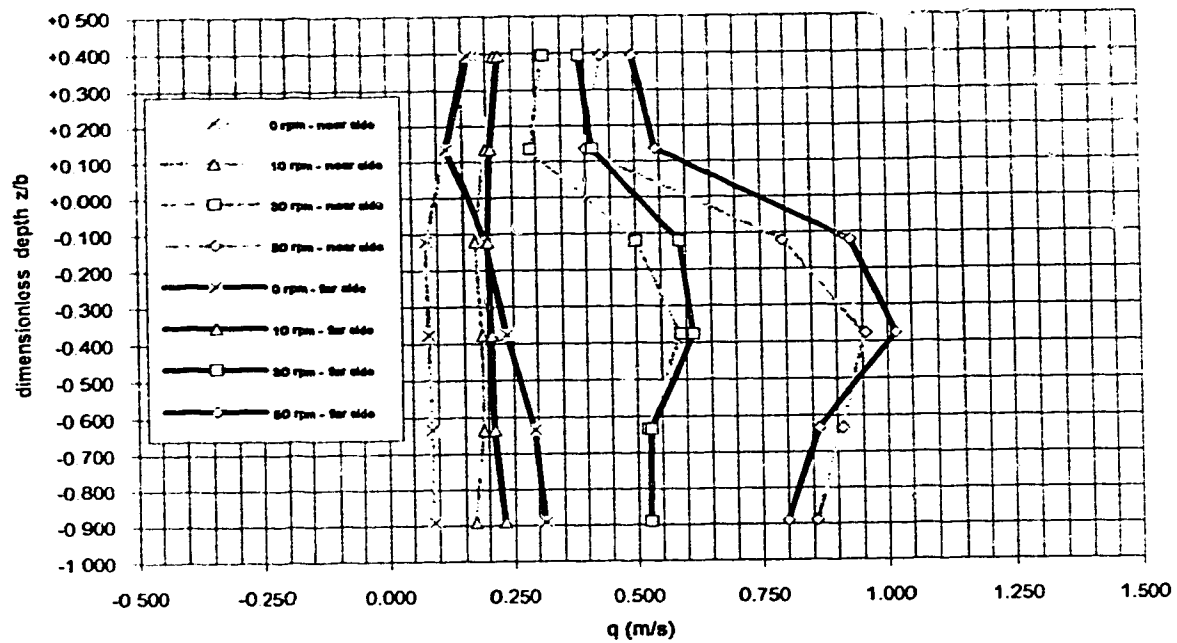


Figure 9-2-3 : trial 2 ; nhc model ; 1:10 scale ; Influent $Q = 7.9 \text{ L/s}$ (Q200)
average velocities along axis of jet - not normalized by tip speed
 $d=42.62 \text{ cm}$; $b=10.8 \text{ cm}$; $2r/d=1.070$

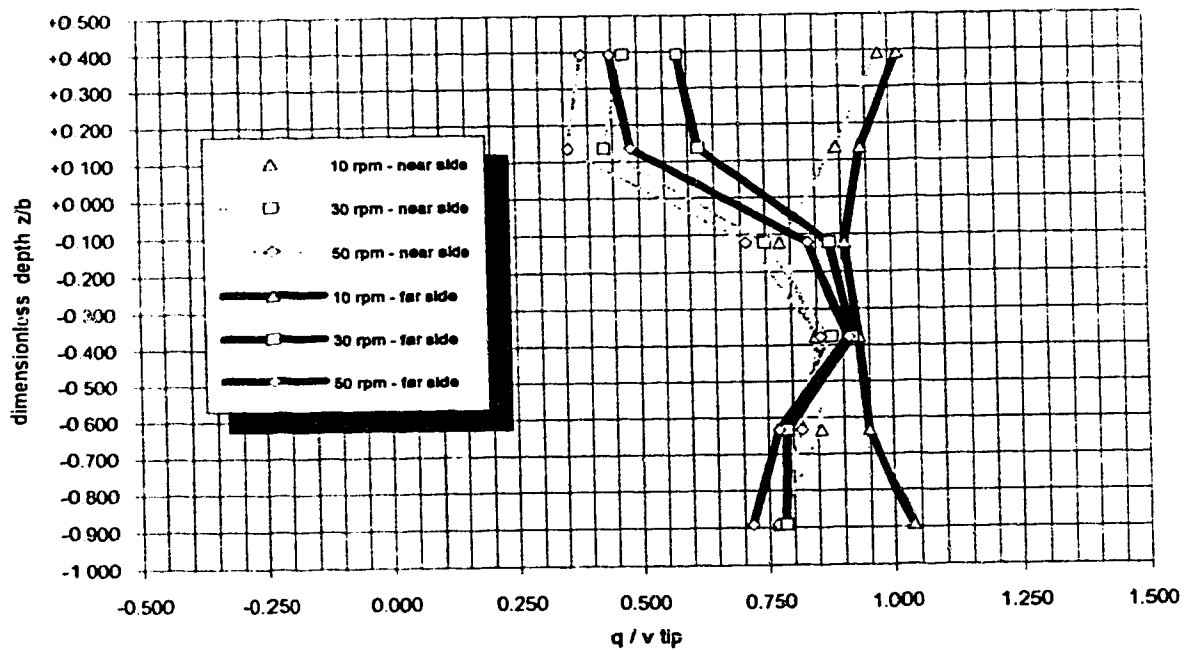


Figure 9-2-3n : trial 2 ; nhc model ; 1:10 scale ; Influent $Q = 7.9 \text{ L/s}$ (Q200)
average velocity along axis of jet - normalized by tip speed
 $d=42.62 \text{ cm}$; $b=10.8 \text{ cm}$; $2r/d=1.070$

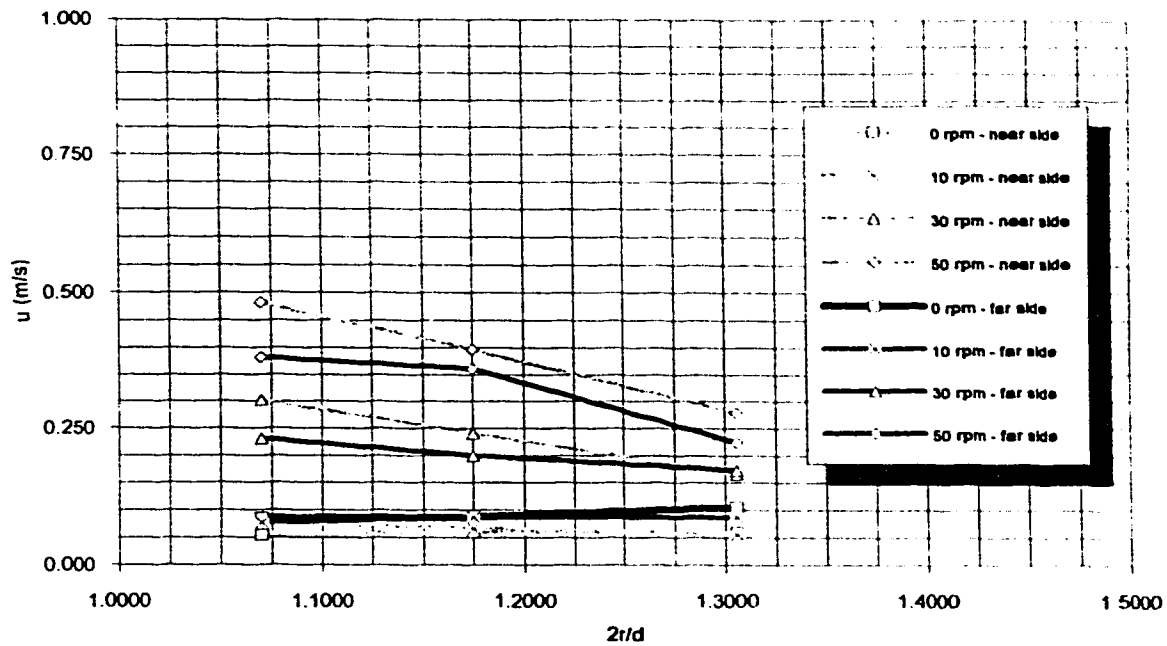


Figure 9-2-4 : trial 2 - nhc model ; 1:10 scale
radial variation of maximum radial velocity - not normalized by tip speed
 $d=42.62$ cm ; $b=10.83$ cm ; Influent $Q = 7.9$ L/s (Q200)

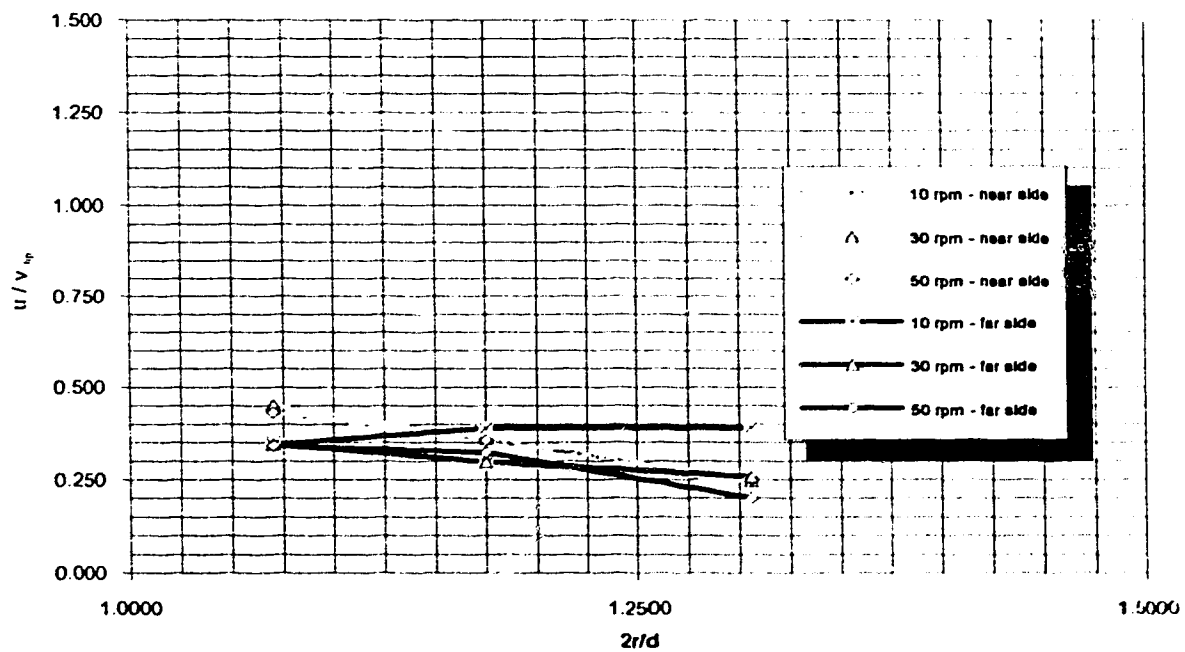


Figure 9-2-4n : trial 2 - nhc model ; 1:10 scale
radial variation of maximum radial velocity - normalized by tip speed
 $d=42.62$ cm ; $b=10.83$ cm ; Influent $Q = 7.9$ L/s (Q200)

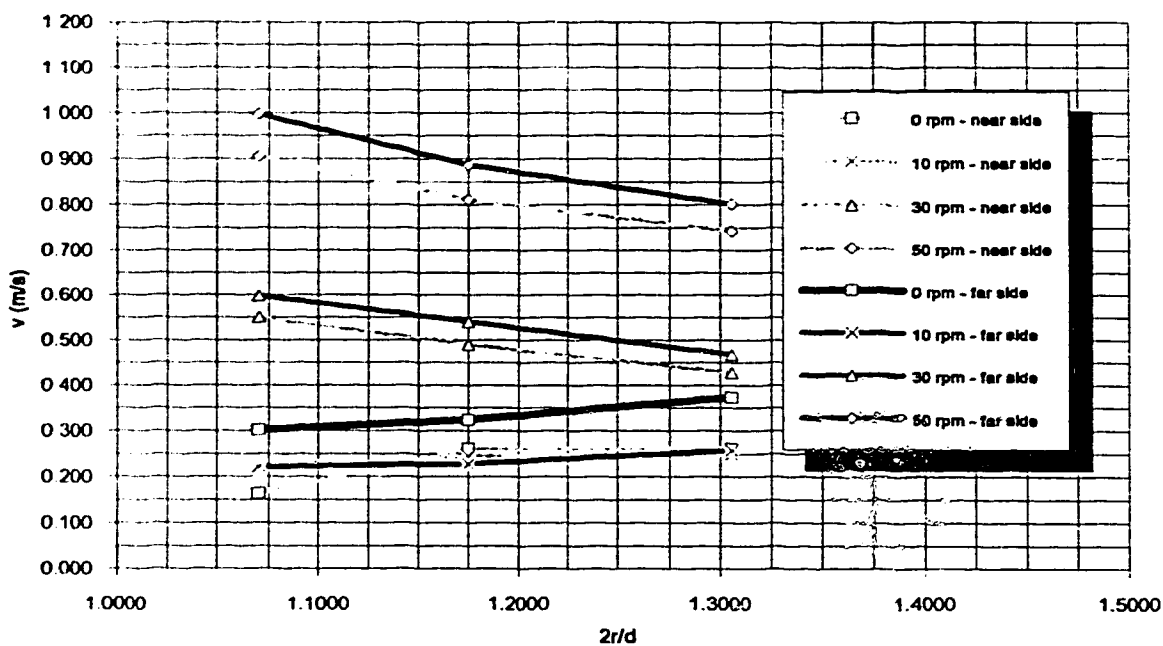


Figure 9-2-5 : trial 2 - nhc model ; 1:10 scale
radial variation of maximum tangential velocity - not normalized by tip speed
 $d=42.62$ cm ; $b=10.83$ cm ; Influent $Q = 7.9$ L/s (Q200)

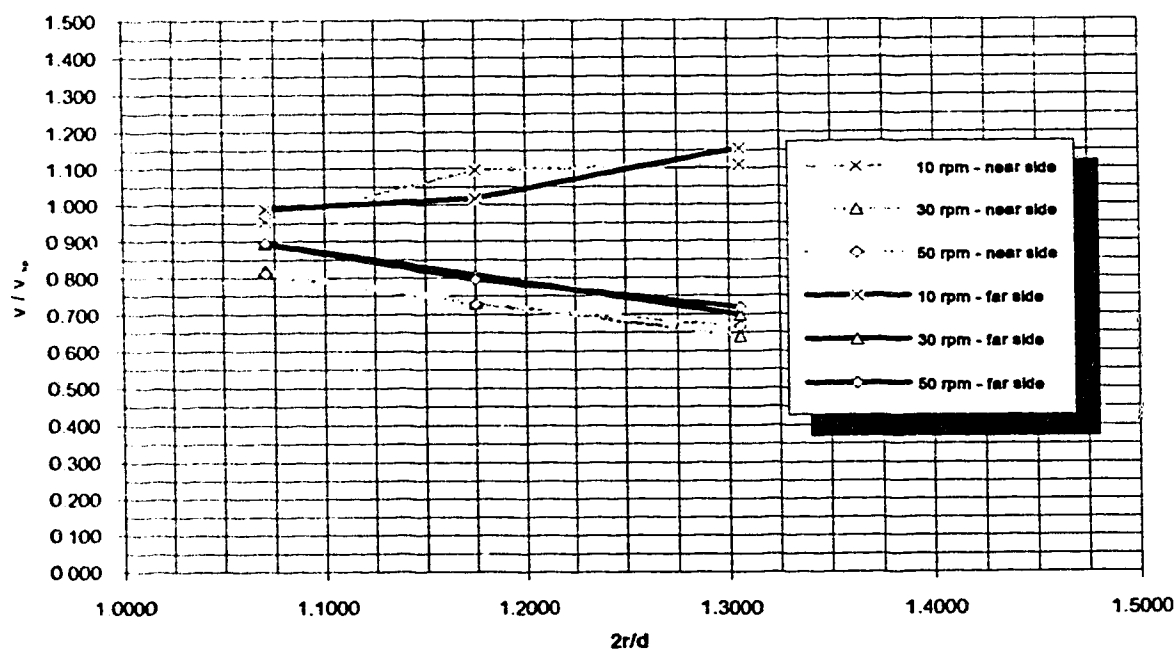
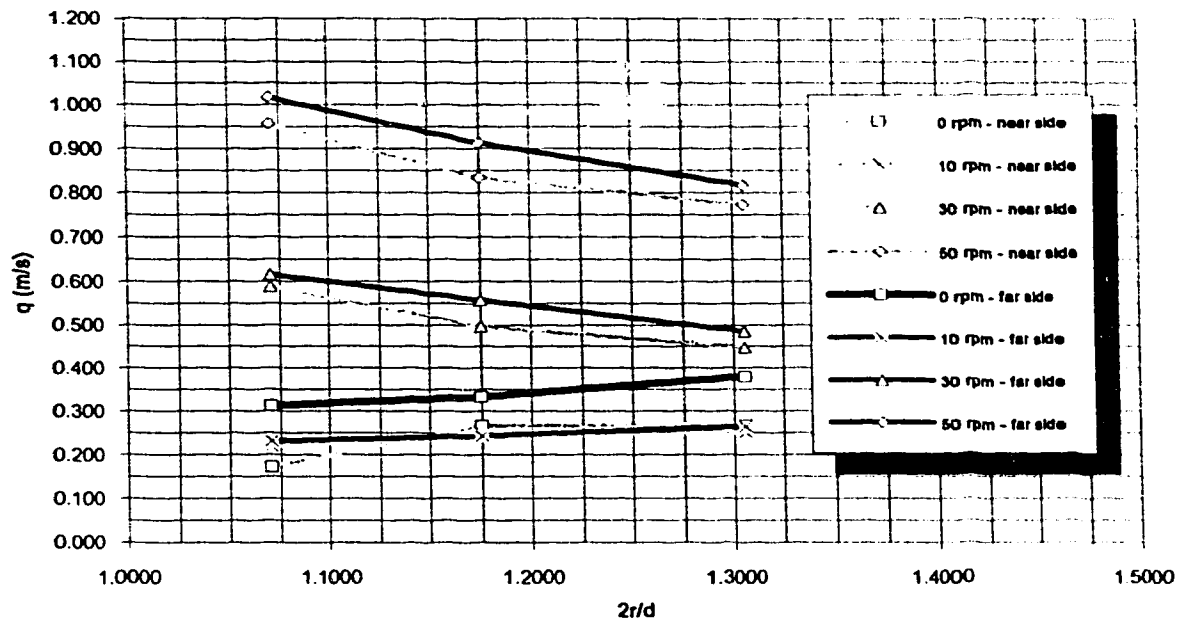
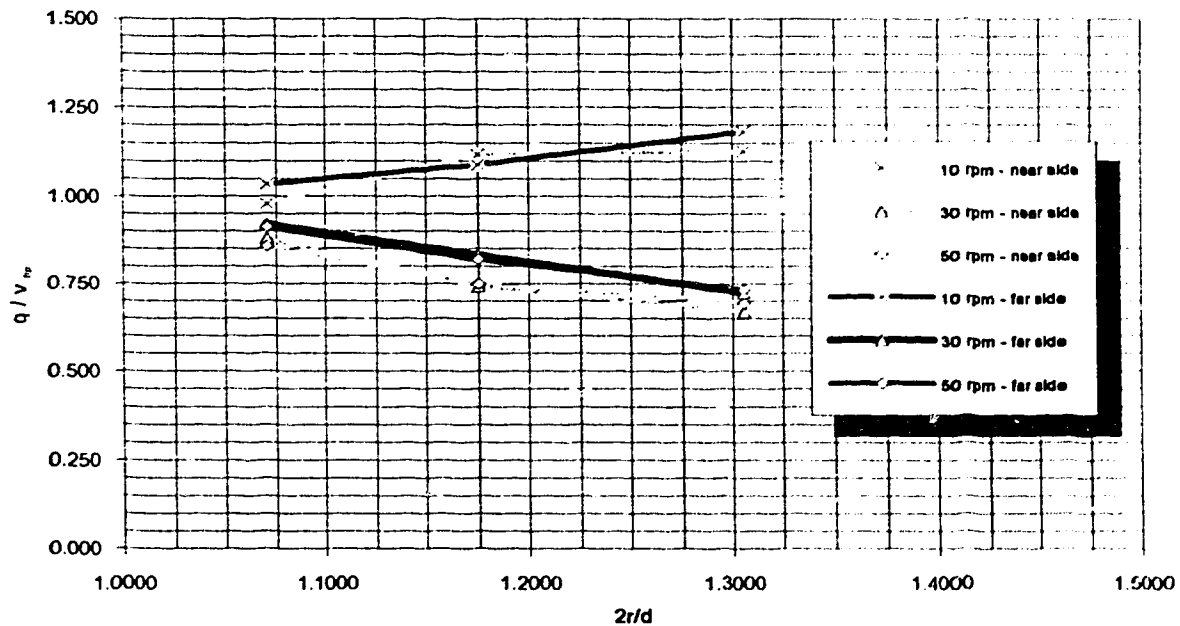


Figure 9-2-5n : trial 2 - nhc model ; 1:10 scale
radial variation of maximum tangential velocity - normalized by tip speed
 $d=42.62$ cm ; $b=10.83$ cm ; Influent $Q = 7.9$ L/s (Q200)



trial 2 - nhc model ; 1:10 scale

Figure 9-2-6 : radial variation of maximum velocity along axis of jet - not normalized by tip speed
 $d=42.62$ cm ; $b=10.83$ cm ; Influent $Q = 7.9$ L/s (Q200)



trial 2 - nhc model ; 1:10 scale

Figure 9-2-6n : radial variation of maximum velocity along axis of jet - normalized by tip speed
 $d=42.62$ cm ; $b=10.83$ cm ; Influent $Q = 7.9$ L/s (Q200)

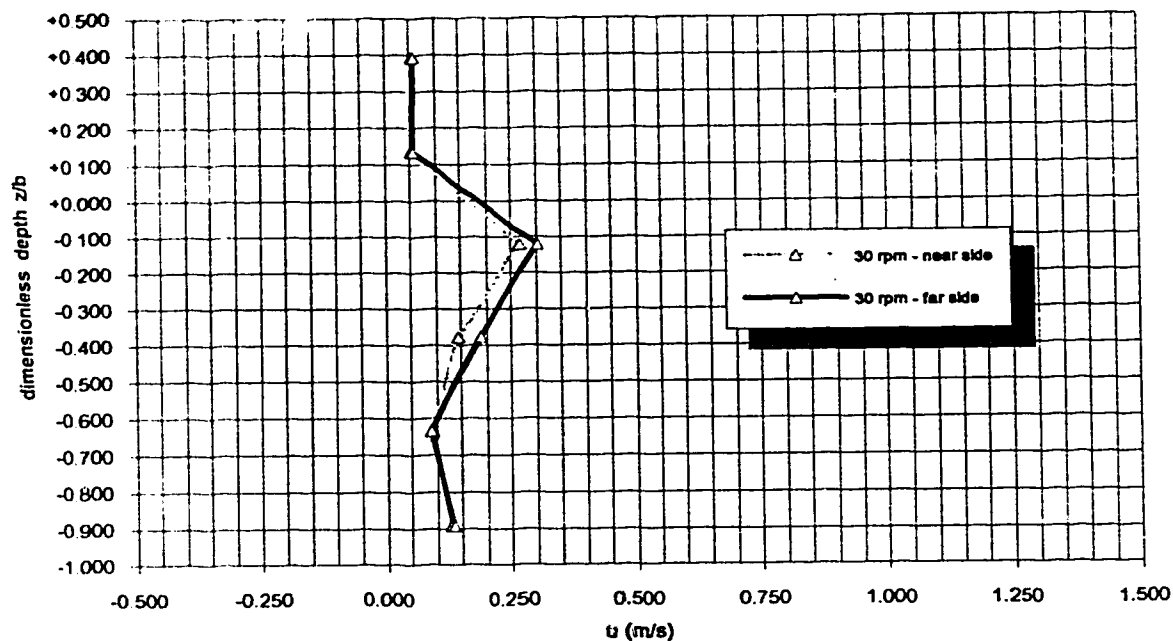


Figure 9-3-1 : trial 3 ; nhc model ; 1:10 scale ; Influent $Q = 4$ L/s (Q100)
radial average velocities near Impeller - not normalized by tip speed
 $d=42.62$ cm ; $b=10.8$ cm ; $2r/d=1.070$

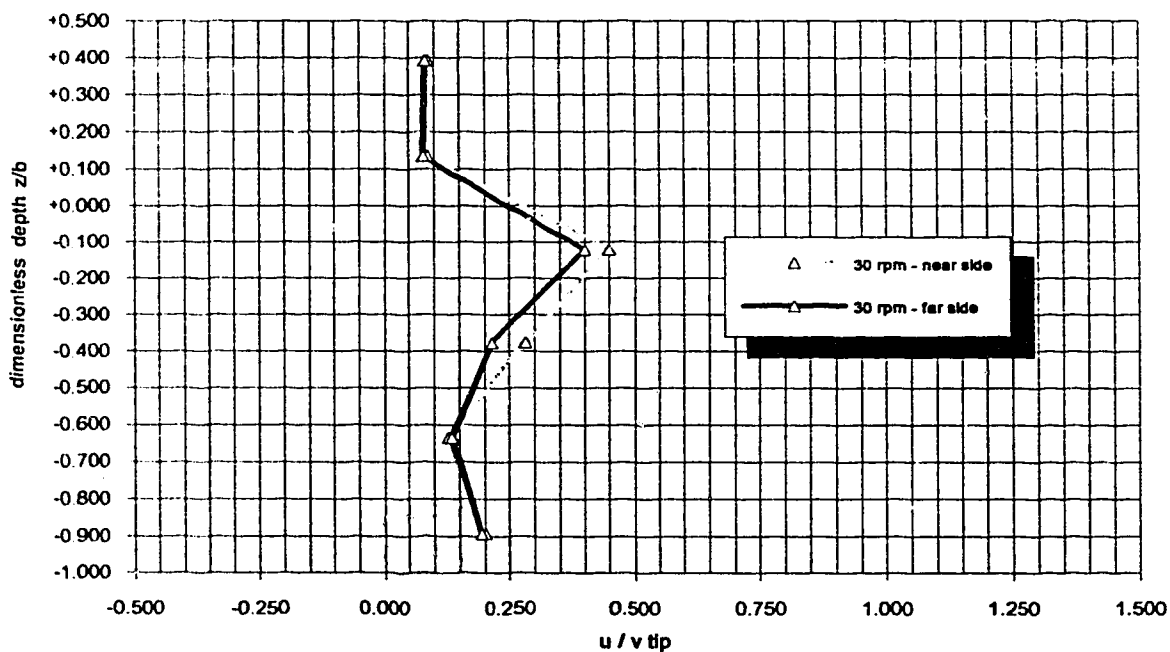


Figure 9-3-1n : trial 3 ; nhc model ; 1:10 scale ; Influent $Q = 4$ L/s (Q100)
radial average velocities near Impeller - normalized by tip speed
 $d=42.62$ cm ; $b=10.8$ cm ; $2r/d=1.070$

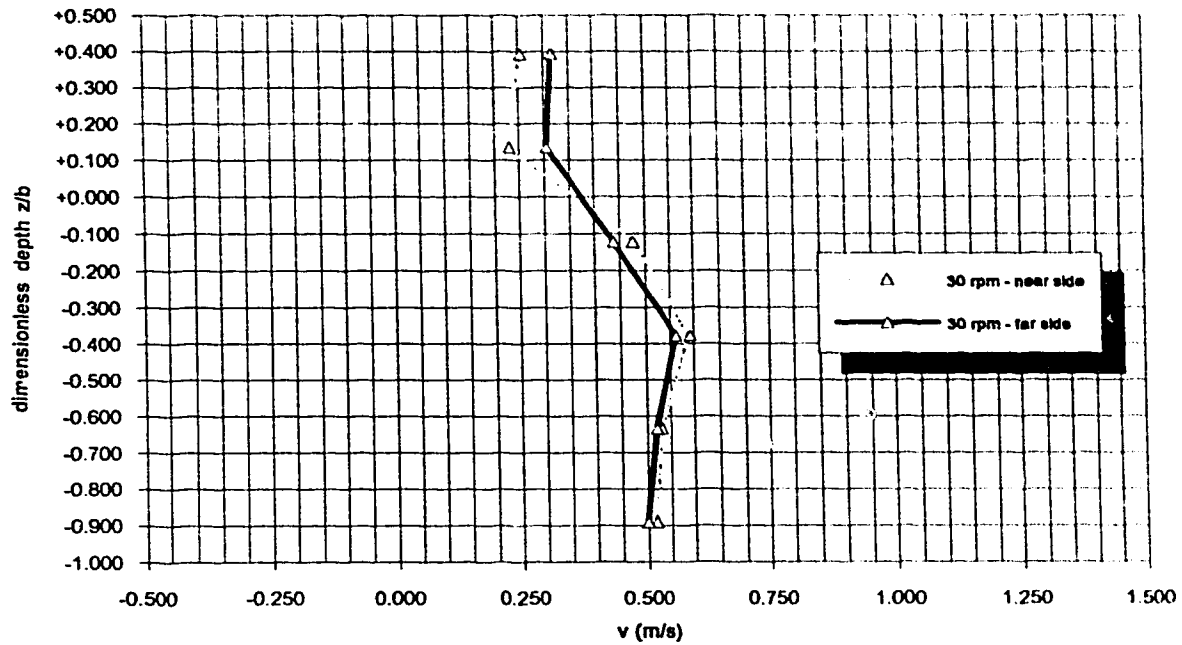


Figure 9-3-2 :

trial 3 ; nhc model ; 1:10 scale ; influent $Q = 4 \text{ L/s}$ (Q100)
 tangential average velocities near impeller - not normalized by tip speed
 $d=42.62 \text{ cm}$; $b=10.8 \text{ cm}$; $2r/d=1.070$

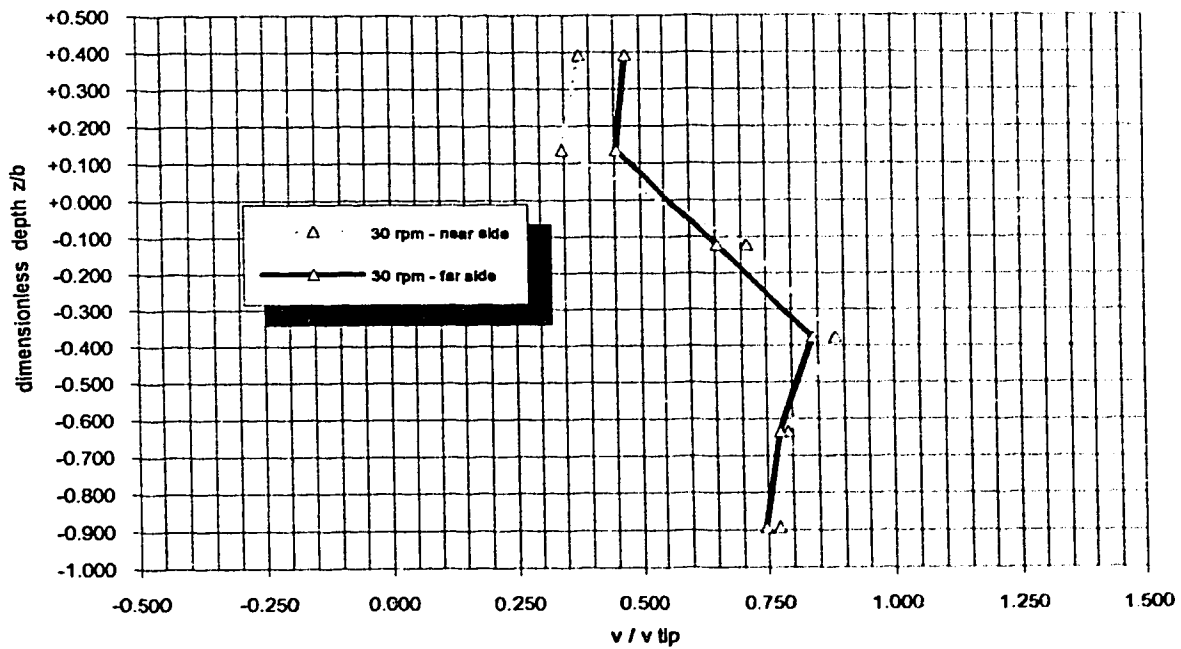


Figure 9-3-2n :

trial 3 ; nhc model ; 1:10 scale ; influent $Q = 4 \text{ L/s}$ (Q100)
 tangential average velocities near impeller - normalized by tip speed
 $d=42.62 \text{ cm}$; $b=10.8 \text{ cm}$; $2r/d=1.070$

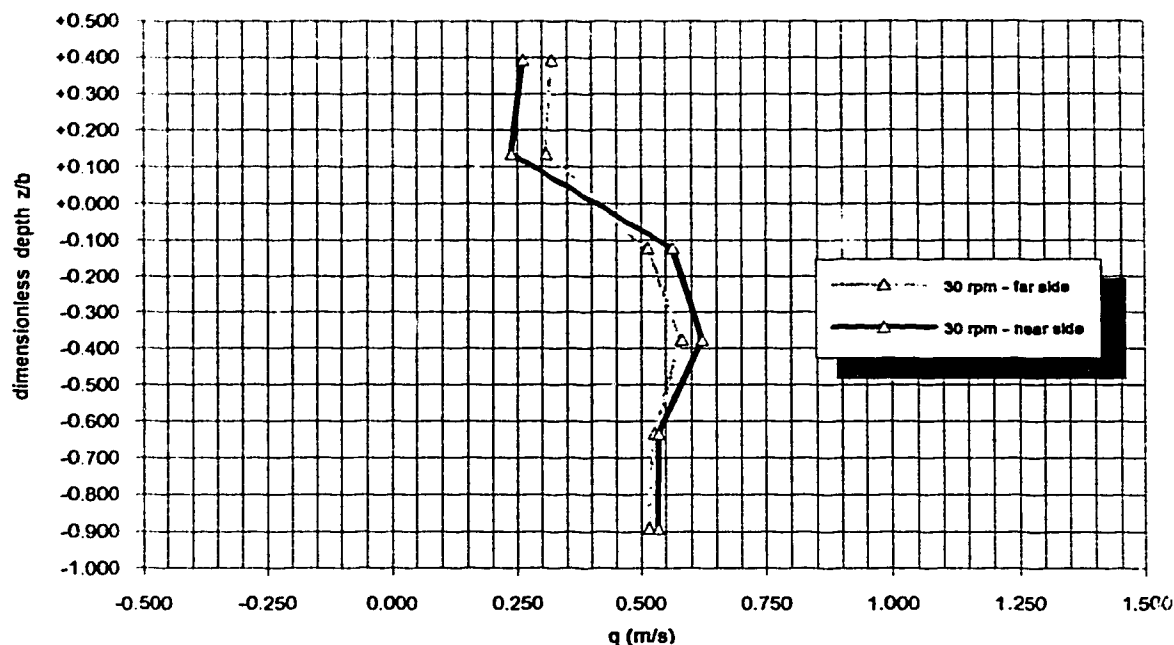


Figure 9-3-3 : trial 3 ; nhc model ; 1:10 scale ; influent $Q = 4$ L/s ($Q100$)
maximum average velocities along axis of jet - not normalized by tip speed
 $d=42.62$ cm ; $b=10.8$ cm ; $2r/d=1.070$

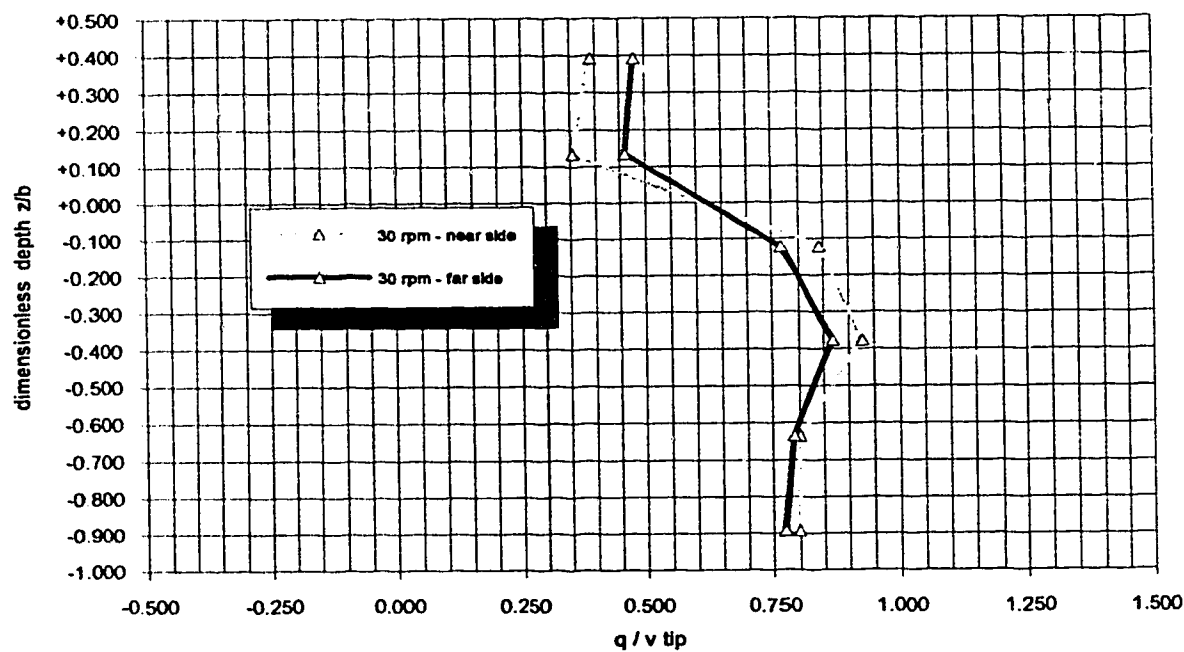


Figure 9-3-3n : trial 3 ; nhc model ; 1:10 scale ; influent $Q = 4$ L/s ($Q100$)
average velocities along axis of jet - normalized by tip speed
 $d=42.62$ cm ; $b=10.8$ cm ; $2r/d=1.070$

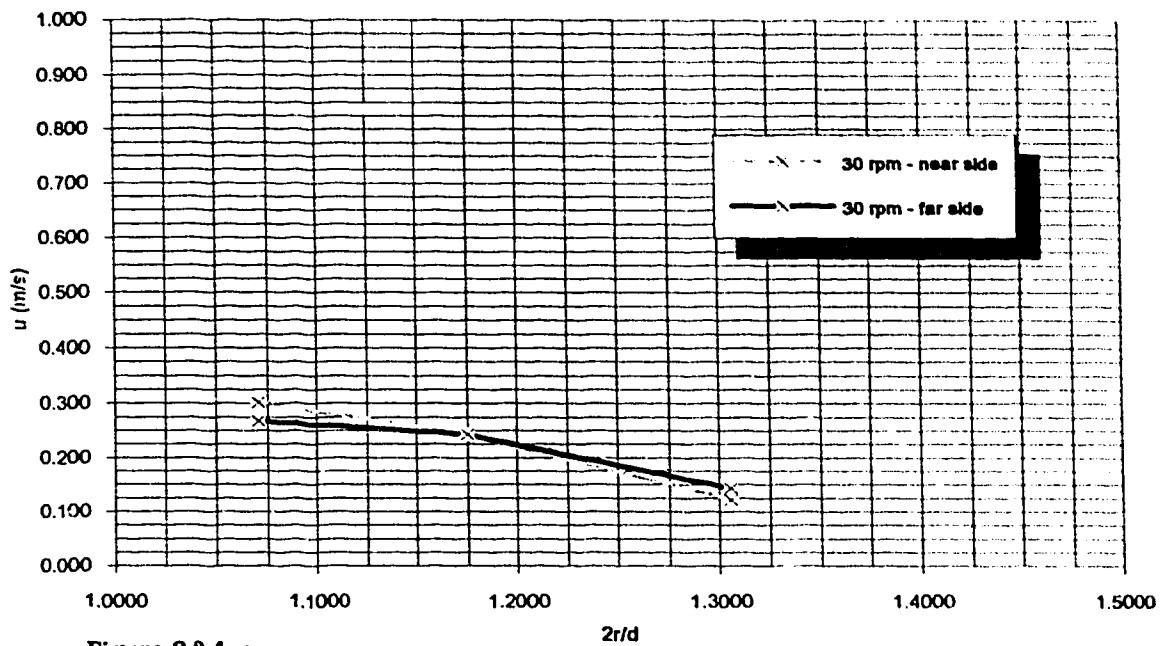


Figure 9-3.4 :
 trial 3 - nhc model ; 1:10 scale
 radial variation of maximum radial velocity - not normalized by tip speed
 $d=42.62$ cm ; $b=10.83$ cm ; influent $Q = 4$ L/s (Q100)

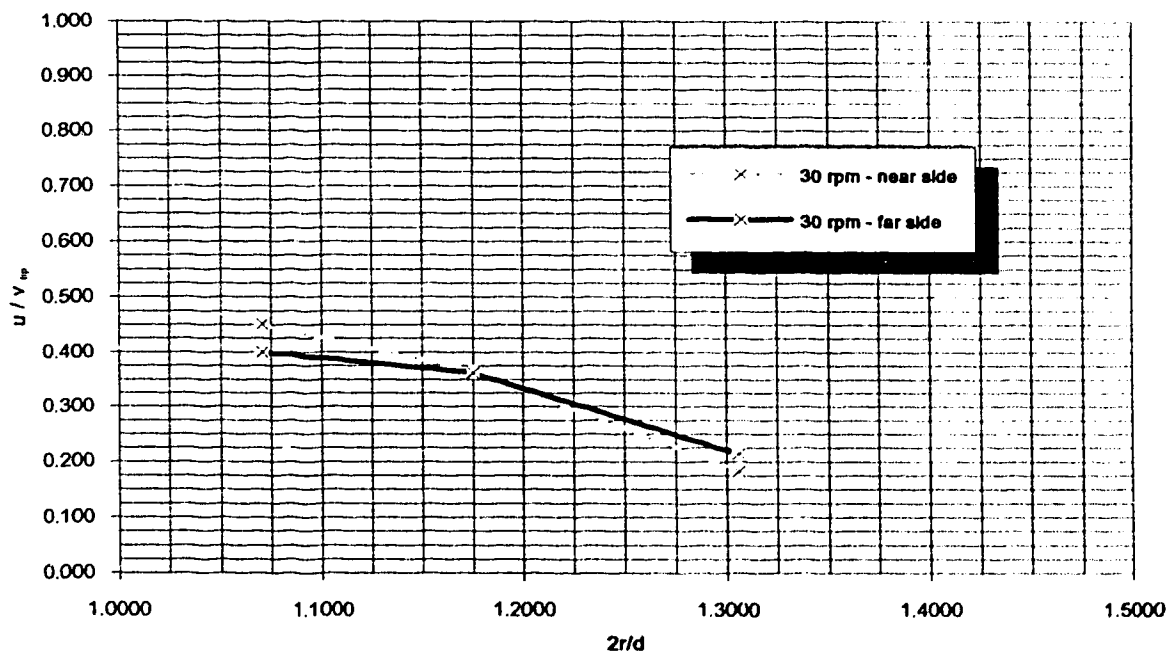


Figure 9-3.4n :
 trial 3 - nhc model ; 1:10 scale
 radial variation of maximum radial velocity - normalized by tip speed
 $d=42.62$ cm ; $b=10.83$ cm ; influent $Q = 4$ L/s (Q100)

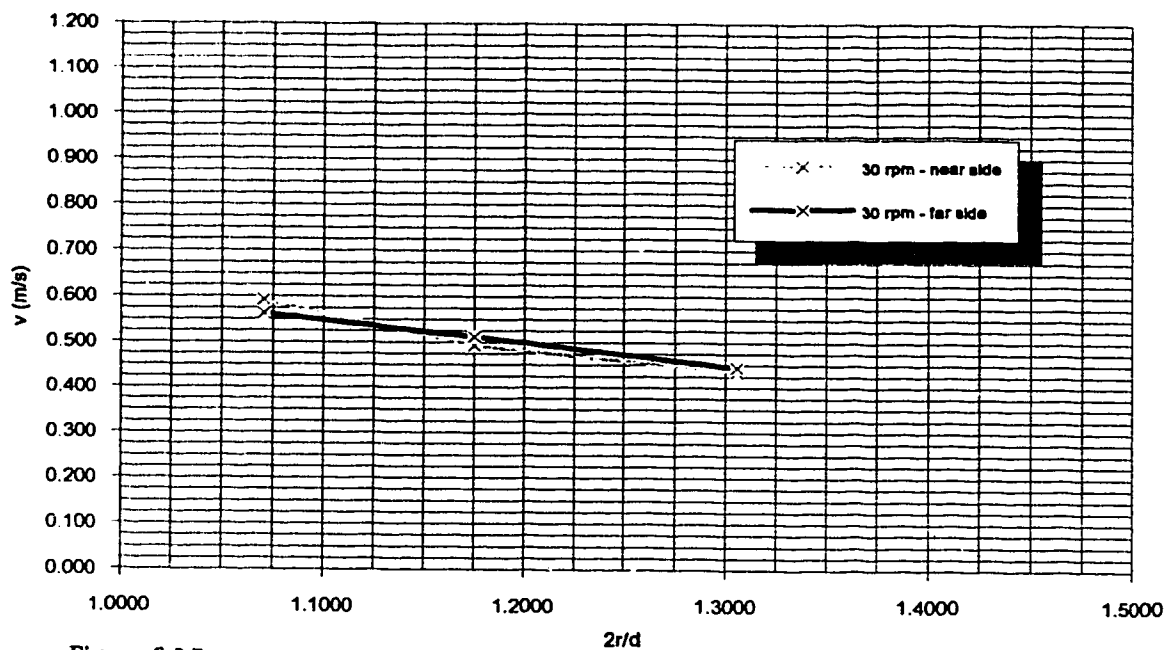


Figure 9-3-5 : trial 3 - nhc model ; 1:10 scale
radial variation of maximum tangential velocity - not normalized by tip speed
 $d=42.62$ cm ; $b=10.83$ cm ; Influent $Q = 4$ L/s (Q100)

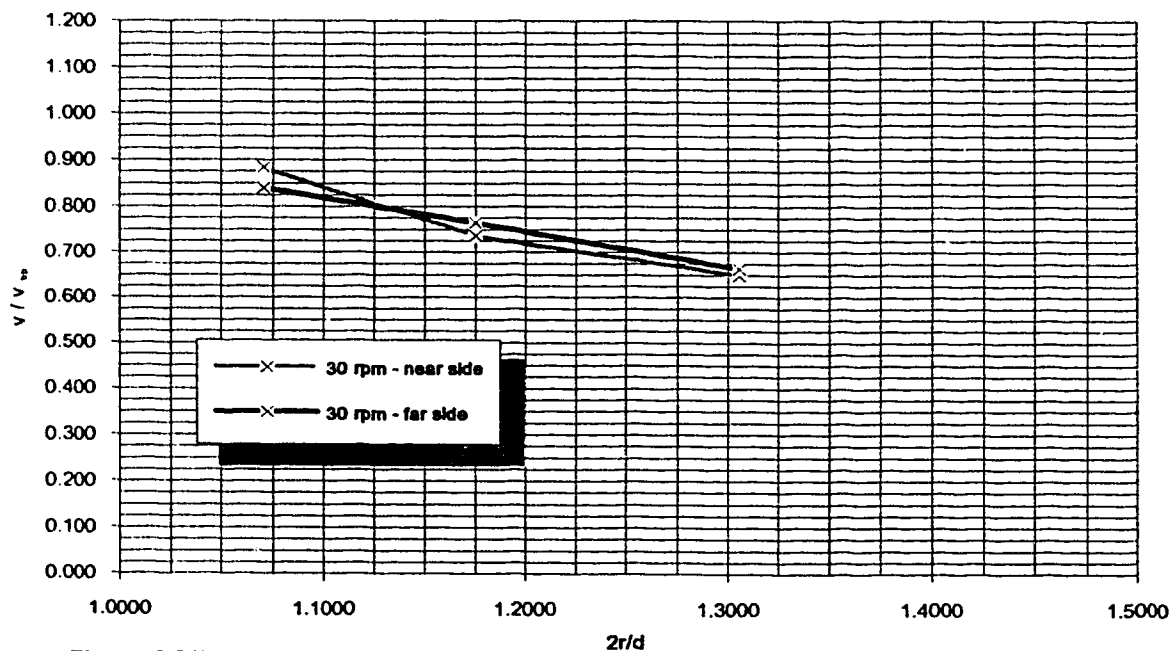


Figure 9-3-5n : trial 3 - nhc model ; 1:10 scale
radial variation of maximum tangential velocity - normalized by tip speed
 $d=42.62$ cm ; $b=10.83$ cm ; Influent $Q = 4$ L/s (Q100)

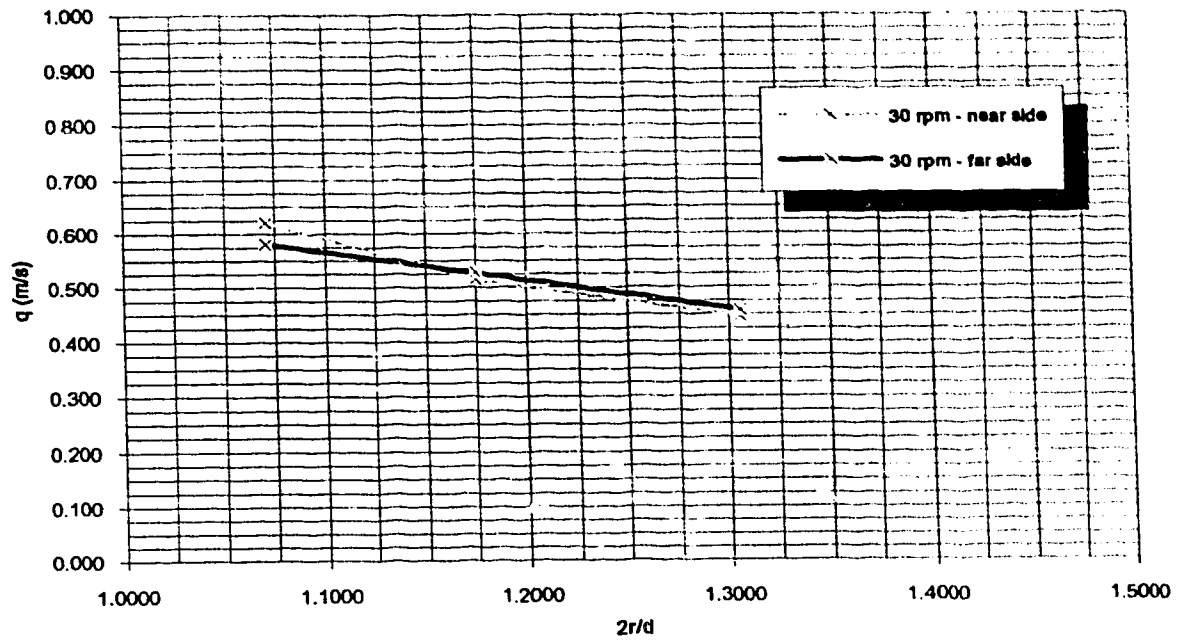


Figure 9-3-6 : trial 3 - nhc model ; 1:10 scale
radial variation of maximum velocity along axis of jet - not normalized by tip speed
 $d=42.62$ cm ; $b=10.83$ cm ; Influent $Q = 4$ L/s (Q100)

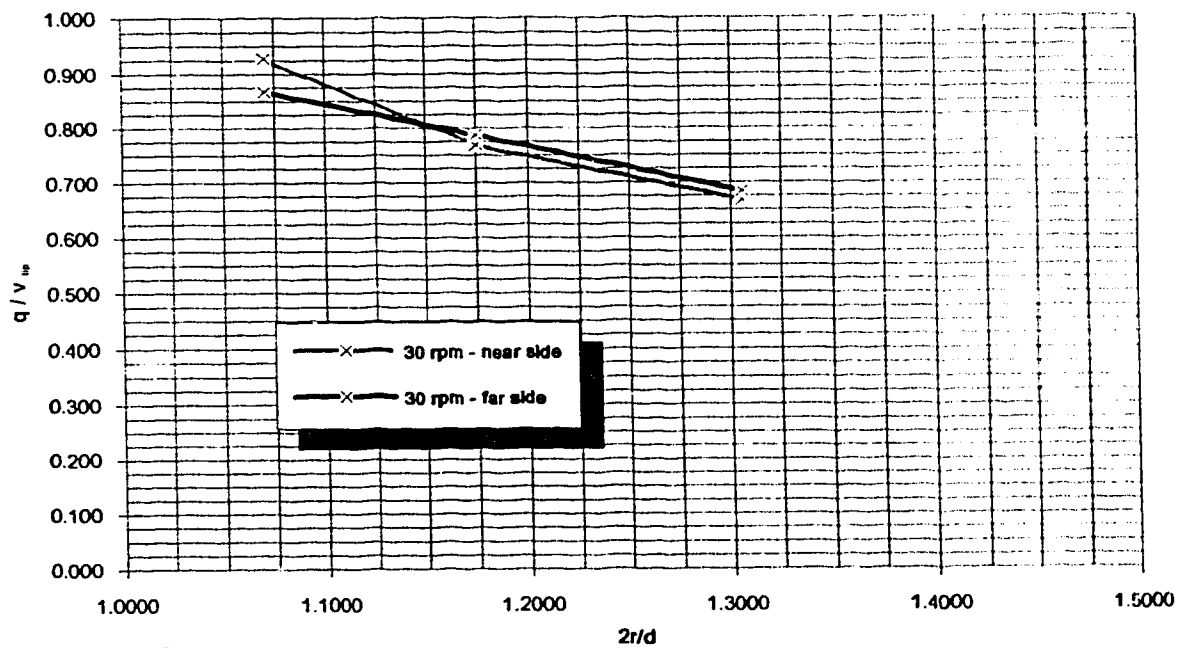


Figure 9-3-6n : trial 3 - nnc model ; 1:10 scale
radial variation of maximum velocity along axis of jet - normalized by tip speed
 $d=42.62$ cm ; $b=10.83$ cm ; Influent $Q = 4$ L/s (Q100)

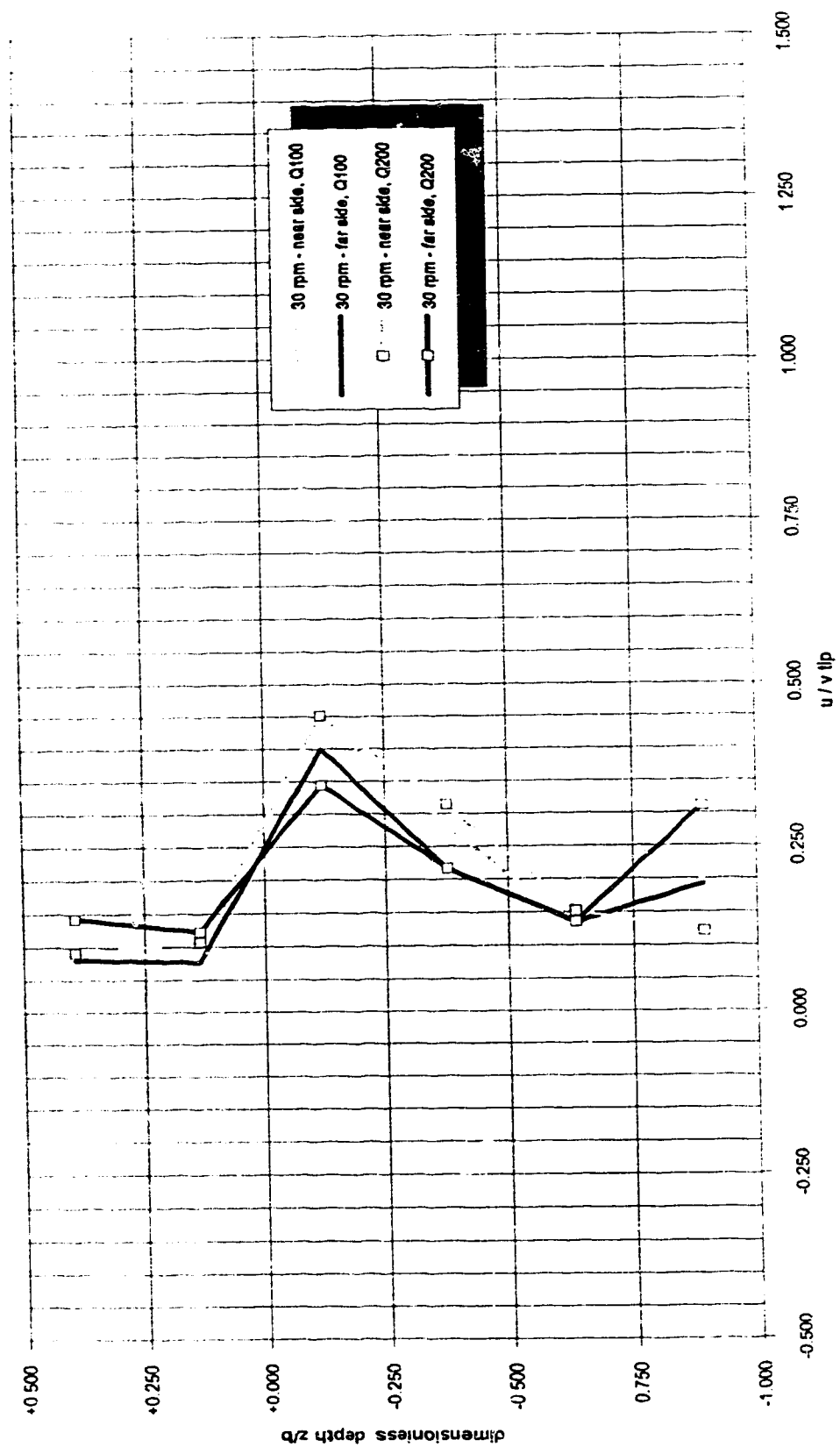


Figure 9.4.1 :
 nht model ; 1:10 scale
 radial average velocities near impeller - normalized by tip speed
 $d=42.62$ cm ; $b=10.8$ cm ; $2r/d=1.070$

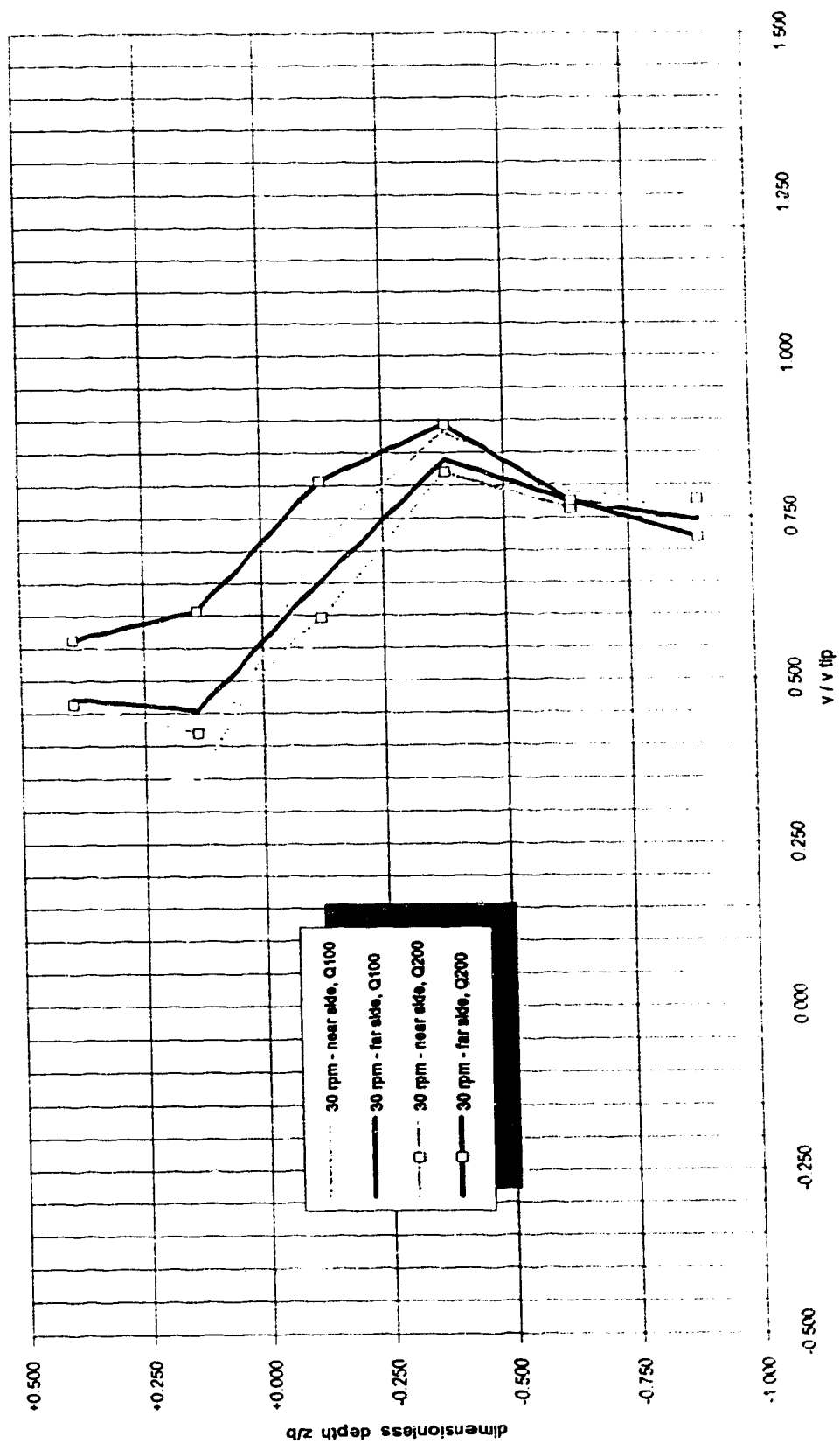


Figure 9-4.2 : nhc model : 1:10 scale
 tangential average velocities near impeller - normalized by tip speed
 $d=42.62$ cm ; $b=10.8$ cm ; $2r/d=1.070$

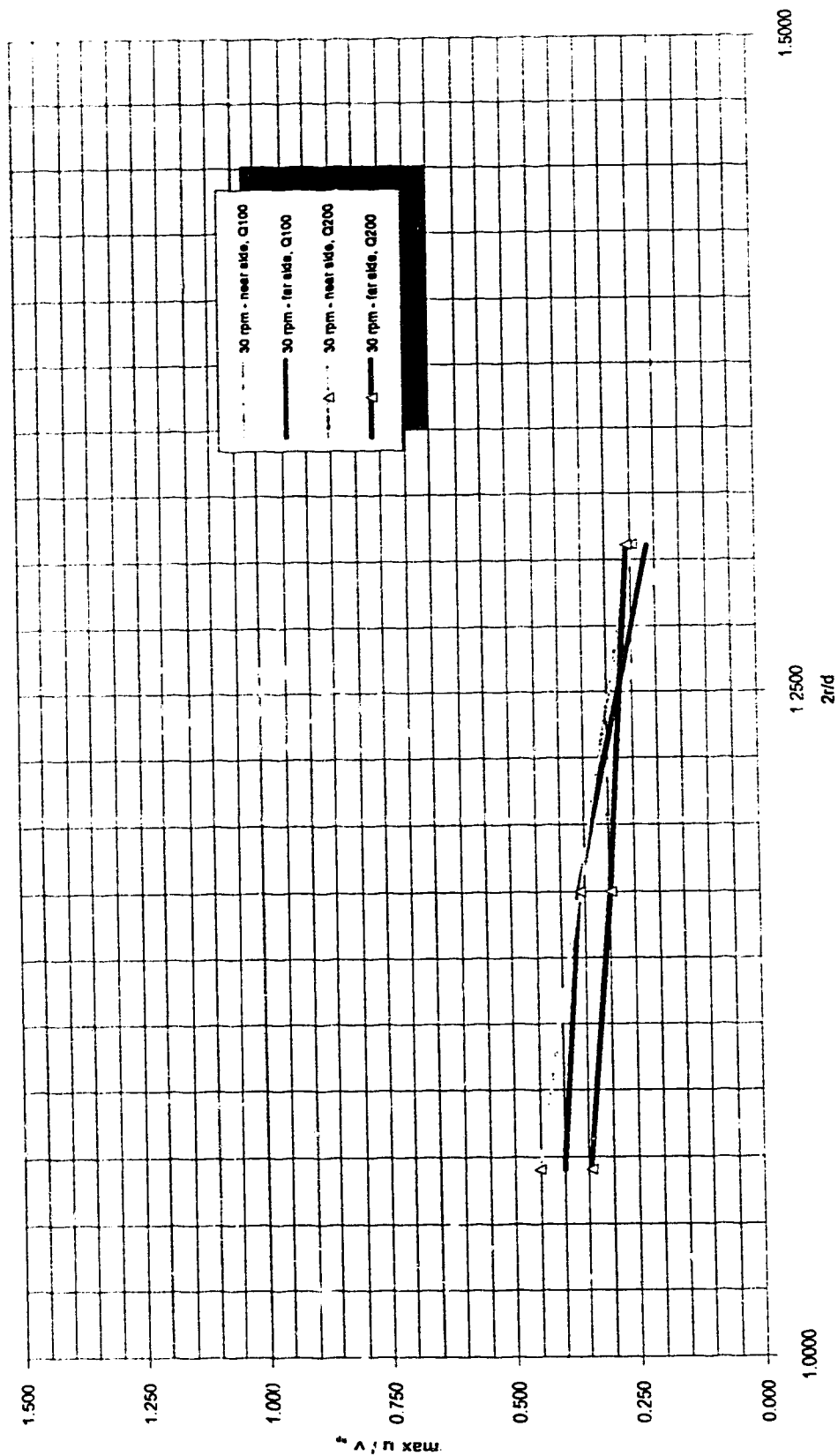


Figure 9-43 :
nhc model : 1:10 scale
radial variation of maximum radial velocity - normalized by tip speed
d=42.62 cm ; b=10.83 cm

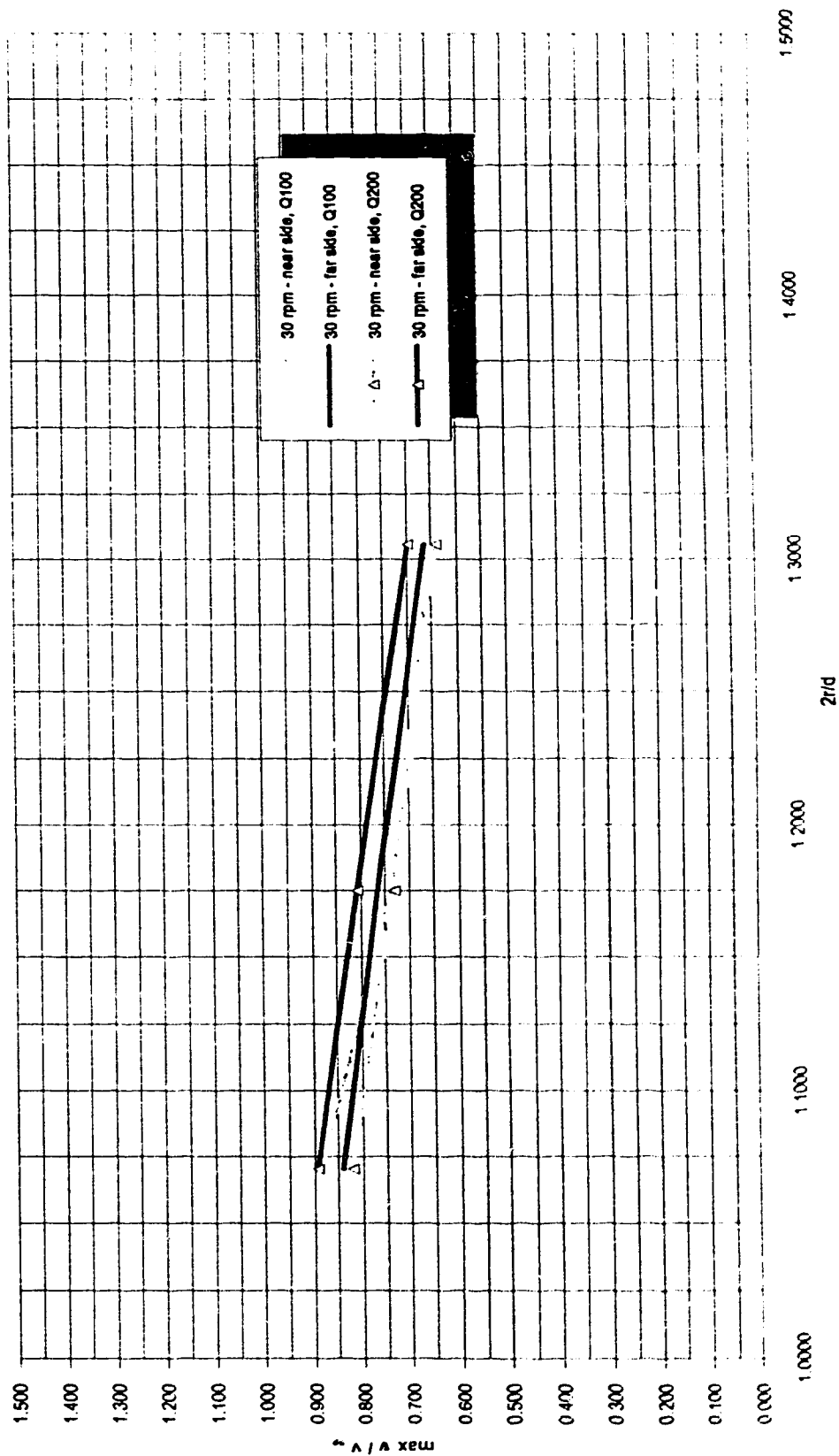


Figure 9-4-1 :
 nhc model ; 1:10 scale
 radial variation of maximum tangential velocity - normalized by tip speed
 $d=42.62$ cm ; $b=10.83$ cm

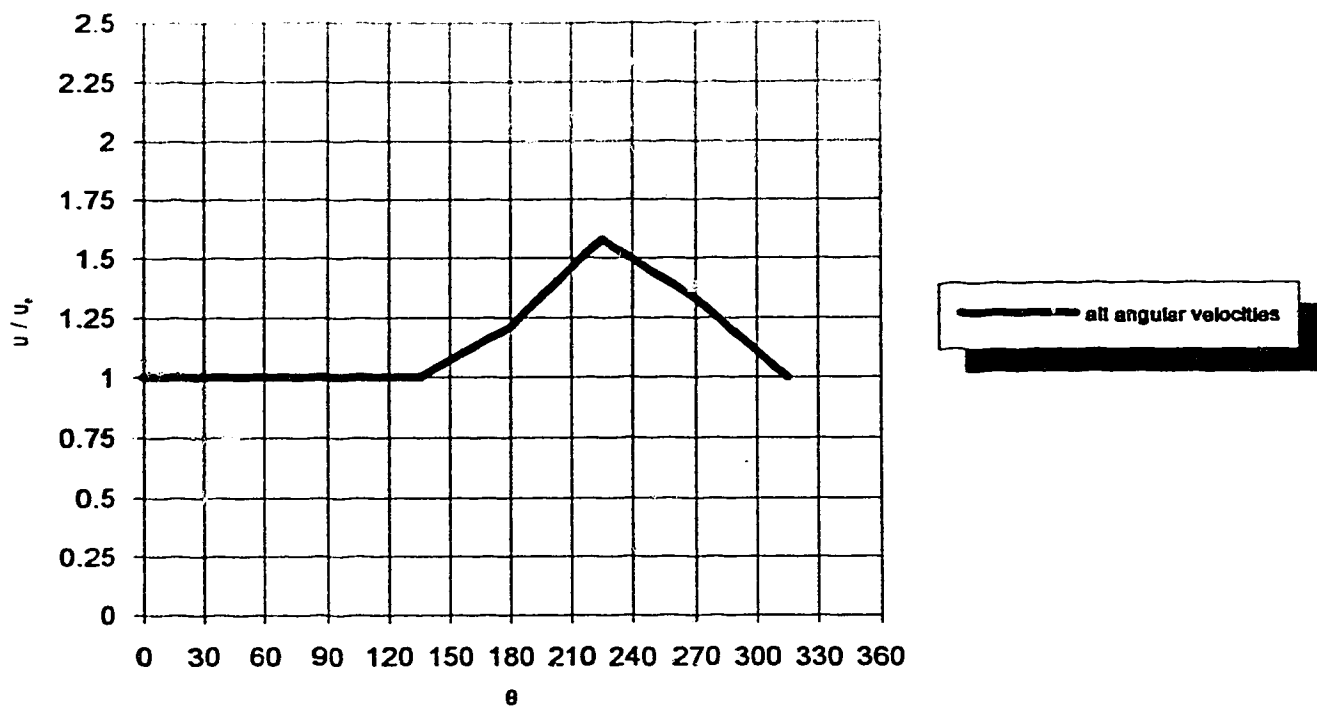


Figure 9-5a : ecodyne clarifier - nhc trials
assumed skirt-influx distribution function
Q-200 equivalent: 8 L/s

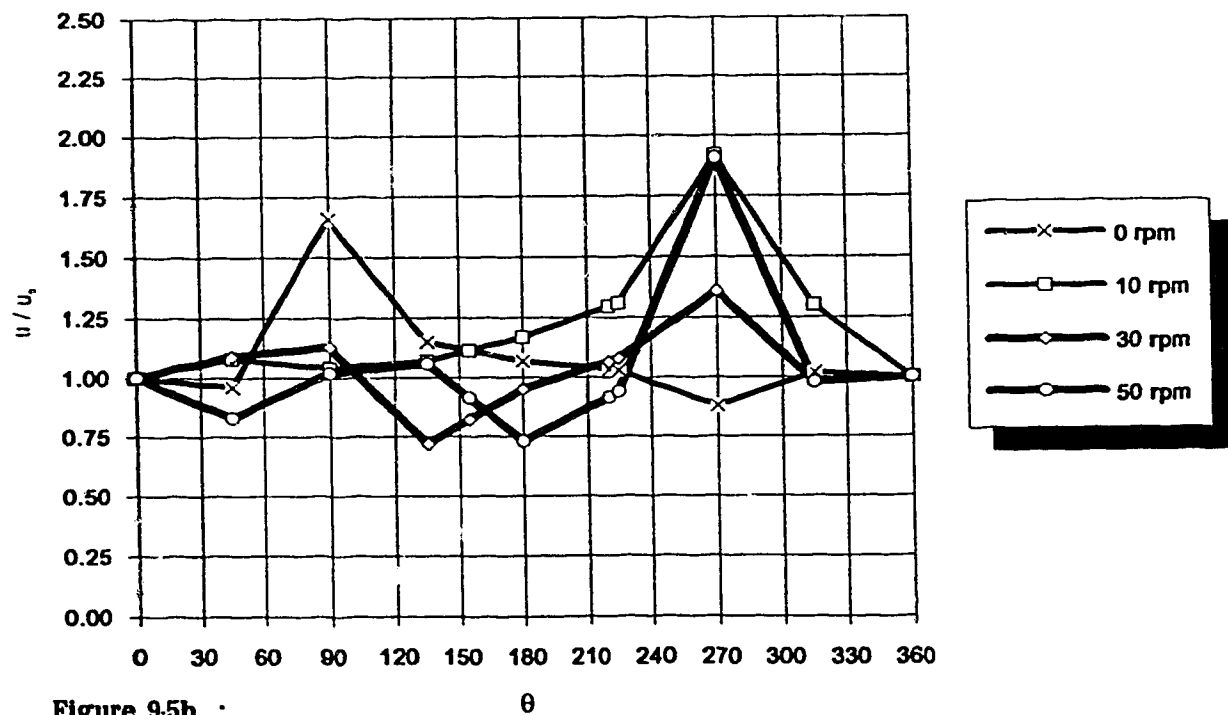


Figure 9-5b : ecodyne clarifier - nhc trials
final assumed rotation-dependent surface-efflux distribution function
Q-200 equivalent: 8 L/s

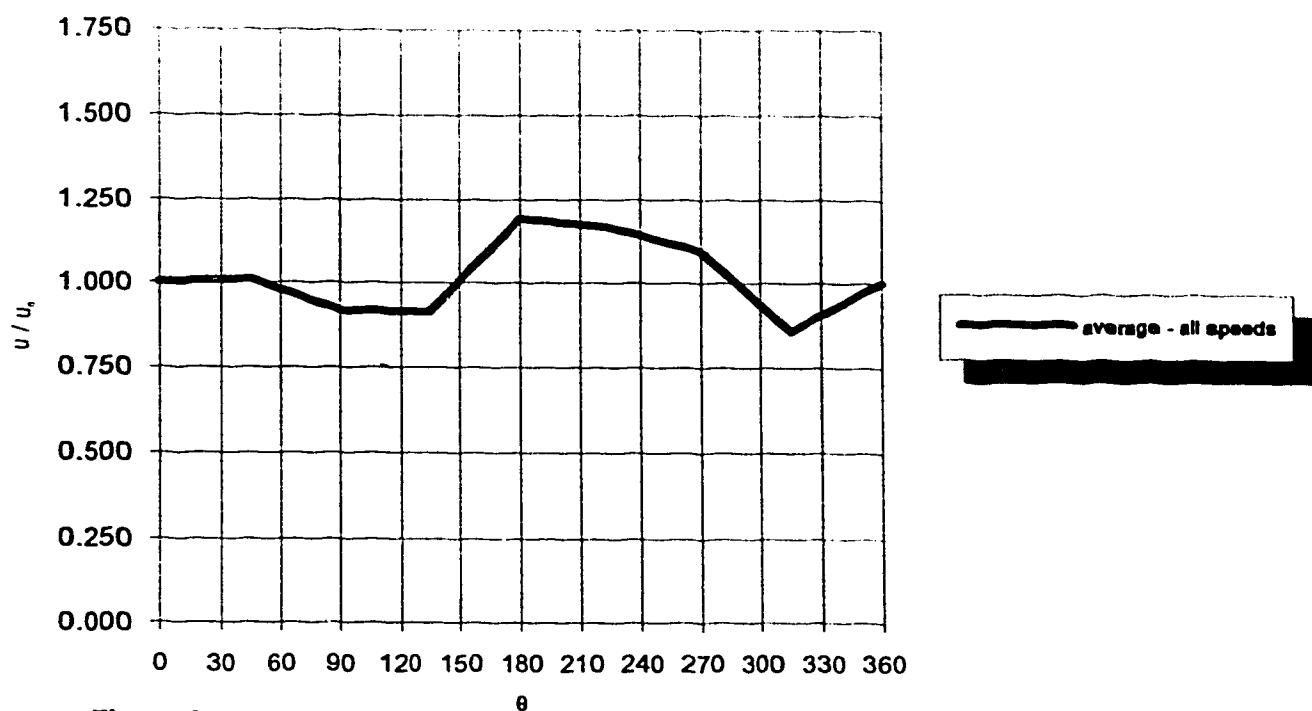


Figure 9-6a :
 nhc model - 1:10 scale
 assumed skirt-influx distribution function
 Q-100 equivalent, 4 L/s

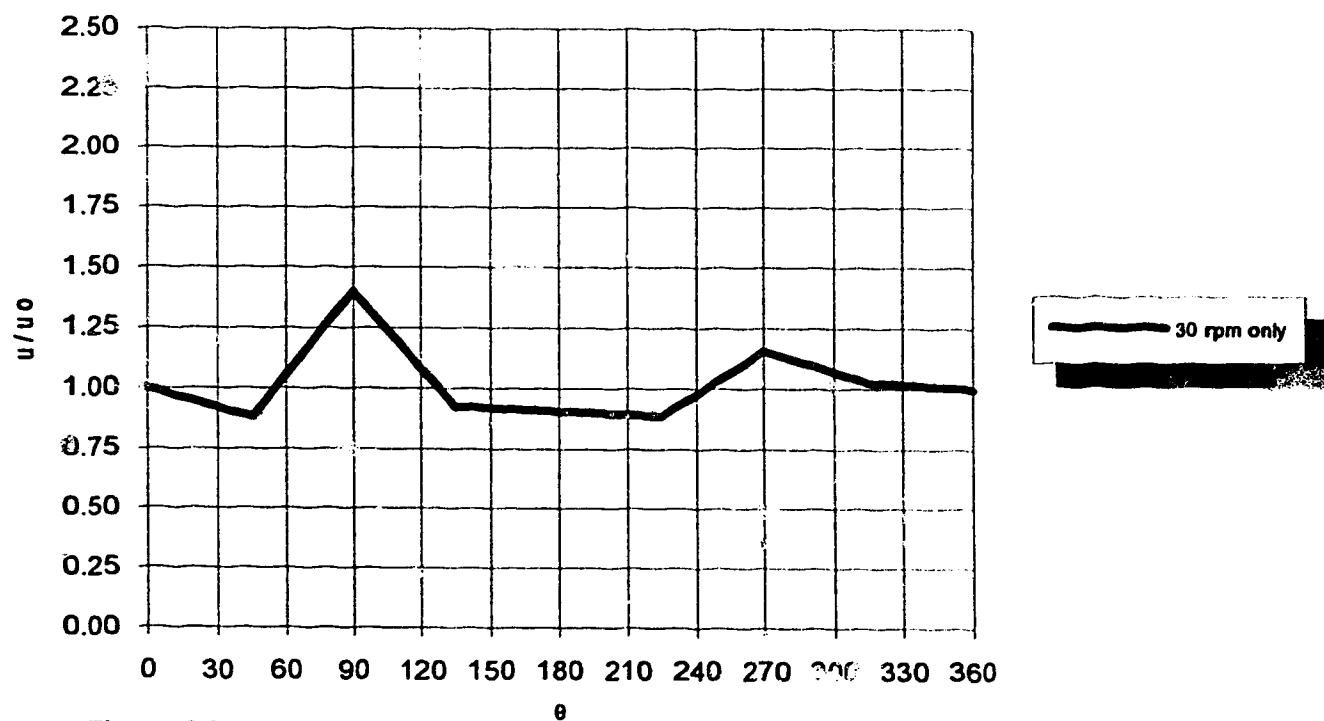
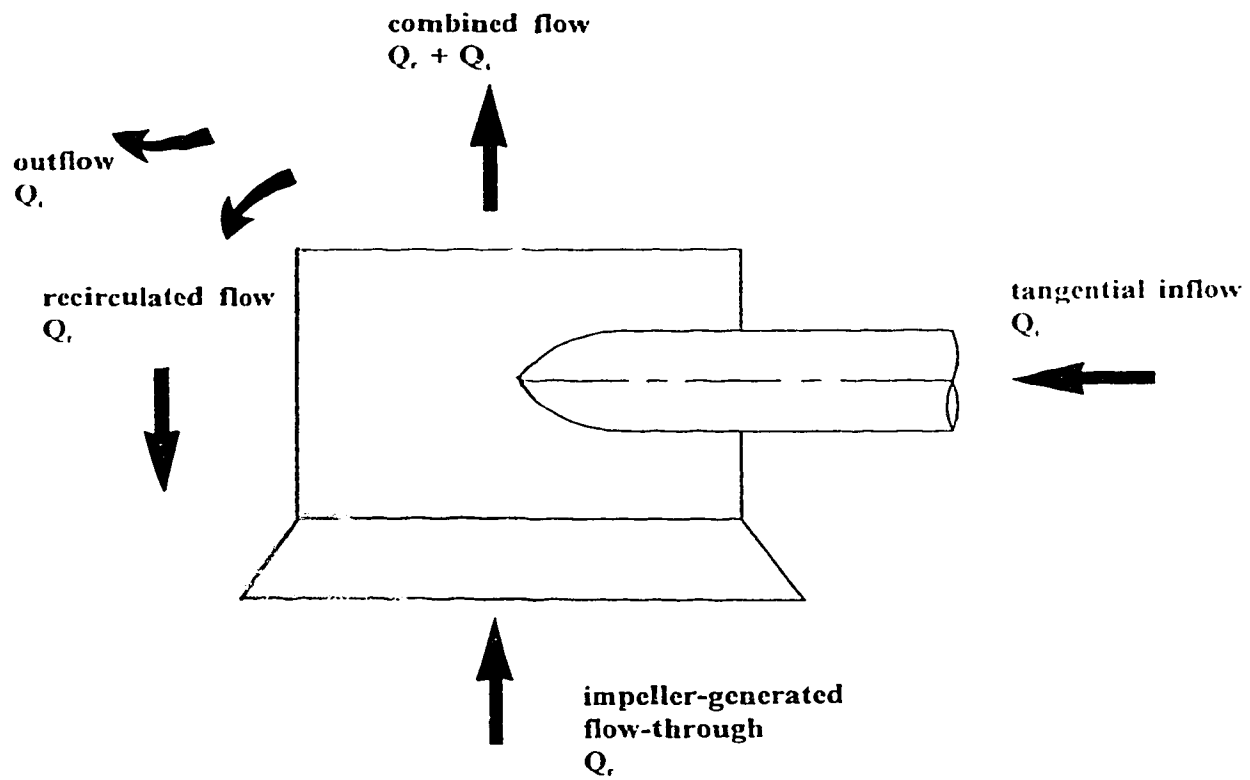


Figure 9-6b :
 ecodyne clarifier - nhc trials
 final assumed surface-efflux distribution function
 Q-100 equivalent: 4 L/s



$$\text{recycle ratio} = \mathcal{R} = \frac{Q_r}{Q_t}$$

figure 9-6c
general illustration of flow-through and recirculation

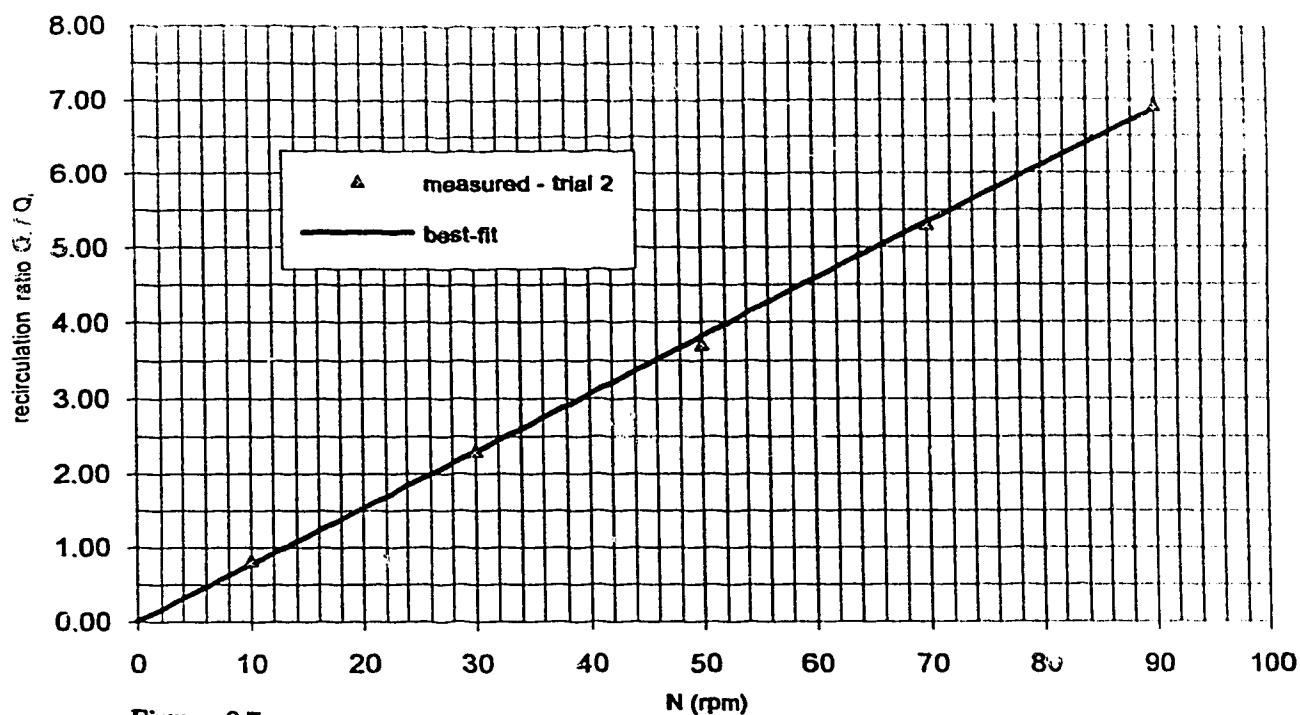


Figure 9-7a : nhc model - 1:10 scale ; model influent $Q_i = 7.9 \text{ L/s}$ ($Q-200$ equivalent)
derived variation of recycle ratio

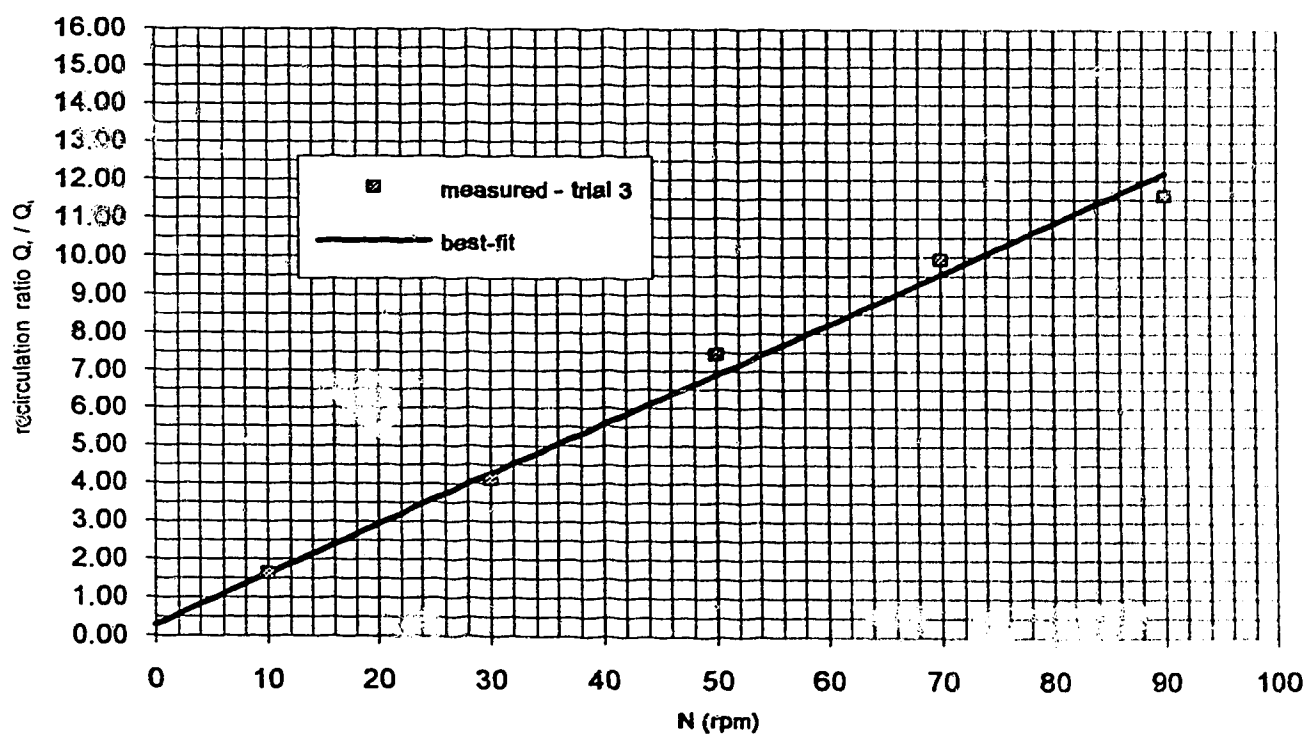


Figure 9-7b : nhc model - 1:10 scale ; model influent $Q_i = 4.0 \text{ L/s}$ ($Q-100$ equivalent)
derived variation of recycle ratio

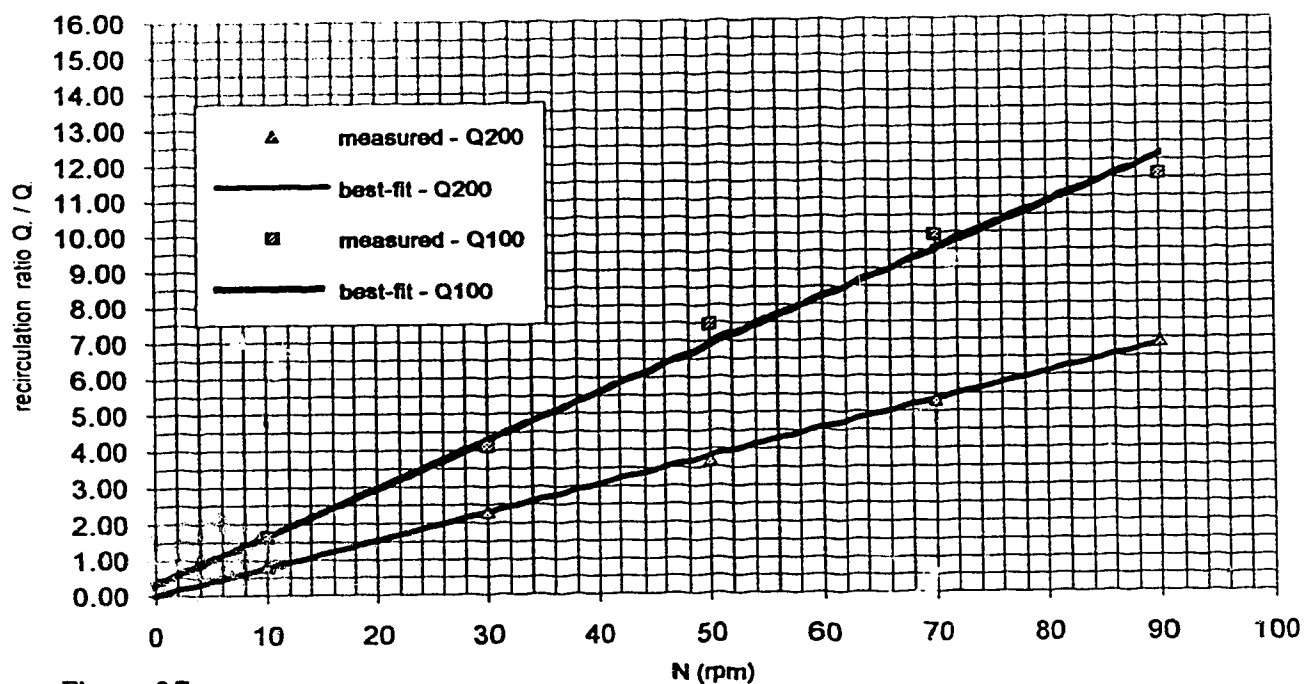


Figure 9-7c :

nhc model - 1:10 scale
comparison: derived variation of recycle ratio
Q200 equivalent = 7.9 L/s ; Q100 equivalent = 4.0 L/s

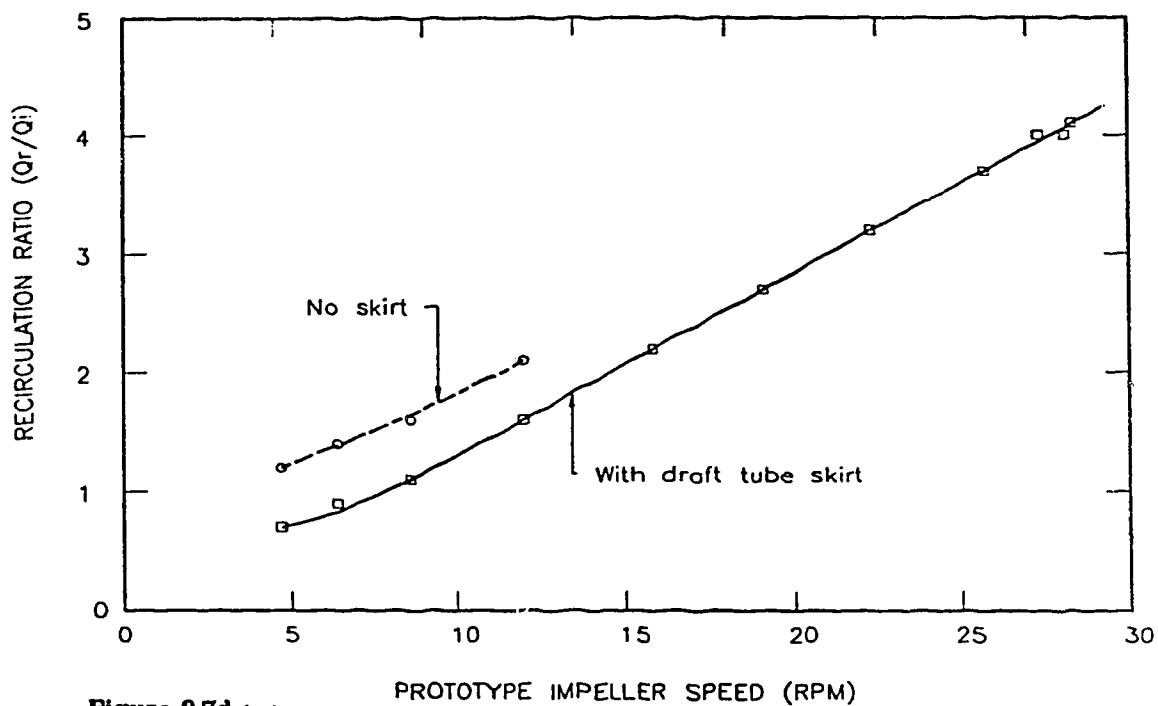
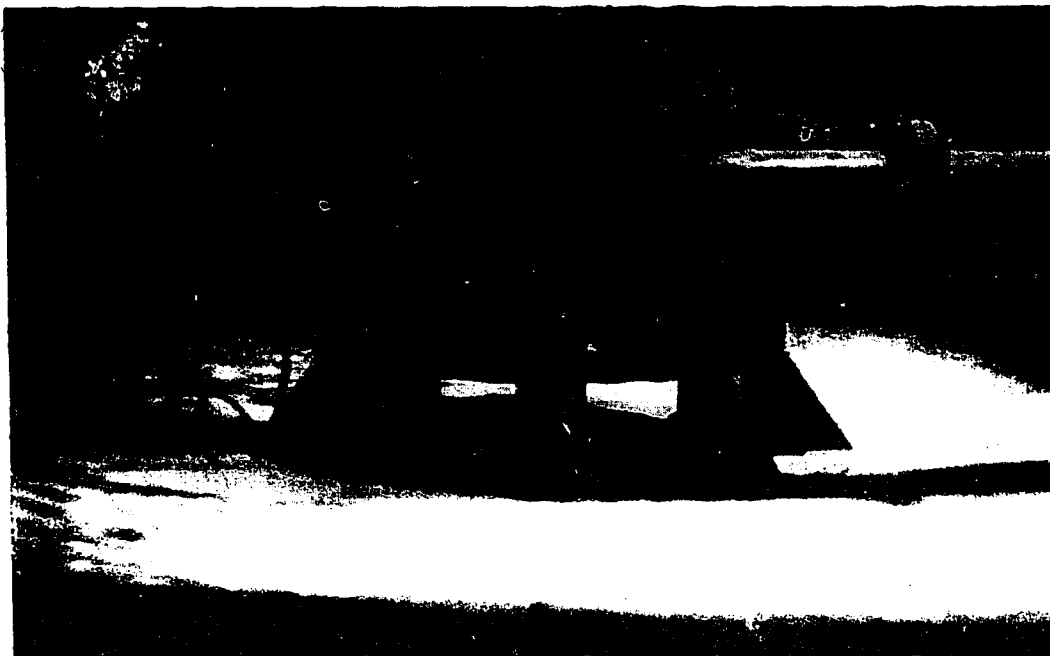
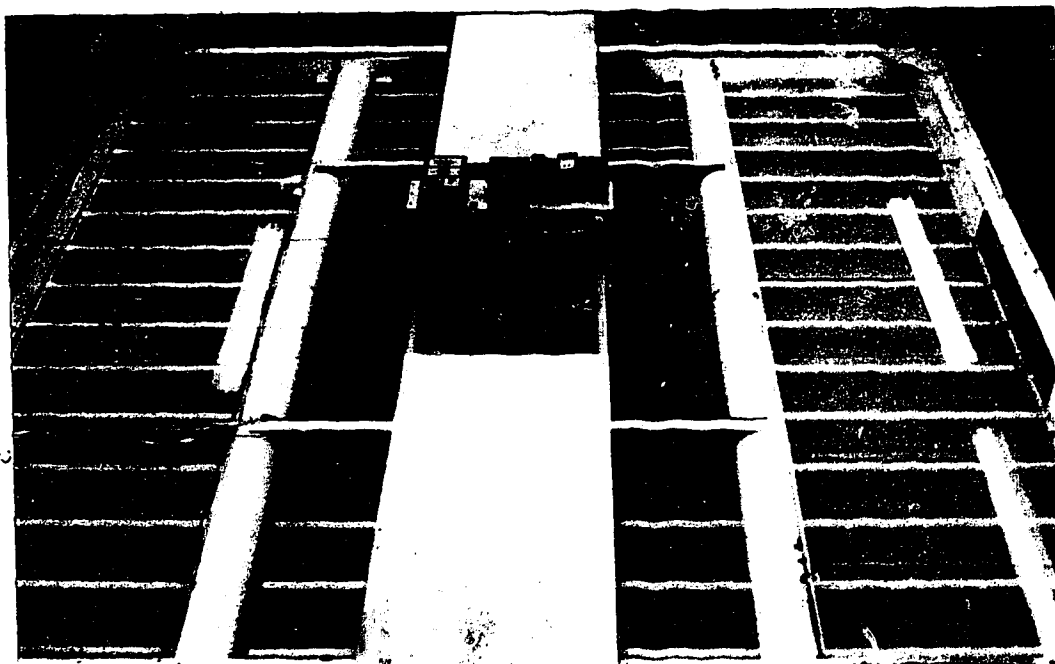


Figure 9-7d :

nhc model - 1:10 scale
comparison: derived variation of recycle ratio
Q200 equivalent = 7.9 L/s ; Q100 equivalent = 4.0 L/s



Photograph 9-1
1:10-scale model during NHC's original testing: Q200, 20.1 rpm
tangential stream does not mix down into impeller stream



Photograph 9-2
1:10-scale model during NHC's original testing: Q200, 20.1 rpm, illustrating
uneven spreading of dye cloud

10.0 Concluding Remarks - Modelling and Scale-Up

Following a fairly extensive analysis of both the bulk-velocities and the turbulence characteristics of an impeller-agitated flow at three different geometric scales, it may be concluded that the analysis of this type of impeller - a type presumably not before encountered in the literature - is amenable to the traditional methods of analysis in terms of velocities, flow-through and dissipation rate when the tangential inflow is constrained to be zero. However, when this discharge is not zero, it has been shown that the spatial distributions of velocity, flow-through and dissipation rate must be subordinated to the interaction between the magnitude of the tangential inflow and the angular velocity of the impeller. Even so, the zero-inflow turbulent dissipation rate is probably still of the same order as that for the case of the non-zero inflow - at least throughout much of the draught tube.

In summary, the significant results of this study are:

1. **The average and turbulent velocities in any direction which exist at a given point within the impeller-generated flow may be scaled as definite and approximately constant multiples of the impeller's tip-speed regardless of geometric scale, impeller angular velocity and structural configuration.**
In this manner, both the average and turbulent velocities are known at any geometric scale, anywhere in the impeller-generated jet-flow so long as the impeller's tip-speed is known.
2. **The estimated turbulent dissipation rate at a particular location within the impeller-generated jet-flow may be estimated by the expression**

$$\frac{u'^3}{\ell}$$

where the turbulent length-scale, ℓ , may be approximated as $\frac{1}{2}$ of the impeller's blade-height.

3. **For any particular model configuration, the dimensionless dissipation rate at a geometrically consistent location within the impeller-generated jet-flow, estimated as**

$$\frac{u'^3 / \ell}{v_{tip}^3 / b}$$

was shown to be a constant, regardless of both the impeller's angular velocity and the geometric scale of the model.

This fact presumably allows the local turbulent dissipation rate to be estimated anywhere in the impeller-generated jet-flow. Based upon general statements found in the literature concerning the hydrodynamics of flocculation, it follows that the spatial variation of the local flocculation rate in the full-scale clarifier may also be estimated throughout the impeller-generated jet-flow.

4. Structural modifications to the impeller-agitated mixing vessel strongly affect the recirculation of water through the draught tube.

Specifically, the draught tube and skirt decrease the recirculated flow over the case of the free impeller ; by lowering the height of the skirt slightly, the flow-through can be increased ; draught tube baffles decrease flow through ; increasing the orifice increases flow through.

5. Structural modifications to the impeller-agitated mixing vessel affect the local turbulence structure to varying degrees.

Specifically, the installation of the draught tube and skirt decreases the local turbulent dissipation rate near the impeller compared to that for the free impeller ; draught tube baffles decrease the local turbulent dissipation rate near the impeller ; enlarging the orifice does not significantly affect the local dissipation rate in the draught tube.

6. The presence of a tangentially entering flow exerts considerable influence upon the local velocity field within the draught tube and is suspected to influence the local turbulent dissipation rate throughout a portion of the draught tube.

In this manner, the presence of the tangential inflow may be assumed to be responsible for the observed hydraulic imbalance in the full-scale clarifier. It is strongly implied that such a hydraulic imbalance accompanies a spatially inconsistent quality of floc particles throughout the tank.

The various methods of scale-up that have traditionally been applied to such problems have very little similarity among themselves. For instance, scaling the bulk inflow Q , by the Froude criterion, as was done for Q_{100} and Q_{200} in the NHC model, has been shown to have very little to do with duplicating the impeller-generated turbulent dissipation rate ϵ at a point in space. As such, it is suggested that one not assume the existence of a universal scale-up rule whereby all aspects of the flow may be scaled simultaneously. Instead, such scale-models should be recognized as being most capable of duplicating a particular property of interest within the flow, usually at the expense of accurate representations of the other properties of the flow.

In practice, the application of geometrically accurate scale-models to the specific design of flocculation systems and other impeller-agitated mixing systems has not been commonplace. It would appear that bench-scale testing still remains the preferred method in such matters. Whenever scale-models are used in any practical manner, it is usually only in modelling the overall bulk improvements to the facility, such as the effects of skirt-opening, orifice size and baffles - exactly the reason why the City of Edmonton commissioned NHC to perform a model study of the clarifier in 1992. Unfortunately, the modelling of dissipation rates represents a whole other matter, where the difficulties of analyzing the turbulent conditions present in slow-mixing processes such as flocculation have perhaps precluded a significant amount of research in this area.

The establishment of an accurate mechanism for scale-modelling of certain turbulence-based descriptive parameters of impeller-agitated flows, such as the turbulent dissipation rate, ϵ , has to this point been of interest primarily to the academic community. It seems reasonable to expect that as the scientific study of mixing processes continues to evolve, there will be ever

more emphasis placed upon the type of work that has been presented here. In doing so, a better understanding will be gained of the manner in which the principles of geometric scale, turbulence and turbulent dissipation may be applied to the design and improvement of mixing-based processes in water treatment. The necessity of such analyses has recently been recognized by Clark, Srivastava, Lang *et alii* (1994) who stated that:

there is a need for a better understanding of how impeller fluid mechanics changes with scale and how these different fluid mechanics regimes affect flocculation-sedimentation performance.

an approach that necessarily demands:

the measurement of fluid flow patterns and energy dissipation induced by different flocculation impellers at different scales

To this end, the results of this project are willingly put forth.

List of References

American Society of Civil Engineers, 1942, ASCE Manuals of Engineering Practice no. 25, Hydraulic Models, prepared by the Committee of the Hydraulics Division on Hydraulic Research.

Amirtharajah, A. & Tambo, N., 1991, Mixing in Water Treatment, from Mixing in Coagulation and Flocculation, American Water Works Association Research Foundation, Denver, Colorado, 3-34.

ASCE → see American Society of Civil Engineers

Antonia, R., Satyaprakash, B. & Hussain, A., 1980, Measurements of Dissipation Rate and Some other Characteristics of Turbulent Plane and Circular Jets, Phys. Fluids, **23**, 4, April, 695-700.

Bin, A. K., 1984, Mass Transfer to the Free Interface in Stirred Vessels, Chemical Engineering Communications, **31**, 155-183.

Bowen, R., 1985, Agitation Intensity: Key to Scaling Up Flow-Sensitive Liquid Systems, Chemical Engineering, 159-168, March 18.

Bowen, R., 1986, Unraveling the Mysteries of Shear-Sensitive Mixing Systems, Chemical Engineering, 55-63, June 9.

Bujalski, W., Nienow, A.W., Chatwin, S. & Cooke, M., 1987, the Dependency on Scale of Power Numbers of Rushton Disc Turbines, Chemical Engineering Science, **42**, 2, 317-326.

Burghardt, A. & Lipowska, L., 1972, Mixing Phenomena in a Continuous Flow Stirred Tank Reactor, Chemical Engineering Science, **27**, 1783-1795.

Camp, T. & Stein, P., 1943, Velocity Gradients and Internal Work in Fluid Motion, Journal of the Boston Society of Civil Engineers, **30**, 4, 219-237.

Chen, K., Wang, C., & Hajduk, 1988, J., Laser-Doppler Anemometry in a Baffled Mixing Tank, Journal of the Chinese Society of Mechanical Engineers, **9**, 4, 249-258.

Chudacek, M. W., 1986, Relationships Between Solids Suspension Criteria, Mechanism of Suspension, Tank Geometry, and Scale-Up Parameters in Stirred Tanks, Industrial Engineering and Chemical Fundamentals, **25**, 391-401.

Clark, M.M., Srivastava, R.M., Lang, J.S., Trussell, R.R., McCollum, L.J., Bailey, D., Christie, J.D. & Stolarik, G., 1994, Selection and Design of Mixing Processes for Coagulation, published by the American Water Works Association Research Foundation, Denver, Colorado and the American Water Works Association, 129.

Connolly, J. & Winter, R., 1969, Approaches to Mixing Operation Scale-Up, Chemical Engineering Progress, **65**, 8, 70-78.

Curev, A., 1980, The Hydromechanical Theory of Continuous Mixing in Baffled Agitated Vessels with Curved-Blade Turbine Impellers, Acta Technica Csav, **2**, 125-137.

- Cutter, L. 1966. Flow and Turbulence in a Stirred Tank, AIChE Journal, **12**, 1, 35-45.
- Dague, R. & Baumann, E., *ca.* 1970 ?. Hydraulics of Circular Settling Tanks Determined by Models. Engineering Experiment Station, Iowa State University, Ames, Iowa, for presentation at the Annual Meeting, Iowa Water Pollution Control Association, Lake Okoboji, Iowa, conference date unknown.
- DeSouza, A. & Pike, R.W., 1972. Fluid Dynamics and Flow Patterns in Stirred Tanks with a Turbine Impeller, Canadian Journal of Chemical Engineering, **50**, 15-23.
- Dzhaugashtin, K.E. & Shelepov, A.A., Solution to the Problem of a Swirling Jet from an Annular Orifice, Fluid Dynamics, **26**, 2, 197-201, September.
- Filip, P., Kolar, V. & Curev, A.G., 1985-1, Space Flow Geometry of the Radial Free, Wall and Liquid Jets with Swirl, Applied Scientific Research, **42**, 185-196.
- Filip, P., Kolar, V. & Curev, A.G., 1985-2, Complex Swirling Radial Jets, Z. Angew. Math. u. Mech., **65**, 9, 441-446.
- Filip, P., Kolar, V. & Curev, A.G., 1986, a Note on the Radial Wall Jet with Swirl, Acta Mechanica, **60**, 41-47.
- Geisler, R., Buurman, C. & Mersmann, A.B., 1993, Scale-up of the Necessary Power Input in Vessels with Suspensions, the Chemical Engineering Journal, **51**, 29-39.
- Godfrey, J C. & Amirtharajah, A, 1991, Mixing in Liquids, from Mixing in Coagulation and Flocculation, American Water Works Association Research Foundation, 35-79.
- Gray, D.J, Treyball, R.E. & Barnett, S.M., 1982, Mixing of Single and Two Phase Systems ; Power Consumption of Impellers, AIChE Journal, **28**, 2, 195-199, March.
- Gunkel, A. & Weber, M., 1975: Flow Phenomena in Stirred Tanks - part I, the Impeller Stream, AIChE Journal, **21**, 5, 931-939 ; Flow Phenomena in Stirred Tanks - part II, the Bulk of the Tank, AIChE Journal, **21**, 5, 939-949.
- Hiraoka, S. & Ito, R., 1975, On the Relation Between Power Input and Jet Flow Rate, Journal of Chemical Engineering of Japan, **8**, 4, 323-326.
- Holland, F.A., 1962, Scale-up of Liquid-Mixing Systems, Chemical Engineering (New York), **69**, 19, 179-184.
- Holland, F.A., 1963, Scale-up of Chemical Reactors, Chemical Engineering (New York), **70**, 19, 145-152.
- Hoogendorn, C. & Den Hartog, A.P., 1967, Model Studies on Mixers in the Viscous Flow Region, Chemical Engineering Science, **22**, 1689-1699.
- Ju, S., Chiu, T. & Hoh, Y., 1991, Scale-up of the Mixer of a Box-type Mixer-Settler, Journal of the Chinese Institute of Chemical Engineers, **22**, 1, 37-44.

Kamienski, J., 1990, Mixing Power of Turbine-type Impellers with Divided, Inclined Blades, International Chemical Engineering, **30**, 3, 517-525.

Kellendonk, D., *ca.* 1989 ?, Optimization of Upflow Solids Contact Clarifiers at the E.L. Smith Water Treatment Plant, Edmonton, Alberta, internal report, City of Edmonton, Water Plants Engineering.

Khang, S. & Levenspiel, O., 1976, New Scale-Up and Design Method for Stirrer Agitated Batch Mixing Vessels, Chemical Engineering Science, **31**, 569-577.

King, H.W., 1954, Handbook of Hydraulics, fourth edition, McGraw-Hill, New York.

Kolar, V., Filip, P. & Curev, A.G., 1982, The Swirling Radial Jet, Applied Scientific Research, **39**, 329-335.

Kolar, V., Filip, P. & Curev, A.G., 1984, Hydrodynamics of a Radially Discharging Impeller Stream in Agitated Vessels, Chemical Engineering Communications, **27**, 313-326.

Kolar, V., Filip, P. & Curev, A.G., 1985, the Swirling Radial Jet Model and its Application to a Radial Impeller Stream, from 5th European Conference on Mixing, Wurzburg, West Germany, 10-12 June, 1985, 483-490.

Kresta, S. & Wood, P., 1991, Prediction of the Three-dimensional Turbulent Flow in Stirred Tanks, AIChE Journal, **37**, 3, 448-460, March.

Laufhutte, H.D. & Mersmann, A., 1985, Laser-Doppler Velocimetry as a Suitable Measuring Technique for the Determination of Flow Behaviour in Stirred Fluids, German Chemical Engineering, **7**, 371-379.

Leentvaar, J. & Ywema, T.S.J., 1980, Some Dimensionless Parameters of Impeller Power in Coagulation-Flocculation Processes, Water Research, **14**, 135-140.

Mack, D.E. & Marriner, R.A., 1949, A Method of Correlating Agitator Performance, Chemical Engineering Progress, **45**, 9, 545-552.

Mamleev, R.A., 1985, Modeling of Turbulent Mixing in Two-phase Dispersed Liquid/Liquid Systems, International Chemical Engineering, **25**, 3, 566-569, July.

Mersmann, A & Laufhutte, H.D., 1985, Scale-up of Agitated Vessels for Different Mixing Processes, from 5th European Conference on Mixing, Wurzburg, West Germany, 10-12 June, 1985, 273-284.

Metzner, A.B. & Otto, R.E., 1957, Agitation of Non-Newtonian Fluids, AIChE Journal, **3**, 1, 3-10.

Mhaisalkar, V., Paramasivam, R. & Bhole, A., 1986, An Innovative Technique for Determining Velocity Gradient in Coagulation-Flocculation Process, Water Research, **30**, 1307-1314.

NHC → see Northwest Hydraulic Consultants Limited.

Nishikawa, M., Mori, N., Fujieda, S. & Kayama, T., 1987, Scale-up of Liquid-Liquid Phase Mixing Vessel, Journal of Chemical Engineering of Japan, **20**, 5, 454-459.

Northwest Hydraulic Consultants Limited, 1993, E.L. Smith W.T.P Clarifier Model, Edmonton, Alberta, Canada, consultant's report prepared for Associated Engineering Alberta Ltd.

Oldshue, J.Y., 1966, Fluid Mixing, Heat Transfer and Scale-Up, Chemical and Process Engineering, **47**, 4, 183-188, April.

Oldshue, J.Y., 1981, Let's Understand Mixing, Chemtech, September, 555-561.

Papastefanos, N. & Stamatoudis, M., 1989, Effect of Vessel and Impeller Geometry on Impeller Power Number in Closed Vessels for Reynolds Numbers Between 40 and 65000, Chemical Engineering Research and Design, **65**, 169-174, March.

Pawinski, J. & Roszkowski, J., 1986, Similarities of Flow with an Exchange of Mass, Momentum and Energy, Archiwum Gornictwa, **31**, 2, 305-309.

Placek, J. & Tavlarides, L.L., 1985, Turbulent Flow in Stirred Tanks, part I: Turbulent Flow in the Turbine Impeller Region, AIChE Journal, **31**, 7, 1113-1120, July.

Placek, J., Tavlarides, L.L. & Smith, G.W., 1986, Turbulent Flow in Stirred Tanks, part II: a Two-scale Model of Turbulence, AIChE Journal, **32**, 11, 1771-1786, November.

Rajaratnam, N., 1975, Turbulent Jets, Elsevier Science Publishers Ltd., Amsterdam.

Rice, R. & Baud, R., 1990, The Role of Micromixing in the Scale-up of Geometrically Similar Batch Reactors, AIChE Journal, **36**, 2, 293-298.

Rosensweig, R.E., 1964, Idealized Theory for Turbulent Mixing in Vessels, AIChE Journal, **10**, 1, 91-97.

Rushton, J.H., 1951, The Use of Pilot Plant Mixing Data, Chemical Engineering Progress, **47**, 9, 485-488.

Rushton, J.H., 1952-1, Applications of Fluid Mechanics and Similitude to Scale-up Problems - part 1, Chemical Engineering Progress, **48**, 1, 33-38.

Rushton, J.H., 1952-2, Applications of Fluid Mechanics and Similitude to Scale-up Problems - part 2, Chemical Engineering Progress, **48**, 2, 95-102.

Rushton, J.H., 1952-3, Mixing of Liquids in Chemical Processing, Industrial & Engineering Chemistry, **44**, 12, 2931-2936.

Rushton, J.H., Costich, E.W. & Everett, H.J., 1950-1, Power Characteristics of Mixing Impellers - part 1, Chemical Engineering Progress, **46**, 8, 395-404.

Rushton, J.H., Costich, E.W. & Everett, H.J., 1950-2, Power Characteristics of Mixing Impellers - part 2, Chemical Engineering Progress, **46**, 9, 467-476.

Ryon, A.D., Daley, F.L. & Lowrie, R.S., 1959, Scale-up of Mixer-Settlers, Chemical Engineering Progress, **55**, 10, 70-75.

Sano, Y. & Usui, H., 1985, Interrelations Among Mixing Time, Power Number and Discharge Flow Rate Number in Baffled Mixing Vessels, Journal of Chemical Engineering of Japan, **18**, 1, 47-52.

Schwartzberg, H.G. & Treyball, R.E., 1968, Fluid and Particle Motion in Turbulent Stirred Tanks, Industrial & Engineering Chemistry Fundamentals, **7**, 1, 1-12.

Seichter, P., 1975, Vyzkum Turbinovych Michadel Pro Prutocne Flokulacni Komory, Chemicky Prumysl, **25**, 9, 453-462.

Shulyak, I.A. & Zapara, E.S., Calculation of Rational Parameters of Mixing Blades, Chemical & Petroleum Engineering, **24**, 3-4, 111-115, November.

Sohn, P. & Bajpai, R., 1987, Characterization of Imperfect Mixing of Batch Reactors by Two Compartment Model, from Kansas State University Institute for Systems Design and Optimization, Report #87, 74-84.

Stanley, S.J. & Smith, D.W., 1994, Environmental Engineering and Science Program, University of Alberta, Edmonton, Alberta, Canada, Hydrodynamics of Mixing in Drinking Water, accepted for publication by ASCE.

Stanley, S.J., Smith, D.W. & Prince, D., 1993, Environmental Engineering and Science Program, University of Alberta, Edmonton, Alberta, Canada, Hydraulic Tracer Tests on Clarifier C-2, E.L. Smith Water Treatment Plant, (preliminary draft).

Tambo & Watanabe (1979) → see Amirtharajah & Tambo (1991)

Tennekes, H & Lumley, J.L., 1972, A First Course in Turbulence, MIT Press, Cambridge, Massachusetts.

Van de Vusse, J.G., 1955-1, Mixing by Agitation of Miscible Liquids - part 1, Chemical Engineering Science, **4**, 178-200.

Van de Vusse, J.G., 1955-2, Mixing by Agitation of Miscible Liquids - part 2, Chemical Engineering Science, **4**, 209-220.

Van't Reit, K. & Smith, J.M., 1975, The Trailing Vortex System Produced By Rushton Turbine Agitators, Chemical Engineering Science, **30**, 1093-1105.

Van't Reit, K., Bruijn, W. & Smith, J.M., 1976, Real and Pseudo-Turbulence in the Discharge Stream from a Rushton Turbine, Chemical Engineering Science, **31**, 407-412.

White, A. & Brenner, E., 1934, Transactions of the American Institute of Chemical Engineers, **30**, 585

Weetman, R. & Oldshue, J.Y., 1988, Power, Flow and Shear Characteristics of Mixing Impellers, from Proceedings, Sixth European Conference on Mixing, Pavia, Italy, 24-26 May, 1988, 43-50.

Wu, H. & Patterson, G.K., 1989, Laser-Doppler Measurements of Turbulent-Flow Parameters in a Stirred Mixer, Chemical Engineering Science, **44**, 10, 2207-2221.

Zlokarnik, M., 1987, Scale-up under Conditions of Partial Similarity, International Chemical Engineering, **25**, 1, 1-9, January.